Max-Planck-Institut für
extraterrestrische Physik

MAX-PLANCK-GESELLSCHAFT

RESEARCH 2010 – 2012

A Book of Highlights

Observations – Measurements

Theory – Simulations

Experiments – Projects – Detector Developments

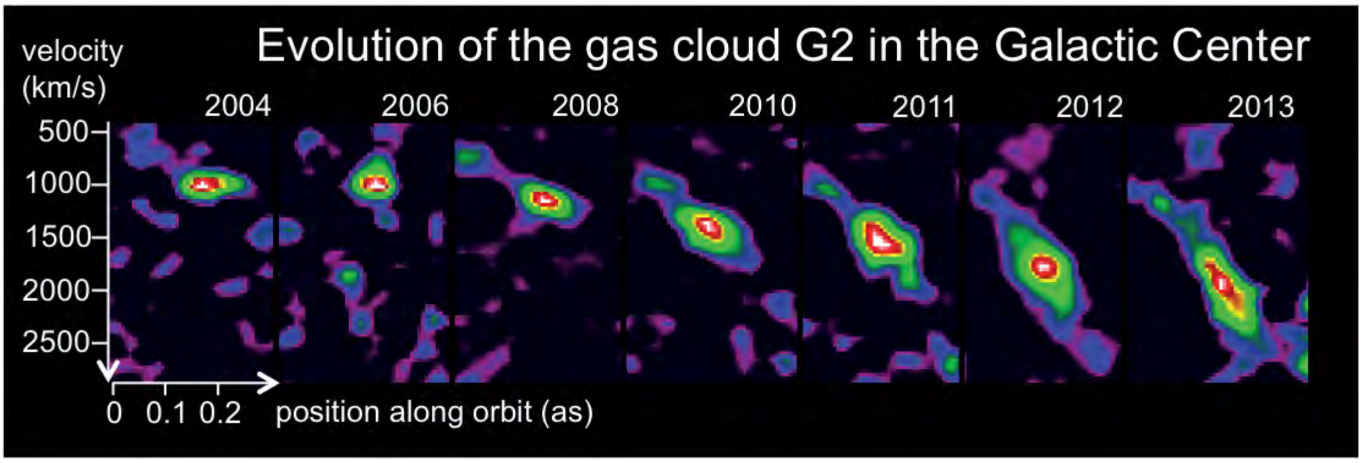

July 2013

Book of MPE Research/Experimental Highlights

This book of MPE research and experimental highlights for the years 2010 to 2012 was produced for the MPE Fachbeirat Meeting of July 8 to 10, 2013. Its goal is to provide a comprehensive overview as well as detailed information on science results, data analysis activities, ongoing experimental projects and detector developments in a fashion that is supplementary to the Science Report for these years. Scientists were encouraged to submit their highlight contribution for the three-years period. The authors of the posters are clearly identified and are solely responsible for their contents.

The contributions are sorted according to MPE groups (the main groups as well as sub-groups). They are also marked by different colors of their abstracts. Inside the groups posters are sorted with respect to science or instrumental/hardware topics.

Edited by R. Bender, W. Collmar, R. Mayr-Ihbe

Table of Contents

Table of Contents

Table of Contents

Table of Contents

Table of Contents

I) Infrared / Submillimeter Astronomy

(including MPG Minerva Group:
Dr. Natascha M. Förster Schreiber)

The SINS/zC-SINF survey: Kpc-scale kinematics and star formation

SINS/zC-SINF is the first and largest survey of spatially-resolved kinematics, star formation, and physical properties of distant galaxies, with the near-IR imaging spectrometer SINFONI at ESO's VLT. The sample of 110 galaxies probes the bulk of the massive z~1–3 star-forming population; for 35 of them, deep AO-assisted observations resolve the line emission and kinematics on ~1.5 kpc scales, 4× smaller than in natural seeing. Over 50% of the galaxies have disk kinematics. The rotation velocity *v* scales roughly linearly with galaxy size but the intrinsic local velocity dispersion σ_0, 5–10× higher than in z~0 disks, is fairly constant with galaxy properties. Widespread star formation-driven outflows are seen to originate from extended regions. The most massive galaxies, all large disks, show evidence for a stellar bulge and nuclear AGN-driven outflows, which may contribute to the shutdown of star formation above ~10^{11} $M_\odot$. Compact, less massive objects have lower v/σ_0, are more gas-rich and metal-poor, and could represent an earlier evolutionary stage. Our findings highlight the importance of efficient secular processes, stellar and AGN feedback, in growing galaxies at early times.

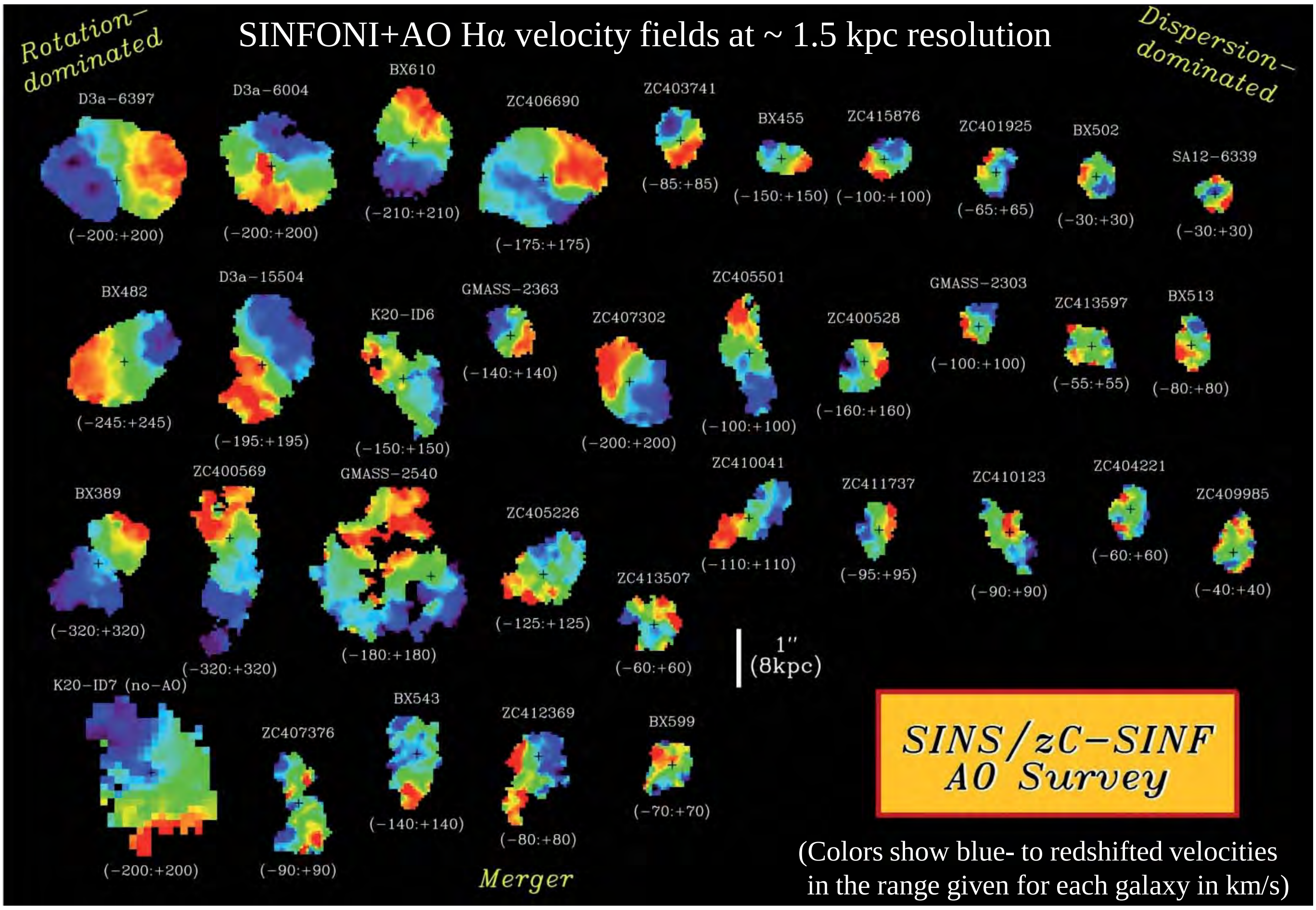

(Colors show blue- to redshifted velocities in the range given for each galaxy in km/s)

Selected References:
• Förster Schreiber, N.M., et al. 2013, ApJ, subm. • Newman, S.F., et al. 2013, ApJ, in press (arXiv:1211.6160)

N.M. Förster Schreiber, R. Genzel, L. Tacconi, S. Newman & SINS/zC-SINF Team

SINS/zC-SINF Survey: Outflows at High-z

Using SINFONI data obtained at the VLT with adaptive optics, we explore the origin and properties of galactic scale outlows coming from z~2 star-forming galaxies. These outflows serve to deplete galaxies of baryons as well as enrich the IGM with metals. They could be launched by both star-formation processes and AGN feedback, and little is known of the source of the outflows from within galaxies and how the strength of outflows varies with galaxy properites. From a sample of 27 galaxies from the SINS and zC-SINF surveys, we find that the strength (or mass loading) of the outflows is strongly correlated with the star formation surface density (ΣSFR) of the galaxy. In addition, for a few of the galaxies for which we have exceptional data quality, we are able to probe the origin of the outflowing gas from within the galaxy and find that much of it is coming from individual Hα-bright star-forming clumps.

Clump Hα line profile

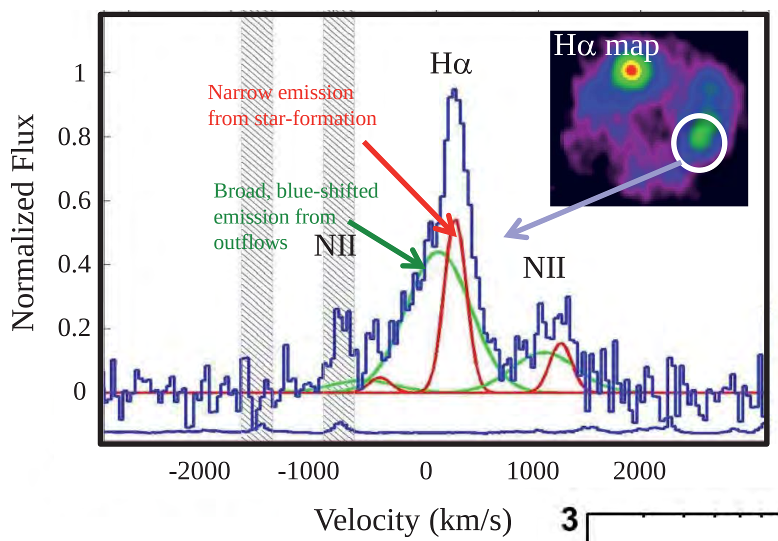

Main Conclusions:

- Much of the **outflows** come from star-forming **clumps**
- The strength of outflows scales with the galaxy **star-formation surface density**

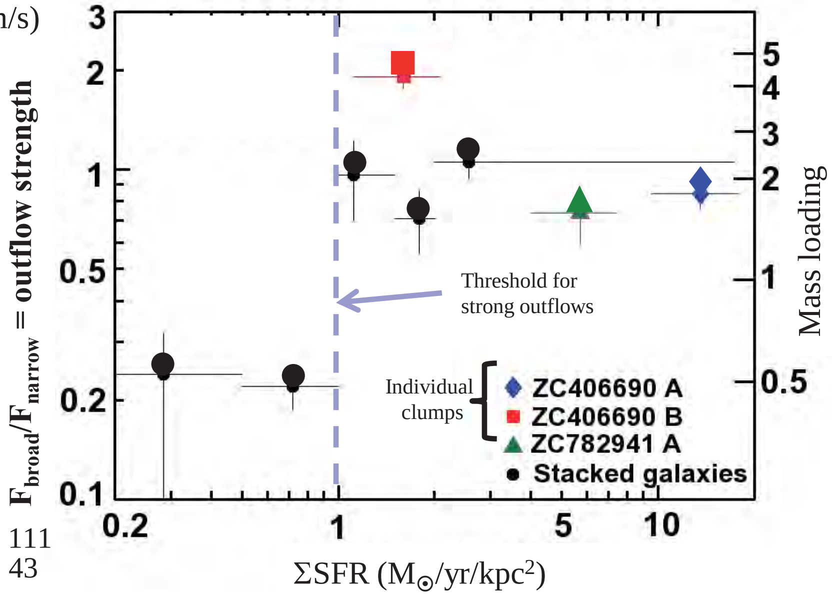

References:

- Newman, S. F. et al. 2012a, ApJ 752, 111
- Newman, S. F. et al. 2012b, ApJ 761, 43

S. F. Newman, R. Genzel, N. M. Förster Schreiber and the SINS team

SINS/zC-SINF survey: connection between stellar mass buildup, kinematics and SF at z~2

We are expanding our detailed SINFONI+AO studies of the kinematics, star formation, and physical conditions of z~2 galaxies with new, sensitive, high-resolution near-IR HST/WFC3 mapping of the stellar light and mass. This powerful combination allows us to gain key insights into the buildup of stellar disks and bulges at early cosmic epochs, investigate the relative importance of secular processes, clump migration, and minor/major merging in shaping galaxies, and explore directly the connection between bulge buildup and AGN activity.

Through deep WFC3/IR F110W and F160W imaging, we map the rest-frame optical continuum and derive the stellar density distribution of 39 spectroscopically confirmed z~2 star forming galaxies that are observed within a SINFONI/AO large program. The adjacent F110W and F160W filters, sampling the Balmer/4000Å break, give a robust estimate of the M/L ratio and therefore of the stellar mass density, only little affected by metallicity or extinction.

Our stellar mass density maps show, unlike clumpy Hα - morphologies, smooth distributions of stellar mass with a prominent central peak in the most massive objects indicating a bulge component. These massive objects also show signs of AGN activity supporting a close connection between bulge and supermassive black hole growth at early epochs.

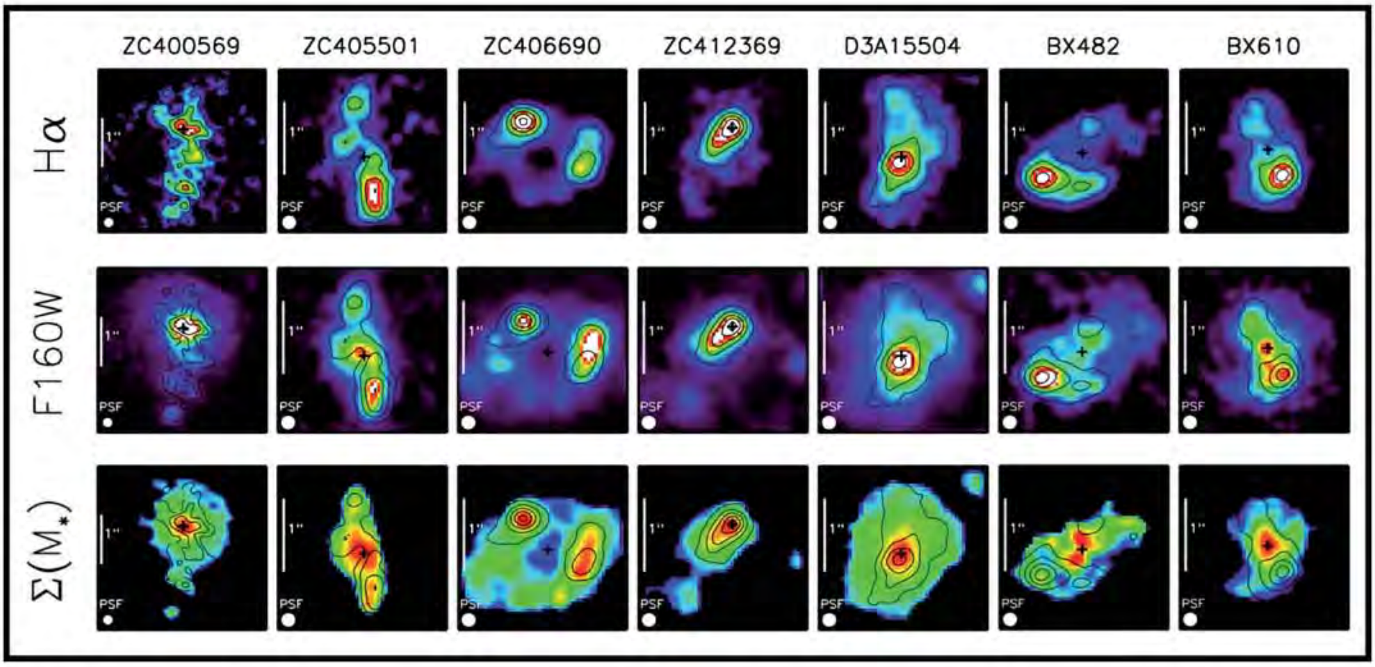

Figure 1. Shown are Hα emission-line maps (upper row), WFC3/IR F160W emission maps (middle row) and stellar mass density maps (lower row) for a subset of our galaxy sample. Overlaid are contours of the Hα emission-line map for each target.

References:

- Förster Schreiber et al. 2009, ApJ,706, 1364
- Mancini et al. 2011, ApJ, 743, 86

P. Lang, N.M. Förster Schreiber, R. Genzel, S.Wuyts and the SINS/zC-SINF Team

Smooth stellar mass maps and the longevity of clumps in high-z galaxies

We perform a detailed analysis of the resolved colors and stellar populations of a complete sample of 649 massive star-forming galaxies at 0.5 < z < 2.5 in the GOODS-South field. By modeling the 7-band optical ACS + near-IR WFC3 spectral energy distributions of individual bins of pixels, we are able to reconstruct the distribution of stellar mass, star formation, stellar age and dust on 1 kpc scales. We find evidence for redder colors, older stellar ages, and increased dust extinction in the nuclei of galaxies. Big star-forming clumps seen in star formation tracers are less prominent or even invisible on the inferred stellar mass distributions. Off-center clumps contribute up to ~20% to the integrated star formation rate, but only 7% or less to the integrated mass of all massive star-forming galaxies at z~1-2, with the fractional contributions being a decreasing function of the wavelength used to select the clumps.

Our results are consistent with an inside-out disk growth scenario with brief (100 – 200 Myr) episodic local enhancements in star formation superposed on the underlying disk. Alternatively, the young ages of off-center clumps may signal inward clump migration, provided this happens efficiently on the order of an orbital timescale.

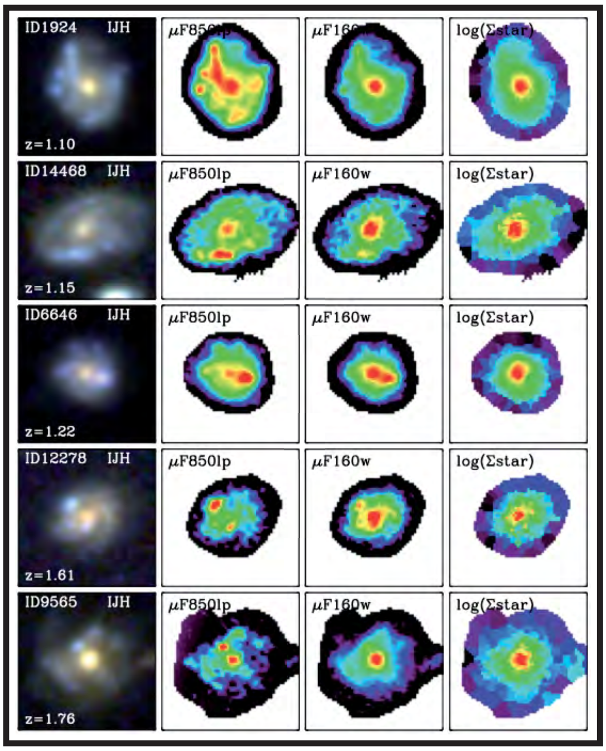

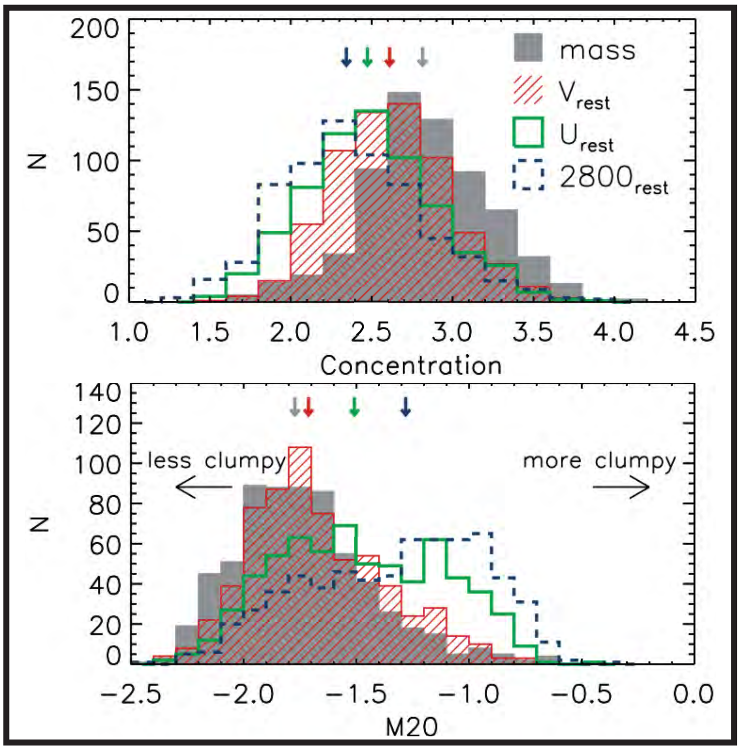

Left: Case examples of star-forming galaxies featuring off-center peaks in surface brightness at short wavelengths (μF850lp). A central enhancement in surface brightness becomes more prominent at rest-optical wavelengths (μF160w). The resolved color information reveals spatial variations in mass-to-light ratio across the galaxies, leading to smoother and more centrally concentrated stellar mass maps (Σstar).

Right: Distribution of concentration and M20 coefficients for the complete sample. High-redshift galaxies appear more compact and less disturbed in mass than in light.

References:

• Wuyts, S., et al. 2012, ApJ, 753, 114

S. Wuyts, N. Förster Schreiber, R. Genzel and the CANDELS team

Global and spatially resolved line excitation in high-redshift galaxies

– Objective and Method –

We investigate line excitation and metallicity in a main sample of 16 massive z~2 star forming galaxies using the key rest-frame optical nebular emission lines, Hα, Hβ, [NII], and [OIII] observed with the integral-field spectrometer SINFONI at the VLT allowing for full two dimensional spatially-resolved mapping on several kpc scale and the LUCI multi-object spectrograph at the LBT.

– Results –

1. Noticeable differences in morphology between different emission lines in several cases, suggesting spatial variations in line excitation mechanism and nebular oxygen abundances.

2. Objects span a range of excitation, from purely-star-forming to AGN-dominated objects. Many exhibit slightly higher excitation than the bulk of z~0 star-forming galaxies, the reasons could be the presence of a central AGN, variations in metallicity, in ionization parameter and/or in the electron density and/or contributions by shocks.

3. Similar mass-metallicity relation as previously reported at z~2.

4. Shallow, negative metallicity gradients (~ -0.02dex/kpc) in some cases

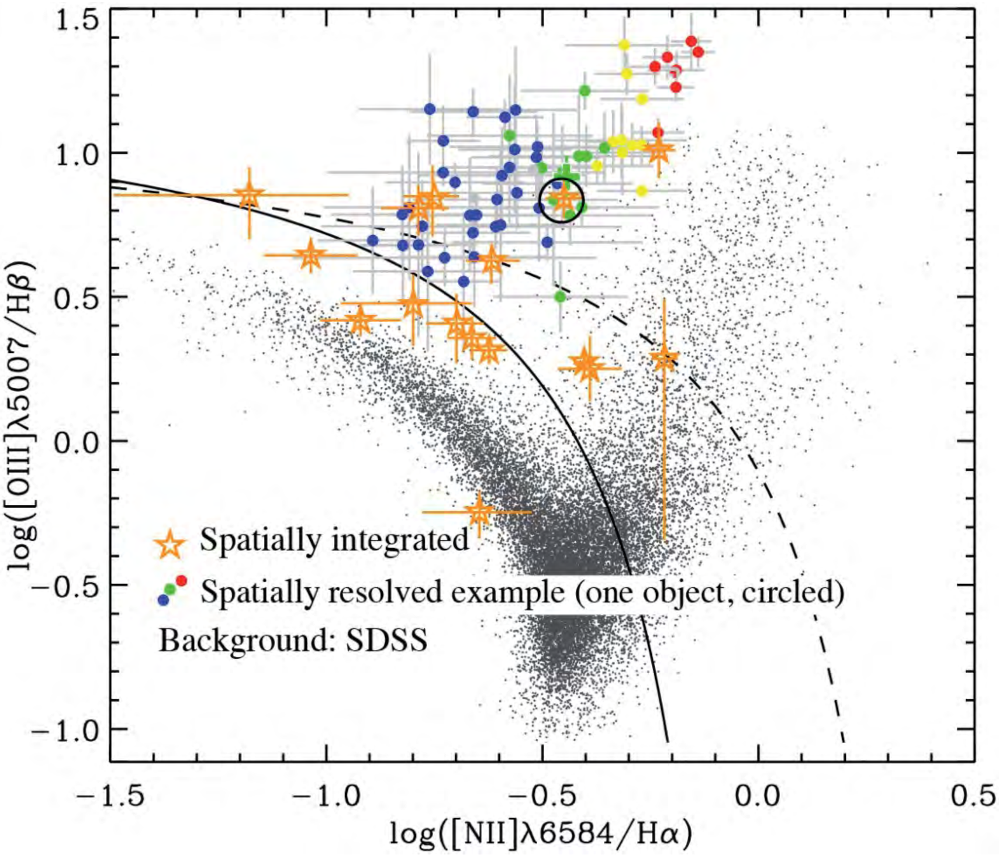

Spatially integrated (star objects) and one example of a spatially resolved analysis (dots=single spatial pixels of the circled object), revealing an AGN in its center and star formation in the outskirts (red to blue = center to outskirts spatial pixel)

References:

• P. Buschkamp, PhD-Thesis, 2012

• Förster Schreiber et al. 2009, ApJ, 706, 1364

P. Buschkamp, N.M. Förster Schreiber, J. Kurk, S. Newman and the SINS Team

The LUCI survey of emission lines: the mass-metallicity relationship at high redshift

MAX-PLANCK-GESELLSCHAFT

We have carried out a survey of galaxies at $1.3 < z < 2.6$ with LUCI, the NIR spectrograph at the Large Binocular Telescope. The sample size and range of galaxy properties covered is unequalled, allowing the determination of the mass-metallicity and fundamental metallicity relation down to stellar masses of 10^9 $M_\odot$. We confirm the evolution of the mass-metallicity relation with redshift, but our results are inconsistent with the fundamental metallicity relation.

LUCI is the NIR spectrograph installed at the Large Binocular Telescope. The MPE/IR-group contributed the mask exchange unit holding 23 user-defined cooled slit masks. This versatility allows to observe rest-frame optical emission lines of a large sample of high-redshift galaxies.

Properties of our LUCI+SINS sample:

- 99 galaxies observed by LUCI having at least one emission line detected
- 50 galaxies observed by SINFONI (SINS; Förster Schreiber et al. 2009)
- HST imaging and multi-band photometry
- stellar mass (M_*) and star formation rate (SFR) from SED fitting (Wuyts et al. 2011)
- covers 2 dex in both M_* and SFR, has an average redshift of $z = 2.1$

We measure the [NII]/Hα ratio, as proxy of metallicity (Z) in stacked spectra binned by mass. We confirm the evolution of the mass-metallicity relation with redshift (e.g. Erb et al. 2006).

Mannucci et al. (2010) find that both local and distant galaxies define a tight surface in the 3D space of M_*, SFR and Z. This *fundamental* metallicity relation does not evolve with redshift. Our results, however, are inconsistent with the fundamental metallicity relation by ~0.2 dex.

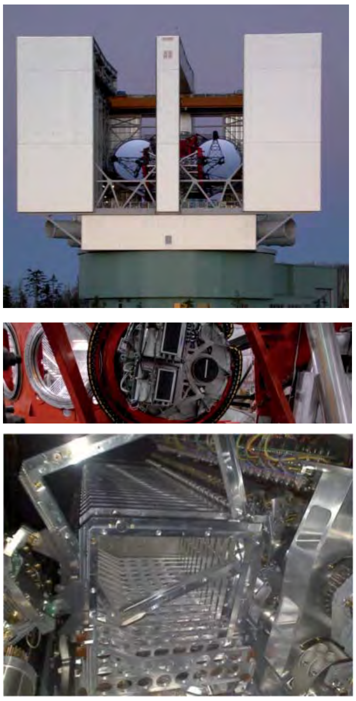

LBT, LUCI and the mask exchange unit (from top to bottom).

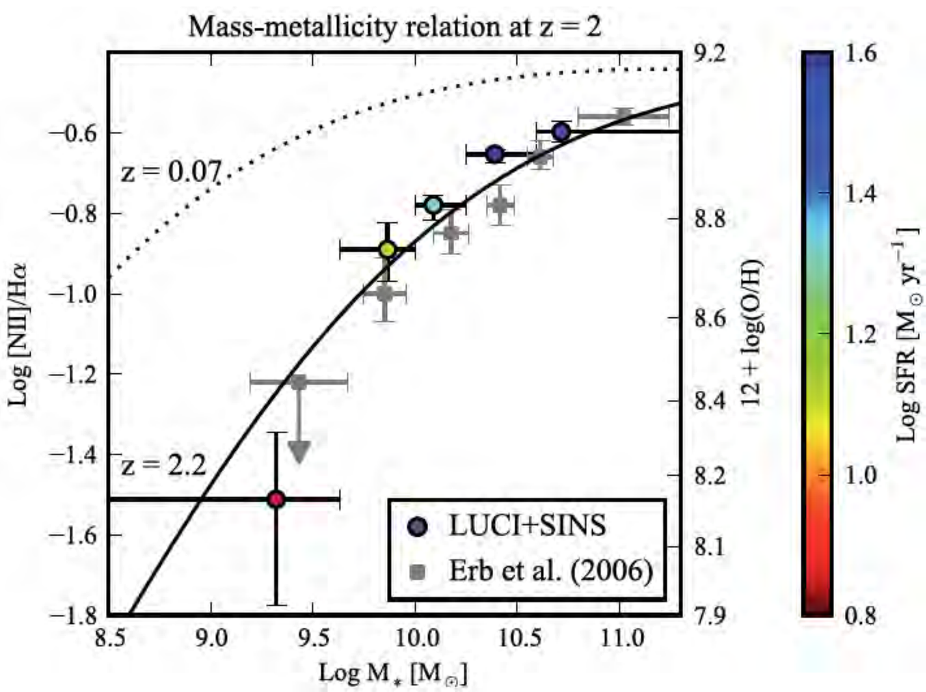

Using [NII]/Hα (left axis) as proxy of gas metallicity (right axis), we confirm the evolution of the mass-metallicity relation with redshift but, considering also the SFR, not that of the fundamental metallicity relation.

References:
- Erb et al. 2006, ApJ 644, 813
- Förster Schreiber et al. 2009, ApJ 706, 1364
- Mannucci et al. 2010, MNRAS 408, 2115
- Wuyts et al. 2011, ApJ 742, 96

J. Kurk, N. Förster Schreiber and the SINS/LUCI team.

KMOS^{3D} Survey: evolution of spatially resolved kinematics of high-z galaxies

The KMOS^{3D} survey is designed to witness the mass growth and life cycle of galaxies between z = 0.5 – 2.5. Using the new K-band Multi Object Spectrograph (KMOS), the KMOS^{3D} Survey will take advantage of joint guaranteed time between the IR and OPINAS groups in order to conduct the first unbiased statistical census of spatially-resolved kinematics and star formation for a sample of 600 galaxies.

The multi-year KMOS ^{3D} *program will:*

- establish the connection between stellar structure and kinematics in order to understand the role/timescale of secular vs. merger-driven evolution,
- study the evolution of outflow properties to establish the role of star formation and AGN in governing stellar mass growth,
- systematically test *for the first time* the imprint of feedback on galaxy formation efficiency via a statistically well defined $M_\star - Z$ relation across a wide z-range,
- quantitatively compare dynamics, structure, star formation, and environment as galaxies transition from star-forming to passive

z>0.5 near-IR IFU Surveys

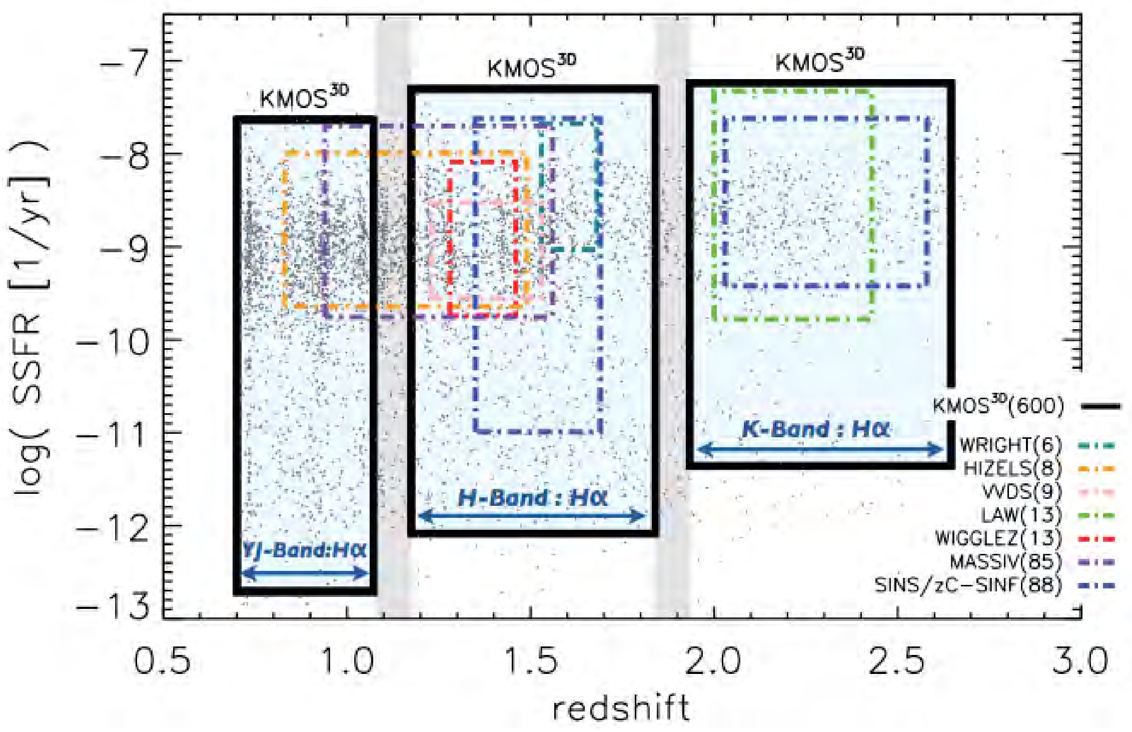

Also see poster by OPINAS group

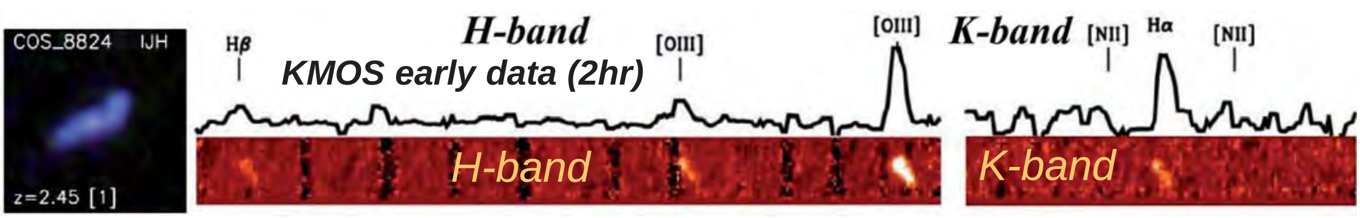

E. Wisnioski, E. Wuyts, N. M. Förster Schreiber, D.Wilman and the KMOS^{3D} team

PHIBSS: Molecular Gas & Scaling Relations in z~1-3 Star-Forming Galaxies

We present PHIBSS, **the Plateau (de Bure) High-z Blue Sequence CO 3-2 Survey** of molecular gas properties in massive, main-sequence star forming galaxies (SFGs) near the cosmic star formation peak. PHIBSS provides 52 CO detections in two redshift slices at z~1.2 and 2.2, with with $\log(M_* (M_\odot)) \geq 10.4$ and $\log(SFR(M_\odot/yr)) \geq 1.5$ (examples at bottom). We infer average gas fractions of ~0.33 at z~1.2 and ~0.47 at z~2.2. Gas fractions drop with stellar mass, in agreement with cosmological simulations including strong star formation feedback. Most of the SFGs are rotationally supported turbulent disks. The molecular gas-star formation relation is near-linear, with a ~0.7 Gyrs gas depletion timescale (below, right panel). At given z and M*, gas fractions correlate strongly with specific star formation rate. The variation of specific star formation rate between z~0-3 is mainly controlled by the fraction of baryonic mass that resides in cold gas (below, left panel).

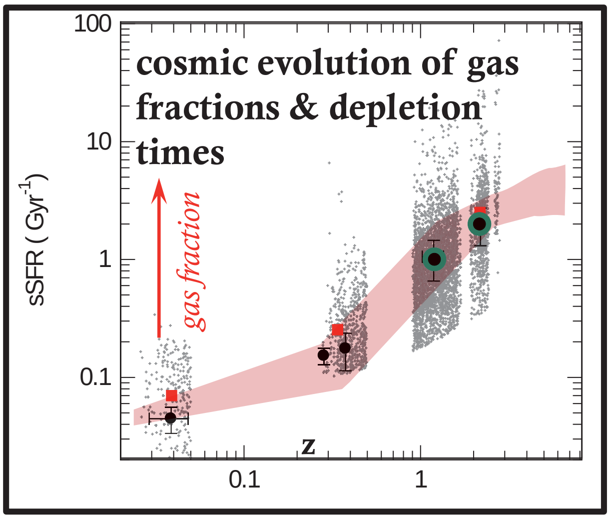

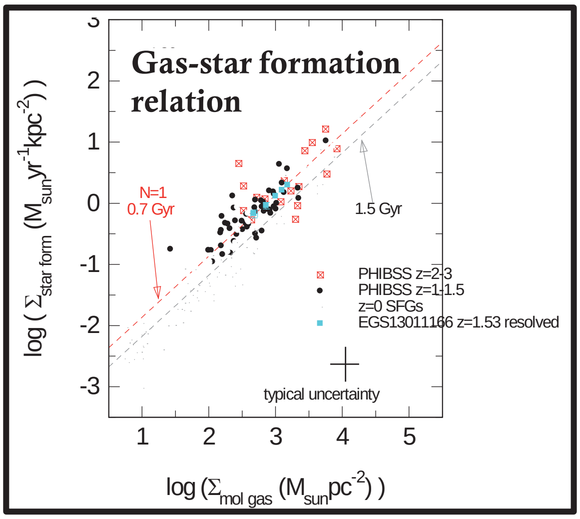

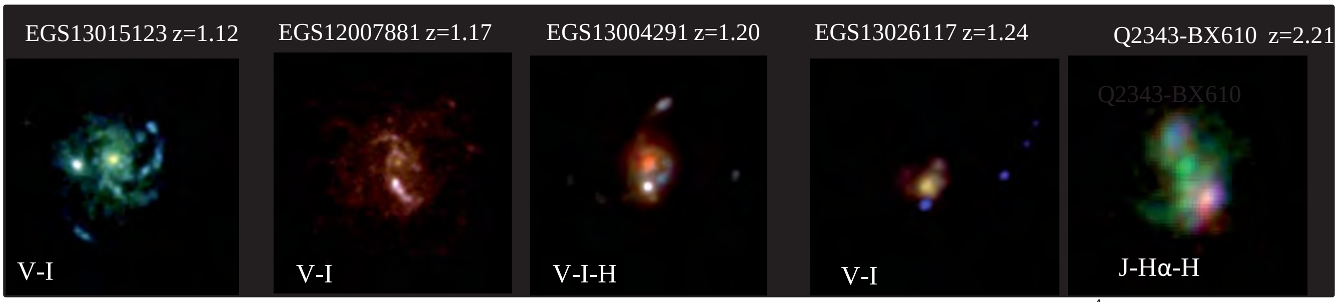

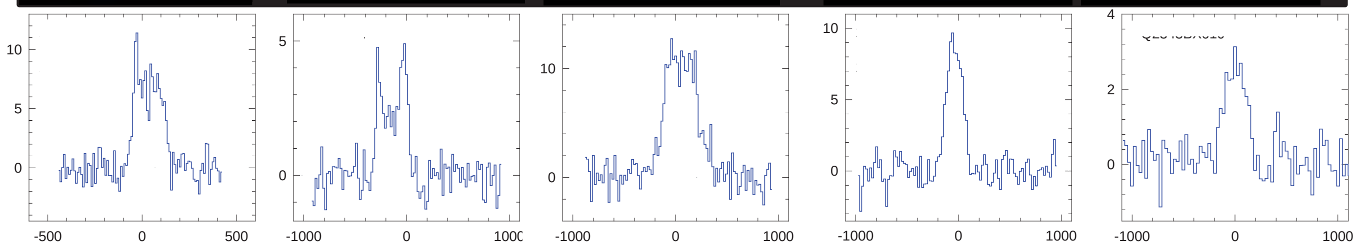

References:

- Tacconi, L.J. et al. 2013, ApJ May 10 in press
- Genzel, R. et al. 2013, ApJ submitted
- Genzel, R. et al. 2010 MNRAS, 407, 2091
- Tacconi, L.J. et al. 2010 Nature, 463, 781

L. Tacconi, R. Genzel, S. Wuyts, A. Burkert, N. Förster Schreiber,
J. Gracia-Carpio, D. Lutz, A. Saintonge and the PHIBSS Team

COLD GASS: an IRAM legacy survey for molecular gas in nearby galaxies

We are using the IRAM 30-m telescope to measure the molecular gas contents of 500 nearby galaxies that form an unbiased subsample of the local galaxy population with $9<\log M^*<11.5$. We have also collected Arecibo HI data and optical long slit spectroscopy to complement the IRAM CO(1-0) observations and the public *Galex* and SDSS photometry. This allows us for the first time to fully and homogeneously quantify the cold baryonic contents of nearby galaxies of all types, and to derive unbiased scaling relations between atomic and molecular gas reservoirs, star formation rates, and galaxy structural and chemical properties.

Highlight from COLD GASS science: The specific rate of star formation in galaxies (i.e. the position in the SFR-M* plane) is determined by variations in both molecular gas contents, and the efficiency to convert this gas into stars. Only with a complete, homogenous, and unbiased sample like COLD GASS can such an analysis be performed successfully.

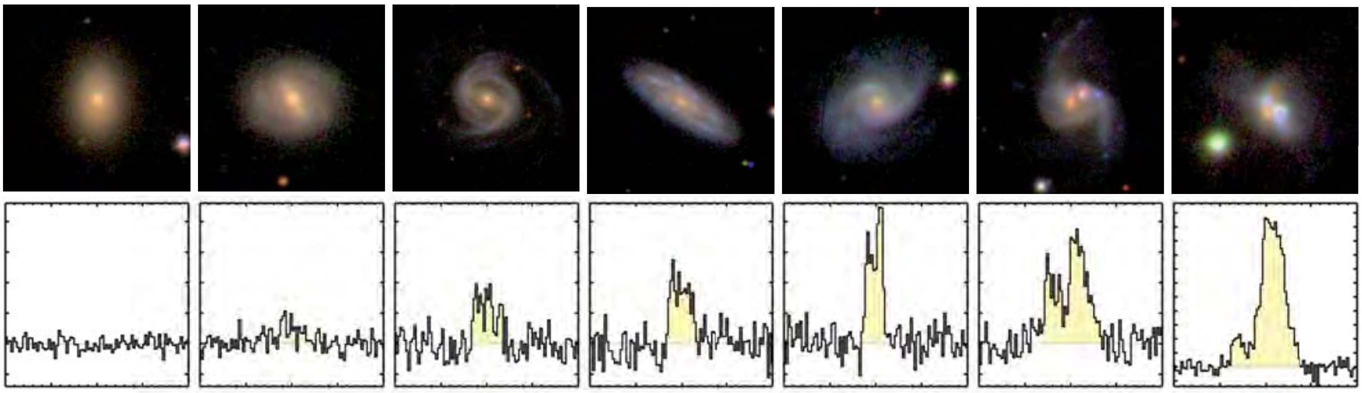

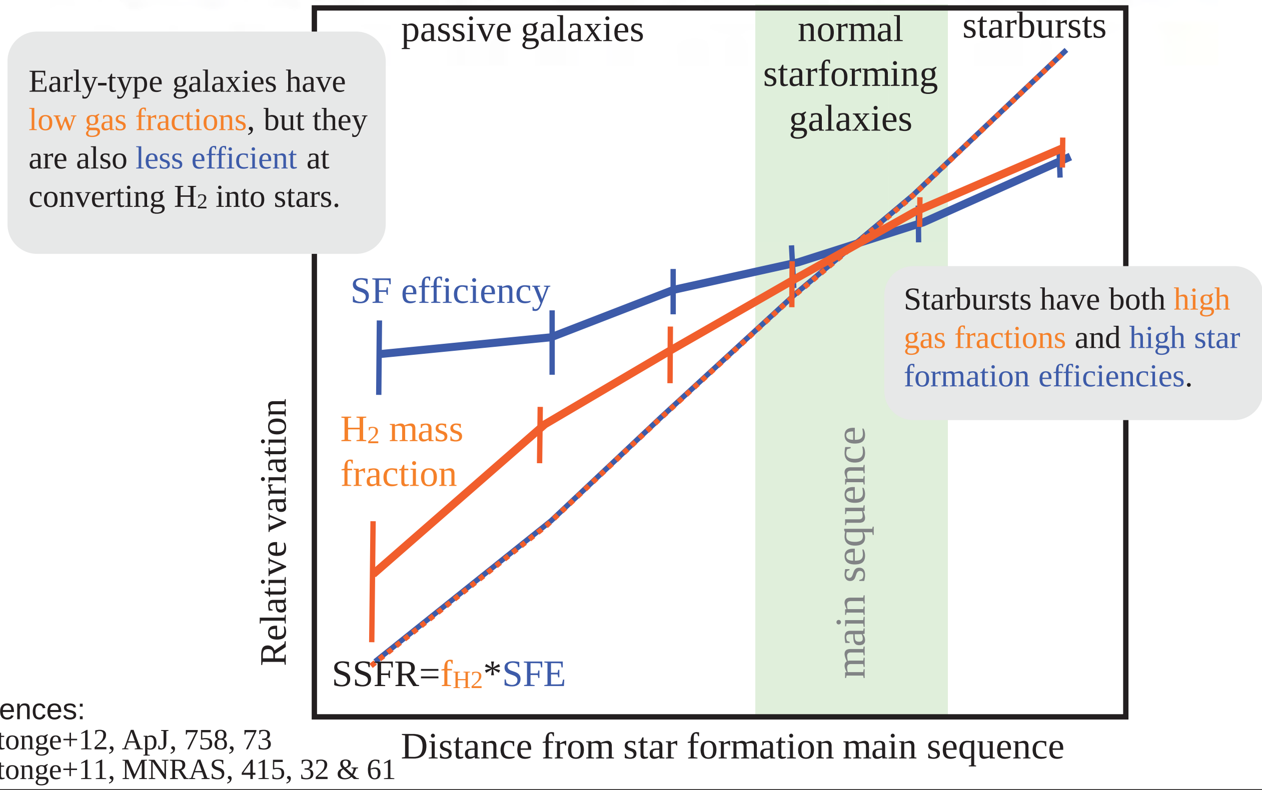

References:

- Saintonge+12, ApJ, 758, 73
- Saintonge+11, MNRAS, 415, 32 & 61

A. Saintonge, L. Tacconi, R. Genzel, J. Gracia-Carpio, K. Lutz

Molecular gas and metallicity profiles in low mass galaxies

Low mass galaxies are known to have very large reservoirs of cold atomic gas, yet are inefficient at converting this gas into stars. We are measuring the stellar, gaseous and chemical contents of a large sample of low mass galaxies (1) to test whether these galaxies are indeed inefficient starformers and (2) to identify the global properties of galaxies where the standard galactic CO → H_2 conversion factor is not valid anymore. This study will not only help us understand the formation histories of low mass galaxies, but also provide important constraints on how to interpret CO measurements in low metallicity and high redshift galaxies.

Right: The average spatial metallicity profile of massive galaxies (COLD GASS [1], dots) is flat [2], whereas less massive galaxies (red stars), show outwards declining metallicities.

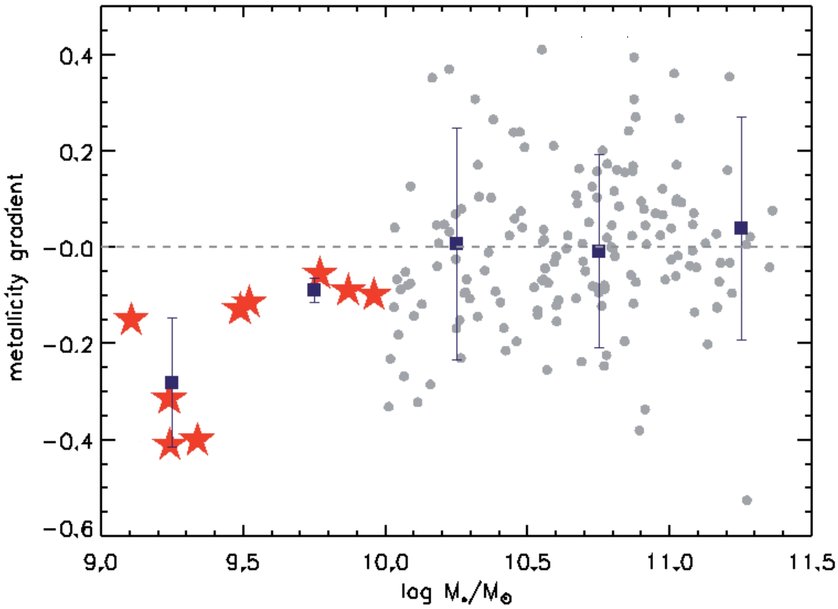

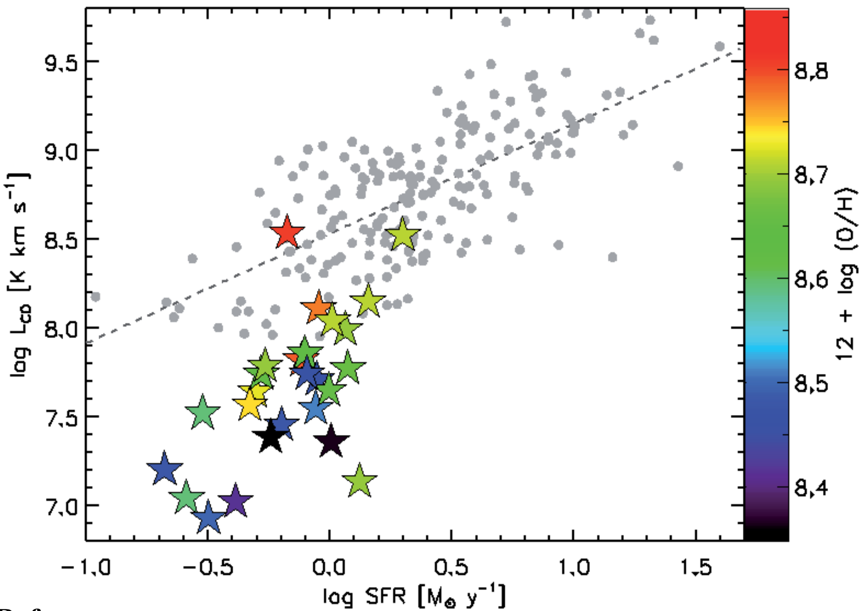

Left: Low mass galaxies (coloured stars) are underluminous in the CO(J = 1→ 0) line for a given star formation rate. Our survey will answer the question: Is this effect driven by a less efficient star formation or a metallicity dependence of the conversion factor?

References:
[1] Saintonge et al. 2011, MNRAS, 415, 32
[2] Moran et al. 2012, ApJ, 745, 66

K. A. Lutz, A. Saintonge, L. J. Tacconi

PEP slices the far-infrared Sky

Our *PACS Evolutionary Probe* (PEP) Herschel key program has completed its far-IR survey of popular multi-wavelength fields. Adding up 631 hours of Herschel time, PEP detected more than 15000 galaxies up to redshift z~2 and beyond. Combined with the rich ancillary datasets, this allowed us not only to resolve the Cosmic Infrared Background (CIB) into individual sources, but also to determine the fraction of CIB emitted at different cosmic epochs. The main results obtained in this context are:

- roughly 75% of the COBE CIB is resolved into individual sources at 100 and 160 μm.
- employing the P(D) statistical analysis, we break the confusion limit and reach 89% of the total CIB at 160 μm.
- To the depth reached by PEP, half of the resolved CIB originates at z>0.58, 0.84, 1.02 at 70, 100, 160 μm, respectively.

Our estimate of the CIB is fully enclosed in the COBE 1σ errors. We reach the point where lower limits - given by resolved counts - are more constraining than direct measurements.

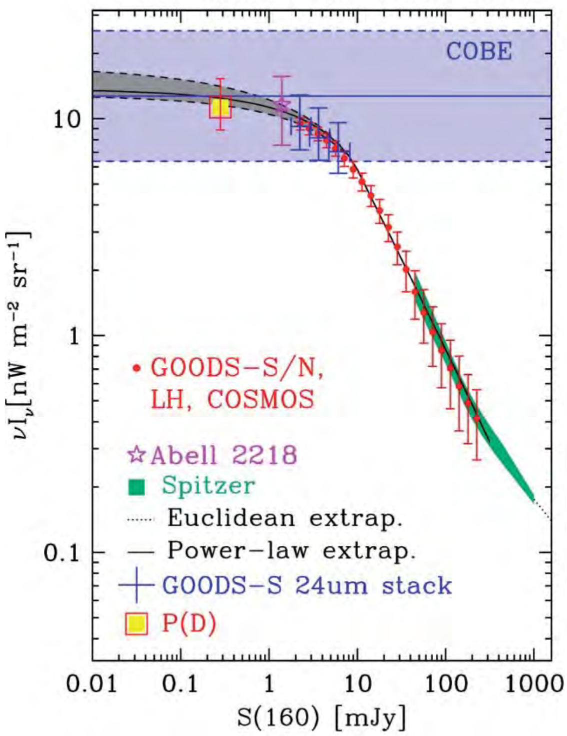

Left: cumulative CIB as a function of flux, compared to the direct measurement by COBE.
Right: resolved CIB as a function of wavelength and redshift.

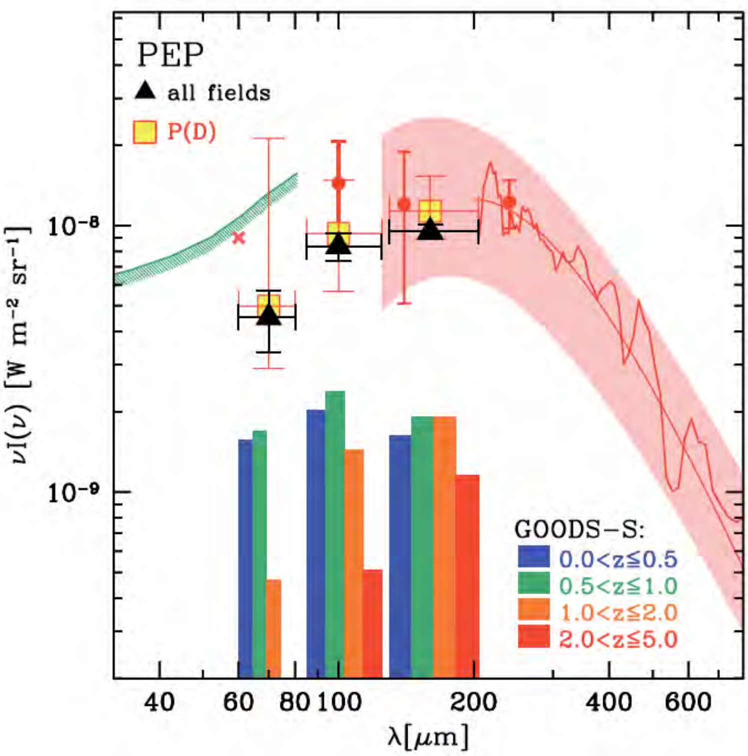

References:
- Berta et al. (2010, A&A, 518, L30)
- Berta et al. (2011, A&A, 532, A49)
- Magnelli et al. (2013, ArXiv/1303.4436)

S. Berta, B. Magnelli, D. Lutz and The PEP Team

Evolving galaxy SEDs and the star forming ‚main sequence‘

Using the Herschel PEP deep survey we have studied properties and infrared SEDs of galaxies out to z~2.5. Infrared astronomers have traditionally characterised galaxies as a function of IR luminosity, creating the LIRG/ULIRG categories with well established trends in a variety of properties. With Herschel we have shown that this approach fails at high redshift. We find that:

- Previous SFR estimates applying local SED families to 24µm surveys need correction.
- A redshift independent picture emerges when expressing properties in relation to the evolving ‚main sequence‘ of star formation.
- Out to z~2, objects near the main sequence contribute ~98% of the star forming objects and 90% of the star formation rate, have typically disk like morphologies, and have infrared SED shapes similar to local normal galaxies, even if (at z~2) having total SFRs similar to local merger ULIRGs.
- Merger morphologies and SEDs resembling local ULIRGs are found for the rare outliers that are placed well above this main sequence.

These results agree with increasing evidence about the gas-richness of high-z galaxies, fed by the cosmic web and minor mergers.

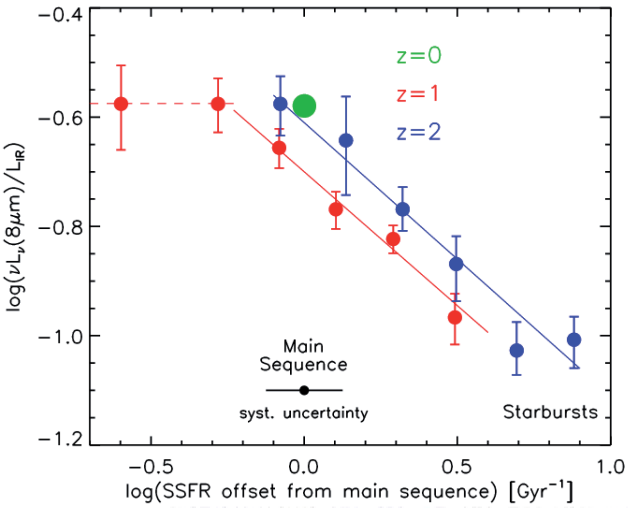

Left: Infrared SED shape (coded by the ratio of rest 8µm and total infrared emission) follows a relation with offset from the star forming main sequence, consistently between z~0 and z~2.
Below: A ladder of star formation indicators including and calibrated on Herschel data, in combination with HST imaging, allows to study morphologies of galaxies in the stellar mass-SFR plane. A morphological main sequence with disk like sersic indices (black) is discernible out to z~2, with de Vaucouleurs like sersic indices (red) both for passive objects below and rare starbursting outliers above this sequence.

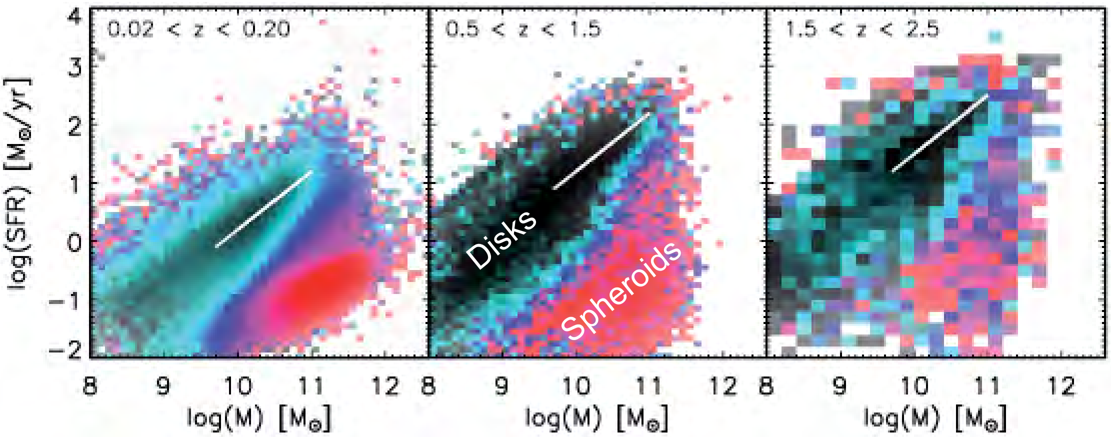

References:

- Nordon et al. 2010 A&A 518, L24 • Wuyts et al. 2011 ApJ 738, 106 • Wuyts et al. 2011 ApJ 742, 96
- Rodighiero et al. 2011 ApJ 739, L40 • Nordon et al. 2012 ApJ 745, 182 • Magnelli et al. in prep.

D. Lutz, R. Nordon, S. Wuyts, B. Magnelli, S. Berta and the PEP team

The mixed cast of Submillimeter Galaxies

In the late 90s, submillimeter galaxies detected by ground-based 850µm to 1200µm surveys (SMGs) gave one of the first glimpses of the dusty side of galaxy evolution. Studies including our IRAM PdBI CO program indicated them to be mostly highly star forming z~2 merger systems, but the key rest far-infrared peak of their SED remained essentially unobserved. Our Herschel survey now provides good quality SEDs for large numbers of SMGs. We find that

- as suspected, the lower luminosity and redshift members of an 850µm selected sample are biased towards cold dust temperature, compared to IR luminosity selected samples
- huge ~1000M_{Sun}/yr star formation rates are confirmed for the subset of bright z~2 SMGs, and are hard to create with steady non-merger mechanisms
- current SMG samples are a diverse mixture of such starbursts far above the main sequence, with colder, very massive objects near the main-sequence

With 'submillimeter selection' now increasingly including fainter sources and observations at shorter wavelengths by Herschel-SPIRE and SCUBA-2, samples need to be explicitly quantified in IR luminosity, redshift, and relation to the star forming 'main sequence', in order to obtain meaningful conclusions on their nature.

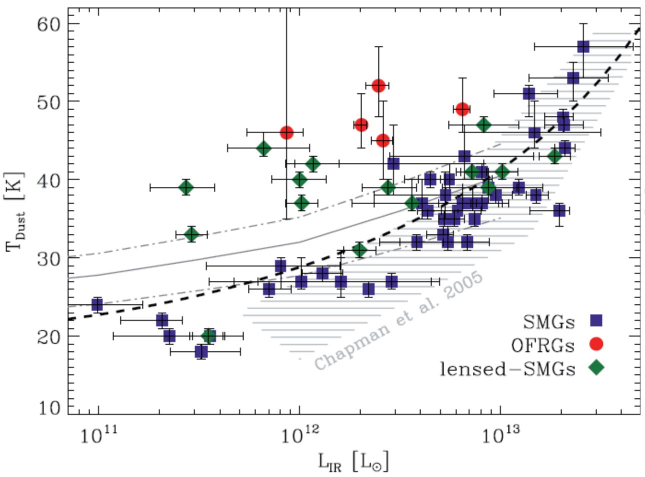

SMGs from classical ground-based 850µm surveys (blue) miss warm objects of moderate luminosity

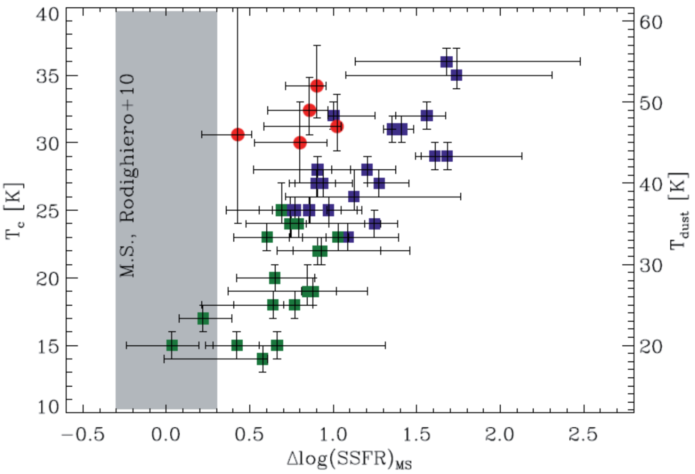

The SMG population includes both luminous starbursting objects with warm dust and placed above the star-forming main sequence (blue) and colder near-main sequence galaxies (green)

Below: Example for complete 24 to 870µm coverage of the FIR SED of a z~2 SMG (60"x60" stamps)

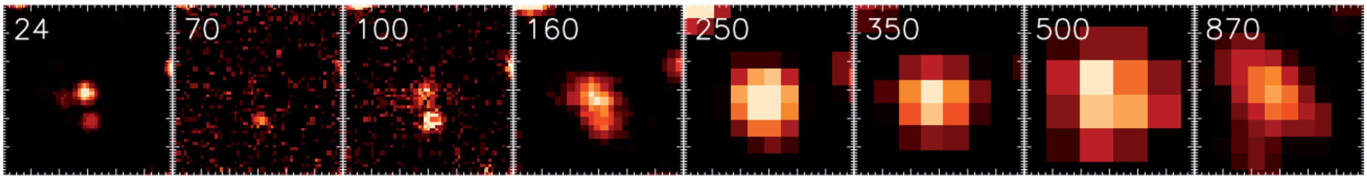

References: Magnelli et al. 2010 A&A 518, L28 Magnelli et al. 2012 A&A 539, A155

B. Magnelli, D. Lutz, S. Berta, R. Genzel, L. Tacconi and the PEP team

Herschel Observations of Gravitational Lenses

We utilize *Herschel* PACS/SPIRE and IRAM Plateau de Bure Interferometer observations to study the dust and gas contents of high-z star forming galaxies. In particular, we present new observations for a sample of 17 lensed galaxies at $z \geq 1.5$, which allow us to directly probe the cold interstellar medium of normal star-forming galaxies with stellar masses of ~ 10^{10} M_*, a regime otherwise accessible only by stacking. We compare the observations of lensed galaxies to reference samples of sub-mm and star-forming galaxies with similar far-infrared photometry. The lensed galaxies at $z > 2$ have high dust temperatures (T_{dust} ~ 50K), despite being located on the star formation main sequence, which can be explained by the high star formation efficiencies and low metallicites. The mean gas depletion timescale of main sequence galaxies at $z > 2$ is indeed found to be a factor of ~1.5 shorter than at $z = 1$. Both the dust and gas masses are low in the high-z lensed sample compared to $z \sim 1 - 2$ galaxies, suggesting a flattening or even a reversal of the trend of increasing gas fractions with redshift recently observed up to $z \sim 2$. The short depletion timescale and low gas fractions of the $z > 2$ normal star- forming galaxies can be fully explained under the "equilibrium model" for galaxy evolution, in which the gas fraction of galaxies is the primary driver of rates.

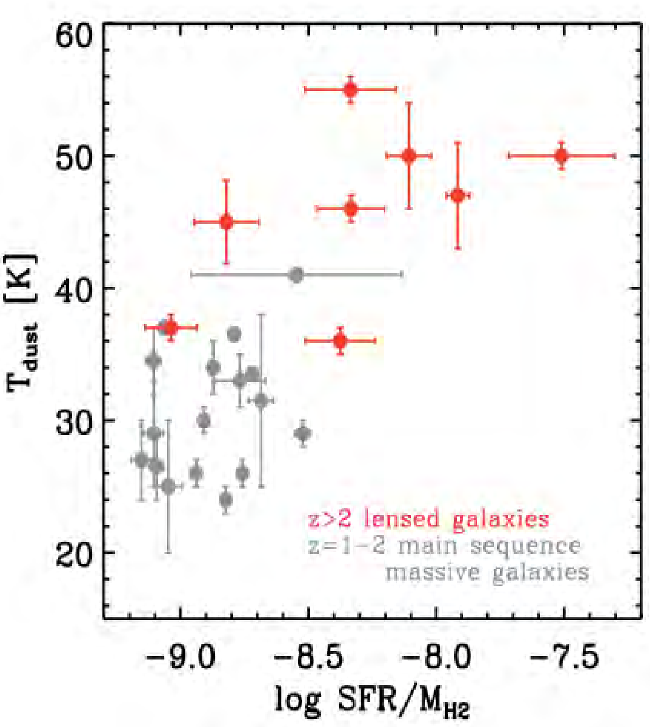

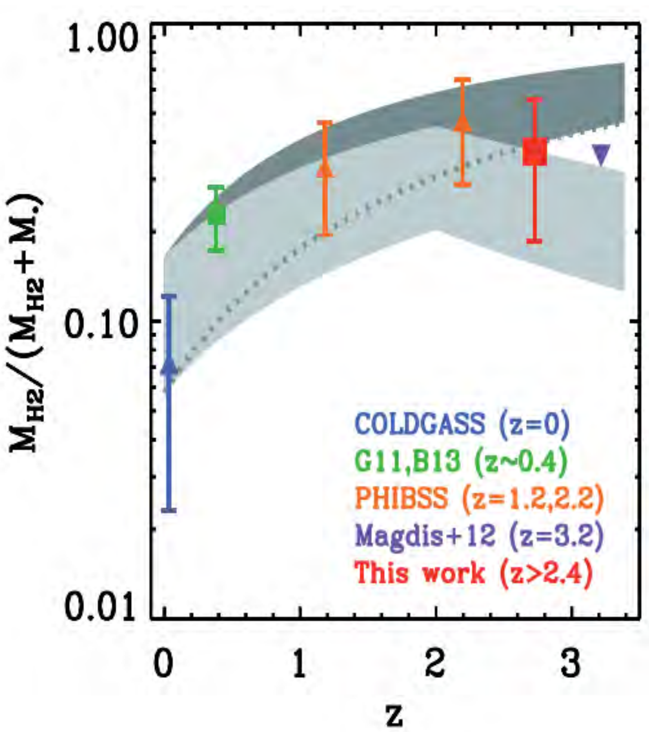

Figure (left): Dust temperature as a function of star formation efficiency (= SFR/M_{H2}). The lensed galaxies, which have higher dust temperatures, are shown as red symbols and the reference sample is shown as light gray symbols. **Figure (right)**: Redshift evolution of the gas fraction (f_{gas}) in star-forming galaxies. The dark gray region shows the redshift dependence of f_{gas} if the specific star formation rate (sSFR) steadily increases with redshift. The light gray region shows the redshift dependence of f_{gas} if the sSFR increases up to $z = 2$ and flattens beyond $z > 2$.

References:

• Saintonge, A., et al. 2013, *ApJ submitted*

K. Bandara, A. Saintonge, D. Lutz, R. Genzel, L. Tacconi, and the PEP team

The Starburst-AGN Connection on Small Scales

Star formation is now a core ingredient in models of gas inflow on nuclear scales. But there is no observational consensus on its role. Our adaptive optics integral field spectroscopy has revealed a link between the characteristic starburst age in the central tens of parsecs, and the accretion rate onto the AGN. This strongly suggests that AGN are associated with young post-starbursts. Hydrodynamical simulations indicate that slow winds (from AGB stars) can accrete efficiently to smaller scales. These imply that the properties of the torus depend on gas inflow and hence on star formation, and that the torus should be considered as a time dependent phenomenon with multiple structures contributing to its different characteristics.

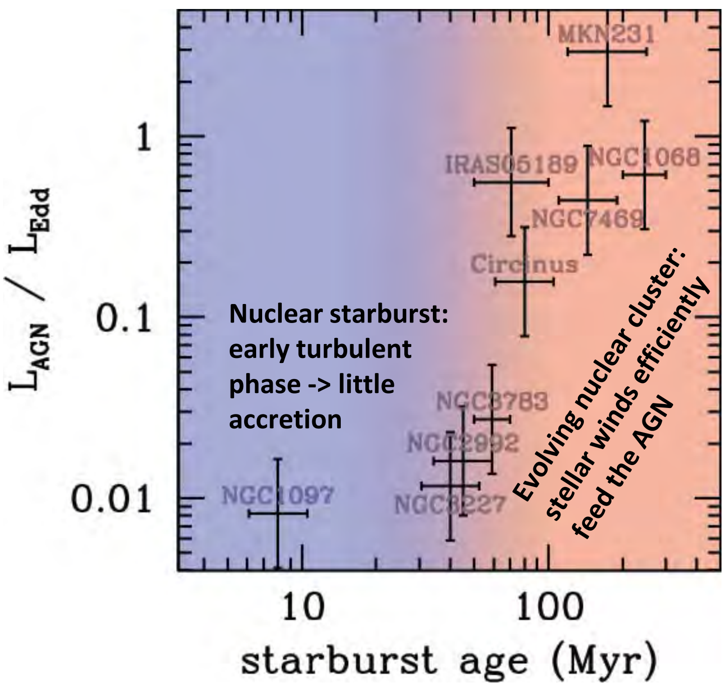

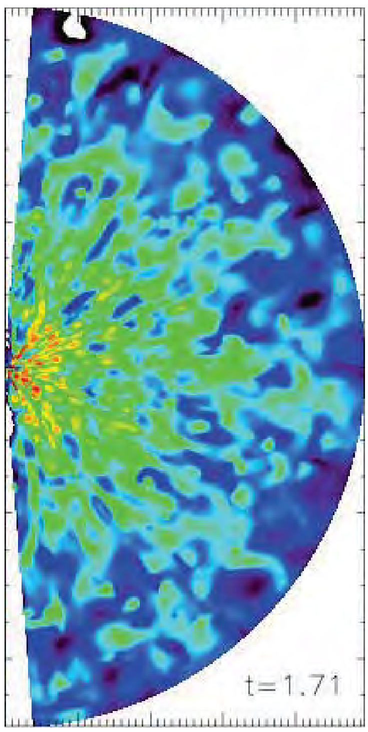

Left:
Observed relation between characteristic starburst age on <50pc scales, and accretion rate onto the AGN. To put this on a statistically robust footing we plan next to observe a complete sample of local active & inactive galaxies selected from the Swift-BAT catalogue.

Right:
3D hydrodynamical simulation of the central 50pc of NGC1068 shows how slow stellar winds can form filaments that flow in to produce a compact turbulent disk. Encouragingly, this was on the same scale as the disks observed in H_2O water masers and mid-infrared interferometry.

References:
- Davies R., et al., 2007: ApJ, 671, 1388
- Schartmann M., et al., 2010: MNRAS, 403, 1801
- Sani E., et al., 2012: MNRAS, 424, 1963
- Davies R., et al., 2012: A&A, 537, 133

R. Davies, L. Burtscher, G. Orban de Xivry, K. Dodds-Eden ,
M. Schartmann, J. Graciá-Carpio, E. Sturm, D. Rosario

The Herschel view of the co-evolution of high-z AGN and their hosts

The star formation rate (SFR) is a fundamental measure of the growth of galaxies. Using the far-infrared as a measure of the SFR, our Herschel/PACS studies of X-ray selected AGN have revealed the importance of “secular” processes in governing the co-evolution of supermassive black holes and massive galaxies over much of cosmic time. Such processes operate over galaxy dynamical timescales and erase any synchronisation between AGN activity and global star-formation. We find that AGN are preferentially located in starbursts only among the most luminous AGN at z<1, where a correlation is seen between the far-IR and AGN luminosity. At high z, and among low luminosity AGN at all redshifts, the SFR of AGN hosts are similar to those of inactive galaxies. However, AGN are significantly more likely to be hosted by a star-forming galaxy and are not generally in systems that are already largely quenched.

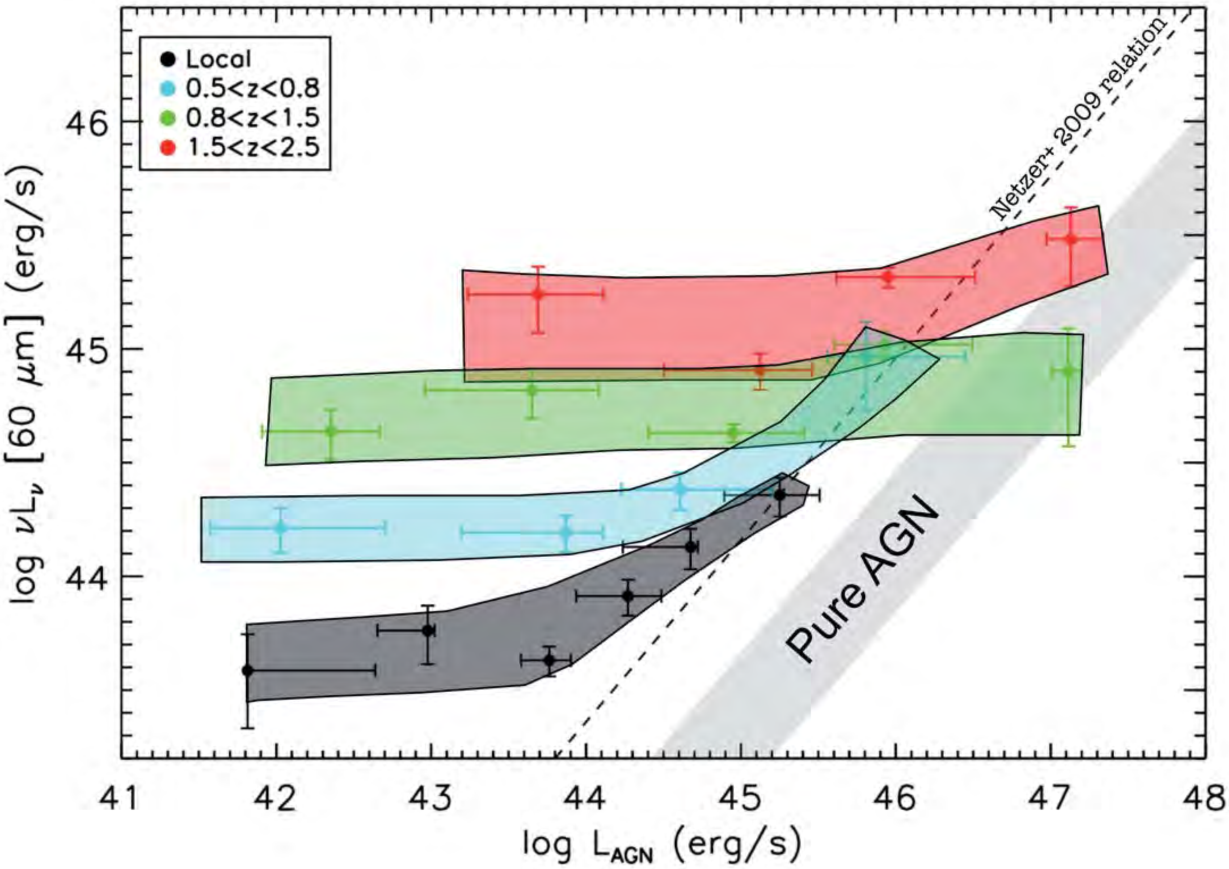

Mean rest-frame 60 μm luminosity of X-ray selected AGN as a function of AGN bolometric luminosity and redshift. The local points come from IRAS measurements of Swift/BAT AGN, while all other points are derived from stacking Herschel/PACS maps. At z<1, luminous AGN show a consistent correlation, which weakens at higher redshift.

References:
- Rosario et al. 2012, A&A, 545, 45
- Rosario et al. 2013, in press

D. Rosario, D. Lutz, P. Santini, R. Nordon, L. Shao

Secular Evolution & Black Hole Growth in NLS1s

Narrow Line Seyfert's represent a class of active galactic nucleus in which the bulge, and hence the black hole, growth is, and has always been, dominated by secular evolution.

Narrow Line Seyfert 1's are commonly interpreted to have particularly **low** – ~10^6 Msun – **black hole masses** and **Eddington-like accretion rate.**
Therefore, NLS1's are considered to be extreme objects among Seyfert type 1 ("BLS1").

Morphology and nuclear star formation show that *present secular processes* are important in NLS1 galaxies, much more than in BLS1's.
Past secular processes seem also to have shaped the NLS1 host galaxies. Indeed NLS1 hosts have "pure" **pseudo-bulges** in contrast to BLS1 galaxies, see Fig.1.
Internal secular processes therefore must have influenced the NLS1 BH growth.

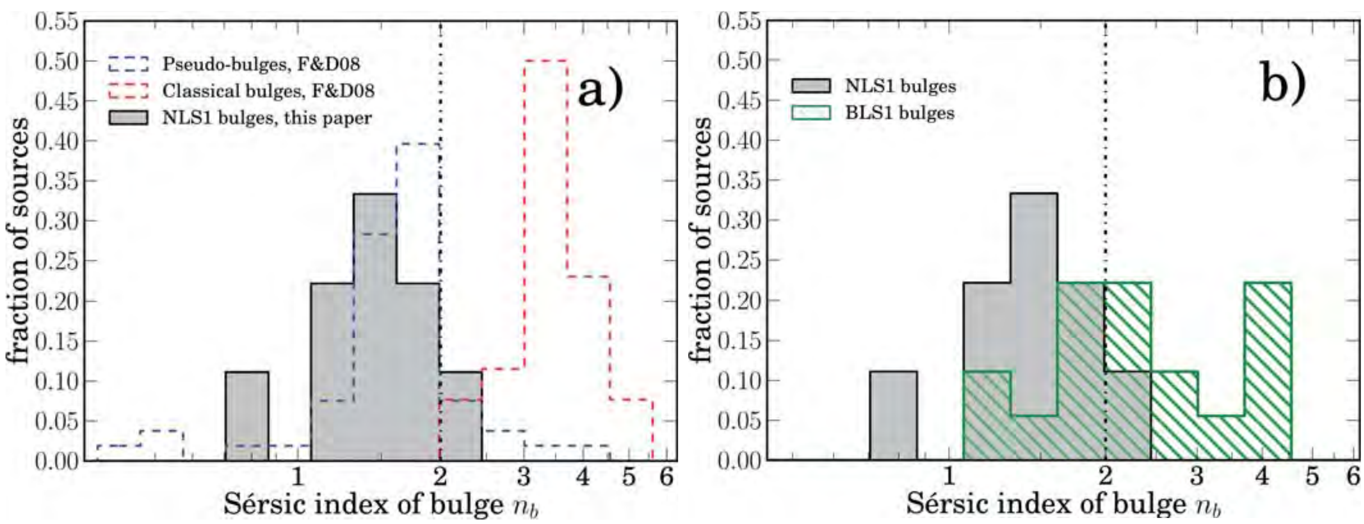

Fig.1. NLS1's have typically pseudo-bulges (n_b<2, low B/T), which is interpreted as a consequence of past secular evolution.

From these results, surveys, and simulations, it appears that NLS1's could have actively accreted on to their BH for ~700Myr since z~1.
For high radiative efficiency – hence high BH spin and slow BH growth –, this would predict ~10^6 Msun BH.

And indeed, observations suggest that NLS1's have **high BH spin**, a possible result of prolonged smooth accretion or a slim accretion disk.

Reference:

- Orban de Xivry G. et al., 2011, MNRAS, 417, 2721, and references therein.

G. Orban de Xivry, R. Davies, M. Schartmann, S. Komossa, A. Marconi, E. Hicks, H. Engel, L. Tacconi

FIR line deficit studies with Herschel

We used Herschel to study the FIR emission line properties of a large sample of galaxies in the local and high-z Universe. We find that the ratio between the FIR luminosity and the molecular gas mass, L_{FIR}/M_{mol}, is a much better proxy for the relative brightness of the fine-structure lines than L_{FIR} alone. Systems with intense star formation tend to have weaker lines relative to their FIR continuum, than less active star-forming galaxies. These line deficits are found both in local and high-z galaxies, and are probably a consequence of their more intense interstellar radiation fields. By resolving the spatial emission in local galaxies, we have been able to extend our analysis to kpc and sub-kpc scales. We find low line to continuum ratios in regions with high FIR surface densities and warm dust temperatures. Only the most compact and obscured regions in some local HII galaxies present line deficits as strong as those found globally in luminous and ultraluminous infrared galaxies (LIRGs and ULIRGs).

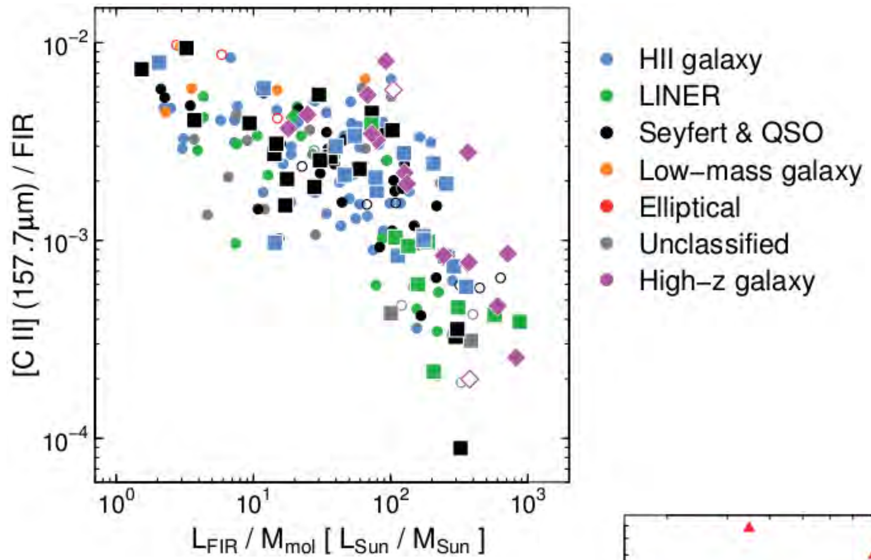

The global [CII] line to FIR continuum ratio in different types of galaxies. The scatter is significantly reduced when L_{FIR}/M_{mol} is used instead of L_{FIR}. Local and high-z Universe galaxies follow similar trends.

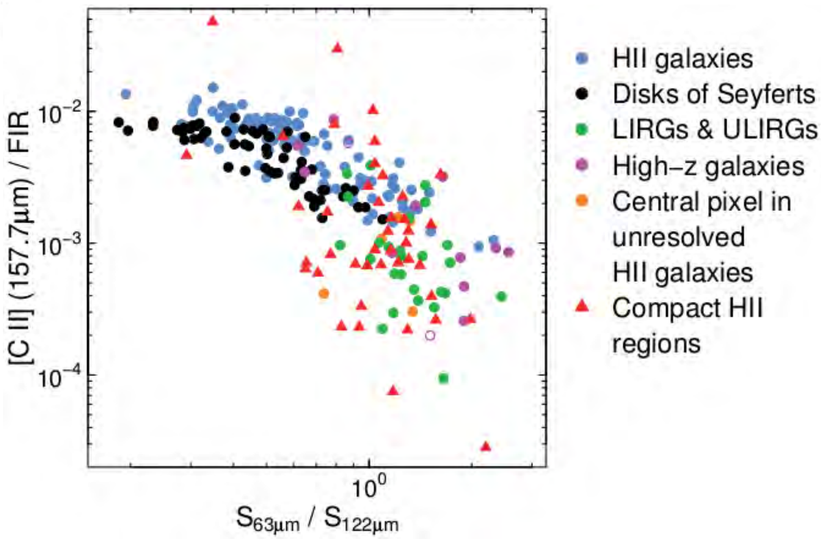

Spatially resolved [CII]/FIR ratio in local Seyferts and HII galaxies as a function of the $S_{60\mu m}/S_{100\mu m}$ continuum colour, which is a proxy of the intensity of the radiation field. Each blue and black point represents an individual Herschel/PACS spatial pixel.

References: Sturm et al. 2010, A&A 528 ● Fischer et al. 2010, A&A 528 ● Genzel et al. 2010, MNRAS, 407 ● Graciá-Carpio et al 2011, ApJ, 728 ● Contursi et al. 2013, A&A 549 ● Graciá-Carpio et al., in preparation

J. Graciá-Carpio, E. Sturm, A. Contursi, A. Poglitsch, R. Davies, R. Genzel, D. Lutz, L. Tacconi, J. A. de Jong, and the SHINING Team

Massive Molecular Outflows and Feedback in ULIRGs and QSOs

We have found unambiguous evidence for massive molecular outflows in the Herschel-PACS spectra of a large number of nearby ULIRGs, traced by the hydroxyl molecule (OH). These outflows may represent the long sought evidence for the strong QSO mode feedback onto the host galaxy required by galaxy evolution models. In some of these objects the (terminal) outflow velocities exceed 1000 km s^{-1}, and their outflow rates (up to~$1200 M_{\odot}$ yr^{-1}) are several times larger than their star formation rates. ULIRGs with a higher AGN luminosity have higher terminal velocities and shorter gas depletion timescales. We are pursuing an extensive follow-up program with Herschel, IRAM/PdBI and ALMA, expanding the sample to PG QSOs and lower luminosity (BAT-)AGNs at various evolutionary stages, confirming the correlation of outflow strength with AGN luminosity, and spatially resolving the outflow geometries.

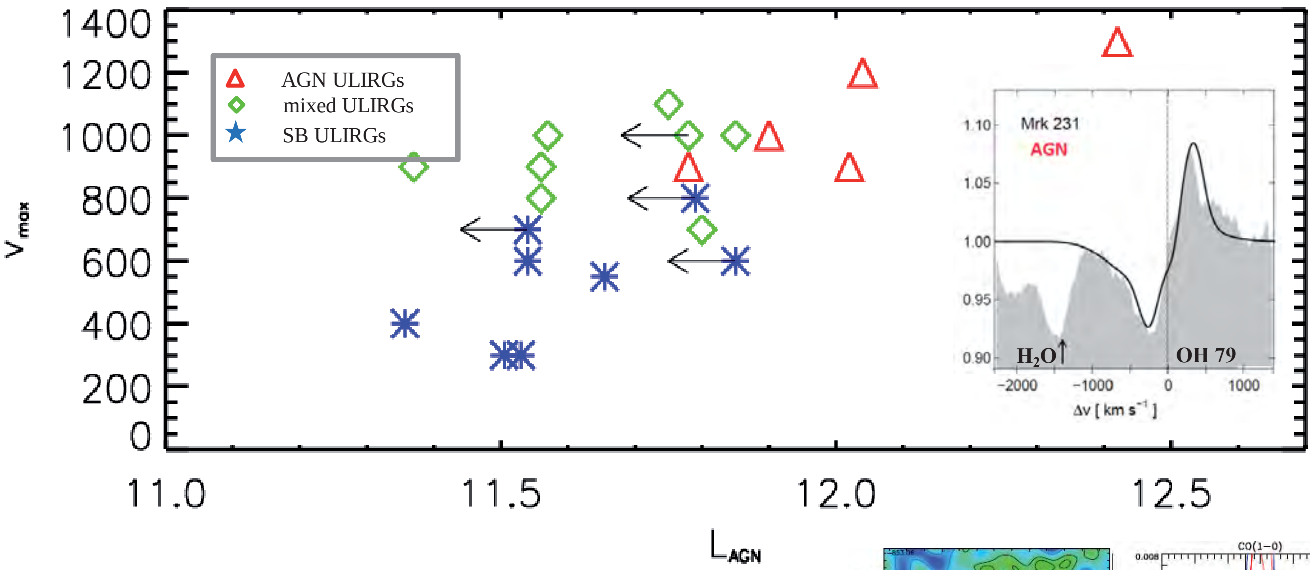

Top: Teminal outflow velocities measured in the OH profiles of different types of ULIRGs. ULIRGs with stronger AGN contribution have stronger outflows (Menendez+ in prep.).
Inlay: Example OH 79µm P-Cygni outflow profiles for an AGN-dominated ULIRG and a starburst galaxy, with typical differences in blue-/red shifts and terminal velocities (Sturm+2011).

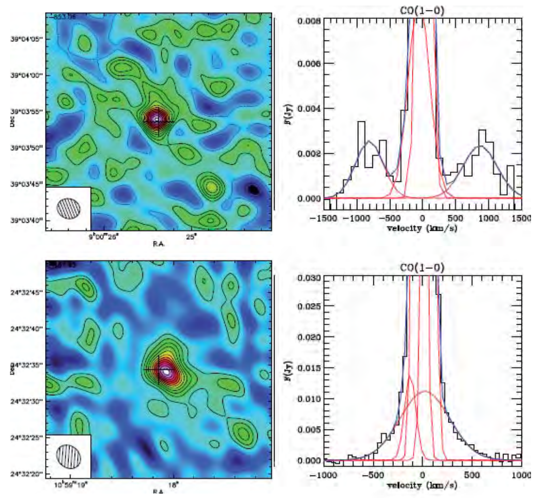

Right: Maps and continuum subtracted spectra of CO(1-0) obtained with IRAM for two of the ULIRGs with strong OH outflow, showing the corresponding outflow in CO as broad wings (Cicone+ in prep.).

References:
- Sturm + 2011, ApJ, 733, L16,
- Fischer + 2010, A&A, 518, L41
- Feruglio+ 2013, A&A, 549, A51
- MPE/ESA press release: http://www.mpe.mpg.de/19543/News_20110509

E. Sturm, J. Graciá-Carpio, A. Contursi, A. Poglitsch, R. Davies, R. Genzel, D. Lutz, L. Tacconi, J. A. de Jong, and the SHINING Team

Resolving the AGN „torus“

Interferometric observations in the mid-infrared made it possible to resolve the nuclear dust structures in Active Galactic Nuclei (AGNs). MIDI observations at the VLTI allow us to observe AGNs at the superb resolution of just a few milli-arcseconds. A large study of 23 AGNs observed with MIDI at the VLTI shows that the mid-IR sizes of „tori“ are more compact and diverse than expected and do not follow a simple scaling relation.

Viewing angle-dependent line of sight obscuration can explain the observed differences in optical spectra, the confinement of ionisation cones and also the different X-ray column densities of „type 1“ and „type 2“ AGNs. However, this „torus“ can only be resolved and thus directly studied in the mid-infrared by employing long-baseline „stellar“ interferometry, specifically using MIDI at the VLTI (Chile).

After the first studies of the two mid-IR brightest galaxies (NGC 1068 and the Circinus galaxy), a big sample of objects has been observed in the MIDI AGN Large Programme. Since this required going to much fainter objects, considerable efforts were necessary to adapt both the observing and analysis methods (Burtscher et al. 2012).

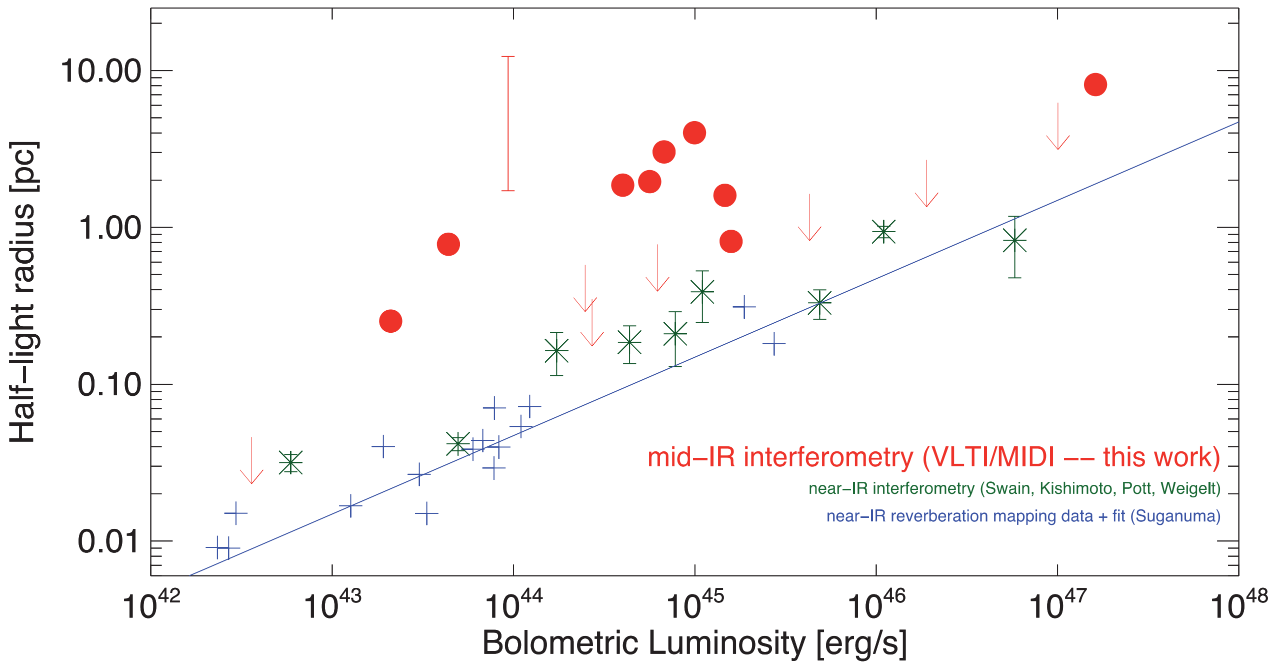

One of the key results is that the mid-IR sizes show an order of magnitude scatter in size. This is surprising as a tight scaling relation of the inner radius of dust with luminosity is now well established in the near-IR (see Figure). While the inner radius is determined by the dust sublimation temperature, the mid-IR radius may have been set by the accretion history of the source. By combining MIDI and SINFONI observations, we will test this link empirically.

References:
• Burtscher, L. et al. 2012, SPIE Proceedings, 8445
• Burtscher L., et al. 2013, A&A, submitted

L. Burtscher, R. Davies, G. Orban de Xivry, D. Rosario
and the MIDI AGN Large Programme team

Extragalactic high-J CO line observations with Herschel/PACS

Far-IR high-J CO lines in galaxies have long been proposed as a tracer of the molecular torus in AGN and of X-ray dominated regions (XDRs). If confirmed, this would be a powerful diagnostic tool for future millimeter studies of high *L* AGN (e.g. ALMA or NOEMA). We performed the first extragalactic observations of high-J CO lines in a sample of local IR luminous galaxies of various types (ULIRGs, Sy1, Sy2, and SB).

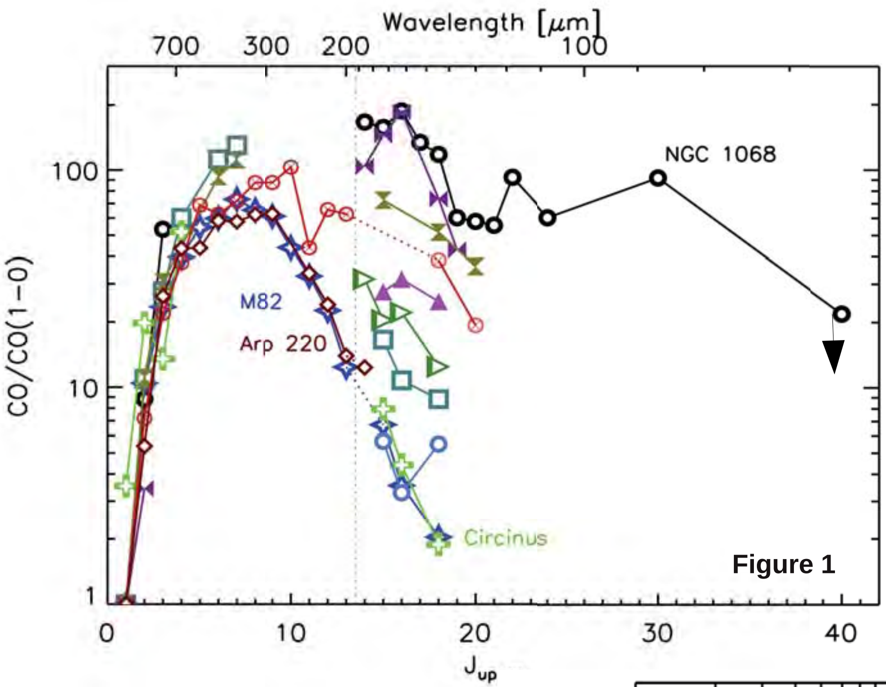

Figure 1

- **Fig. 1** shows how the CO spectral line energy distribution of different types of galaxies starts to differ at J≳ 8.
- The J=40 lower limit in NGC1068 allows to exclude any significant contribution from a compact (~1-pc) torus as in the model of Krolik & Lepp.
- We explore a CO-ratio-ratio diagram as diagnostic to characterize the role of AGN and starbursts in high-z galaxies. The first results (**Fig. 2**) show a good correlation.

- On the other hand, this diagnostic has to be used with caution as suggested by the considerable scatter and by the fact that an AGN dominated galaxy like Circinus, occupies the same part of the diagram of the typical starburst galaxy M82 (see also **Fig. 1**).

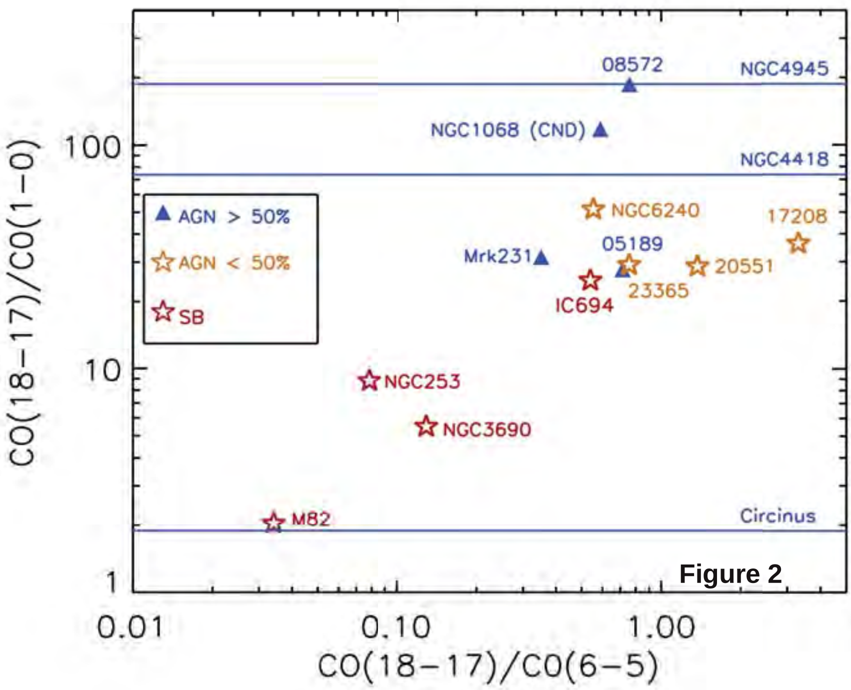

Figure 2

References

- Krolik & Lepp, S. 1989, ApJ, 347, 179

J.Gr aci á′-Cp J.oci á, C J.ESa′′t aCEJ.u áSm-AsGSáP-r C J.g r l h-c′mRCDJ.v Se-t ′Cv J.z i dLCDJ.u t aLt hC
z J.TSmr a-CEJ J.dt .Er al ...Sad.cRt .oHININu .ct S, .

A gas cloud on its way towards the Galactic Center supermassive black hole

Measurements of stellar orbits show that the compact radio source Sagittarius A* at the Galactic Center is a black hole four million times the mass of the Sun. With the exception of modest X-ray and infrared flares, Sgr A* is surprisingly faint, suggesting that the accretion rate and radiation efficiency near the event horizon are currently very low. This might change soon.

In 2011, we discovered a dense gas cloud ("G2") approximately three times the mass of Earth that is falling into the accretion zone of Sgr A*. Our observations tightly constrain G2's orbit to be highly eccentric (e = 0.966), with a pericenter distance of only 2,200 Schwarzschild radii that will be reached in late 2013. Over the past four years G2 has begun to disrupt through tidal shearing arising from the black hole's gravitational force. Ultimately, the gas might feed the black hole, leading to an overall, broad-band increased emission of Sgr A*.

L-band (3.8μm) images of the central arc second, obtained with NACO at the VLT (top). The arrow marks G2 falling rapidly towards Sgr A* (asterisk). Bottom: Hydro-simulation of the infall.

Position-velocity-diagrams of G2 from hydrogen and helium recombination lines observed in deep integral-field spectroscopy with SINFONI/VLT (top). As the cloud moves along the orbit (yellow line) it gets tidally more and more sheared in accordance with a test-particle simulation (bottom).

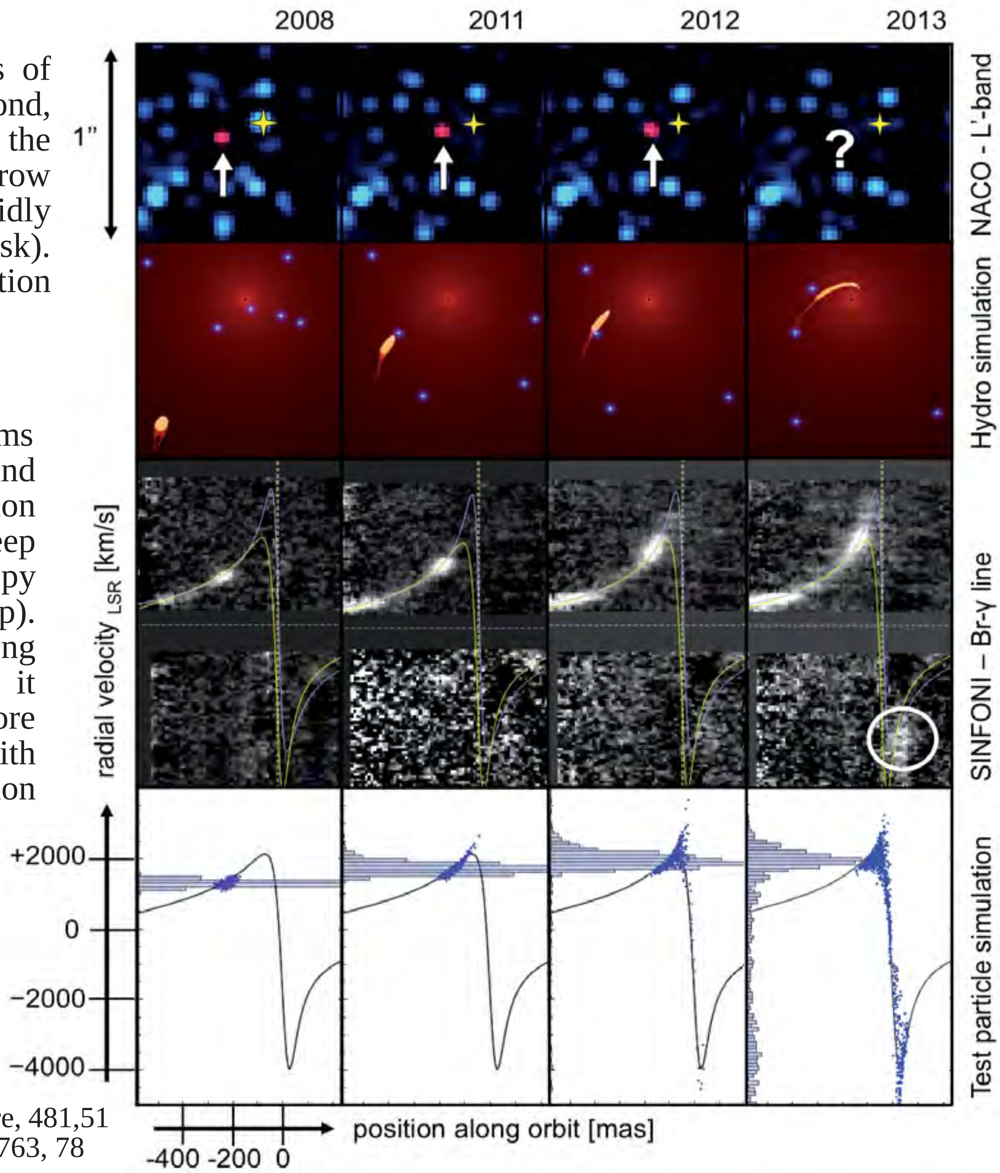

References:
• Gillessen et al., 2012, Nature, 481,51
• Gillessen et al., 2013, ApJ, 763, 78

S. Gillessen, R. Genzel, F. Eisenhauer, T. Fritz, O. Pfuhl, T. Ott

Update on S-stars

The center of the Milky Way hosts a massive black hole. The observational evidence for its existence is overwhelming. The compact radio source Sgr A* has been associated with a black hole since its discovery. In the last decade, high-resolution, near-infrared measurements of individual stellar orbits in the innermost region of the Galactic Center have shown that at the position of Sgr A* a highly concentrated mass of $4 \times 10^6\ M_\odot$ is located. Assuming that general relativity is correct, the conclusion that Sgr A* is a massive black hole is inevitable.

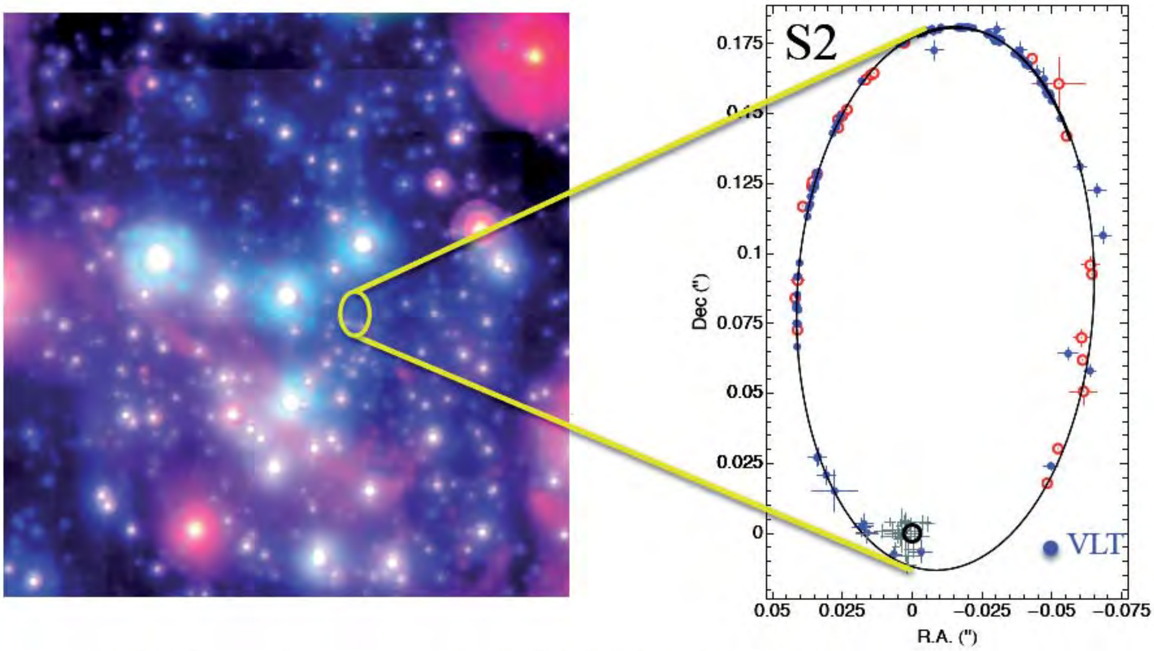

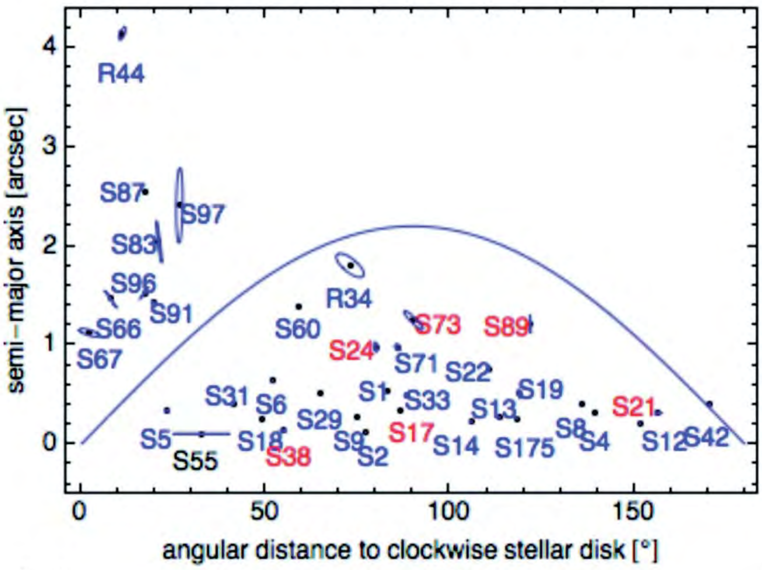

We find a group of orbits at larger radii that share a common plane. This explicitly confirms the existence of the clockwise stellar disk.

References:
• Gillessen S., et al, 2011, ASPC 439, 157
• Gillessen S., et al., 2009, ApJL 707, 114
• Schödel R., et al., 2002, Nature 419, 694

T. Ott, S. Gillessen, O. Pfuhl, T. Fritz, F. Eisenhauer, R. Genzel

The Star Formation History of the Galactic Center

We used spectroscopically derived temperatures of 450 cool giant stars within 1 pc from Sgr A* to construct a Hertzsprung–Russell diagram of the Galactic Center stellar population. By fitting the observed diagram with model populations we were able to derive the star formation history of the nuclear cluster.
We find:
(1) that the average nuclear star formation rate dropped from an initial maximum ~10 Gyrs ago to a deep minimum 1–2 Gyr ago and increased again during the last few hundred Myrs,
(2) that roughly 80% of the stellar mass formed more than 5 Gyrs ago, and
(3) that mass estimates within *R* ~ 1 pc from Sgr A* favor a dominant star formation mode with a “normal” Chabrier/Kroupa initial mass function for the majority of the past star formation in the GC.

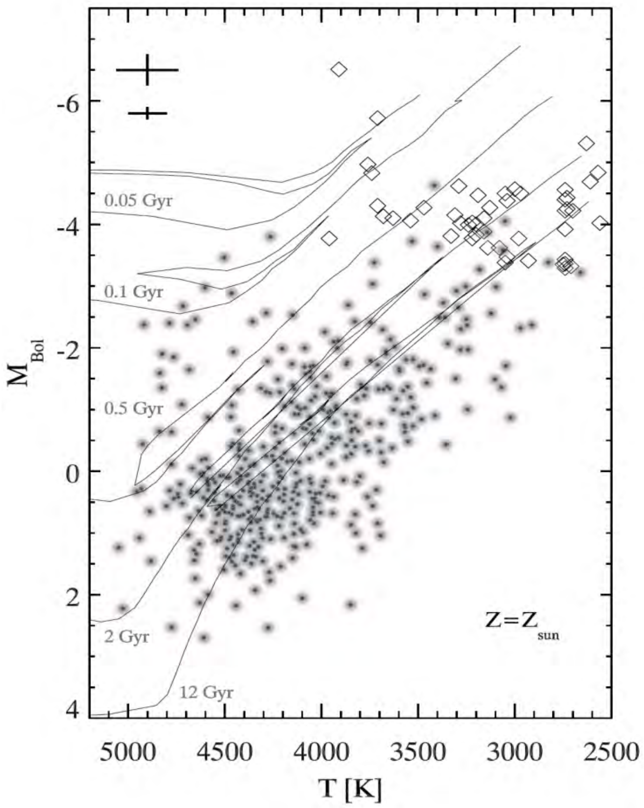

H-R diagram of the cool Galactic Center stars (filled circles). Overplotted are isochrones for ages (from left to right) 0.05, 0.1, 0.5, 2, and 12 Gyr with solar metallicity.

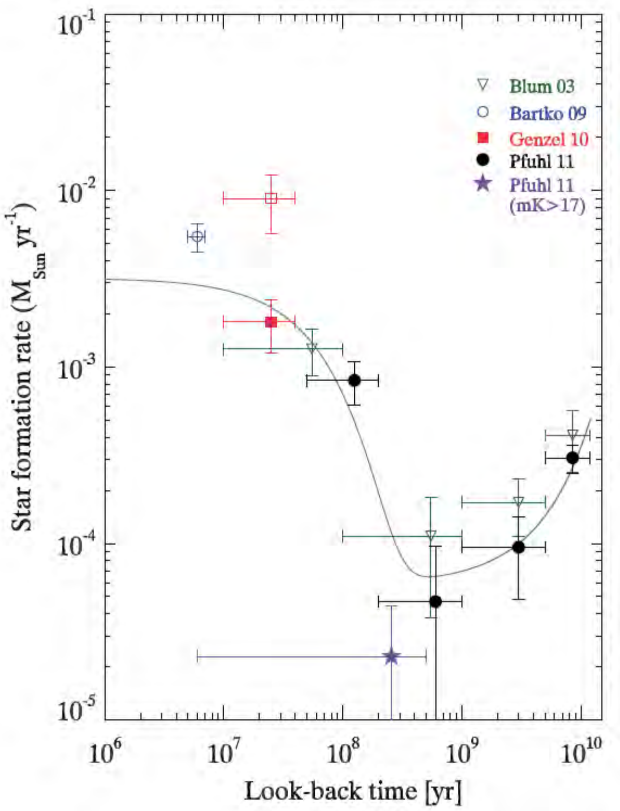

The star formation rate of the Galactic Center as a function of time. The black circles represent the best-fit to the H-R diagram. The solid gray line shows an exponential model of the star formation as function of time.

References:
• Pfuhl O. et al., 2011, ApJ, 741, 108
• Genzel R et al. 2010, Rev. Mod. Phys., 82, 3121
• Blum R.D. et al., 2003, ApJ, 597, 323

O. Pfuhl, T.K. Fritz, F. Eisenhauer, R. Genzel, S. Gillessen, T. Ott, et al.

The extinction curve towards the Galactic Center

We derived the extinction curve towards the Galactic Center from 1 to 19 µm. We used the emission of the HII region; in the infrared hydrogen lines and as extinction-free reference, radio continuum. We measured an extinction of A_{Ks}=2.62 0.11. The extinction curve follows a steep power-law of -2.11 0.06 shortward of 2.8 µm. At larger wavelengths the extinction is grayer and more complex showing also absorption features. We found that a dust model which contains only pure carbonaceous and silicate grains (Weingartner et al. 2001) cannot fit the extinction curve. In addition, also composite particles which contain ices in addition to other components (Zubko et al. 2004) are necessary to fit the extinction curve. Combining our results with the red clump magnitude in Schödel et al. 2010 we obtained an estimate of the distance to the Galactic Center of 7.95 0.65 kpc.

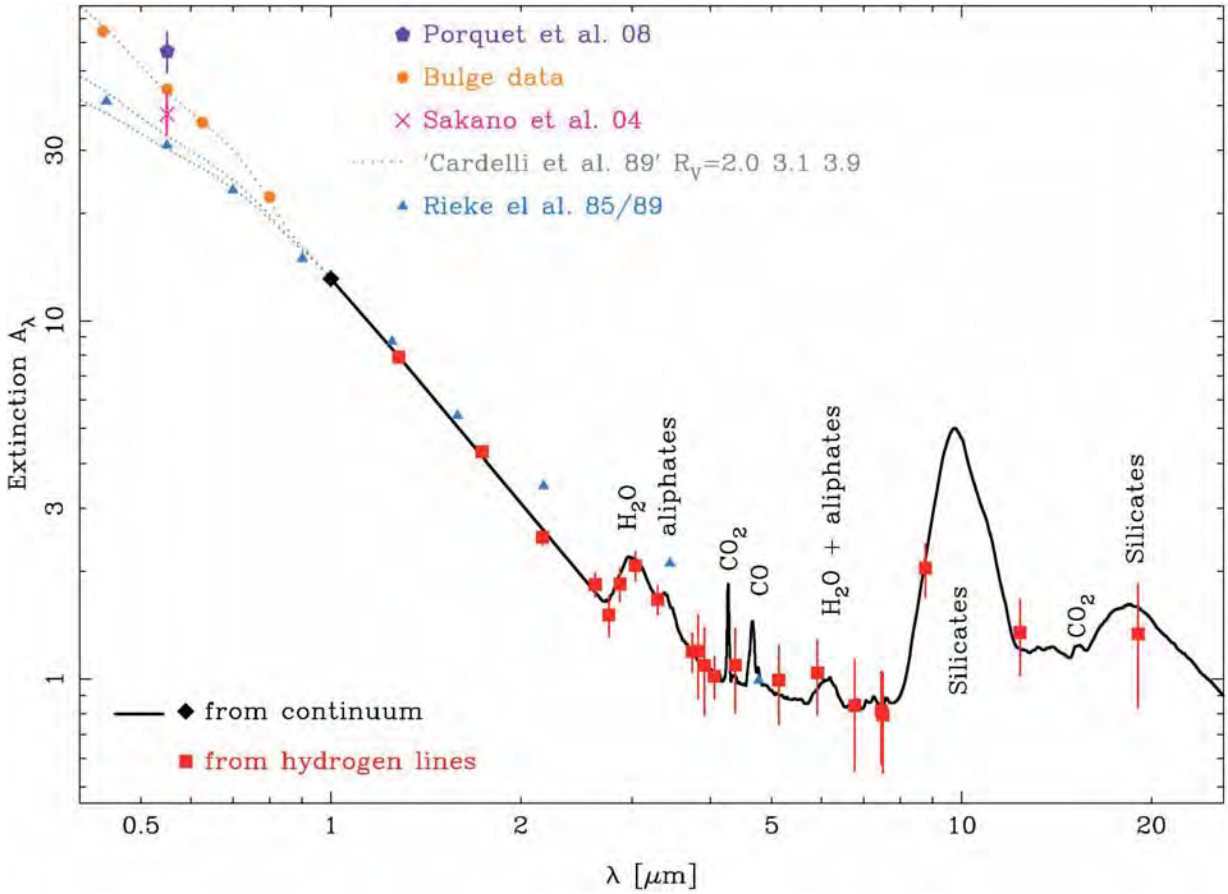

Extinction curve towards the Galactic Center. In our work we tied the ISO results of Lutz 1999 (λ>2.5µm) into the newly calibrated absolute extinction and added new measurements at shorter wavelengths. In the mid infrared the absorption features of different species are visible. The curve is different from the results of Rieke et al. 1985, 1989 but consistent with recent works e.g. Schödel et al. 2010. Indirect measurements hint to a steep curve in the optical with R_V<3.1

References:
- Fritz et al. 2011, ApJ, 737, 37
- Weingartner et al. 2001, ApJ, 548, 296
- Zukbo et al. 2004, ApJS, 152, 211
- Lutz 1999, ESASP, 427, 623
- Schödel et al 2010 A&A, 511, A18
- Rieke et al. 1985, ApJ, 288, 618
- Rieke et al. 1989, ApJ, 336, 752

T.K. Fritz, S. Gillessen, K. Dodds-Eden, D. Lutz, R. Genzel, W. Raab, T. Ott et al.

Studies of trans-Neptunian objects with Herschel Space Observatory

Many stars have debris disks indicating the presence of dust-producing planetesimals. Trans-Neptunian objects (TNO) may be analogous to those unseen dust parent-bodies. As leftovers from the formation process of our Solar System, TNOs' physical properties provide information on the outer protoplanetary disk and constrain theoretical models explaining the formation and evolution of the Solar System. Combining data from optical wavelengths to thermal emission data, which for TNOs peak at far-infrared, allows us to determine size and albedo simultaneously (instead of assuming an albedo) and to infer thermal and surface properties. We observed 132 TNOs with Herschel/PACS/photometer in order to derive their basic physical properties as well as sample properties of the different dynamical TNO classes.

Observations: We use data from two *Herschel* programs: 400 hours from the open time key program "TNOs are Cool: A Survey of the Trans-Neptunian region" (PI T. G. Müller) and 29 hours from "Probing the extremes of the outer Solar System" (PI E. Vilenius).

Results

- We find very diverse albedos among TNOs in the size range 100 to 2400 km (see figure).
- We calibrated the size scale of Plutinos (orbital 2:3 mean motion resonance with Neptune) using our measured sample (1st row in the figure).
- There is a positive correlation between size and albedo in the SDO class (objects scattering off Neptune, 2nd row in the figure) which is compatible with the fact that large objects can retain bright ices more easily than small ones. However, we do not find this correlation among other dynamical classes.
- We confirm that classical TNOs with low inclination orbits (left half of 3rd row in the figure) have higher average albedo than any other dynamical class. This difference, together with different optical colors, is compatible with the hypothesis of a different evolutionary path.
- The dwarf planet Makemake has dark areas on its surface, enabling a local atmosphere.

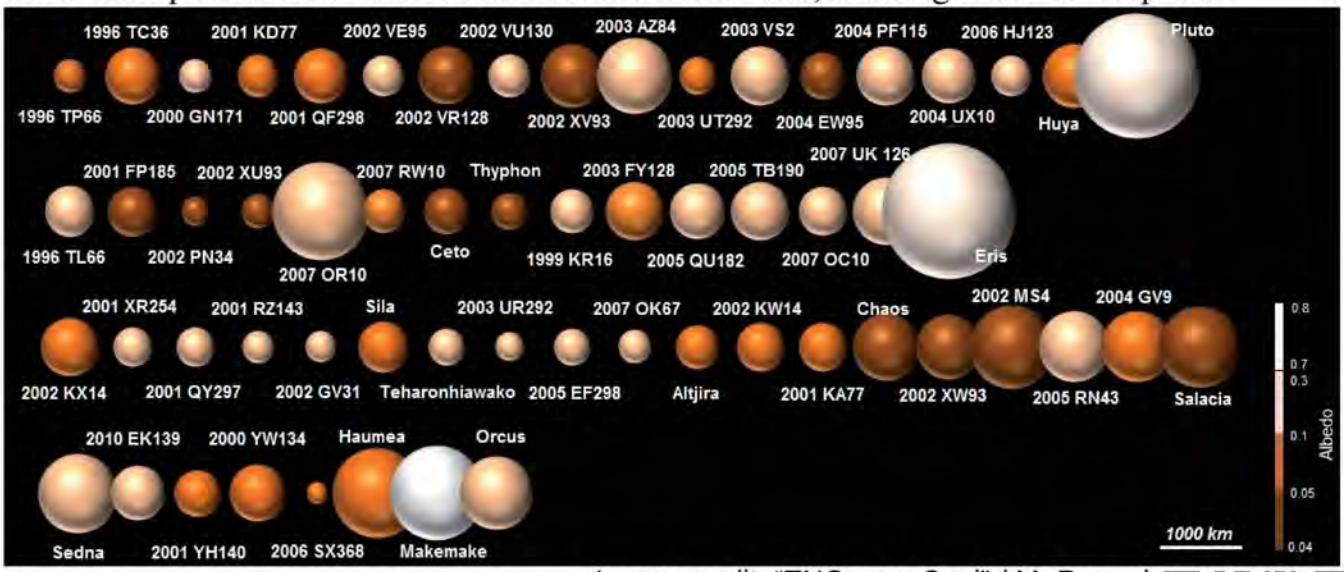

Image credit: "TNOs are Cool" / M. Rengel

References:
- Müller et al., Earth, Moon, Planets, 105:209-219, 2009.
- Müller et al., A&A, 518, L146, 2010. • Lellouch et al., A&A, 518, L147, 2010.
- Lim et al., A&A, 518, L148, 2010. • Santos-Sanz et al., A&A, 541, A92, 2012.
- Mommert et al., A&A, 541, A93, 2012. • Vilenius et al., A&A, 541, A93, 2012.
- Pal et al., A&A, 541, L6, 2012. • Ortiz et al., Nature, 491, 566-569, 2012.

E. Vilenius, T. G. Müller, and "TNOs are Cool" team

Symbiotic stars at high angular resolution

Symbiotic stars are (semi-)detached interacting binaries, generally constituted of a red giant transferring material to a hot, compact white dwarf companion. They are excellent laboratories to study mass transfer and accretion processes, relevant to many other astrophysical objects, and could be linked to type Ia supernovae and some chemically peculiar stars. They are however poorly understood: it appears necessary to probe the sub-AU inner parts of these systems (where occurs the mass transfer) with optical interferometers to go further.

A fundamental question posed by symbiotic binaries is the process of mass transfer. Is it by Roche-lobe overflow (RLOF), stellar wind, or something in between, such as “wind RLOF”? [1] “Classical” studies suffer from their incapacity to resolve such systems and lead to strong inconsistencies [2]. In general, it is not possible to determine the exact nature of the mass transfer and its efficiency, and consequently the evolution and fate of the system. Optical interferometry can directly resolve the inner, sub-AU parts of these systems, and allows to determine the size and the distortion of the giant star, as well as the orbital parameters of these systems, without any a priori on their characteristics. We present below the example of SS Lep.

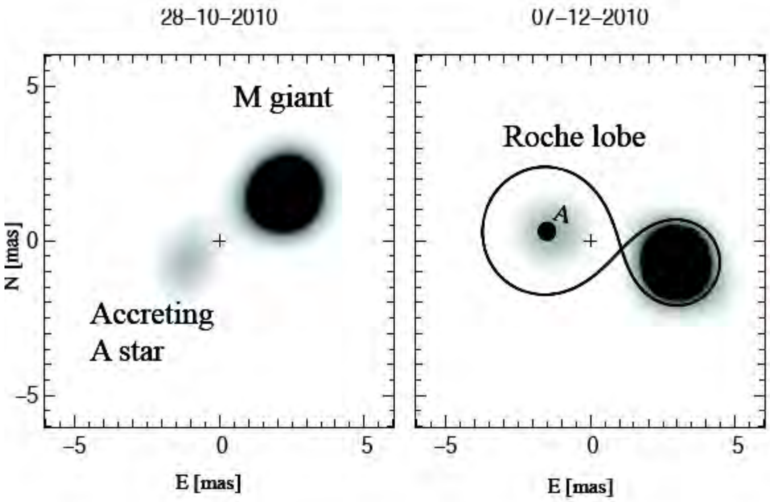

The first images of the symbiotic star SS Lep with the 4-telescope combiner PIONIER/VLTI showed that, conversely to previous claims, the red giant star does not fill its Roche lobe [3]. However it is close to fill it, so that it is not clear what could actually fill this lobe: e.g. extended molecular layers? or a slow wind leading to “wind RLOF”?

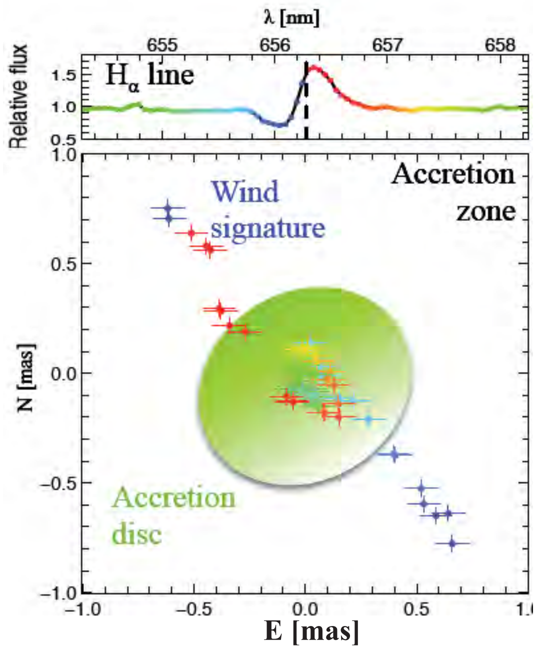

Interferometric observations of SS Lep in the visible allows to focus onto the accreting A star, revealing an accretion disk and the spectro-astrometric signature of a wind.

References:
- [1] Mohamed, S. & Podsiadlowski, P., 2010, American Institute of Physics Conference Series, 1314, 51–52
- [2] Mikołajewska, J. 2007, Baltic Astronomy, 16, 1
- [3] Blind, N., Boffin, H. M. J., Berger, J.-P., et al. 2011, A&A, 536, A55

N. Blind

GRAVITY – Approaching the Black Hole

GRAVITY is the 2nd generation VLTI instrument for precision narrow-angle astrometry and interferometric imaging. With its fiber-fed integrated optics, wavefront sensors, fringe tracker, beam stabilization, and a novel metrology concept, GRAVITY will push the sensitivity and accuracy far beyond what is offered today. Providing ten micro-arcsecond precision astrometry and four milli-arcsecod resolution imaging, GRAVITY will address a number of fundamental open questions on the Galactic Center black hole and its surrounding: What is the nature of its flares? What is the spin of the black hole? How can we resolve the "Paradox of Youth" of the stars in its vicinity? Does general relativity hold in the strong field around the black hole?

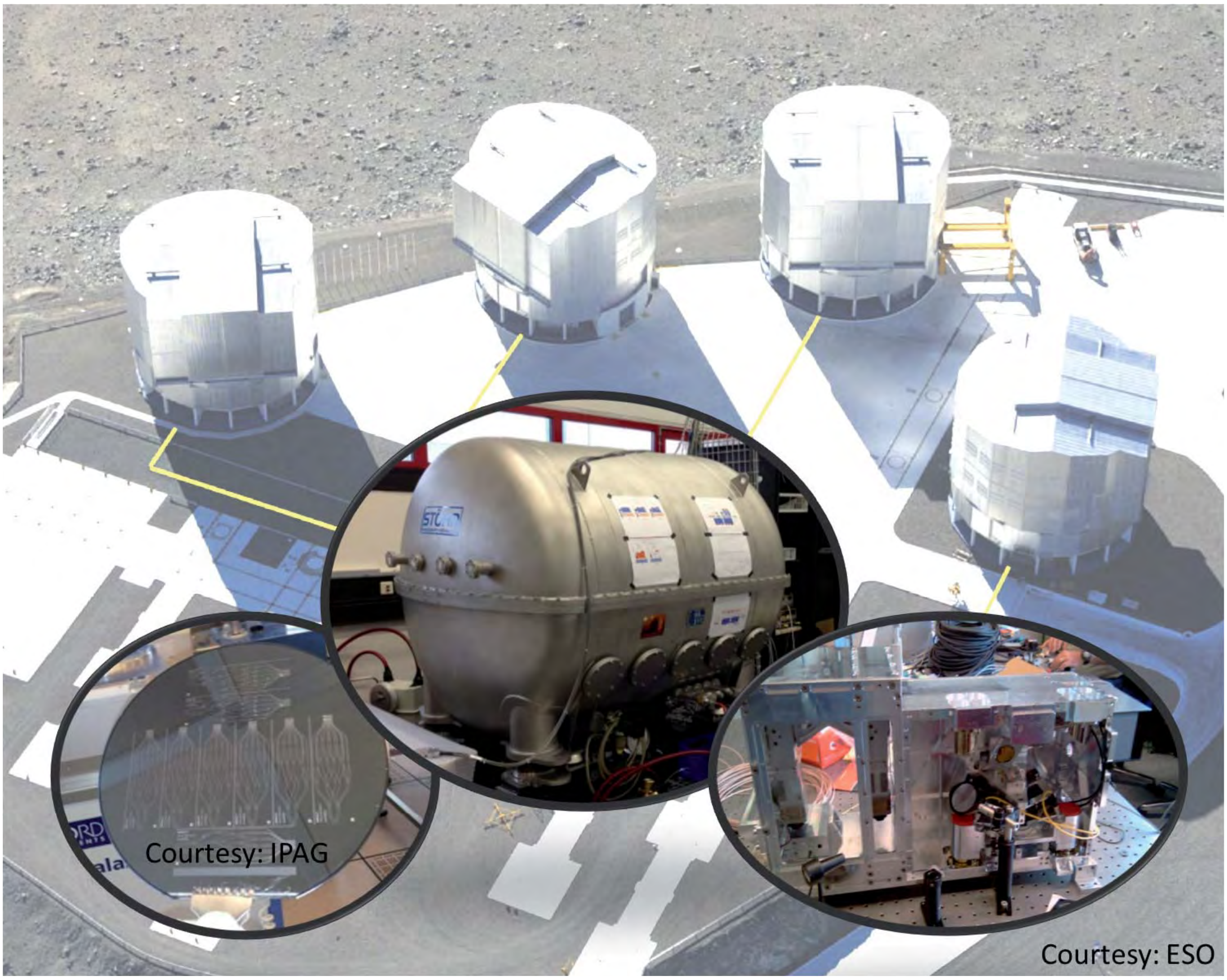

GRAVITY combines the light from the four UT or AT telescopes measuring the interferograms for six baselines simultaneously. The insets depict the GRAVITY instrument (middle) and two of its main components, the integrated optics beam combiner (left), an optical equivalent of an electronic IC, and the fiber coupler (right), which stabilizes and injects the starlight into single mode fibers.

Reference: F. Eisenhauer et al. 2011, The Messenger, 143, 16

F. Eisenhauer, R. Genzel, S. Gillessen, O. Pfuhl, M. Haug, S. Kellner, E. Sturm, M. Lippa, A. Janssen, E. Wieprecht, T. Ott, N. Blind, L. Burtscher, F. Haußmann, R. Hofmann, O. Hans, S. Huber

GRAVITY – Beam Combiner Cryostat

GRAVITY is an adaptive optics assisted four beam combiner for the **second generation VLTI** instrumentation. The cryostat hosts all functions of the beam combiner instrument. It provides the required temperatures for the various subunits ranging from 40 K up to 280 K. The bath-cryostat is cooled with liquid nitrogen and uses the exhaust gas to cool the intermediate temperature (240 K) subsystems. The 40 K level is achieved with a newly developed pulse-tube cooler. All temperature levels are actively stabilized by electric heaters. The cold bench is supported separately from the vacuum vessel and the liquid nitrogen reservoir to minimize transfer of acoustic vibrations onto the instrument. The key functions are the stabilized temperature levels down to **40 K**, the **mechanical stiffness** and the **vibration insulation**.

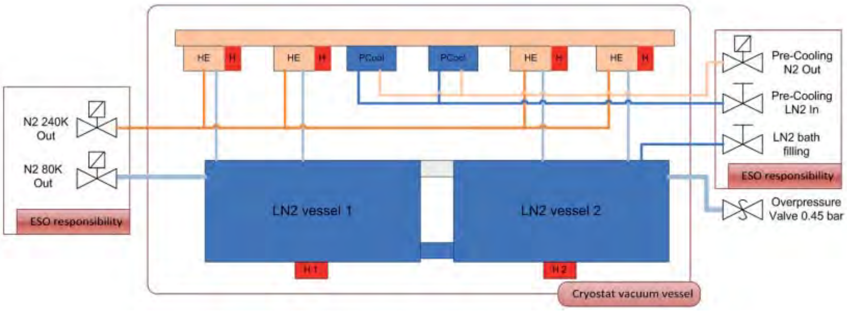

Temperatures to provide

- the two Hawaii-Detectors at 80 K
- the Saphira-Detector at 40 K
- the two Spectrometers at 85 K
- the metrology injection at 280 K
- the IO chip at 200 K
- Different baffles at 85 K to 120 K

How to achieve the 240 K level

The optical bench is at 240K. It is cooled by the **evaporating nitrogen gas** from the liquid nitrogen bath. The gas flow can be adjusted by heaters mounted on the bottom side of the tank. The temperature will be controlled by heaters mounted on the **gas heat exchangers** which are placed on the lower side of the bench.

How to achieve the 40 K level

Via **pulse-tube cooler**.
It's "warm" side will be on **80K**, the cold side at **40K** at a heat load of **2W**. The main aim is to develop a cooler with very low vibrations.

How to achieve the 80 K levels

The 80 K components are connected to massive copper bolts. They are mounted at the bottom of the liquid nitrogen tank. To avoid influence through a change of the **liquid nitrogen level** they are housed in aluminum tubes.

Vibration insulation

The vacuum vessel is **vibration insulated** from the optical bench. The optical bench is mounted stiffly via a stainless steel frame work to the support structure. The vacuum vessel is mounted on elastomer **dampers** and is connected to the bench only via flexible bellows.

M. Haug, F. Haußmann, S. Kellner, R. Hofmann, J. Eder, O. Hans, F. Eisenhauer

Fiber Coupler for GRAVITY

The fiber coupler is a part of the gravity interferometer instrument. Its main function is to separate the light from two stars, and couple this light into two fibers. Moreover it includes some parts for alignment of the whole instrument, and parts of the metrology system. Because all these functions are combined, the fiber coupler houses a lot of (moving) optics, fibers, a prism, and a dichroic.

In the end, there should be four fiber couplers: one for every telescope of the VLTI. At the moment we are finishing the first one. Many functions have been tested already, and work as they should. Now the last changes have to be implemented and verified. An overview of the main functions is shown in the picture below.

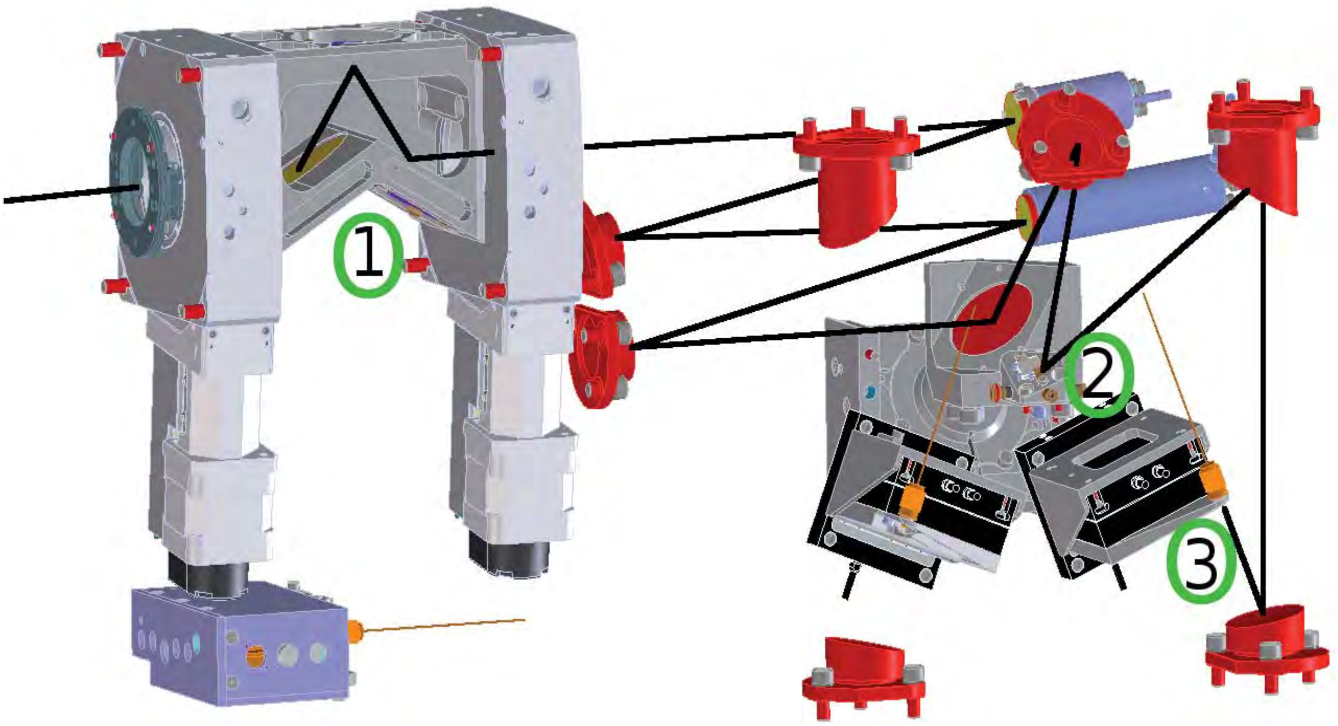

1. Light enters the fiber coupler through the k-mirror. This k-mirror rotates during observations, in order to correct for drifts caused by earth rotation.

2. The roof prism is a roof-shaped mirror, which separates the light from two stars. Each star is projected on one side of the roof-top, so the light of the two stars is reflected in different directions.

3. Finally, the light is coupled into fibers. These fibers must be aligned very well with the rest of the fiber coupler. Also, they have to move in spatial directions, to track the star. Therefore the fibers can move in spatial and angular directions.

A. Janssen, O. Pfuhl, F. Eisenhauer, F. Haussman, M. Haug, S. Kellner

GRAVITY – The Metrology System

The VLTI instrument GRAVITY will provide powerful astrometry. It will measure the angular separation between two astronomical objects to a precision of 10 µas. This corresponds to a differential optical path difference (dOPD) between the targets of few nanometers, and the paths within the interferometer have to be known to that level. For this purpose, the novel metrology system of GRAVITY will monitor the internal dOPD from the beam combination of the astronomical light back to the telescopes using phase-shifting interferometry.

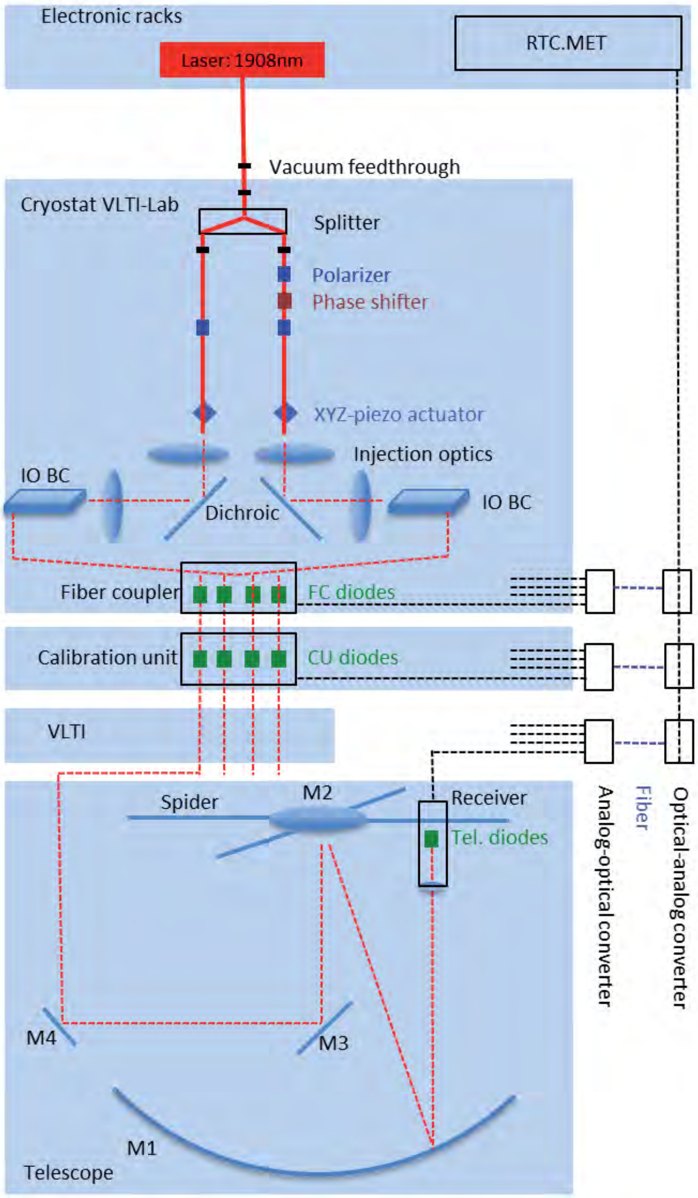

The figure shows an overview of the metrology system. The basic concept is to

- split laser light guided by optical fibers (red solid lines) into two beams.
- inject each beam backwards into one of the beam combiners (IO BC) of the two observed objects.
- let the beams trace the optical paths of the astronomical light back to the telescopes and interfere again.
- resolve the interference fringes with receivers by phase shifting one of the beams in 4 steps (ABCD).
- measure the intensity I for each step at each telescope to determine the fringe phases Φ according to the relation:

$$\Phi = \arctan\left(\frac{I_A - I_C}{I_B - I_D}\right)$$

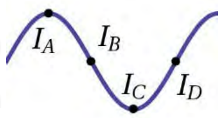

- calculate the dOPDs within the interferometer, which occur between the beam combination and the telescopes, from those phases.
- subtract this internal dOPDs from the measured astronomical dOPDs to extract the angular separation between the observed objects on sky.

Reference:
• S. Gillessen et al. 2012, Proc. of the SPIE, Vol. 8445, Paper No. 8445-58

M. Lippa, S. Gillessen, N. Blind, F. Eisenhauer, O. Pfuhl, A. Janssen, M. Haug, F. Haußmann, S. Kellner, T. Ott, E. Wieprecht, L. Burtscher, E. Sturm, R. Genzel

GRAVITY Metrology Real Time Software

For GRAVITY, MPE is writing the major part of the Instrument Control Software driving motors, lamps, shutters etc. up to special devices, but also the real time software controlling the Metrology system.
The Metrology system is based on the ESO VLT near Real Time framework (TAC), pushing it to the frequency limit of 4KHz.

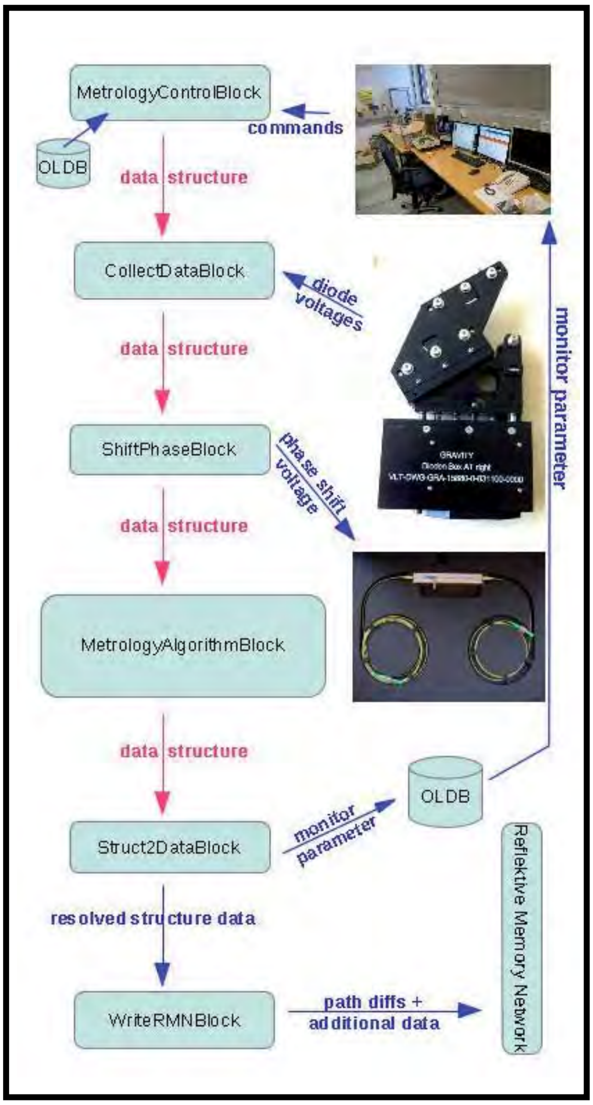

Figure: The Metrology RT data flow

The control block is reacting on runtime commands. A data structure is filled with DB configuration parameters and initialized data & flags.

Photo diodes record light intensities caused by the interferometric fringe patterns generated above each primary mirror by the Metrology laser.
The values are collected, combined and filled into the GRAVITY data structure.

To guarantee high performance, only one number is passed between the different TAC blocks. This parameter is mapped to a pointer address pointing to the GRAVITY structure. This little trick permits passing only a pointer between the TAC blocks.

The phase is shifted.

The Metrology Algorithm is a big, highly optimized TAC Block, calculating the unwrapped phases for the DDLs.

In order to write the data to the ESO Reflective Memory Network the GRAVITY data structure need to be resolved.

The data needed for the DDL control are written to the RMN. Other control parameter are fed back via the DB to the Metrology NRT Control GUI for monitoring purposes.

References:

M.Lippa et al. 2013, GRAVITY – The Metrology System, this booklet
S.Gillessen et al. 2012, Proc. Of SPIE, Vol. 8445, Paper No. 8445-58

E. Wieprecht, S. Gillessen, F. Eisenhauer, T. Ott, M. Lippa, L. Burtscher

ARGOS: Laser guide stars for the LBT

ARGOS is a multi laser guide star adaptive optics system for the LBT, designed to perform GLAO correction for a very wide FoV. The system uses high powered, pulsed, 532 nm lasers to generate three guide stars at an altitude of 12 km above each LBT mirror. The light returning from the individual laser guide stars is detected by gated wavefront sensors, directly driving the adaptive secondary mirrors of the LBT. ARGOS is designed to operate with the multiple object spectrograph LUCI.

ARGOS is developed and built by an MPE-led consortium with contributions from Italian, US and other German research institutes . It will be available for observations towards the end of 2014. ARGOS is expected to improve the FWHM of LUCI by 2-3.

ARGOS comprises the following components:

- **Laser System**
Three 18 W lasers, beam steering mirrors and position control cameras.
- **Laser Launch System**
A refractive, aspheric beam expander and a two flat fold mirrors.
- **Wavefront Sensors**
A Shack Hartmann system with shutters that open for 2 µs on the returning pulses.

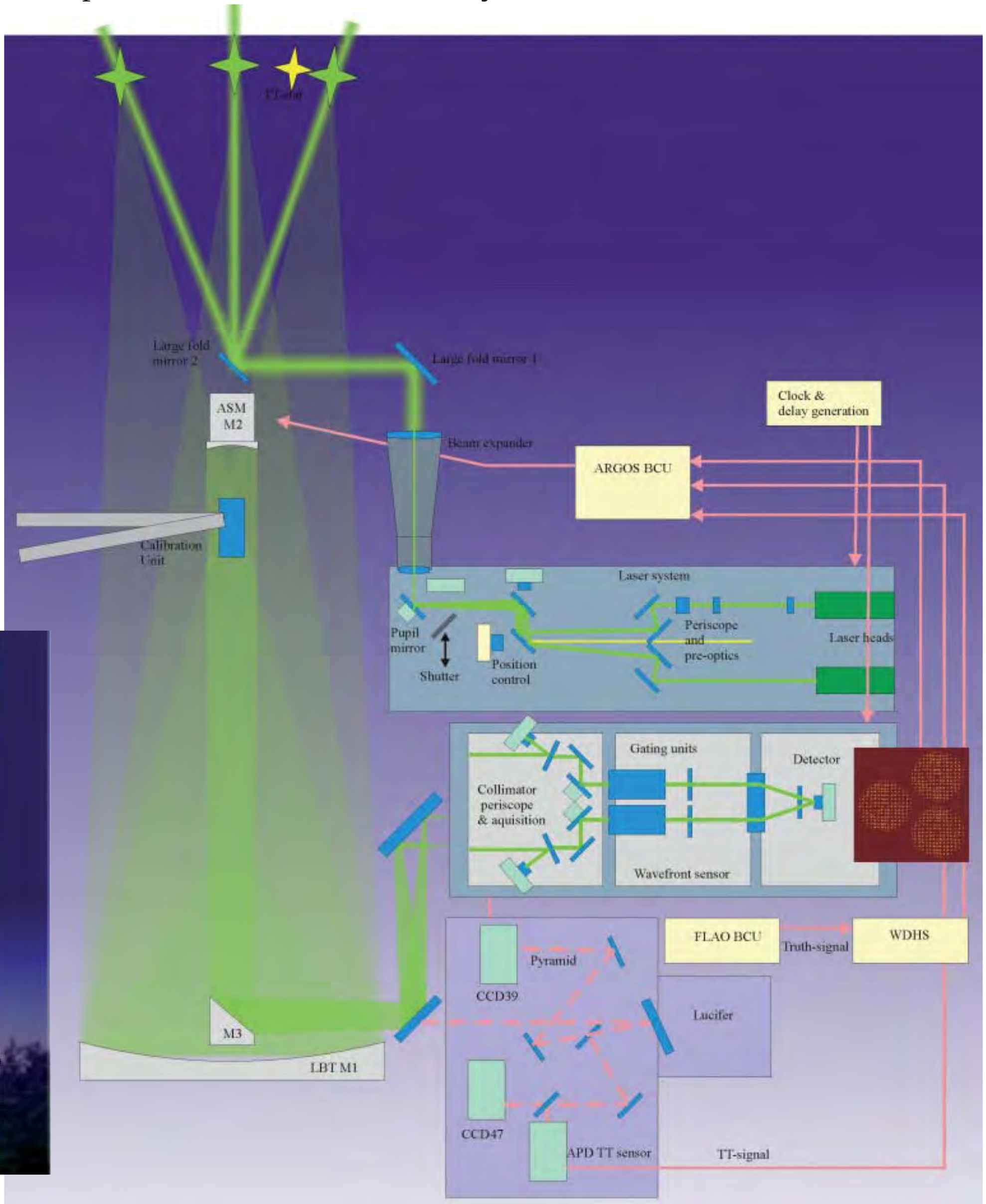

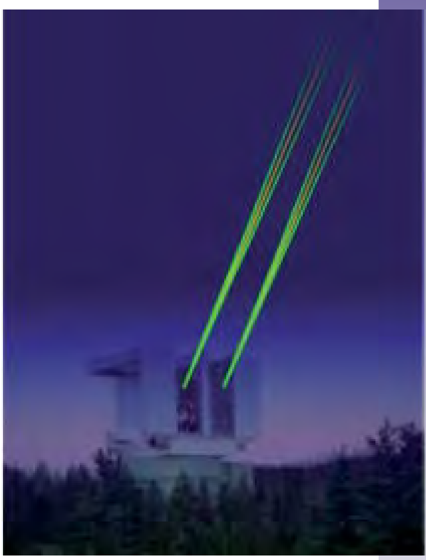

References:

• http://www.mpe.mpg.de/ir/argos
• Rabien et al., Proc. SPIE, Volume 7736, 2008

W. Raab for the ARGOS team

ARGOS WFS Detector & Gating

ARGOS is the Laser Guide Star adaptive optics system for the Large Binocular Telescope. Aiming for a wide field adaptive optics correction, ARGOS will equip both sides of LBT with a multi laser beacon system and corresponding wavefront sensors. Amongst several developments, MPE contributes to the wavefront sensor of ARGOS the high speed large frame CCD, slope computers and wide field Pockels cells.

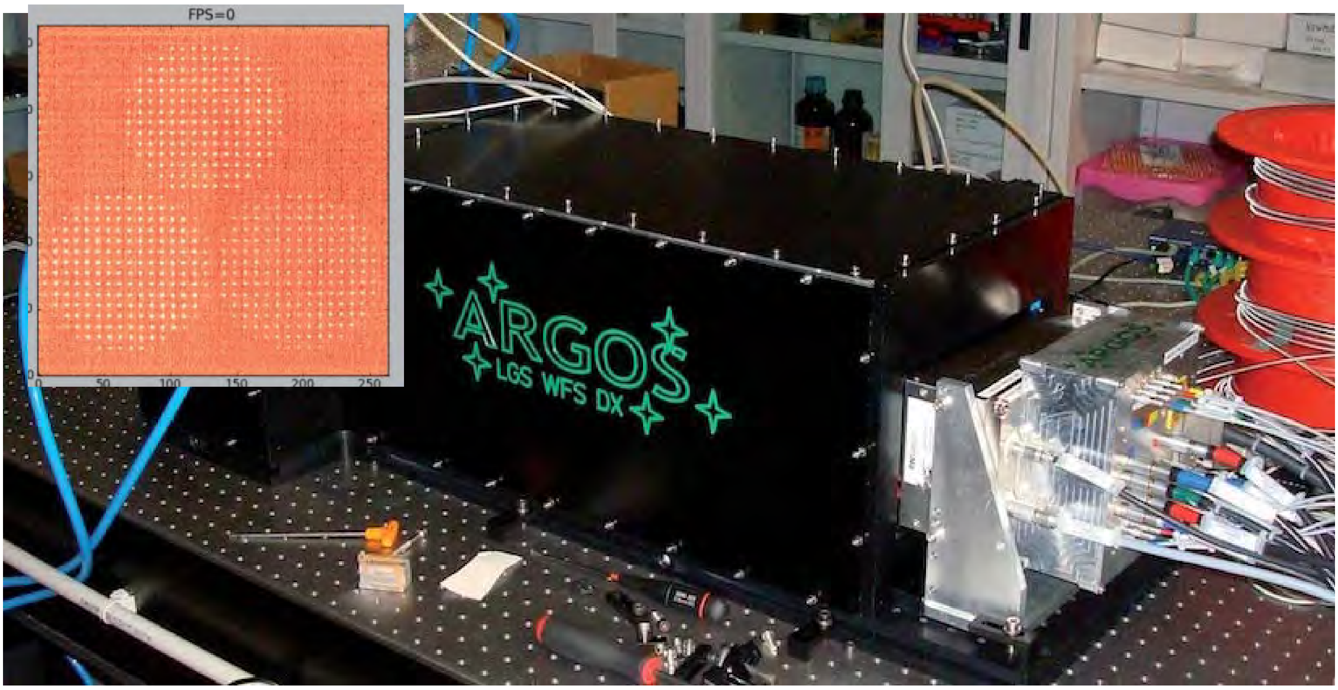

Developed together with PnSensor and the HLL, the ARGOS WFS camera can be operated at 1 kHz framerate with less then 3 electrons readnoise on its 256x256 pixel frame. The picture shows the camera system already attached to the wavefront sensor. On the first light image inset three SH spot patterns can be seen.

ARGOS utilizes Rayleigh scattering of high power laser beams in the earths atmosphere. The height of the guide star is determined with a Pockels cell system custom developed at MPE. The setup features:

- BBO double crystal system
- 10ns risetime
- negligable ringing
- 1:2000 suppression rates
- wide field suppression

Running at ~10kHz and 2µs opening time the cells discriminate the selected guide star distance of 12km and 300m range gate. To the right one of the cells is shown in the laboratory test setup.

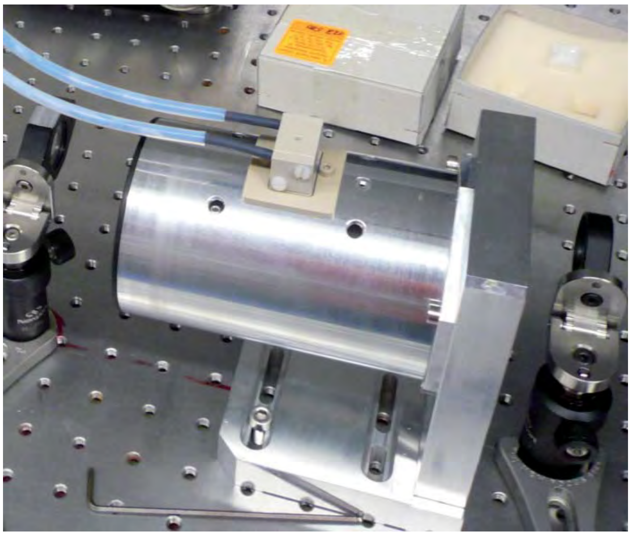

S. Rabien, G. Orban de Xivry

Laser System of ARGOS, Rayleigh guide star facility for LBT

ARGOS is the multi laser guide star facility for the Large Binocular Telescope (LBT), designed for ground-layer adaptive optics correction over a wide field of view. The laser system was developed, assembled and tested at MPE. Per each of the LBT telescopes, one of the thermally isolated, twin 'laser boxes' houses three high-power, pulsed, green lasers, along with optics to project the constellation of Rayleigh beacons to 12km altitude. Diagnostics are implemented for alignment, monitoring and flexure compensation. Prior to its recent shipment for installation, the system underwent an alignment and integrated testing phase.

Laser system components

- three commercial 18W lasers per LBT side, Nd:YAGs pulsed at 10kHz for range gating
- cameras imaging field and pupil plane, internal and auxiliary alignment cameras
- two tip-tilt mirrors control each beam
- beam power, polarization and collimation are monitored and controlled

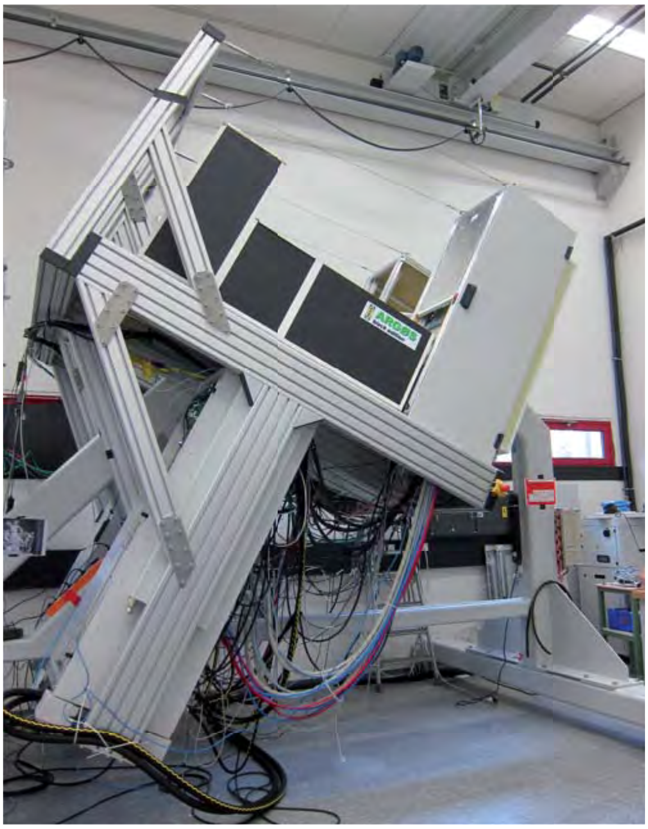

Alignment and integrated tests

- nominal constellation defined on a 2' radius, each beacon can be moved within 0.5'
- aligned using a focal mask (below), centered on a dedicated alignment laser
- 'telescope simulator' tests (left) confirmed very stable operation at up to 60° inclination, for full assembly with electrical supply racks
- position control loop compensates flexure, pointing accuracy of 0.1" before launch optics

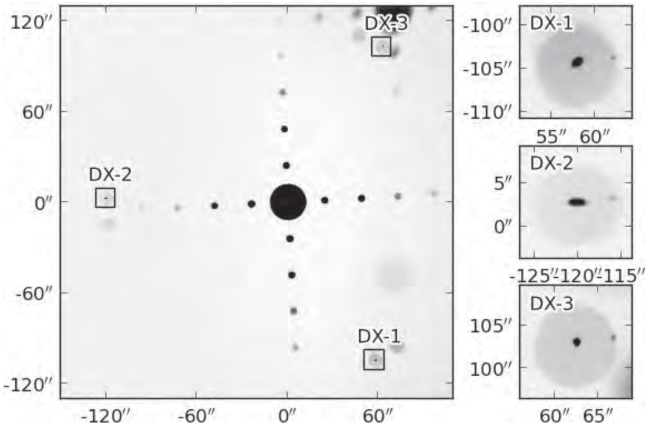

References:
- Loose et al., Proc. SPIE, Volume 8447, 2012

C. Loose for the ARGOS team

LUCI 1 & 2 at the LBT

LUCI-1&2 are the infrared imagers and spectrographs at the Large Binocular Telescope. LUCI-1 is used for science since 2009, LUCI-2 will be installed in summer 2013. Their unique multi-object spectroscopy capabilities allow for -among others- detailed studies of spectroscopic properties of galaxies over a wide range of redshift and classes of statistically significant samples leading to new insights on galaxy formation processes.

LUCI-1 & 2 (formerly LUCIFER) are the near-infrared imagers and spectrographs for the Large Binocular Telescope. They support seeing and diffraction limited direct imaging, long-slit, and multi-object (MOS) spectroscopy. The LUCIs are operating in the 0.9 - 2.5 micron spectral range, covering a field of view of up to 4x4 arcmin. The devices are built by a German consortium led by the Landessternwarte in Heidelberg. LUCI-1 is used for scientific observations since 2009, LUCI-2 will be installed at the telescope during summer 2013.

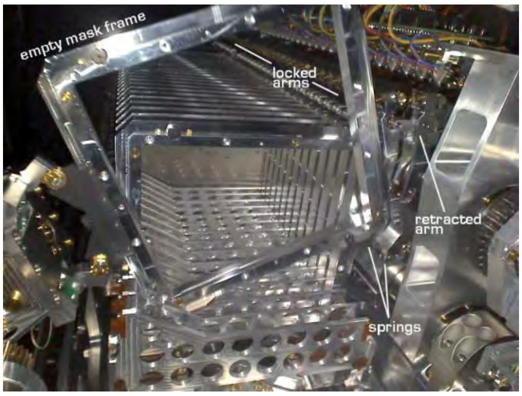

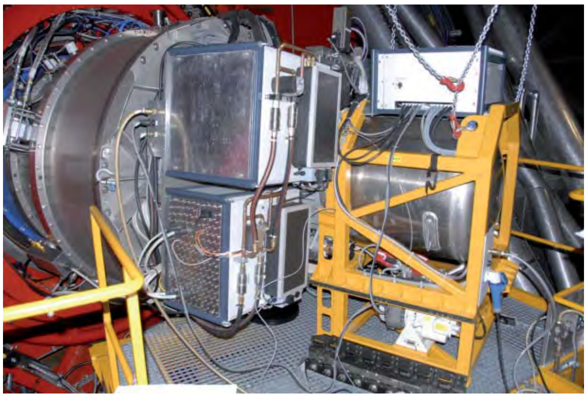

In the left picture an (empty) mask frame is taken out of the storage cabinet for transport to the focal plane. The image on the right shows LUCI-1 at the telescope with one of the auxiliary cryostats (yellow frame) attached during a cabinet exchange.

The IR/Submm group at the MPE contributes the complex, fully cryogenic MOS-units, featuring two main functionalities:

- **Mask exchange**: Selection, transport, and reproducible positioning in the focal plane of one out of 33 different long slit and multi slit masks for spectroscopic observations in any orientation and state of the instrument within a few minutes
- **Cabinet exchange**: removal of the cabinet containing “observed“ masks and insertion of a cabinet with “new“ masks during daytime operation - without loosing the cryogenic conditions of the instrument, a unique feature of the LUCI instruments

References:

- Buschkamp et al., Proc. SPIE, Vol 8446 (2012)

H. Gemperlein, P. Buschkamp, R. Hofmann

KMOS Data Analysis Software (pipeline)

KMOS is a multi-object near-infrared integral field spectrometer with 24 deployable pick-off arms installed at the VLT. The data processing pipeline, developed at MPE, has been used successfully for analysis of commissioning data since the instrument's first light in Nov 2012. A novel aspect of the pipeline is that the raw data can be reconstructed into a cube in a single step. The pipeline is now available to the community for reduction of KMOS data.

The KMOS pipeline calibration recipes create look-up tables instead which associate each measured value on the detector withs its spatial and spectral location. Using these look-up tables to interpolate the 3D data cube, has the following advantages:

- Bad pixels are simply ignored (they don‘t appear in the look-up table)
- Calibration does not fix the pixel scale in the final data cube
- Interpolating more than one frame simply increases the size of the look-up tables but still only a single interpolation step is needed
- Flexure (spatial and spectral) can be compensated by applying the measured offsets back to the look-up tables. The 3D data cube can then be re-interpolated again.

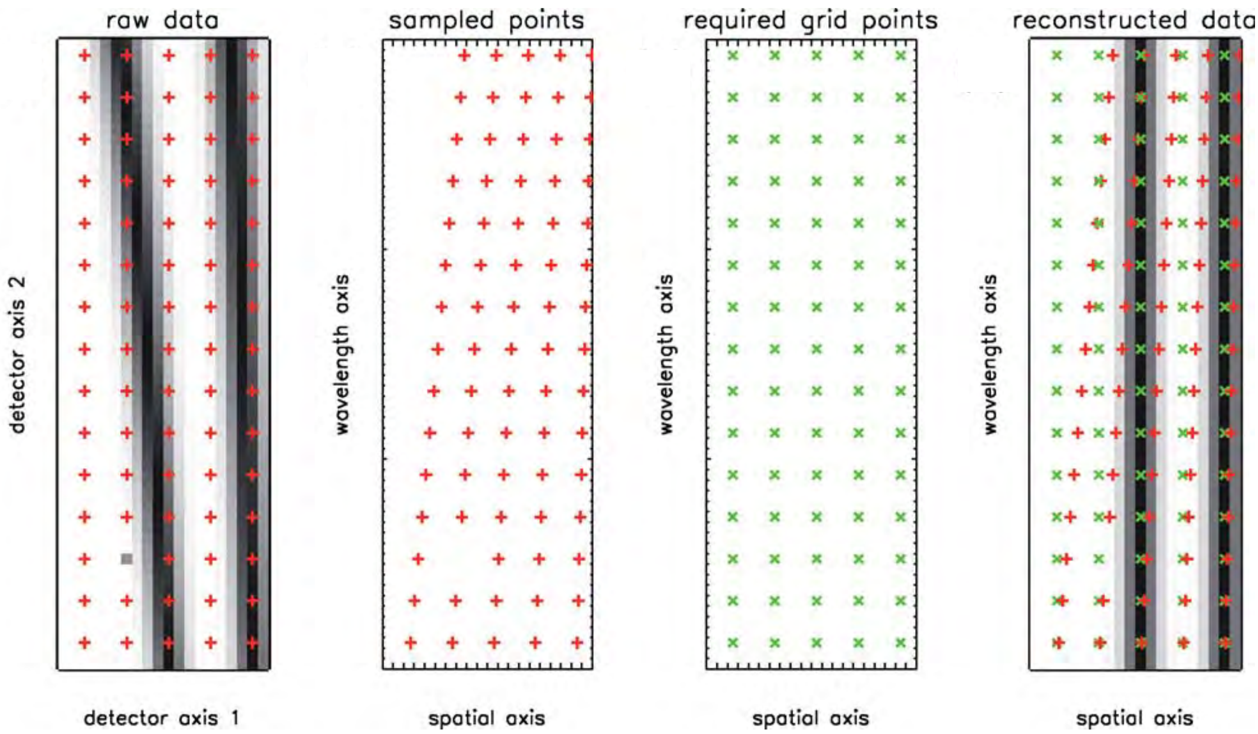

Figure: Dark shadows show the signal, red crosses the sample points where data is taken on the detector. Green crosses indicate the required, regular grid points.

References:

• KMOS Data Flow: Reconstructing Data Cubes in One Step , R. Davies et al., 'Ground-based and Airborne Instrumentation for Astronomy III', SPIE, Vol. 7735, June 2010
• KMOS Data Reduction Library Design & User Manual, R. Davies et al., VLT-MAN-KMO-146611-007, https://wiki.mpe.mpg.de/KMOS-spark/InstallationPages

E. Wiezorrek, R. Davis, A. Agudo Berbel, N. M. Förster Schreiber

ERIS Overview

ERIS (Enhanced Resolution Imager and Spectrograph) is a new ESO instrument for the Cassegrain focus of VLT UT4 to be commissioned in late 2017. It combines the existing integral field spectrograph SPIFFI with a new near infrared camera and a wavefront sensor module for the ESO adaptive optics facility. MPE upgrades SPIFFI and builds the camera.

For VLT UT4 ESO builds an adaptive optics (AO) facility featuring
- a deformable secondary mirror,
- four laser guide stars.

At the time when this facility will be installed, two instruments become obsolete:
- the near infrared integral field spectrograph SPIFFI,
- the diffraction limited imager CONICA.

SPIFFI and CONICA will be replaced by ERIS which comprises:
- an upgraded version of SPIFFI,
- a near infrared camera which provides most of the CONICA observing modes,
- a wavefront sensor module feeding the AO facility.

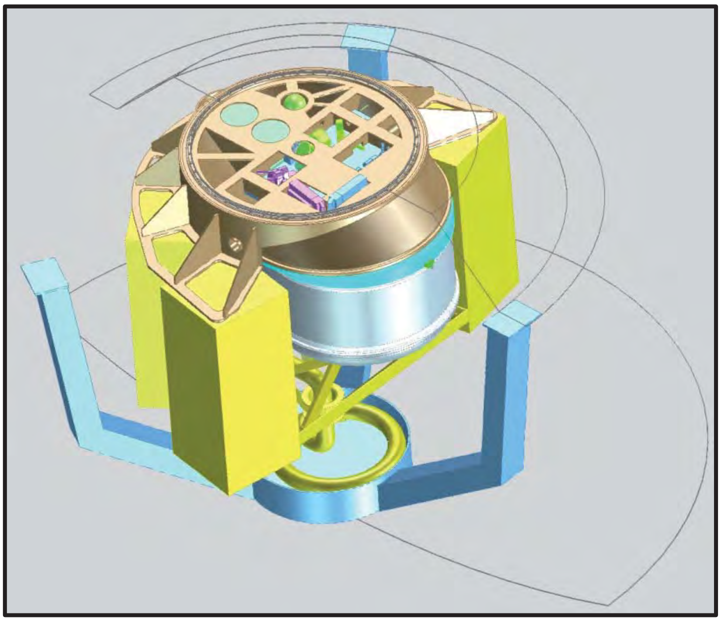
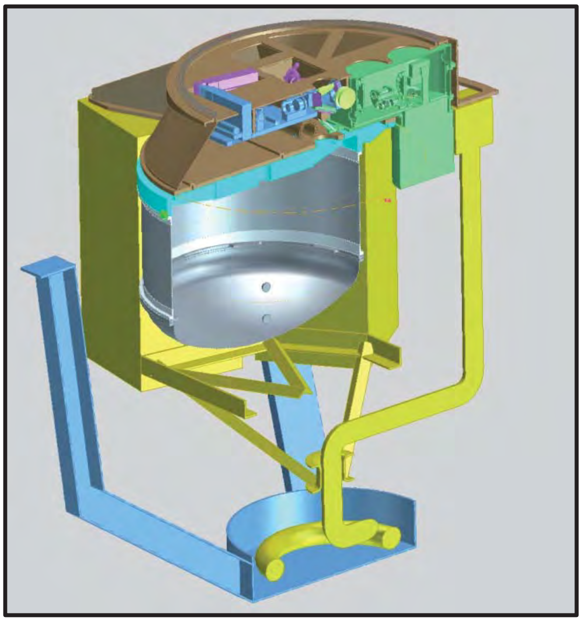

MPE has been involved in the ERIS phase A study which ended in May 2012. The concept emerging from this study is presented in the two pictures:
- The telescope interface (brown) carries the wavefront sensor module (blue and magenta), the near infrared camera (green), and the calibration source (light green).
- SPIFFI (the large cylindrical vessel) is attached to the bottom of the telescope interface.
- Four yellow boxes mounted around SPIFFI house the instrument electronics.
- The blue tripod carries the cable wrap.

In December 2012 ESO issued a call for proposal for the upgrade of SPIFFI, the ERIS camera, and subunits of the wavefront sensor module. MPE applied for the first two items and has been selected by ESO in March 2013 to provide both.

R. Hofmann, F. Eisenhauer, H. Feuchtgruber, M. Hartl, J. Schubert, E. Sturm, K. Tarantik, E. Wiezorrek

MICADO: First Light Instrumentation for the E-ELT

MICADO, the Multi-AO Imaging Camera for Deep Observations, is one of two first-light instruments identified by the European Southern Observatory (ESO) for the 40m-class next generation European Extremely Large Telescope (E-ELT). MICADO will provide diffraction limited imaging and long-slit spectroscopy in the near infrared (NIR) wavelength range.

The MICADO consortium – led by MPE – successfully completed a Phase A study commissioned by ESO. The start of Phase B is scheduled for early 2014.

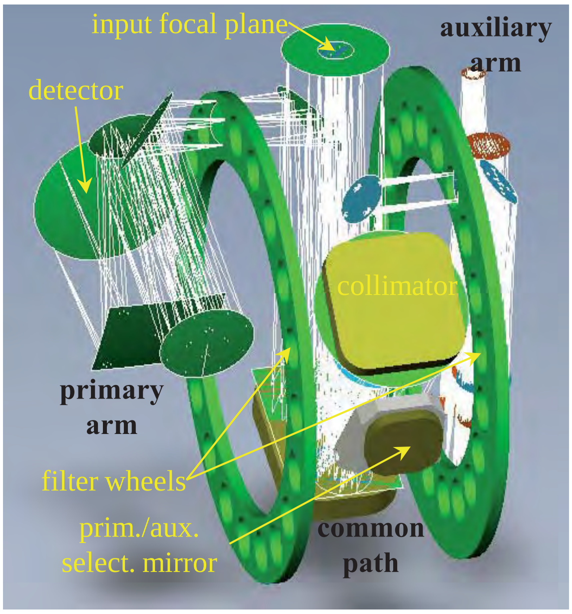

MICADO optical design overview at the end of Phase A

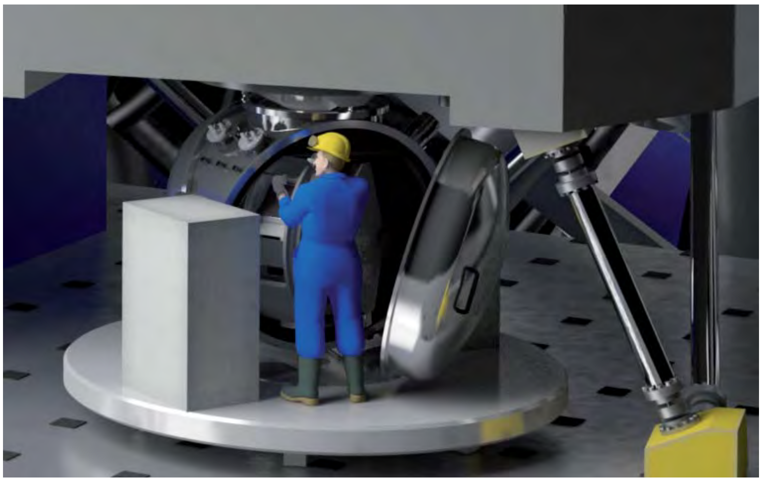

MICADO as it might look under the multi-conjugate AO system MAORY

Challenging technical requirements are imposed on the instrument design by the science cases:

- *precision astrometry* of stellar motions within light hours of the Galaxy's black hole, of intermediate mass black holes in stellar clusters, of orbits of globular clusters around the Galaxy, and of exo-planets around nearby stars.
- *high sensitivity, resolution, and contrast imaging* of stellar populations out to the Virgo cluster, of solar system bodies to characterise physical properties, of galaxy structures at z>1 and to detect galaxies at z>7, and to characterise young massive exo-planets.
- *wide wavelength coverage spectroscopy* of stellar types and 3D orbits in the Galactic Center, of metallicities from absorption lines in elliptical galaxies at z~2-3, of high z transients (e.g. supernovae to z~6), and of emission lines of starburst galaxies at z~4-6.

References:

• Trippe S., et. al., MNRAS, **402**, 1126 (2010): *High Precision Astrometry with MICADO at the E-ELT*
• Davies R., et. al., Proc. SPIE, **7735**, 77352A-1 (2010): *MICADO: the E-ELT Adaptive Optics Imaging Camera*

M. Hartl, R. Davies, J. Schubert, E. Sturm, J. Kurk

SPICA - SAFARI

The Japanese space agency JAXA is presently performing an assessment study of the planned Space Infrared Telescope for Cosmology and Astronomy (SPICA), with the aim to decide on the mission implementation in late 2013 for a scheduled launch in 2022. SPICA will cover the wavelength range from 5 – 210µm with focal plane instruments provided by Japanese and international consortia. ESA would contribute the cryogenic telescope (diameter: 3.2m). A European consortium, lead by SRON (NL) and including MPE, is planning to contribute the core instrument SAFARI, an imaging spectrometer and photometer for the 35 – 210µm range.

- Herschel has resolved the Cosmic Infrared Background, around its peak in emission, into individual galaxies, but with very little spectroscopic information
- Spectroscopic follow-up of these sources in the diagnostic mid/far-infrared lines will need an actively cooled (< 10 K) telescope to reach the required sensitivity
- New detector technology is needed to match low background photon noise
- The European SAFARI instrument on the Japanese SPICA combines these capabilities:
    - Flexible, imaging Fourier-transform spectrometer / camera
    - Low-noise detector technology – TES bolometers with multiplexed SQUID readout
    - Spectral/spatial multiplexing → 30 x better line sensitivity than PACS spectrometer!

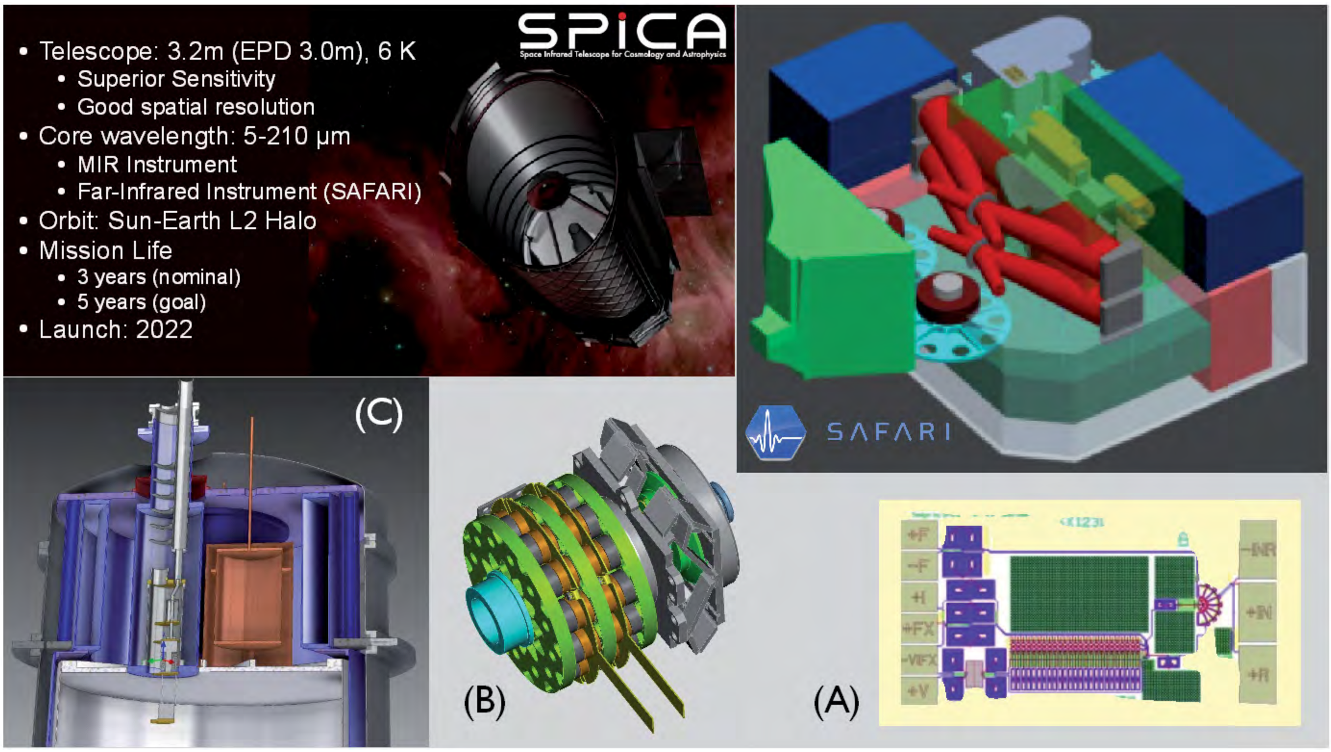

MPE will provide – through a collaboration with PTB (Berlin) – the SQUID circuits (A) for the readout of the TES detectors and the signal line drivers, ultra-low dissipation motors (B) for the cryo-mechanisms, and the cryogenic test facility for detector characterization (C).

A. Poglitsch, L. Barl, W. Raab, J. Schubert, E. Sturm and the SAFARI Team

Herschel-PACS: absolute flux calibration

The PACS flux calibration is based on regular observations of 5 fiducial stars: β And, α Cet, α Tau, α Boo, and γ Dra. With the recently established corrections for detector temperature effects (Fig. 1) we reach an intrinsic uncertainty (repeatability) of better than 2%. The absolute flux calibration is limited by the model errors for the fiducial stars, given with **5% at the PACS reference wavelengths of 70.0, 100.0 and 160.0 µm**.

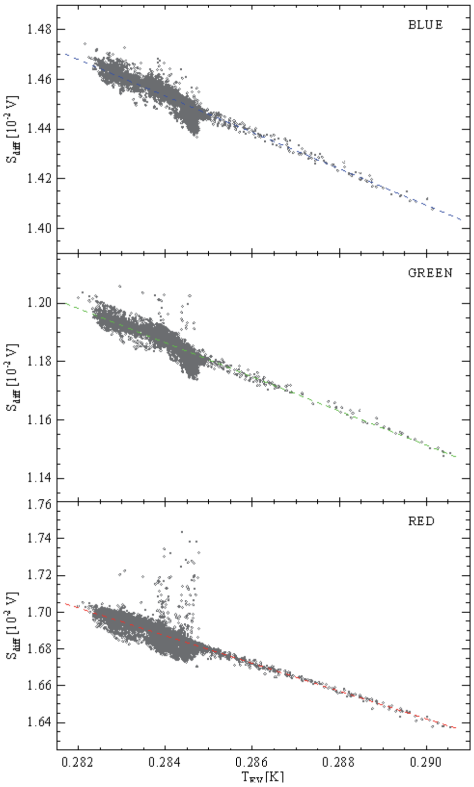

Fig. 1: Correlation between PACS bolometer signal and evaporator temperature

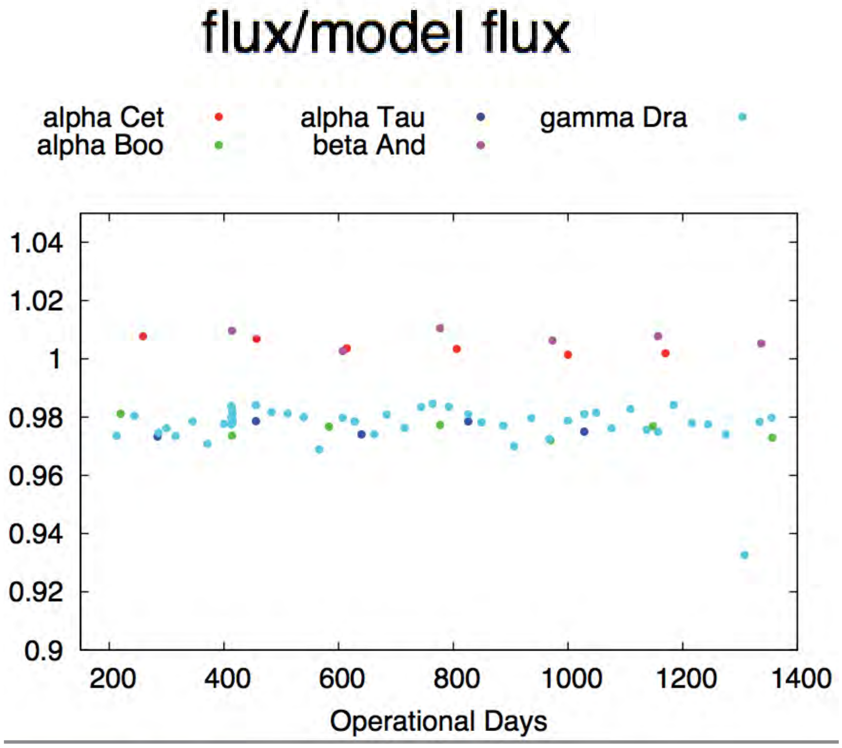

Fig. 2: PACS Photometer absolute flux calibration via stars and stability during the Herschel mission

The high absolute accuracy level and the detector stability was confirmed via observations of well-known asteroids and the planets Neptune/Uranus. These measurements were also used to complement instrument calibration activities:

- characterization of detector non-linearity: linear response up to ~100Jy, small corrections for brighter sources
- colour corrections: tabulated for a wide range of source SEDs
- point-spread-function characterisation: library of PSF-measurements & models available
- search for filter leaks: nothing found
- establishment of the spectrometer's relative spectral response function
- cross-calibration of sub-instruments (photometer & spectrometer fluxes agree within 10%) and observing modes (4-6% flux offset between chop-nod & scan-map observations).

The PACS photometer results for point- and extended sources are found to agree within 5-20% with SPIRE and previous far-IR observations (ISO, Akari, Spitzer) at similar wavelengths.

T.G. Müller and the PACS ICC team

Herschel Spacecraft Pointing Improvements

The pre-launch requirement for the absolute spacecraft pointing error (APE) of the Herschel Space Observatory was <3.7“. This requirement is indeed fullfilled, but generous given PSF sizes down to 5“. Growing knowledge of the satellite pointing system and the statistics of observed pointing errors facilitated substantial improvements to the on-board attitude determination and the a posteriori on-ground spacecraft pointing reconstruction by:

- Application of image corrections, in the star tracker (STR) on-board software for optimized real-time performance
- On-ground removal of residual STR CCD pixel-structure induced distortions
- Identification and removal of badly performing guide stars from the star catalog

Finally the APE could be improved down to <0.9“. However the relative pointing error (RPE) or pointing jitter turned out to be the main source for pointing induced noise in PACS spectrometer observations. We developed a new algorithm to combine the STR reconstructed absolute pointing with the Herschel gyroscope attitude information, resulting in a relative pointing reconstruction precision of better than 0.1“ and improved Strehl ratios for numerous PACS photometer observations.

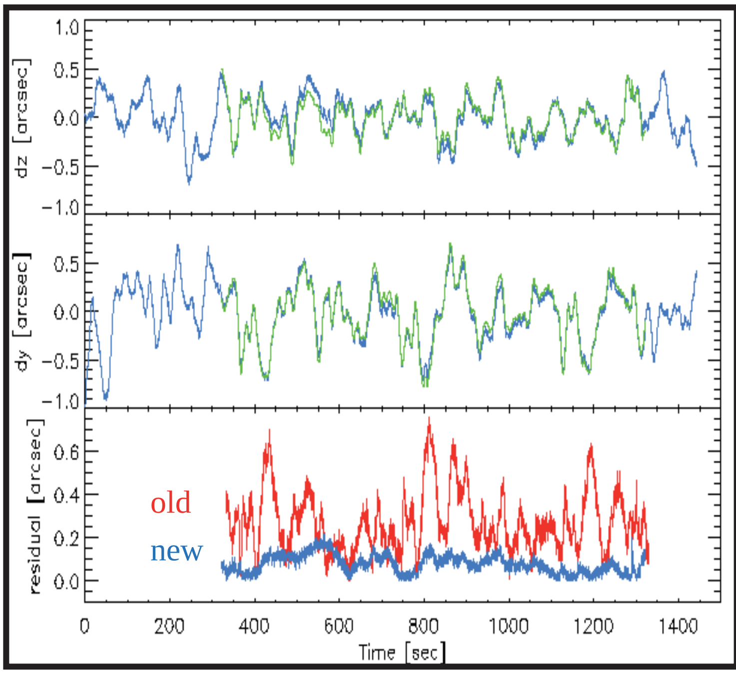

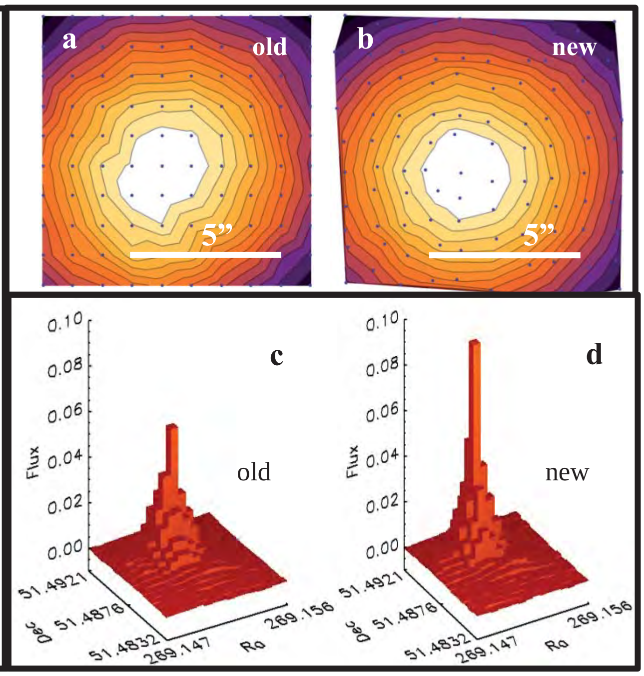

Figures:
Left: time sequence of spacecraft coordinates during an observation of R Dor as measured (green) on the blue PACS photometer array and as reconstructed (blue) by STR+Gyro information (upper plot: dz; middle plot: dy). The residual deviation of the reconstructed attitude from the observed position (lower plot) for the nominal pointing reconstruction (red) and for the improved algorithm (blue).
Right: Central part of the PACS spectrometer PSF at 94µm reconstructed from default attitude information (a) and from the new algorithm. Blue 70µm PACS photometer image of γ Dra, processed without (c) and with (d) the new STR+Gyro attitude reconstruction algorithm.

H. Feuchtgruber, A. Poglitsch

The PACS Spectrometer
Data Processing and Analysis Software

The PACS Instrument Control Centre (ICC) team at MPE develops a large part of the software for processing the PACS[1] spectrometer raw data to obtain calibrated spectra. In addition, we provide interactive tools and guidelines to adapt this processing for specific scientific goals, and to further analyse the calibrated spectra to produce publication ready data. All this software runs within the Herschel Interactive Processing Environment (HIPE[3]) and/or is used for automatic processing at the Herschel Science Centre (HSC).

Data Processing

The data processing[2] to obtain calibrated spectra involves organization in blocks, spatial and wavelength calibration, flux calibration, flagging of glitches, saturation, etc., background subtraction, rebinning and mapping.

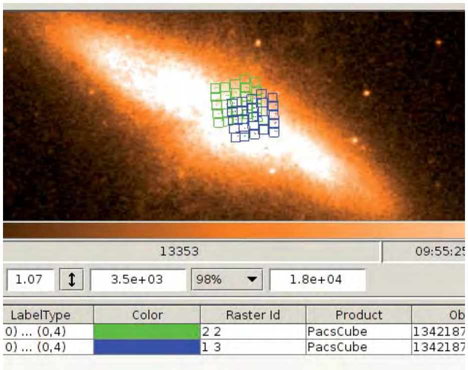

Fig 1: Footprint viewer showing some PACS spectrometer pointings on a galaxy image

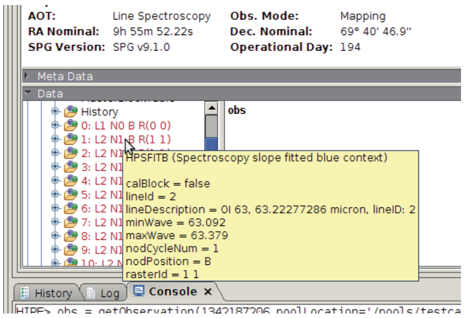

Fig 3: Organized data in the HIPE observation viewer

Interactive Analysis

- We provide Python scripts for step-by-step processing of each type of observation.
- These scripts contain elaborate guidelines on how to use the tools we provide for interactive analysis of intermediate data.
- One of these tools is the Spectrum Explorer (see Fig. 2), with which one can explore individual spectra in a cube, mask data, compute velocity and intensity maps, extract/fit spectral lines, etc.
- Other tools for exploring an observation are shown in Figures 1 and 3.

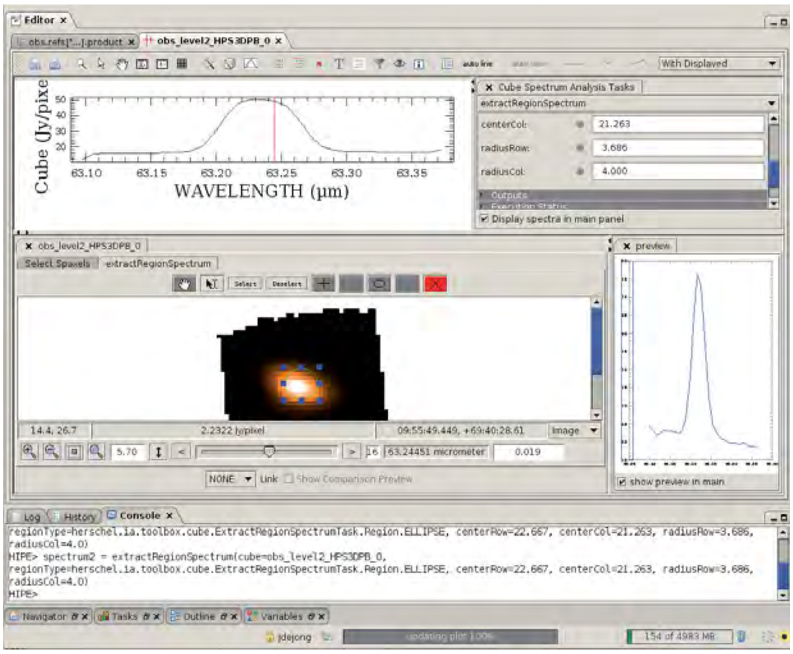

Fig 2: Spectrum Explorer showing the [O I] 63 µm spectral line map of a galaxy and the integrated spectrum

References:
1. Poglitsch, A. et al., 2010, A&A 518, 2
2. Schreiber, J. et al. 2009, ASPC 411, 478
3. Balm, P. 2012, ASPC 461, 733

J.A. de Jong, A. Contursi, H. Feuchtgruber, A. Poglitsch, E. Sturm, E. Wieprecht and the PACS Spectrometer Team

Herschel Interactive Processing Environment: the PACS photometer pipeline

The PACS photometer pipeline is developed and maintained by the PACS Instrument Control Centre at MPE, with contributions from NHSC and HSC. It allows PACS users and archive diggers to visualise and re-process the PACS data according to specific scientific goals. In addition to providing a suit of tools to display and analyse the data, HIPE also allows plugin-in from external add-ons and to use VO capabilities for source identification and external visualisations.

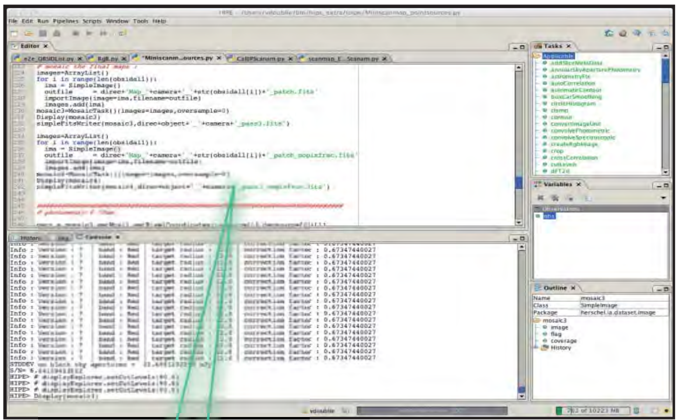

Fig. 1 PACS data reprocessing and analysis environment

1- PACS pipeline runs in a java based standalone environment, HIPE*, that allows to extract PACS observations from the Herschel archives, visualise and manipulate the automatically processed products.

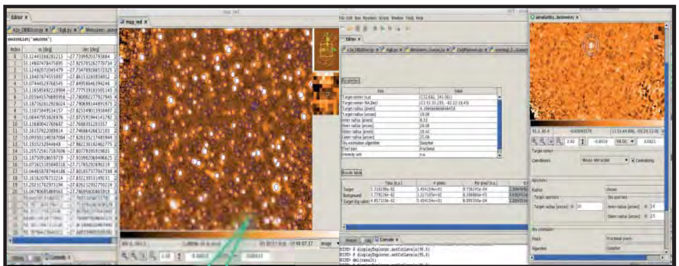

Fig. 4 Hipe tools: Source Extractor, Aperture photometry

3- Analysis tools such as aperture photometry and source extractions are available in both command-line and in dialog windows (GUIs) options

(*)HIPE is a joint development by the Herschel Science Ground Segment Consortium, consisting of ESA, the NASA Herschel Science Centre, and the HIFI, PACS and SPIRE consortia.

2- Interactive/tuneable scripts are available to the users according to science cases.

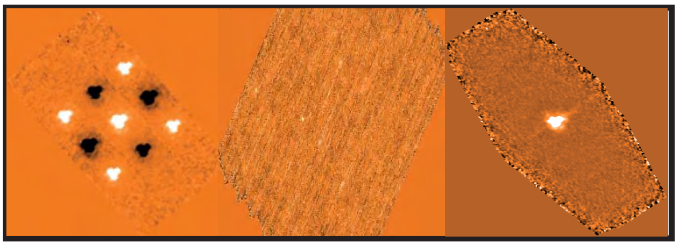

Fig. 2 PACS point sources observing modes: chop/nod, Parallel, scans

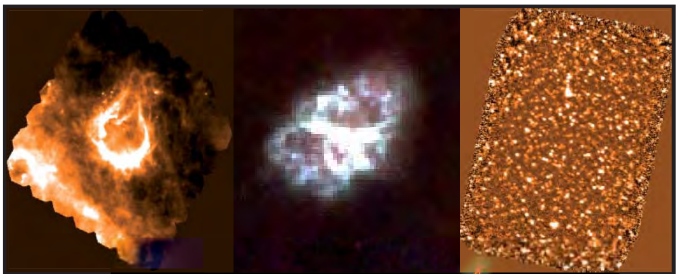

Fig. 3 PACS large maps: galactic, extragalactic, cosmic

4- PACS data processing and analysis environment, still being improved, allows to re-process data to science grade quality and provides tools to analyse the PACS photometer data for publications and/or prepare follow-up observations for coming missions e.g. ALMA or SPICA.

References:

•http://herschel.esac.esa.int/hcss-doc-10.0/index.jsp#pacs_phot:pacs_phot

•http://herschel.esac.esa.int/twiki/bin/view/Public/PacsCalibrationWeb

V. Doublier Pritchard and PACS-MPE Team

QFitsView – A versatile FITS viewer

QFitsView is an open source FITS viewer and manipulator developed at MPE, available for all major operating systems. It combines the power of a comprehensive scripting language and the ease of use of an interactive graphical user interface.

- Displaying 1D, 2D and 3D FITS files
  - as interactive wiregrid, contour, linemap or volume rendering
  - with multiple extensions simultaneously
- Online display of spectra in FITS cubes
  - with optional source-continuum subtraction on selected regions
- Access to commonly used data reduction functions and analyses via dialog boxes
- Interactive fitting of multiple gaussians and lorentzians to spectra

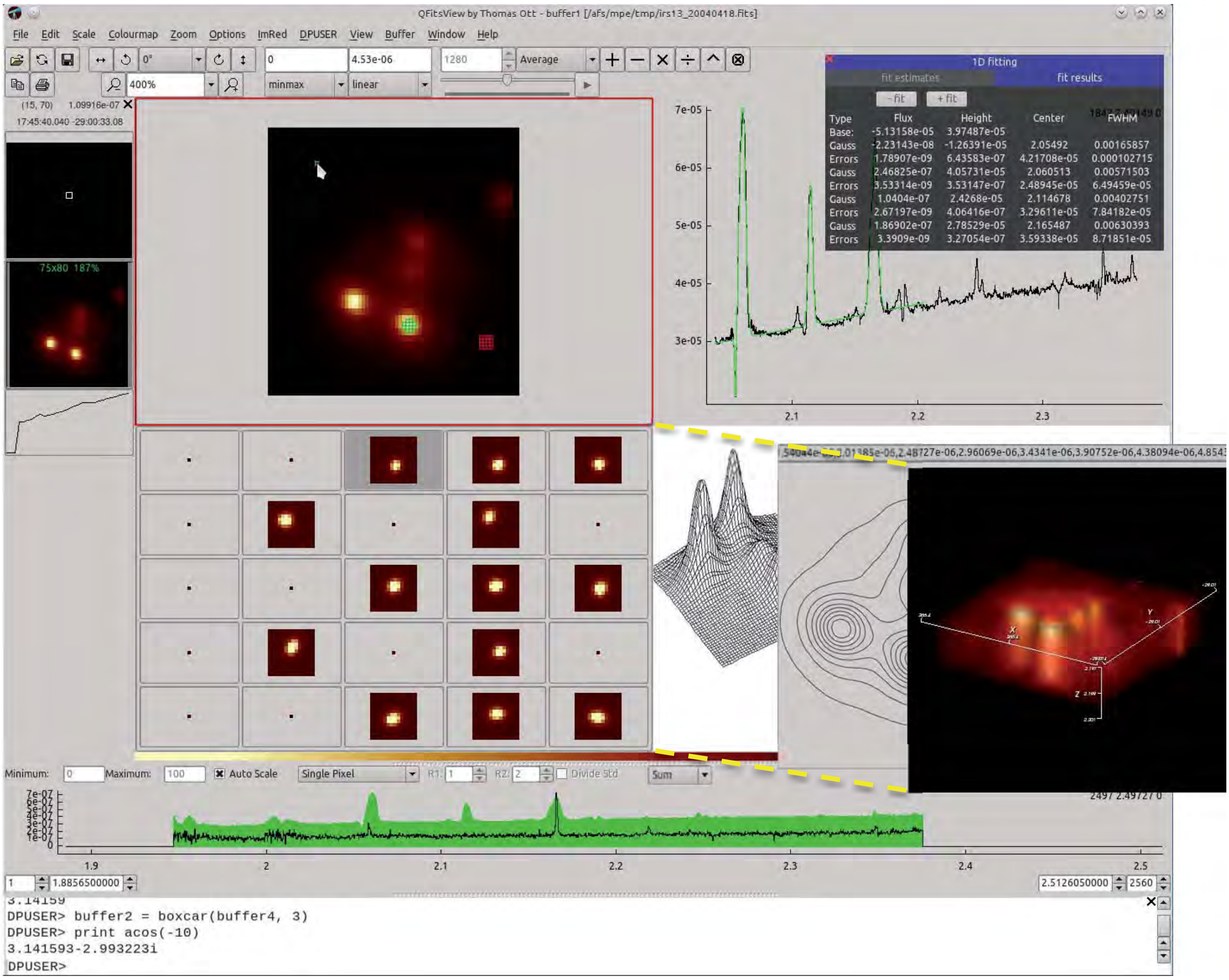

References:
- www.mpe.mpg.de/~ott/QFitsView

A. Agudo Berbel, T. Ott

I.1) Group: Prof. Ewine F. van Dishoeck

Water in star-forming regions with Herschel
A WISH come true

MAX-PLANCK-GESELLSCHAFT

Water is a key molecule in astrochemistry and origin of life. The WISH program observes water and related molecules in 80 sources, from low- to high-mass protostars, and from cold cores prior to collapse to the late stages of protoplanetary disks using Herschel-HIFI and PACS. Both the physical and chemical evolution are probed.

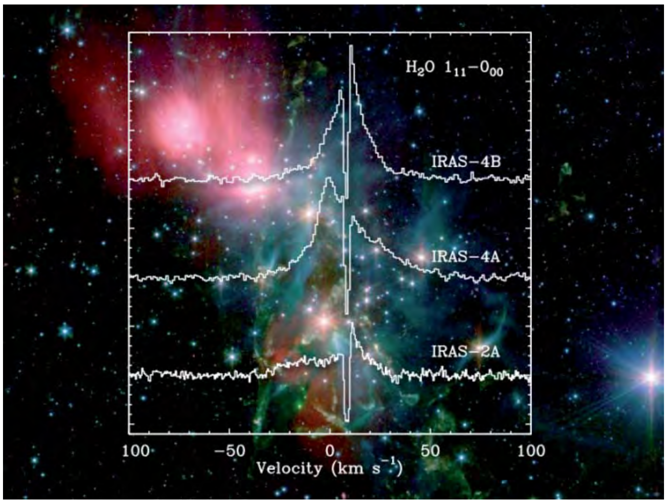

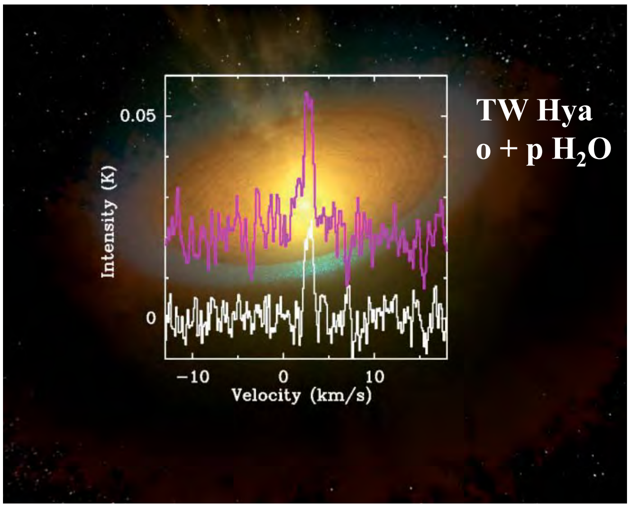

Left: HIFI spectra of water toward low-mass protostars in NGC 1333, indicating warm fast-moving water in outflows as well as cold absorption (Kristensen et al. 2012). Right: First detection of cold water in a protoplanetary disk (Hogerheijde et al. 2011).

Main results

- Water is formed mostly as ice in the pre-stellar stage and transported to disks (see cartoon)
- Water and CO probe the physics of hot, dense irradiated shocks in protostars (see poster Karska)
- The cold water reservoir in disks is equivalent to several thousand oceans, available for planet formation

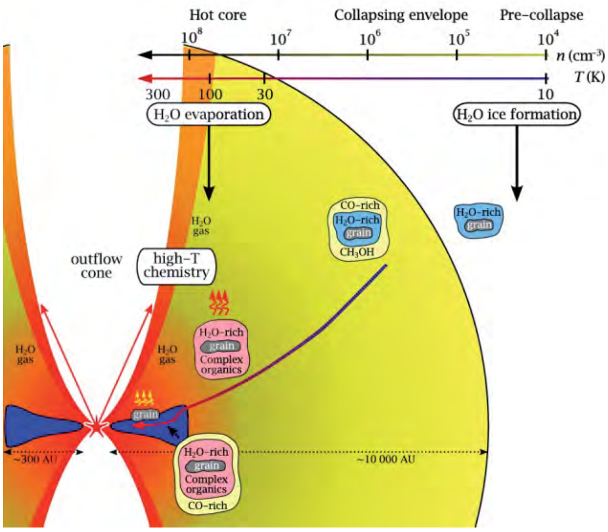

References:

• van Dishoeck et al. 2011, PASP 123, 138; Caselli et al. 2012, ApJ 759, L37; Hogerheijde et al. 2011, Science 334, 338; Kristensen et al. 2012, A&A 542, A8; Visser et al. 2009, A&A 495, 881

E. van Dishoeck, A. Karska, S. Bruderer and the WISH team

Herschel survey of very young low-mass protostars

Protostars interact with their surrounding envelopes through shocks and UV radiation resulting in warm molecular gas (T~100-1000 K). We present a *Herschel*-PACS survey of 18 deeply embedded low-mass protostars at different stages of evolution. With PACS's unprecedented sensitivity, spatial and spectral resolution at 55-210 μm, all major far-IR gas cooling lines are detected: CO, H_2O, OH, [OI] and [CII]. Both the excitation and spatial distribution are used to distinguish the different physical processes involved.

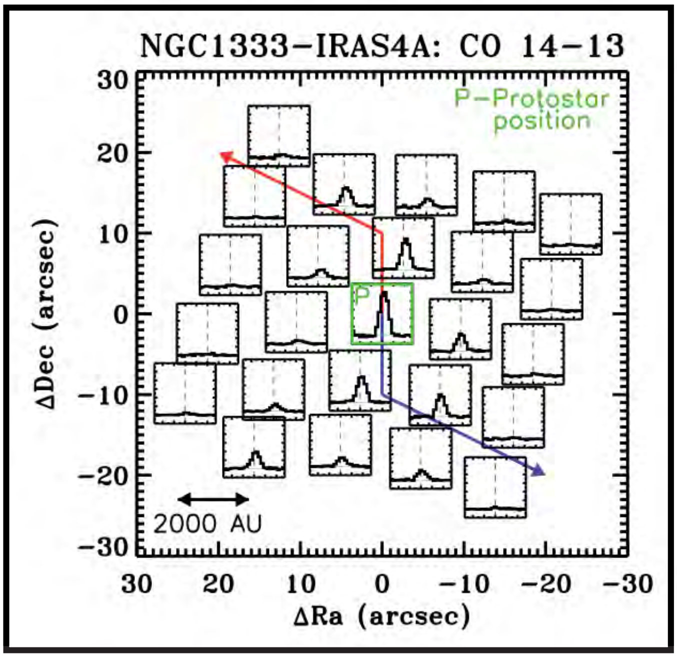

Fig.1. PACS spectral map of Class 0 object NGC1333-IRAS4A in CO 14-13. Outflow direction from sub-mm observations is shown.

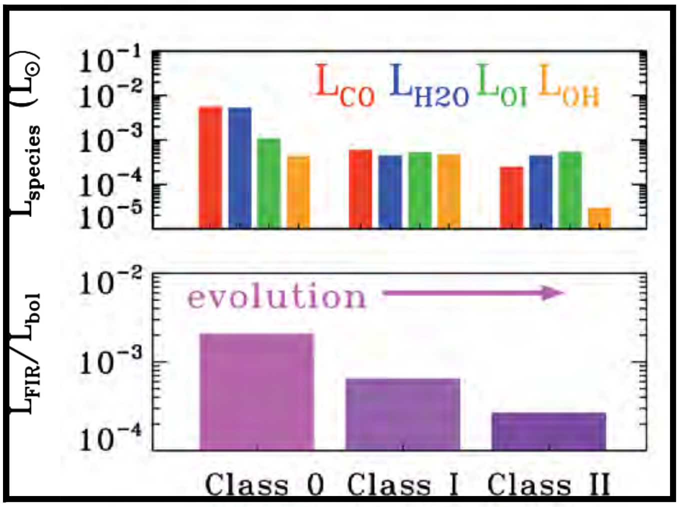

Fig.2. (*Top*) Cooling in CO, H_2O, OH, and [OI] lines for Class 0, I, and II objects. (*Bottom*) Evolution of the total far-IR gas cooling over bolometric luminosity.

RESULTS:

✧ H_2O is detected in all sources, up to high excitation (E_{up}/k_B~1000 K);

✧ Excitation diagrams of CO show two distinct components at T_1~300 K and T_2~700 K; H_2O diagrams show T~150 K;

✧ Strong correlation between high-*J* CO and H_2O line fluxes and (extended) pattern of emission; no correlation with [OI];

CONCLUSIONS:

✧ Two physical components probed by PACS data: non-dissociative (irradiated) shocks (traced by H_2O and CO) and dissociative shocks (seen in OI, OH along outflows);

✧ Total far-IR cooling dominated by H_2O and CO. Fraction contributed by [OI] increasing for more evolved sources;

✧ L_{FIR}/L_{bol} decreases with evolution.

References:
• Karska, A., Herczeg, G., van Dishoeck, E.F., et al. 2013 (A&A, in press)

A. Karska, G. J. Herczeg, E. F. van Dishoeck, and WISH team

Anatomy of a low-mass protostar: VLA1623's "merry-go-round" with ALMA

VLA1623 is a triple non-coeval protostellar system in ρ Ophiuchus (120 pc). The system's young protostar, VLA1623A, presents structures in molecular lines that have characteristics of a disk and a ring. Using ALMA observations, we study their physical structure and chemistry.

How do multiple stellar systems form?
When do disks form?

- Fragmentation: during collapse vs. envelope
- Disk formation influenced by fragmentation?

Methods: ALMA and SMA observations
Models

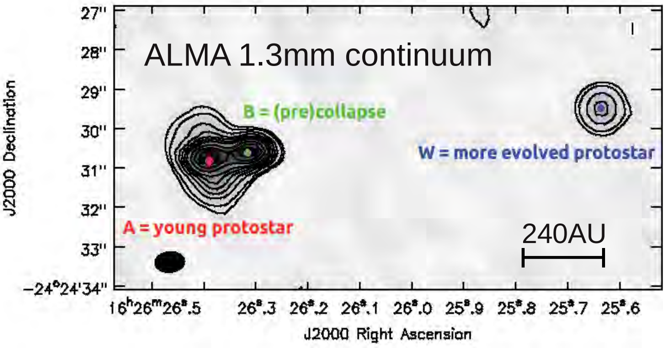

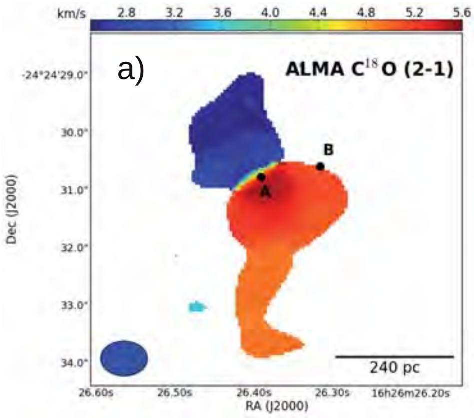

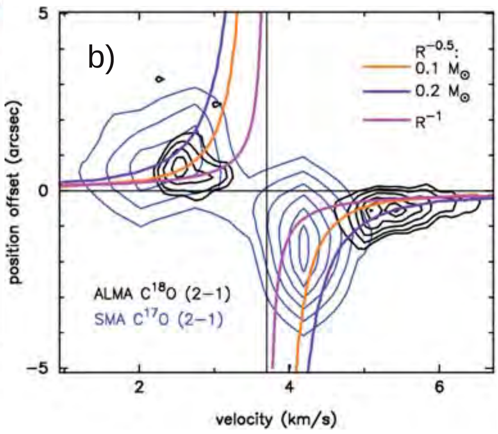

$C^{18}O$ and $C^{17}O$ emission show rotating disk-like structure centered at VLA1623A and consistent with Keplerian rotation $v \propto R^{-0.5}$ (fig. b).

VLA1623A's disk is the **youngest** yet observed.

DCO^+ shows a clumpy ring-like structure bordering on the $C^{18}O$ emission (fig. c).

CO isotopologues freeze out below temperatures of 20~30K, which enhances DCO^+.

Observed DCO^+ emission consistent with physical chemical models (red and green circles; model of Jørgensen et al. 2002).

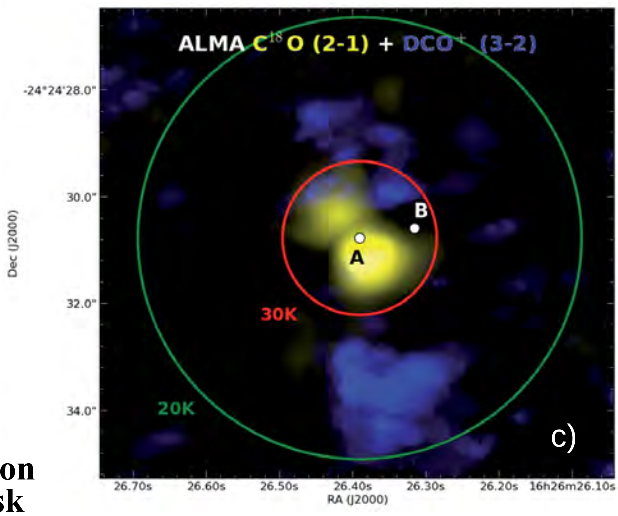

Conclusions:

- Non-coeval VLA1623 → **envelope fragmentation**
- VLA1623A shows the **youngest protostellar disk** yet observed
- DCO^+ traces a ring around VLA1623A, reflecting the cold gas and depleted CO regions → **chemical tomography.**

References:

- Jørgensen et al. 2002, 2005
- Murillo & Lai, 2013

N. Murillo, S. Bruderer, E. van Dishoeck, et al.

Molecular gas in the cavities of transition disks
The cradle of gas giant planets?

Understanding the evolution of protoplanetary disks is crucial to constrain theories of planet formation. After a few million years, protoplanetary disks disperse from gas-rich to gas-poor disks. Giant planet formation needs to take place before this dispersal.
In the transition disk phase, submillimeter continuum images and the spectral energy distribution reveal the presence of dust free cavities with radii of several 10 of AUs. Different scenarios for the formation of these cavities have been suggested, including the most exciting one: clearing by a young planet.
ALMA allows for the first time to study the gas in cavities of transition disks (e.g. van der Marel et al. 2013). We have developed new chemical, thermal and radiative transfer models of transition disks (Bruderer et al. 2012, Bruderer 2013). We find that observations of CO and isotopologue rotational lines allow to measure the gas mass in the cavity, which in turn constrains physical conditions in planet forming regions and the mechanism leading to dust cavities.

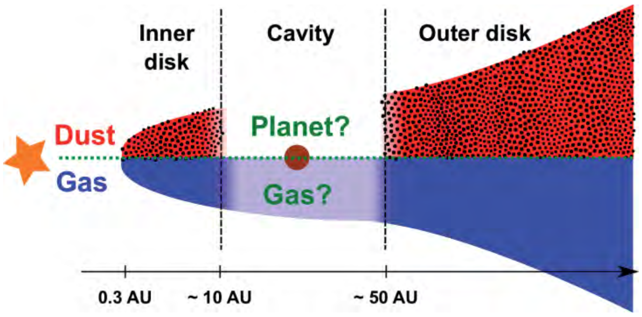

Figure 1: Possible scenario of a transition disk.
Upper half: dust structure with a cavity carved out by a planet.
Lower half: gas structure. It is currently not known if gas remains in the cavity and can form further planets.

Figure 2: Simulated CO fractional abundance. Panels from left to right show decreasing gas masses in the cavity (0.006, 0.6, 6000 M_{earth}). Stellar UV light photodissociates CO to C^+ in the upper disk. This C^+/CO transition shifts to larger heights with increasing gas mass. Note that CO survives inside the cavity down to very low masses and is thus a good gas mass tracer.

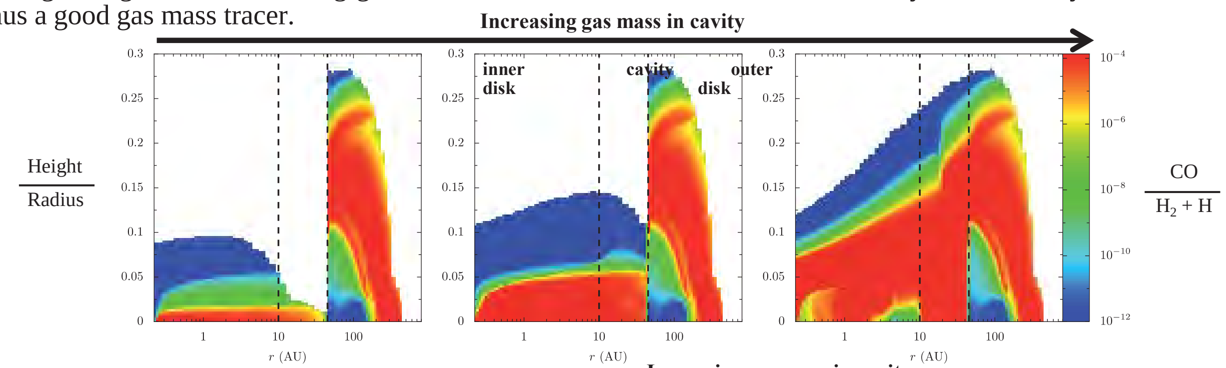

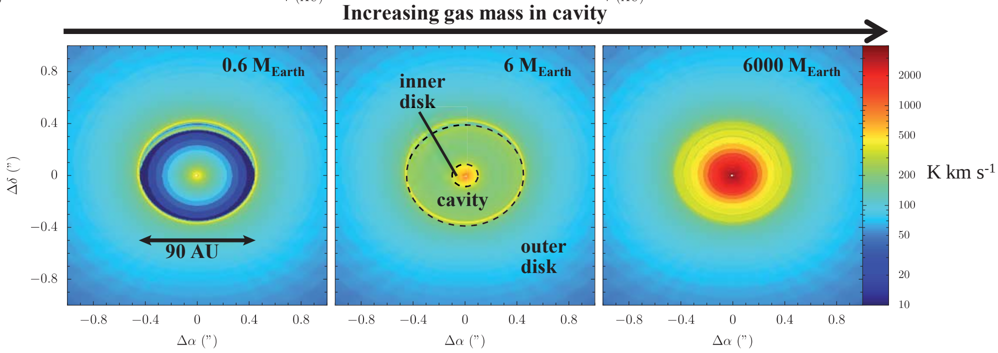

Figure 3: Simulated integrated intensity map of ^{12}CO(J=3-2) from a transition disk. ALMA can readily distinguish these cases.

References:

- S. Bruderer, E.F. van Dishoeck, S.D. Doty, G.J. Herczeg 2012, A&A, 541, A91
- S. Bruderer, 2013, submitted
- N. van der Marel, E.F. van Dishoeck, S. Bruderer et al. 2013, submitted

S. Bruderer, E. F. van Dishoeck

Gas in planet-forming disks with Herschel

What determines the composition of planet atmospheres? How were the volatile species (e.g. H_2O) delivered to Earth? To answer these questions we study the chemical composition of planet-forming disks around newly born stars.
Multi-wavelength spectroscopy allows us to constrain the radial distribution of different species in the disk (Fig. 1). The near-IR spectrum of young stars reveals an H_2O-rich disk atmosphere around T Tauri stars ($M < 1.5\ M_{sun}$). In contrast disks around the more massive Herbig AeBe stars ($M > 1.5\ M_{sun}$) are OH-rich and H_2O-poor due to photodissociation. With Herschel/PACS, 22 Herbig AeBe and 8 T Tauri disk have been surveyed as part of the key-project DIGIT. Overall HAeBe disks show a high OH/H_2O column density with disk radius while T Tauri disks show a drop at long wavelengths.

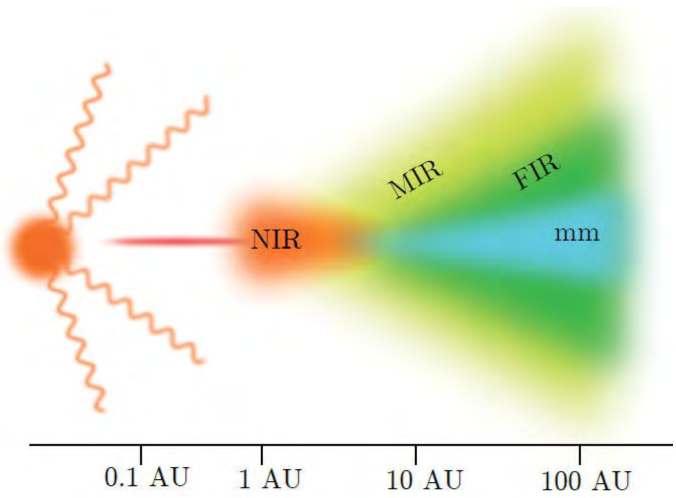

Figure 1: Schematic picture of a protoplanetary disk showing the regions traced by different wavelengths.

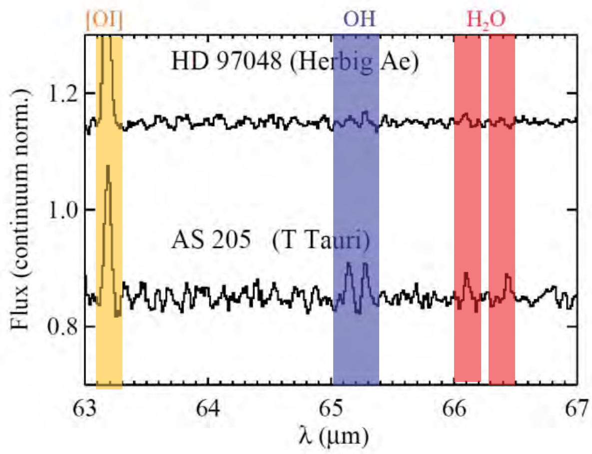

Figure 2: Herschel/PACS spectra of an Herbig Ae (top) and T Tauri (bottom) source.

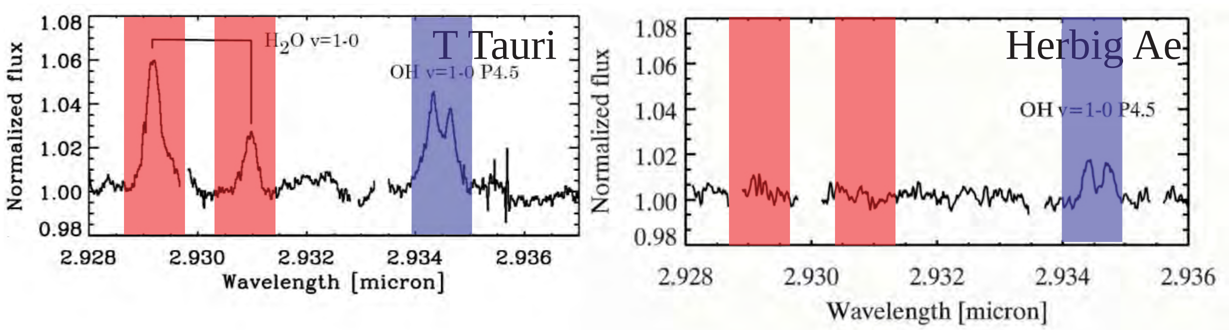

Figure 3: Near-IR spectra of a T Tauri (left) and Herbig Ae (right) disk showing different OH/H_2O abundance ratios as in Fig. 2

References:
Fedele et al. 2011 ApJ, 732, 106; Fedele et al. 2012, A&A, 544, 9; Fedele et al. 2013 submitted

D. Fedele, S. Bruderer, E.F. van Dishoeck and DIGIT team

II) Optical & Interpretative Astronomy

Kinematics, dynamics and stellar populations in M31

We observed the nearby spiral galaxy M31 with the VIRUS-W integral field unit spectrograph on the 2.7m telescope at the McDonald Observatory in Texas. VIRUS-W has a spectral resolution of R=9000 (σ=15 km/s). One pointing has a field of view of 105" x 55" and results in 267 individual spectra. With 190 pointings, we covered the whole bulge and sampled the disk along six different directions. We fitted the line-of-sight velocity distribution (LOSVD) of the stars and the gas, for the latter we used the [OIII] and [NI] emission lines. From these data we produced kinematical maps of impressive quality. Future work will involve modeling dynamics and stellar populations, from which we will construct a detailed three-dimensional mass model of M31. This will help in the interpretation of the micro-lensing events we are collecting in the PAndromeda project [1] and allow us to better understand the nature of the massive halo objects (MACHOS).

The positions of the observed pointings are shown in Fig.1. Data reduction resulted in ca. 50,000 individual spectra, from which 2393 binned ones were produced with a Voronoi binning code by Cappellari and Copin [2]. Stellar and gas kinematics were fitted using a Maximum Penalized Likelihood code. The resulting maps for v and σ are shown in Figs. 2 and 3 for the stars and in Figs. 4 and 5 for the gas. They agree with the kinematics obtained by Saglia et al. [3].

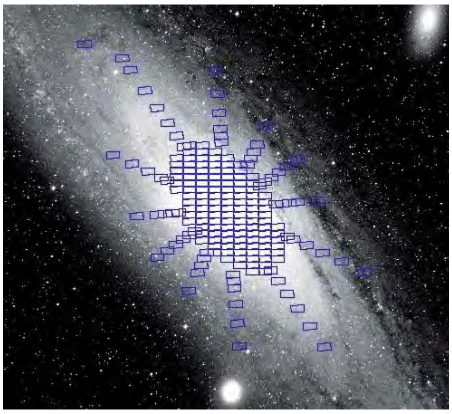

Fig.1: Observed VIRUS-W pointings superposed on a Sloan g-band image.

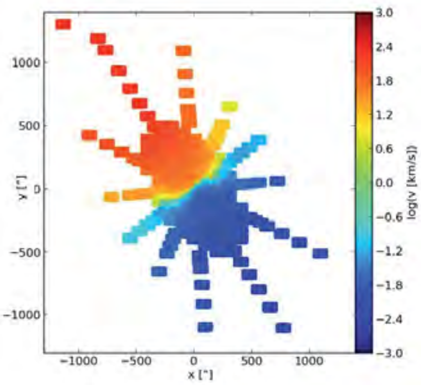

Fig.2: Stellar velocity field. The line of zero velocity seems to be twisted.

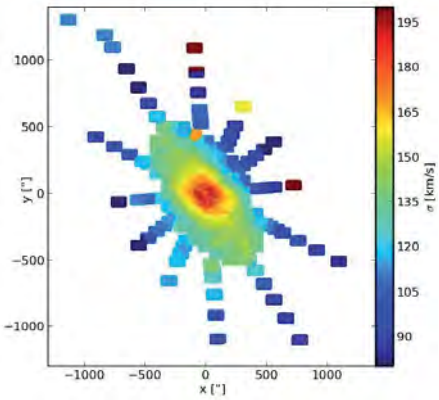

Fig.3: Stellar velocity dispersion field. σ is lower in the north-western (i.e. upper right) region of the bulge than on the opposite side. This may be due to dust obscuring the view in the northwest.

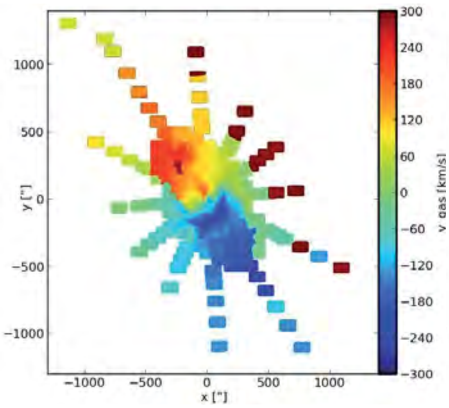

Fig.4: Gas velocity field, fitted to the [OIII] and [NI] lines. The velocity can change dramatically between neighboring pointings. This is due to double peaks in the gas features, hinting at two gas components with different v.

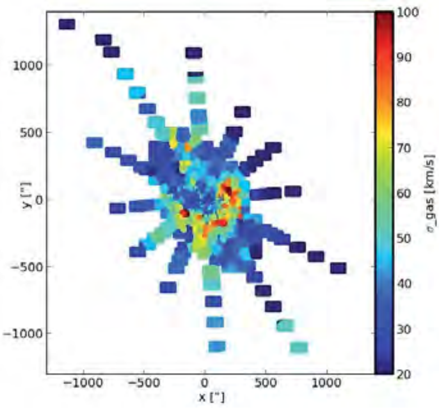

Fig.5: Velocity dispersion field of the gas. The arc of high σ corresponds to a region of low velocity (see Fig.4). In the disk, σ is lower for the gas than for the stars.

References:

[1] Lee C.-H. et al 2012, AJ, 143, 89
[2] Cappellari M. & Copin Y. 2003 MNRAS, 342, 345
[3] Saglia et al. 2010, A&A, 509, 61

M. Opitsch, R. Saglia, R. Bender, M. Fabricius, S. Rukdee, M.Williams

Probing the dynamical structure of bulges with VIRUS-W

In October 2010 we commissioned VIRUS-W, a new fiber based Integral Field Unit spectrograph at the McDonald 2.7m Telescope. We are currently conducting a study of the dynamical structure of bulges in nearby disks. With its large field of view and high spectral resolution this instrument is ideally suited to study the stellar and gaseous kinematics of local low-dispersion galaxies giving a unique insight into their formation history.

We are obtaining observations of a sample of bulges of local (D < 20 Mpc) S0 to Sc type galaxies. Fig. 1 shows kinematic maps of three of the galaxies that we observed. All three galaxies show regular rotation and a central increase of stellar velocity dispersion. But on top of this NGC7331 exhibits along the minor axis an asymmetric increase of dispersion that even exceeds the central values. The stellar disk of this galaxy seems to be embedded in a hot stellar halo. Fig. 2 shows that the full LOSVD of NGC7217 consists of two distinct stellar components that can be decomposed into two Gaussian distributions: A rapidly rotating low dispersion component is imbedded in a slowly rotating high dispersion component. The fast component is only responsible for about 30% of the total light. Its rotation and dispersion match very well those of the diffuse gas in this galaxy (as measured from the [OIII] emission). Imaging data show sites of active star formation and blue colors where the fast component dominates. It is conceivable that NGC7217 may be in the process of regrowing a stellar disk inside a hot spherical halo as result of a recent accretion event.

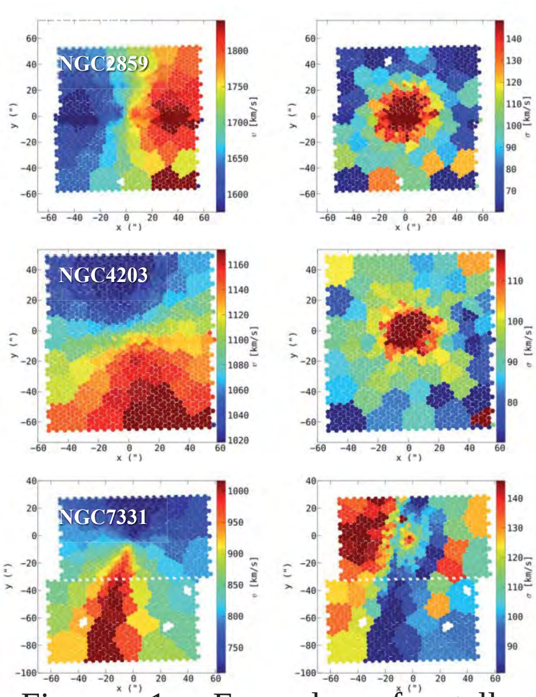

Figure 1: Example of stellar velocity and dispersion maps.

A kinematic decomposition as shown here requires a high spectral resolution and high signal to noise. With VIRUS-W we will obtain similar data for a large number of galaxies. This will give us a new dynamical perspective on the formation of bulge/disk systems that was so far only available for higher dispersion elliptical galaxies.

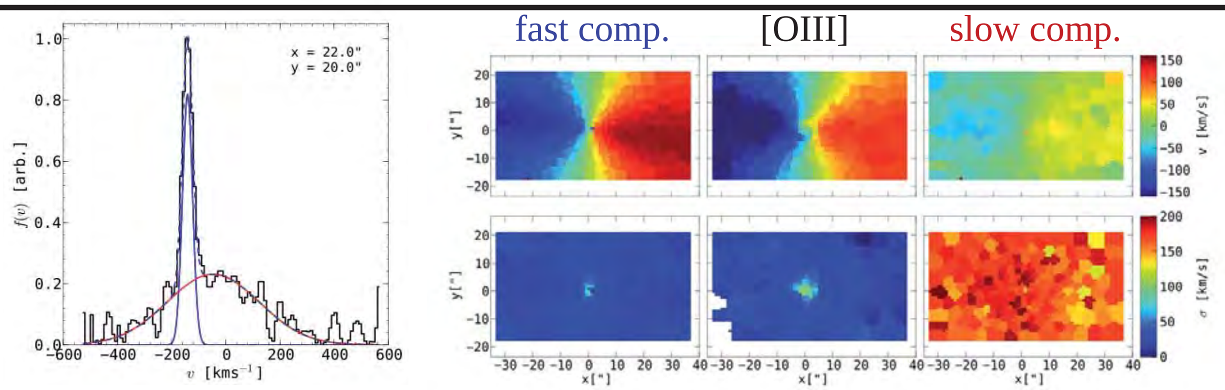

Figure 2: Kinematic decomposition of NGC7217. left: Example for the two-Gaussian fit. right: Velocity (upper row) and σ (lower row) of the two stellar components and the gas.

References: Fabricius et al. 2012, SPIE, 8446E

M. Fabricius, R. Bender, R. Saglia, M. Williams

Secular evolution in action in boxy bulges

Boxy/peanut-shaped bulges are the thick, buckled projection of galactic bars seen in half of edge-on galaxies. They provide a unique perspective on bars, whose dynamics are the dominant force driving the slow, non-violent secular evolution of disk galaxies. We determine central values and radial trends in the stellar populations of bulges for a sample of 28 edge-on S0-Sb disk galaxies, 22 of which are boxy/peanut-shaped (and therefore barred).

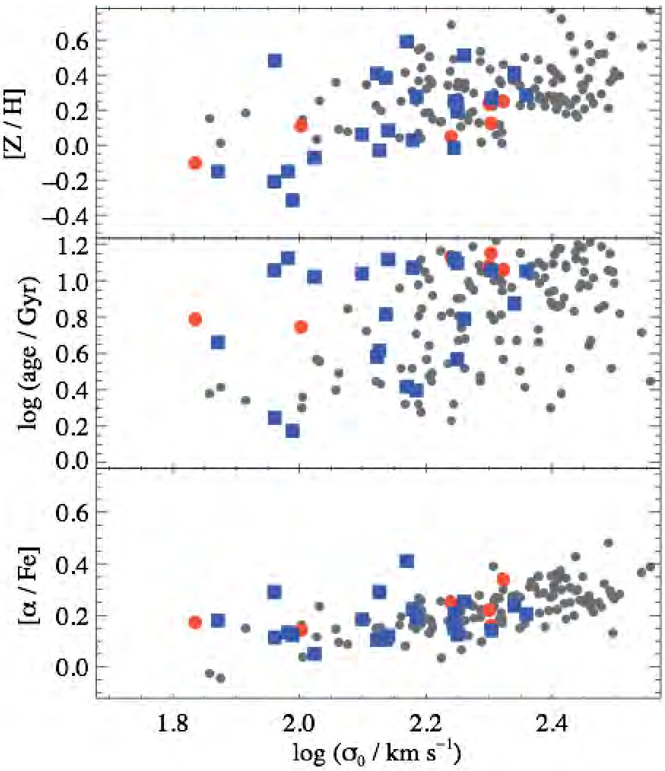

Fig 1. Central stellar populations of boxy bulges (■), round bulges (●), and ellipticals and S0s (●, from Thomas, Maraston & Bender, 2005). At a given velocity dispersion, the central stellar populations of galaxies with boxy/peanut-shaped bulges are indistinguishable from those of early-type (elliptical and S0) galaxies of the same velocity dispersion. Either secular evolution affects stellar populations no differently to monolithic collapse or mergers, or secular evolution is not important in the central regions of these galaxies, despite the fact that they are barred.

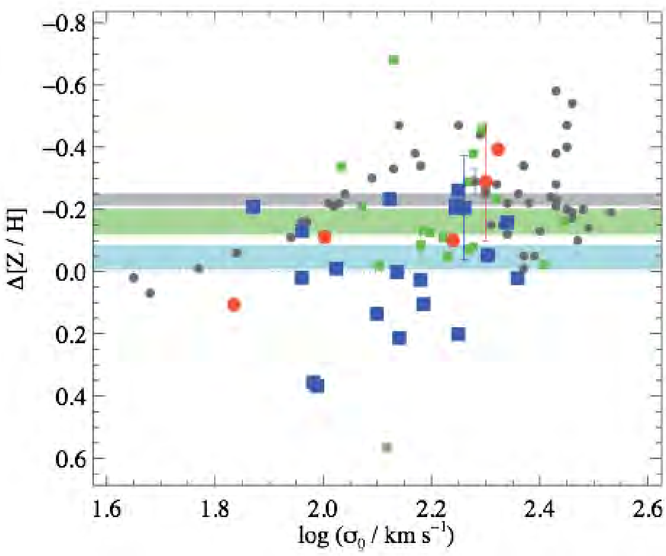

Fig 2. Radial metallicity gradients of boxy bulges (■), round bulges (●), face-on barred galaxies (■, from Pérez & Sánchez-Blázquez 2011), and ellipticals and S0s (●). Sample averages indicated by the blue, green and grey stripes. The radial metallicity gradients of boxy/peanut-shaped bulges and face-on barred galaxies are uncorrelated with velocity dispersion and are, on average, shallower than those of unbarred early-type galaxies. This is qualitatively consistent with chemodynamical models of bar formation, in which radial inflow and outflow smears out pre-existing gradients.

References:
• Williams, Bureau and Kuntschner, 2012, MNRAS Letters, 427, L99-103 • Thomas, et al., 2005, ApJ, 621, 673
• Pérez and Sánchez-Blázquez, 2011, A&A, 529, 64,

M.J. Williams, M. Bureau and H. Kuntschner

New Angles on Box/Peanut Bulges

The majority of disk galaxies have bars, which simulations show become unstable and thicken vertically in their interiors, forming "boxy/peanut-shaped" (B/P) bulges. We show that these structures can be detected when galaxy inclinations are as low as ~40°, contrary to the common belief that they can only be seen in edge-on galaxies. This enables us to compare B/P bulges with the rest of the bar, as well as to find bars *without* B/P bulges. For local S0–Sb galaxies, we find that ≥ 2/3 of bars have B/P bulges, which typically span the inner 40% of the bar—but at least 10% of bars lack them and are uniformly thin, suggesting very recent formation.

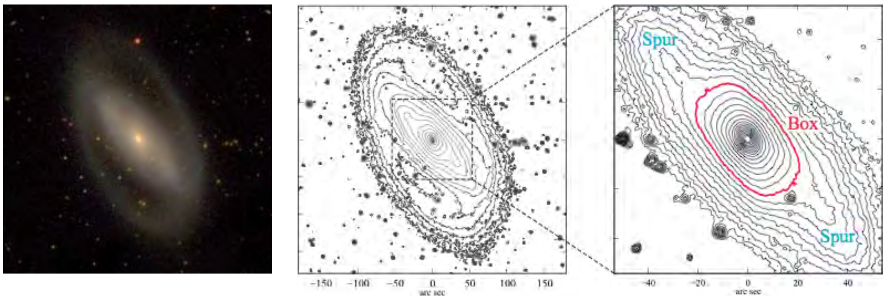

Barred galaxy NGC 5377, with "box+spurs" morphology. The "box" is a projection of the inner, vertically thick part of the bar (the B/P bulge); the "spurs" are the vertically thin outer region of the bar.

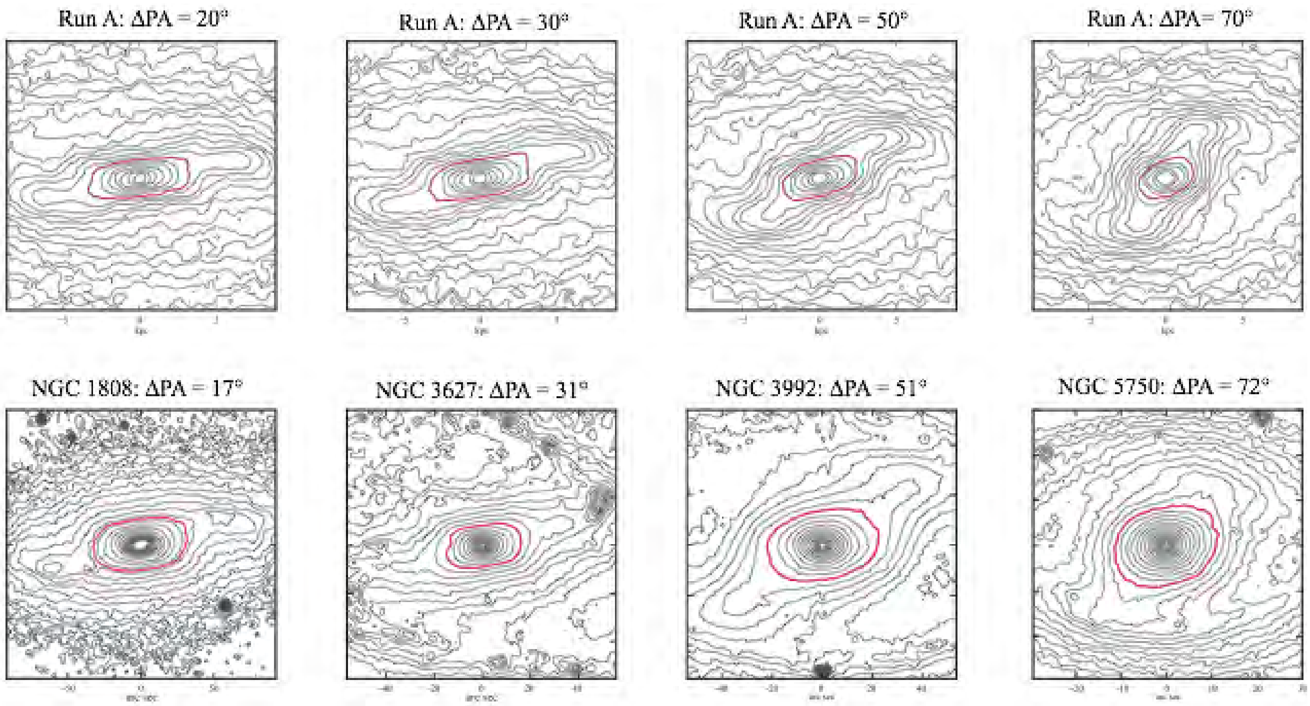

Real and simulated galaxies seen at similar inclinations and orientations, with disk major axis horizontal; angle ΔPA between bar and major axis increases to the right. **Top:** projected isodensity contours of *N*-body simulation seen at $i = 60°$; **Bottom**: Near-IR isophotes of real galaxies with $i = 50–60°$. The boxy zone (the projection of the B/P bulge) is outlined in red.

References:

• Erwin & Debattista, 2013, MNRAS, in press

P. Erwin & V. P. Debattista

A Revised Parallel-Sequence Classification of Galaxies: Formation of S0s and Spheroidals

We update van den Bergh's parallel sequence galaxy classification in which S0 galaxies form a sequence S0a-S0b-S0c that parallels the sequence Sa-Sb-Sc of spiral galaxies. We make one major improvement by extending the S0a-S0b-S0c sequence to spheroidal (Sph) galaxies that are positioned in parallel to irregular galaxies in a similarly extended Sa-Sb-Sc-Im sequence. This provides a natural home for spheroidals, which previously were omitted from galaxy classification schemes or inappropriately combined with ellipticals. We present detailed photometry of four rare, late-type S0s that bridge the gap between the more common S0b and Sph galaxies, among them NGC4452, which has a pseudobulge-to-total ratio of PB/T = 0.017 and is the first known S0c, and VCC2048, which contains an edge-on disk, but its bulge plots in the structural parameter sequence of spheroidals; it is therefore a disky Sph. Furthermore, we show that Sph galaxies of increasing luminosity form a continuous sequence with the disks (but not bulges) of S0c-S0b-S0a galaxies. Remarkably, the Sph-S0-disk sequence is almost identical to that of Im galaxies + spiral galaxy disks. We suggest that Sph galaxies are transformed, ``red and dead" Scd-Im galaxies in the same way that many S0 galaxies are transformed, red and dead Sa-Sc spiral galaxies.

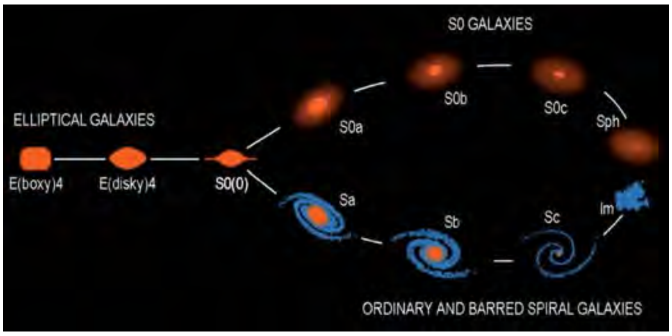

Fig.1 (above): Revised parallel-sequence morphological classification of galaxies. E types are from Kormendy & Bender (1996), ranging from boxy to disky. Bulge-to-total ratios decrease toward the right; Sc and S0c galaxies have tiny or no pseudobulges. Sph and Im galaxies are bulgeless.

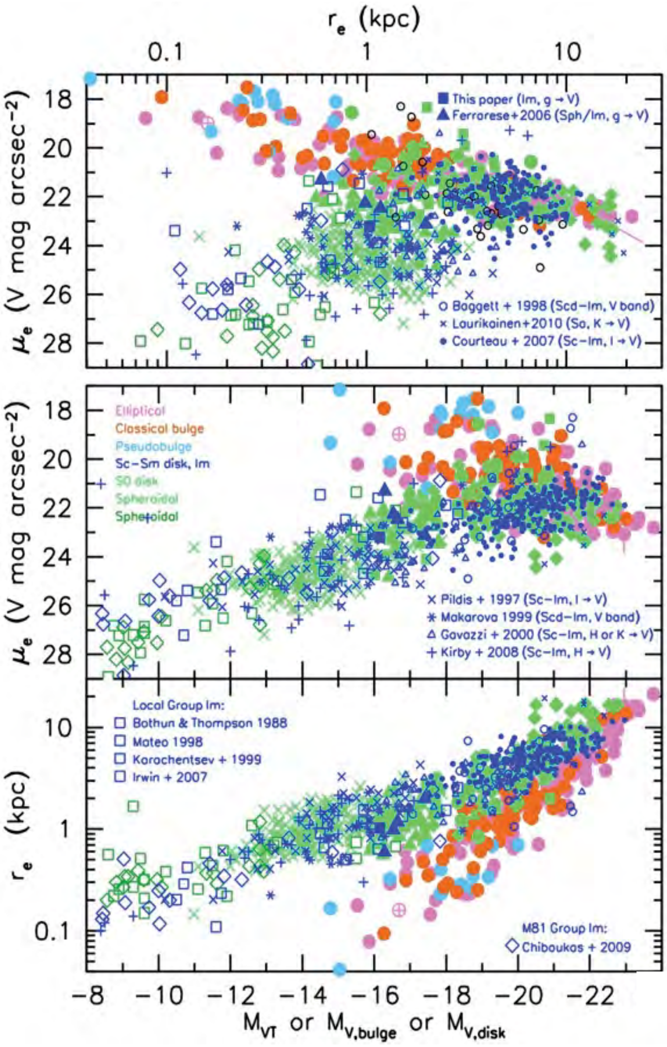

Fig. 2 (right): Parameter correlations for ellipticals, bulges, Sphs, and S0 disks, plus disks of Sa-Im galaxies. When (pseudo)bulge-disk decomposition is necessary, the two components are plotted separately. Spiral disks, S0 disks, Im and Sph galaxies form one sequence (green and dark blue symbols); ellipticals, and (pseudo-)bulges another one (red, orange turquoise symbols). Most disks that have lower-than-normal surface brightnesses are in galaxies that have outer rings, and most disks that have higher-than-normal surface brightnesses are either edge-on or starbursting. Blue Compact Dwarfs are omitted.

References:

• Kormendy, J. & Bender, R: 2012, ApJS 198, 2

R. Bender and J. Kormendy

Large central M/L in cluster ellipticals

In the Milky Way, the stellar initial-mass-function (IMF) flattenes below ~1 $M_\odot$ (Kroupa IMF). Even a massive population of low-mass stars, as predicted by steeper IMFs (e.g. Salpeter IMF), can hardly be observed directly in the optical spectra of distant galaxies. However, dynamical models are sensitive to the extra mass of such a faint population. In 24 early-type galaxies in the Coma and Abell 262 clusters we measure dynamical stellar mass-to-light ratios and compare them to predictions from stellar-population models based on spectral line indices and a Milky-Way IMF. In the most massive early-type galaxies we find a disagreement: dynamical stellar masses are up to 2x larger than expected for a Milky-Way IMF.

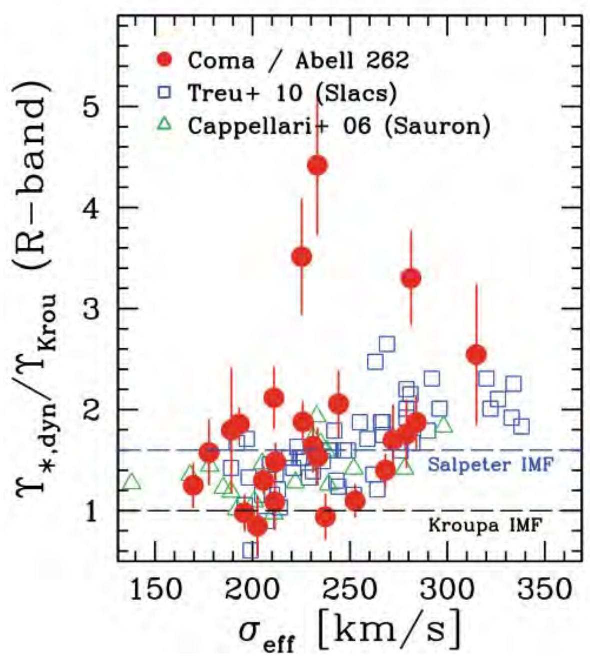

The ratio of the dynamical stellar mass-to-light ratio over the stellar-population prediction for a Milky-Way (Kroupa) IMF increases with galaxy velocity dispersion.

• If all ellipticals have maximum stellar mass then the IMF has to vary with increasing σ

• If the IMF is universal and Milky-Way like then the most massive early-type galaxies have sub-maximal stellar masses

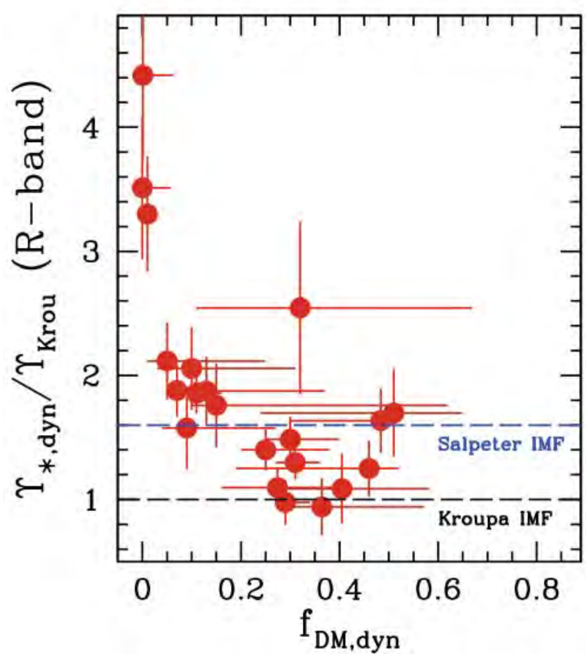

Cluster galaxies where the IMF is most discrepant from the Milky-Way have almost no central dark matter (dark matter fraction of total mass along the x-axis).

• Dynamical models distinguish stars from dark matter if they follow distinct spatial profiles, otherwise they become degenerate

• If dark matter follows the light closely in high-σ galaxies, the IMF can be universal.

References:

• J. Thomas, R. P. Saglia, R. Bender, et al., 2011, MNRAS, 415, 545
• G. Wegner, E.M. Corsini, J. Thomas, R. P. Saglia, R. Bender, S. Pu, 2012, AJ, 144, 78

J. Thomas, R. P. Saglia, R. Bender et al.

Dark matter halos of massive ellipticals

Our current Λ-CDM paradigm predicts cuspy dark-matter halo profiles. During the formation of a galaxy the dark-halo profile is altered by the baryon infall, which might lead to halo contraction or halo expansion, depending on assumptions upon the feedback process which are not well understood yet. Our measurements of halo profiles in 16 Coma cluster ellipticals indicate a strong degeneracy similar to the disk-halo degeneracy in spiral galaxies. If ellipticals have maximum bulges (i.e. all the mass that follows the light is in stars) then cored halos can fit the observations as well as Λ-CDM halos. If not, then halos must be close to isothermal, i.e. steeper than predicted by Λ-CDM .

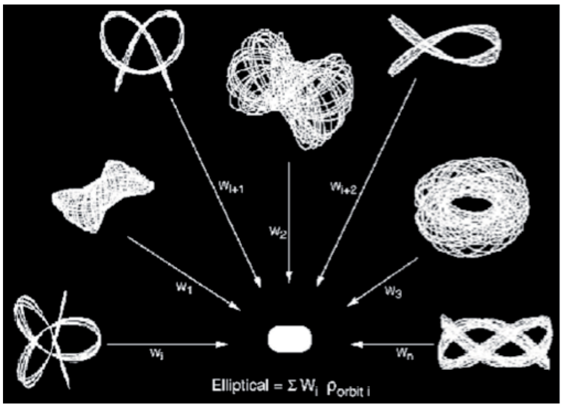

Data and models.

We use state-of-the-art Schwarzschild orbit superposition models to determine the stellar masses and dark-halo profiles in 16 elliptical galaxies in the Coma cluster. Right: stellar kinematics of IC 843.

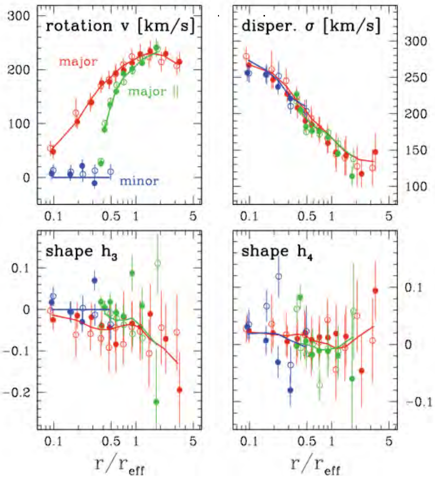

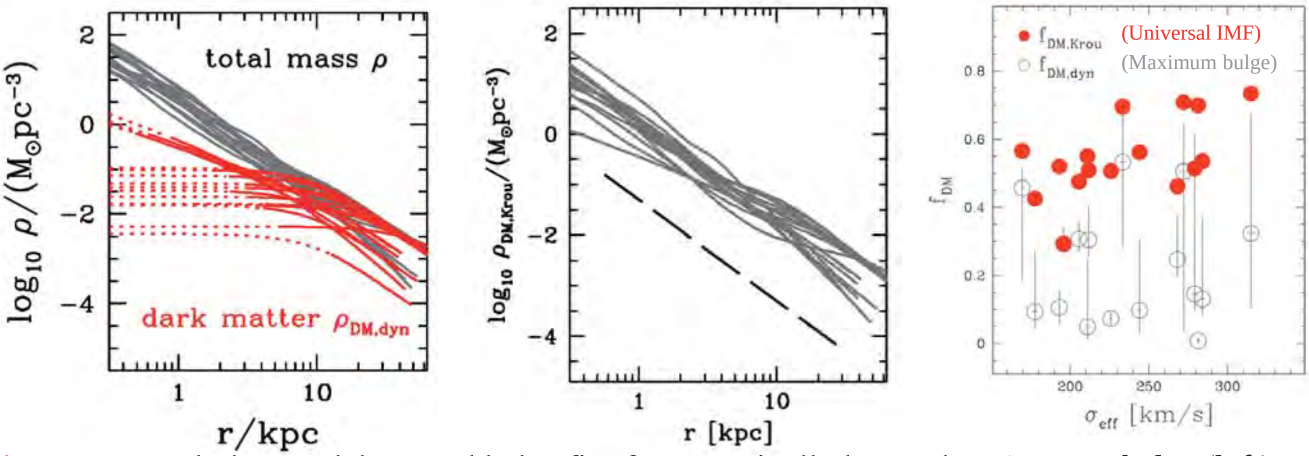

- Maximum-bulge models: cored halos fit often marginally better than Λ-CDM halos (left)
- Universal-IMF models: halos are steeper than Λ-CDM (middle panel; dashed = isothermal)
- Dark-matter fraction: 25% for maximum bulges, 56% for universal IMF (right)

References:
• J. Thomas, R. P. Saglia, R. Bender, et al., 2011, MNRAS, 415, 545

J. Thomas, R. P. Saglia, R. Bender et al.

Central mass density profiles of elliptical galaxies from strong gravitational lensing

We use exceptional strong gravitational lensing systems like SDSS J1430+4105 to measure their central mass profiles from lensing alone. We split the mass profile of the elliptical galaxy into a luminous and dark component and constrain these two components separately. We can measure the mass to light ratio for the luminous mass purely based on gravitational lensing and compare this to results from fitting the galaxy photometry to composite stellar populations. Our results require Salpeter IMF mass to light ratios.

We search for exceptional strong lensing systems in the SLACS (www.slacs.org) archive with multiple sources that are imaged over a large radial range in the lens plane. This configuration allows us to reconstruct the total mass profile on a large radial range. We combine a NFW profile for the dark matter and a de Vaucouleurs profile for the luminous matter to directly derive properties of the dark and luminous matter in these systems. Here, we present the results for SDSS J1430+4105.

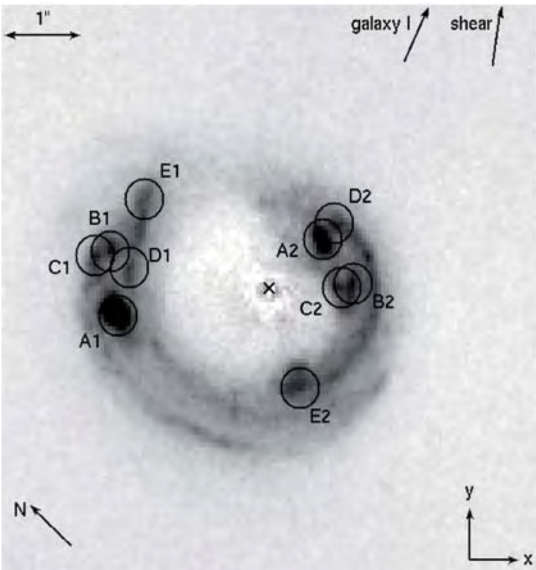

Fig. 1 shows the observed lensed image with the lensing galaxy already subtracted. The identifiers A to E mark the corresponding multiple image sub-systems. The background source itself forms an almost complete Einstein ring in this configuration.

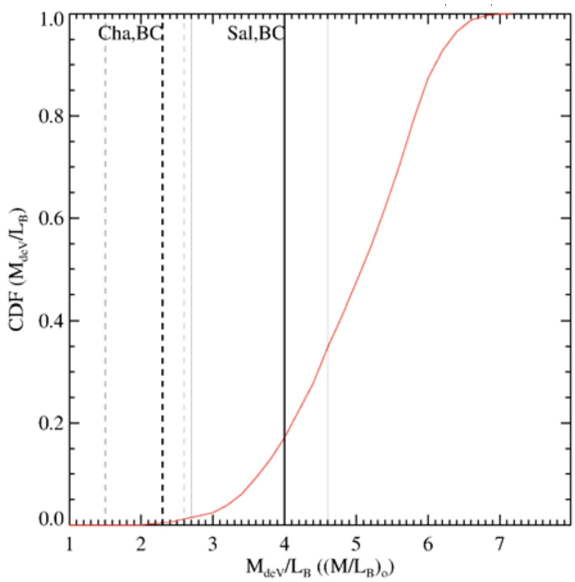

Fig. 2. The red curve is our lensing derived cumulative distribution function for the mass to light ratio of the luminous mass. We also plot the estimates for the mass to light ratios derived in [2] from SDSS photometry for this system: the vertical lines give the estimates for a Chabrier and Salpeter IMF and the 68% c.l., respectively.

We can reconstruct the observed positions of the multiple images with an accuracy of ~0.05". Our model reveals that approximately half of the total matter within the Einstein radius has to be dark. Fig. 2 shows the cummulative PDF for the mass to light ratio from our strong lensing analysis. The luminous mass is best reconciled with a Salpeter-IMF, agreeing with recent dynamical results for nearby massive elliptical galaxies. (Thomas et al., 2011, MNRAS, 415, 545, see Poster of J. Thomas)

We are currently expanding this sample, to get a more complete picture of dark and luminous matter properties in early-type galaxies at intermediate redshifts, see also [3].

References:

- [1] Eichner, T., Seitz, S., Bauer, A., MNRAS, 2012, 427, 1918
- [2] Grillo, C., et al., A &A, 2009, 501, 461
- [3] Grillo, C., Eichner, T., Seitz, S., Bender, R., Lombardi, M., Gobat, R., Bauer, A., 2010, ApJ, 710, 372

T. Eichner, S. Seitz

Galaxy Halo Truncation in the CLASH Cluster MACSJ1206.2-0847

We analyze the mass distribution of MACSJ1206.2-0847 (z=0.44) using strong gravitational lensing, especially focusing on the sizes of the cluster galaxies. We reconstruct the surface brightness (SB) of a spectacular giant arc which is bent by several neighboring cluster galaxies. We show that the halos of cluster members are significantly smaller than for field elliptical galaxies, likely due to tidal stripping.

MACSJ1206.2-0847 was observed by the CLASH collaboration (Postman et al., 2012). A strong lensing model was published by [1]. Among the observed multiple images in MACSJ1206.2-0847 - originating from 12 background sources - are a spectacular arc (at z=1.033) and its counterimage shown in Fig. 1. We construct a projected mass density model for the cluster and its member galaxies that reproduces the observed multiple image positions with a mean accuracy below 1". We reconstruct the surface brightness of the arc and its counterimage by optimizing the parameters of neighboring galaxies thus measuring their halo size vs luminosity relation.

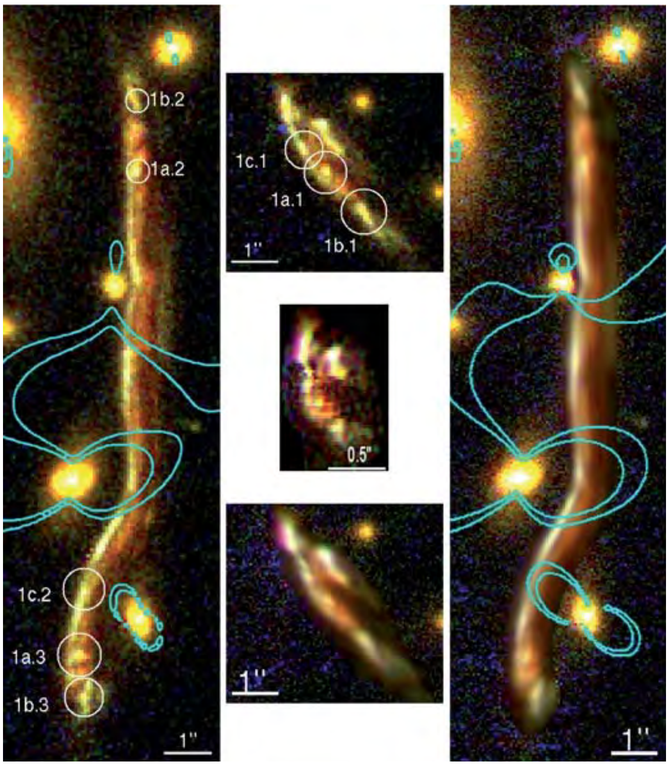

Fig. 1. The giant arc and its counterimage are shown in the left row and the middle, top panel. The reconstruction of the arc by the strong lensing model is shown in the right and middle row, bottom panel. The cyan curves are contours of very high magnification. The center of the figure hosts the image of the reconstructed source. The colors are made of the F435W-F606W-F814W filter data.

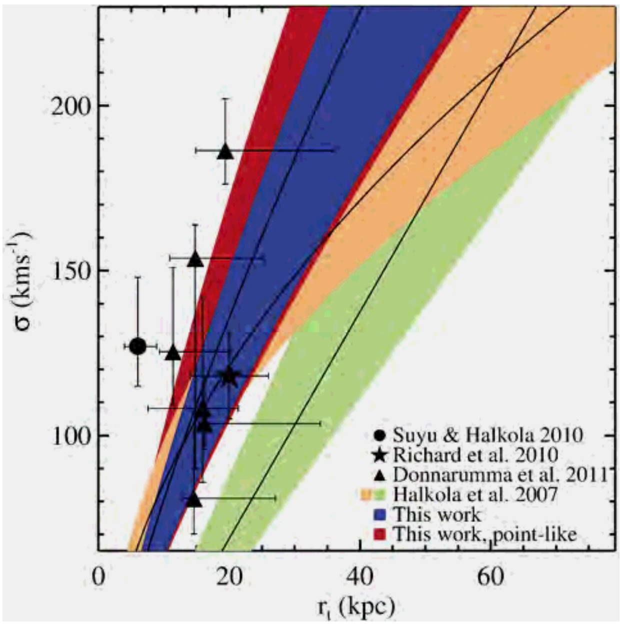

Fig. 2. This figure shows the size-velocity dispersion relation we can derive in this cluster (red, blue). The results for several other studies on different objects are also plotted, giving similar results. All these studies are done in environments with similar density, i.e. the centers of clusters and groups of galaxies.

We derive the size-magnitude relation as shown in Fig. 2 from the reconstruction. In numbers, the relation reads: $\log(r_t[\mathrm{kpc}]) = \log(35\pm8) - 0.16 M_{B,\,\mathrm{Vega}} - 3.372$

For a galaxy with $m_{F160W,AB} = 19.2$ ($M_{B,\mathrm{Vega}} = -20.7$) this converts to $\sigma = 150\,\mathrm{kms}^{-1}$, $r_t \approx (26 \pm 6)$kpc.

References:

[1] Zitrin et al., 2012, ApJ, 749, 97

[2] Eichner, T. et al., 2013, ApJ submitted

T. Eichner, S. Seitz and the CLASH Team

Dark Matter Halo Properties from Galaxy-Galaxy Lensing

We analyzed the galaxy-galaxy lensing (GGL) signal in the CFHTLS-Wide as function of lens luminosity for red and blue galaxies and for the combined galaxy lens sample and measured the scaling relation between halo parameter and luminosity for SIS and NFW profiles. For the SIS velocity dispersion we find $\sigma_{red} \propto L^{0.24\ 0.03}$ for red, $\sigma_{blue} \propto L^{0.23\ 0.03}$ for blue and $\sigma \propto L^{0.29\ 0.02}$ for combined galaxies. The NFW mass-to-light scaling with luminosity is described by a broken power law with a break luminosity of ~ 10^{10} h^{-2} $L_{\odot}$. If we translate this luminosity into a stellar mass for red galaxies we find a minimum for M_{200}/M_{star} ratio at M_{star}~ 3-4 10^{10} h^{-2} $M_{\odot}$.

We performed a GGL analysis based on 89 deg^2 imaging data from the CFHTLS-Wide. We used photometric redshifts (u*g'r'i'z', PhotoZ-code: Bender 2001 et al.) to define foreground and background samples and measured the lensing signal as a function of luminosity and SED type. We fitted SIS profiles out to scales of 100 h^{-1} kpc and measured the velocity dispersions σ. The result is shown in Fig.1. The scaling relations for the red and blue galaxies are σ_{red}=162 2 km/s $(L/L^*)^{0.24\ 0.03}$ and σ_{blue}=115 3 km/s $(L/L^*)^{0.23\ 0.03}$ with L^*=1.6 10^{10} h^{-2} $L_{\odot}$ measured in the r'-band. The different σ-amplitudes and the varying fractions of red and blue galaxies as a function of luminosity lead to a steeper relation of σ=135 2 km/s $(L/L^*)^{0.29\ 0.02}$ for the combined galaxy sample.

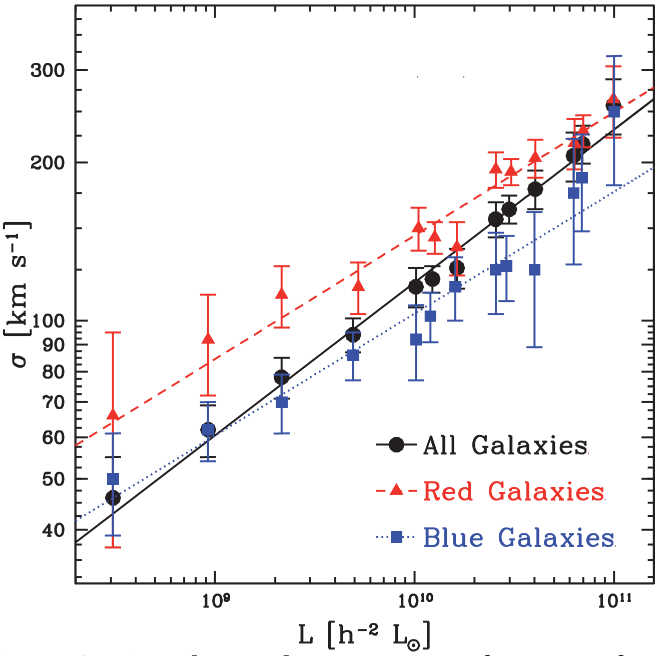

Fig. 1. Velocity dispersion as a function of luminosity and SED type.

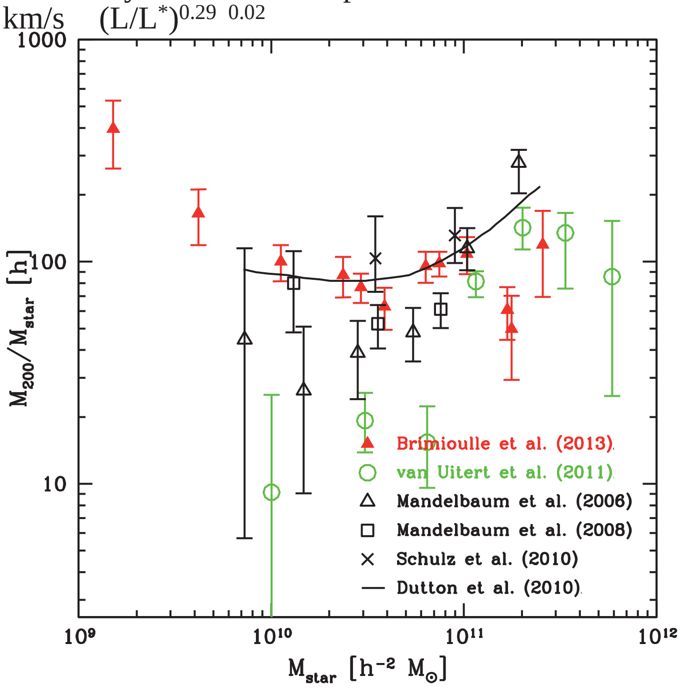

Fig. 2. M_{200}/M_{star} for red galaxies as a function of stellar mass.

We further fitted NFW profiles (Navarro et al. 1997) to the lensing signal out to scales of 100 h^{-1} kpc assuming the concentration-mass relation of Duffy et al. (2008). We obtain broken power law relations for the scaling of the virial masses M_{200} with luminosity. For the red galaxies we can turn the luminosities into stellar masses and obtain a minimum of the M_{200}/M_{star} – ratio for a stellar mass of M_{star}~ 3-4 × 10^{10} h^{-2} M_{star} (see Fig. 2). The existence and location of this minimum is consistent with results from Abundance Matching (see Guo et al. 2010, Dutton et al. 2010).

References:

- Bender et al. (2001)
- Brimioulle et al. (2013)
- Duffy et al. (2008)
- Dutton et al. (2010)
- Guo et al. (2010)
- Navarro et al. (1997)

F. Brimioulle, S. Seitz, M. Lerchster, R. Bender, J. Snigula

THE $L \propto \sigma^8$ CORRELATION FOR ELLIPTICAL GALAXIES WITH CORES: RELATION WITH BLACK HOLE MASS

We construct the Faber–Jackson correlation between velocity dispersion σ and galaxy luminosity L_V separately for elliptical galaxies with and without cores. The coreless ellipticals show the well known, steep relationship $d\log\sigma/d\log L_V=0.268$ or $L_V \propto \sigma^{3.74}$. This corresponds to $d\log\sigma/d\log M=0.203$, where M = stellar mass and we use $M/L \propto L^{0.32}$. In contrast, the velocity dispersions of core ellipticals increase much more slowly with L_V and M: $d\log\sigma/d\log L_V = 0.120$, $L_V \propto \sigma^{8.33}$, and $d\log\sigma/d\log M = 0.091$. Dissipationless major galaxy mergers should roughly preserve σ according to the simplest virial-theorem arguments. However, numerical simulations show that σ increases slowly in dry major mergers, with $d\log\sigma/d\log M \simeq +0.15$. In contrast, minor mergers cause σ to decrease, with $d\log\sigma/d\log M \simeq -0.05$. Thus, the observed relation argues for dry major mergers as the dominant growth mode of the most massive ellipticals. This is consistent with what we know about the formation of cores. We know no viable way to explain galaxy cores except through dissipationless mergers of approximately equal-mass galaxies followed by core scouring by binary supermassive black holes. The observed, shallow $\sigma \propto L^{+0.12}$ relation for core ellipticals provides further evidence that they formed in dissipationless and predominantly major mergers. Also, it explains the observation that the correlation of supermassive black hole masses with velocity dispersion, $M_{BH} \propto \sigma^4$, "saturates" at high M_{BH} such that M_{BH} becomes almost independent of σ .

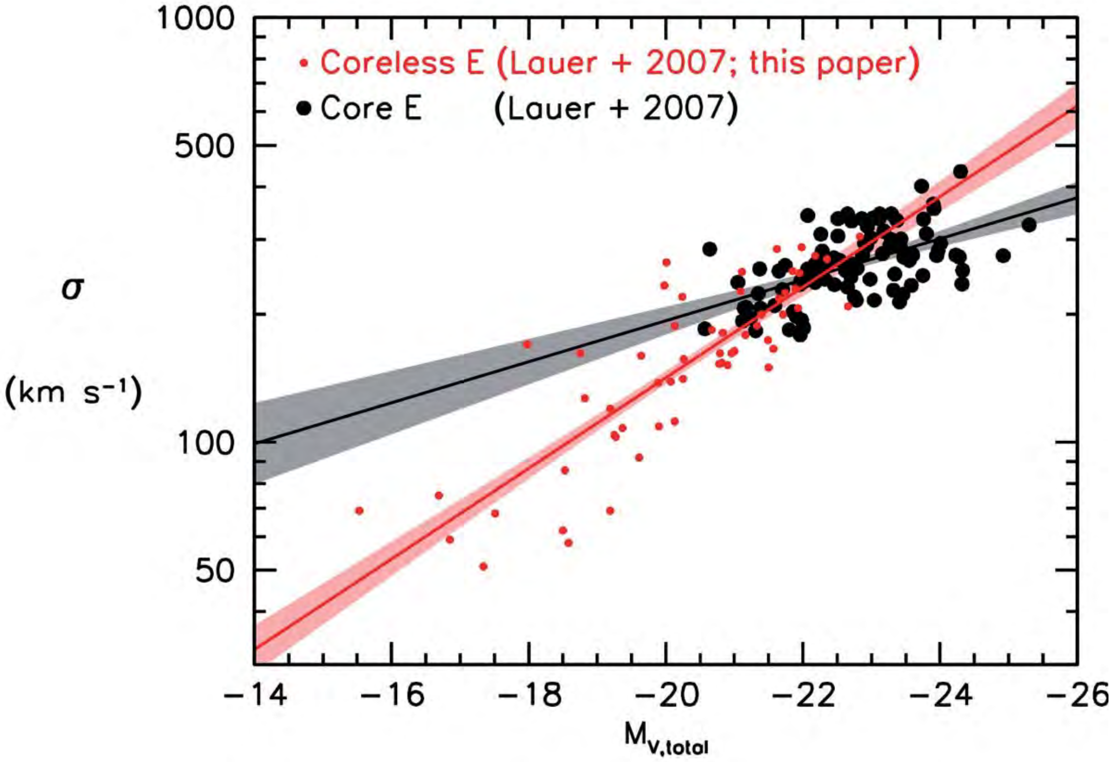

Faber & Jackson (1976) correlations for elliptical galaxies with and without cores. Total galaxy *V*-band absolute magnitudes, velocity dispersions σ, and central profile types are from Lauer et al. (2007a) and others. The lines are symmetric least-squares fits to the core galaxies (black line) and to the coreless galaxies (red line). The shading shows 1σ fit uncertainties. The coreless galaxies show the familiar Faber–Jackson relation, $L_V \propto \sigma^4$(red line). However, velocity dispersions in coreless galaxies increase much more slowly with luminosity $L_V \propto \sigma^8$ (black line), approximately as found in numerical simulations of dissipationless major galaxy mergers (Boylan-Kolchin et al. 2006; Hilz et al. 2012).

References: • Kormendy, J. & Bender, R: 2013, ApJ 767, L1

J. Kormendy and R. Bender

Core scouring and Black Holes (BHs)

We study the sizes r_b and mass deficit M_{def} of the cores of 23 masssive elliptical galaxies with dynamically measured central BH masses M_{BH}, with one third of the sample coming from our Sinfoni Black Hole survey. We find that r_b predicts M_{BH} to less than 0.3 dex. Most of the galaxies have mass deficits in the range 1-5 M_{BH}, indicative of one or more past major mergers.

When galaxies with central BHs merge, a BH binary is formed that by hardening and finally merging ejects stars from the center, creating a core with a 'mass deficit' of $\lesssim 5M_{BH}$. We fit core-Sersic profiles to the photometry of our sample and measure r_b and M_{def}. We find that the velocity dispersion or the luminosity predict r_b worse than M_{BH}. Both the luminosity and the mass deficit correlate with M_{BH} and velocity dispersion.

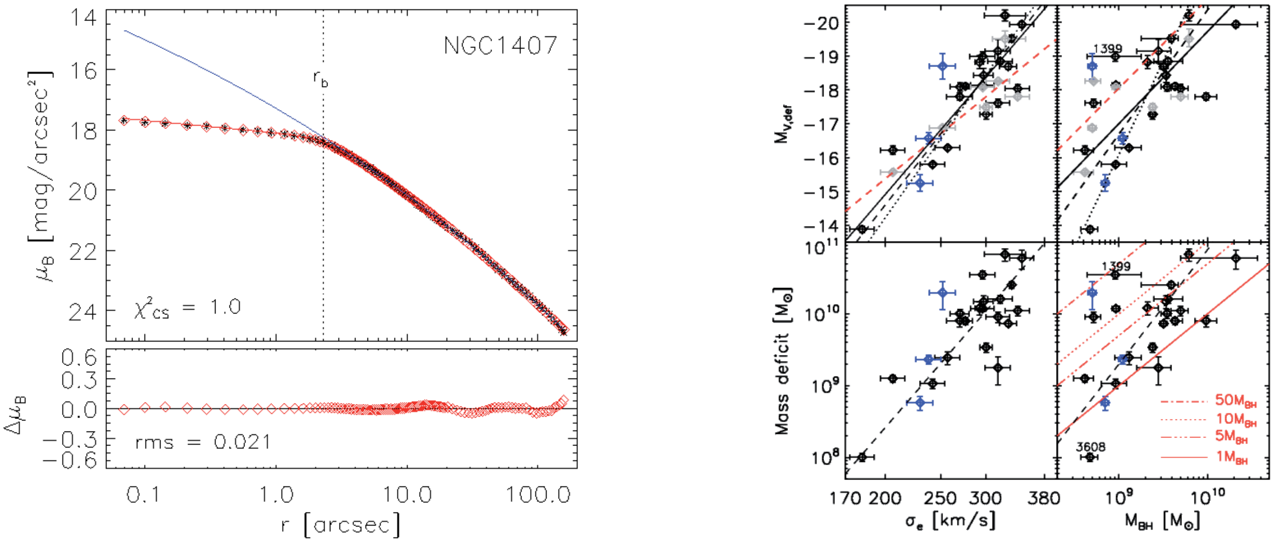

Fig. 1. Left: the fit to the photometry of the core galaxy NGC 1407. **Right:** the correlation between velocity dispersion σ_e, M_{BH} and M_{deff}. The blue points show galaxies with uncertain M_{BH}

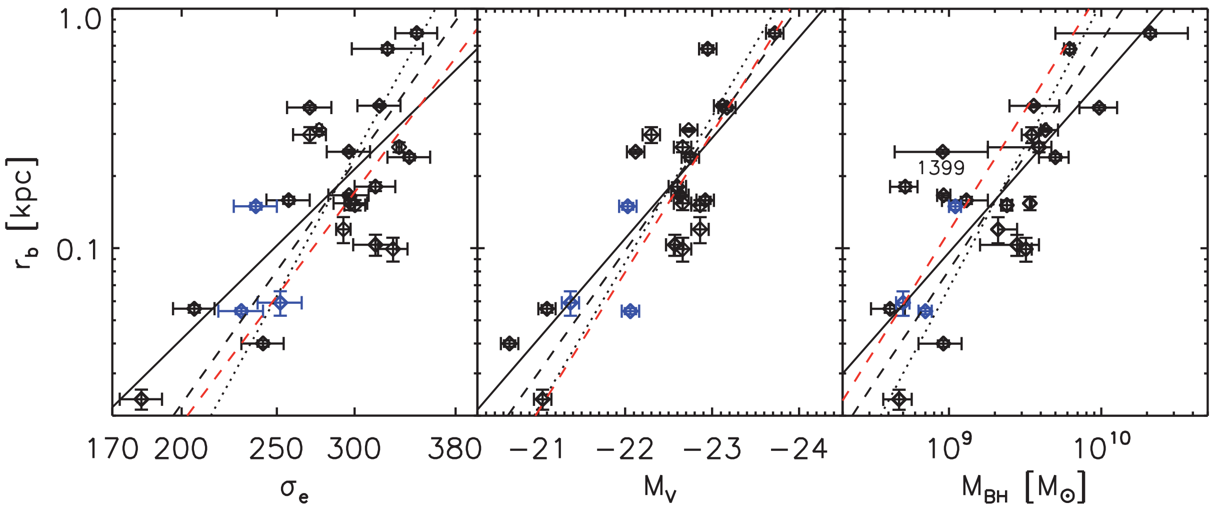

References:
- Rusli et al. 2013, AJ, submitted

Fig. 2: The core radius correlates best with M_{BH}. The blue points show galaxies with uncertain M_{BH}.

R. Saglia, S. Rusli, P. Erwin, J. Thomas, M. Fabricius, R. Bender, N. Nowak

Black-hole merging & depleted stellar cores

The most massive early-type galaxies exhibit shallow power-law cores in their light distributions. The cores are believed to form in gas poor mergers, when the central black holes of the progenitor galaxies spiral inwards by dynamical friction to form a binary. Stars on orbits with pericentres small enough to reach the sphere of influence of the black-hole binary can be ejected through 3-body interactions. However, cores have also been suggested to form through expansion when an active black hole ejects gas from the centre. We present the first evidence for black-hole scouring in the orbital structure of 7 core galaxies observed with SINFONI.

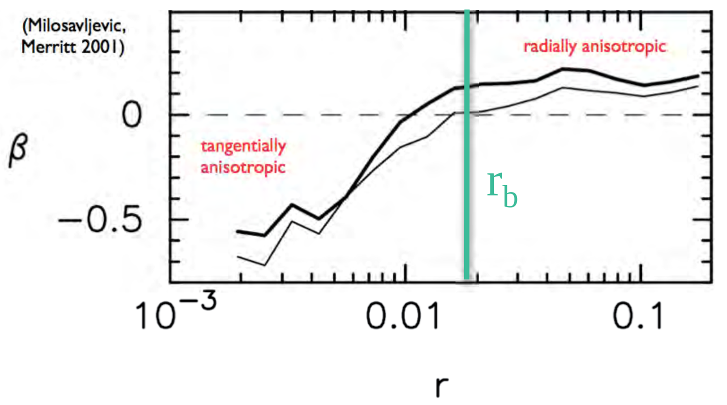

Core formation model

Numerical simulations predict a drop of the anisotropy $\beta=1-(\sigma_t/\sigma_r)^2$ inside the core radius r_b: stars on radial orbits (large σ_r) with pericentres inside the sphere of influence of the binary are ejected. Stars on high angular-momentum orbits (large σ_t) are not affected. Outside the core, ejected stars increase the radial anisotropy.

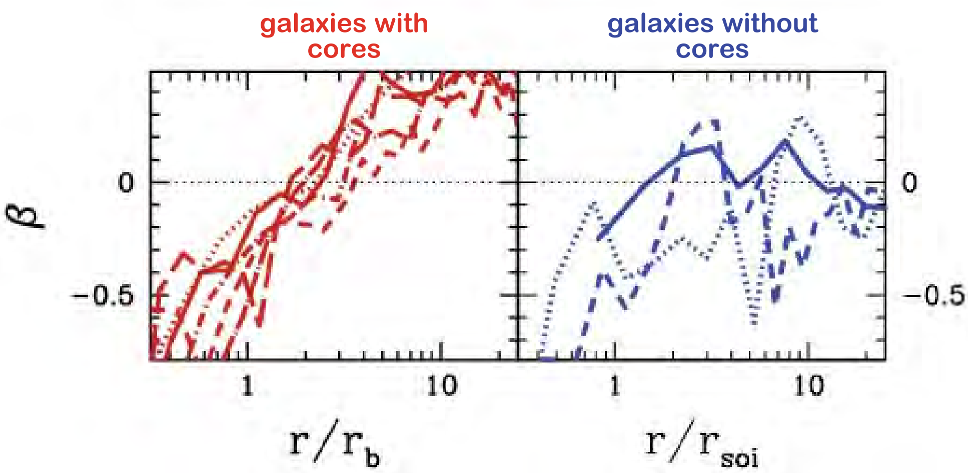

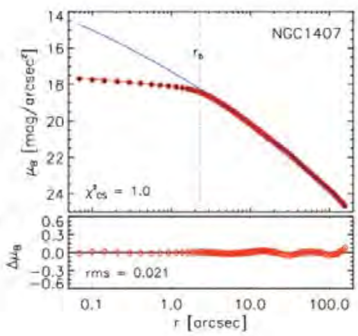

➢ We use Schwarzschild orbit-superposition models to determine the anisotropy in the central region of 10 high-σ galaxies observed with SINFONI

➢ Galaxies with a shallow core in their light distribution show the predicted change from tangential to radial anisotropy at the core radius r_b. Galaxies without cores lack this signature inside the sphere-of-influence r_{soi} of the black hole.

References:
• Thomas et al., in preparation; Rusli et al., AJ, submitted

J. Thomas, S. Rusli, P. Erwin, M. Fabricius, R. P. Saglia, R. Bender et al.

Black holes in the most massive galaxies

The correlation between black-hole mass and galaxy velocity dispersion is uncertain for the most massive galaxies. We present ten new dynamical black-hole mass determinations in high-dispersion galaxies (σ~300 km/s). Accounting for the presence of dark-matter halos turns out to be necessary. Without dark matter, black-hole masses are underestimated by a factor of ~2 on average. All new black-hole masses are larger than expected from the luminosity of their host galaxy and seven are larger than implied by the velocity dispersion of their host galaxy. The slope of the M-σ relation increases significantly.

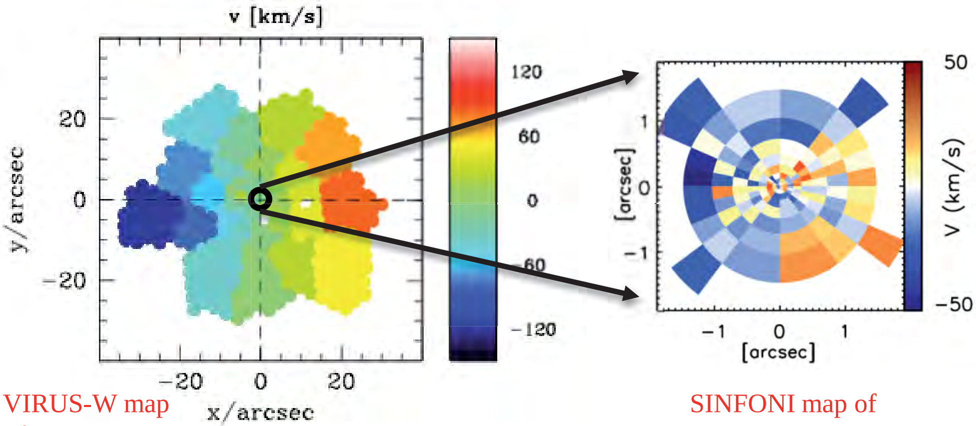

VIRUS-W map of NGC 5328

SINFONI map of NGC 5328, FWHM ~0.15”

***Left:* the rotation field of NGC 5328.**

We combine wide field kinematic data with high-resolution adaptive-optics SINFONI data to determine black-hole, stellar and dark-halo masses at the same time.

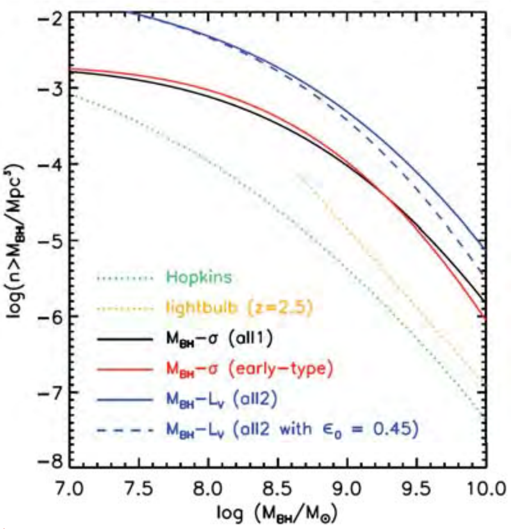

➤ Using our updated M_{BH} scaling relations, we find the space-density of massive black holes (M_{BH}>10^9 M_{sun}) estimated from M_{BH}-L higher than from M_{BH}-σ, and the latter higher than model predictions from quasar counts (each by an order of magnitude).

➤ Our SINFONI sample (red) doubles the number of galaxies with black-hole masses at σ~300 km/s

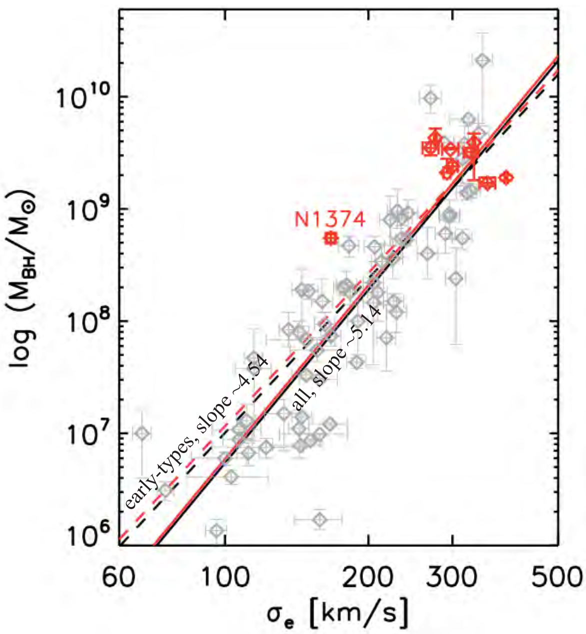

References:

• S. Rusli, J. Thomas, R. P. Saglia, M. Fabricius, P. Erwin, R. Bender et al., AJ, accepted

S. Rusli, J. Thomas, R. P. Saglia, M. Fabricius, P. Erwin, R. Bender

Supermassive black holes do not correlate with galaxy disks or pseudobulges: Two modes of black hole growth

The masses of supermassive black holes are known to correlate with the properties of the bulge components of their host galaxies. In contrast, they appear not to correlate with galaxy disks. Disk-grown pseudobulges are intermediate in properties between bulges and disks; it is unclear whether they do or do not correlate with black holes in the same way that bulges do. At stake are conclusions about which parts of galaxies coevolve with black holes, possibly by being regulated by energy feedback from black holes. Here we confirm that black holes do not correlate with disks and show that they correlate little or not at all with pseudobulges. Our results are based in part on new measurements of velocity dispersions in the biggest bulgeless galaxies and on new bulge-pseudobulge classifications. In a companion paper, we show that black holes do not correlate with dark matter halos, either. We suggest that there are two different modes of black hole feeding, (1) Black holes in bulges grow rapidly to high masses when mergers drive gas infall that feeds quasar-like events; (2) small black holes in bulgeless galaxies grow as low-level Seyferts. Growth of the former is driven by global processes, so the biggest black holes coevolve with bulges, but growth of the latter is driven locally and stochastically, and they do not coevolve with disks and pseudobulges.

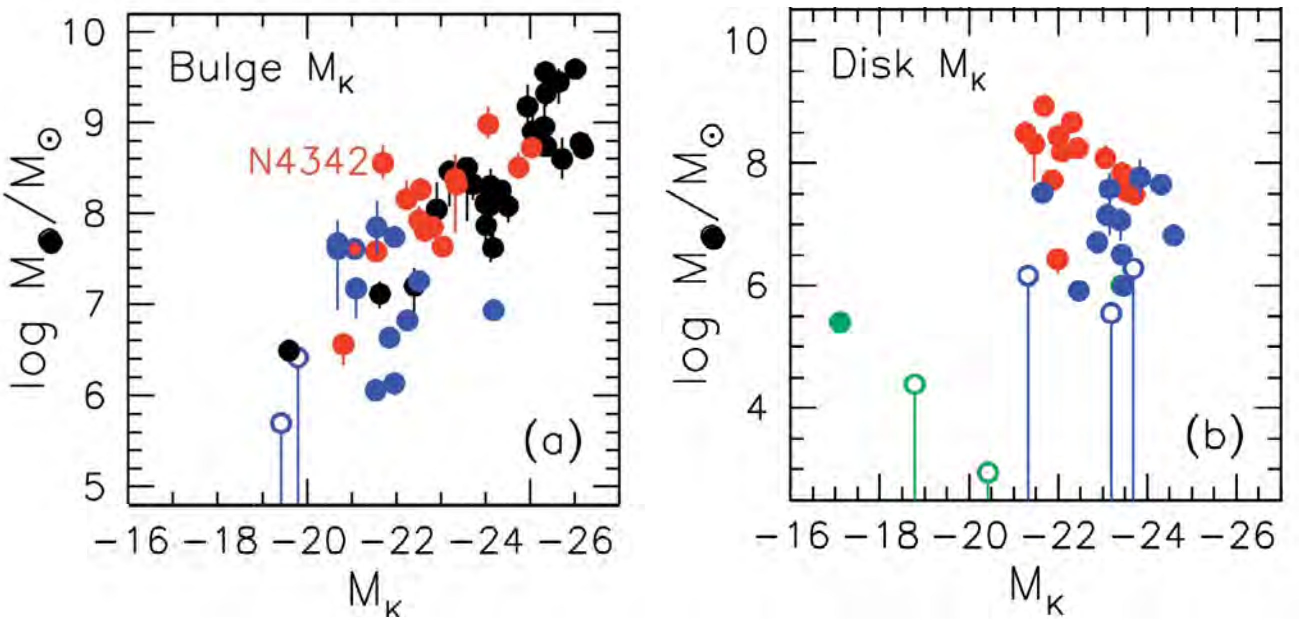

Correlations of dynamically measured black hole masses M_{BH} with (a) bulge absolute magnitude and (b) disk absolute magnitude. Elliptical galaxies are plotted with black points; classical bulges are plotted in red; pseudobulges are plotted in blue. In panel (a) the red and black points show the well-known correlation between M_{BH} and bulge luminosity; a symmetric, least-squares fit of a straight line has $\chi^2 = 12.1$ per degree of freedom and a Pearson correlation coefficient of r = -0.82. In contrast, the blue filled circles for pseudobulges show no correlation: $\chi^2 = 63$ (p.d.o.f) and r = 0.27. In panel (b), the red and blue points together confirm previous results that BHs do not correlate with disks: $\chi^2 = 81$ (p.d.o.f.) and r = 0.41. In panel (b), green points are for galaxies that contain neither a classical nor a pseudo bulge but only a nuclear star cluster; i. e., these are pure-disk galaxies. They are not included in the above analysis, but they strengthen our conclusion. In both panels, galaxies that have only M_{BH} limits are plotted with open symbols; they were chosen to increase our dynamic range. They, too, support our conclusions. We use K-band magnitudes to minimize effects of star formation and internal absorption, that is, of mass-to-light ratio variations among galaxies.

References:

• Kormendy, J, Bender, R., Cornell, M.: 2011, Nature 469, 374

J. Kormendy, R. Bender and M. Cornell

Supermassive black holes do not correlate with dark matter halos of galaxies

Supermassive black holes have been detected in all galaxies that contain bulge components when the galaxies observed were close enough so that the searches were feasible. Together with the observation that bigger black holes live in bigger bulges, this has led to the belief that black hole growth and bulge formation regulate each other. That is, black holes and bulges "coevolve". Therefore, reports of a similar correlation between black holes and the dark matter halos in which visible galaxies are embedded have profound implications. Dark matter is likely to be nonbaryonic, so these reports suggest that unknown, exotic physics controls black hole growth. Here we show – based in part on recent measurements of bulgeless galaxies – that there is almost no correlation between dark matter and parameters that measure black holes unless the galaxy also contains a bulge. We conclude that black holes do not correlate directly with dark matter. As they do not correlate with galaxy disks, either, black holes coevolve with bulges only. This simplifies the puzzle of their coevolution by focusing attention on purely baryonic processes in the galaxy mergers that make bulges.

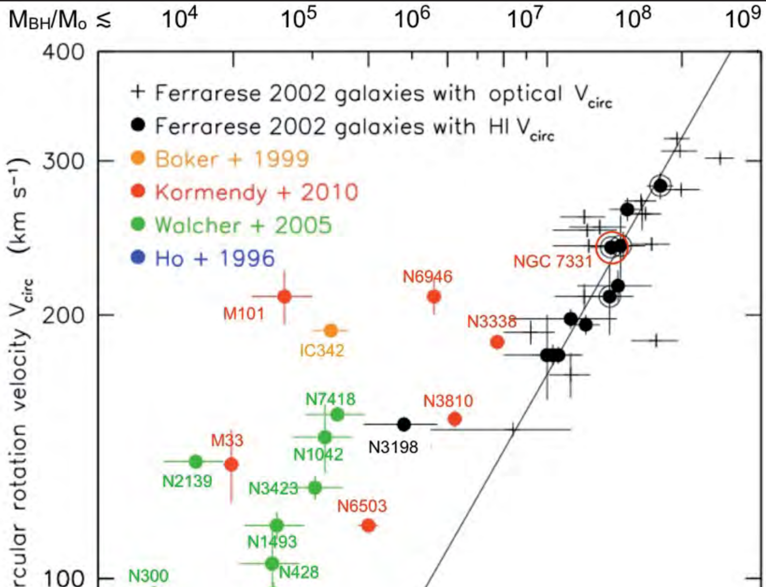

Outer rotation velocity V_{circ} vs. near-central velocity dispersion σ. We use σ as a surrogate for black hole mass. All objects with reliably measured black hole mass and velocity dispersion have a black hole mass that is similar to or smaller than the surrogate mass given at the top of the diagram for the velocity dispersion σ given at the bottom of the diagram. The BH–DM correlation of Ferrarese 2002 is shown in black symbols (circled if the galaxy has a classical bulge) except that points have been omitted if the σ measurement had insufficient velocity resolution. Error bars are 1 sigma. We add points (color) for galaxies measured with $\sigma_{instr} < 10$ km/s, i. e., high enough resolution to allow measurement of the smallest dispersions seen in galactic nuclei. The line (equation at bottom; velocities are in units of 200 km/s) is a symmetric least-squares fit to the black filled circles minus NGC 3198. It has $\chi^2 = 0.25$. The correlation coefficient is r = 0.95. This correlation is at least as good as $M_{BH} - \sigma$. The correlation for the + points has $\chi^2 = 2.6$ and r = 0.77. In contrast, the correlation for the color points plus NGC 3198 has $\chi^2 = 15.7$ and r = 0.70.

References: • Kormendy, J., Bender, R.: 2011, Nature 469, 377

J. Kormendy, R. Bender

Gas in the centre of nearby galaxies from SINFONI integral field spectroscopy

The gaseous material is considered to be the primary fuel source of the nuclear activity in galaxies. It is not only necessary for the formation and growth of nuclear black holes (BHs) but it is also a fundamental ingredient for the nuclear and circumnuclear starburst activity. We investigate the emission-line gas in the centre of six nearby galaxies by means of AO-assisted K-band integral field spectroscopy obtained with SINFONI/VLT. The spectra of the galaxies in the sample display several H_2 emission-lines and, in some cases, ionized hydrogen and helium emission lines. This, together with the high-spatial resolution provided by the observations, allow us to study in detail the morphology, physical properties and kinematics of the gas located in the innermost regions of the galaxies, and the star-forming regions associated with it. Additionally, we derive the gas mass content of the galaxies and analyse the role of the gas on the methods used to estimate the mass of the central BH.

From the SINFONI data we derived the 2D distribution and kinematics of the warm molecular and ionized gas of the nuclear regions (r ≤ 300 pc) of six nearby galaxies. The figure on the right shows an example of the H_2 distribution, velocity and velocity dispersion maps of two of the galaxies in our sample: NGC4536 and NGC3627.

A diversity of morphologies (bar- and ring-like distributions and either centrally peaked or off-centre emission) are observed. Similarly, the galaxies display a range of gas kinematics: circular rotation, highly-elliptical/quasi-radial flows, and irregular motions. Also, signatures of shocks are present in some of the galaxies, which could be driving the gas into the nucleus.

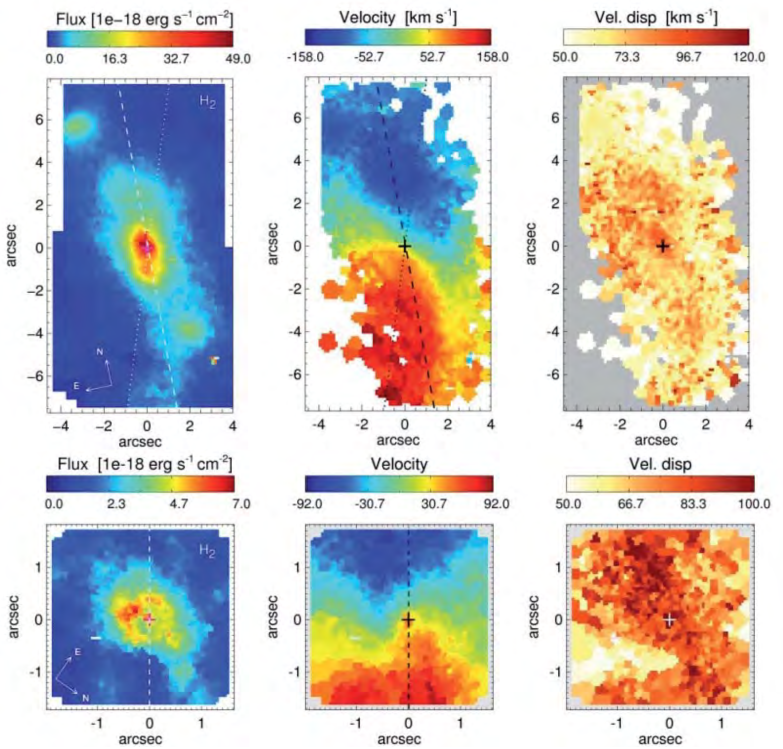

Flux, velocity and velocity dispersion maps for NGC3627 (upper panels) and NGC4536 (lower panels).

The galaxies in the sample contain large quantities of gas in their centres (up to ~10^8 $M_\odot$). Nevertheless, these masses are only 3% (at most) of the corresponding stellar masses. Hence, BH mass estimates based on the dynamical modelling of the stars should not be affected by the presence of gas. On the other hand, the complexity of the observed kinematics warns about the validity of the simple assumptions commonly made to derive BH masses from gas kinematics, and highlights the importance of full 2D information.

References:

• Mazzalay et al., 2013a, MNRAS, 428, 2389
• Mazzalay et al., 2013b, in preparation

X. Mazzalay, R. Saglia, P. Erwin, M. H. Fabricius, S.P. Rusli, J. Thomas, R. Bender, M. Opitsch, N. Nowak and M. Williams

Black Holes scaling relations

We analyse a sample of 91 galaxies with measured black hole (BH) masses, for which we determine the spherically averaged bulge density (ρ_h) and mass (M_{Bu}). We find that for early-type and classical bulges the M_{BH}-σ and M_{BH}-M_{Bu} residuals correlate with ρ_h. This is not the case for pseudo-bulges and points to different formation histories of the two classes of objects.

Our Sinfoni Black Hole (BH) survey measured the black hole masses at the centers of 23 galaxies (plus 3 upper limits). We joined our sample to the literature data to investigate correlations between global galaxy properties and BH masses. We measured the spherically averaged densities ρ_h within the half luminosity radius of 63 early-type plus 10 classical bulges and of 18 pseudo-bulges with measured BH masses. For the first class, M_{BH} correlates with M_{Bu} and σ (as already well known). Taking into account ρ_h as a further parameter reduces the scatter significantly. ‚Classical' bulges and black holes grow together. Low density, high M_{BH} systems (the core galaxies plotted in red below) result from gas-free (‚dry') merging of power-law early-types (plotted in black). These in turn are the product of gas-rich mergers. Present-day, young remnants of almost equal mass mergers of gas rich disky systems (plotted in green) are found below the M_{BH}-M_{Bu} correlation, because the bulge mass increases by a factor equal to the total to disk mass ratio of the progenitors, while the BH increases by just a factor two, not having had the time yet to accrete gas. At higher redshifts, when gas densities were higher, one expects the M_{BH}/M_{Bu} ratio to be higher than today. Therefore, compact local early-types or classical bulges (plotted in blue) with high average densities have M_{BH} larger than expected by their M_{Bu}.

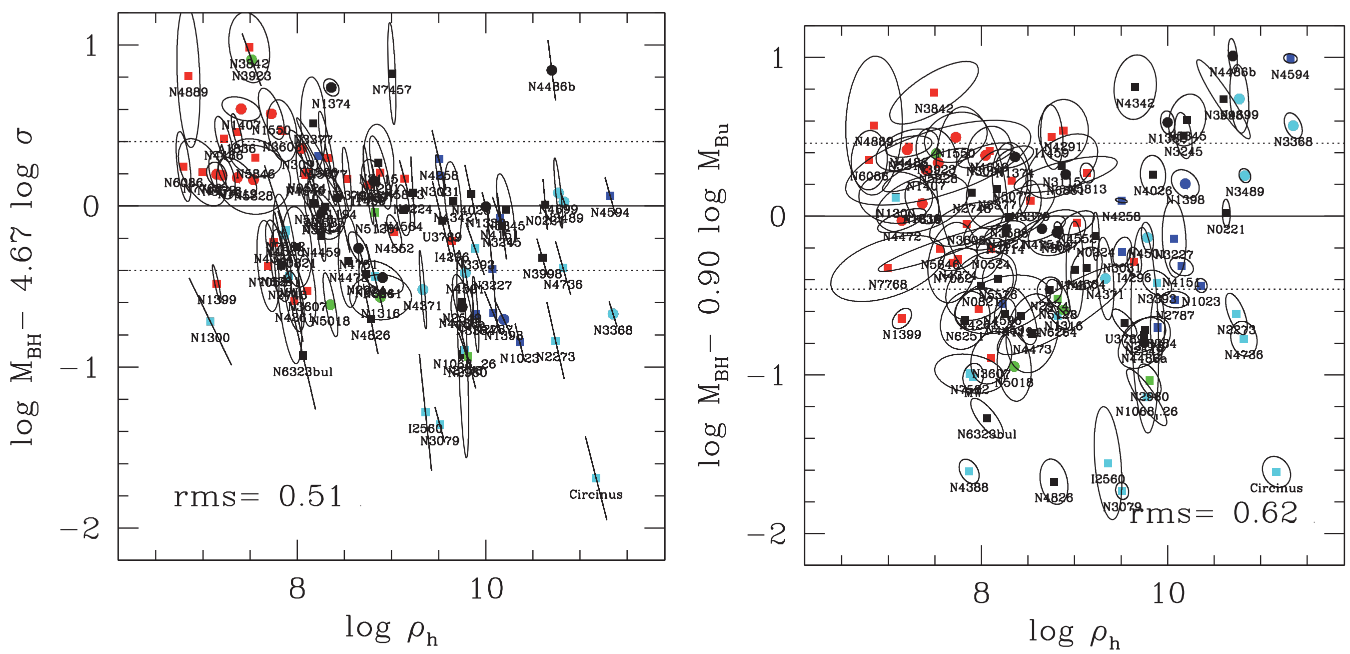

This is not the case for pseudo-bulges (plotted in cyan). The growth of pseudo-bulges (or disks) and black holes is decoupled, because it does not involve mergers. Composite systems like NGC 3368, NGC 3489 and NGC 4699 have both pseudo and small classical bulge. These last components do follow the known correlations.

References: Saglia et al. 2013, in preparation

R. Saglia, M. Optisch, R. Bender, P. Erwin, M. Fabricius, N. Nowak, S. Rusli, J. Thomas

SEDs of Luminous Red Galaxies
Photometric Redshifts and Stellar Populations

We create spectral energy distributions (SEDs) that optimally match the photometry of spectroscopic SDSS luminous red galaxies (LRGs) in five different redshift bins. We achieve this by superposing SEDs of composite stellar populations (CSPs) with a burst SED and allowing for extinction. From these SEDs we select a subset which represents the data in color space, thereby defining our novel template set for photometric redshift (photo-z) estimation. We show that templates that optimally describe the brightest galaxies indeed vary from z = 0.1 to 0.5, consistent with aging of the stellar population. Furthermore, we find that best fitting SEDs from galaxies at z < 0.1 strongly differ as a function of the absolute magnitude, indicating an increase in star formation activity for less luminous galaxies.

We generate SEDs for spectroscopic SDSS LRGs by fitting a superposition of a model and a burst SED from Bruzual & Charlot 2003 to the photometry of the LRGs with the fitting routine SEDfit (Drory+04). Thereof we select model SEDs that describe the data in five z bins from 0 to 0.5 for our photo-z template set. The results with the novel templates and the Bayesian photo-z code PhotoZ (Bender+01) are shown in Fig. 1. They exhibit a very low bias and scatter throughout the SDSS z range.

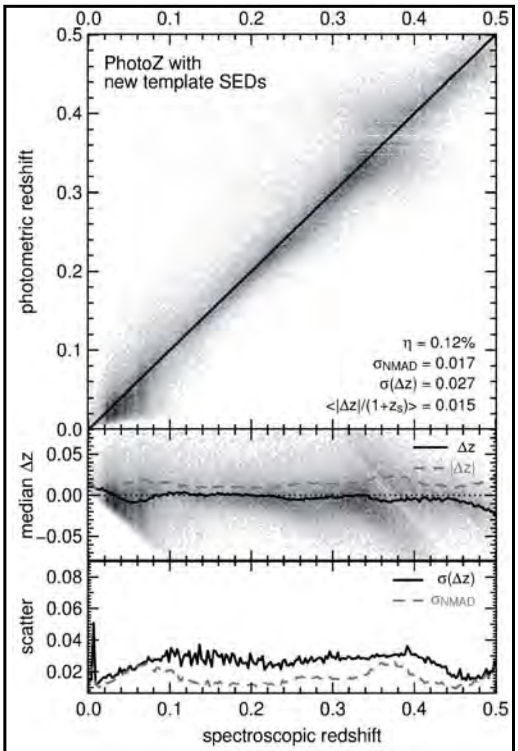

Figure 1. Photometric redshift results with the novel templates and spectroscopic SDSS LRGs. (Greisel+13)

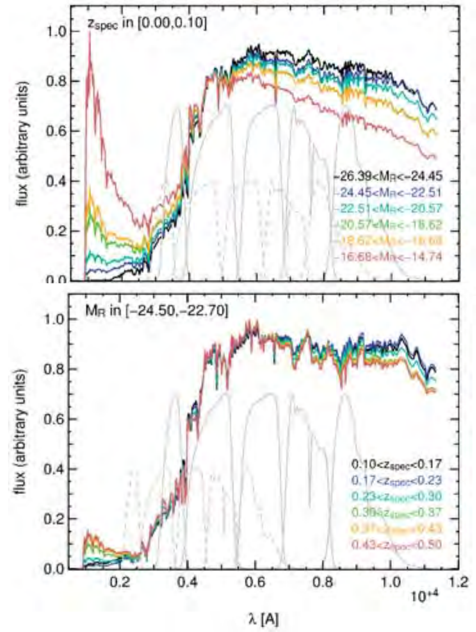

Figure 2. Flux weighted superposition of best fitting model SEDs as a function of R band luminosity for $z < 0.1$ (upper panel), and as a function of redshift for $z > 0.1$ and M_R in [-24.5, -22.7] (lower panel). (Greisel+13)

We perform a fit of the LRG photometry (at known z) to our novel template set and analyze the flux weighted superposition of best fitting SEDs for galaxies from different z-M_R bins (Fig. 2). We infer that local (z < 0.1) galaxies show increasing signs of star formation for decreasing luminosity (Fig. 2, upper panel). We observe the same behavior for stacked SDSS spectra within the same z-M_R bins.

The SEDs that describe the brightest galaxies best change with redshift in a way predicted by aging of stellar populations (Fig. 2, lower panel). Using SDSS emission line strength ratios as a measure for star formation confirms the results of the best fitting model SEDs (Greisel+13).

Our novel LRG-SEDs will be used by the PANSTARRS Photometric Classification Client (see Poster of Saglia+).

References:
- Bender R. et al. 2011, in Deep Fields
- Bruzual, G., & Charlot, S. 2003, MNRAS, 344, 1000
- Drory, N. et al. 2004, ApJ, 616, L103
- Greisel, N. et al. 2013, ApJ, in press, astroph

N. Greisel, S. Seitz, N. Drory, R. Bender, R. P. Saglia, J. Snigula

Morphology and quenching in the SDSS

Star-forming galaxies are dying. This process – dubbed quenching – has led to the buildup of a large population of passive elliptical galaxies over the last 8 billion years; however, the underlying mechanism(s) that govern quenching remain largely unknown. In this paper we use the combined spectroscopic and photometric data of the Sloan Digital Sky Survey to show that bulge formation plays an integral part in the shutdown of galaxies' star-formation activity.

In Mendel et al. (2013) we select quenched galaxies based on their spectroscopic properties: we require that they host a relative young stellar population and no ongoing star formation. Such galaxies comprise only 3% of the 680,000 galaxy SDSS DR7 sample. By comparing the morphology of these quenched galaxies with their presumed parent and destination populations – star-forming and passive galaxies, respectively – we can single out features immediately associated with the transition from star-forming to passive on short timescales.

The Galaxy Zoo project (Lintot et al. 2008) provides visual classifications for hundreds of thousands of galaxies in the SDSS by means of their mophological probabilities, $P_{\mathrm{elliptical}}$ and P_{spiral}. Star-forming and passive galaxies conform to the well-known properties of their populations: while passive galaxies are predominantly classified as ellipticals, star-forming galaxies are preferentially spirals. In contrast, quenched galaxies are neither clearly elliptical nor clearly spiral; instead, they fall between the star-forming and passive poulations, suggesting intermediate (bulge + disk) morphologies.

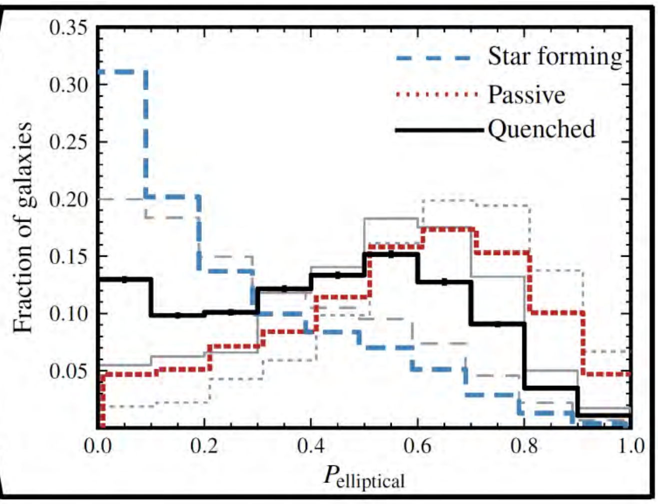

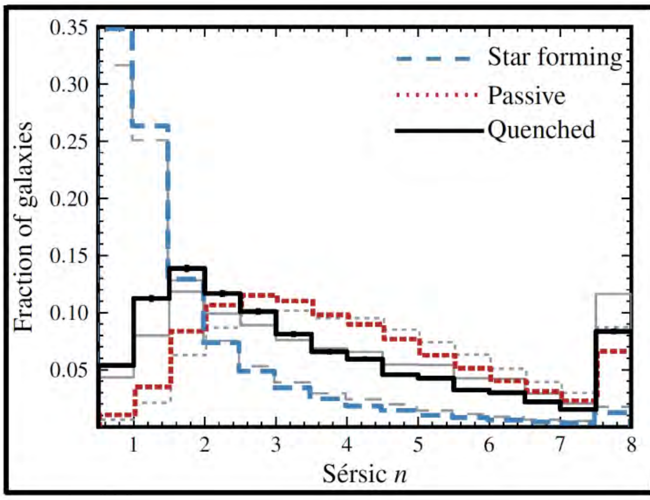

Sersic indices trace the 'cuspiness' of a galaxy's light profile and provide a quantitative measure of its morphology. By comparing the distribution of Sersic indices measured by Simard et al. (2011) for quenched galaxies with those of the star-forming and passive galaxy populations we show that the hallmark of quenching is the buildup of a cuspy light profile. Taken together the qualitative (visual) and quantitative morphlogies point towards bulge formation as playing a critical role in the quenching process.

References: Lintott et al., 2008, *MNRAS*, 389, 1179; Mendel et al., 2013, *MNRAS*, 429, 2212; Simard et al. 2011, *ApJS*, 196, 11

J. T. Mendel, L. Simard, S. L. Ellison, and D. R. Patton

The Origins of Galaxy Morphology

To understand the origin of galaxy morphological types in a hierarchical Universe, we measure the morphological mix in different environments and redshifts and compare with hierarchical models. Ellipticals form hierarchically in mergers but are less common than expected. To compensate, central galaxies with B/T$\gtrsim$0.2 must be passive, typically S0s. A second mode of S0 formation is required to explain the excess of lower mass S0s as satellites in >$10^{13}M_\odot$ halos.

Two Modes of S0 production:

Right: At redshift ~ 0, ~20% of central galaxies are S0s independent of stellar or halo mass. The same fraction of high-mass *satellite* galaxies are S0s, suggesting they are accreted central S0s. But in high-mass halos (>$10^{13}M_\odot$), the S0 fraction for lower mass (<$10^{11}M_\odot$) galaxies is much larger. This can be explained if spiral galaxies accreted from the field lose their star forming gas reservoirs and fade to form S0s [1]. Our observations at z~0.4 tell a consistent story [2].

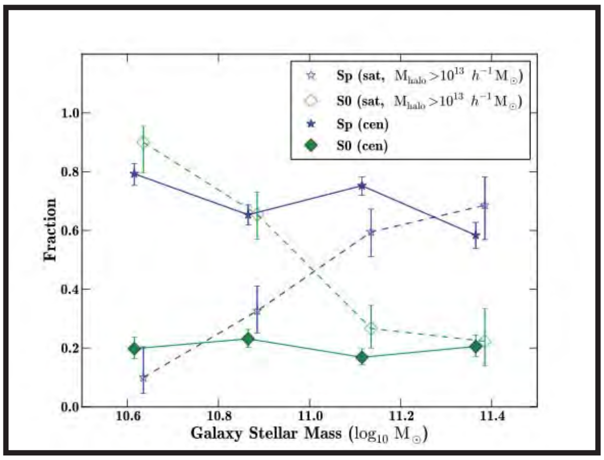

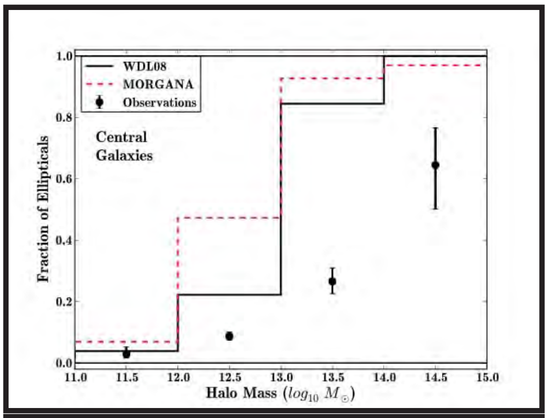

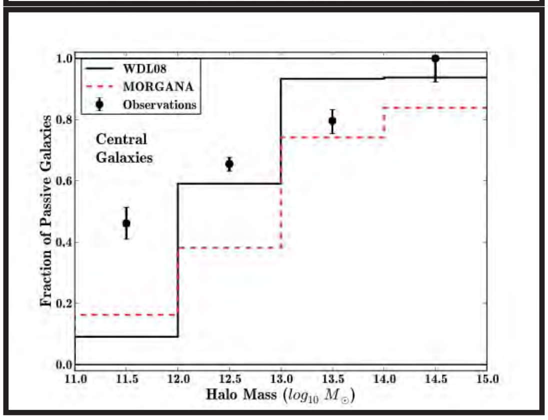

Hierarchical Origin of Ellipticals, and Passive Central Galaxies [4]:

Left (top): Ellipticals form hierarchically via major mergers, producing an increasing fraction with halo mass (for central galaxies). But elliptical (B/T>0.7) fractions are overpredicted by hierarchical models, even assuming ellipticals and bulges form only in mergers (lines, see [3]) when compared to the fraction of observed, visually classified ellipticals (data points). The impact of major mergers may be reduced if tidal stripping of satellite galaxies reduces the mass ratio of mergers and thus the frequency of major mergers.

Left (bottom): The passive (star formation rate x 100 Gyr < stellar mass) population of massive central galaxies is reasonably well reproduced in the same models, primarily because AGN feedback stops star formation in elliptical galaxies (which host particularly massive black holes). To successfully reproduce *both elliptical* and *passive fractions*, galaxies with B/T$\gtrsim$0.2 must have their star formation effectively quenched. This might explain the existence of central S0 galaxies.

References:
• [1] Wilman & Erwin, 2012, ApJ, 746, 160
• [2] Wilman et al., 2009, ApJ, 692, 298
• [3] De Lucia, Fontanot, Wilman & Monaco, 2011, MNRAS, 414, 1439
• [4] Wilman et al., 2013, MNRAS, submitted

D. Wilman, P. Erwin, F. Fontanot, G. De Lucia, P. Monaco

High-z absorption line kinematics with KMOS

At high redshift, when massive galaxy clusters first virialize, we have a unique opportunity to view the physical processes governing galaxy evolution in high-density environments. We are therefore using the superior multiplexing capabilities of KMOS on the VLT to undertake a comprehensive study of cluster galaxy dynamics at z ~ 1.5. The addition of spectroscopic data to high-quality HST imaging allows a *quantitative* connection between galaxies' internal dynamics, stellar populations, morphology, and surrounding environment, providing important constraints to current models of galaxy evolution. These data will increase the current number of stellar kinematic measurements by a factor of 5 at these redshifts, and for the first time facilitate a homogeneous study of galaxies' joint evolution in size, velocity dispersion and stellar mass during the peak of passive galaxy formation at z > 1.

The **KMOS-cluster** program will target key science areas:

- Evolution of the *velocity dispersion function* and its link to galaxy size growth [e.g. Fig. 1],
- The role of high-density environments in regulating star formation,
- Evolution of *mass-to-light* ratios and their connection to galaxy dynamics,
- A census of *early-type galaxy kinematics* at their peak formation epoch [2].

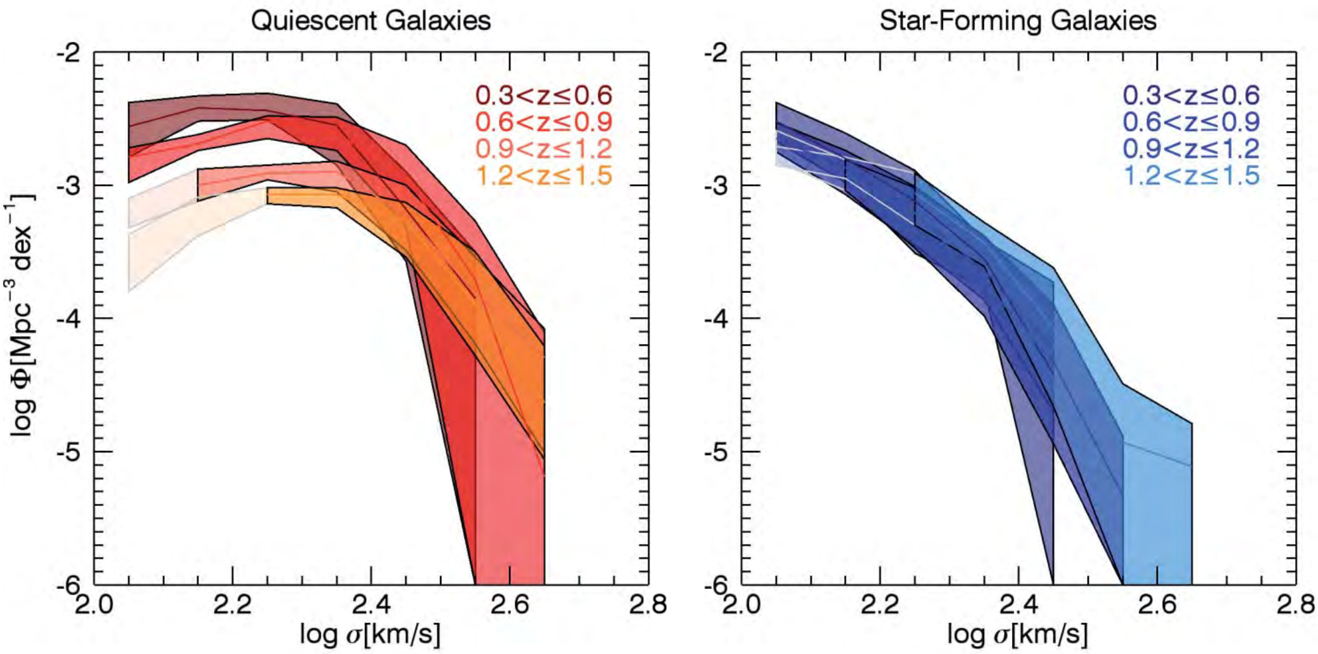

Fig. 1 - *Predicted evolution of the galaxy velocity dispersion function [1]. The functional form of the velocity dispersion function depends on the details of star-formation quenching as well as the evolving relationship between stellar and halo mass.*

References:
[1] Bezanson et al., 2012, *ApJ*, 760, 62; [2] Cappellari et al., 2011, MNRAS, 416, 1680

A. Beifiori, J. T. Mendel, R. Bender and the KMOS cluster survey team

Mass and Light in Clusters of Galaxies

Clusters of galaxies provide a unique test-bed of the physics of the dark universe, since they reside in a regime of size and mass sensitive to the interplay of dark matter and dark energy, the two most important puzzles of modern cosmology. We analyze seven clusters of galaxies, five selected by the SPT / Planck SZ signal and two targets of the CLASH survey, using shapes and photometric redshifts measured with MPG/ESO-2.2m WFI data. This allows a test of SZ mass calibration with weak gravitational lensing (WL), insights into the (sub)structure of clusters in terms of both mass and light and a comparison with our early DES results on two of these systems (Melchior+ in prep).

We perform a parametric reconstruction of mass profiles for our cluster sample, using galaxy shapes measured with a noise-calibrated pipeline based on KSB and PSFEx (Young, Gruen+ 2013). Our results confirm previous mass-observable relations at the high mass end (Fig.1). At lower masses, the statistical uncertainty of individual cluster measurements increases, yet there is evidence of deviations between weak lensing and SZ/X-ray masses of our cluster sample , likely due to the astrophysical state and orientation of the systems (Marrone+ 2012). Our low WL mass for one of the SPT clusters is in agreement with the result of McInnes+ 2009 (black symbol).

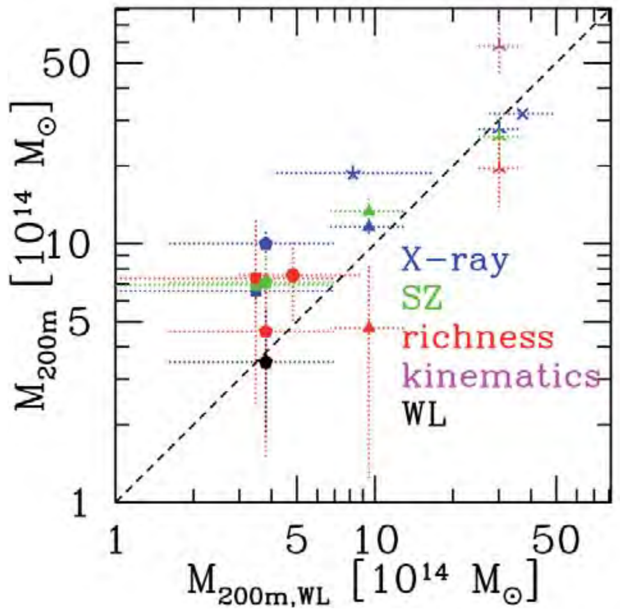

Figure 1: Mass estimates for our sample of seven clusters versus our weak lensing mass.

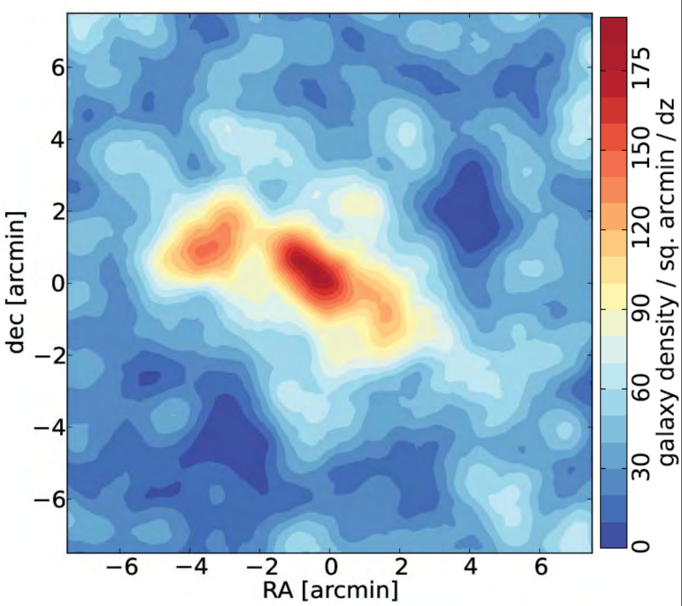

Figure 2: Complex structure of galaxy density (calculated with minimum variance kernel of 1‘ radius inside $|\Delta z|<0.08$) around RXC J2248.7-4431 (Gruen+ 2013).

Apart from the astrophysical state, one important factor influencing mass estimates (including lensing) are sub- and neighboring structures (Gruen+ 2011). Using galaxies as a tracer, we therefore study the environment of our clusters (Fig. 2), confirm the sensitivity of weak lensing to the complexity of matter profiles and measure the abundance of subpeaks (Kosyra+ in prep).

References:
- Gruen, Bernstein, Lam, Seitz (2011), MNRAS, 416, 1392
- Gruen, Brimioulle, Seitz+ (2013), MNRAS in press
- Kosyra, Bender, Brimioulle, Gruen, Seitz+, in prep, author list tbd
- Marrone+ (2012), ApJ, 754, 119
- McInnes+ (2009), MNRAS, 399, L84
- Melchior, Brimioulle, Gruen, Seitz+, in prep, author list tbd
- Young, Gruen+, in prep, author list tbd

D. Gruen, S. Seitz, F. Brimioulle, R. Kosyra

High redshift galaxies in CLASH RXCJ2248: z~6 quintuple lensed galaxy

Clusters of Galaxies, acting as gravitational lenses, offer a unique tool to observe high redshift galaxies magnified by the cluster and thus to investigate the galaxy population of the early Universe. In the context of the CLASH survey, we use a wide photometric data set to identify z>5 galaxies through the 'dropout' technique, with the aim to explore the faint end of the LF at z>5 taking advantage of the high magnification in the inner region of Cluster.

The Cluster Lensing And Supernovae with Hubble (CLASH) multi-cycle treasury program (PI. M. Postman, Core Team Member S. Seitz, Postman et al. 2012) is targeting 25 galaxy clusters in 16 HST filters spanning the range from the UV to the NIR (Fig.1). One of the main goals of the survey is to investigate high-z galaxies magnified by the clusters. Galaxies at z>5 appear as optical dropouts in photometric data set, since their restframe UV emission is redshifted in the NIR range. The dropout technique (Steidel et al. 1996) is widely used to identify the Lyman-α break (λrest=1216Å) redshifted in the NIR range for z>5 (Fig.1). Early type galaxies at z~1.5 appear as optical dropouts as well, thus the analysis of the NIR colors is needed to discriminate low- and high-z dropouts (see Fig2). We use the CLASH photometric data set to identify robust z>5 candidates which are optical dropouts, with blue NIR colors (as expected for star forming galaxies at z>5) and with photometric redshift zphot>5. So far, we selected ~30 candidates at z>5 which satisfy these criteria in 6 CLASH clusters.

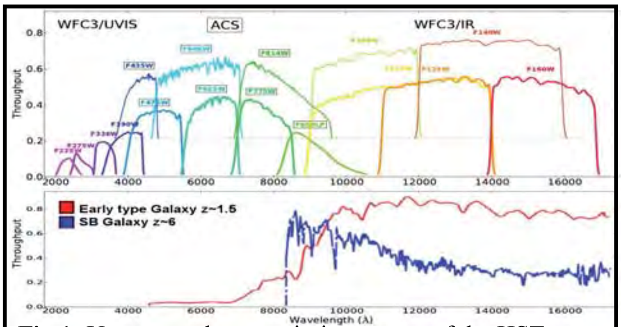

Fig 1: Upper panel: transmission curves of the HST filters of the CLASH survey. Lower panel: template SED of a star forming galaxy at z~6 (blue) and an early type galaxy at z~1.5(red): both are observed as optical dropout.

<u>The case of RXCJ2248</u>: we selected 4 high-z candidates in the field of the galaxy cluster RXCJ2248 (zcl=0.35) which are likely multiple images of a galaxy at z~6 (Monna et al, in prep.). Photometric analysis support the high-z nature of these sources (Fig.2): they are optical dropouts, first detected in the f814 filter, with blue NIR colors and zphot ~5.9. We performed a strong lensing analysis of the cluster using further 10 multiple lensed systems, and our best final model predicts z~6 for this system, with magnification of ~13 for the brighter image. Thanks to the lensing prediction, we identified a fifth dropout image in the central region, clearly detected after removing the BCG (Fig.2). The delensed photometry leads to a faint galaxy with Luv = 0.35L*, referring to the luminosity function at z=6 (Bouwens et al. 2012). We modeled the observed SED of these sources to estimate physical properties, obtaining best fit for very young galaxy (~Myr), with M~109 Msun.

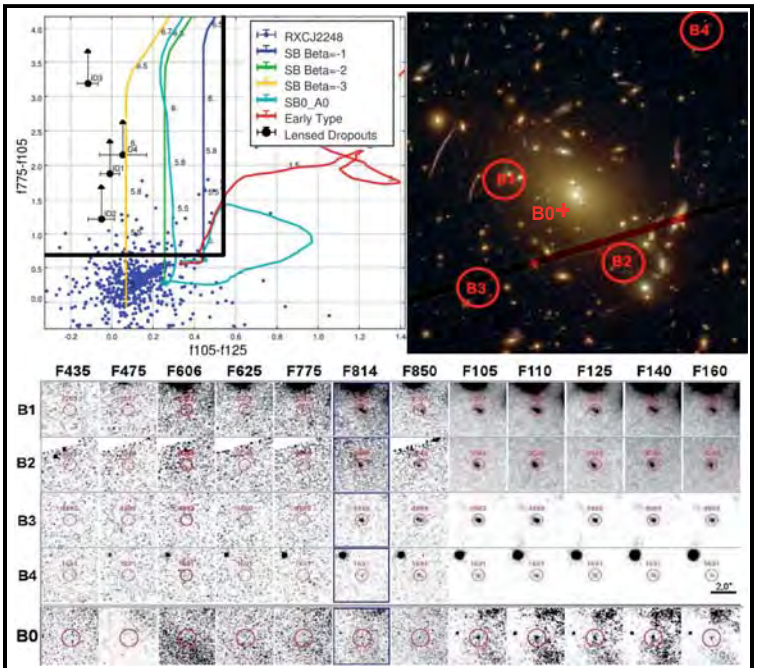

Fig 2: Upper left: NIR color diagram with redshift-color galaxy Tracks overplotted.The black lines trace the color area limit for star forming galaxies at z>5. The black points are our 4 dropouts. Upper right: HST color image of RXCJ228, red circles are our 4 dropout, the red '+' is the central image predicted from the lensing model. Lower panel:postages of the 5-image system at z=6. The central image (B0) is detected after the BCG subtraction.

References: Postman et al 2012, ApJS, 199, 25
Steidel et al. 1996, ApJ 462, L17
Bouwens et al 2012, ApJ 754, 83B
Monna et al., in prep.

A. Monna, S. Seitz

An HOD model of multiscale measurements of the influence of environment on galaxy properties

The fraction of galaxies with red colours depends sensitively on environment. To distinguish competing theories for the quenching of star formation and its dependence on halo mass, we have developed a model using the Millennium simulation (Springel 2005) and a simple HOD (halo occupation distribution) prescription which describes the **multiscale density field** of Sloan Digital Sky Survey DR7 galaxies (Phleps et al., submitted). We model the red fraction of central galaxies as a constant while we use a functional form to describe the red fraction of satellites as a function of halo mass which allows us to distinguish a sharp from a gradual transition. The data can only be explained by a gradual transition. We also rule out a sharp transition for central galaxies, within the halo mass range sampled.

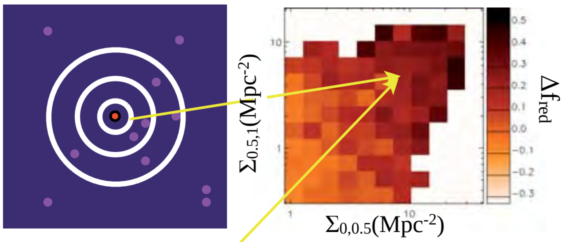

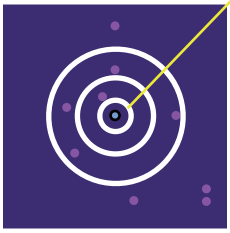

Annuli of variable inner and outer radii are centred on each galaxy, and the surface density $\Sigma_{ri,ro}$ of neighbouring galaxies within these annuli and within δv = 1000 km s^{-1} is measured. We then explore the dependence of the excess red galaxy fraction Δf_{red} on these multiscale densities.

We parametrise the fraction of red satellite galaxies in the model as a function of halo mass using a tanh function with two free parameters, a transition mass M_t, and a slope, Γ. We find that a model with a shallow slope fits the data best: A very steep slope can be ruled out for both central and satellite galaxies. For the satellites, we find log M_t=13.8 and Γ=3.0 to fit the data best.

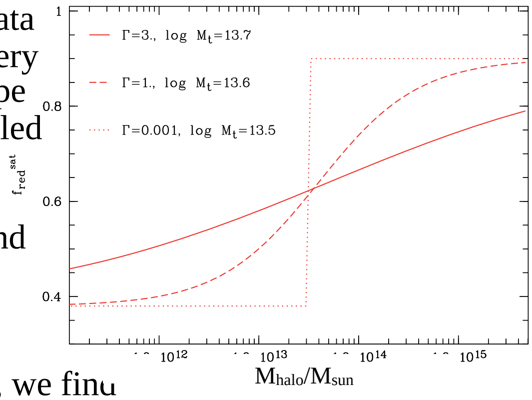

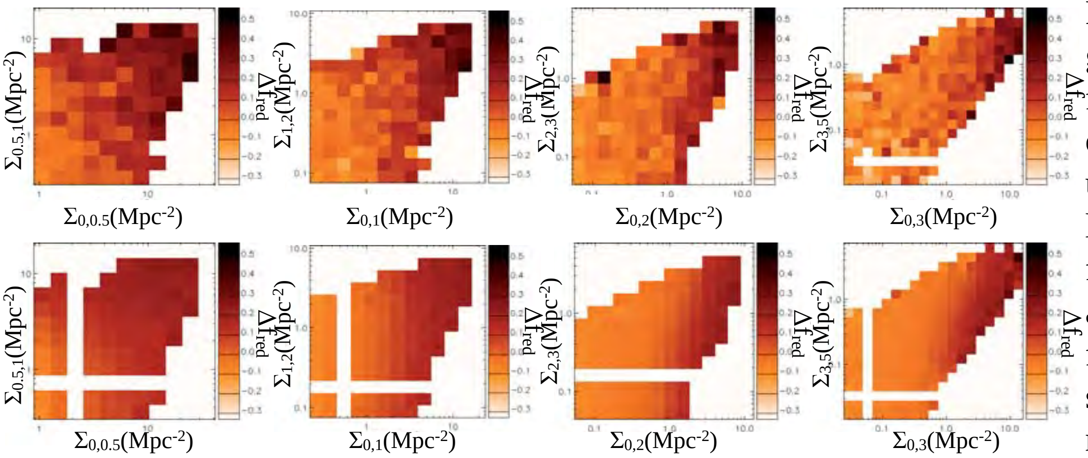

Fraction of red galaxies as a function of density on different scales, upper panel: data, lower panel: best-fitting model (with a slowly rising fraction of red satellites with halo mass).

References:
•Phleps, Wilman, Zibetti and Budavári, submitted to MNRAS
•Springel, 2005, Nature, 435, 629
•Wilman, Zibetti and Budavári, 2010, MNRAS, 406, 1701

S. Phleps, D. J. Wilman, S. Zibetti, and T. Budavâri

The clustering of galaxies in BOSS

The Baryon Oscillation Spectroscopic Survey (BOSS) is one of the four components of SDSS-III. Thanks to its large volume and average number density, BOSS will measure the large-scale structure (LSS) of the Universe with unprecedented precision, providing new insights on the origin of cosmic acceleration. By applying state-of-the-art modeling techniques we explore the cosmological implications of the galaxy clustering measurements in BOSS. The accuracy of our cosmological constraints is a clear demonstration of the constraining power of LSS observations in the current era of precision cosmology.

Early results from BOSS show a strong detection of the baryon acoustic oscillations (BAO). This can be seen in the figure on the left, where the red points correspond to the two-point correlation function, $\xi(s)$, of the CMASS sample from BOSS DR9 (Sánchez et al. 2012). The BAO signal can be seen as a broad peak on large scales. A comparison of this measurement with the results from Eisenstein et al. (2005, blue points), shows the improvement in the statistical uncertainties of LSS measurements since the first detection of the BAO signal.

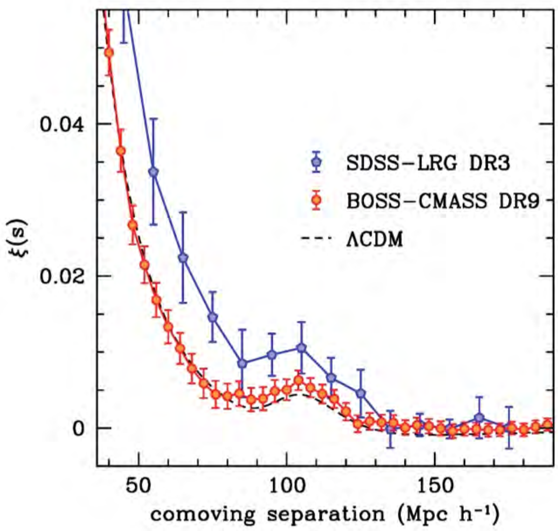

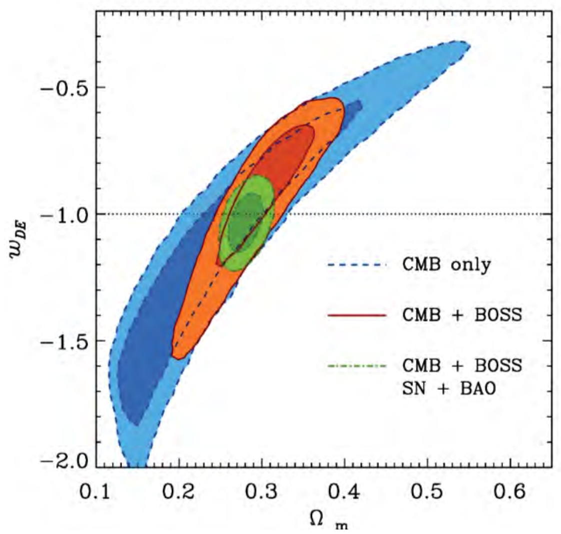

The information contained in $\xi(s)$ can be used to constrain cosmological parameters. As an example, the figure on the right shows the joint 68% and 95% confidence levels in the Ω_m - w_{DE} plane inferred from CMB data alone (blue) and its combination with the CMASS $\xi(s)$ (red). The CMB-only constraints show a strong degeneracy, which is alleviated by the inclusion of BOSS data. Adding also SN information and BAO measurements from other surveys (green) leads to a final constraint of $w_{DE} = -1.03 \pm 0.07$, in good agreement with a cosmological constant.

These results are based on the first spectroscopic data release of BOSS. The larger volume that will be probed by subsequent data releases will reduce the uncertainties in the clustering measurements. These new datasets will push the achievable precision on our cosmological constraints to a new level, allowing us to put the ΛCDM paradigm under even stricter scrutiny.

References:
- Eisenstein et al., 2005, ApJ, 633, 560
- Sánchez A., et al. 2012, MNRAS, 425, 415

A. G. Sánchez, F. Montesano

The three point statistics for large scales
The bispectrum: Estimation of the bias parameters

Galaxies are biased tracers of the underlying dark matter density field. In order to use the spatial distribution of galaxies as a means to constrain cosmological parameters, it is of pivotal importance to understand and quantify how they relate to the dark matter. This relation is called biasing. The linear and quadratic bias parameters b_1 and b_2 can be extracted from three-point statistics, such as e.g. the bispectrum. For our model of the bispectrum we modified the commonly used tree-level ansatz [1] by replacing the linear power spectra by the 3rd order perturbation theory equivalents, in order to be able to put tighter constraints on b_1 and b_2.

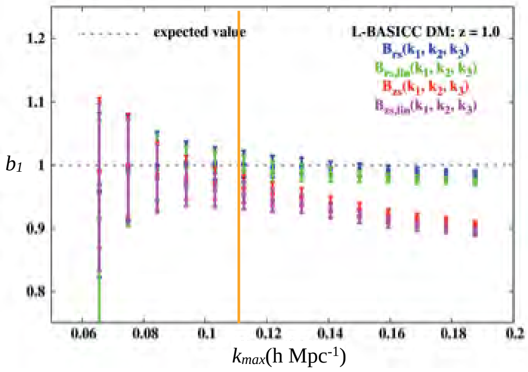

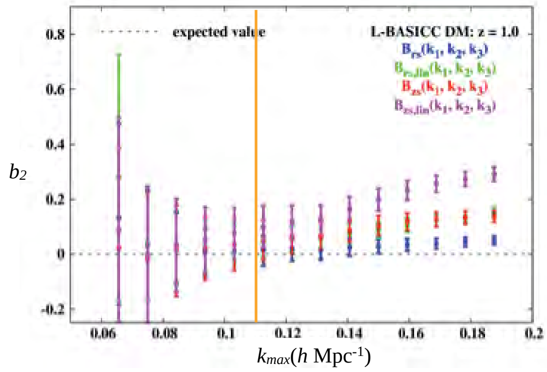

Above: Bias parameters for the dark matter L-BASICC II simulation [3] (where the bias parameter are known, b_1=1.0 and b_2 = 0.0) vs. maximum k-modes k_{max} included in the fit of the model at redshift z=1.0. Green and purple: original tree-level ansatz, blue and red: modified tree-level ansatz (each for real and redshift space, respectively). **The fit can thus be extended to larger k_{max}.**

Below: Linear and quadratic bias for L-BASICC dark matter halos at z=1.0 in real and redshift space (including linear Kaiser effect [3] in that case).

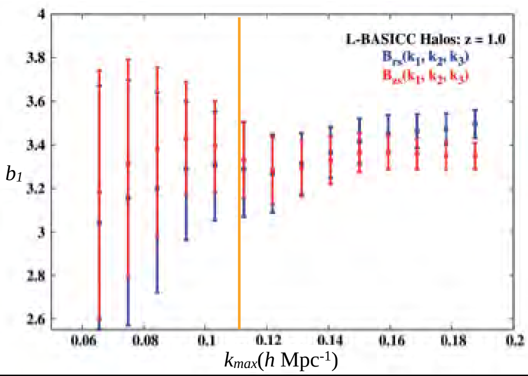

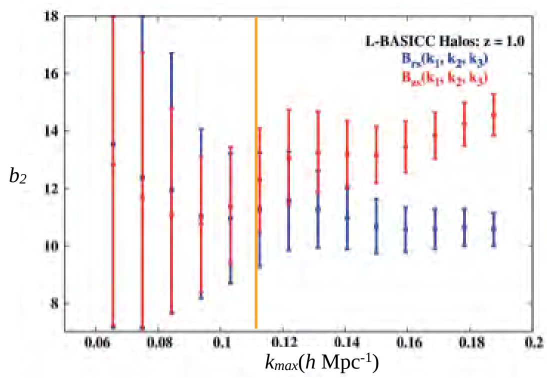

A consistent estimate of both bias parameters in real and redshift space can be achieved for scales up to 0.11 h Mpc^{-1}. For larger k the model has to be further improved.

References:

[1] Bernardeau F., Colombi S., Gaztanaga E. & Scoccimarro R. 2002, PhysRep, 367, 1
[2] Angulo R. E., Baugh C. M., Frenk C. S. & Lacey C. G. 2008, MNRAS, 383, 755
[3] Kaiser, N. 1987, MNRAS, 227, 1

H.A. Schlagenhaufer, S. Phleps and A.G. Sánchez

Modelling the galaxy power spectrum

The power spectrum (PS) of the galaxy distribution contains information about the origin, evolution and composition of the Universe. Because of non-linear evolution, galaxy bias and redshift-space distortions, an accurate modelling of the full shape of the PS is necessary for a precise measurement of cosmological parameters and to improve our knowledge of dark energy (DE), one of the great mysteries of modern physics. We have proposed a new phenomenological model of the PS that can account for the above distortions, and used it to obtain accurate cosmological constraints.

Present and future galaxy redshift surveys, like the Sloan Digital Sky Survey III (SDSS), are designed to provide very accurate measurements of the large scale structure of the Universe. The blue lines and shaded regions in Fig. 1 show the PS measured from a set of mock catalogues built to mimic data release (DR) 9 of the SDSS [1]. It deviates from the predictions of linear theory (green lines) already at k~0.07 h/Mpc. We developed a new model for the PS, shown by red lines, that clearly improves over the linear prediction. The inset in Fig. 1 shows the same PS divided by a reference one in order to enhance the baryon acoustic oscillations feature.

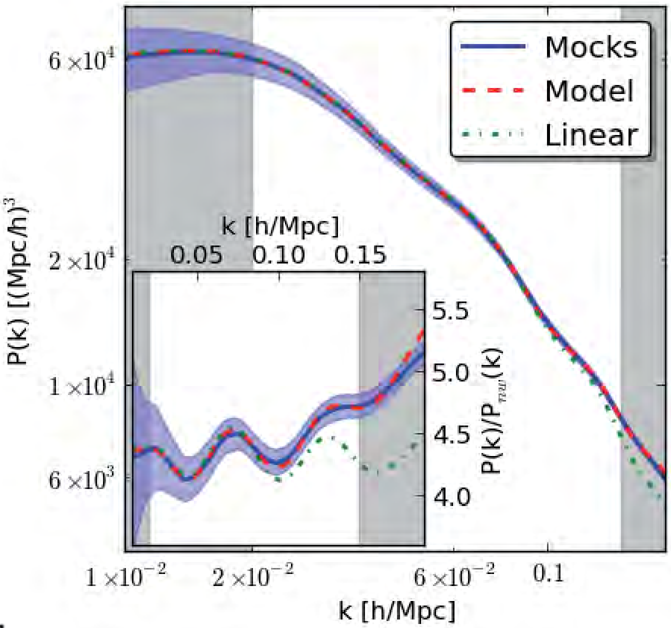

Figure 1

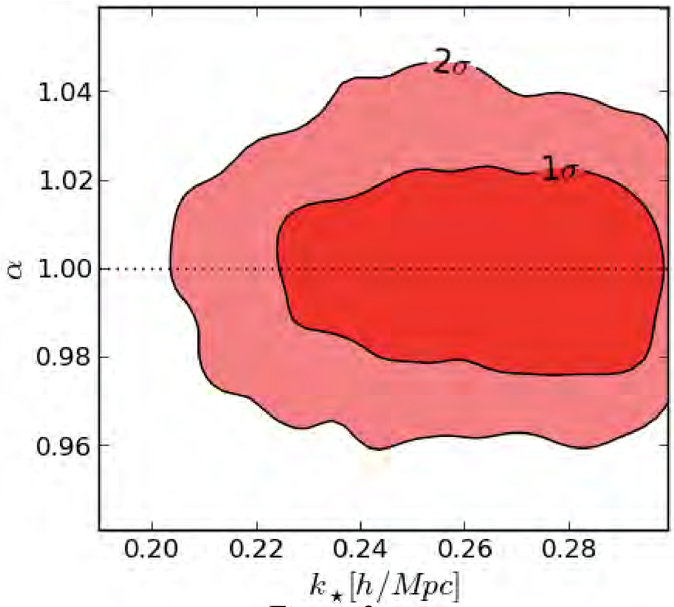

Figure 2

To test its accuracy, we allow the model to stretch adding a parameter α and fit it against the mock PS. For an unbiased model, we expect α to be 1. Fig. 2 shows the 1σ and 2σ constraints on α and a model parameter k_*, when fitting the model in the range k=0.02-0.15 h/Mpc (white background in Fig. 1). We measure α=1.00± 0.02, showing that the model provides unbiased constraints on cosmological parameters. Indeed, this model has been already successfully used in the analysis of a galaxy sample from the SDSS DR7 [3] and will be soon applied to a sample about 500000 galaxies that will be publicly released as part of the SDSS DR10.

References:
[1] Manera M. et al., 2013, MNRAS, 428, 1036
[2] Montesano F. et al., 2010, MNRAS, 408, 2397
[3] Montesano F. et al., 2012, MNRAS, 421, 2656

F. Montesano, A.G. Sánchez, S. Phleps and the BOSS clustering working group

Correcting for Non-Linearities in Galaxy Clustering Measurements

Non-linear evolution distorts the galaxy two-point correlation function, however, modelling this effect is extremely challenging. We investigate two reconstruction techniques aiming at correcting for these distortions. First, reconstruction of the displacement field removes bulk flow distortions. Second, we apply logarithmic transformations of the measured density field. Using large-volume N-body simulations, we show that these methods can improve the accuracy of the cosmological constraints derived from large-scale structure observations.

1) Displacement Field Reconstruction

The BAO feature in the statistics of the matter density field can be sharpened using the displacement field from Lagrangian perturbation theory (Eisenstein et al. 2007). We apply this technique to the density field of our simulations.

2) Logarithmic Transformations

The density field can also be linearised by applying logarithmic transformations, $\delta \rightarrow \log(\delta)$, which enhances correlations with the initial conditions (Neyrinck 2011). We apply such transformations to the density field of our simulations.

Two-Point Correlation Function

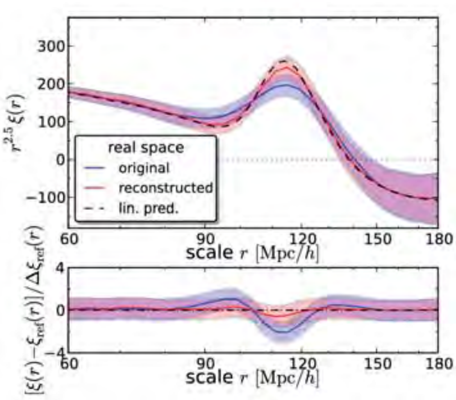

The figures show the effect of displacement field reconstruction (left panel) and a logarithmic transformation (right panel) on the matter correlation function, ξ(r), from our N-body simulations. The reconstructed results are in closer agreement with the linear-theory prediction down to scales r ~ 30 Mpc/h, with a sharper BAO peak.

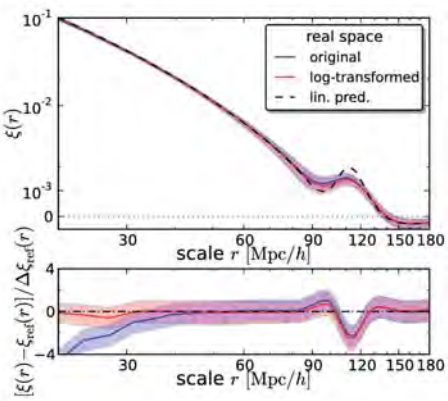

Dark Energy Constraints

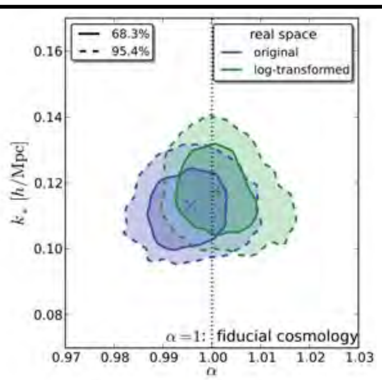

These reconstruction techniques can lead to significant improvements in the attainable cosmological constraints. We explore this using the parameter space of the dewiggled model for ξ(r) and find improved constraints on the stretch parameter α, which can be converted into constraints on the dark energy equation of state parameter, w. The effects of redshift-space distortions and halo bias are also analyzed.

We plan to extend our analysis of improved constraints to ongoing galaxy-redshift surveys such as BOSS in the near future.

References:

- Eisenstein, Seo, Sirko, & Spergel 2007, ApJ, **664,** 675
- Sanchez, Baugh, & Angulo 2008, MNRAS, **390**, 1470
- Grieb, Sanchez, Montesano 2013, in. prep.
- Neyrinck 2011, Astrophys.J., **742**, 91, and references therein

J. Grieb, A. G. Sánchez and F. Montesano

Clustering Tomography

We tested a new technique to detect the Baryon Acoustic Oscilation (BAO) signal in the angular two-point correlation function $\omega(\theta)$ of thin redshift bins, aiming to determine distances and providing unbiased constraints on cosmological parameters, without assuming a fiducial cosmology in order to transform angular positions and redshifts into comoving distances.

Using a set of 160 mock catalogues [1] designed to reproduce the properties of the SDSS DR7 spectroscopic LRG sample within $0.16 < z < 0.44$, we have measured angular correlation functions of thin redshift shells of $\Delta z = 0.028$. Additionally, based on renormalized pertubation theory [2], we constructed a model for the full shape of $\omega(\theta)$, including effects such as redshift space distortions, nonlinear growth of density fluctuations and bias.

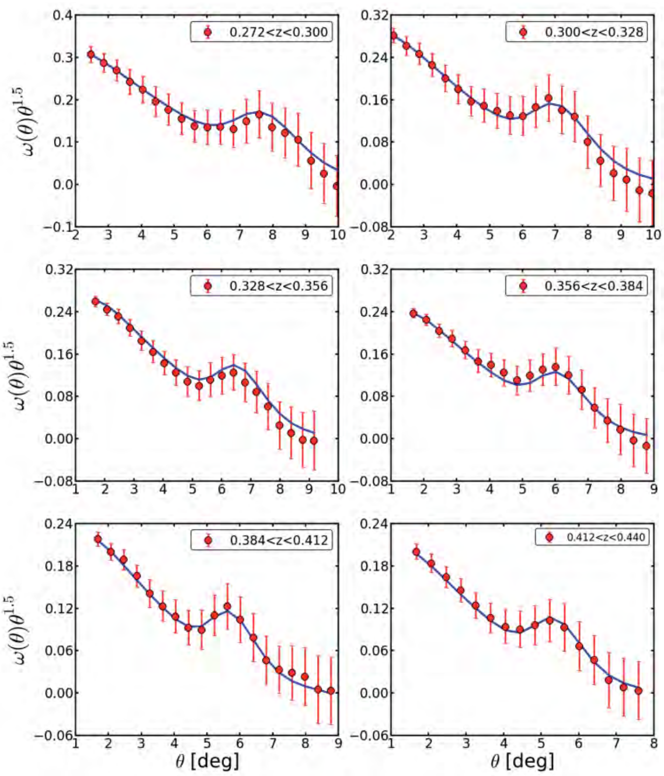

Figure 1: *Measurements of the mean angular correlation function for 6 redshift shells (red dots). In the Y-axis, $\omega(\theta)$ is amplified by $\theta^{1.5}$ in order to highlight the BAO peak. The errorbars correspond to the error in the mean. The solid blue lines correspond to the predictions of our model, which simultaneously reproduce $\omega(\theta)$ for all the shells.*

We applied this model simultaneously to the measurements of all redshift shells, in order to extract the information contained in $\omega(\theta)$ and provide constraints on cosmological parameters. In this case, we focused on the dark energy equation of state, w_{DE} , for a flat ΛCDM model, and on the mean bias of the sample. We are able to extract the correct values used to construct the mocks, showing that this method can provide unbiased constraints on cosmological parameters.

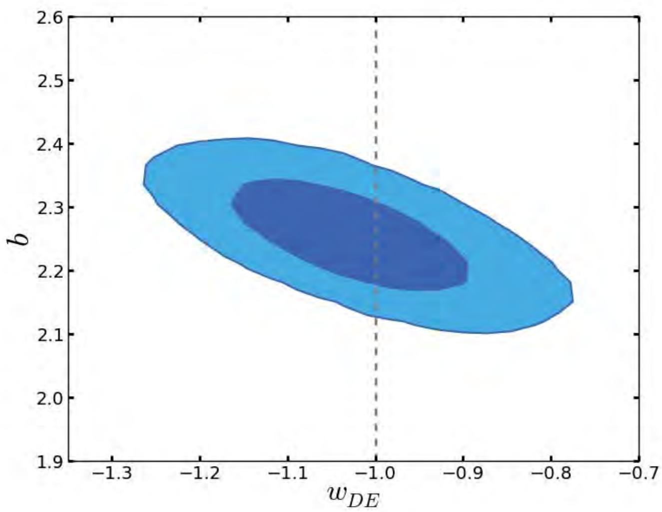

Figure 2: *Constraints on the dark energy equation of state and the mean bias of the sample. These results show that our method can provide unbiased constraints on cosmological parameters from the information enclosed in $\omega(\theta)$.*

References:

• [1] LasDamas project, *http://lss.phy.vanderbilt.edu/lasdamas/*

• [2] Crocce M.,Scoccimarro R., 2006a, Phys. Rev. D, 73, 063519.

S. Salazar, A. G. Sánchez, C. Baugh, N. Padilla.

PAndromeda - the high-cadence monitoring of M31 with Pan-STARRS 1

The Pan-STARRS 1 (PS1) survey of M31 (PAndromeda) is designed to identify gravitational microlensing events caused by bulge and disk stars (self-lensing) and by compact matter in the halos of M31 and the Milky Way (halo lensing or lensing by massive compact halo objects). With the 7 deg^2 field of view of PS1, the entire disk of M31 can be imaged with one single pointing. Between 2009 and 2012 we were able to monitor M31 in r_{P1} and i_{P1} bands with a daily sampling (limited by weather) for 20 minutes per night for up to 5 months per year.

From a preliminary analysis of the 2010 season (91 nights, 30 h integration, 12% of the field) we published (Lee et al. 2012) light curves for six candidate microlensing events in the central 40′ × 40′ region of M31 (Fig. 1 and 2). This is a competitive rate compared with previous M31 microlensing surveys. The identification of four short-duration microlensing events with t_{FWHM}~1–3 days shows that the time resolution of the PAndromeda project is comparable with the best two seasons of the WeCAPP project (where we coordinated two telescopes, see Riffeser et al. 2008). We are currently analyzing the full data set of all four PAndromeda seasons (see Tab. 1).

filter	frames	hours	nights
g	248	4.2	28
r	2619	46.3	243
i	1301	21.7	150
z	80	1.2	16
y	205	3.7	35
grizy	**4453**	**77.2**	**256**

Tab. 1 The full data amount for the PAndromeda seasons 2009-2012 is 22.4 TeraBytes consisting of 4453 frames observed in 256 nights

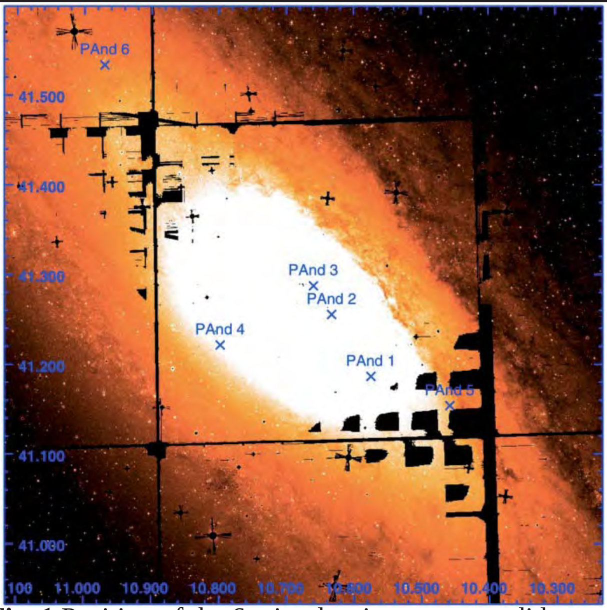

Fig. 1 Position of the 6 microlensing event candidates detected in the central 40' x 40' region of M31

By finding or excluding microlensing events in the outer disk of M31, the PAndromeda survey will manifestly exceed the accuracy of previously derived M31-halo-MACHO fractions. Actual studies of the dynamics of the M31 bulge (Saglia et al. 2010) help to better quantify the bulge self-lensing contribution in the center of M31. We further use the data for novae detection and investigation of other variables like cepheids (Kodric et al. 2013), eclipsing binaries (Lee in prep), LBVs (Lee in prep) and LPVs (Snigula in prep). For these studies we correct fluxes with our M31 extinction map (Montalto et al. 2009).

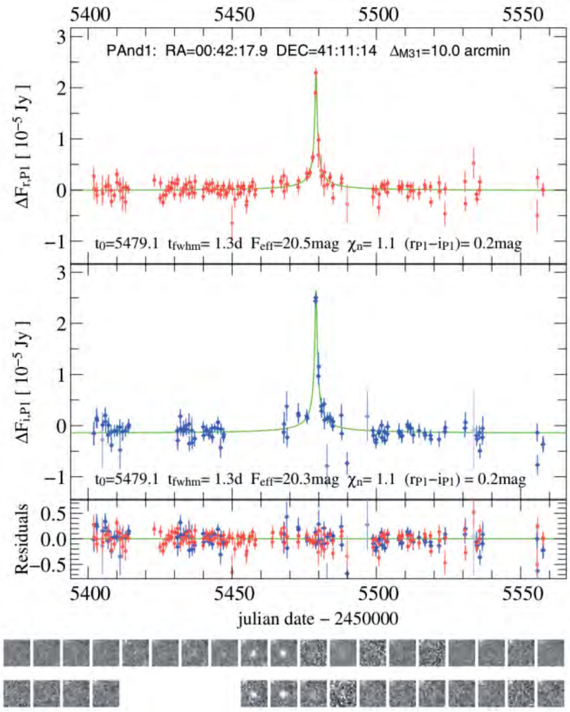

Fig. 2 Light curves of the PAnd-1 event, r_{P1}-band *(red dots)*, i_{P1}-band, *(blue dots)*, *grey:* difference image postage stamps

References:
- Kodric, M., et al. 2013, AJ, 145, 106
- Lee, C. H., et al. 2012, A&A, 537, A43
- Montalto, et al. 2009, A&A, 507, 283
- Riffeser, A., et al. 2008, ApJ, 684, 1093
- Saglia, R. P., et al. 2010, A&A, 509, A61

A. Riffeser, C. Lee, S. Seitz, R. Bender, M. Kodric, J. Koppenhoefer, V. Hopp, J. Snigula, C. Goessl

PAndromeda Cepheids

We derive a sample of Andromeda galaxy (M31) Cepheids based on the first year of the Pan-STARRS 1 survey in the $_{rP1}$ and i_{P1} filters. The 2009 Cepheids we find constitute the largest Cepheid sample in M31 known so far. By determining the age of the Cepheids we are able to show that the 10 kpc ring in M31 has an age gradient. The M31 Period-Luminosity relation (PLR) we derive indicates that the PLR has a curvature term.

We develop an automatic Cepheid detection using Fourier decomposition and the location of the instability strip to find 2009 Cepheids in the first year of PAndromeda data (for a description of these data see Lee et al. 2012).
Using period-age relations [1] we obtain a deprojected spatial age distribution (top panel Fig. 1). The Cepheids nicely follow the 10 kpc ring found previously [2]. The bottom panel of Fig. 1 shows the median age for bins withs width of ≈6.8 kpc. The first and the last two bins contain less than 10 Cepheids and thus can be neglected. The errors determined with the bootstrap method are shown in magenta. The dispersion of each bin is shown in black. We observe an age gradient and the fit to the median age is shown as a solid magenta line. The age gradient suggests that the star formation related twe detect old (faint) Cepheids in the seventh bin, but no young Cepheids. This leaves us with the conclusion that there is an age gradient in the 10 kpc ring of M31.
Our period luminosity relation (Fig. 2), is dominated by the long period Cepheids. This is due to the Malmquist bias and the detection limit for faint (small period) Cepheids. The Bono et al. 2010 predictions for long period Cepheids are in good agreement with our PLR-slopes. Bono et al. also predict a curvature term in the PLR, which we will be able to analyze after we determine the slope of the faint end of the PLR with our final M31 data. The existence of a curvature term in the PLR has ramifications on the determination of extra galactic distances. This is because most of the commonly used calibrations of the PLR are dominated by the short period o the interaction with M32 moved inwards. In this first data set we can not find Cepheids in the center of M31. We hardly detect old (faint) Cepheids in this region, most likely due to the low signal to noise ratio of our data in the center of M31. The lack of young Cepheids in the outer region of the ring is not due to a selection bias, since Cepheids whereas the typical Cepheids that are used for the extra galactic distance determination are long period, bright Cepheids.
Our final goal is to determine the PLR of M31 more precicely over a broader period range, and then to combine this with distance estimates for M31 eclipsing binaries (see poster of Lee et al.) to finally obtain a calibrated PLR.

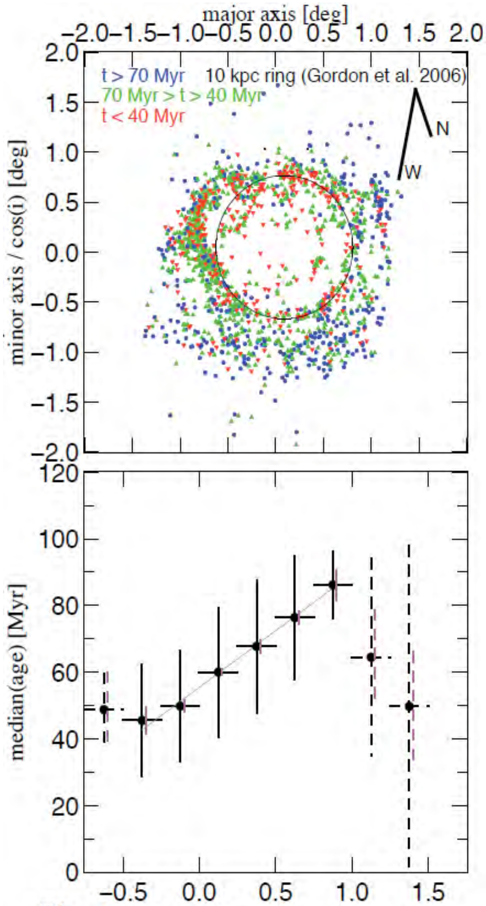

Fig. 1 Δ r [deg] relative to the 10 kpc ring

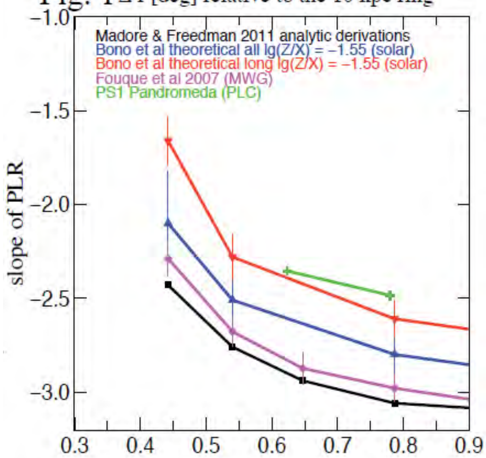

Fig. 2 λ [μm] of PLR

References:
• [1] Bono et al. 2005 • Bono et al. 2010 • Kodric et al. 2013
• [2] Gordon et al. 2006 • Lee et al. 2012

M. Kodric, A. Riffeser, U. Hopp, S. Seitz, J. Koppenhoefer, R. Bender et al.

PAndromeda Eclipsing Binaries

The Pan-STARRS-1 PAndromda Survey monitored the M31 galaxy in the years 2010-2012. High precision light curves of several hundred thousand resolved sources have been obtained in the r- and i-bands. We search for periodic eclipses in this data and fit the folded light curves with realistic binary models in order to determine the system parameters (Teff, gravity, radii). We find 36 detached or semi-detached eclipsing binaries (EBs) with V<20 suitable for follow-up spectroscopically and M31 distance determination.

We apply our detection algorithm to the PAndromda light curves of all resolved sources down to the detection limit. The algorithm is based on the box-fitting least squares algorithm proposed by Kovacs et al. 2002 with an additional fit for a secondary eclipse and a trapezoidal re-fit of the primary and secondary eclipse (for details we refer to Zendejas et al. 2013).
Figure 1 shows the folded r-band light curve of an eclipsing binary system with a period of 2.7 days together with the trapezium fit of our detection algorithm in green.

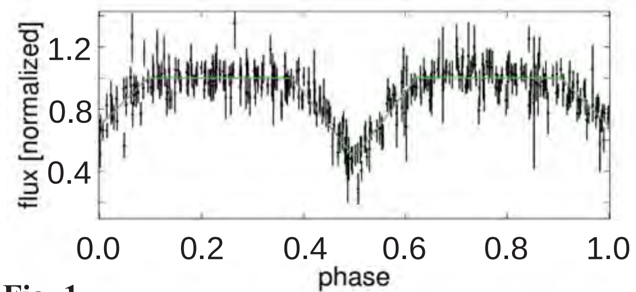

Fig. 1

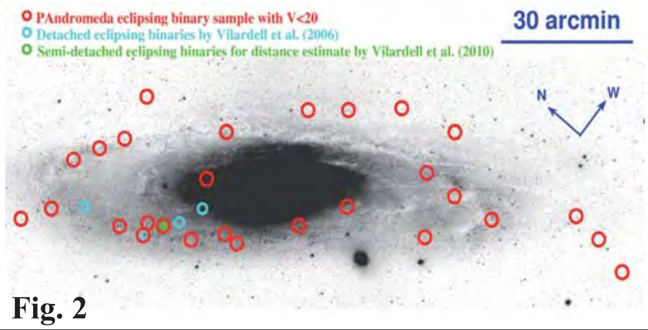

Fig. 2

Using optical and NIR multiband photometry from the Local Group Survey and the HST PHAT project we estimate the effective temperatures of the two components which we then use as a prior in the detailed light curve fitting with an analytical binary model proposed by Wilson and Devinney (1971).

Our dedicated box-fitting algorithm is efficient in filtering out over-contact eclipsing binaries and leave us with detached and semi-detached ones. Since the detached eclipsing binaries are more favorable for distance determination, we used the results of the Wilson-Devinney routine to finally select the detached eclipsing binaries.

To find out the most suitable eclipsing binaries for measuring the distance to M31, we select the ones that are brighter than 20 mag in V. Our sample is shown in Figure 2, with red circles. To compare with previous studies, we also plot the bright, detached eclipsing binaries from Vilardell et al. (2006). This shows that our sample has a better coverage of the full disk of M31. This Figure also shows the two eclipsing binaries that Vilardell et al. (2010) used to determine the distance to M31 (in green circle); these two eclipsing binaries are, however, semi-detached. The most interesting systems from our sample will be followed-up spectroscopically in order to derive radii and masses and to estimate the distance to M31 with high precision. An accurate M31 distance plays an important role in calibrating the PL relation of Cepheids, which is essential to our Cepheid project (see Kodric et al. 2013).

References:

1. Kodric et al. 2013, accepted by AJ
2. Kovacs et al. 2002, A&A 391, 369
3. Vilardell et al. 2006, A&A 459, 321
4. Vilardell et al. 2010, A&A 509, 70
5. Wilson and Devinney 1971, ApJ 166, 605
6. Zendejas et al. 2013, submitted to A&A

C.-H. Lee, J. Koppenhoefer, S. Seitz, A. Riffeser, U. Hopp, R. Bender

Pan-Planets

The Pan-STARRS1 Planet Survey is a wide field search for transiting extra-solar planets in the Galactic disk. In the years 2009-2012 we monitored the brightness of more than a Million stars. The main focus of the project is to study the occurance rate of Hot Jupiters around M-dwarfs and to potentially detect the first extra-solar planet orbiting a White dwarf.

Pan-Planets is one of the key projects of the Pan-STARRS1 science consortium. The survey utilizes the PS1 telescope which is operated at Haleakala Observatory. In four years we collected a total of 170 observing hours. The survey strategy has been optimized using Monte-Carlo simulations (Koppenhoefer et al. 2009). Seven slightly overlapping fields in the Cygnus region of the Milky Way have been observed for approximately 1 hour per night over a period of 4 years. The total survey area of 40 square degrees.

The data analysis is based on the MDia package (Koppenhoefer et al. 2013), a high precision photometry tool which utilizes the image subtraction technique. At the present time we have completed the analysis of about 25% of the data. Figure 1 shows the RMS of all normalized light curves as a function of the i-band magnitude. The red line indicates the expected photometric precision based on photon noise calculations. At the bright end, a precision of 5mmag is reached.

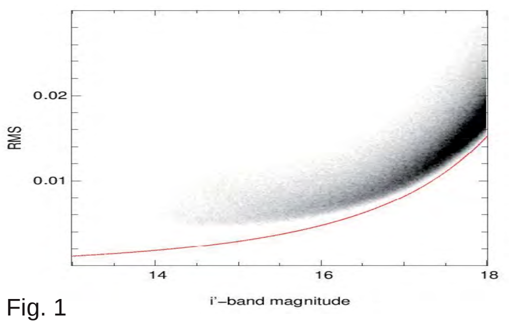

Fig. 1

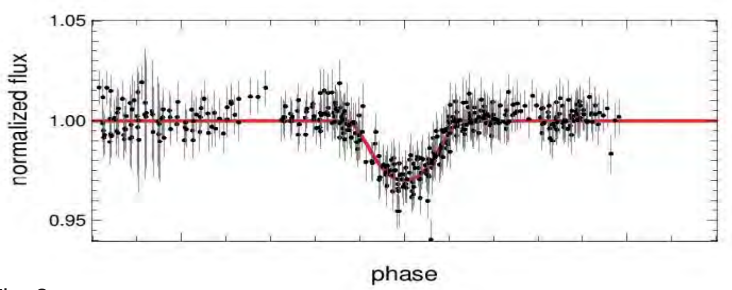

Fig. 2

Using a modified version of the box-fitting least squares algorithm we identified several planet candidates around faint M-dwarfs which are currently being followed-up. In addition we found a promising planet candidate around a brighter star (i=15 mag) of spectral type F/G. Figure 2 shows the folded light curve together with the best fitting transit model in red.

In addition we found a few planet candidates around White dwarfs. These objects show extremely short transits (in the order of a few minutes only) and therefore have only few points in transit. Photometric follow-up with a very high temporal resolution will be crucial to investigate the true nature of these candidates.

Our follow-up strategy is making use of the low-resolution spectrograph at the Hobby-Eberly-Telescope (HET). A comparison of the observed spectra to synthetic templates allows us to derive the effective temperature of our candidates. Photometric observations with the Calar Alto 1.23m telescope centered on predicted transit times enable us to derive more precise period estimates for our candidates and provide light curves with a better time resolution. This helps us to remove false detections. Promising candidates will be further followed-up with high-resolution spectroscopy at the HET and the Keck telescopes.

References:

- Koppenhoefer et al. 2009, A&A, 494, 707
- Koppenhoefer et al. 2013, ExA, 35, 329

J. Koppenhoefer, Th. Henning, R. P. Saglia, C. Obermeier, R. Bender, A. Riffeser

The RoPACS ITN FP7 Project

During the period 2009-2012 the RoPACS ITN FP7 project searched for planets around cool dwarf stars using the Widefield Transit Survey lightcurve dataset collected in the J band at UKIRT. We discovered 2 planets very near to an F and a K star and several M-dwarf binaries, but no hot Jupiters around these cool systems.

We followed up our best candidates spectroscopically with the HET telescope, confirming two planets (WTS-1b, Cappetta et al. 2012; and WTS-2b, Birkby et al. 2013), both of them (very) hot Jupiters orbiting an F7V and an K2V star respectively. WTS-1b has one of the largest radius anomalies among the known hot Jupiters in the mass range 3-5 M_J. WTS-2b is unusally close-in, at just 1.5 times the distance at which it would be destroyed by Roche lobe overflow, with a predicted lifetime of just ~38 Myr. In contrast, we did not find any hot Jupiter around M-dwarfs, our prime target population. This allowed us to set up an interesting upper limit (1.9% at 95% confidence) to the fraction of M-dwarfs brighter than 17 J mag hosting Jupiter-like planets on orbits with periods shorter than 10 days (Kovacs et al. 2013). Furthermore, we pushed the analysis of the light curves to J=18 mag using difference imaging without finding any candidate planet around M-dwarf (Zendejas et al. 2013).

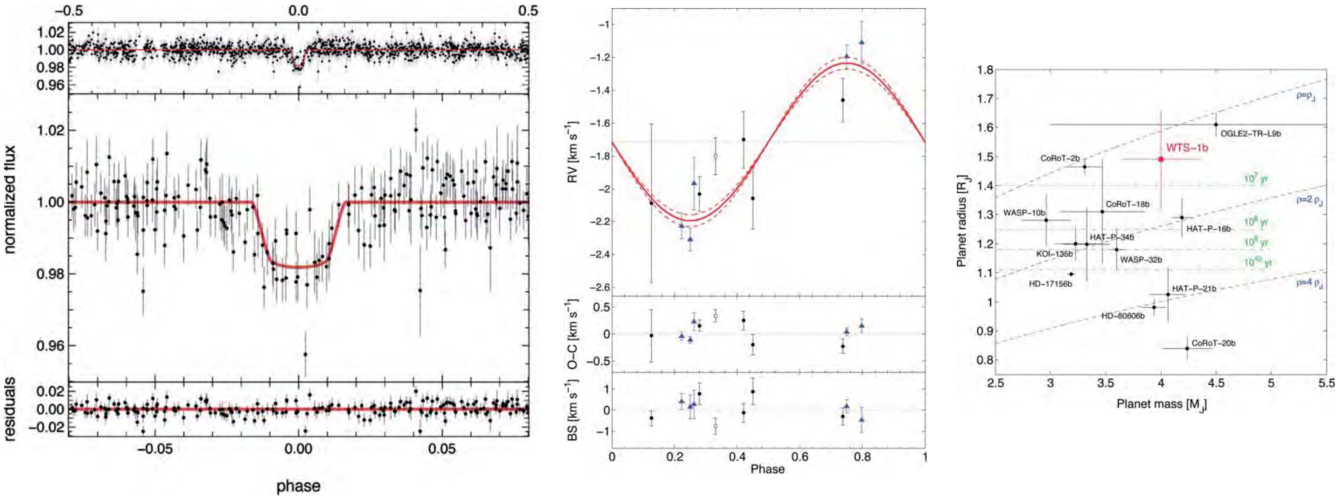

Left: the J-band light-curve showing the transit of WTS-1b**. Middle:** the HET radial velocity curve of WTS-1b. Right: the position of WTS-1b in the Radius-Mass diagram.

A by-product of the survey was the discovery of several detached M dwarf eclipsing binaries, in particular four with ultra-short periods (≤0.18 d, Nefs et al., 2012). Such systems are interesting for both measuring in a model independent way the fundamental parameters of these poorly understood yet numerous stars, and for probing the models of formation of low-mass binaries (Birkby et al. 2012). In our HET search for binaries we also found a white dwarf – brown dwarf (of 56 Jupiter masses) system rotating with an amazingly short period of 102 minutes, the shortest ever detected (Steele et al. 2013).

References:
• Birkby et al. 2012, MNRAS, 426, 1507 ; Birkby et al. 2013, MNRAS, sub.; Cappetta et al. 2012, MNRAS, 427, 1887 ;Kovacs et al. 2013, MNRAS, in press, astro-ph/1304.1399; Nefs et al. 2012, MNRAS, 425, 950 ; Steele et al. 2013, MNRAS, 429, 3492; Zendejas et al. 2013, A&A, sub.

R. Saglia, M. Cappetta, J. Koppenhöfer, P. Steele, J. Zendejas

Search for giant planets in M67

Precise stellar radial velocities are used to search for massive (Jupiter masses or higher) exo-planets around stars in the open cluster M67. We aim to obtain a census of massive exo-planets in a cluster of solar metallicity and age in order to study the dependence of planet formation on stellar mass and to compare in detail the chemical composition of the stars with and without planets. This work presents the sample, the radial velocity distribution of the stars and individuates the most likely planetary candidates.

Method: The Radial Velocity Spectroscopy is an indirect method, based on Doppler effect measurements, used to determine periodic RV changes in the stars that can be attributed to the gravitational influence of one or more planets on a host star or to intrinsic pulsations of the stellar surface. We observed 88 main sequence stars, subgiants and giants, all highly probable members of M67 (cfr. Fig.1), using four telescopes and instruments combinations: the HARPS spectrograph at ESO 3.6m, the SOPHIE spectrograph at OHP, the CORALIE spectrograph at the Euler Swiss telescope and the HRS spectrograph at HET telescope. We investigate whether exo-planets are present by obtaining radial velocities with a precision as good as ~10 m/s. To date, we have performed more than 740 single observations and a preliminary analysis of the data, spanning a period of 9 years. After reducing all the observations to the HARPS zero point, we evaluated the RV variability of the observed stars versus the V magnitude (cfr. Fig.2) to individuate some possible candidates for planet hosts.

Results: Although the sample was preselected to avoid the inclusion of binaries, we identify 11 previously unknown binary candidates. The RV variance (including the observational error) for the bulk of the stars is almost constant with stellar magnitude at ~20 m/s. Nine stars show a RV variability greater then 45m/s (corresponding to the red dashed line in Fig.2): they are interesting candidates for planets host (cfr. Fig.3).

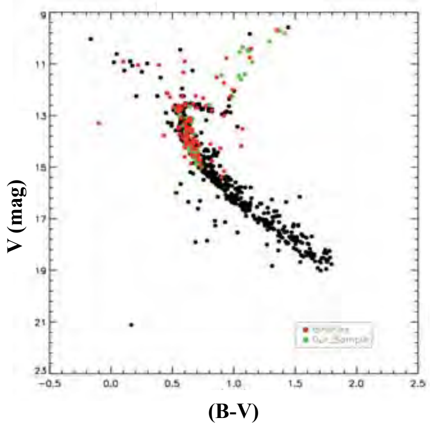

Fig.1: Color-magnitude diagram of M67. The photometry is from Yadav et al. 2008. Binaries either from this work or literature are marked in red colors. The stars of our sample are in green .

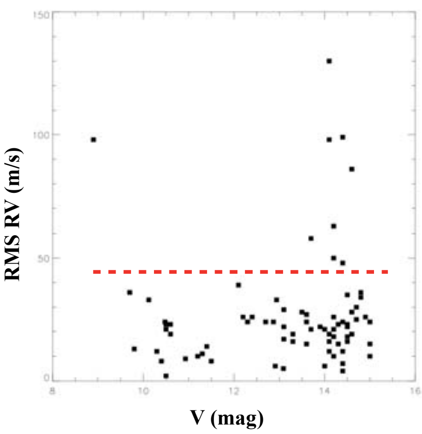

Fig.2: Radial velocity variability of the observed stars vs V mag. Nine stars show a RV variability >45m/s (red dashed line in the plot): they are interesting candidates for planets host.

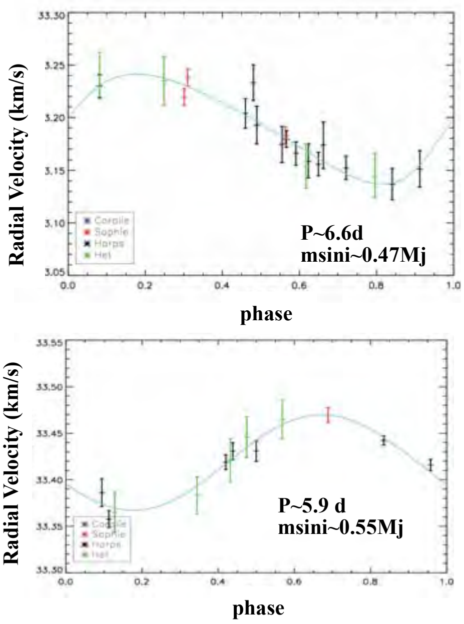

Fig.3: Phased Radial velocity curves and preliminary fits for two stars belonging to the list of our candidates.

References:

- Pasquini,L., Brucalassi, A. et al. 2012, A&A..545A.139P
- Yadav, R.K.S.,Bedin L.R., et al. 2008, A&A, 484, 609

A. Brucalassi, R. P. Saglia, et al.

The photometric classification server (PCS) for Pan-STARRS1 (PS1)

MAX-PLANCK-GESELLSCHAFT

MPE

The PS1 survey is obtaining multi-epoch imaging in five bands ($g_{P1}r_{P1}i_{P1}z_{P1}y_{P1}$) over the entire sky north of declination -30 deg. PCS (Saglia et al. 2012, 2013) allows the automatic classification of objects into star/galaxy/quasar classes based on colors and the measurement of photometric redshifts for extragalactic objects.

The object classificationPanDiSC is based on a support vector machine, a statistical learning algorithm. The photometric redshifts produced by PanZ are derived performing Bayesian spectral energy distribution fitting. The codes are interfaced to the PS database (see Figure, left), run unsupervised on our multinode cluster when new data become available, and publish the results back to the database in Hawaii.

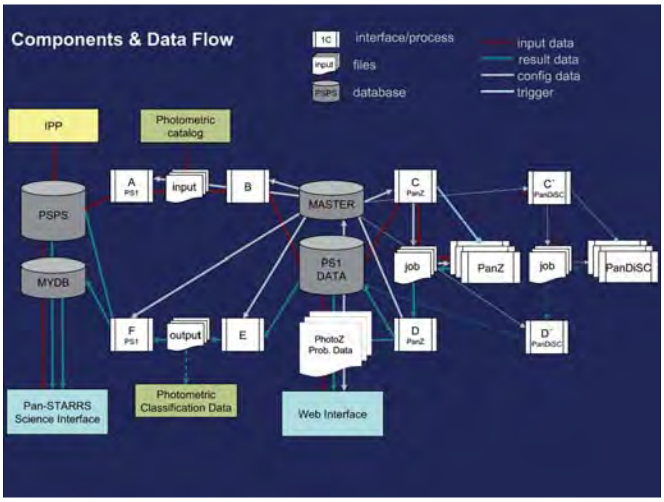

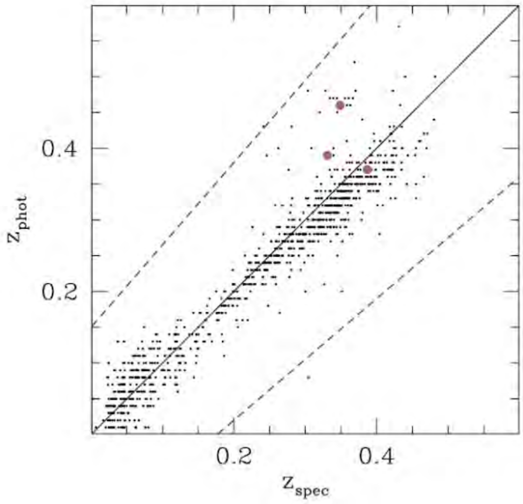

Left: the schema of PCS. **Right:** the precision of photometric redshifts for RLGs. The magenta points show the 3 objects for which the QSO SEDs would give the best.

We used the photometry derived from the Medium-Deep Fields of Pan-STARRS1 to test the system in combination with available spectroscopic surves as training and or verification sets. The table demonstrates the success of the PanDIsC classifications (85% for stars, 97% for galaxies, 83% for QSOs). The purity of the corresponding samples is highest for galaxies (99%), while it can be improved for stars (81%) and QSOs (72%) when morphologies are taken into account. Photometric redshifts are of excellent qualities for red luminous galaxies (RLGs, 2.4% in $\Delta z/(1+z)$, see figure to the right and histogram below) thanks to a newly developed set of templates (Greisel et al. 2013). The quality is slightly degraded for blue objects (in $\Delta z/(1+z)=0.042$) and rather poor for QSOs (the correct redshift is found in only 22% of the cases) due to the lack of u-band data.

True Classes	N_{tot}	Star	Galaxy	Quasar
Star	450	412	23	15
		0.916	0.051	0.033
Galaxy	4750	99	4525	126
		0.021	0.953	0.026
Quasar	550	25	15	510
		0.046	0.027	0.927

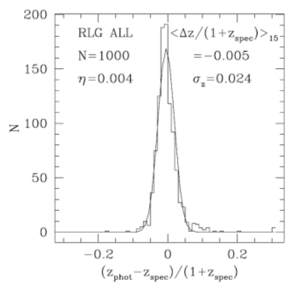

References:

• Saglia et al. 2012, ApJ, 746, 128;Saglia et al. 2013, EA, 35, 337; Greisel et al. 2013, MNRAS, in press

R. Saglia, R. Senger, R. Bender, J. Snigula, N. Greisel, S. Seitz

KMOS: a multi-IFU NIR spectrograph for the VLT

KMOS is a second generation VLT instrument for multi-object near-infrared spectroscopy and the most complex VLT instrument built so far. KMOS uses deployable integral field units of 2.8”x2.8” size to obtain spatially-resolved spectra for up to 24 objects simultaneously from within a field of view of 7 arcminutes diameter. KMOS had first light on VLT UT1 in November 2012. The OPINAS group has provided all electronics, instrument control software and observing preparation tools for KMOS.

Right: KMOS on the VLT Nasmyth focus in November 2012. The cryostat provides the cold infrastructure (<140 K, detectors <80K) for pick-off module, IFU units, spectrographs and detectors with a total of over 60 motor-driven cryogenic functions. Bottom: optical path through the various KMOS components.

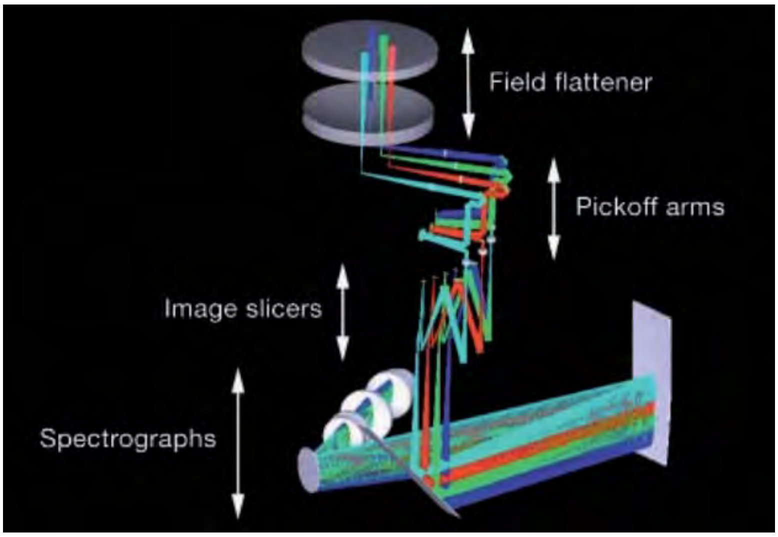

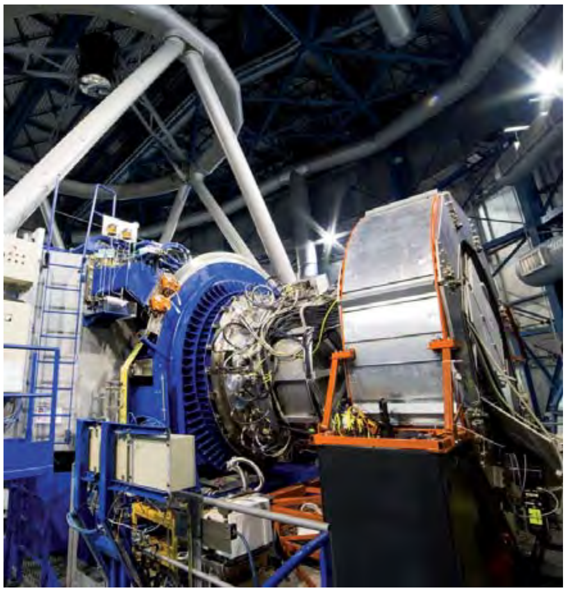

Grating/Band	λ range [μm]	λ_c [μm]	R ($\equiv \lambda/d\lambda$)
Iz	0.80 - 1.08	0.98	2800
YJ	1.02 - 1.35	1.18	3200
H	1.50 - 1.90	1.65	3800
K	1.95 - 2.50	2.23	3000
HK	1.50 - 2.38	1.94	1800

The 24 KMOS arms, arranged concentrically around the field of view, pick off incoming light by fold mirrors and relay it to image slicers, where each 2.8”x2.8” deployable IFU field is divided into 14 slices, i.e. each IFU pixel covers 0.2”x0.2”. Realigned to pseudo-slits and fed into 3 identical spectrographs, these slices end up as 24x14x14 spectra on the three 2kx2k HgCdTe detectors. Deployable IFUs have a significant advantage relative to multi-slit spectrographs because of the reduced slit contention in crowded fields and their insensitivity to slit losses due to extended galaxy morphology and orientation.

The KMOS consortium: University of Durham, University Observatory Munich, Max Planck Institute for Extraterrestrial Physics, Astronomy Technology Centre Edinburgh, University of Oxford, European Southern Observatory. In the application phase, the KMOS PI was Ralf Bender and the co-PI Ray Sharples, in the implementation phase their roles were reversed. KMOS was funded in Germany by the Federal Ministry of Research (BMBF), the Ludwig-Maximilians-University and MPE.

References: e.g., Sharples, R., Bender, R. et al. 2010, The Messenger, 139, 24; and 2013, The Messenger, 151, 21

R. Bender, B. Muschielok, H.J. Hess, R. Häfner and the KMOS team

KMOS^{3D} - Regulation of Galaxy Formation

The efficiency of galaxy formation and growth is a strong function of halo mass - but the precise reasons are elusive. The KMOS^{3D} survey will use newly commissioned NIR spectrograph KMOS on the VLT to target the Hα+[NII] emission complex for a mass-complete sample of ~600 galaxies with NIR grism redshifts from 3d-HST and CANDELS HST imaging. This will provide the first representative view of galaxy growth and the quenching of star formation at z~0.5-2.5, as star formation in the Universe peaks and starts to decline.

KMOS has been commissioned and KMOS^{3D} will have 75 nights GTO time from OPINAS and IR groups

KMOS provides spatially resolved spectra for ~600 Galaxies @ z~0.5-2.5, with simultaneous observations in 24 IFUs

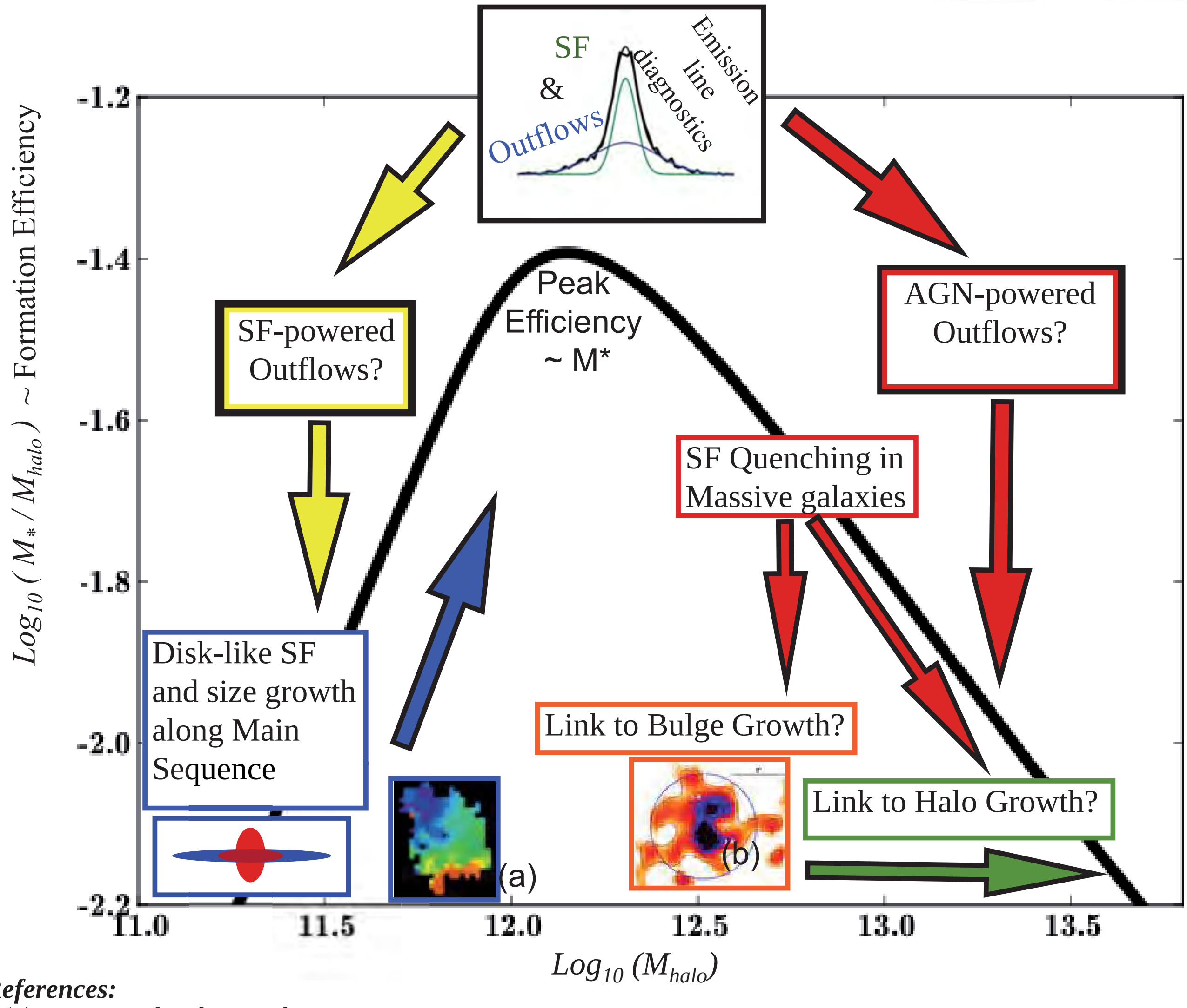

References:

- *(a) Förster Schreiber et al., 2011, ESO Messenger, 145, 39*
- *(b) Nastasi et al., 2011, A&A, 532, L6*

See also poster from IR group

D. Wilman, N. Förster Schreiber, R. Bender, R. Genzel, KMOS^{3D} Team

The Hobby-Eberly Dark Energy Experiment

The Hobby-Eberly Telescope Dark Energy Experiment (HETDEX) will map the expansion history of the universe at 1.9 < z < 3.6 using 800,000 Lyman-α emitters detected by a blind spectroscopic survey as probes of large scale structure. It will reach sufficient precision in H(z) and $D_A(z)$ to directly detect Λ at z ~ 3 at 3-σ. MPE leads the data analysis software development, survey scheduling, and is heavily involved in the experiment design.

HETDEX will outfit the 10 m HET with an array of 75 integral-field spectrographs. Each IFU spectrograph will cover 3500-5500Å at ~5Å resolution, sampling 50” × 50” using 448 fibers on the sky. The 75 IFUs are distributed within a 22’ field. This instrument, called VIRUS, will blindly survey a 420 deg^2 field in 3 years starting early 2014 (with probable 2 year extension). In this survey, we will detect 0.8 million Lyman-α emitting (LAE) galaxies at 11.9 < z < 3.6. The 3-D map of LAEs in a 9 Gpc^3 volume will be used to measure the expansion history and the growth of structure at that early epoch. HETDEX is designed to provide a 3-σ direct detection of dark energy at z ~ 3 (for w = -1). HETDEX will constrain the evolution of dark energy and will also provide 0.1%-level accuracy on the curvature of the Universe, ten times better than current measurements; HETDEX will also provide competitive (Planck-level) constraints on the total neutrino mass (from the small scale power spectrum) on on inflation models (from the power spectrum on largest scales). A prototype of the VIRUS unit spectrograph (VIRUS-P) has been built and is operating on the McDonald 2.7 m since 2007. VIRUS-P has been used for a pilot survey to better characterize the properties of LAEs in support of HETDEX and develop and test data reduction procedures.

The HETDEX Dataset will include:
- 0.8 million Lyman-α emitters (5σ detection) at 1.9 < z < 3.5
- 1.0 million [O II] emitters at z < 0.5
- 10^4 galaxies with spatially resolved spectroscopy at R~900
- 0.4 million unresolved galaxies (S/N > 3 per resolution element)
- 0.25 million stars with spectra (S/N > 3 per resolution element)
- 2000 Abell galaxy clusters
- 10,000-50,000 AGNs at z < 3.5

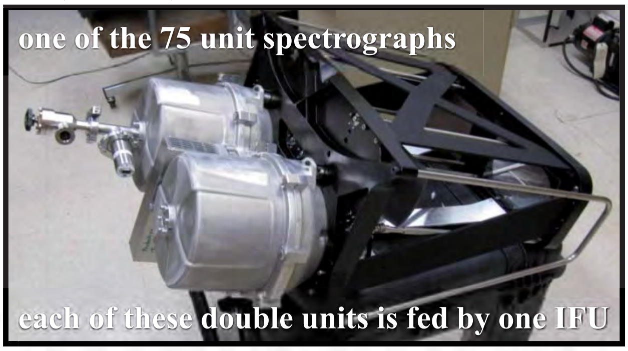

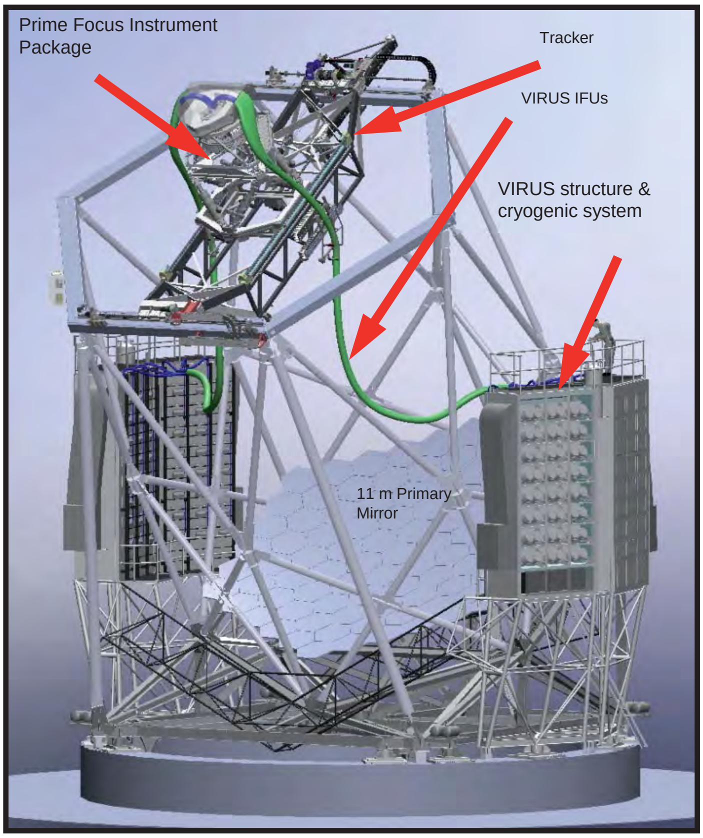

N. Drory, M. Fabricius, R. Bender, U. Hopp, M. Landriau, A. Sanchez, J. Snigula, J. Weller and HETDEX team

Cure-WISE: HETDEX data reduction with Astro-WISE

We expect the Hobby-Eberly Telescope Dark Energy Experiment (HETDEX) to produce more than 35000 individual FITS images on a typical night during its expected five years of observations. To analyze and catalog this data volume we implemented the CURE pipeline within the Astro-WISE system[1,2] (Astronomical Wide- field Imaging System for Europe).

The Cure-WISE pipeline provides:

- automated object detection, flux and redshift measurements
- full dependency tracking of the all the data reduction steps
- database backed management
- bookkeeping of the observed data
- organization of the detected sources
- user and project management
- access to the database and data reduction facilities for all HETDEX consortium members through its federated structure.

Cure is the data reduction and object detection pipeline for HETDEX. We created python wrappers for all the reduction steps in Cure (Cure-WISE), encapsulating it in Astro-WISE. The wrappers give us access to the Astro-WISE batch systems for parallel data reduction of all IFUs at once. The system includes automated quality control checks at various steps in the pipeline. First tests with mock HETDEX data show, that we will be able to reduce the observations in real time. Since Astro-WISE is designed to be used with many instruments, it enables us to reduce the accompanying imaging survey and to match the resulting catalog against our emission line detections.

Additionally we developed a simulation framework for HETDEX. The simulated data allow us to estimate the completeness of the source detections, test the correctness of flux recovery and sky subtraction schemes, and to stress-test the Cure-WISE system on the equivalent of a full 5-year data volume.

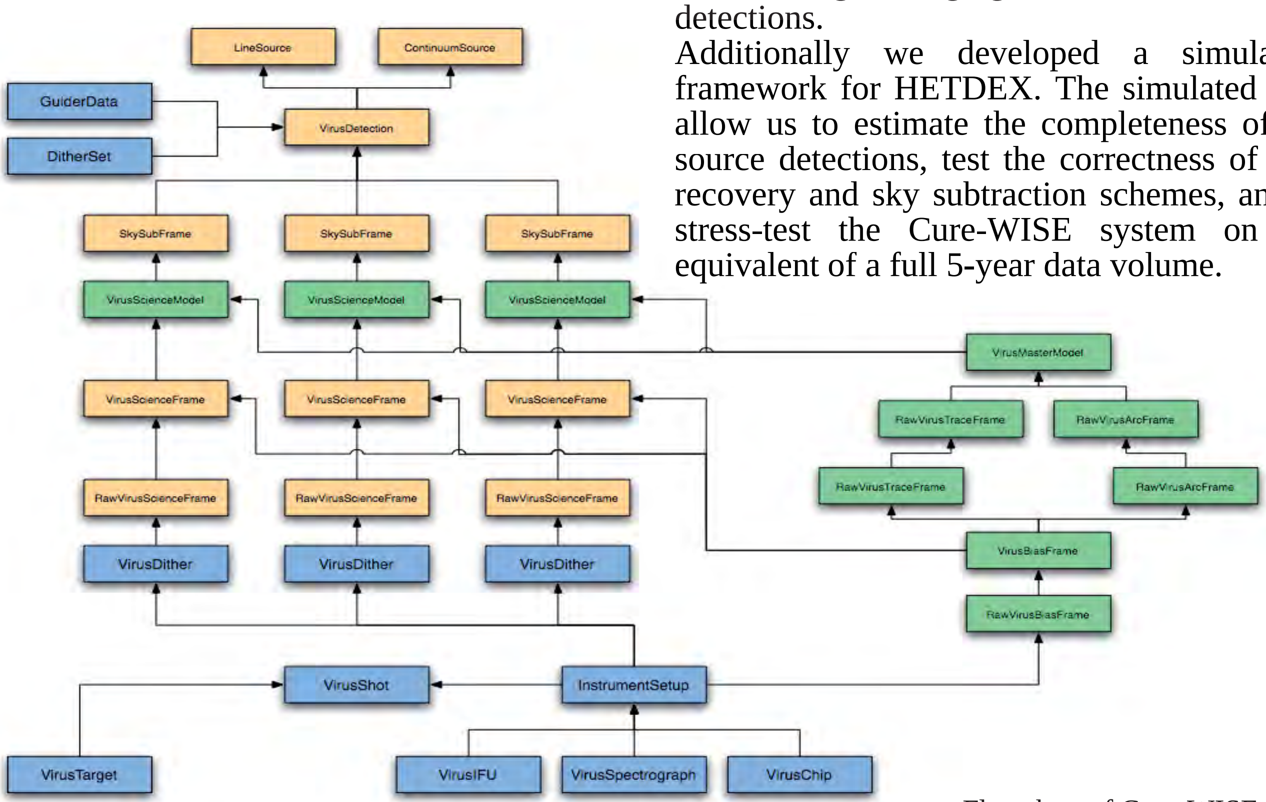

Flowchart of Cure-WISE pipeline.

References:
1) Valentijn, E. A., et al. ASP Conference Series 376, 491 (Oct. 2007)
2) http://www.astro- wise.org

J. Snigula, M. Cornell, N. Drory, M. Fabricius, M. Landriau, G. Hill, K. Gebhardt and HETDEX team

Calibration unit for the Hobby-Eberly Telescope Dark Energy Experiment

The primary survey instrument of HETDEX is the Visible Integral field Replicable Unit Spectrograph (VIRUS). The ability to calibrate the instrument swiftly at multiple times during a night is critical to our ability to detect faint emission line sources. The Facility Calibration Unit (FCU) provides arc lamps and a novel flat field source.

In order to detect faint emission line sources the instrumental point spread function and its nightly variation has to be measured with high accuracy. For this, frequent calibrations of the spectrograph are necessary. To minimize the impact of repeated calibrations on the survey efficiency a dedicated Facility Calibration Unit (FCU) was developed. This device provides ten different spectral line calibration-lamps and a tunable flat field unit: An array of 16 different LEDs can be adjusted in power output to provide almost constant signal over the whole spectral range from 3500 to 5500Å. Two movable pickoff heads allow to select and combine the light of two different sources at a time.

The calibration unit is part of the prime focus assembly which also houses the new 22‘ wide field corrector (WFC), and the instrumental focal plane.

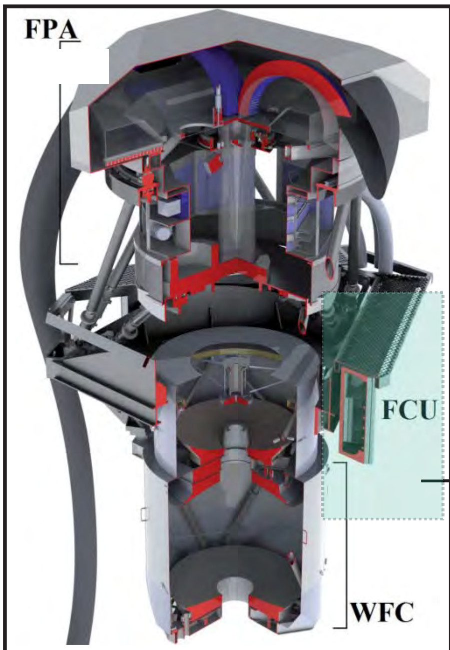

Sketch of the prime focus assembly. The high-lighted area indicates the location of the actual calibration unit. The light is injected below the wide field corrector.

FCU Characteristics:

- Two groups of five spectral calibration sources and a tunable flat field source.
- Simultaneous calibration exposures of one lamp per group and the flat field unit are possible. The exposure times can be set separately.
- Individual adjustment of the LED power output eliminates the problem of strongly varying flux levels as a function of wavelength of traditional light sources.

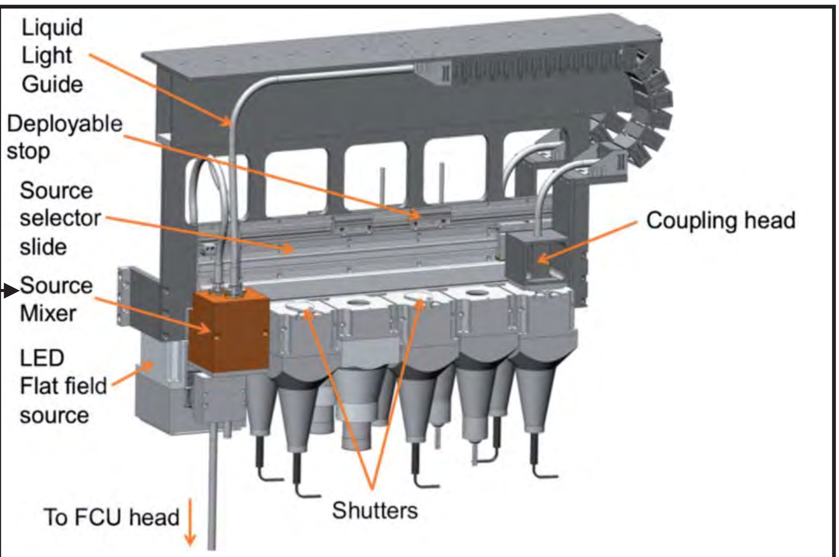

Solid model of the calibration unit. The actual light sources are arranged on the bottom of the unit.

References:
- Gary Hill, et. al., 2004, SPIE Conf. Ser. 5492, DOI: 10.1117/12.552474
- Hanshin Lee, et. al., 2012, SPIE Conf. Ser. 8444, DOI: 10.1117/12.926736
- John A. Booth, et. al., 2006, SPIE Conf. Ser. 6267, DOI: 10.1117/12.672694

M. Häuser, M. Fabricius and HETDEX-Team

Dark Energy with Euclid

EUCLID is a high-precision ESA medium class mission dedicated to the investigation of the nature of Dark Energy. EUCLID will image the entire extragalactic sky with high spatial resolution in one optical and three near-infrared bands. This will allow to analyse the evolution of large scale clustering out to redshifts of ~2 using the cosmological weak lensing (WL) shear signal of ~10^9 galaxies. In addition, slit-less spectrosopy will be employed to probe the characteristic scale of the Baryonic Acoustic Oscillations (BAO) and the galaxy power spectrum as a function of redshift at z>1.

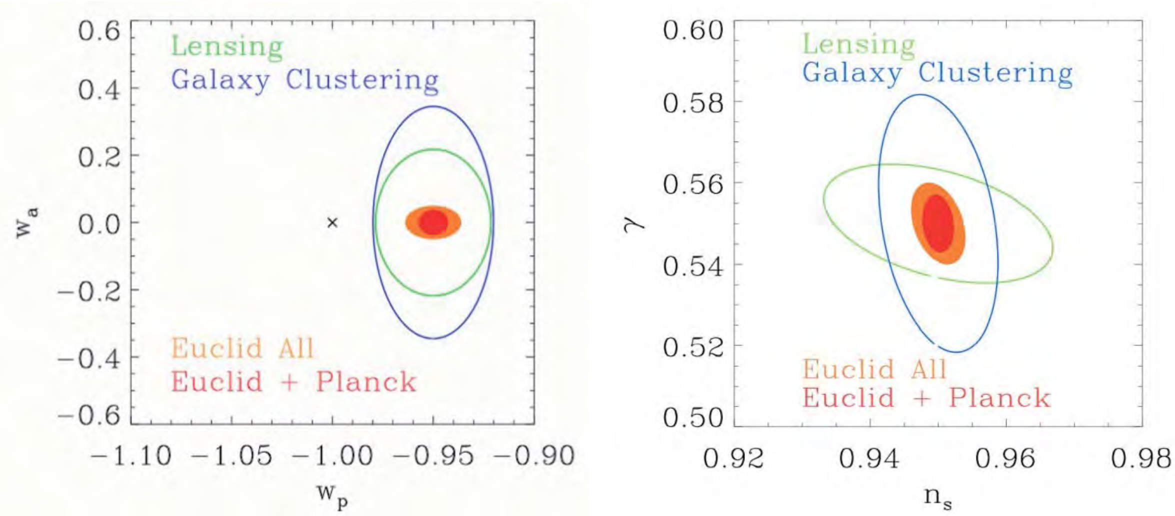

The properties of dark energy relevant for cosmology can be parameterized by the equation of state factor "w", which is the ratio of pressure to density of the dark energy fluid. A cosmological constant would correspond to a constant w=-1. Most dark energy models give a "w" which is evolving in time. It is common to parameterize this evolution with the value of w today (w_0) and at early times (w_0+w_a). The quality of the experiment to constrain dark energy can hence be estimated by the errors in the w_0-w_p plane (left). We show lensing only (green), galaxy clustering only (blue), all the Euclid probes (orange) and all Euclid with Planck CMB constraints (red*).* If the cause of accelerated expansion of the Universe is in fact due to a modification of gravity, not only the expansion history of the Universe is changed, but also the way large scale structures grow over time. The growth of these structures can be parameterized by "γ", where a value of 0.55 corresponds to standard Einstein gravity. On the right panel we show how exquisitely EUCLID can measure this value. In addition EUCLID can provide tight cosmological constraints on the neutrino mass and primordial non-Gaussianity.

MPE, together with its partners at the University Observatory Munich (USM) is prominently represented in EUCLID at various levels, Ralf Bender is member of the EUCLID Board, Joseph Mohr is member of the ESA EUCLID Science Team, Jochen Weller is co-lead of the cluster working group, Frank Grupp is the chief optical architect for the mission and responsible for the optical design of NISP, several more MPE/USM scientists are represented in the various science working groups. Moreover, MPE is hosting the German Science Data Center and provides the optics including mounts for the NISP instrument.

References: "Euclid Definition Study Report", R. Laureijs et al., ESA/SRE(2011)12, arXiv:1110.3193

J. Weller, R. Bender, F. Grupp, J. Koppenhoefer, R. Saglia, A. Sanchez, S. Seitz

Euclid near infrared optical system

Understanding the nature of dark matter and dark energy are the key science goals of the *ESA Cosmic Vision* mission Euclid. In collaboration with industrial partners the MPE is developing optics, opto-mechanics and alignment procedures for the NIR imaging spectrometer.

A 168mm diameter near infrared optical system with close to diffraction limit performance is needed to reach the science goals of the Euclid 1.2m space telescope mission. This is the largest ever flown lens optics in combin-ation with the most stringent tolerances on lens shaping and positioning.

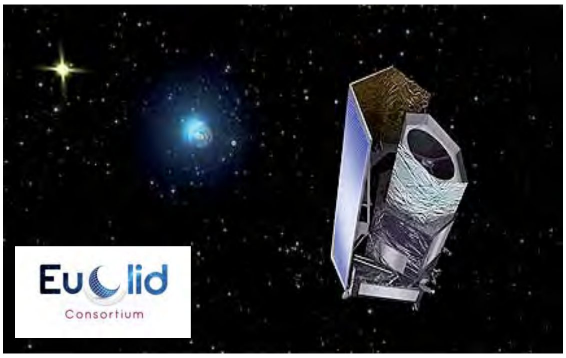

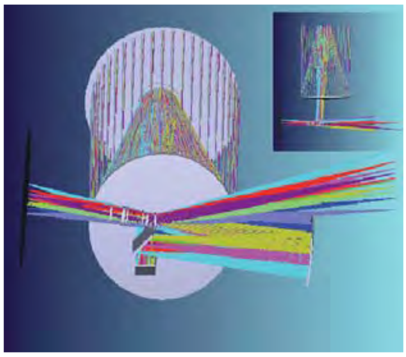

Left: An artists view on the Euclid spacecraft in the outer Lagrange point L2. **Right:** Euclid optical design. The MPE contributes the near infrared optics design and opto-mechanical implementation.

Basic parameters and specification:

Field of view: ≈ 0.5 sq.deg
Spectral bands: Y, J, H + 2 spectroscopy bands
Spectral resolution: R ≈ 500
Photometric limiting magnitude: 24.5 mag

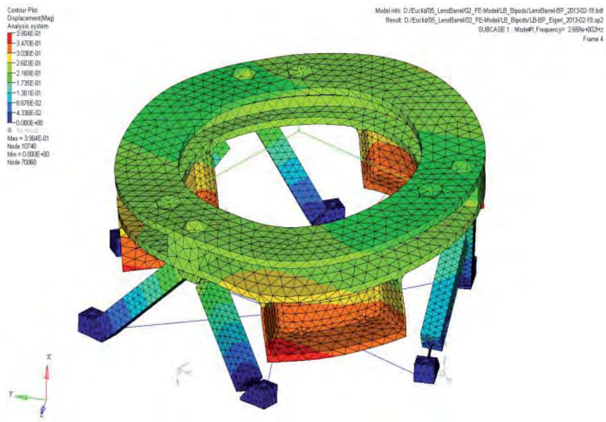

Extensive simulation is carried out to achieve a system that withstands the launch conditions and cool-down to the operational temperature of 137K. First representative lens systems, including the most critical optical material CaF_2, have been tested for vibrational and thermo-elastic behaviour. All tests have been passed sucessfully.

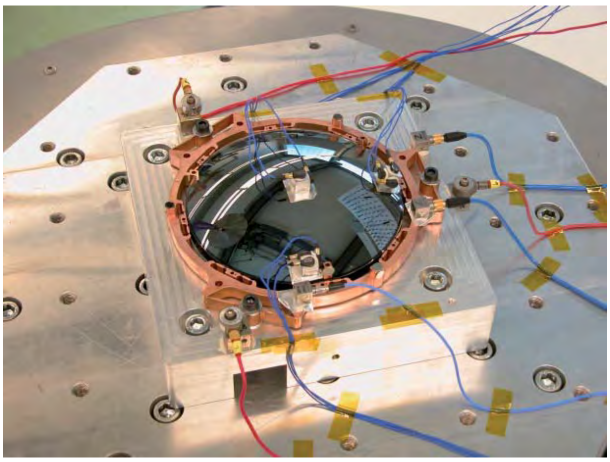

Top: A thermo elastic simulation of the lens barrel connecting three of the Euclid near infrared lenses. Stiffness, maximum exportit moments and torques are nominal and in spec. for this design.
Bottom: Calcium-fluoride lens after passing the vibration test on the MPE shaker facility. The lens is partially mirrored in order to allow precise interferometric shape measurements after shaking and during cool-down.

References:

- Laureijs, R.; Amiaux, J.; Arduini, S. and 216 co authors, 2011, Euclid definition study report, ESA
- Grupp, F.; Prieto, E.; Spano, P.; Zerbi, F. M.; Geis, N.; Bode, A.; Junk, V.; Bender, R., 2011, SPIE, 8146, 283

F. Grupp, R. Bender, A. Bode, C. Bodendorf, N. Geis, R. Katterloher, J. Snigula , C. Vogel, I. Weiss

The German Euclid Science Data Center

The German Euclid Science Data Center (SDC-DE) is one of eight data centers of the ESA space mission Euclid. The main responsibility of the SDC-DE is the processing and storage of large external data sets such as the Dark Energy Survey (DES) and Pan-STARRS1/2. The computer hardware is set-up at the Rechenzentrum of the Max Planck Society and the Institute for Plasma Physics in Garching (RZG). The SDC-DE collaborates with the Euclid groups at the Ludwig Maximilians University in Munich (LMU), the Argelander Institute for Astronomy in Bonn (AIfA) and the Max Planck Institute for Astronomy in Heidelberg (MPIA).

The Euclid space mission has recently been selected as part of ESA's Cosmic Vision Program (Laureijs et al. 2011). The satellite is expected to be launched in 2020. The main goal of the mission is to study the nature of dark energy and dark matter using several complementary cosmological probes. The Euclid satellite will be equipped with an optical imager (VIS) and a near infra-red imager (NIR) and spectrograph (see poster "Euclid near infrared optical system"). During its seven year mission, the Euclid instruments will collect 300 TByte of raw data that will be processed by the ESA Science Operations Center (SOC) and the eight national Science Data Centers (SDCs) of the Euclid Consortium. All results will be collected in a centrally organized Euclid Mission Archive (EMA).

In addition to the satellite data, the success of the mission depends on external data sets coming from ongoing and planned ground based extragalctic surveys which will provide broad band photometry in optical bands. Together with the Euclid NIR measurements the external data will allow to derive precise photometric redshifts of all galaxies in the Euclid sample. Fig. 1 shows the relative sizes of the Euclid and external data sets. The storage and processing of these large data sets requires huge investments in computer hardware as well as efficient processsing and data management strategies.

At the SDC-DE we prepare for processing and storing the external data sets from DES and Pan-STARRS. Both surveys have already started to take data. Therefore, the time scale for development and execution of the external data pipeline is very much different from the other Euclid pipelines. We recently bought a 500 TByte storage which we use to store all DES and Pan-STARRS1 raw data. A dedicated 576 core cluster allows us to test and optimize our processing pipeline which is being developed in close collaboration with the Euclid team at the LMU.

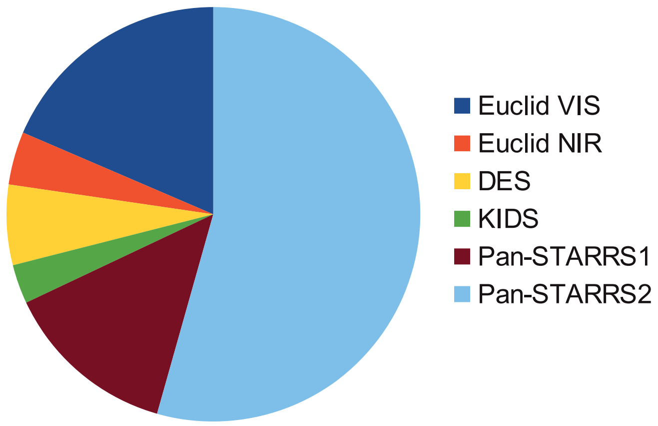

Fig. 1: The data volumes of the Euclid mission. With 1 PByte of raw data, the external data sets (DES, KIDS and Pan-STARRS1/2) outnumber the Euclid data by a factor of 3.

References:

Laureijs et al. 2011, eprint arXiv:1110.3193

J. Koppenhoefer, F. Raison, R. Bender, A. Bohnet, R. P. Saglia, R. Senger, J. Snigula

The Wendelstein 2m Fraunhofer Telescope

The OPINAS branch at the University Observatory Munich is currently commissioning a new 2m telescope on Mt. Wendelstein in the Bavarian Alps. The site has an altitude of 1840m, provides approximately 1100 clear hours per year and excellent Seeing (median <0.8”). The telescope will be equipped with a wide-field imager (WWFI with 0.5˚x0.5˚ field of view and minimal ghosting), a three-channel camera (3KK which allows simultaneous observations in two optical bands and one NIR band) and two fiber-coupled spectrographs (FOCES, an R=70000 Echelle spectrograph for single object spectroscopy, and VIRUS-W, an R=9000 integral field spectrograph with 250 fibers for nearby galaxy kinematics and populations studies). All instruments will be permanently mounted at/connected to the telescope; switching between instruments is possible within minutes. The telescope will be used to support and complement OPINAS projects at large telescopes or satellites, for transient follow-up and long-term monitoring projects. As the telescope is run privately by the University Observatory Munich, it offers maximum flexibility in scheduling and fast response to data needs. Last-not-least, master-students can make first hands-on experience with observations and data analysis.

Basic parameters of the 2m Fraunhofer telescope:

- free aperture 2.00m, f/7.8, scale 0.2”/15µm
- compact design with two Nasmyth stations
- Port 1: 0.7° diameter field of view (with 3-lens corrector) for wide-field imaging with WWFI
- Port 2: 0.2° diameter field of view for 3-channel imager 3KK and fiber-coupled spectrographs FOCES and VIRUS-W (see separate posters)

Mt. Wendelstein (1840m) with the Observatory on top.

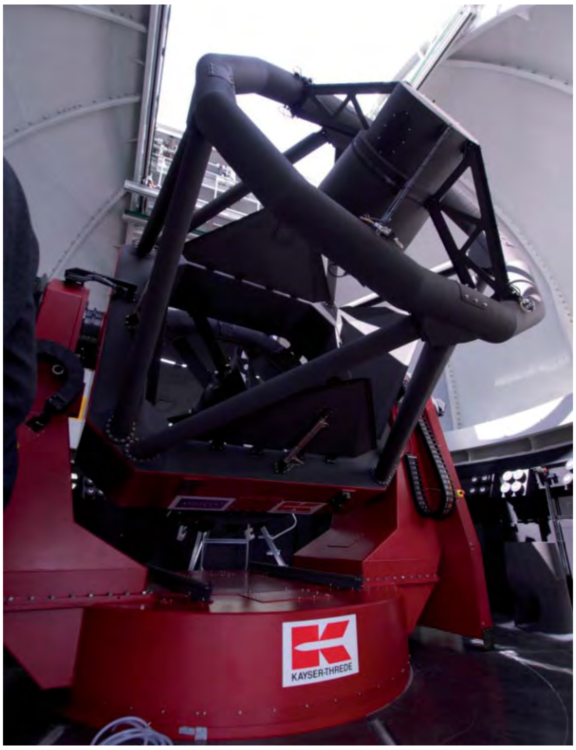

Acknowledgements: The telescope was built by Kayser-Threde and Astelco and was funded by the Freistaat Bayern and the BMBF. Instruments have been supported by the Ludwig-Maximilians-University, the Excellence Cluster ‘Origin and Structure of the Universe’, and the MPE.

References:

- Hopp, U. et al. 2012, SPIE 8444,2
- Gössl, C. et al:, 2012, SPIE 8446,3

U. Hopp, R. Bender, F. Grupp, C. Gössl, F. Lang-Bard, R. Kosyra, W. Mitsch

3KK – an Optical-NIR Three-Channel Imager

The 3-channel camera 3KK is currently being built by the OPINAS branch at the University Observatory Munich for the new 2m Fraunhofer Telescope on Mt.Wendelstein in the Bavarian Alps. 3KK has two optical channels (split at 695 nm) and one NIR channel (beyond 970 nm) with 7 arcmin and 8 arcmin field-of-view, respectively. 3KK is optimized for fast multi-wavelength follow-up of transients and efficient photometric redshift estimation of galaxy clusters identified in optical (e.g. PanSTARRS) or X-ray (e.g. eROSITA) surveys.

The optical part of 3KK is composed of commercially available CCD cameras (Apogee Alta E3041, 15 µm Pixel, 2kx2k Fairchild CCD), coupled with Bonn Shutters, and mounted on commercial high precision linear stages for differential focusing. A specially designed beam-splitter system provides high optical quality in all channels. The NIR camera (HAWAII-2RG detector, 18 µm Pixel, 2kx2k) has been built in collaboration with the Institute for Astronomy in Hawaii.

Upper left: Optical design of the WNIR camera. It consists of 6 lenses for reimaging, a cold stop and a filterwheel with 8 positions.
Lower left: Optical design of the two optical channels. Two wedge shaped beam-splitters and a corrector plate separate the wavelengths for the different channels and correct for optical aberrations. The colors indicate the wavelength that are reflected/transmitted.
Upper and lower right: FEM analysis (undeformed and deformed view) of the 3KK structural parts.

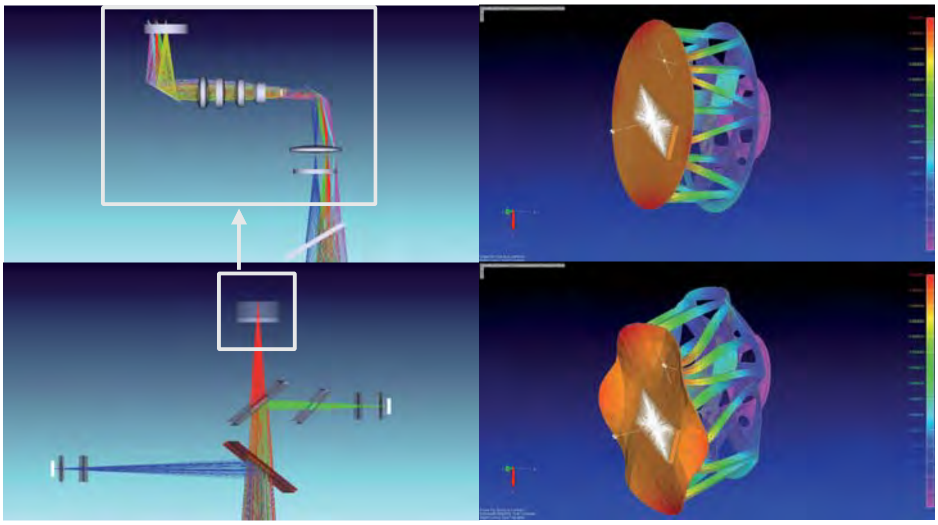

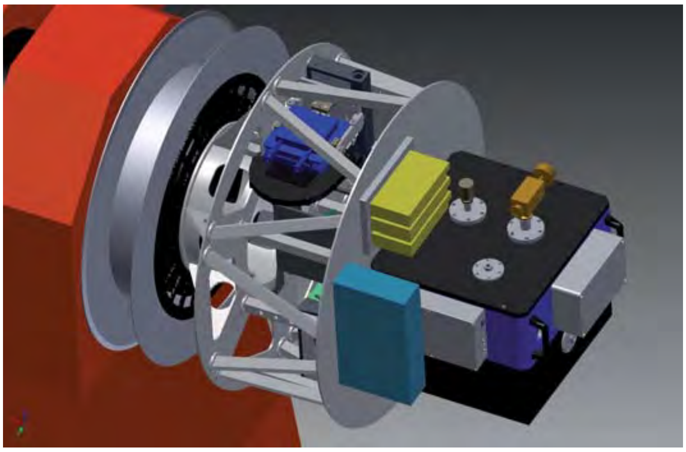

Current state of the mechanical design. The two optical channels are to the left of the circular plate, the NIR channel to the right, together with electronics, temperature controllers and power supplies.

Overall specifications:

Blue channel:	340 nm – 695 nm (u', g', r' filters)
Red channel:	695 nm – 970 nm (I', z' filters)
NIR channel:	970 nm – 2310 nm (Y, J, H, Ks, H_2, Br_γ filters)
EE:	80 % in two Pixels for all channels
Distortion:	~ 0.001 % (blue/red)
	~ 0.2 % (NIR)
FOV:	6.8 arcmin (optical channels)
	8.2 arcmin (NIR channel)
Pixelscale:	0.2 arcsec/pixel

Acknowledgements: 3KK is funded by the Ludwig-Maximilians-University, the Excellence Cluster 'Origin and Structure of the Universe' and MPE.

References: Lang-Bardl, F. et al:, 2010, SPIE 7735-133

F. Lang-Bardl, R. Bender, M. Kodric, F. Grupp, C. Gössl, U. Hopp and W. Mitsch

FOCES a planet finder for Wendelstein

Detecting and characterizing exo-planetary systems is the goal of the FOCES Échelle spectrograph project. By means of intense environmental stabilization, a high level of fiber optical decoupling between telescope and spectrograph and by using simultaneous frequency comb calibration we aim for the <1m/s regime in radial velocity accuracy.

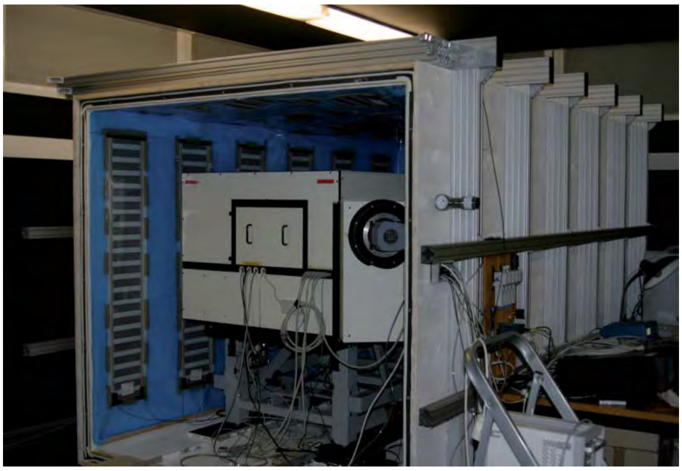

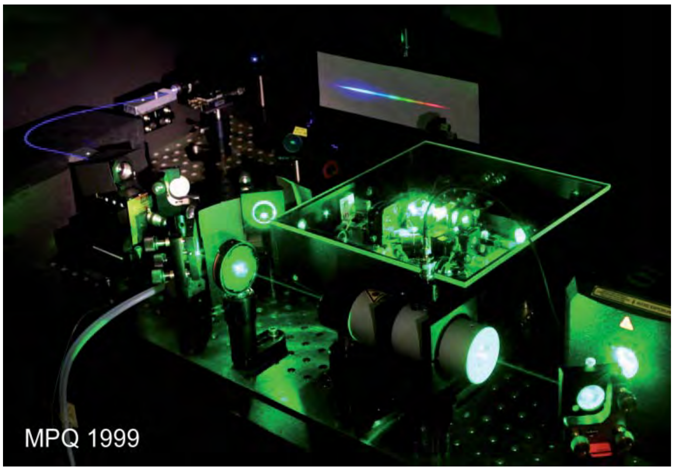

Left: FOCES in its pressure box, note the outer layer heating elements on the walls. **Right:** Frequency comb system developed at the MPQ in collaboration with Menlo Systems, a more integrated system will be used to calibrate FOCES.

Super-earth type planets around solar type stars generate a radial velocity signal of the order of 1m/s. This signal corresponds to a physical shift of a spectral line of 1/3000 of a pixel on a typical high resolution Échelle spectrograph. This small signal can only be detected if the spectrographs stability is extremely high and if remaining drifts are being monitored with the highest precision.
The necessary temperature and pressure stability have been reached by a two layer thermal and one layer pressure stabilization. The figure to the right shows the movement of the Échelle orders within a 30 minutes period. Un-calibrated drift is already down to <1/1000 of an order in many orders. Simultaneous calibration will allow to go for even higher calibrated pixel-wavelength accuracy.
FOCES will be able to observe 65 single stars brighter than V=7mag. The limiting magnitude will be 8.5 mag.

Basic parameters and specification:

Resolution: R = λ/dλ = 70000
Spectrograph stability: <0.001pix (averaged)
Temperature stability: < 0.01 K
Pressure stability: < 0.1 hPa
Radial velocity accuracy: ≤ 1 m/s

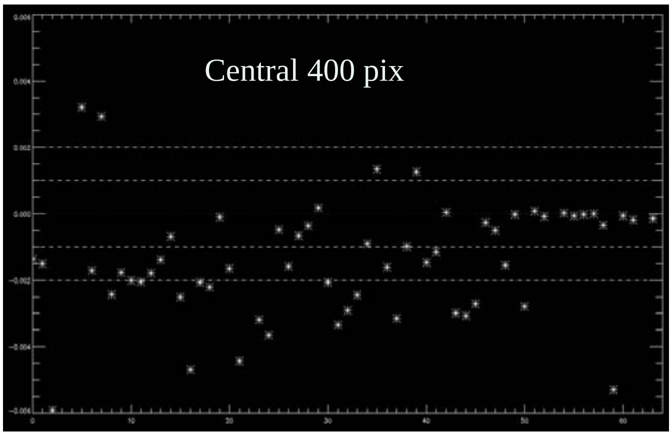

References:
•Brucalassi, A.; Feger, T.; Grupp, F.; Lang-Bardl, F.; Hu, S.M.; Hopp, U.; Bender, R., 2012, SPIE, 8446, 2
•Grupp, F.; Udem, T.; Holzwarth, R.; Lang-Bardl, F.; Hopp, U.; Hu, S.M.; Brucalassi, A.; Wang, L.; Bender, R, 2010, SPIE, 7735, 232

F. Grupp, A. Brucalassi, L. Wang, T. Pfleger, F. Lang-Bardl, S.M. Hu, U.Hopp, R. Bender

II.1) Group: Prof. Ortwin Gerhard

Planetary nebulae in the halos of early-type galaxies

The halos of early-type galaxies are faint and not straightforward to explore, but they preserve long-lasting substructures as record of formation and accretion processes. We trace this diffuse stellar component using PNe out to 13 R_e from the galaxy centre.

The long-lasting substructures preserved in the outer halos of early-type galaxies (ETGs) are the best records of merger and accretion events in these systems. Far from the galaxy's centre, where conventional spectroscopy is not feasible due to low surface brightness, we can still detect Planetary Nebulae (PNe) thanks to their strong [OIII] emission line. With PNe as kinematic tracers we extend the phase-space information to large radii where dynamical times are long.

The PN Spectrograph (PNS, ref.[4]) is a dedicated instrument installed at the William Herschel Telescope. As part of the PNS team we gathered kinematic measurements for some 20 ellipticals and S0s out to typically ~5-8 Re ([2],[3], Fig. 1), with the aim of quantifying the angular momentum (Fig. 2), halo dynamics, and dark matter content in these systems. Analysis of the full PNS data is on-going.

To push to even larger radii we carried out an imaging PN survey around the Virgo-central giant elliptical galaxy NGC 4486 (M87) with Suprime-Cam at the Subaru Telescope, reaching 150 kpc (~ 13 Re) in the M87 halo.

PNe were identified using automatic selection criteria [1], obtaining a statistically complete PN sample of ~700 objects, that allowed us to get an unprecedented photometric study of the PN population in M87's outer regions including the transition to the intracluster light (ICL). The logarithmic PNe density profile is shallower than the surface brightness profile of M87, consistent with the superposition of two photometric components, the halo and the ICL, with different luminosity-specific PN number for both components (Fig.3).

With forthcoming spectroscopic follow-up we will complete the analysis of the PN population in the outermost regions of M87, studying the orbits and looking for substructures in the observed phase-space.

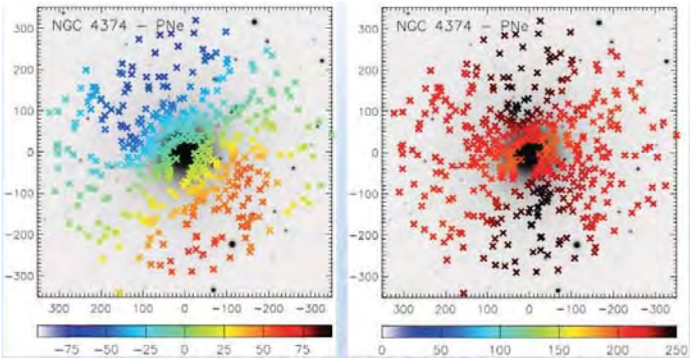

Fig.1 Two dimensional velocity (right) and velocity dispersion (left) fields for NGC4374, reaching ~7 half-light radii Re in this galaxy [3].

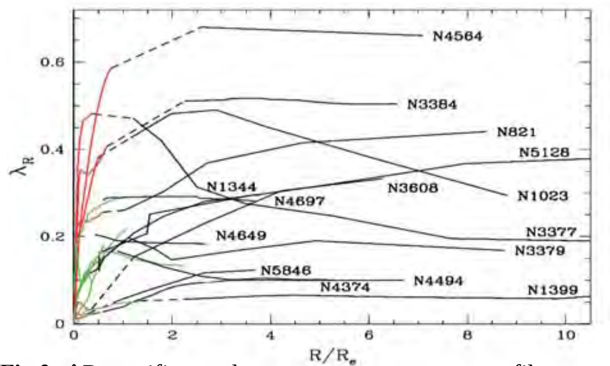

Fig.2: λR specific angular momentum parameter profile extracted from PNe kinematics. $\lambda R=0.1$ separates fast and slow rotators. The red and green curves are based on SAURON data. From [3].

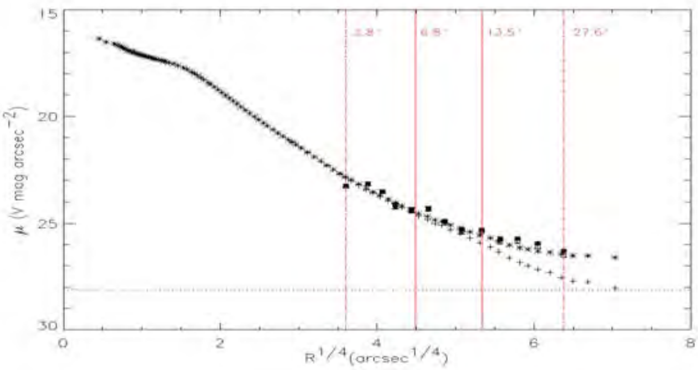

Fig.3: Comparison between M87's logarithmic PN number density profile (circles), surface brightness profile ([5],crosses), and PN density model, with α2.5,halo=8.2e-9 PN/Lsolar and α2.5,halo/α2.5,ICL=3 (asterisks) [6].

References:
[1] Arnaboldi et al. 2002,AJ,123,760
[2] Cortesi et al. 2013,A&A,549, A115
[3] Coccato et al.2009,MNRAS,394,1249
[4] Douglas et al. 2009,PASP,114,1234
[5] Kormendy et al. 2009,ApJS,182,216
[6] Longobardi et al. 2013, A&A, subm.

A. Longobardi, O. Gerhard, M. Arnaboldi, L. Coccato, et al.

Mass distribution of quasi-Keplerian elliptical galaxies

Several elliptical galaxies such as NGC 4494 have been inferred to have unusually diffuse dark matter halos – based on their rapidly decreasing, quasi-Keplerian velocity dispersion profiles. We probed the dark matter content and orbital structure in the halo of NGC 4494, using the NMAGIC particle method to construct axisymmetric models for extended multiple slitlets data out to 3.5Re, as well as hundreds of planetary nebulae velocities out to ≃7Re. We also compared with the halos of the similar galaxies NGC 3379 and NGC 4697 for which less constraining data allow greater degeneracy between anisotropy and mass. The best-fitting outer circular velocity curves and dark matter halos of all three galaxies are quite similar. NGC 4494 shows a particularly high dark matter fraction inside ~ 3Re, and a strong concentration of baryons in the center.

The best-fitting models for NGC 4494 have a dark matter (DM) fraction of about 0.6±0.1 at 5Re (70% C.L.), and are embedded in a DM halo with circular velocity ~200kms^{-1}. The total circular velocity curve is approximately flat at v_c=220kms^{-1} outside ~0.5Re, and the orbital anisotropy of the stars is moderately radial (Fig.1). Results obtained for NGC 4697 and NGC 3379 based on the likelihood of PN velocities (Fig.2) are qualitatively similar, with lower DM fractions and larger radial anisotropy.

We devised a Monte Carlo method to estimate confidence boundaries for the halo parameters, given our data and modelling set-up. We find that the correct ΔG(merit function)~26 ($\Delta\chi^2$~59) at 70% C.L., much larger than the usually assumed $\Delta\chi^2$ = 2.3 for two free parameters at 70% C.L. This may be case-dependent, but calls into question the general validity of the standard assumptions used for halo and black hole mass determinations.

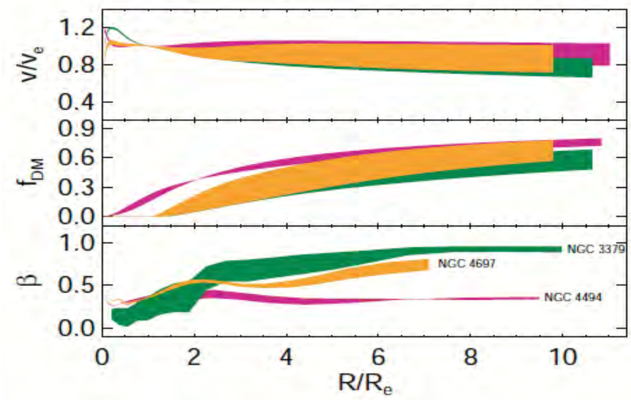

Fig.2: Circular velocity normalized by its value at 1Re (top), dark matter fraction (middle), and anisotropy parameter (bottom), for the range of valid NMAGIC models obtained for NGC 4494 ([3], violet), NGC 4697 ([1], orange) and NGC 3379 ([2], green).

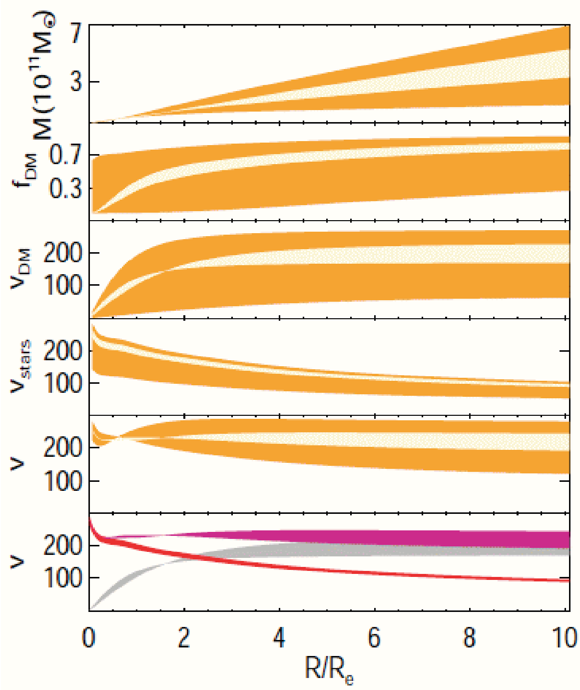

Fig.1: Structure of NGC 4494. From top, 1) total mass, 2) DM fraction within R, circular velocity curves corresponding to 3) dark matter, 4) stars, and 5) total potential, 6) contribution of DM (grey) and stars (orange) to total (violet). Orange regions show all edge-on NMAGIC models investigated, other shaded regions shows 70% confidence regions.

References:
[1] De Lorenzi, Gerhard, et al. 2008, MNRAS, 385, 1729
[2] De Lorenzi, Gerhard, et al. 2009, MNRAS, 395, 76
[3] Morganti, Gerhard, et al. 2013, MNRAS, in press

L. Morganti, O. Gerhard, L. Coccato, I. Martinez-Valpuesta, M. Arnaboldi

Structure of the Milky Way Bulge from VVV

Using red clump giants in the VVV survey as a standard candle, we have reconstructed a three-dimensional map of the density in the central 1.5 kpc of the Galactic bulge. Our reconstruction shows a peanut/X-shape together with a triaxial bar lying at 20° to the line-of-sight.

Red clump (RC) stars provide a standard candle with dispersion $\sigma(K_S)\approx0.17$mag. The VVV survey is a near-infrared survey of the Galactic bulge. It has sufficient depth to detect the RC in the Galactic bulge in all but the most highly extincted regions, with better coverage and resolution than previous surveys (Gonzalez *et al.* ’11). The RC has been used to probe the Galactic bulge previously, mostly focusing on estimating the peak of the RC luminosity function along different lines of sight, and thereby tracing the shape of the Galactic bar (e.g. Stanek *et al.* ’94). Here we utilize this information, but also their number density as a function of position both in (l,b) and along the line-of-sight.

First the change in $J-K_S$ color of the RC is used to construct the extinction map in Fig. 1. Then extinction-corrected K_S-band luminosity functions such as that shown in Fig. 2 are used to measure the density along each line-of-sight, after deconvolving from the intrinsic RC luminosity function.

Finally, the combined line-of-sight densities are converted to a three-dimensional measurement of the structure of the bulge. Our result is non-parametric, but by assuming 8-fold mirror symmetry about the galactic center we can provide a complete map despite missing VVV fields. In Fig. 3 we show a slice through the resultant 3D density map. It demonstrates a peanut/X-shape together with the triaxial bar.

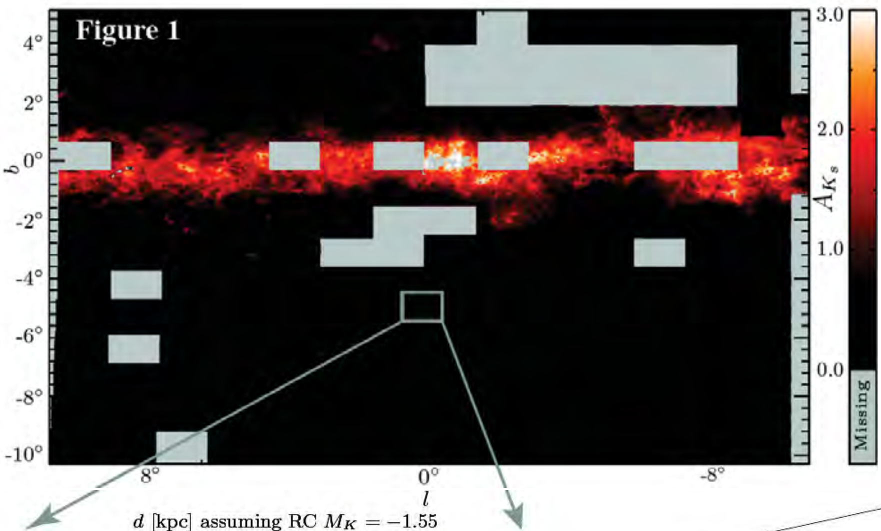

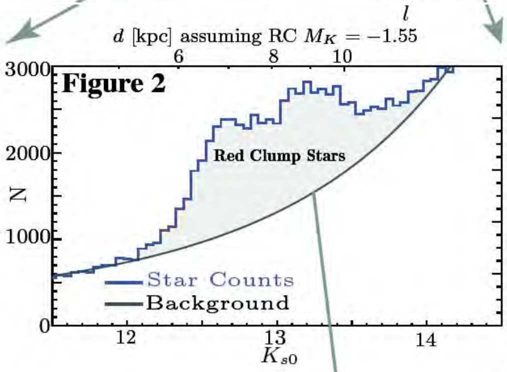

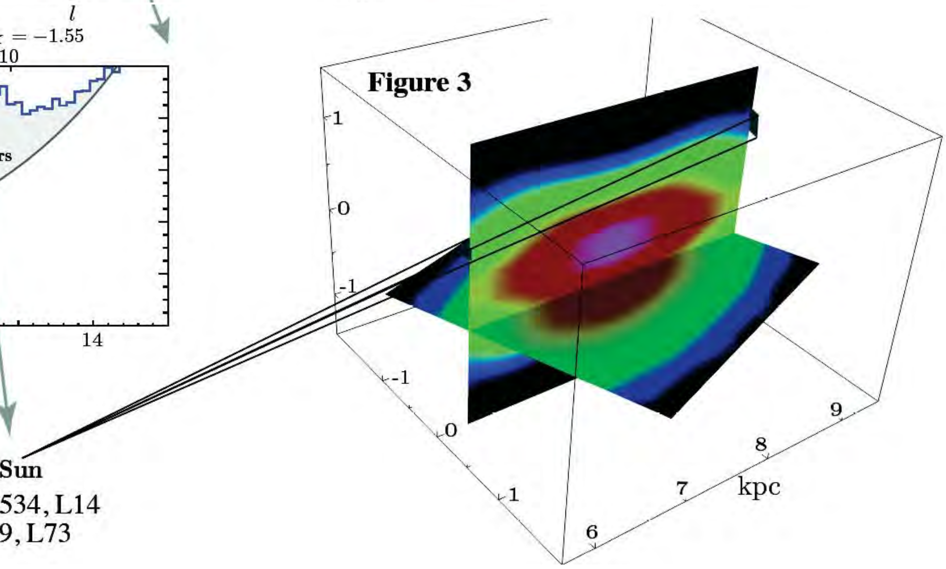

References:

- Gonzalez *et al.* 2011, A&A, 534, L14
- Stanek *et al.* 1994, ApJL, 429, L73

C. Wegg, O. Gerhard

Dynamical models for the Milky Way's boxy bulge and bar

The Milky Way (MW) is a barred galaxy with a boxy bulge representing the inner three-dimensional (3D) part of the bar. We analyzed the MW bulge using an N-body model which formed a boxy bulge from an exponential disk through bar and buckling instabilities. [1] Based on comparisons with star counts in for longitudes |l| < 26°, |b| < 10°, the so-called "long bar" (e.g., Benjamin et al 2005) and the main Galactic bulge can be understood as the planar and 3D parts of the MW bar, which ends at ~4.5 kpc. [2] The nearly axisymmetric central bulge explains the structural change seen at |l|<4° in recent VVV star counts. No separate nuclear bar is needed. [3] Radial metallicity gradients in the disk survive through the bar and buckling instabilities, possibly explaining part of the vertical metallicity gradients seen in the bulge (e.g., Zoccali et al 2008). – Using NMAGIC dynamical models, we also showed [4] that the cylindrical rotation and velocity dispersions seen in the BRAVA data (Kunder et al. 2012) can be reproduced, arguing for a low pattern speed in of the bar. – All results support a secular origin of the MW bulge, with no clear evidence remaining for a classical bulge.

The N-body simulation is here viewed at time T~1.9 Gyr when the bar is growing again after formation of the boxy bulge. The bar consists of a planar "long bar" part whose inner 2/3 are thickened as the boxy bulge. In agreement with MW star count data, the inner 600 pc is nearly axisymmetric [2], and the bar shows leading ends from interaction with spiral arms [1].

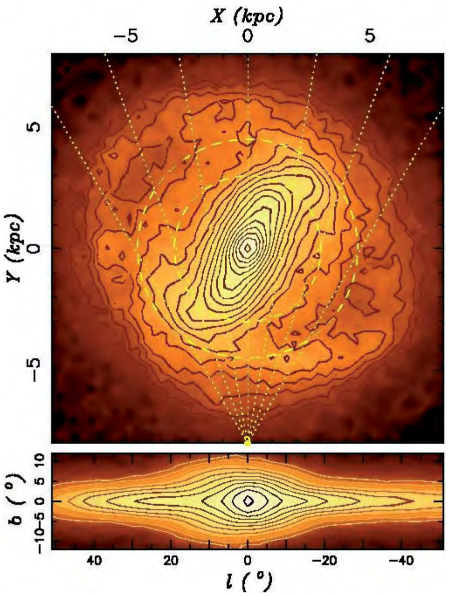

Fig.1: Face-on view of the model with the bar oriented at 25° (top). Edge-on view (bottom) as seen from the Sun at 8 kpc. High density corresponds to bright colors. From [1].

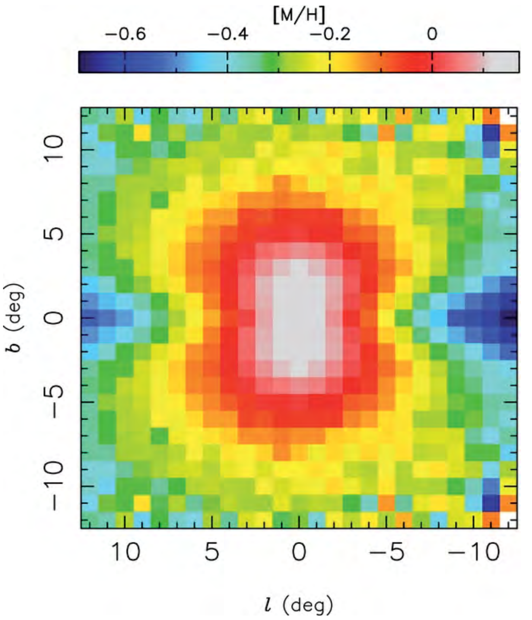

Fig.2: Metallicity map of the model bulge in galactic coordinates. Color corres-ponds to the average metallicity. From [3].

Bulge dynamics

Kinematics of bulge stars from the recent BRAVA and ARGOS (Ness et al 2013) surveys show cylindrical rotation, as predicted by barred bulge models evolved from unstable disks.

Fig.3: Different lines show the models obtained with various bar pattern speeds, overplotted on BRAVA data. Only small differences can be seen, but based on χ^2 the model would prefer a low pattern speed of $\Omega_b \sim 42$ km sec^{-1} kpc^{-1}.

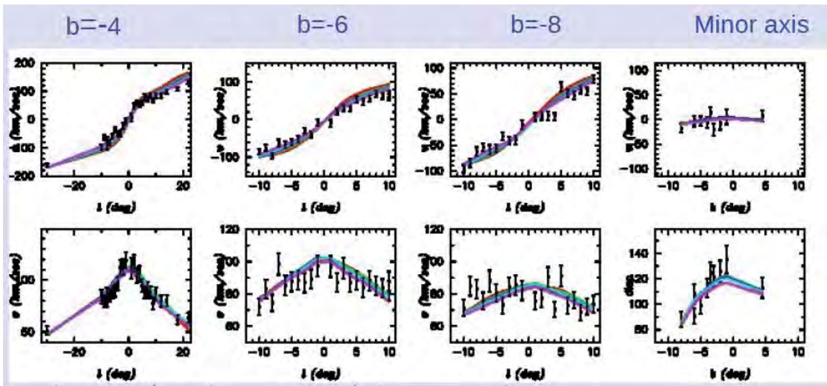

References:

[1] Martinez-Valpuesta & Gerhard 2011, ApJ, 730, L20

[2] Gerhard & Martinez-Valpuesta 2012, ApJ, 744, L8

[3] Martinez-Valpuesta & Gerhard 2013, ApJ, 766, L3

[4] Martinez-Valpuesta & Gerhard 2013, in prep.

I. Martinez-Valpuesta, O. Gerhard

Spin-up of classical bulges in barred galaxies

Classical bulges in spiral galaxies are known to rotate faster than elliptical galaxies of the same luminosity but much slower than the boxy bulges that form through disk instability. However, the origin of angular momentum in classical bulges is not well understood. We studied the dynamical evolution of initially axisymmetric disk galaxies with preexisting classical bulges using self-consistent N-body simulations. Low mass classical bulges gain angular momentum from the bar mostly through resonant orbits, and thereby transform into fast-rotating, triaxial objects with cylindridal rotation, embedded in the similarly fast rotating boxy bulge formed from the disk. The long-term kinematics of the composite final bulge is independent of the rotation in the initial classical bulge. Surprisingly, also massive classical bulges gain a significant fraction of angular momentum emitted by a bar that forms self-consistently in the disk. For nearly equal bar strength, the angular momentum gain of the classical bulge increases with its mass, and even massive classical bulges can be spun-up to (v/σ*)~1 in less than half a Hubble time if they are not too compact or too diffuse.

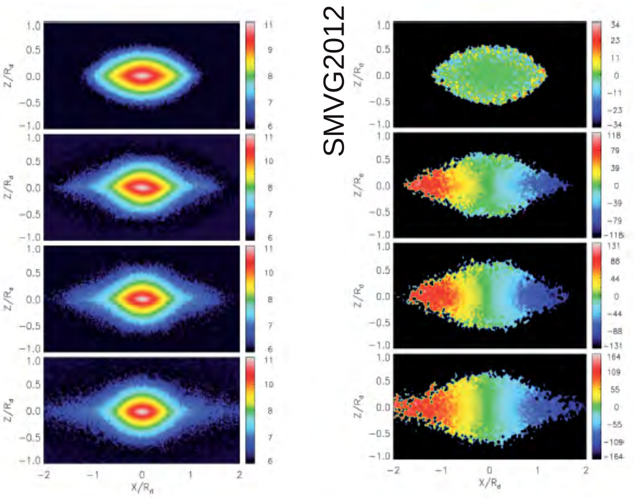

Fig.1: The initially non-rotating classical bulge acquires cylindrical rotation by angular momentum transfer from the bar. The right panel shows the time evolution of the edge-on velocity field (top: t=0); the left panel shows the surface density. The boxy/bulge formed from the disk (not shown) also has cylindrical rotation. From [1].

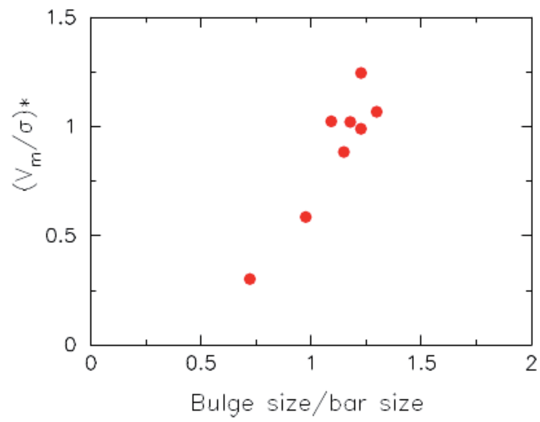

Fig.2: Spin-up is most efficient (v/σ*~1 at 4 Gyr) for classical bulges whose outer (King model) radius is about equal to the size of the bar. Too compact or too diffuse classical bulges do not gain as much angular momentum and thus rotate only slowly. This indicates that some of the classical bulges in spiral galaxies might have acquired rotation through secular processes [3].

Cylindrical rotation of rotating classical bulges:
The long-term kinematics of the composite BP bulges in our simulations is independent of the rotation of the initial classical bulge (models 0,A,B,C), and is always described by cylindrical rotation. However, as a result of the co-evolution between bulge and bar, deviations from cylindrical rotation are seen during the early phases of secular evolution and may correspond to similar deviations observed in some bulges.

Fig.3 shows the degree of cylindrical rotation (δ_{CL}) at different major axis radii of our N-body models of BP bulges plotted at the end of 2.9 Gyr. Overplotted is the degree of cylindrical rotation for two galaxies NGC 7332 and NGC4570. From [2].

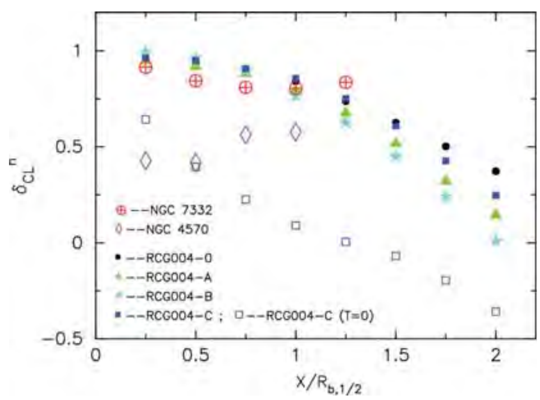

References:
[1] Saha, Martinez-Valpuesta & Gerhard 2011, MNRAS, 421, 333 [2] Saha & Gerhard 2013, MNRAS, 430, 2039
[3] Saha, Gerhard & Martinez-Valpuesta 2012, in prep.

K. Saha, O. Gerhard, I. Martinez-Valpuesta

Rotation and dynamics of the old nuclear cluster at the Galactic centre (GNC)

The main goal of this project is to put constraints on the mass, rotation, orbit structure and statistical parallax of the GNC. For this we combine star counts and kinematic data in various fields from Fritz et al. (2013), including 2500 radial velocities and 10000 proper motions obtained with VLT instruments, and 200 maser velocities. First we fit the surface density with a 2-component oblate-spheroidal model. Then we use the fitted density to calculate the 2-integral DF using the contour integral method of Hunter & Qian (1993). We add rotation self-consistently by adding an odd part in Lz to the initially even DF(E,Lz). The addition of self-consistent rotation to the model does not affect the projected dispersions along the l & b directions. The difference between σ_l and σ_b can only be explained by assuming an axial ratio of $1/q = 1.4 \pm 0.1$ for r<70". The orbit structure of the 2-I DF is also able to predict the observed double peak in the velocity histogramms (VHs). This is independent of the net rotation, but depends of the flattening of the GNC.

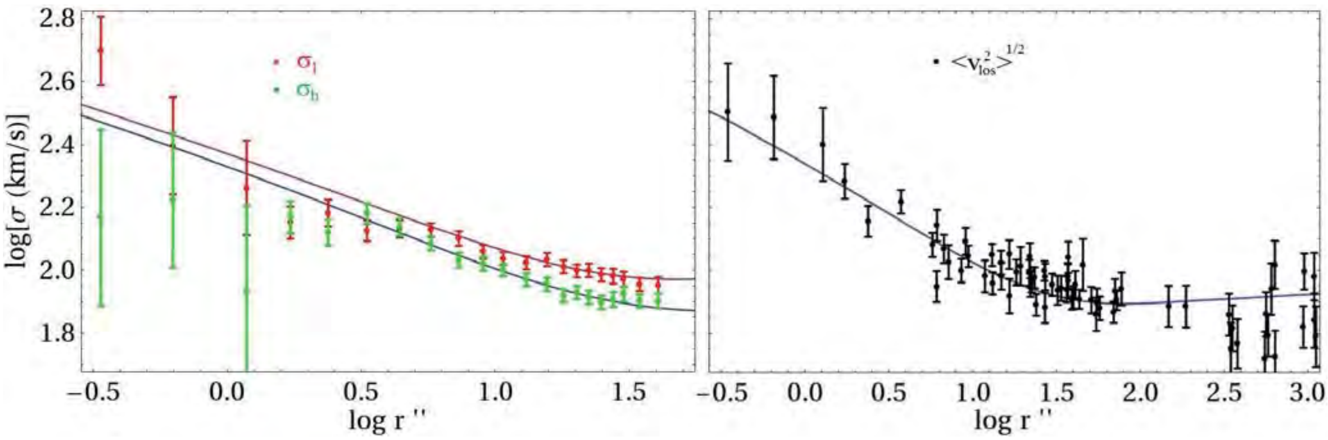

Figure 1. Left plot shows how our model predicts the difference in the observed dispersions in the l and b directions. The observed difference is a result of the flattening of the GNC. Right plot shows the mean square line-of-sight velocity compared with our model. We used a stellar mass of 0.75×10^6 M_{solar} for r < 1pc, a BH mass of 4×10^6 M_{solar} and a distance of 8 kpc.

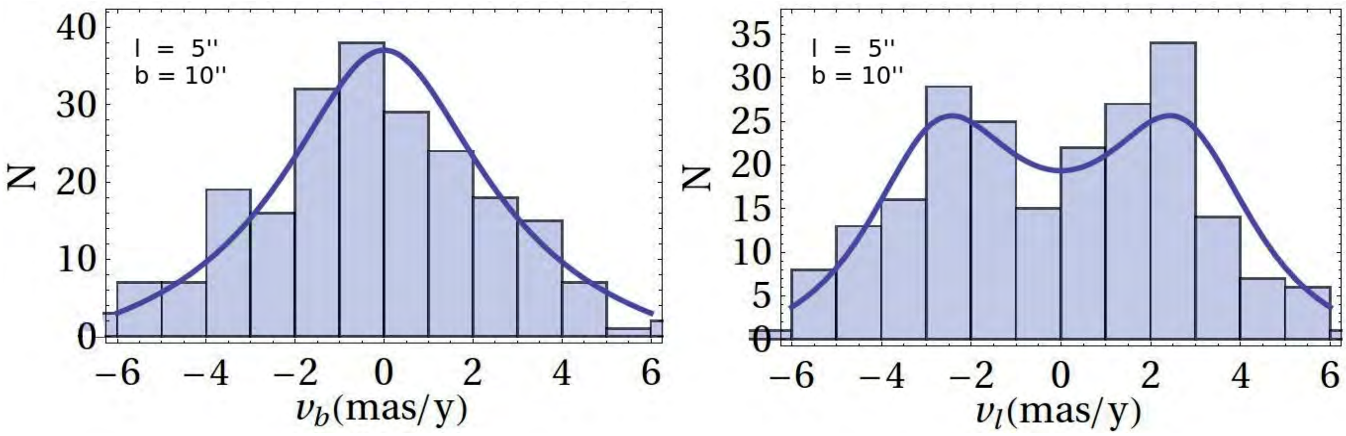

Figure 2. An example of how our model compares with the observed VHs along l and b.

References:

• Fritz et al. 2013, Hunter & Qian 1993, Qian et al. 1995, Schodel et al. 2009, Trippe et al. 2008

S. Chatzopoulos, O. Gerhard, T. Fritz, S. Gillessen, R. Genzel

III) High-Energy Astrophysics

Host galaxies of AGN in COSMOS

Using the rich multi-band photometry in the COSMOS field we explored the host galaxy properties of a large, complete, sample of X-ray selected AGN. Based on a two-component fit to their Spectral Energy Distribution (SED; Fig. 1) we derive rest-frame magnitudes, colors, stellar masses and star formation rates up to z ~ 3. The universal shape of the AGN fraction as a function of accretion rate (Fig. 2) in galaxies of different stellar mass, implies, that the same, probably stochastic, process of AGN activation and triggering seems to be in place in galaxies of all masses, and across a wide redshift range. The evolution of its normalization, on the other hand, suggests that AGN activity and star formation are globally correlated.

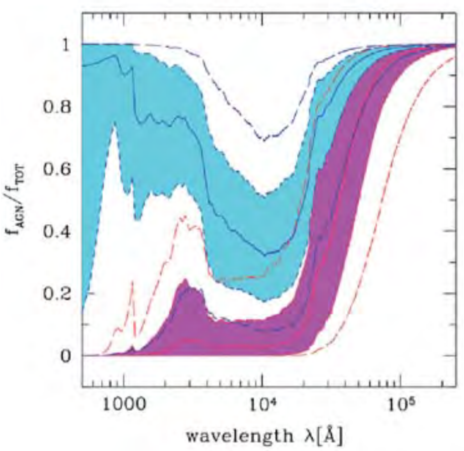

Figure 1: For all AGN in COSMOS, we were able to separate the AGN SED into a stellar (galaxy) and nuclear (AGN) components. This figure shows the median AGN contribution to the total SED at different (rest-frame) wavelengths for un-obscured (blue continuum line) and obscured (red continuum line) objects. Shaded areas correspond to the range within the 25th and 75th percentiles, long dashed lines that within the 10th and 90th percentiles. Crucially, we see that at wavelengths of about 1μm, three quarters of un-obscured objects have AGN fractions smaller than about 50%, implying that, even for un-obscured quasars, our method allow a robust determination of the host total stellar masses (Merloni et al. 2010).

Figure 2: By comparing the AGN hosts with a complete parent sample of IR detected galaxies, we can measure the *probability for a galaxy to host a black hole growing at any given specific accretion rate* (L_X/M_*), shown here for three redshift bins (0.3<z<0.8; 0.8<z<1.5; 1.5<z<2.5, from Bongiorno et al. 2012). We found that this obeys a power-law distribution (with a break consistent with the Eddington limit, vertical dotted line), and *is independent of the host galaxy stellar mass* and follows a power-law distribution in L_X/M_* (a proxy of the Eddington ratio). The incidence of AGN increases with redshift as rapidly as ~$(1 + z)^4$, in close resemblance with the overall evolution of the specific star formation rate. These empirical relations reveal fundamental properties of AGN triggering in galactic nuclei, and will be a useful tool for theoretical studies of black holes within galaxy evolution models.

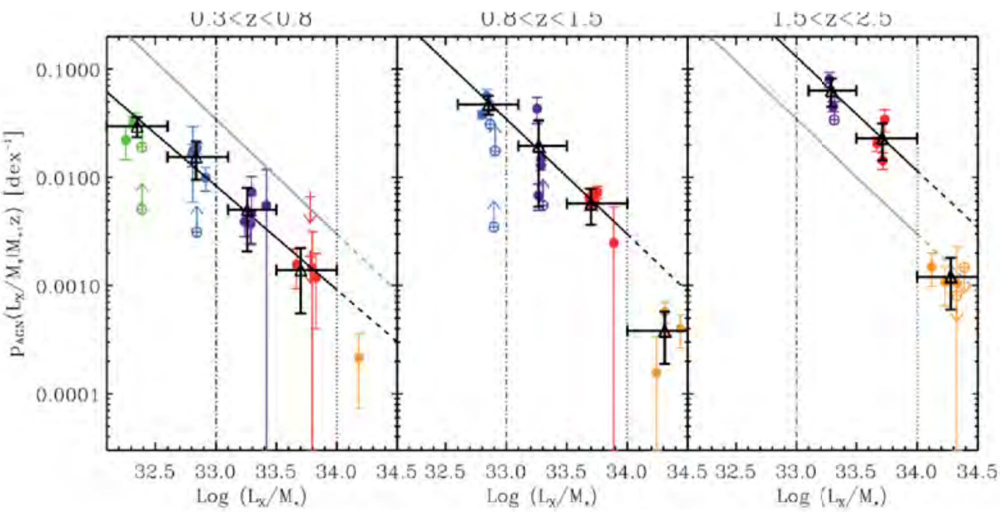

References:

- Merloni et al. 2010, ApJ, 708, 137
- Brusa et al. 2010, ApJ, 716, 348
- Bongiorno et al. 2012, MNRAS, 427, 3103

A. Merloni, A. Bongiorno, and the COSMOS team

The AEGIS Deep X-ray Survey

The AEGIS field (Davis et al. 2007) is one of the richest regions of the extragalactic sky in terms of multi-wavelength data. We have acquired two of the largest *Chandra* observing programs providing X-ray data in this field, motivated by investigation of the co-evolution of AGN and their host galaxies. The AEGIS-XD (deep) survey provides coverage over an area of 0.3 deg^2 to 800ks depth, complementing the wider but shallower (200ks) AEGIS-XW (wide) survey (Laird et al. 2009). We use the outstanding supporting data to perform identifications of the X-ray sources and provide high fidelity photometric redshifts, complementing the excellent spectroscopic coverage in the field provided by the DEEP2 and DEEP3 surveys.

The AEGIS-XD *Chandra* data were taken at three nominal pointing positions (see figure) in the central region of the Extended Groth Strip. The new 600ks exposures were added to the existing AEGIS-XW pointings in this region for a nominal exposure of 800ks. The data were analysed using the methods of Laird et al. (2009), yielding a total of 937 X-ray point sources, to flux limits of 4×10^{-17} erg cm^{-2} s^{-1} (0.5-2 keV band) and 4×10^{-17} erg cm^{-2} s^{-1} (2-10 keV).

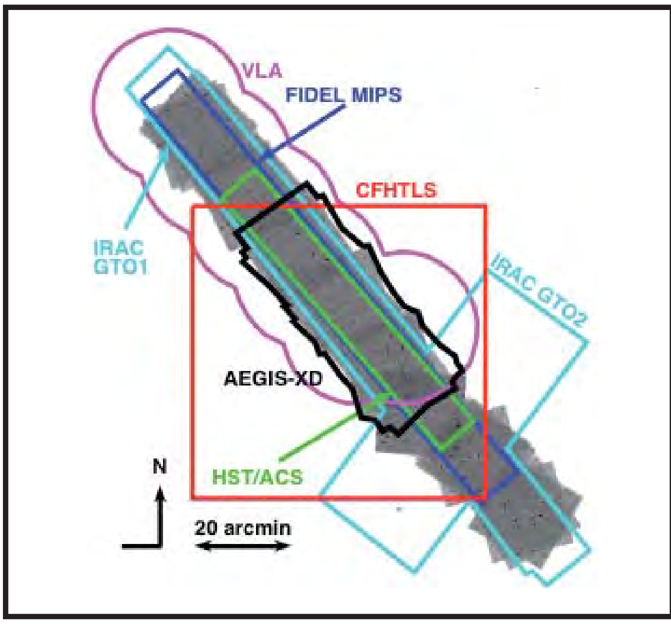

Fig. 1: Layout of the AEGIS-XD Chandra pointings (black) overlaid on the AEGIS-XW data. Excellent Multiwavelength data are available via *Spitzer*, *HST* and the CFHT legacy survey.

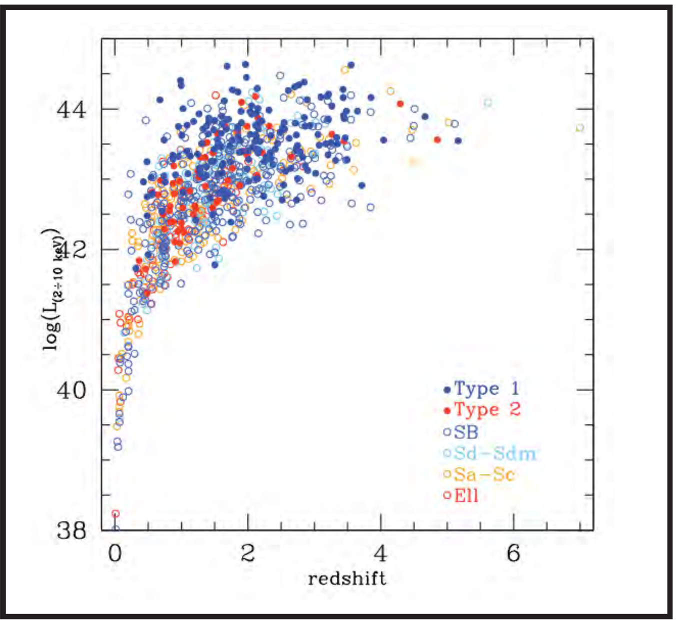

Fig. 2: X-ray luminosity versus redshift for the AEGIS-XD sample. High spectroscopic completeness is complemented by photo-z employing a variety of templates, colour coded.

Using likelihood-based methods, counterparts to 929 of the X-ray sources were identified from deep ground-based, *HST* and *Spitzer* images, including dedicated IRAC imaging acquired as part of the *Chandra* program. Accurate multiband photometry was derived using the methodology of Barro et al. (2011). Spectroscopic redshifts for the X-ray source counterparts are available for ~40% of the sample. For the remainder, we compute photometric redshifts using the method of Salvato et al. (2011), incorporating AGN templates. The accuracy is excellent for an X-ray selected sample with a scatter σ=0.05 and outlier fraction 6%. The sample forms the basis for a large number of further AGN evolution and co-evolution studies.

References:

• Barro, G., et al. 2011, ApJS, 193,13
• Laird, E.S, et al., 2009, ApJS, 180, 102
• Salvato, M., et al., 2011, ApJ, 742, 61

K. Nandra, M. Salvato, A. Georgakakis and the AEGIS team

Bayesian spectral characterisation of X-ray selected AGN in the CDF-S

Active Galactic Nuclei (AGN) show obscuration due to cold, neutral material in the line of sight. With a Bayesian analysis method, X-ray selected AGN in the Chandra Deep Field South (CDF-S) were analysed using a range of X-ray models. Using Bayesian model selection, we find that the obscurer has to have a large covering geometry with strong Compton reflection.

AGN are thought to intrinsically emit a Comptonized spectrum in X-rays which can be approximated by a powerlaw. The variety of observed spectra is attributed largely to viewing angles (unification scheme). Interaction processes such as photoelectric absorption, Fe fluorescence and Compton-scattering determine the spectral shape in dependence of the obscurer geometry and density.

Using a Bayesian approach, we analyse X-ray spectra of 413 X-ray detected AGN in the CDF-S. This method allows us to

(1) extract the most information from typically low signal-to-noise spectra of z~1 AGN, which represent the majority of black hole growth in the Universe.
(2) compare various non-nested models using Bayesian model selection (see Figure 1, left column) corresponding to different geometries.

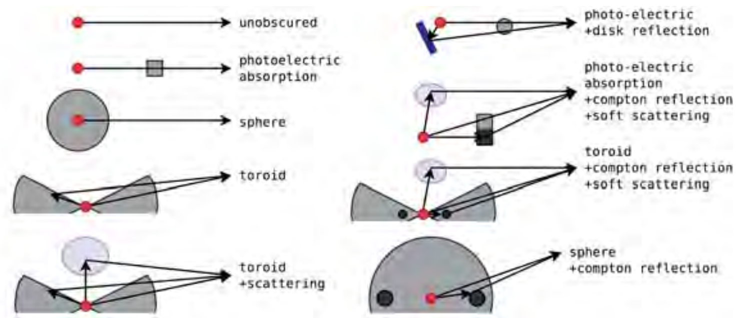

Figure 1. Various geometries considered. The left first four cases represent zero, small, medium and large covering fractions respectively. Additional components, such as Thomson-scattering off ionized clouds (`soft scattering`) and `reflection` are considered (see text).

The sphere or torus geometry with a scattering component (see Figure 2) rule out all other geometries with very strong evidence (Bayes factor > 30). We find:

- *Obscured AGN require a model based on multiple photon interactions.*
- *The obscurer extends outside the line of sight with a large covering fraction.*
- *Thomson scattering is important in ~10% of sources, making an unobscured opening physically necessary*

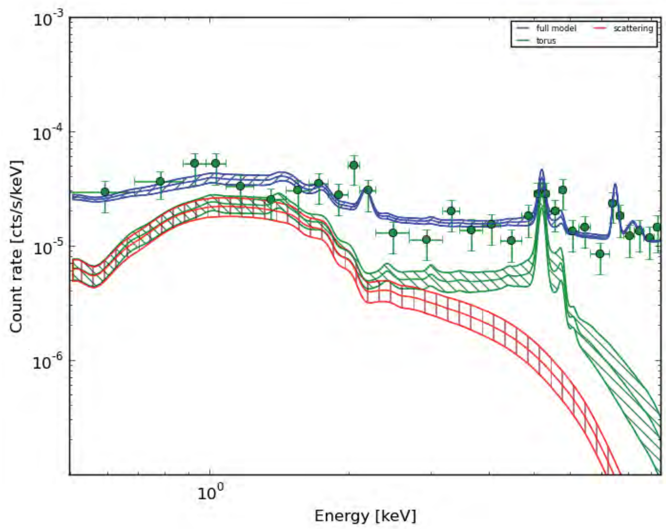

Figure 2. Most observed spectra, like the strongly obscured one shown here, can be described by a powerlaw source embedded in a torus of constant density ("torus", green area) and a "scattering" powerlaw (red area). The model with background (blue) is in agreement with the observed counts (green points).

Ongoing research deals with the problem that the reflection hump and Fe-line is pronounced to various degrees. Introducing additional reflection (see Figure 1, right column) is very strongly preferred by model selection, however there are sources which show a weaker Fe-line than the torus model predicts, potentially indicative of a different geometry, ionization state or metallicity.

J. Buchner, A. Georgakakis, A. Merloni, K. Nandra

Powerful obscured AGN in COSMOS

The large body of XMM-COSMOS multi-wavelength data allowed us to devise a robust method to isolate objects transitioning from being starburst dominated to AGN dominated, such as those expected in the ‘feedback’ phase in AGN-galaxy co-evolutionary models (Hopkins et al. 2008). We make use of the high spectroscopic completeness and the availability of spectral classifications to assess the reliability of color cuts and flux ratios (e.g. R-3.6>4 and 24micron/R>10) as diagnostics of the presence of such rare objects (Fig. 1). The analysis of the optical emission and absorption line properties, the morphological appearance, and the overall spectral energy distribution of the brightest object (in a sample of ~150) revealed high-ionization AGN lines, extended morphology, vigorous on-going star formation (SFR>1000 $M_\odot$) and evidence for outflow (300 km/s). All these are properties expected in the ‘feedback’ phase, confirming the efficiency of the proposed color-color selection (Fig. 2a,b).

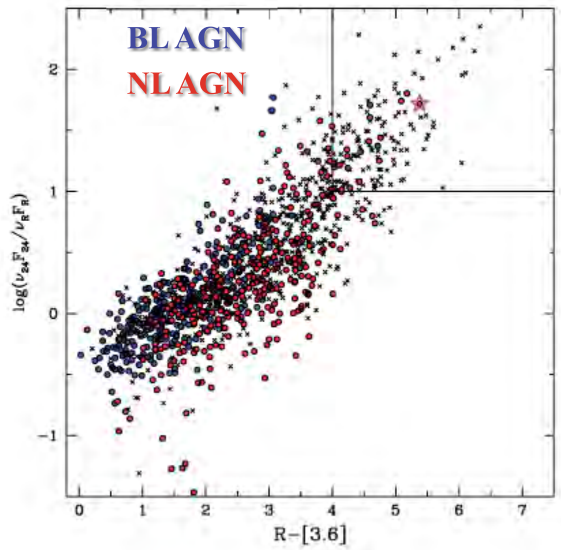

Fig. 1: The solid lines mark the color-color cuts used to select luminous obscured QSO among the XMM-COSMOS sources (complemented by a similar one based on the X/O flux ratio and the R-K color). The magenta star mark the position of XID2028.

Fig. 2: the HST/ACS image (left) revealing extended emission, and the Keck optical spectrum (right) of XID 2028, with superimposed emission and absorption lines, as labeled. The inset shows the zoom on the MgII and MgI absorption lines. A shift of these lines with respect to the systemic velocity can be interpreted as outflow of gas with v=300 km/s.

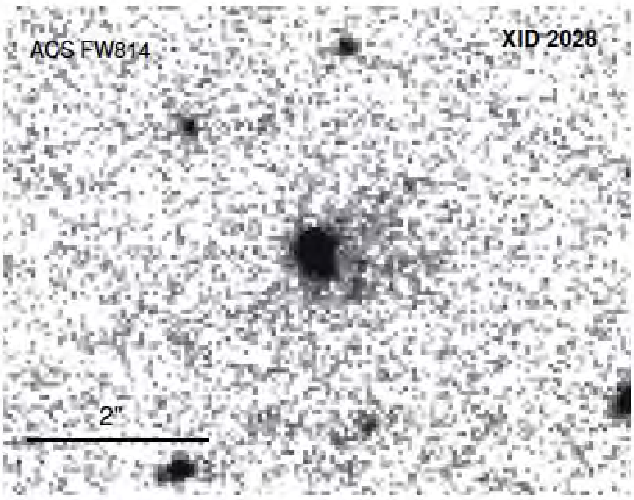

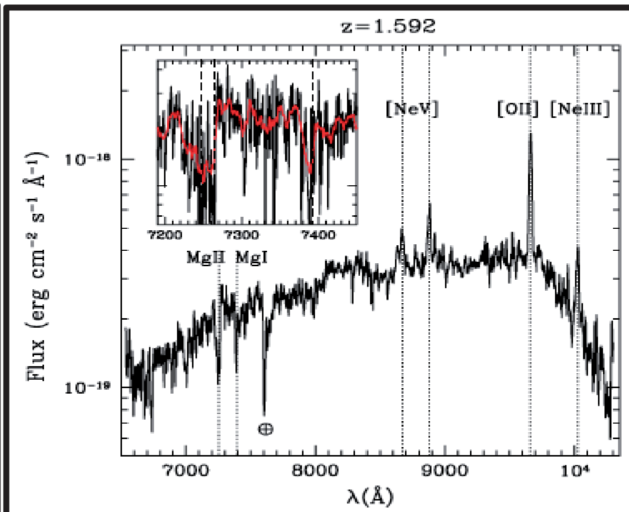

References:
• Brusa et al. 2010, ApJ 716, 348
• Hopkins et al. 2008, ApJS 175, 356

A. Merloni, M. Brusa, and the COSMOS team

The Evolution of Hard x-ray selected AGN

The evolution of Active Galactic Nuclei (AGN) is a tracer of the growth and evolution of supermassive black holes, found in the centers of most galaxies. Using as a proxy of the evolution, the luminosity function of AGN in the X-rays, we catch 'in the act' actively accreting objects and we shed light on their accretion history, up to redshift 4.

With the advantage of being affected the least by photoelectric absorption, we study the evolution with redshift of AGN in the 5-10 keV energy band. Using the latest available surveys (MAXI, HBSS, Lockman Hole, COSMOS, CDFS, AEGIS), we created an unprecedented sample of ~780 AGN, with 98% redshift completeness utilizing the complete probability distribution function in the case of photometric redshifts (37% of the sample).

By means of Maximum Likelihood Estimation, we identified the ***Luminosity Dependent Density Evolution*** as the best evolutionary model to describe our data (*Miyaji et al., 2000*).

Our result, supports the anti-hierarchical growth of supermassive black holes. The most luminous AGN, and therefore the more massive ones, where more numerous at earlier epochs of the Universe (*Fotopoulou et al., 2013 in prep*.).

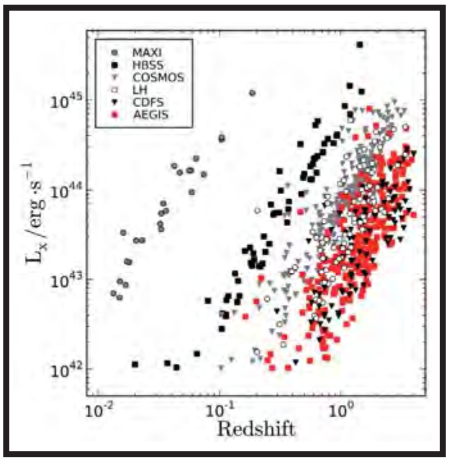

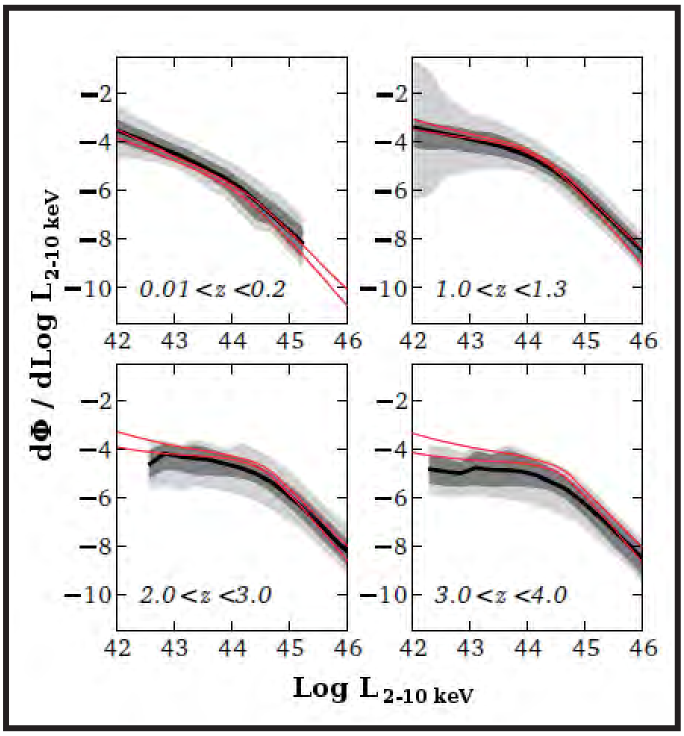

To create the most comprehensive view of the AGN luminosity function, we performed a meta-analysis (*Fotopoulou, Buchner et al., in prep*) of the evolutionary models found in the literature in the 2-10 keV energy band (*Aird et al., 2010, Yencho et al., 2009, Silverman et al., 2008, Ueda et al., 2003*).

Our result in the 5-10 keV (red lines, 90% credible interval) is in remarkably good agreement with the *meta*-luminosity function in the 2-10 keV (gray area, 68% and 90% credible intervals) at low redshift. However, discrepancies are present at the faint end of the luminosity function at high redshifts. This effect could be due to incomplete samples and crude incompleteness corrections.

Since the result is still governed by low number statistics, particularly at high z (z>1) eROSITA with the detection of millions of AGN, will pave the way to a definite answer as to which is the true evolution of AGN.

References:

Miyaji, T.,et al., 2000 A&A 353

Aird et al., 2010, MNRAS 401

Yencho et al., 2009 ApJ 698

Silverman et al., 2008 ApJ 679

Ueda et al., 2003 ApJ 59

S. Fotopoulou, M. Salvato, J. Buchner, K. Nandra, M. Brusa, et al.

AGN X-ray Variability in XMM-COSMOS

Using 4 years of XMM observations in COSMOS, we study the long term variability of a large sample of AGN (1058 sources with $0.3 < z < 3$ and $10^{42} < L_{2-10} < 10^{45.3}$ erg/s). The fraction of sources found to be variable at >99% confidence, given enough statistic, is 0.6±0.2. We used the Normalized Excess Variance (σ^2_{rms}) to obtain a quantitative measure of the variability, and to study the dependencies with other quantities such as L_{2-10}, z, BH mass, Eddington ratio.

Variability, on timescales from minutes to years, is one of the defining characteristics of AGN/BH accretion. The X-ray variability at high frequency can be modeled with a power law of slope >1 (Barr & Mushotzky 1986). It flattens below a break frequency ν_b (Edelson & Nandra 1999) that scales linearly with M_{acc} and with M_{BH}^{-1} (Koerding et al. 2007). X-ray variability at low freq. is difficult to study, due to the long time scale observations required. Deep X-ray surveys such as the Chandra Deep Fields and COSMOS, are a powerful new tools, thanks to the repeated observations performed for large samples of AGN (Paolillo et al. 2004). The typical timescales between multiple observations for sources in the XMM-COSMOS catalog (Hasinger et al. 2007) is in the range 100-1000 days (rest frame), i.e. we are sampling the PSD at frequencies lower than ν_b for any BH mass $<10^9 M_\odot$.

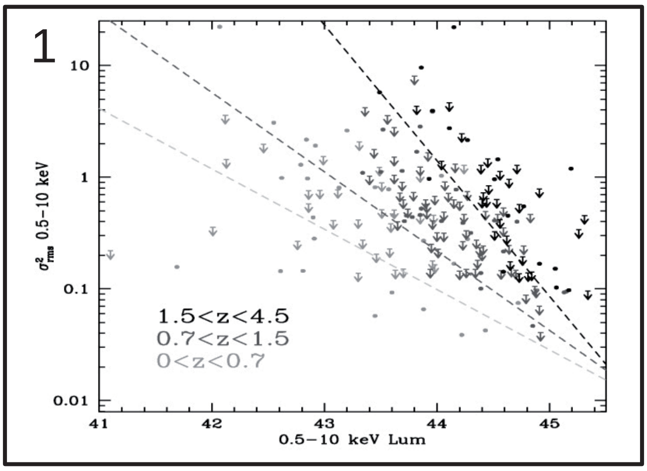

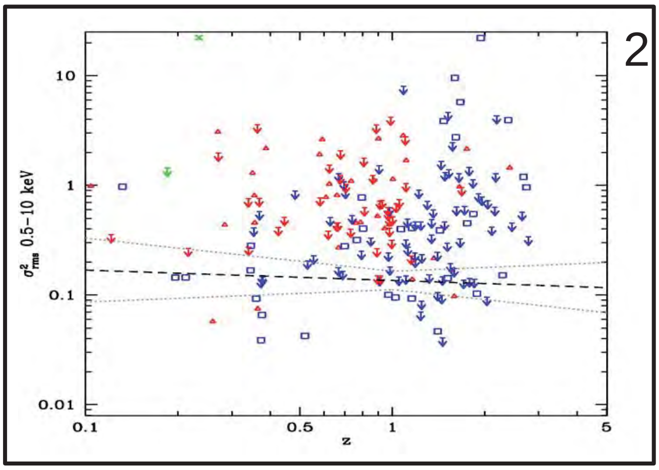

The fraction of sources found to be variable at 99% confidence is strongly dependent on the total number of counts. For sources with good statistic (>1000 counts), the fraction is 0.6±0.2, and decrease to <0.05 for sources with < 100 counts. The total fraction of variable sources is constant with L_{2-10} but decrease with redshift, i.e. our ability to select variable sources decreases with z, due to a decreasing number of counts. For all sources found to be variable we computed the σ^2_{rms} in order to have a quantitative estimate of the variation. The well known anti-correlation between σ^2_{rms} and L_{2-10} is observed also in our sample and, thanks to unprecedented size and z-L_{2-10} plane coverage, we can observe it in 3 redshift bins (Fig. 1). The slopes are consistent within 1σ but, for a given luminosity range the typical σ^2_{rms} it's higher at higher redshifts. No correlation instead is found directly between σ^2_{rms} and redshift (Fig. 2). We do not find any strong correlation of σ^2_{rms} with the BH mass, in agreement with the fact that we are sampling very long time scales, i.e. the flat part of the PSD for our sources. Finally we do not find any evident correlation with the Eddington ratio (Lanzuisi et al. 2013 to be submitted).

References:

- Barr, P., & Mushotzky, R. F. 1986, Nature, 320, 421
- Edelson, R., & Nandra, K. 1999, ApJ, 514, 682
- Koerding, E. G., Migliari, S., Fender, R., et al. 2007, MNRAAS, 380, 301
- Paolillo, M., Schreier, E. J., Giacconi, R., Koekemoer, A. M.,& Grogin, N.A. 2004, ApJ, 611, 93
- Hasinger, G., Cappelluti, N., Brunner, H., et al. 2007, ApJS, 172, 29

G. Lanzuisi, G. Ponti, M. Salvato, et al.

Occupation of X-ray Galaxy Groups by X-ray AGN in the COSMOS field

We present the first direct measurement of the mean Halo Occupation Distribution (HOD) of X-ray selected AGN in the COSMOS field at $z \leq 1$, based on the association of 41 XMM and 17 C-COSMOS AGN with member galaxies of 189 X-ray detected galaxy groups from XMM and Chandra data. We find the mean HOD of AGN among central galaxies to be modelled by a softened step function at logMh $[M_\odot] >$ $\log M_{min}$=12.75(12.10;12.95) while for the satellite AGN HOD we find a preference for an increasing AGN fraction with Mh ($\alpha_s < 0.63$), suggesting that the average AGN number grows slower than the satellite HOD of samples of galaxies (α_s = 1-1.2).

The clustering analysis of AGN can powerfully test theoretical models of galaxy formation and address which physical processes trigger AGN activity. In the HOD framework, the dark matter halos are described in terms of the probability of a halo of mass M_h of having N AGN. A simple way to model the complicated shape of $\langle N(M_h)\rangle$ is by assuming the existence of two separate galaxy populations within halos, central and satellite galaxies $\langle N_{AGN}\rangle(M_h)=\langle N_{cen}\rangle(M_h)+\langle N_{sat}\rangle(M_h)$.
Despite the diverse methods for studying the HOD, we estimated the mean AGN HOD $\langle N_{AGN}\rangle(M_h)$, by using the mass function of galaxy groups hosting AGN among satellite and central galaxies (Fig. 1), i.e. directly counting the number of AGN in galaxy groups.

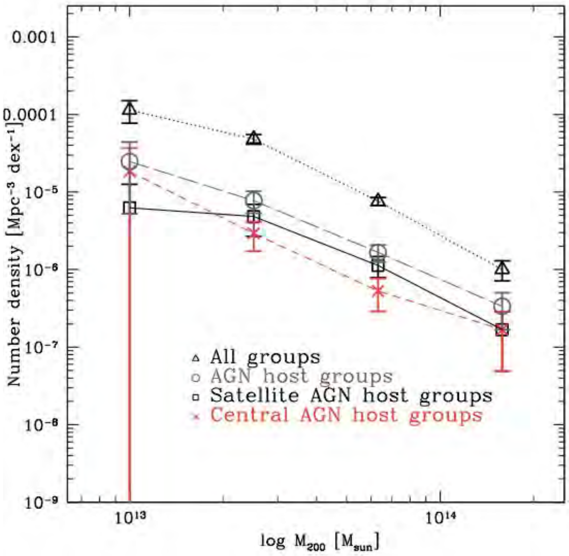

Fig 1: Mass function of X-ray galaxy groups

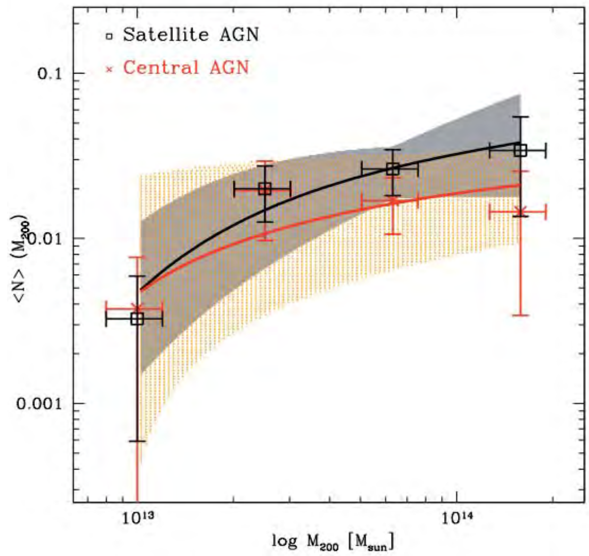

Fig 2: Mean HOD of satellite and central AGN

Using a galaxy membership catalog, we associated 58 AGN in galaxy groups with 22 in central and 36 satellite galaxies, respectively. We found the mean HOD of AGN among central galaxies to be modelled by a softened step function (Fig. 2) at logMh$[M_\odot]$>logMmin=12.75(12.10;12.95). We constrained that the average number of AGN in satellite galaxies might be equal or even larger than the average number of AGN in central galaxies, i.e. AGN do not avoid satellite galaxies. A high fraction of AGN in satellite galaxies is expected in a picture where other phenomena like secular processes, might become dominant in the AGN activation. The mean HOD of satellite AGN increases slower (α_s<0.63) with the halo mass with respect to the linear proportion (α_s=1) of the satellite galaxy HOD, i.e. the number of satellite AGN is not only triggered by the halo mass.

V. Allevato, A. Finoguenov, M. Salvato, M. Brusa and the COSMOS TEAM

Photometric redshift and SED fitting for AGN

Only a large sample of different types of AGN with reliable redshift can allow us to test AGN/galaxy (co)evolutionary models. Given the low number density and the faintness of the majority of AGN, gathering spectroscopic redshift is an not efficient way and we need to rely on photometric redshift. In this context, our group is working on improving the technique and obtaining SED fitting that are informative on the nature of the object

The photometric and spectroscopic ancillary data available for the 2 sq.deg covered by the COSMOS survey allowed a dramatic leap in the accuracy of photometric redshift for AGN (QSOs, type 1 and type 2), comparable to the accuracy obtained routinely for normal galaxies (1%), keeping at the same time the fraction of outliers lower than 6% (Salvato+, 2011). This is due to the creation of a library of hybrid templates representative of the AGN population (Salvato+, 2009). The library is currently used in our group for Ext. Groth Strip (Fig 1, left; Nandra+, 2013), Lockman Hole (Fotopoulou+, 2012), Ext. Chandra Deep South (Hsu+, 2013).

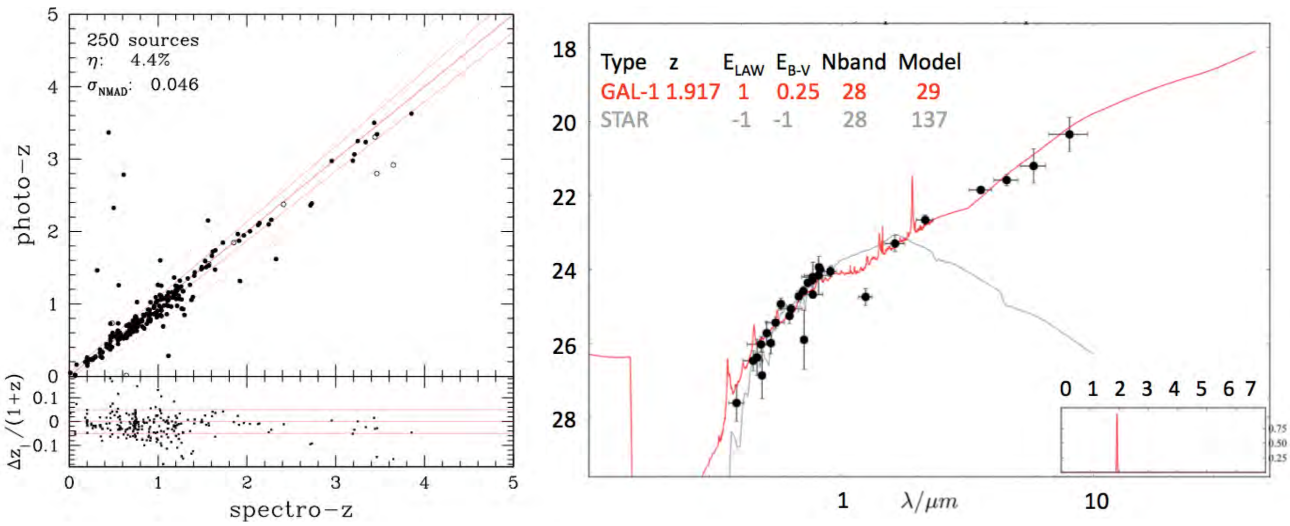

*Fig.***1 Left***: The same procedure defined in XMM- and Chandra-COSMOS allows us to get accurate photometric redshift also for other X-ray sources (EGS in the example), even if lacking intermediate band photometry.***Right***: SED fitting for a IRAC power-law selected AGN, non X-ray detected. The fitting with the hybrids templates recover the right redshift at z=1.9. Normal templates used for these kind of sources would provide false solutions at z=0.7 and z=3.5.*

Although less biassed, the X-ray selection is not complete as, for example, AGN characterized via IRAC power-law are often missed (Donley+, 2012). Erroneously, those sources are usually fit by normal galaxies templates, while a hybrid template would be more appropriate (Fig. 1, right). Beside been able to represent a large variety of AGN population, the hybrids are also providing a reliable estimate of the AGN/host relative contribution when comparing with X-ray and spectroscopic classification (Cappelluti+ 2009, Brusa+ 2010, Donley+2012).

References:

• Donley, J. L.; Koekemoer, A. M.; Brusa, M.; Capak, P. et al., 2012, ApJ, 748, 142
• Fotopoulou, S.; Salvato, M.; Hasinger, G.; Rovilos, E.; Brusa, M. et al. 2012, ApJ, 98,1
• Nandra, K., Laird, E.S., Aird, J.,A., Barro, G., Salvato, M., et al ApJ, 2013, to be submitted
• Salvato, M.; Hasinger, G.; Ilbert, O.; Zamorani, G.; Brusa, M. et al, 2009, ApJ, 690, 1250
•Salvato, M.; Ilbert, O.; Hasinger, G.; Rau, A.; Civano, F.; Zamorani, G. et al., 2011, ApJ, 742, 61

M. Salvato

A BOSS Ancillary Survey of X-Ray AGN in the XMM-LSS

Based on a BOSS ancillary survey in the XMM-LSS field, we performed a study of QSO selection criteria comparing X-ray, variability, and optical colour selection, to prepare for upcoming programs for spectroscopic follow-up of eROSITA AGN. We present our first results of the colour properties and redshift distribution of ~300 X-ray detected AGN.

1. Introduction

The Ancillary Survey of X-ray AGN with BOSS aims for the determination of reliable and unbiased QSO selection criteria for large spectroscopic surveys. In the field of the XMM-LSS, dense spectroscopy with BOSS allows to characterize active galactic nuclei (AGN) sources and hone targeting algorithms for the e-ROSITA X-ray source follow up planned for the SDSS IV program (SPIDERS).

2. Target Selection

The first target sample has been extracted from the XMM-LSS field and consists of 312 X-ray point-like sources ($F_{0.5\text{-}2\ keV} > 10^{-14}$ erg cm^{-2} s^{-1}) over an area of 7 deg^2 with uniform XMM coverage. We observed them with the BOSS spectrograph, and obtained reliable redshift and classification (broad (BL) or narrow (NL)emission lines in the spectrum) for 268 objects. We compare the properties of that sample with those of ~500.000 QSO candidates from the eBOSS survey. The latter are supposed to be optically point-like and in the redshift of $0.8<z<2.2$ with colours defined as in the XDQSO targeting algorithm[1].

3. Colour-Colour Diagrams

In general, optical colours of X-ray selected AGN and optically selected QSO are very similar. However, the X-ray selection provides 35% of the sources that are not represented by the optical QSO candidates, being redder. About 50% of these sources are low luminosity/host galaxy dominated low redshift AGN (see Fig. 1 and 2). The combined selections improve our census of the AGN population.

4. Outlook

Our goal is to characterize the sources detected in the SPIDERS eROSITA follow-up program with SDSS-IV, and optimizing their use for cosmological investigations. For further investigation, we will analyse colour selection criteria by using additional surveys and study spectral properties as a function of M_{BH}, M_{host} and redshift.

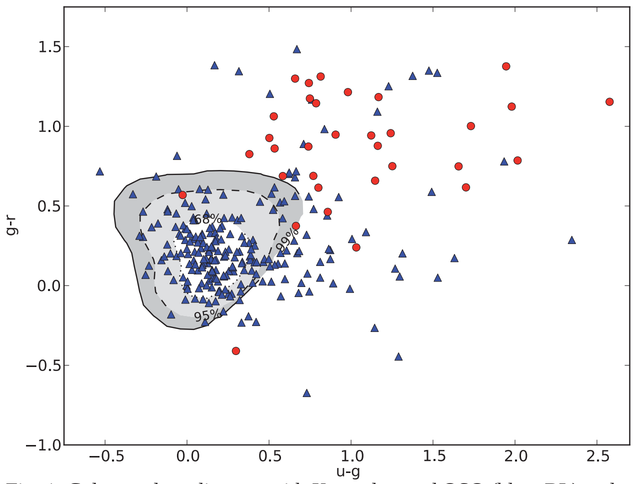

Fig. 1: Colour-colour diagram with X-ray detected QSO (blue, BL) and galaxies (red, NL) from XMM-LSS, and optically selected QSO candidates from SDSS imaging (black, contours for 68%, 95%, 99% of distribution).

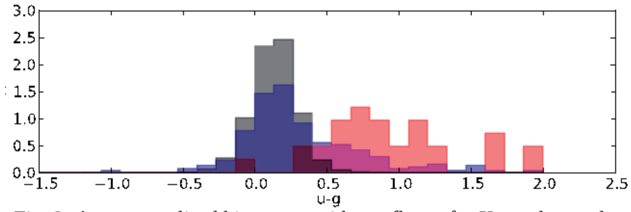

Fig. 2: Area-normalised histogram with u-g fluxes for X-ray detected QSO (blue) and galaxies (red) and only optically detected QSO (black)

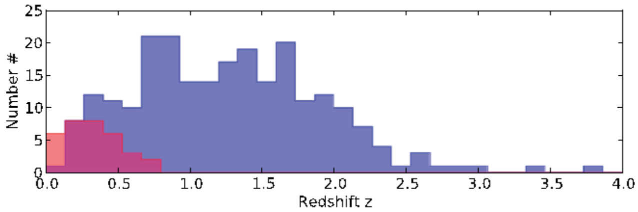

Fig. 3: Redshift distribution by number for X-ray detected QSO (blue) and galaxies (red)

References:

- P. Green & A. Merloni, TDSS/SPIDERS/eBOSS Pilot Survey,2011
- [1] Bovy et al., Probabilistic Target Selection and the SDDS-XDQSO Quasar Targeting Catalog, 2011

M.-L. Menzel, A. Merloni, M. Salvato, N. Clerc, K. Nandra

An X-ray Point Source Catalog for the Chandra Survey in the AKARI NEP Deep Field

Science background: The contribution of Compton-thick, absorbed AGN to accretion onto super-massive black holes across cosmological time is still poorly quantified. By combining Chandra X-ray data with the deep IR survey, the Japanese AKARI satellite conducted in the North ecliptic pole region, we are able to separate IR-detected AGN into unabsorbed, Compton-thin absorbed and Compton-thick (CT) objects, allowing us to address still unresolved questions, such as the contribution of CT AGN to the cosmic X-ray background and their role in host galaxy/AGN evolution.

Data analysis: X-ray source detection in overlapping Chandra raster pointings suffers from the large variability of the Chandra point response across the field of view. Based on software included in the XMM-Newton science analysis software package and previous Chandra-COSMOS work, we fine-tuned and improved a Maximum Likelihood point response fitting method to derive a sensitive and reliable point source catalog, exploiting the full information content of the data. The method was tested and calibrated using simulated Chandra datasets.

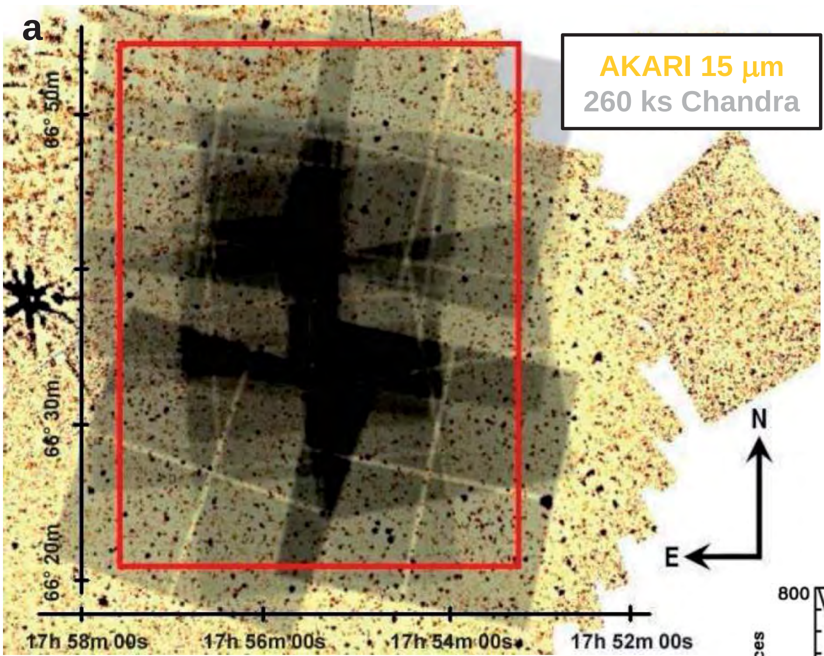

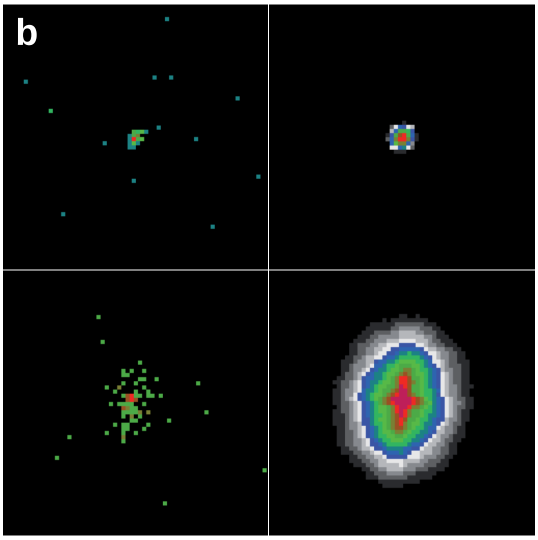

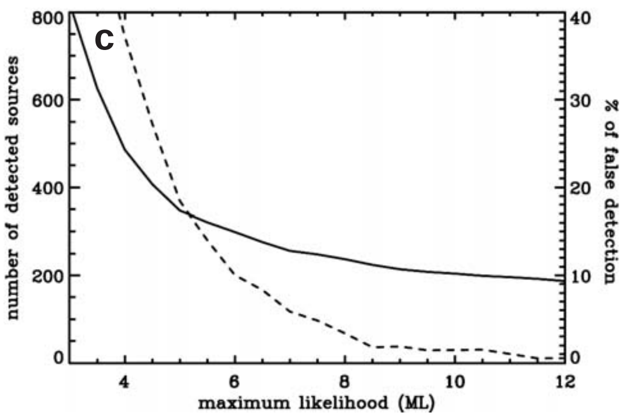

a. 13 Chandra ACIS-I pointings (grey) overplotted on AKARI 15 μm map (yellow) **b.** In overlap areas, same Chandra source displays widely different point response (top, bottom). This is modeled by simultaneous Maximum Likelihood fits of Chandra point response (right: log-scale best fit models). For application of method to Chandra–COSMOS data, see Puccetti et al., 2009.
c. Number of detected sources (left axis, solid line) and % of false detections (right axis, broken line) is determined from simulated Chandra-AKARI data as a function of detection likelihood.

Krumpe, Miyaji, Brunner, et al., MNRAS, in prep.
Puccetti,…, Brunner, et al., 2009, ApJS, 185, 586

H. Brunner et al.

Identification and Photometric Redshift of X-ray Detected Active Galactic Nuclei in the CANDELS

Taking the advantage of the high-resolution and the depth of HST/WFC3 near-infrared (NIR) imaging from the Cosmic Assembly Near-IR Deep Legacy Survey (CANDELS), we present accurate photometric redshift (photo-z) for normal galaxies and X-ray detected sources in this region, and obtain a high fraction of counterparts for the X-ray sources as well. In particular the depth of the CANDELS data in NIR allows more accurate photo-z in the redshift range z >1.5 and J >23 mag. Similarly, using the newly available TENIS data (Taiwan ECDFS Near-IR Survey; Hsieh et al. 2012), which reaches a depth of 25.6 mag for J-band, we implemented the same procedure in the 4 Msec Chandra Deep Field-South (CDFS) and the Extended-CDFS (ECDFS). To compute photometric redshift for AGN, we adopted new sets of AGN/galaxy hybrids (Fig. 1) for the spectral energy distributions (SEDs) fitting. Compared to the AGN/galaxy hybrids defined by Salvato et al. (2009), the new sets make use of semi-empirical spectra with emission lines (Bender et. al. 2001) for the host component. We show the importance of the NIR deep data and the intermediate band (IB) photometry to acquire accurate photo-z for X-ray detected sources.

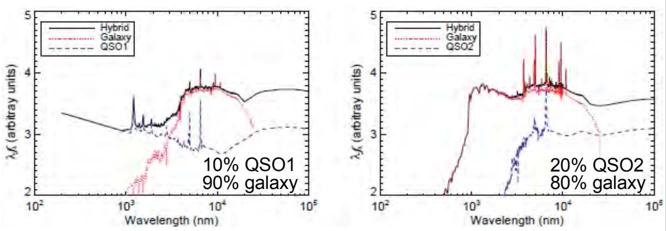

Fig. 1. Two examples for the SED hybrids. The emission line components allow a better fit also for low luminosity AGN (Hsu et al. 2013).

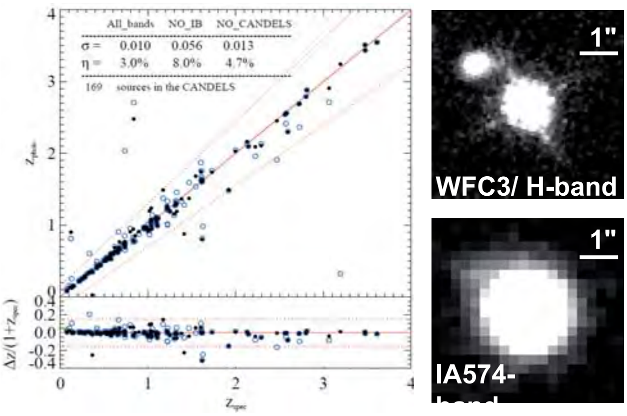

Fig. 2. Left: Photo-z vs. spec-z of the X-ray sources in the CANDELS-GOODS-South. The cyan open circles indicate the photo-z computed without CANDELS data. A clear improvement is shown by adding the CANDELS data (black dots). The remaining outliers are due to the low-resolution and not de-blended photometry in the intermediate bands (see the example of cutouts). Future re-computation of the photometry will improve results for these kind of objects.

To compute photo-z, in addition to the CANDELS photometry (Guo et al. 2013) on 16 bands (mostly from space), we used data from the GALEX, TENIS, and 18 intermediate bands from Cardamone et al. (2010), for a total of up to 48 bands. We achieved an accuracy of σ_{NMAD} = 0.010 and have 3.0% outliers for 169 X-ray sources with secure spectroscopic redshifts (Fig. 2). Comparing the result with Luo et al (2010), the improvement is shown especially in the NIR-faint sources (Fig. 3).

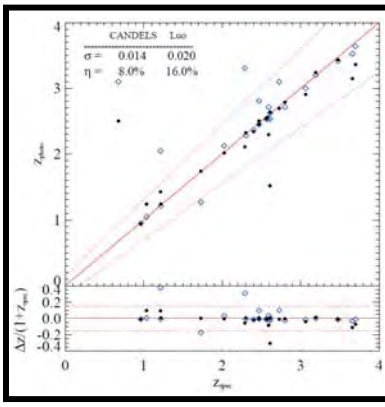

Fig. 3. Photo-z vs. spec-z of the NIR-faint (J >23) sources in the CANDELS GOODS-S. The black dots indicate the photo-z results in this work, and the cyan diamonds indicate the photo-z results from Luo et al. (2010).

References:
- Bender, R., et al. 2001, The ESO Messenger
- Cardamone, C. N., et al. 2010, ApJS, 189, 270C
- Hsieh, B.-C., et al. 2012, ApJS, 203,23H
- Guo, Y., et al. 2013, ApJS, submitted.
- Luo, B., et al. 2010, ApJS, 187, 560
- Salvato, M., et al. 2009, ApJ, 690, 1250

L.-T. Hsu, M. Salvato, K. Nandra and the CANDELS team

GROND Photometric Redshifts of Fermi BL Lac Objects Leading to EBL Constraints

We performed Swift/UVOT and GROND optical-near-IR imaging in order to obtain spectral energy distributions (SEDs) of 103 Fermi/LAT blazars. Photometric redshifts were derived through SED fitting pushing the known redshift boundary of BL Lacertae (BL Lac) objects out to z~1.9. These redshift estimates facilitated the detection of the attenuation of Fermi/LAT gamma-ray photons by the UV/optical extra-galactic background light (EBL) and the measurement of the EBL flux density.

A significant fraction of the Fermi/LAT source population is formed by BL Lac objects. However, their featureless UV/optical spectra make redshift estimates very challenging and, thus rare. We obtained photometric redshifts using SED fitting of quasi-simultaneous 13-band GROND [1] and Swift photometry (left figure) utilizing the flux suppression caused by the absorption through neutral hydrogen along the sight line. We provided the first reliable measurements for 8 sources (6 of them BL Lacs) and upper limits for an additional 66 targets. The 6 BL Lac objects, including the new record holder at z~1.9, quadruple the known z>1.3 sample, demonstraing the power of the photometric redshift technique. [2]

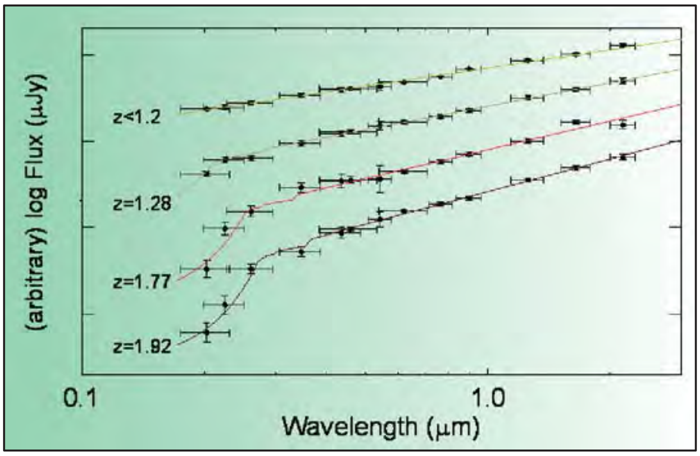

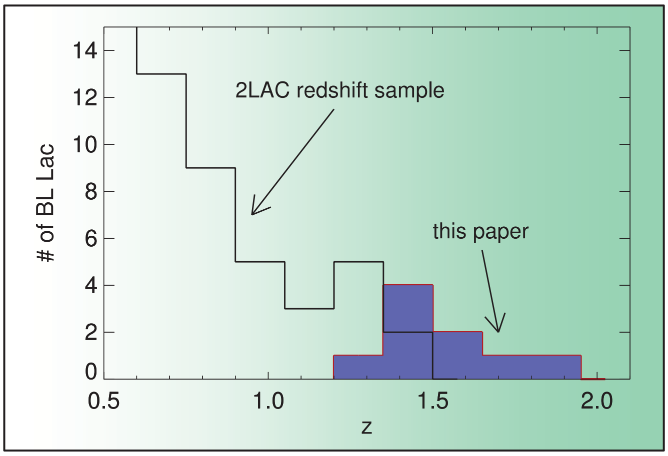

The EBL is produced by the emission from stars and accreting compact objects throughout the history of the Universe and thus a powerful tool to study star and galaxy formation. γ-γ absorption of high-energy gamma-rays emitted by BL Lacs (thought to be free of intrinsic absorption) allows an indirect probe of the EBL. As the attenuation signature increases with redshift, our work on extending the redshift distribution (see above) was crucial. The right figure shows the absorption feature present in the combined Fermi/LAT BL Lac spectra at 0.5<z<1.6, together with the best fit attenuation model (dashed line). Models containing a source intrinsic exponential cut-off (solid line) do not fit the data well. [3]

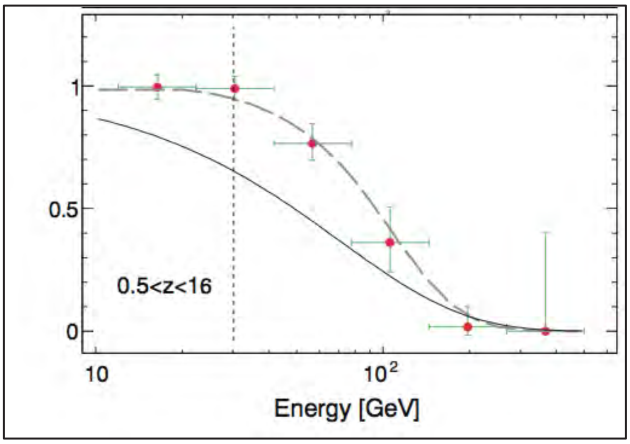

References:

- [1] Greiner et al. 2008, PASP, 120, 405;
- [2] Rau et al. 2012, A&A, 538, A26;
- [3] Ackermann et al., 2013, Science, 338, 1190

A. Rau, P. Schady, J. Greiner, M. Salvato, et al.

Obscured AGN: new X-ray spectral models

New X-ray spectral models for heavily obscured active galactic nuclei (AGN) are presented. These models self-consistently account for signatures of obscuration, including absorption, Compton scattering, iron Kα fluorescence and the geometry of the absorber under one scheme. Characterising AGN obscuration is important for understanding the accretion history of the universe.

INTRODUCTION: AGN are understood to be powered by the accretion of material onto a supermassive black hole, and that the evolution of these black holes are somehow linked to their host galaxies (Ferrarese & Merritt 2000). Thus understanding the accretion history of the universe is important in understanding the evolution of galaxies. Much of this accretion is hidden from sight, however, by obscuring material surrounding the AGN (Antonucci 1993). X-ray spectral analysis is ideal for assessing this obscuration due to the ability of X-rays to penetrate even the most heavily obscured systems. We present here new models from Brightman & Nandra (2011) specifically designed to unveil obscured accretion in X-rays

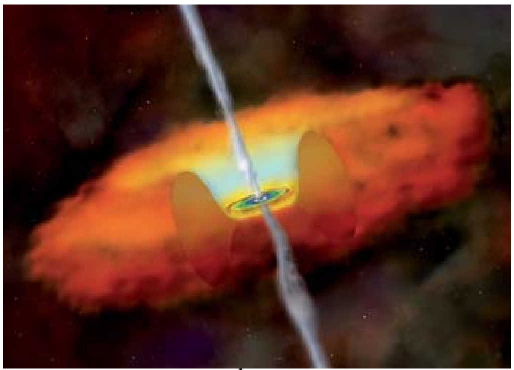

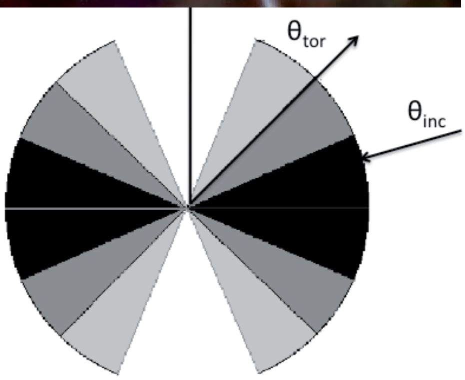

Fig. 1. A ‘torus‘ geometry is assumed in the model, thought to be the geometry of material obscuring AGN.

MOTIVATION: X-ray spectral signatures of obscuration in AGN include soft X-ray absorption, Compton reflection and Fe Kα emission. Most spectral analyses of heavily obscured AGN model each signature separately. Our new models include all these effects self-consistently in one shceme.

MODEL DESCRIPTION: Monte-Carlo methods are employed to calculate radiative transfer from an isotropic point source of X-rays, using interaction cross sections for scattering and absorption, with an input spectrum of $F\gamma = E^{-\Gamma}$. Fluorescent emission lines of Fe Kα (6.4 keV), Fe Kβ (7.1 keV) + Kα lines from several other elements are also included. A torus geometry (Fig.1) is used which is believed to be the configuration of obscuring material in AGN. Line of sight column densities considered: $10^{20} \leq N_H \leq 10^{26}$ cm^{-2}, with power-law indices $1 \leq \Gamma \leq 3$. Viewing angle and torus opening angle are also parameters. Fig. 2 shows some example model spectra, for a range of N_H and torus opening angles

Fig. 2. Simulated X-ray spectra, for $N_H=10^{20}$, 10^{23}, 10^{24}, 10^{25} cm^{-2} (left to right), for torus opening angles of 30° (black) and 60° (red).

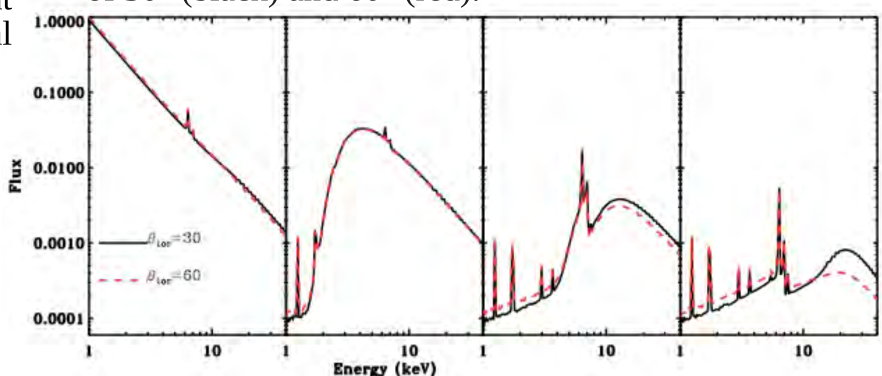

References:
• Antonucci R., 1993, ARA&A, 31, 473
• Brightman M., Nandra K., 2011, MNRAS, 413, 1206
• Ferrarese L., Merritt D., 2000, ApJ, 539, L9

M. Brightman, K. Nandra

The dark matter halo masses of X-ray AGN

The environment of AGN, i.e. the mass of the dark matter halo in which they live, provides important information on the physical conditions under which black holes at the centres of galaxies grow their mass. We present a novel method that uses photometric redshifts to measure the clustering of X-ray AGN and which is superior in certain aspects to traditional clustering estimators. We show that the bulk of the X-ray AGN at z~1 live in haloes with masses logM~12.5 (solar), suggesting cold-gas accretion as the dominant AGN fueling mode.

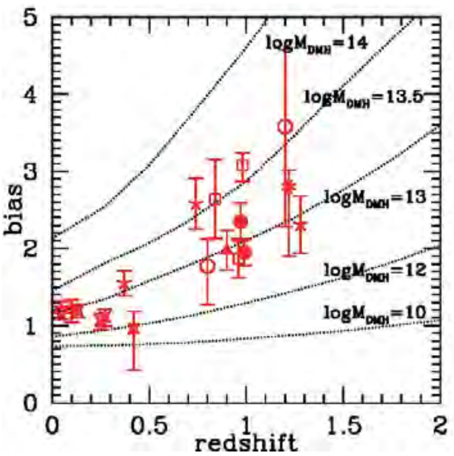

Fig. 1: Current state of the art in measurements of the bias of X-ray AGN as a function of redshift. Data points correspond to different samples in the literature. Curves correspond to different halo masses. At any given redshift there is substantial scatter among individual bias measurements. This is partly because of random errors and systematics affecting different samples,

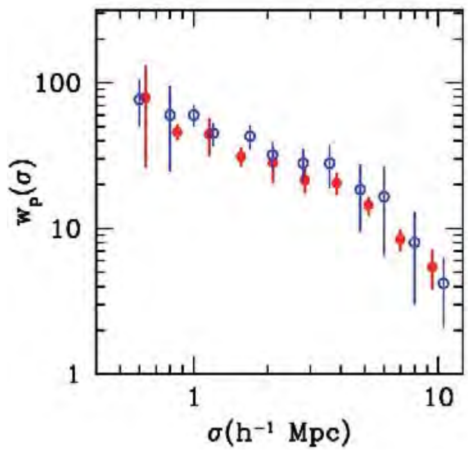

400 spec-z AGN (ECDFS, COSMOS, AEGIS) correlated with 10^5 galaxy photo-z PDFs

100 spec-z AGN (AEGIS) correlated with 5000 spec-z galaxies (DEEP2)

Fig. 2: Redshift-space AGN/ga;axy cross-correlation function, wp. Blue points are the traditional estimator that uses spectroscopic redshifts for both populations. The red circles are the new method that replaces spectroscopy for galaxies with photo-z PDFs. The new method recovers the clustering signal and also allows wp estimates in fields without extensive spectroscopy for galaxies.

Fig. 1 presents the current state of the art in X-ray AGN clustering measurements. There is significant scatter among studies, partly because of statistical errors (e.g. small sample sizes) and systematics (e.g. sample variance). Both these issues are related to the strong dependence of current clustering estimators on spectroscopy to get robust measurements.

We relax this requirement by developing a methodology which uses the photometric redshift PDFs (Probability Distribution Function) of galaxies to determine the AGN/galaxy cross-correlation function and infer from that the DMH mass of AGN (Mountrichas et al. 2013, MNRAS, 430, 661). The power of this approach is demonstrated in Fig. 2. Our method is superior to traditional AGN clustering estimators because (i) random errors are suppressed when counting AGN/galaxy pairs, (ii) the impact of sample variance is minimised and (iii) the requirements for spectroscopy are minimal: only spec-z for AGN are needed.

This methodology is applied to Chandra deep surveys (AEGIS, ECDFS, COSMOS). We estimate an average halo of mass of logM~13.2 (solar) for AGN at z~1 and Lx~1043erg/s. We also find that this mean is biased high because of the small number of AGN in haloes >1013Mo. Removing 5% of the AGN associated with X-ray groups above this mass cut reduces the clustering signal of the overall population to logM~12.5 solar, close to the halo mass scale where star-formation proceeds more efficiently (e.g. Behroozi et al. 2013, ApJ, 762, 31). This favors cold gas accretion as the dominant mode for fueling the bulk of AGN at z~1.

A. Georgakakis, G. Mountrichas, A. Finoguenov and the AEGIS collaboration

Galaxy Clusters as Cosmological Probes

Galaxy clusters are ideal probes for assessing the statistics of the cosmic large-scale structure and to test cosmological models. Based on the ROSAT All-Sky Survey we have compiled the largest, statistically well defined galaxy cluster sample in the nearby Universe with the REFLEX II and NORAS II cluster redshift surveys comprising ~1834 clusters. With the REFLEX survey we have obtained cosmological constraints from the cluster X-ray luminosity function and determined the power spectrum of the cluster distribution on large scale.

We have compiled highly complete catalogs of galaxy clusters from the ROSAT All-Sky Survey in the north (NORAS II survey) and in the south (REFLEX II survey) to a flux-limit of 1.8 10^{-12} erg s^{-1} cm^{-2} (0.1 – 2.4 keV). The sky distribution of the two surveys is shown in Fig. 1. We have applied the REFLEX II sample to a number of astrophysical and cosmological studies, and e.g. determined a very precise X-ray luminosity function.

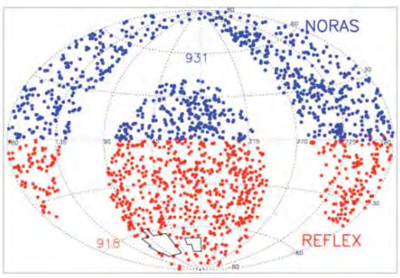

Fig. 1 (left) Sky distribution of the galaxy clusters in the REFLEX II (red) and NORAS II survey (blue). **Fig. 2** (right) X-ray luminosity and redshift distribution of the REFLEX II clusters, with Abell clusters marked by solid points.

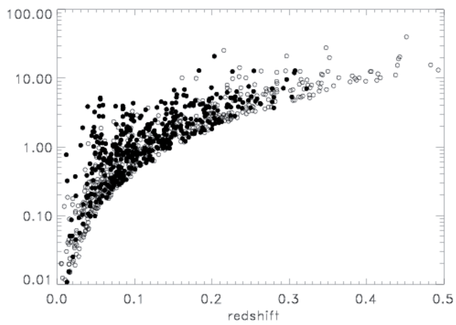

The X-ray luminosity of the clusters is tightly correlated to the cluster mass. The mass function, as predicted by cosmic structure formation theory, is exponentially dependent on some of the cosmological parameters. Therefore the X-ray luminosity function can be used to provide good constraints on cosmological parameters, particularly on the density fluctuation amplitude, σ_8, and the cosmic matter density parameter, Ω_m (shown in Fig. 3). The power spectrum of the galaxy cluster density distribution provides information of the inhomogeneous matter density distribution in an amplified (biased) way. With galaxy clusters we therefore obtain an amplified view of the density structure of the Universe compared to that of the dark matter and the galaxies (as shown in Fig. 4).

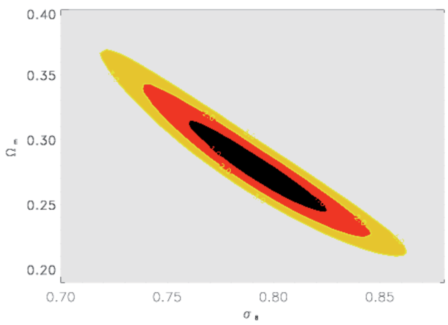

Fig. 3 (left) Constraints on the cosmological parameters, Ω_m and σ_8 from the REFLEX X-ray luminosity function. **Fig 4** (right) Power spectrum of the density distribution of REFLEX clusters compared to that of dark matter and galaxies. The cluster function is biased high.

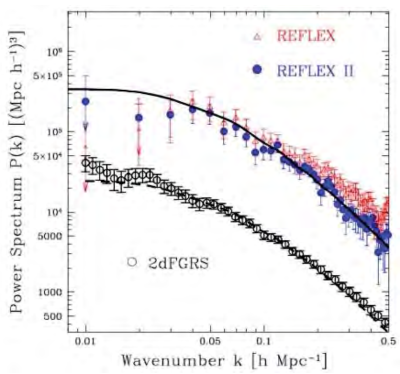

References:
Böhringer, H., et al., 2004, A&A, 425, 367; Böhringer, H., 2011, AIP Conf. Proc. 1381, 137, Chon G. & Böhringer, H., 2012, A&A, 538, 35; Balaguera-Antolinez, A., et al., 2011, MNRAS, 413, 386; Böhringer, H., et al., 2013, A&A, submitted

H. Böhringer and G. Chon

Superclusters from REFLEX II survey

Superclusters are the largest structures that we can observe in our Universe. They are located at a special place in terms of structure formation hierarchy being not virialised unlike clusters of galaxies. Here we construct the first X-ray flux-limited supercluster catalogue with the extended ROSAT-ESO (REFLEX) flux-limited X-ray galaxy cluster survey to study the nature of X-ray superclusters and to use them as astrophysical laboratories.

Using the friends-of-friends algorithm we construct an X-ray supercluster catalogue. With our choice of the linking length parameter we select superclusters that will eventually collapse in the future. We find 164 superclusters out to redshift z=0.4. We examine the statistical robustness and contamination of our catalogue by constructing four Volume-Limited Samples (VLS) to trace the superclusters through different luminosity cuts and redshift (Fig 2.). We conclude that even for binary superclusters the fraction of spurious detection is less than 6%. A major result is that the volume occupied by the superclusters is only 2% which is made up of slightly more than half of the REFLEX clusters. In addition we confirm for the first time the theoretical expectation that there are more X-ray luminous clusters in the supercluster than the field thanks to the homogeneously selected X-ray cluster sample with a well-understood selection function.

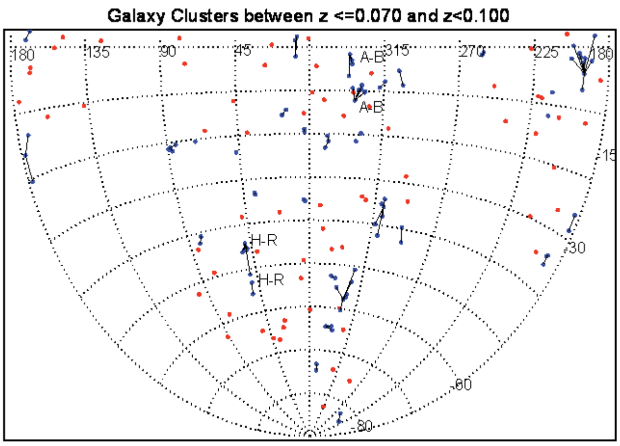

Fig 1. Spatial distribution of the REFLEX superclusters in a redshift shell. The clusters in superclusters are linked by lines (blue) and field clusters are shown in red.

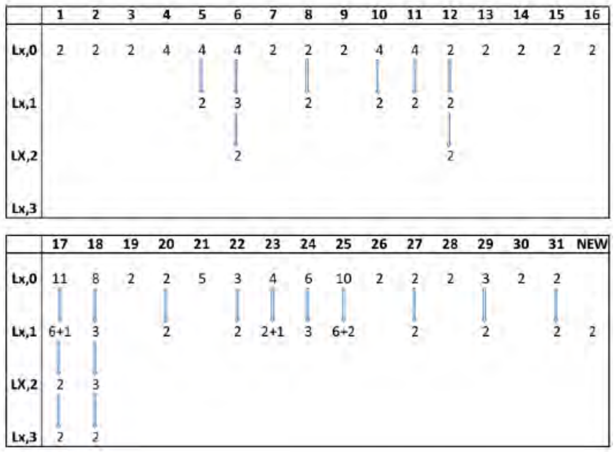

Fig 2. Test of the robustness of superclusters. The nature of superclusters is traced through successively lower luminosity cuts.

Fig 3. Comparisons of the X-ray luminosity functions in different environments. The luminosity function of the clusters in superclusters (green), the field clusters (red), and all clusters(black). The curves are normalised by the volume occupied by the corresponding clusters.

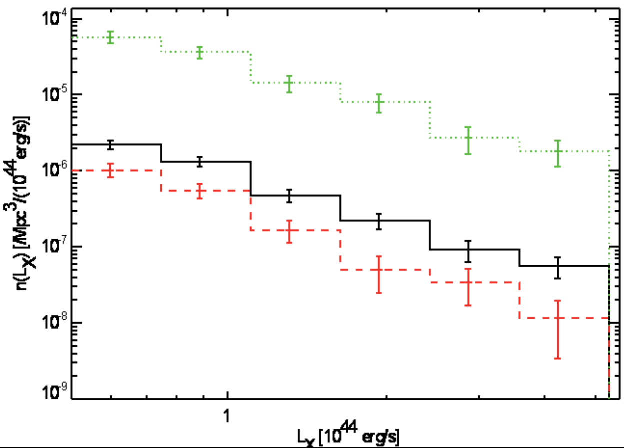

References:

- Chon, Böhringer, Nowak, 2013, MNRAS, 429, 3272
- Böhringer, Chon, et al., 2013, A&A, in press
- Chon, Böhringer, 2012, A&A, 38, 35

G. Chon, H. Böhringer

Comparison of the X-ray and Optical Structure of Galaxy Clusters

Galaxy clusters, the largest bound objects in the universe, can be used to study astrophysics and probe cosmology. Dark matter, intra-cluster gas and galaxies are bound in the deep gravitational potential of a cluster. Comparing the density profiles of galaxies and intra-cluster gas can provide information on how the energy released by the gravitational collapse was distributed between the two components. We also compare the two-dimensionally projected cluster structures seen in optical and X-ray in more detail.

Deep XMM-Newton observations and wide-field optical imaging with the MPG/ESO 2.2m telescope for a representative sample of X-ray luminous clusters (REXCESS) are used to compare their gas and galaxy distribution. For the determination of the galaxy distribution a local background of "field galaxies" was estimated and statistically subtracted from the cluster objects. The galaxy density and X-ray surface brightness distribution for one of the clusters is compared in Fig. 1. Both distributions show a similar East-West elongation.

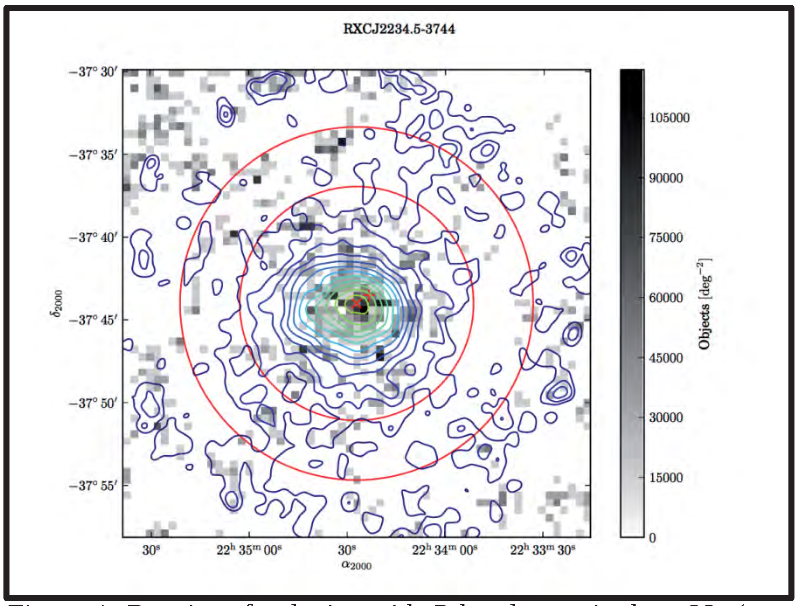

Figure 1. Density of galaxies with R band magnitude < 22. (grey histogram), X-rays in 0.5-2.0 keV (coloured contours, smoothed by symmetric Gaussian with 20 arcsec FWHM). The inner and outer red circles indicate $R500$ and $R200$.

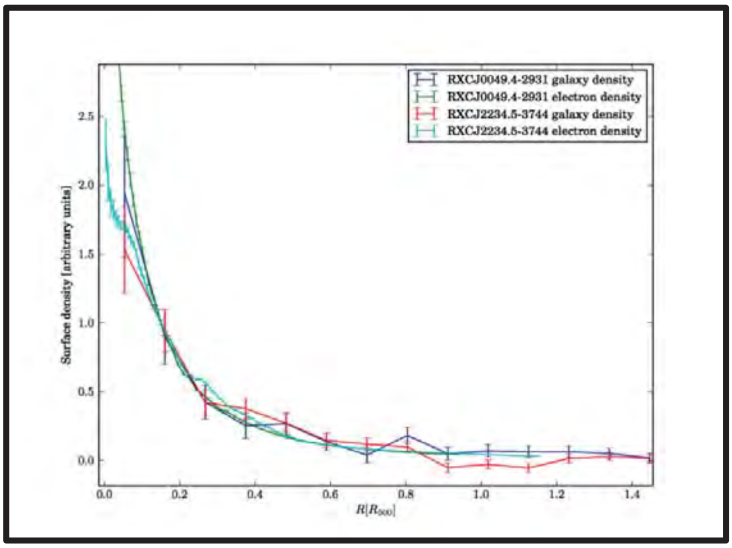

In Fig. 2 we compare the radial gas density and galaxy density profiles of two of the clusters. The profiles have been normalised at a radius of 0.15 R_{500}, outside a possible cool core region. These first preliminary results show a very similar distribution of gas and galaxies. We expect to obtain more precise results from the stacked profiles of our complete sample of clusters.

Figure 2. Surface density profiles of galaxy and electron density (a proxy for the intra-cluster medium) for two galaxy clusters, normalized at 0.15 R_{500}.

References:

- J. Holland et al., in prep.
- H. Böhringer et al., 2007, A&A, 469, 363
- H. Böhringer et al., 2010, A&A, 514, 32

J.G. Holland, H. Böhringer, G. Chon

Substructure Analysis of X-ray Galaxy Clusters

X-ray observations of the Intra-Cluster Medium (ICM) provide excellent means to study the dynamical state of galaxy clusters. A variety of morphologies has been revealed and a substantial fraction of clusters seems to be dynamically disturbed. This indicates that the assumptions of hydrostatic equilibrium and spherical shape which are generally used to determine the cluster mass from X-ray data are not always satisfied. It is therefore important for the understanding of cluster properties as well as for cosmological applications to mark clusters which show substructure in their X-ray images.

Using simulated X-ray images, we analyzed the statistical properties of the morphology estimators power ratio ***P3/P0*** and center shift ***w***, including their sensitivity to Poisson noise and background. We present a method to correct for these effects and give morphological boundaries to divide the sample into relaxed and disturbed objects (Fig. 1). Based on a visual classification of the simulated images, we found useful boundaries for the classification at $P3/P0=10^{-7}$ and $w=0.01$. In the case of high-quality observations, we go into more detail and define three morphological $P3/P0$ ranges: relaxed ($P3/P0<10^{-8}$), mildly disturbed ($10^{-8}<P3/P0<5\times10^{-7}$) and disturbed ($P3/P0>5\times10^{-7}$) objects.

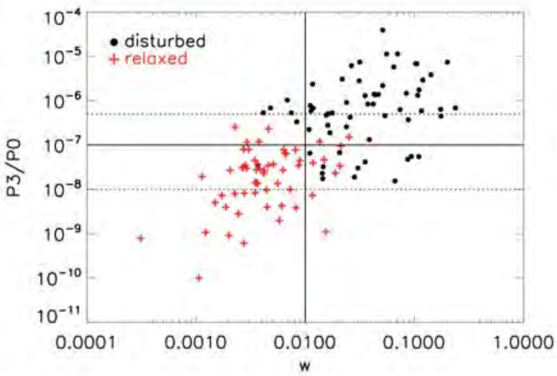

Fig. 1: $P3/P0$-w plane for simulated X-ray images. We visually classified the clusters as relaxed (red crosses) and disturbed (black circles) objects and show the morphological boundaries at $P3/P0=10^{-7}$ and $w=0.01$ as solid lines. A more detailed analysis can be done using two $P3/P0$ boundaries at $P3/P0=10^{-8}$ and $P3/P0=5\times10^{-7}$ (dotted lines).

With these estimators we study the evolution of substructure frequency up to z~1 using 78 z<0.35 and 36 z>0.35 observed galaxy clusters. Poisson noise has a strong influence on the $P3/P0$ determination, especially for high-z observations with low photon statistics. This leads to an overestimation or non-significant $P3/P0$ signal of relaxed objects. Degrading the high-quality low-z observations to the photon statistics of the high-z data yields a very mild positive evolution of the substructure frequency with redshift (Fig. 2). Within the significance limits our result is also consistent with no evolution. Without degrading (undegraded case), we find a too steep slope in the $P3/P0$-z plane. For w, which is more robust against Poisson noise, we find a similar trend for the undegraded and degraded case.

Fig. 2: $P3/P0$-z plane. We show the comparison between the fit of the $P3/P0$-z relation using the undegraded (green) and degraded (red) low-z observations and the high-z 400SD data including their 1-σ errors (dotted lines).

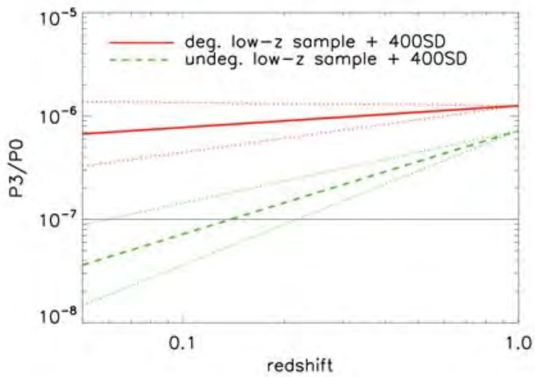

References:
· Weißmann et al. 2013, A&A, 456, 55
· Weißmann et al. 2013, A&A submitted

A. Weißmann, H. Böhringer, G. Chon

Brightest X-ray Clusters in CFHTLS

We present the results of the XMM and Hectospec follow-up programs on the brightest X-ray clusters identified using a combination of faint X-ray sources from the ROSAT survey data and a multi-wavelength coverage of CFHTLS wide (1, 2 and 4) fields.

CFHTLS survey presents a unique data set for weak lensing studies. To utilize the CFHTLS data for cluster calibration, we need to perform a search for clusters. We present the results of identification of faint RASS sources using the multi-wavelength data of CFHTLS. To detect the optical counterparts of X-ray clusters, we introduce a multi-color red sequence method and also verify the results visually. Red sequence configuration parameters, such as color model and characteristic magnitude, are derived from a sample of early-type galaxies and different stellar population models.

In order to fully utilize the XMM data, we adopted the method of using the clusterspatial extent to separate the clusters from point sources to the shallow depths of the XMM data in our program. For each detected source we calculated the red sequence significance parameter to identify galaxy clusters up to a redshift of 1. The top figure shows a color-magnitude plot for a cluster at redshift 0.2. Selected red-sequence member galaxies were targeted by our spectroscopic follow-up program, yielding both spectroscopic identification and dynamical mass estimates. We obtain samples of 135 and 27 X-ray selected clusters from XMM and ROSAT X-ray sources respectively, with 16 clusters in overlap between the two samples, limited by the XMM follow-up. The bottom figure illustrates the X-ray luminosity versus redshift for XMM-CFHTLS clusters (filled circles). For comparison, we also plot COSMOS clusters (open circles). We show that our red sequence finder is a robust tool for identifying a pure sample of X-ray clusters out of a sample of X-ray sources. The final catalog of XMM clusters includes X-ray luminosity, X-ray mass (from scaling relation between X-ray luminosity and weak-lensing mass), integrated optical luminosity, and also velocity dispersion for clusters with more than five spectroscopic members. We find the integrated z-band luminosity of red sequence cluster galaxies to correlate well with the total mass of the cluster, derived from the X-ray luminosity. This can therefore be used to improve the identification of sources in X-ray missions of insufficient spatial resolution.

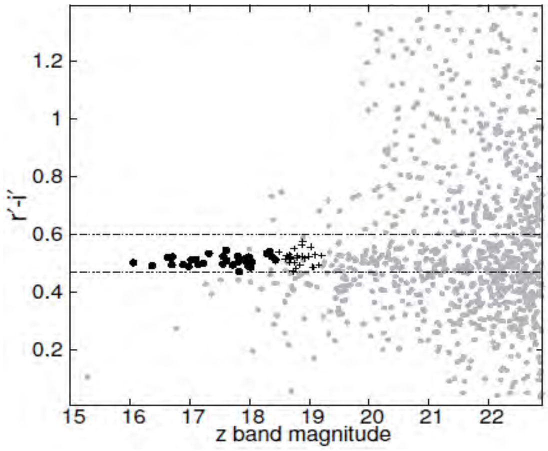

The red sequence galaxies (black dots) in color-magnitude diagram for a cluster at redshift 0.2.

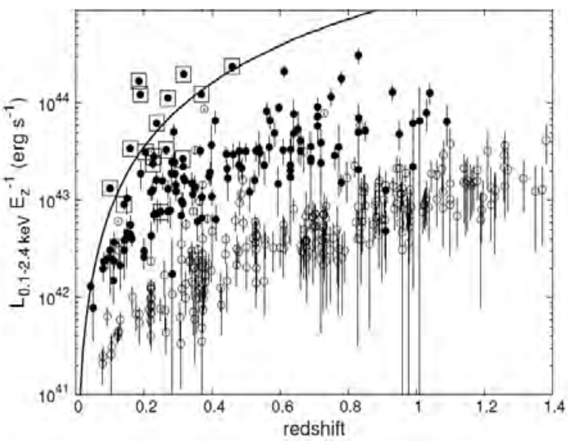

The X-ray luminosity versus redshift for XMM-CFHTLS sample (black dots) and X-ray selected groups in COSMOS (open circles).

References:
Mirkazemi et al. 2013 (in prep.)
Finoguenov et al. 2009, ApJ, 704, 564

M. Mirkazemi, A. Finoguenov, et al.

X-ray Groups of Galaxies in the AEGIS Deep and Wide Fields

We present the results of a search for extended X-ray sources and their corresponding galaxy groups from 800 ks Chandra coverage of the All-wavelength Extended Groth Strip International Survey (AEGIS).

This yields one of the largest X-ray-selected galaxy group catalogs from a blind survey to date. The red-sequence technique and spectroscopic redshifts allow us to identify 100% of reliable sources, leading to a catalog of 52 galaxy groups. These groups span the redshift range z∼0.066–1.544 and virial mass range $M_{200} \sim 1.34\times10^{13}$–$1.33\times10^{14}\ M_{\odot}$ (left figure).

For the 49 extended sources that lie within DEEP2 and DEEP3 Galaxy Redshift Survey coverage, we identify spectroscopic counterparts and determine velocity dispersions from the gapper estimator method. We select member galaxies by applying different cuts along the line of sight or in projected spatial coordinates. A constant cut along the line of sight can cause a large scatter in scaling relations in low-mass or high-mass systems depending on the size of the cut. A velocity dispersion-based virial radius (red circles in right figure) can cause a larger overestimation of velocity dispersion in comparison to an X-ray-based virial radius (black circles in right figure) for low-mass systems. There is no significant difference between these two radial cuts for more massive systems. Independent of radial cut, an overestimation of velocity dispersion can be created in the case of the existence of significant substructure and compactness in X-ray emission, which mostly occur in low-mass systems.

We also compared X-ray galaxy groups and optical galaxy groups detected using the Voronoi–Delaunay method for DEEP2 data in this field. The X-ray groups are preferentially found at z>0.6, compared to the optical groups, but, in general, the two distributions are similar. The distribution of the velocity dispersion of these two samples are also similar. During the optical group identification using spectroscopic data, we discovered a high-z group candidate at z = 1.54. Our detection of a high-z group illustrates that megasecond Chandra exposures are required for detecting such objects in the volume of deep fields. Smaller exposures only yield a marginal detection.

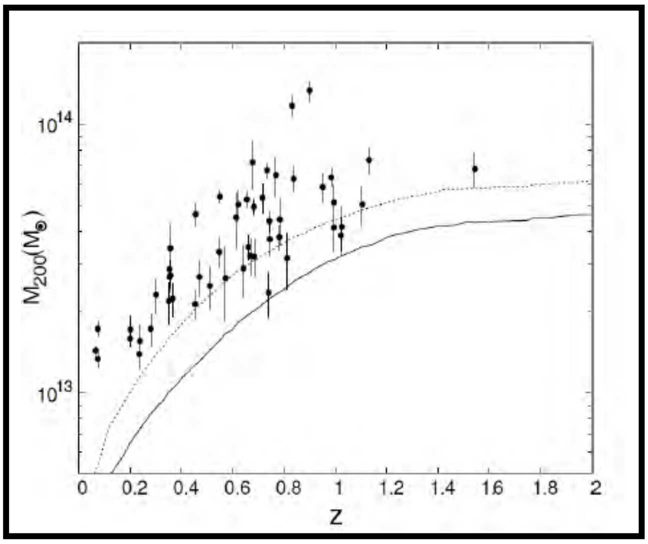

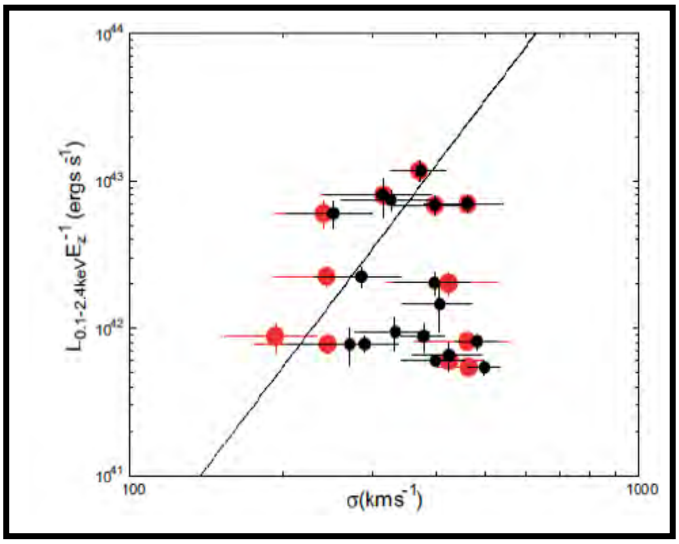

References:
• Erfanianfar et al. 2013, ApJ, 765, 117E
• Finoguenov et al. 2009, ApJ, 704, 564F

G. Erfanianfar, A. Finoguenov, K. Nandra, et al.

The evolution of the star formation activity in different environments up to z~1.6

In the local Universe, the level of star formation (SF) activity in galaxy systems is known to be suppressed relative to the field. In fact, it has been found that the star formation rate (SFR)-density relation is an anti-correlation at z≤0.1 (Gomez 2003) . In order to follow the evolution of the SF activity in systems through the different phases of the structure formation, we build a catalog of X-ray selected groups at 0≤z≤1.6 in the ECDFS and the GOODS regions (see also Popesso et al. 2012), with very deep Herschel PACS and Spitzer MIPS observations. We use the infrared data to get an accurate estimate of the SFR. In addition, we fit SEDs to derive galaxy stellar mass and SFR for the infrared-undetected galaxies.

SFR-density relation: Dynamical approach

We distinguish among X-ray group members, filament-like environments (at the same density of groups but not detected in X-ray), and field to build the <SFR>-environment relation. The strong difference in the evolution of group galaxies with respect to filament-like galaxies at similar density reveals that processes related to the presence of a massive dark matter halo must be dominant in the suppression of the SF activity in group galaxies below z~1.

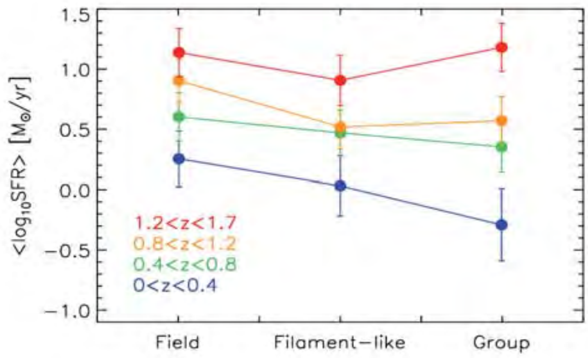

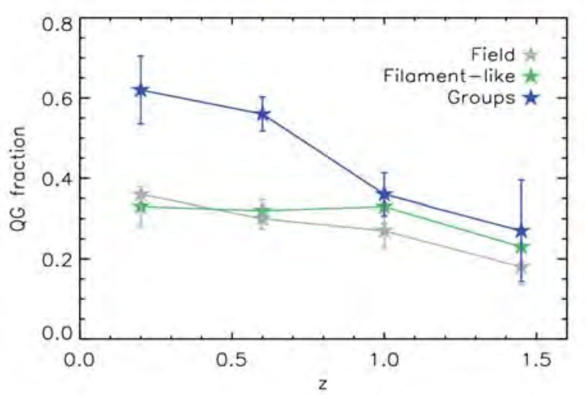

We study the location of group, filament-like and field galaxies in the SFR-stellar mass plane. The group galaxies show a much higher fraction of quiescent galaxies (QG) which evolve faster with respect to the other environments. Galaxies at similar density, but not belonging to the X-ray detected structures, exhibit a similar fraction of quiescent galaxies as in the field at any redshift. At z≥1 the QG fraction is similar for groups, filament-like environments and field.

CONCLUSIONS

X-ray groups seem to be the most efficient environment for quenching the SF. This suggests that a fundamental difference exists between bound (groups) and unbound objects (galaxy overdensity such as filaments), or between dark matter halos of different masses. Thus, processes like ram pressure stripping (Gunn & Gott 1972) or strangulation (Larson et al. 1980), are more efficient in quenching the SF below z~1 with respect to pure density-related quenching processes (e.g. galaxy-galaxy interaction).

References:

- Gomez, P. et al. 2003, ApJ, 584, 210
- Gunn & Gott, 1972, 172, 1
- Larson, Tinsley & Caldwell 1980, Apj, 237, 692
- Popesso et al. 2012 A&A 537, A58

F. Ziparo, P. Popesso, A. Finoguenov, S. Wuyts, D. Wilman, M. Salvato, K. Nandra, D. Lutz and PEP and GOODS Herschel team

Structure in the Coma cluster core

We made a 500 ks set of deep Chandra observations of the Coma galaxy cluster core. We found a set of four linear high-density low-entropy arm-like structures, extending over 100 kpc in the core of the cluster. The likely origin of the features is that they are material stripped from merging subclusters. When viewed on larger scales, two arms appear connected to the NGC 4911 subgroup at 650 kpc radius, implying ages of 300 Myr. Our data have revealed that merger structures can remain intact in the core of a rich galaxy cluster for these timescales.

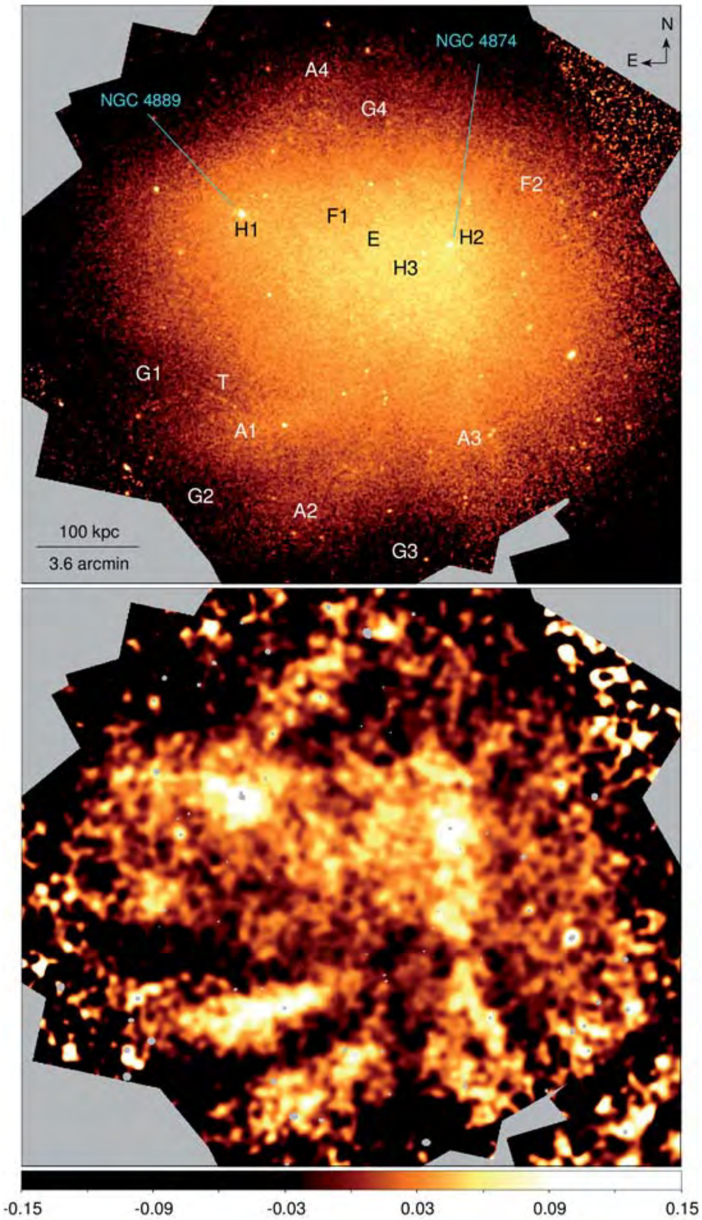

Figure 1: (Top panel) Chandra X-ray image of the cluster. The arms are labelled A1-A4. (Bottom panel) Unsharp-masked cluster image of same region. The scale is fractional surface brightness enhancement.

The intracluster medium (ICM) in galaxy clusters should have a contribution from turbulent and random motions with an energy density which can be up to several tens of per cent of the thermal energy density. Unsharp masking analysis of the X-ray image (Fig. 1) has revealed a number of linear features in the core of the cluster. These features are 10% increases in surface brightness. We estimate that they are 40% density enhancements, accounting for projection. Spectral analysis of the arms shows that they are cooler than their surroundings. Accounting for projection, we examined two arms (A1 and A3), finding that they are either mildly over-pressured by ~20% or are in pressure equilibrium with their surroundings.

The arms A1 and A2 appear connected with the merger of the NGC 4911 subgroup. This is seen most easily in an XMM image on larger scales, where the average at each radius is subtracted (Fig. 2).

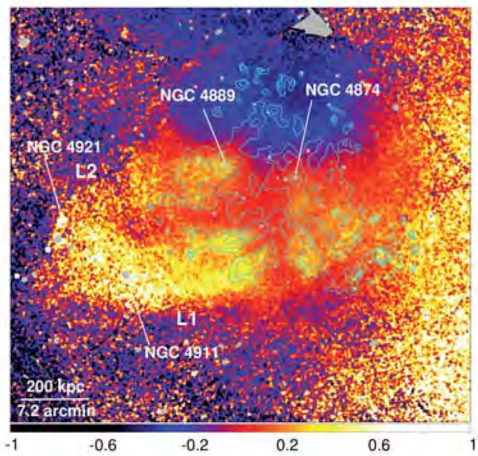

Figure 2: XMM image showing fractional difference from radial average.

J. S. Sanders et al.

Testing strong gravity: AGN soft X-ray lags

The primary X-ray spectral component of active galactic nuclei (AGN) is a power law describing the Compton up-scattering of the thermal disc emission in a centrally concentrated corona of hot electrons. Extrapolation of this power law to soft X-ray energies leaves an excess of emission, the so-called soft excess, whose origin is still widely debated [3, 4, 5]. We carried out a systematic study of X-ray lags between the soft excess-dominated (~0.3-1 keV) and the power law-dominated (~1-5 keV) energy bands, in a large sample (32 sources) of radio quiet AGN observed with XMM-Newton [1]. We found significant evidence that the soft excess variations lag behind the power law variations in all the sources where this measurement was possible (15 out of 32). These soft lags are characterized by very short time scales, of the order of the light crossing time at few gravitational radii, rg, implying that the soft excess is likely produced very close to the power law emitting region. We demonstrated the existence of a mass-scaling law for soft X-ray time lags which well explains the apparent difference in lag profiles among sources with different black hole (BH) mass (Figs.1-2, [2]). This suggests that the physics and geometry of the system are similar in all the radio quiet AGN.

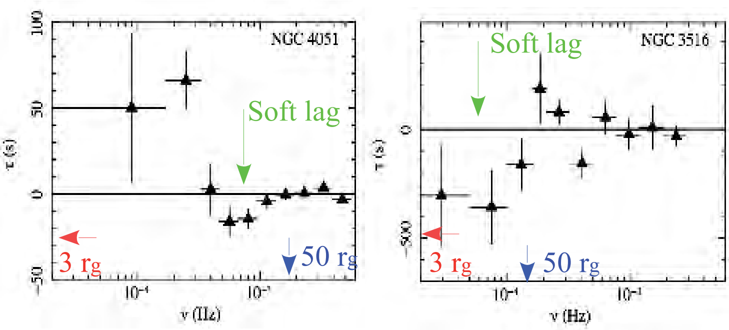

Fig. 1: Examples of X-ray lag profiles in two sources with different values of BH mass. NGC 4051 (BH mass ~10^6 M⊙) has the typical lag profile of a low-mass source, showing both a low-frequency, hard/positive lag and a high-frequency, soft/negative lag. NGC 3516 (BH mass ~10^7 M⊙) shows only a soft/negative lag, but shifted to lower frequencies and larger amplitudes. The shift in lag frequency and amplitude is of the same order of the ratio in BH mass (about a factor 10).

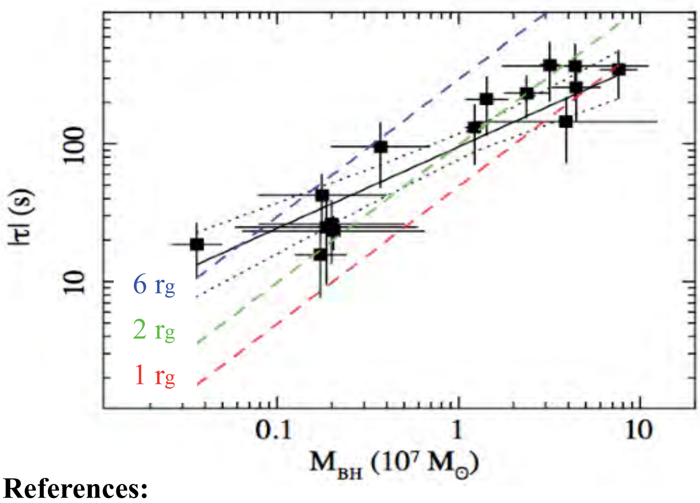

Fig. 2: The relation between lag amplitude and BH mass for the 15 soft X-ray lags detected in our sample. The coloured dashed lines represent the light crossing time at 1, 2 and 6 rg as a function of BH mass. All the data points fall within this range, meaning that the lags map very short distances. A similar relation is obtained for the lag frequency.

References:
·[1] De Marco B., Ponti G., et al., arXiv:1201.0196
·[2] De Marco, B., Ponti G., et al., 2011, MNRAS, 417, 98
·[3] Fabian A. C., et al., 2009, Nat, 459, 540
·[4] Miller L., et al., 2009, MNRAS, 399, 69
·[5] Petrucci, P.-O., et al., 2013, A&A, 549, 73

B. De Marco, G. Ponti, et al.

Tests of General Relativity with X-ray/NIR spectroscopy in the GC and in bright AGN

Gravitation is very well described by Einstein´s General Relativity (GR). However, several theoretical predictions like the existence of curvature singularities and event horizons are under debate. This motivated to modify the standard theory of gravity. Here, we contrast predictions made by GR with the pseudo-complex field theory (pc-GR) proposed recently.

A new formulation of a field theory of gravity, based on a pseudo-complex description has been first published by [1]. A pseudo-complex number X can be written as: $X=X_R+I\times X_I$ with $I^2=+1$. From this a new Einstein equation follows and can be formulated as $R^{mn} - ½g^{mn}R = 8p(G/c^2)\, T^{mn}s_{-}$ with $s_{-} = ½\,(1-I)$ where the energy-stress tensor represents a field with repulsive properties. s_{-} is called zero divisor basis. From this a new metric tensor can be deduced where its 00 component satisfies: $g_{00} = \dfrac{r^2 - 2mr + a^2\cos^2\theta + \frac{B}{2r}}{r^2 + a^2\cos^2\theta}$ with the spin a and an integration constant B. An interesting new feature in pseudo–complex field theory is that it removes the coordinate singularity at the Schwarzschild radius $r = 2\,R_G \equiv R_S$, which is a prediction of GR. Interestingly, there is therefore also no event horizon. This means that a classical black hole is absolutely dark at the horizon whereas a pseudo–complex black hole is rather gray, i.e. light originating at this region might escape to an external observer.

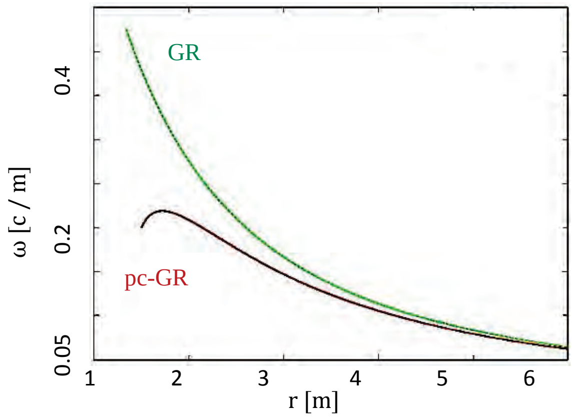

Fig. 1. Keplerian frequencies as a function of the distance to a black hole with a mass of $M = 4.3\times10^6$ solar masses and a black hole spin of $a = 0.995$ for GR (green) and pc-GR (red).In pc-GR the Keplerian frequencies are lower compared to GR.

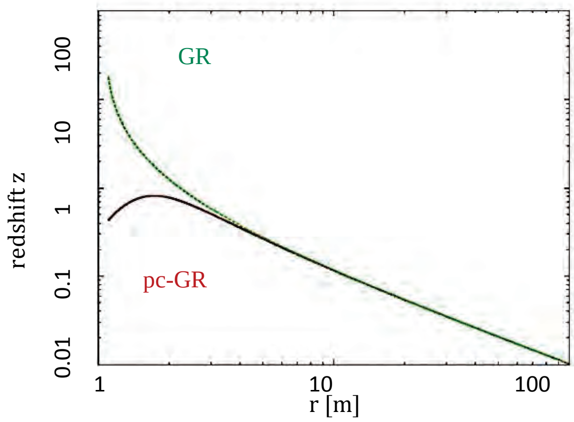

Fig. 2. Gravitational redshift as a function of r for the pc-GR theory (green curve) and the standard theory (red curve) for a black hole spin of a = 0.998. Close to the BH the gravitational redshift is decreased in pc-GR with respect to standard GR.

We contrast predictions made by GR with pc-GR [2]. We show that the orbital frequency of test particles at a given radius in pc-GR is in general lower compared to standard GR (Fig. 1). Concerning the gravitational redshift we find that it is lower in pc-GR than in GR (Fig.2). We have performed simulations for the Athena+ X-ray mission and have worked out tests including relativistic Fe K line emission and QPO frequencies in the GC, Galactic Binaries and in bright AGN. We find that GR and pc-GR can be disentangled when the emission originates closer than about $3R_G$. In Galactic Binaries we find already indications, that the discrepancy between the Fe K emission- and the QPO emission region is the same when applying pc-GR.

References:

[1] Hess, P.O. , Greiner, W., Pseudo-Complex General Relativity, Int. J. Mod. Phys. E 18, 51-77, 2009

[2] Th. Boller , A. Müller, Astronomical tests of GR and the pseudo–complex field theory, Springer 2013

Th. Boller

The SED of the Blazar 3C 279 during the Fermi/LAT Era

Time-resolved broadband multiwavelength campaigns on the blazar 3C 279 were carried out during the first two years (2008 – 2010) of the Fermi mission. The data are compiled to multifrequency light curves and broadband SEDs for different γ-ray flux levels. The main observational and modeling results are summarized.

The Fermi Gamma-ray Space Telescope scans the sky continuously, thereby measuring the γ-flux of strong sources on a daily basis, like for the blazar 3C 279. To understand its emission physics, we performed multi-band campaigns, which yielded the best multifrequency coverage ever on the blazar [1]. The upper figure shows the light curves between August 2008 and August 2010 and the lower figure the SEDs for selected interesting time periods (A – H). In the following we summarize the main new conclusions, based on these compilations:

1) Two significant γ-flares were observed, which did not show a significant correlation between γ-flux and photon index. The two-year average γ-spectrum shows a broken power-law shape which is not varying with source flux.

2) The optical signal appears to be delayed by about 10 days with respect to the γ-rays.

3) A pair of significant X-ray flares seems without contemporaneous counterparts in γ- and optical bands.

4) A coincidence of a γ-ray flare with a dramatic change of the optical polarization angle (red circle in upper figure, [2]) provides evidence for co-spatiality of the γ-ray and optical emission regions, indicating a highly ordered jet magnetic field.

5) Within a leptonic emission scenario, we explain the evolution of the SED from D to E by a shift of the emission region and a change of the viewing angle.

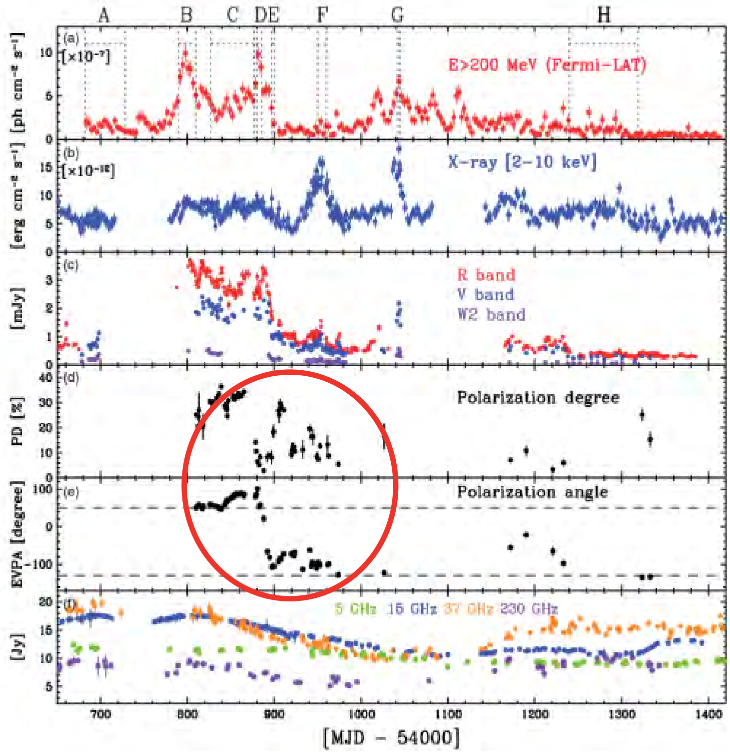

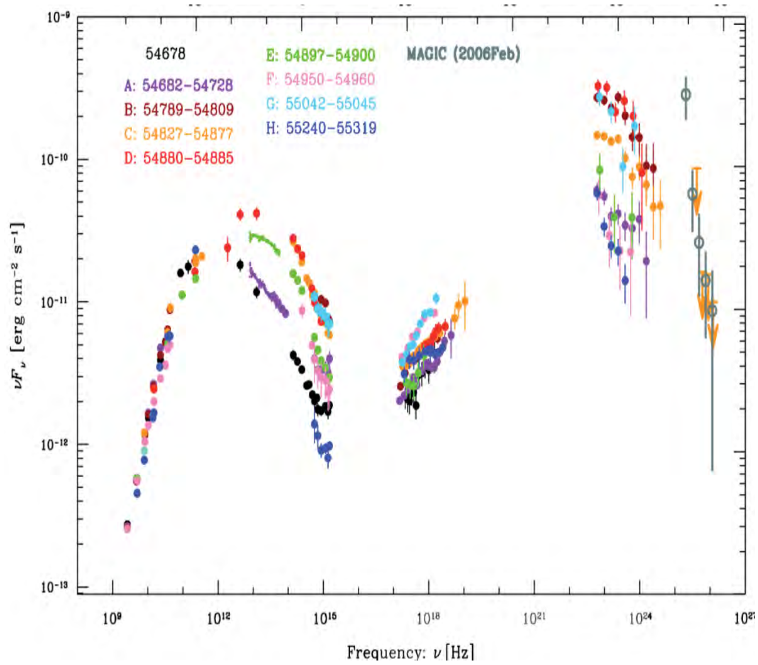

References: • [1] Hayashida et al., ApJ 754:114 (2012) • [2] Abdo et al., Nature 463, 919 (2010)

W. Collmar for the Fermi/LAT AGN Collaboration

Testing strong gravity using the bright Seyfert 1: IC4329A

MAX-PLANCK-GESELLSCHAFT

MPE

The aim of the project is to extend the work of Bhayani & Nandra (2011). The authors justify the apparent absence of a broad FeKα line (Nandra et al. 2007) in the XMM-Newton spectra of AGN with the presence of strong relativistic blurring: the broad iron emission line, being highly blurred, is difficult to distinguish from the continuum. Our work will be to test the correlation between the emission of the FeKα line and the Compton reflection component, taking into account strong relativistic effects.

We analyze the Suzaku spectra (XIS and PIN) of the Seyfert 1, IC4329A, in order to reach high energies (Compton hump). We fit them with the 'pexmon' model (Nandra et al., 2007), which links the emission of the FeKα line and the Compton reflection component, allowing us to test whether they are emitted by the same material around the black hole. First, we adopt a model (NarrowPexmon, NP, in Table 1) which contains one narrow component of the FeKα line, a neutral absorber at the redshift of the source (zwabs) and a power law (cutoffpl) with high energies cut-off: zwabs*(cutoffpl+pexmon). In Table 1, we reported the χ^2 and the degree of freedom. In Figure1a, we show the data/model (NP) ratio between 3-10 keV. Residuals are present at 6.4 keV, extended to lower energies (blurred emission line), and at higher energies (Figure1b). This can be explained with a strong reflection component correlated to the broad emission line.

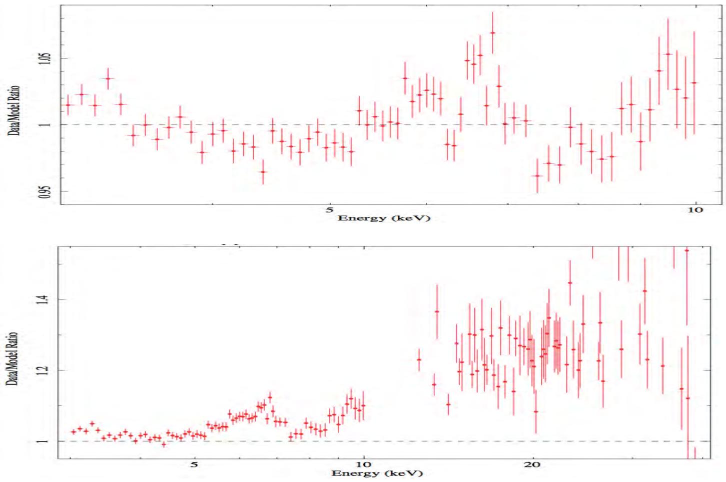

Figure 1: Ratio of data/model for the NP model between 3-10 keV (a) and 3-40 keV (b).

Table1: The best fitting χ^2/d.o.f. of model NP and the $\Delta\chi^2$/d.o.f for the (NP+BP) model.

Observation	NP	NP+BP
702113010	1547.43/1494	14.35/1
702113020	1633.81/1603	14.84/1
702113030	1607.39/1563	14.32/1
702113040	1556.51/1492	20.53/1
702113050	1341.66/1345	26.15/1

Then, we include a blurred pexmon ('kdblur2*pexmon' NP+BP model) in order to fit also the broad component of the line. From Table1, a significant χ^2 improvement (99.998%) can be seen. In Figure2, we can note that the model well fits the data, without significant residuals (except for the ~6.96 keV residual, due to the non-fitted ionized iron emission line).

Conclusions: We demonstrate the presence of the broad component of the FeKα line, blurred by strong relativistic effects and correlated to a strong reflection component.

Future analysis: We aim at carrying out a systematic analysis of the broad FeKα line and its correlation with the Compton hump, applying the same method on a large sample of sources.

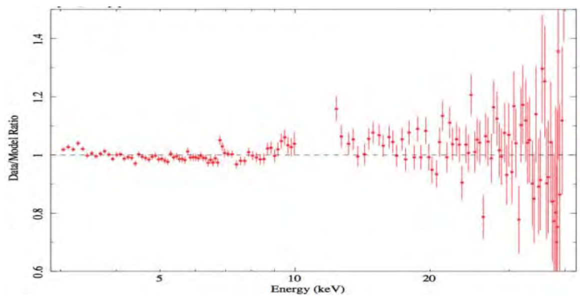

Figure 2: Ratio of data/model for the NP+BP model between 3-40 keV.

References:
- Bhayani S., Nandra K., 2011, MNRAS, 416, 629
- Nandra K., O'Neill P.M., Geroge I.M., Reeves J.N., 2007, MNRAS, 382, 194.

G. Mantovani, K. Nandra, G. Ponti

Traces of past activity in the Galactic Center

The Milky Way center hosts a supermassive Black Hole (BH) with a mass of ~4×10^6 M$_{sun}$, Sgr A*. Its electromagnetic counterpart, currently appears as an extremely weak source with a luminosity L~10^{-9} L$_{edd}$, the lowest known Eddington ratio BH. However, it was not always so; traces of "glorious" active periods can be found in the surrounding medium. The echo(es) (e.g. X-ray reflection) of past flare(s) still illuminate some Molecular Clouds (MC) of the Central Molecular Zone (CMZ). In particular, with XMM-Newton, we discovered an apparent superluminal motion of a light front illuminating a molecular nebula (Bridge), thus ruling out models based on low energy cosmic rays or sources located inside the cloud and suggesting illumination from an external source (e.g. Sgr A*). X-ray emission from MC can be used to reveal the past activity of Sgr A*.

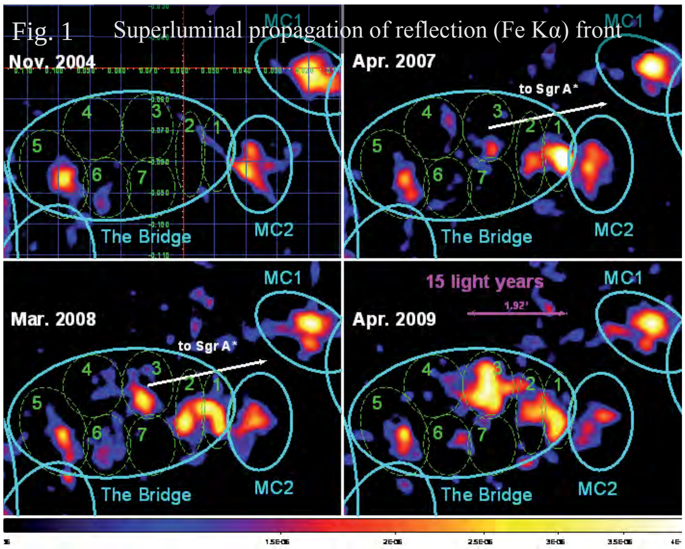

Fig. 1 Superluminal propagation of reflection (Fe Kα) front

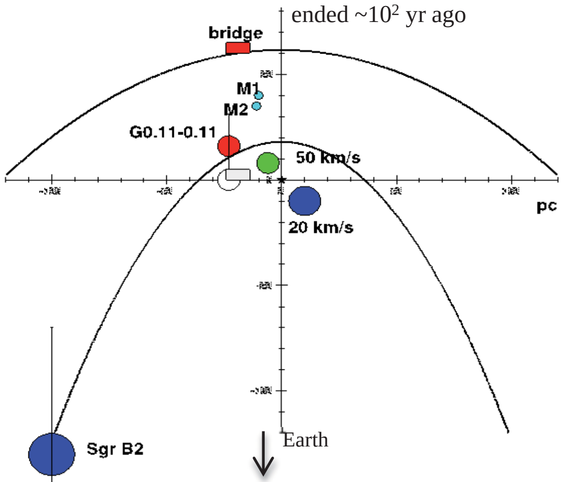

Fig. 2 Possible distribution of MC in CMZ. ➔ Sgr A* outburst might have started few centuries ago and ended ~10^2 yr ago

Extended, hard X-ray and Fe Kα emission elongated along the Galactic plane, corresponding spatially with massive MC, was first detected in the 1990s. This emission could be induced by: i) cosmic ray protons or electrons interacting with the MC; ii) irradiation by a source inside the MC; iii) illumination by a distant powerful transient source (e.g. Sgr A*).

The analysis of all XMM-Newton observations of the CMZ allowed us to discover a super-luminal Fe Kα echo (Fig. 1) that indicates external illumination by a powerful transient source in the direction of Sgr A* [1]. This, in addition to the emission from the other MC, suggests a bright (L~10^{39} erg s^{-1}) Sgr A* outburst ending ~10^2 yr ago (Fig. 2) and allow us to constrain Sgr A*'s activity during the past ~10^3 yr, although the uncertainties on the MC distribution and column densities do not allow a clear determination yet [3,4,5, see 2 for a review]. However, the continuous monitoring of the CMZ will soon reveal correlated variations between the different MC allowing us to perform a tomography of the CMZ distribution and to detail Sgr A*'s history. We are leading the publication of an XMM large program to scan the CMZ and of all triggered observations of any X-ray satellite, would a new Sgr A* outburst occur.

References **(MPE lead):**

• [1] Ponti et al. 2010, ApJ, 714, 732;
• [2] Ponti et al. 2013, Chapter of book: "Cosmic ray induced phenomenology in star forming environments
• [3] Capelli et al. 2012, A&A, 545, 35;
• [4] Capelli et al. 2011, A&A, 530, 38;
• [5] Capelli et al. 2011, A&A, 525, 2.

G. Ponti, P. Predehl, R. Capelli, K. Nandra, F. Haberl, R. Sturm et al.

X-Ray Source Variability Study of the M 31 Central Field

The central field of the Andromeda galaxy (M 31) has been monitored, using the Chandra HRC-I detector during the years from 2006 to 2012 with the main aim to detect X-rays from optical novae. We performed a systematic analysis of the 41 monitoring observations, along with 23 M 31 central field HRC-I observations available from the Chandra data archive starting in December 1999. We created a catalogue of sources, detected in the 64 individual observations with up to 46 ks exposure and in the merged observation, which adds up to a total exposure of about 1 Ms. To study the variability, we derived long-term light curves for each source over the 13 years of observations. In the merged images we also searched for extended X-ray sources. The catalogue, contains 318 X-ray sources with detailed long-term variability information, 28 of which are published for the first time. From the light curves we classified 115 sources as X-ray binary (XRB) candidates due to high X-ray variability or outbursts in addition to 14 globular cluster XRB candidates showing no significant variability. The analysis may suggest, that outburst sources are less frequent in globular clusters than in the field of M 31. We detected 7 supernova remnants and in addition resolved the first X-rays from a known radio supernova remnant. Besides 33 previously known optical nova/X-ray source correlations, we discovered one super-soft X-ray outburst and 12 new novae.

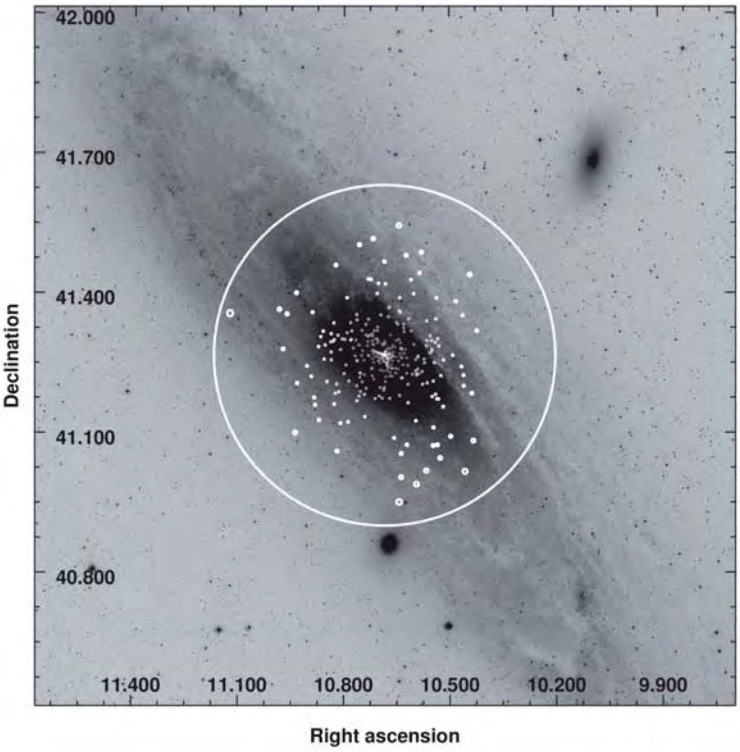

*The figure **above** shows an optical image of M 31 and the X-ray sources as small white circles. The large white circle marks the approximate field of view of the HRC-I observations. The plots on the **right** show representative X-ray light curves (0.2-10 keV). From **top** to **bottom** the plots show No. 104, which is the brightest persistent XRB in our catalogue, No. 54 which is discussed as an XRB hosting a black hole, No. 79 which shows the super-soft X-ray state of a classical nova and No. 149, which shows an ultra-luminous X-ray outburst in M 31.*

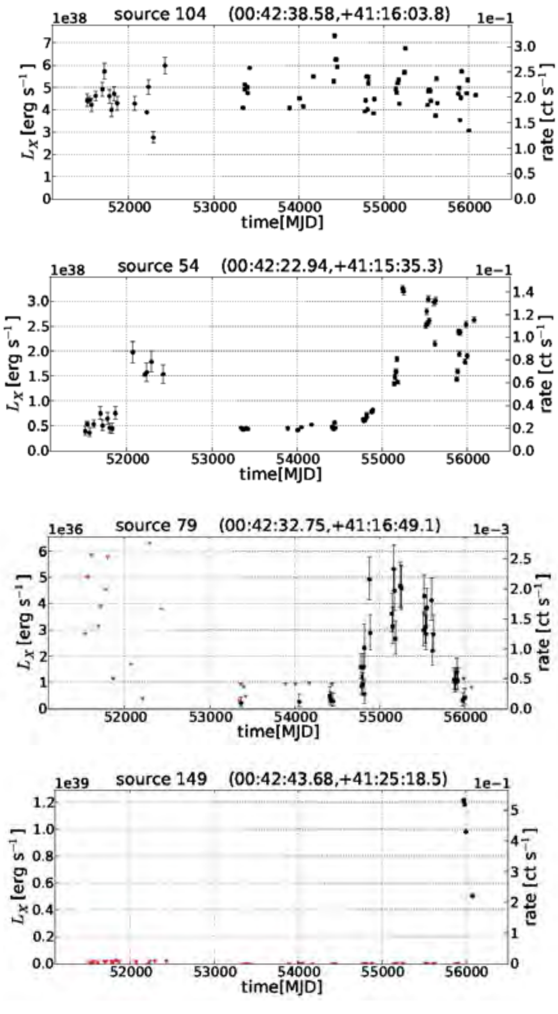

References:
· Hofmann et al. 2013, submitted to A&A

F. Hofmann, W. Pietsch, M. Henze, F. Haberl, R. Sturm

Globular Cluster Novae in X-ray observations of M 31

X-ray monitoring observations of our neighbour galaxy M 31 with XMM-*Newton*, *Chandra* and *Swift* have led to the discovery of two confirmed and one suspected nova in M 31 Globular Clusters (GC). We estimate an enhancement of GC novae with respect to the rest of the galaxy.

The first known nova in an M 31 GC was discovered optically in 2007 in the GC Bol 111 and soon found as a supersoft X-ray source (SSS) in X-ray monitoring observations. The same monitoring revealed a second transient SSS in the GC Bol 194, for which no optical counterpart could be found. In 2010, a third GC nova was discovered, first as a SSS before its optical outburst was confirmed in retrospect (see Figure). This nova in the GC Bol 126 was only the forth confirmed nova in any GC of any galaxy including the Milky Way. Novae in GCs are therefore extremely rare. X-ray monitoring turned out to be a good strategy to find these elusive objects.

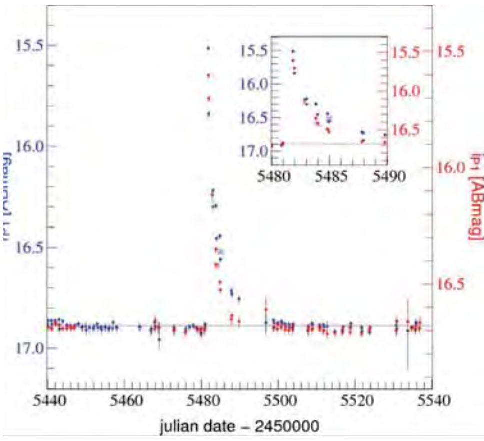

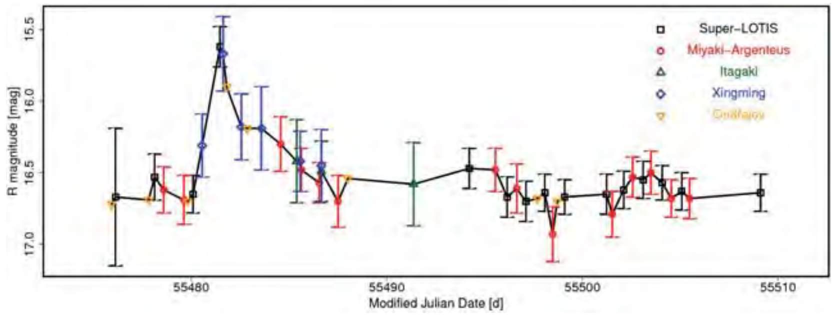

Figure: Top: optical light curves of Bol 126 from the PanSTARRS survey (left) and five different small telescopes (right) ;
Bottom: light curves of the nova in Bol 126 in optical and X-rays

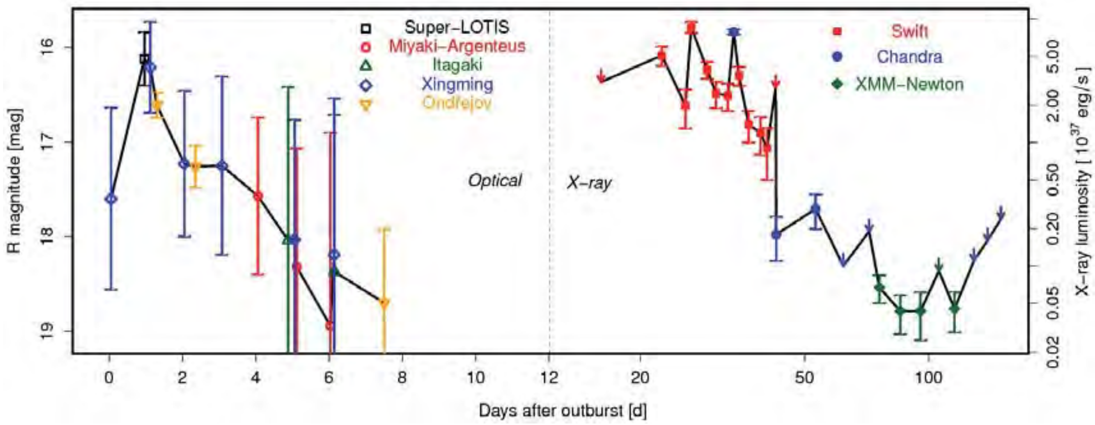

Surprisingly, both confirmed M 31 GC novae (and the suspected nova) were fast and hot SSSs. Such properties are normally associated with younger stellar populations. Assuming that the suspected object was a nova, we used our monitoring coverage in five observing seasons to estimate that the nova rate in M 31 GCs might be an order of magnitude higher than expected from stellar evolution or earlier optical surveys. This could suggests additional formation mechanisms for WD binary systems in GCs, similar to known effects on neutron star binaries.

References:
· Henze, M., Pietsch, W., Haberl, F. et al. 2009, A&A, 500, 769
· Henze, M., Pietsch, W., Haberl, F. et al. 2011, A&A, 533, A52
· Henze, M., Pietsch, W., Haberl, F. et al. 2013, A&A, 549, A120

M. Henze, W. Pietsch, F. Haberl for the M 31 monitoring collaboration

The XMM-Newton survey of the Large Magellanic Cloud: first results

The XMM-Newton large-program survey of the Large Magellanic Cloud (LMC) combined with archival observations, has homogeneously covered a ~10 square degree area of the LMC down to a limiting point source luminosity of ~2 x 10^{33} erg/s. The LMC offers a unique possibility to investigate the X-ray source population of a galaxy as a whole, including supernova remnants (SNRs), high mass X-ray binaries and super soft X-ray sources in an environment with about half the metallicity of the Milky Way. This project will create a unique data set that allows us to extend the study of SNRs and their properties to fainter fluxes, study the star formation history of LMC as written in the record of compact X-ray sources and to investigate the morphology of the hot interstellar medium in the LMC.

The observations of the 70 fields have recently been completed and we have started to analyse the data. First mosaic images reveal unprecedented details. From a preliminary point source catalogue, we selected the most interesting sources which are currently investigated in detail.

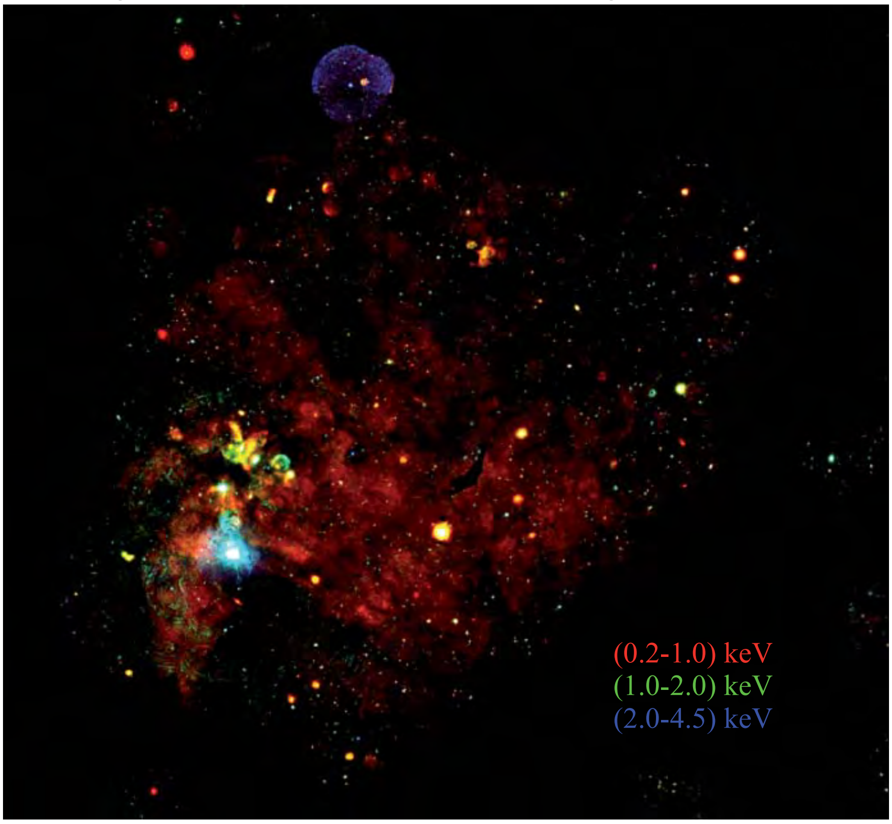

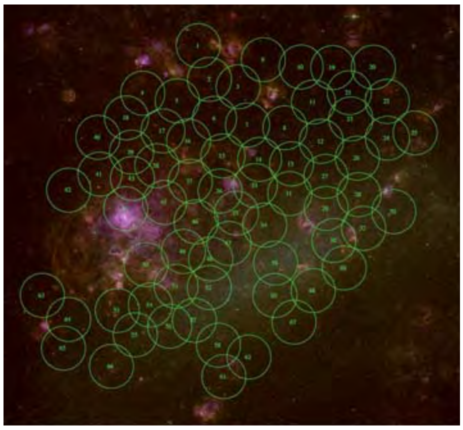

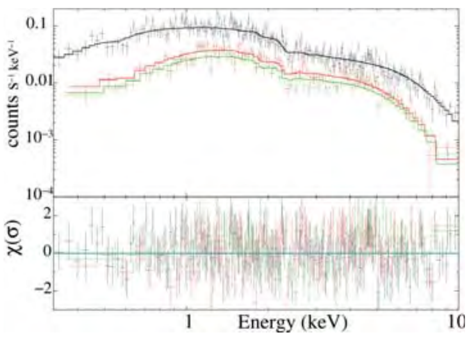

Left: Mosaic colour image of the LMC combining the EPIC data from the XMM-Newton LMC survey (70 observations: ~1750 ks in total) and archival observations. The RGB colour image is composed from three energy bands 0.2-1.0 keV, 1.0-2.0 keV and 2.0-4.5 keV. *Up right*: MCELS image (red: H-alpha, green: [S II], blue: [O III]) from the same region. The green circles indicate the fields (13 arcmin radius) covered by the survey. *Bottom right*: Example of source products of bright point sources: Spectrum of a newly discovered Be/X-ray binary [4] and the residuals for the best fit absorbed power-law, based on observations of the LMC survey.

References:

- [1] R. Sturm et al. A&A 542, A109 (2012)
- [2] P. Maggi et al. A&A 548 L3 (2012)
- [3] P. Maggi et al A&A .546A 109 (2012)
- [4] P. Maggi et al. arXiv:1302.4665 (2013)

G. Vasilopoulos, P. Maggi, F. Haberl, R. Sturm, W. Pietsch

Orbital inclination of Galactic BH binaries

The quest for the spin of Galactic black holes requires accurate knowledge of its mass. However, in most cases only the mass function is known. We have observed several black hole systems with GROND to measure the orbital inclination, and ultimately mass and spin.

Some of the most compelling evidence for the existence of black holes in nature comes from dynamical studies of so-called X-ray novae, Galactic X-ray binaries in which matter is transferred from a late-type companion onto an accreting black hole. With the uncertain orbital inclination, estimates of the black hole mass typically have a 50-100% error. Knowing the black hole mass is not only important in order to derive the spin of the black hole (e.g. via fitting of the X-ray spectrum), but also for models of stellar evolution of massive stars, as well as population synthesis models of binary systems.
The best way to derive the orbital inclination is through measuring the ellipsoidal variations over the orbital phase due to the tidal and rotational distortions of the Roche-lobe filling secondary as well as it‘s non-uniform surface brightness distribution. NIR light curves are particularly useful because they are less contaminated by the accretion stream and disk.

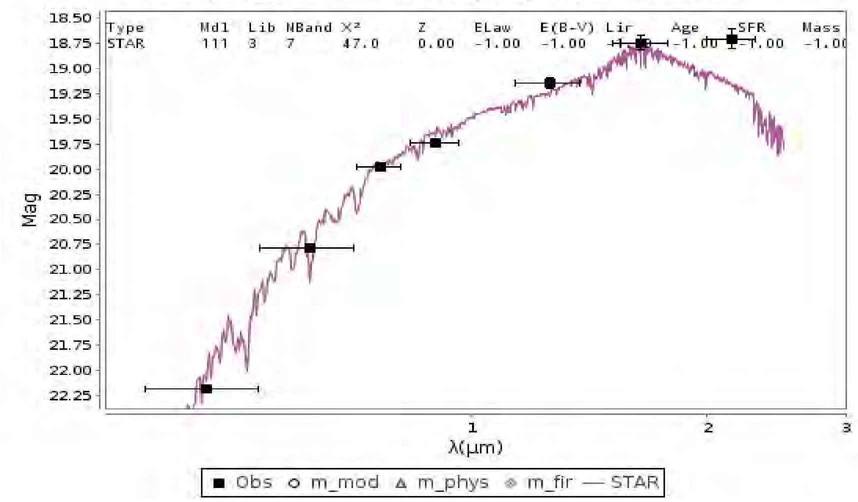

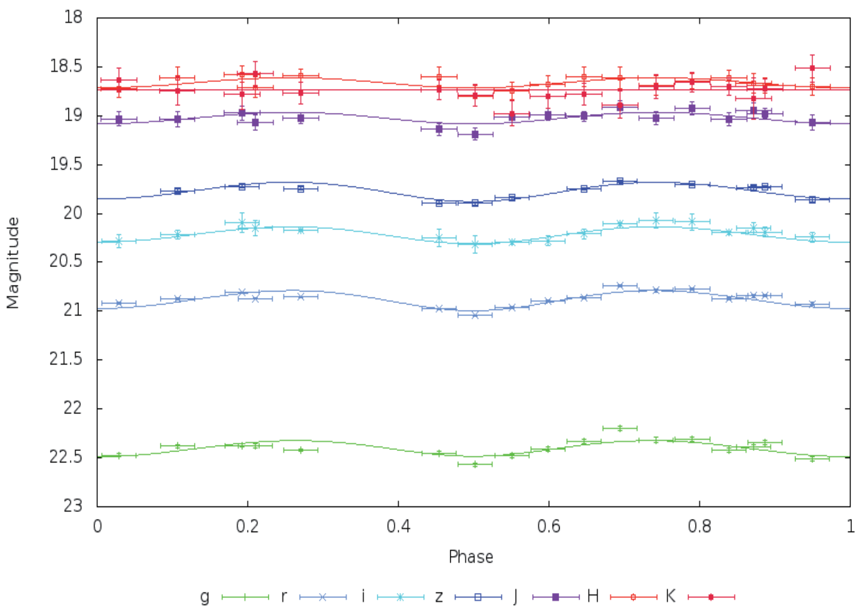

From the spectral energy distribution during the primary minimum we determine the spectral type of the companion star (and implicitely it‘s mass).

We model the orbital light curve with the program *XRbinary* (by E.L. Robinson). This allows us to model not only the ellipsoidal variation, but also a remnant accretion disk and/or the impact point of the accretion stream onto the disk.

The figure to the left shows the example of GRS 1124-68 with known mass function and rough inclination which we used as test case to develop the modelling strategy and fitting software. Different phases of the maxima of the orbital light in different filters hint at a non-negligible hot spot at the outer rim of the accretion disk. This leads to a lower inclination.

References:

- Knust F., 2013, Diploma Thesis, TU Munich (to be subm.)

F. Knust, A. Rau, J. Greiner

On the Physics of Magnetars

The classical magnetar model (ref.1) of Soft Gamma Repeaters (SGRs) and Anomalous X-ray pulsars assumes that these sources are isolated neutron stars with very high magnetic dipole fields (10^{14}-10^{15} G) which power the super-Eddington bursts and the quiescent X-ray emission by magnetic field decay and are responsible for the observed braking (dP/dt).

We discuss an alternative model which explains the quiescent X-ray emission by accretion from a fall-back disk and the braking by the interaction of the disk with the stellar magnetosphere. This model (e.g. ref. 2, 3) requires „normal“ dipole fields (10^{12}-10^{13} G) and explains the observed period clustering of these sources between 2 and 10 sec. The super-Eddington bursts are produced in superstrong multipole fields. There is some evidence for the IR/optical detection of the low-mass accretion disks (10^{-4}-10^{-5} solar masses, ref.4). Furthermore, this model avoids the problem of the low magnetic dipole field ($<7\times10^{12}$G) of the magnetar SGR 0418+5729 (ref.5).

In our model the accretion flow is stopped by a radiative shock close to the stellar surface (Fig. 1). Seed photons from the hot post-shock region and from the hot polar photosphere are upscattered to higher energies by bulk motion Comptonization (BMC) with the infalling electrons and thermal Comptonization (TC) (c.f. Fig. 1) and escape sideways in a fan beam. Supported by gravitational deflection part of this fan beam hits the polar cap leading to heating of the photosphere. Some part of the impinging photons are scattered off and form a polar beam together with the thermal photons from the polar cap.

This model results in a good fit to the total energy spectrum of AXP 4U 0142+61 (Fig.2, ref. 6) and its energy-dependent pulse profiles (Fig.3, ref.7).

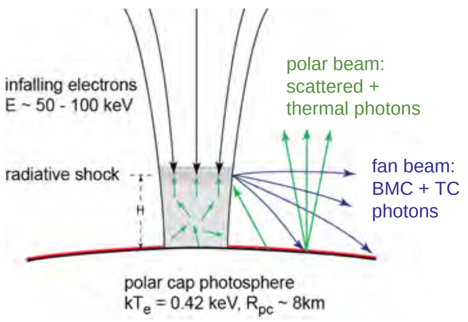

Fig. 1

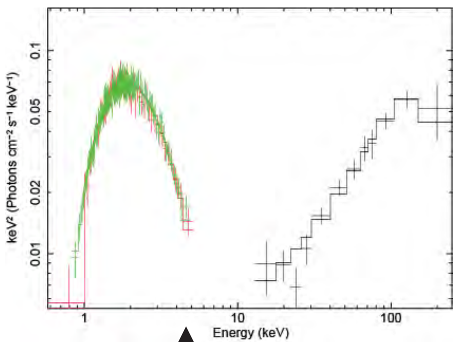

Fig. 2

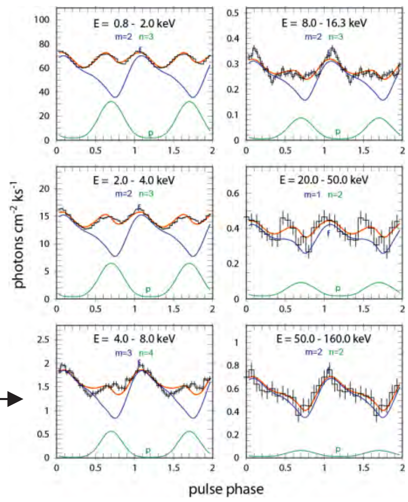

Fig. 3

Fig. 4

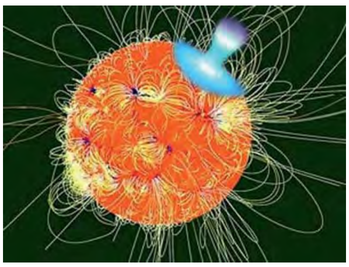

References:

1. Thompson & Duncan 1995, MNRAS 275, 255
2. Alpar, 2001, ApJ 554, 1245
3. Ertan & Alpar 2003, ApJ 593, 576
4. Ertan et al. 2007, ApJ 657, 441
5. Rea et al. 2010, Science 330, 944
6. Trümper et al. 2010, A&A 518, 46
7. Trümper et al. 2013, ApJ 764, 49

Conclusions (Fig. 4):

The magnetar has a dipole field of 10^{12-13} G channeling the accretion flow and multipole fields of 10^{14-15} G responsible for the bursts.

J.E. Trümper, K. Dennerl, et al.

SXP 1062, a Be/X-ray binary pulsar with long spin period in a supernova remnant

We discovered a supernova remnant (SNR) around the Be/X-ray binary pulsar SXP 1062 in radio and X-ray images. The Be/X-ray binary system is found near the centre of the SNR, which is located at the outer edge of the eastern wing of the Small Magellanic Cloud (SMC). SXP 1062 is the first Be/X-ray binary with robust SNR association, allowing to constrain its age to 10−25 kyrs. This is not long enough to spin down the neutron star (NS) from a few 10 ms to its current value of 1062 s. Possible scenarios to explain the long spin period involve high magnetic fields (a magnetar) or a longer spin period of the NS at birth.

The SMC is ideally suited to investigate the recent star formation history from X-ray source population studies. It harbours a large number of Be/X-ray binaries (Be stars with an accreting NS as companion), and the SNRs can be easily resolved with present-day imaging X-ray instruments. From *XMM-Newton* and radio observations we found an SNR around the Be/X-ray binary SXP 1062. The NS with a spin period of 1062 s (the second longest known in the SMC) showed a very high average spin-down rate of 0.26 s per day over the *XMM-Newton* observing period of 18 d. We infer a lower limit of 0.5 s for the birth spin period of the NS, assuming an upper limit of 25 kyrs for its age and the extreme case that it was spun down since its birth by the high accretion torque that we have measured during the *XMM-Newton* observations. For more realistic, smaller long-term average accretion torques our results suggest that the NS was born with a correspondingly longer spin period. This implies that NSs in Be/X-ray binaries with long spin periods can be much younger than currently anticipated.

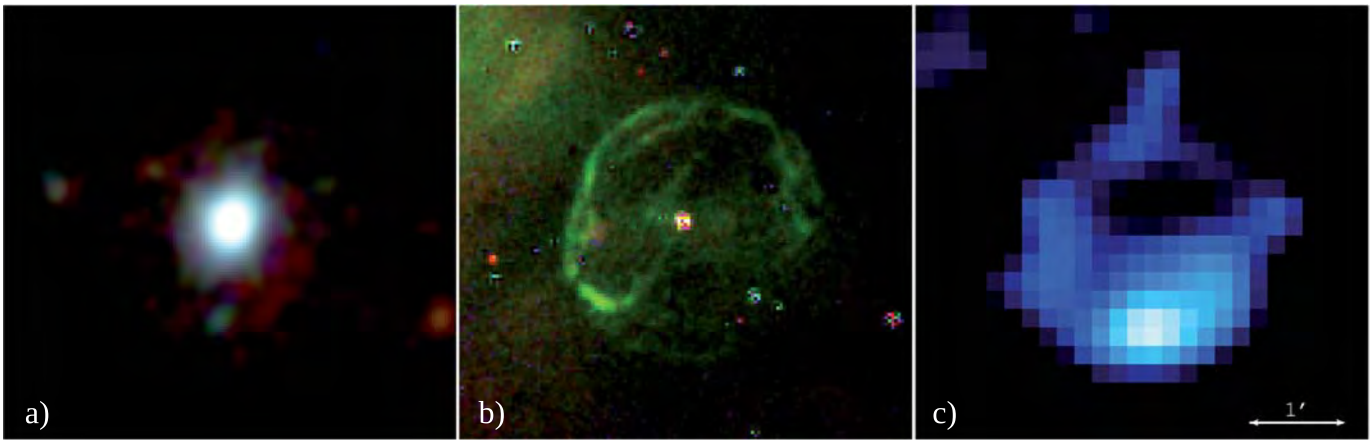

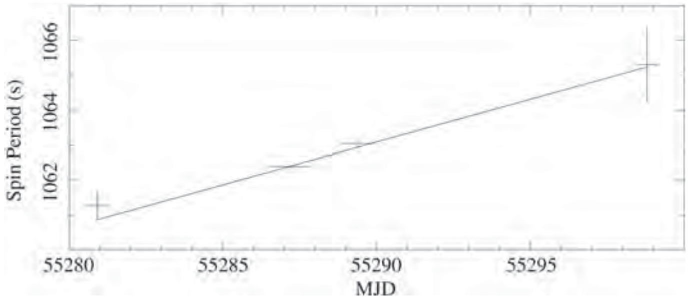

Images of the region around the Be/X-ray binary SXP 1062: a) EPIC colour image obtained from the XMM-Newton observations. Red, green, and blue denote X-ray intensities in the 0.2−1.0, 1.0−2.0, and 2.0−4.5 keV bands. b) Continuum-subtracted MCELS images. Red, green, and blue correspond to Hα, [O III] and [S II]. c) MOST 36 cm radio image. Right: Spin period evolution of SXP 1062 as obtained from the EPIC data in March/April 2010.

Reference:
Haberl F., et al., 2012, A&A 537, L1

F. Haberl, R. Sturm, W. Pietsch

Two transient ULX sources in M 31

From 2006 to 2012 we monitored the core region of the Andromeda galaxy M 31 with XMM-Newton/Chandra to search for supersoft X-ray emission from optical novae. In Dec 2009 and Jan 2012 we detected the first two ultra-luminous X-ray sources (ULX, $L_X > 10^{39}$ erg s^{-1}) in M 31 as transients with luminosities at maximum of 3.8 and 1.3 10^{39} erg s^{-1}, respectively. The X-ray spectra during outburst appeared similar to Galactic black hole X-ray binaries accreting close to or above the Eddington limit and indicated black hole masses of about 5-20 M_{sun}. ULX 2 was detected as an extremely bright radio source that showed variability on a timescale of tens of minutes, arguing that the source is highly compact and powered by accretion close to the Eddington limit onto a stellar mass black hole. In similar Galactic sources the X-ray and radio emission are coupled, with the radio emission originating in a relativistic jet thought to be launched from the innermost regions near the black hole, with the most powerful emission occuring when the rate of infalling matter approaches the Eddington limit.

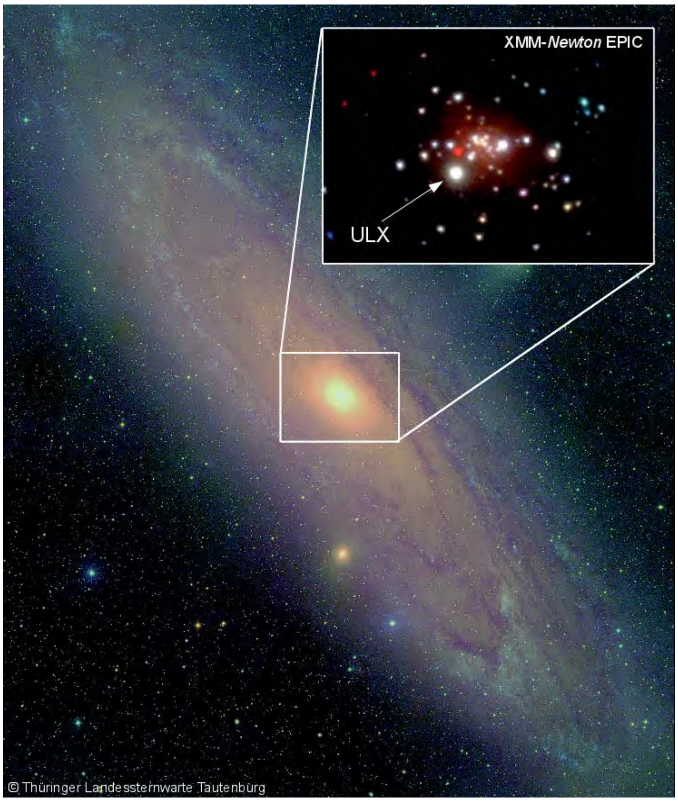

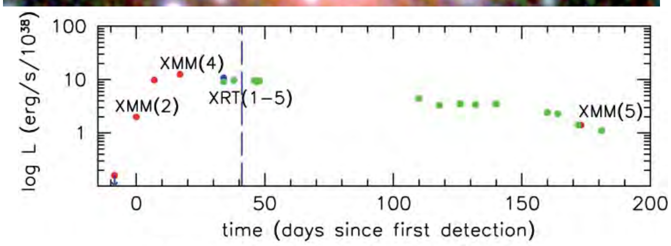

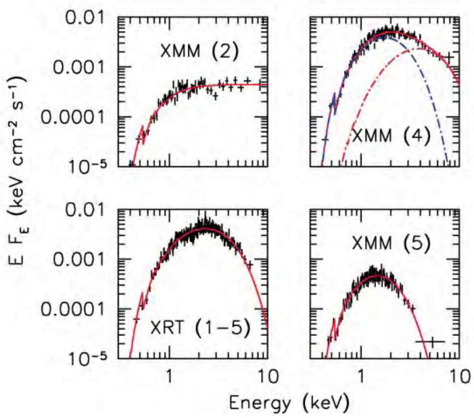

Figures: *XMM-Newton X-ray images of ULX 1 (above, with field of the X-ray image marked on an optical image of M 31) and ULX 2 (right above, bright source north of M 31 center). For ULX 2 XMM-Newton and Swift X-ray light curve and changing spectrum are given (right below).*

References:
- Kaur A. et al. 2012, A&A 538, A49
- Middleton M.J. et al. 2013, Nature 493, 187

W. Pietsch, M. Henze, F. Haberl, V. Burwitz, M. Freyberg, J. Greiner, A. Rau

CHANDRA LETGS Observations of the White Dwarfs GD153, HZ43A, and Sirius B

White dwarf spectra are ideally suited for calibrating the low energy end of the effective area of instruments aboard X-ray observatories. The available model spectra, that are used to fit the X-ray data include detailed white dwarf atmosphere physics for given abundances, with the surface gravity, temperature, and radius as free parameters. Based on our cross calibration of the three white dwarfs GD153, HZ43A, and Sirius B an improved effective area calibration of the LETGS has been made available. Using this new calibration of the LETGS we have been able to refine the physical parameters of these three white dwarfs.

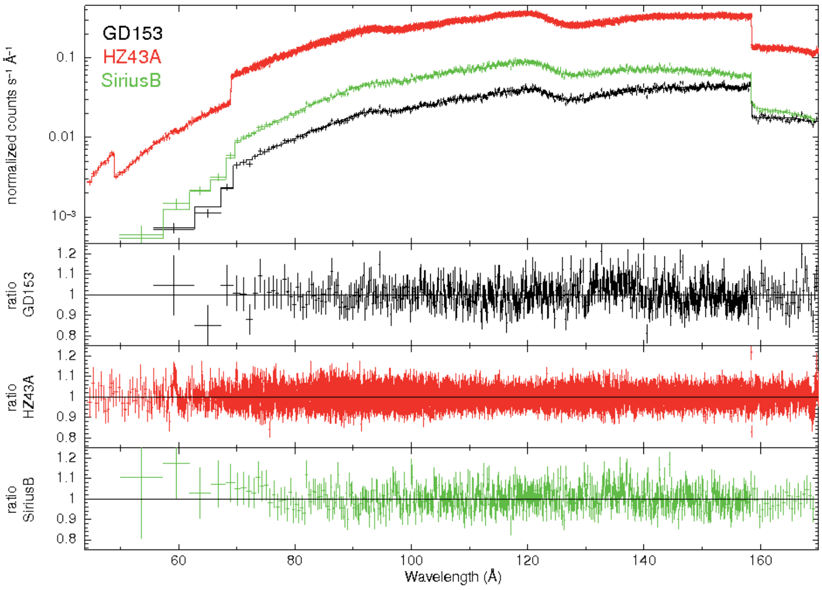

The Chandra LETGS white dwarf spectra of GD153, HZ 43 A, and Sirius B shown on the left have been fitted using non-LTE model atmospheres of pure hydrogen calculated with TMAP, the Tübingen NLTE model Atmosphere Package. The same interstellar absorption parameters as described in Beuermann et al. 2006 were used.
The updated calibration of the Chandra LETGS clearly shows the good agreement between the models and the data.

The effective temperature and the surface gravity parameters are in good agreement with those obtained for FUV and EUV observations.
This shows that we now have a consistent picture for these white dwarfs covering a large spectral range. This allows us to use these objects as standard candles for in flight calibration of new X-ray optics and detectors in the soft X-ray regime.

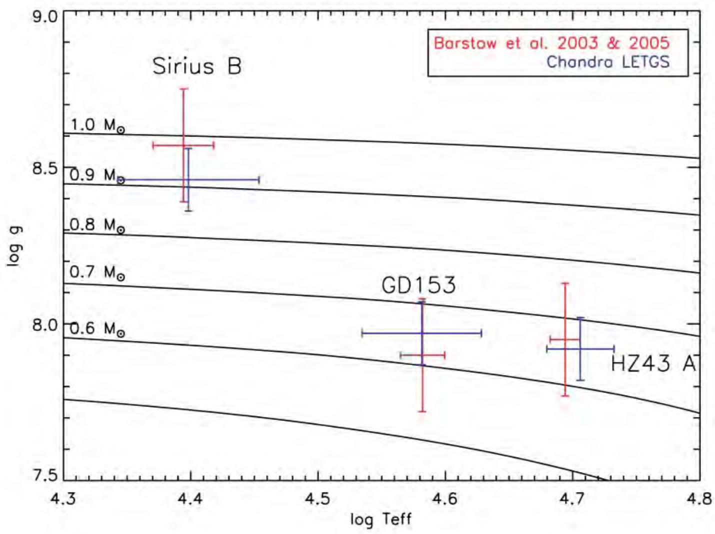

References:
• Barstow M. A., Good S. M., Burleigh M.R., et al. 2003, MNRAS, 344, 562
• Barstow M. A., Bond H. E., Holberg J. B., et al., 2005, MNRAS, 362, 1134
• Beuermann K., Burwitz V., Rauch T., 2006, A&A, 458, 54
• Menz B., 2011, Diploma Thesis Technical University Munich

B. Menz, V. Burwitz et al.

Autonomous Spacecraft Navigation with Pulsars

Pulsars can be used as natural beacons for navigation, similar to the use of GPS satellites for navigation on Earth. In contrast to standard navigation methods, which rely on radio measurements by tracking stations on Earth, pulsar-based navigation can operate autonomously and is, therefore, independent from ground-based control and maintenance. This is particularly interesting for space missions that require a higher degree of autonomy, e.g. exploration of the outer solar system or manned missions to Mars, but could also be beneficial as augmentation of existing space technologies, such as GPS and Galileo satellite systems. Our research project aims at proposing telescope/detector configurations feasible for application in future pulsar-based navigation systems.

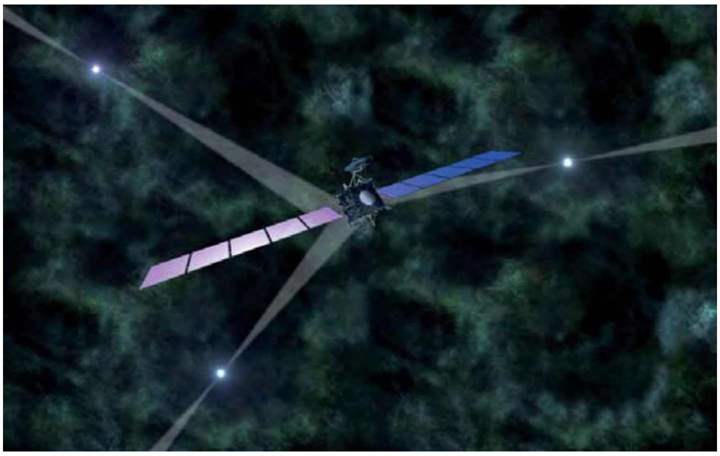

Figure 1 Artist's impression of pulsar-based navigation. A spacecraft that carries the means to detect and analyse the periodic signals from pulsars can determine its position and velocity by comparing pulse profiles and pulse arrival times measured on-board with those predicted at a reference location and epoch.

As pulsars emit broadband electromagnetic radiation from radio to X- and γ-rays, a pulsar-based navigation system can be designed for any energy band that is optimal in terms of pulsar characteristics (luminosity, pulse shape, pulse period etc.), hardware specifications (type and collecting power of the antenna, temporal resolution of the detector etc.) as well as boundary conditions given by the spacecraft (size, weight, power consumption etc.). We have been analysing the performance of pulsar-based navigation systems as a function of these parameters by simulating pulse profiles as measured by an arbitrarily moving virtual observer. According to our studies, an implementation of this novel technology seems particularly promising in the light of new telescope and detector developments, such as low-mass X-ray mirrors and active pixel detectors. Currently, we are working on high-level designs of pulsar-based navigation systems for different mission requirements.

References:

- W. Becker, M. G. Bernhardt, A. Jessner, 2013. Autonomous Spacecraft Navigation with Pulsars. In Proc. of *Relativistic Global Navigation Satellite Systems*. (In print.)
- M. G. Bernhardt, W. Becker, T. Prinz, F. M. Breithuth and U. Walter, 2011. Autonomous Spacecraft Navigation Based on Pulsar Timing Information. In Proc. of *2nd International Conference on Space Technology*.
- M. G. Bernhardt, T. Prinz, W. Becker and U. Walter, 2010. Timing X-ray Pulsars with Application to Spacecraft Navigation. In Proc. of *High Time Resolution Astrophysics IV*.

M. G. Bernhardt, W. Becker

The ultrafast optical photometer OPTIMA:

results from observations of highly variable sources

The OPtical TIMing Analyzer (OPTIMA) is a high-speed photo-polarimeter designed specifically to study highly variable sources (e.g., X-ray binaries, pulsars, cataclysmic variables, GRBs) with ns timing at optical wavelengths. OPTIMA has been successfully operated as a visiting instrument at a number of worldwide telescopes. The recent upgrade to a FPGA-based data acquisition and time tagging system has led to significant improvements of the duty cycle of the instrument. The new online monitoring and data visualization tools provide improved operation controls as well as the basis for standardized data analysis. Selected science results obtained in 2011/12 refer to the eclipsing AM Her type binary 1RXS J1845+48 [1]; the intermediate polar (IP) V2069 Cyg, where X-ray and optical observations are compared [2]; and the long term orbital ephemeris of HU Aqr, where accurate eclipse timing revealed the presence of a planetary companion in the binary system [3]

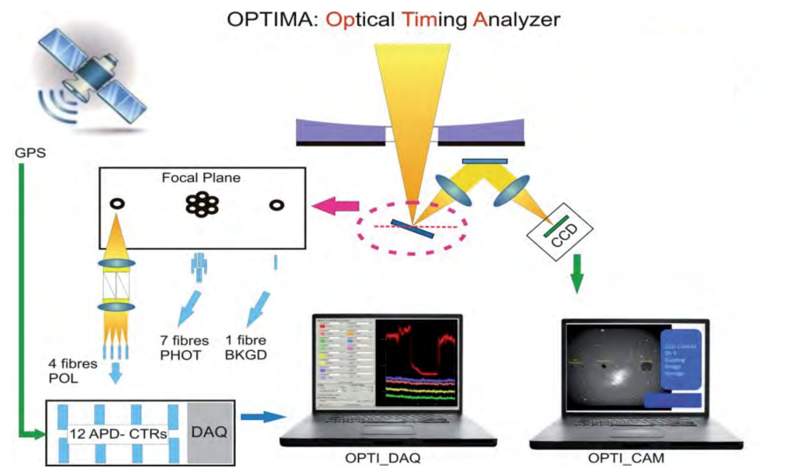

Fig. 1: Schematic layout of the OPTIMA system. Observing modes of photometry and polarimetry (twin Wollastone optics) can be chosen by placing the target object onto separate apertures in the focal plane. Single photons are registered in APD detectors and their time stamps are stored on-line in the DAQ computer. Pointing and guiding control are achieved with a field viewing CCD camera.

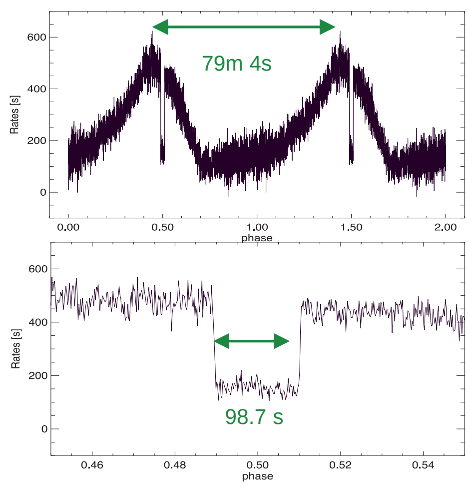

Fig. 2: OPTIMA lightcurve of the eclipsing AM Her binary RXS J1845+48. The extremely short orbital period of 79m 04s and eclipse duration of 98.7s show this system to be in an extreme state of binary evolution [1].

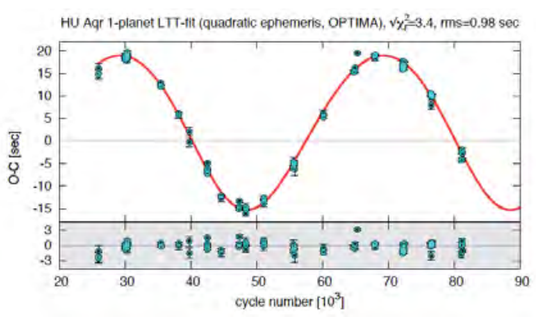

Fig. 3: Planets in eclipsing binaries can be revealed through deviations of the observed eclipse times from those predicted from the binary orbital motion (O-C). This requires high-precision measurements and long baselines as provided by OPTIMA for the polar HU Aqr. Fitting the orbital ephemeris over more than 10 years uncovered a periodic offset. This can be interpreted as the gravitational pull exerted by a planet of about 7 M_{Jup} in a 10 year orbit at a distance of 4.5 AU around the close binary ([3]+new 2012 data).

The intermediate polar (IP) V2069 Cyg, with an orbital period of 7.48h and a white dwarf (WD) spinning with 743s, shows partly anti-correlated double-peaked lightcurves in X-ray and optical emissions. This might indicate different emission regions in a weakly magnetized WD: X-rays come from the accreting polar caps and optical emission from a larger X-ray heated area on the WD [2].

References: [1] Rau et al, 2013, in prep.; [2] Nasiroglu et al, MNRAS, 420, 3350, 2012;
[3] Gozdziewski et al, MNRAS, 425, 930, 2012

G. Kanbach, A. Rau, et al.

The *Fermi*/GBM Gamma-Ray Burst and Spectral Catalogs: The First Four Years

The *Fermi* Gamma-ray Burst Monitor (GBM) has triggered on 953 cosmic gamma-ray bursts (GRB) in the first four years since trigger enabling on July 12, 2008. The catalogs presented here are the continuation of the first GBM two year catalogs (Paciesas et al. 2012, Goldstein et al. 2012). The now larger GRB statistics allows for more reliable conclusions and comparisons with the results obtained by other missions.

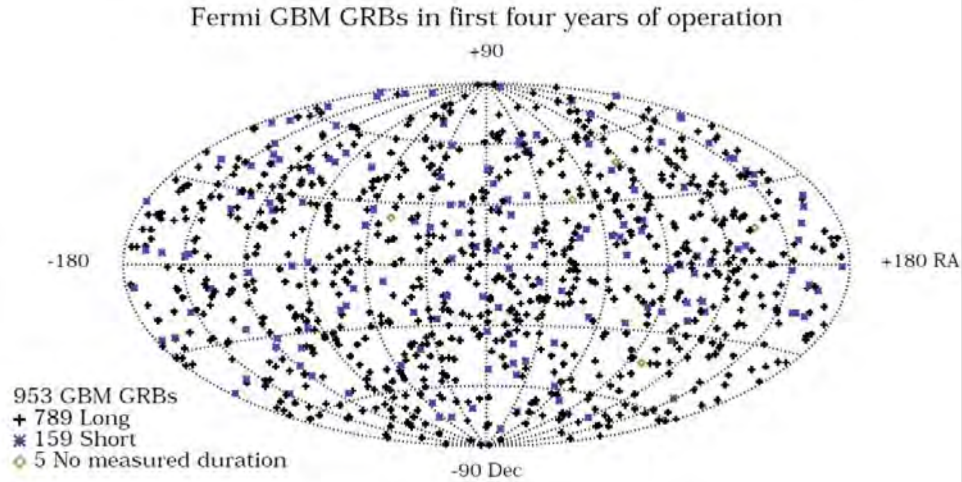

Sky distribution of GBM triggered GRBs in celestial coordinates. Crosses indicate long GRBs ($T_{90} > 2$ s); asterisks indicate short GRBs

The **GBM GRB catalog** (A. von Kienlin et al. 2013) contains the location and main characteristics of the prompt emission, the duration, peak flux and fluence for each GRB. The latter two quantities are calculated for the 50 to 300 keV energy band, where the maximum energy release of GRBs in the instrument reference system is observed and for a broader energy band from 10 to 1000 keV, exploiting the full energy range of the low-energy detectors of GBM.

The spectral analysis of the entire GRB sample obtained by GBM can be useful to infer physical properties and characteristics of GRBs. The **GBM spectral catalog** (D. Gruber et al. 2013) shows two types of spectra for each GRB: time-integrated spectra describing the average emission and peak flux spectra which are representative for the most luminous epoch of the GRB emission. A set of four empirical models (PL, COMPT, BAND, SBPL) was applied to the data of both spectral types, resulting in a compendium of over 7540 spectra. For each GRB we derive the best model and present the distribution and characteristics of the model parameters (see Figures on the right).

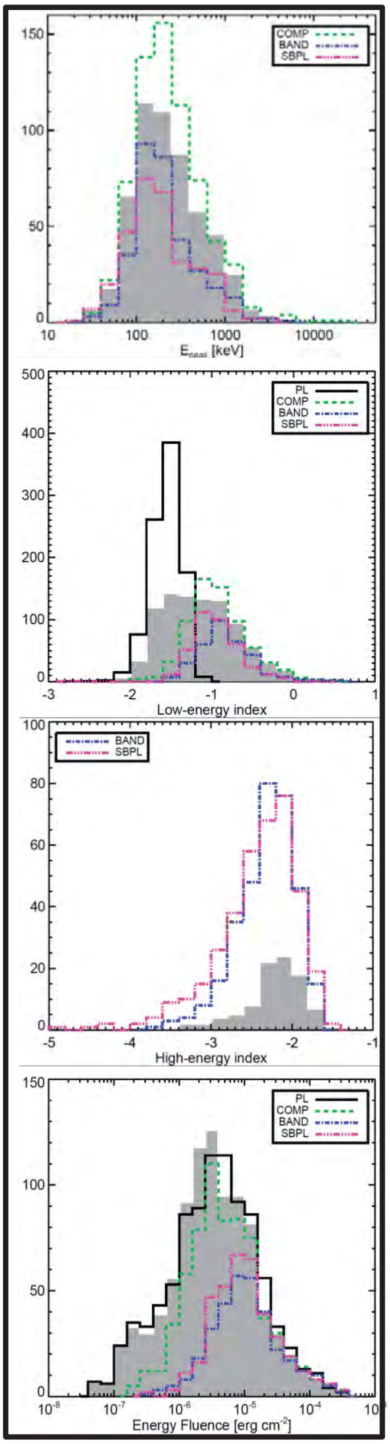

A. von Kienlin , D. Gruber et al. on behalf of the Fermi/GBM team

Photospheric emission in Fermi GBM GRB spectra

We present systematic time-resolved analysis of the brightest gamma-ray bursts observed by the Gamma ray Burst Monitor (GBM) on *Fermi* up to September 2011. Some of the prompt spectra show evidence for photospheric emission. These spectra can be fit with a combination of the Band function and a blackbody component, with the blackbody component observed below the peak energy of the Band function.

Since the launch of the *Fermi* Gamma-ray Space Telescope in 2008, deviations from the canonical Band function at both low and high energies have been observed in gamma ray burst spectra. Bissaldi et al (2011) performed temporal and spectral analysis of a sample of 52 bright and hard gamma-ray bursts (GRBs) observed with the Fermi GBM during its first year of operation. They estimated the burst durations up to 10 MeV and expanded the duration-energy relationship in the GRB light curves to high energies.

Fig. 1: Spectrum with Band+BB fit:

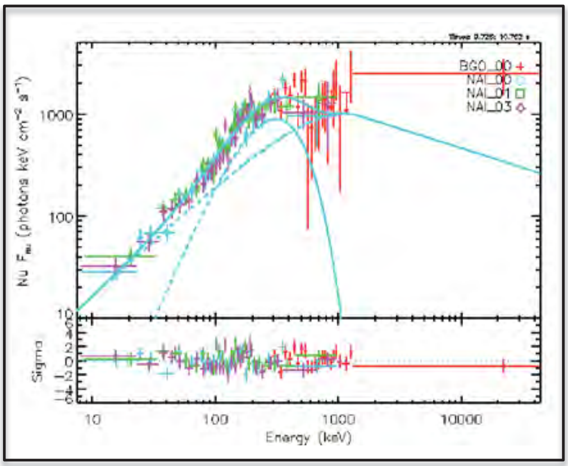

Fig. 2: distributions of E_{peak} (left) & α (right):

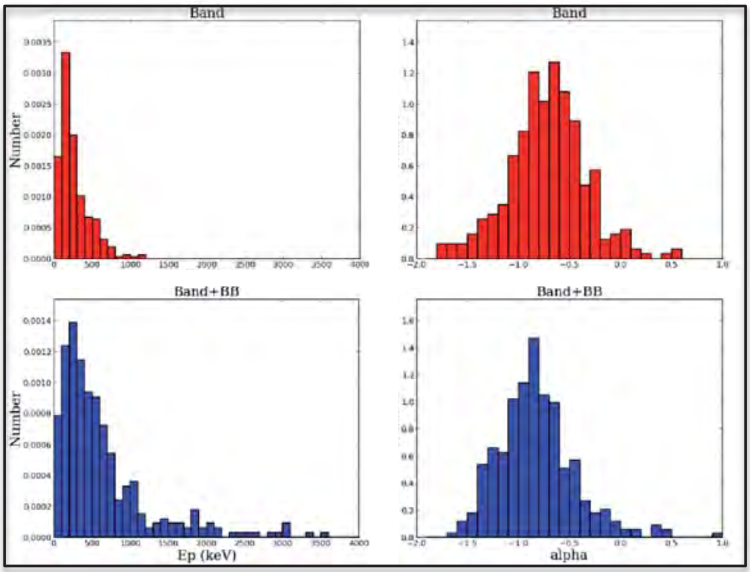

This sample of bright and hard GRBs was then updated to the end of September 2011 (McGlynn et al., 2012). This resulted in 64 bursts whose spectra were split into time-resolved bins. 19 bursts can be fit with a combination of a Band and blackbody (BB) function. We interpret the combination of the two functions as two separate components, where the blackbody corresponds to the photosphere.

The general trend in the subsample is as follows:

- the peak energy of the Band function E_{peak} is shifted to higher values, creating a double-peaked spectral effect (Fig. 1), and the distribution is broadened (Fig. 2).
- α shifts towards a mean of -1, consistent with synchrotron emission models (Fig. 2).

References:

• S. McGlynn & *Fermi* collaboration, Proceedings of Science, POS (GRB 2012) 012
• E. Bissaldi & *Fermi* collaboration, 2011, ApJ, 733, 97

S. McGlynn, E. Bissaldi, J. Greiner

Rest-frame properties of GBM GRBs

We present the main spectral and temporal properties of Fermi/GBM gamma-ray bursts with known redshift. Key-properties of these events in the rest-frame of the GRB are investigated to better understand the intrinisc nature of these events.

The sample comprises 47 GRBs with measured redshift that were observed by GBM until May 2012. For all of these events we derive the intrinsic peak energy in the F spectrum ($E_{peak,rest}$), the duration in the rest-frame ($T_{90,rest}$) and the isotropic equivalent bolometric energy (E_{iso}).

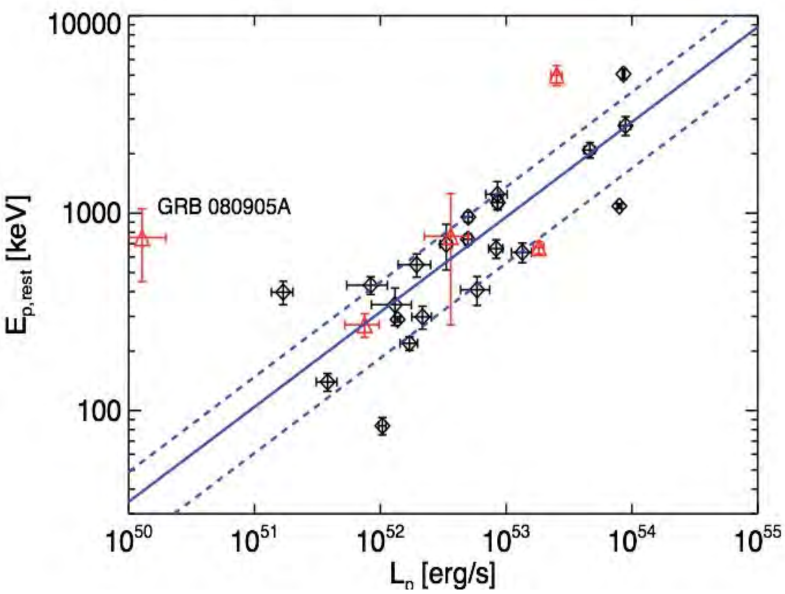

We <u>confirm</u> the tight correlation between $E_{peak,rest}$ and E_{iso} (Amati relation) with a <u>larger scatter</u> than previously reported.

We also confirm the relation between $E_{peak,rest}$ and the 1-s peak luminosity (L_p) (Yonetoku relation Fig. 1).

Short GRB 080905A, whose host galaxy was identified at z = 0.1218 is a peculiar outlier to this relation. This may be because the host galaxy is a foreground object and not related to the burst emission site.

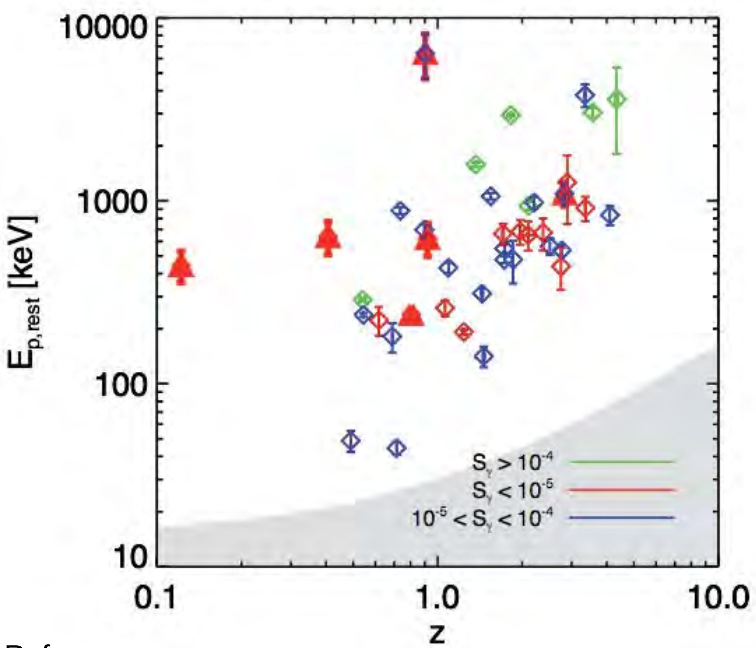

Salvaterra et al. (2007) conclude that high-z GRBs must be more common and/or intrinsically more luminous than bursts at low-z. Assuming that the luminosity function of GRBs indeed evolves with redshift and that the Yonetoku relation is valid, <u>we would also expect a positive correlation of $E_{peak,rest}$ with z.</u>
Indeed such a correlation is evident in Fig. 2. While it is intriguing, <u>selection effects</u> need to be taken into account before a reliable claim on redshift-evolution of $E_{peak,rest}$ can be made. This is under thorough study (but see Gruber et al. 2011)

References:
• Amati et al., 2009, A&A, 508, 173; Gruber et al., 2011, A&A, 531, 20
• Salvaterra et al. 2007, ApJL, 656, 49; Yonetoku et al., 2004, ApJ, 408, 383

D. Gruber, J. Greiner, A. von Kienlin on behalf of the GBM collaboration

The nature of „dark“ Gamma-Ray Bursts

A complete sample of GRB afterglows followed-up with GROND has been used to investigate the nature of ‘dark‘ GRBs, i.e. those with lacking optical emission. With our detection-completeness of 92% and the NIR-coverage, we find that ‘dark‘ bursts are due to moderate dust extinction at moderate redshifts.

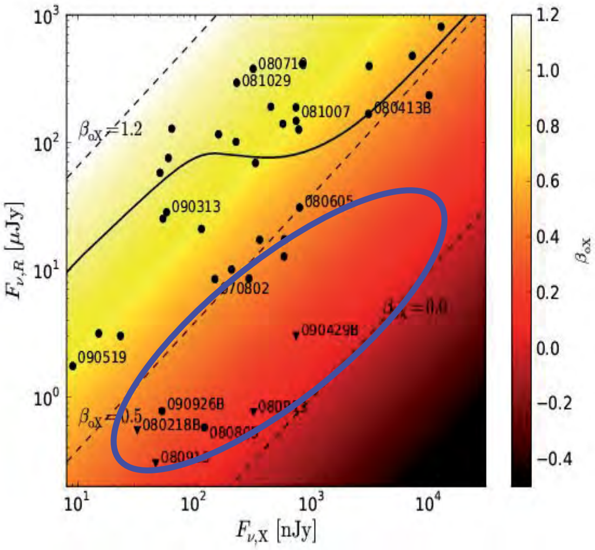

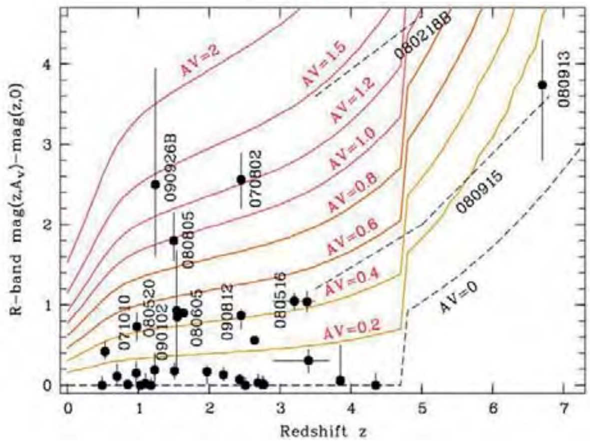

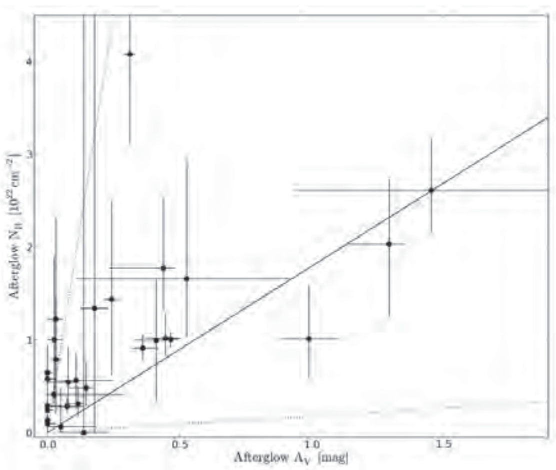

When follow-up observations with GROND start within 240 min after the prompt emission, a detection rate of 92% is reached. Using observations between 2007-2010, we form a sample of 39 GROND-detected GRBs which is (>90%) complete in detection, and the redshift and A_V-distribution.

This sample contains about 25% of ’dark’ bursts (Fig. 1). For these, fitting the GROND spectral energy distribution, we find substantially more afterglows with solid A_V detections than ever seen before: in particular we find ~25% of GRBs have A_V~0.5 mag; and ~10% have A_V > 1 mag.

Combined with the available redshifts, ’dark’ bursts are revealed as due to moderate dust extinction along the sight line, enhanced for the observer due to redshift effect (Fig. 2).

The fraction of high-z (z>5) bursts in the total sample is 5.5 2.8%.

Combined fits of the GROND and Swift/XRT data also provide constraints on the total hydrogen absorption N_H. A comparison of N_H vs. dust extinction shows that along GRB sight-lines there is substantially more dust than neutral hydrogen, by factor ~10-100 over the Galactic dust-to-gas ratio (Fig. 3). The cause is unknown so far: it could be due to ionization of the nearby surrounding, or implying different locations for dust and gas.

References:
Greiner J., Krühler T., Klose S. et al. 2011 A&A 526, A30

J. Greiner, T. Krühler, P. Schady for the GROND Team

Constraining high redshift star formation using long GRBs

MAX-PLANCK-GESELLSCHAFT

MPE

The association of long gamma-ray bursts (LGRBs) with the death of massive stars gives the prospect of utilising LGRBs to trace high redshift cosmic star formation history (CSFH), competing or even surpassing conventional methods. Using the Gamma-Ray burst Optical Near-infrared Detector (GROND), mounted at the 2.2m telescope in La Silla (Chile), highly complete LGRB samples have recently been collated, opening the avenue for using LGRBs as cosmological probes. For the first GROND sample, we have shown that it is not necessary for LGRBs to occur in a specific type of galaxy, and that any galaxy selections could be a result of incomplete samples.

GROND is a multi-channel imager, located at the 2.2m telescope in La Silla (Chile), covering the four sloan filters g', r', i' z' and three 2MASS filters, JHK contemporaneously **[1]**. This unique capability facilitates the measurements of GRB redshifts, when spectra are not available or fruitless (right). Over the past four years of its operation, GROND, has compiled a highly complete redshift sample of ~40 LGRBs (~95% complete in redshift), with a selection criteria of: (i) GRBs followed by GROND < 4 hours after the GRB alert and (ii) the GRB exhibits an X-ray afterglow **[2]**. The poster by Greiner et al. describes the dust properties of this sample.

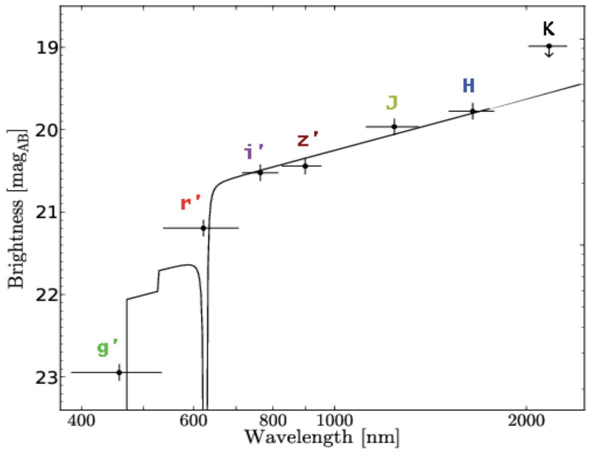

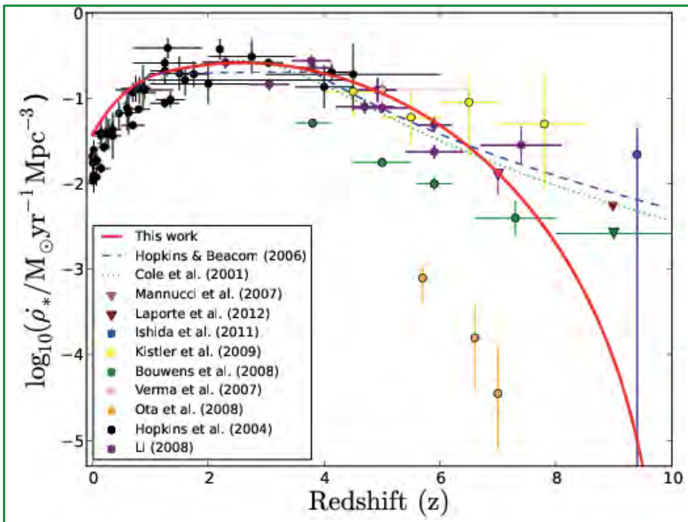

COSMIC STAR FORMATATION measurements at redshifts z>9, is a daunting task for conventional methods that use Lyman-break galaxies and Lyman-alpha emitters. LGRBs have opened a new avenue of probing such cosmological distances. As a result, constraints on early star formation, the period of reionisation and other cosmological processes can be constrained by LGRBs before waiting for the next generation instrumentation, e.g. JWST (left).

THE CONNECTION between CSFH and the LGRB rate may not be linear, and is still an on going debate. Utilising the GROND sample and a LGRB model **[3]**, we determine that it is possible for the LGRBs to trace the CSFH in a linear fashion, i.e. LGRB~CSFH, allowing constraints to be placed on the high-z star formation.

References:

1. J. Greiner, W. Bornemann, C. Clemens et al., 2008, PASP, **120**, 405, 2008.
2. J. Greiner, T., Krühler, S., Klose et al., 2011, A&A, **526**, A30.
3. J. Elliott, J. Greiner, S. Khochfar et al., 2012, A&A, **539A**, 113E.

J. Elliott, J. Greiner, S. Khochfar, P. Schady, J. L. Johnson, A. Rau and the GROND team

Testing the GRB afterglow fireball scenario

We have initiated a dedicated collaboration to obtain radio and sub-mm data in conjunction with our regular GROND observations and publicly available Swift/XRT data in order to test the predictions of the fireball scenario. Here we show the results of our first two cases.

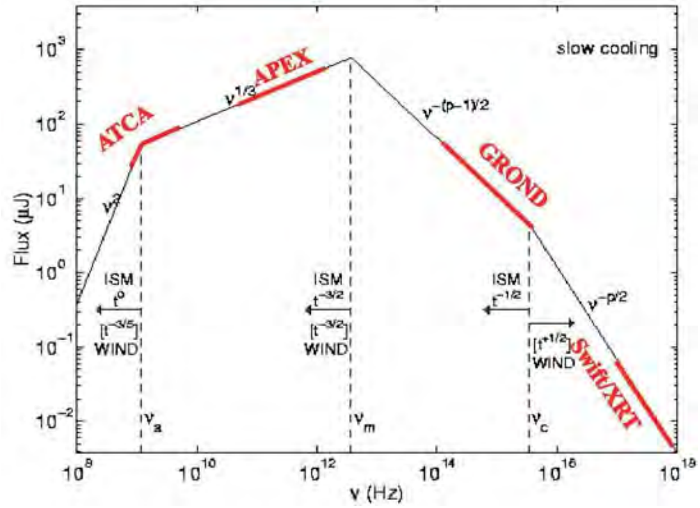

The generally believed scenario to describe the GRB afterglow properties is the so-called fireball scenario. Many observations are consistent with the fireball predictions, but a rigorous test has not been possible so far. With multi-epoch spectral energy distributions built from simultaneous ATCA, APEX (in the future ALMA), GROND and Swift/XRT data we will be able to test the predicted movement of the cooling and injection frequency (Fig. 1). This in turn allows to determine the energetics of the burst, and the energy partition between electrons and magnetic field.

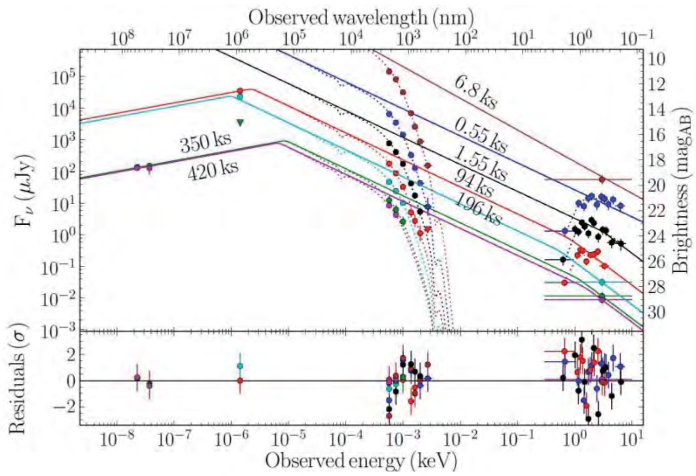

Our first succesful observational campaign was for GRB 100621A (Fig. 2), for which 3 epochs with ATCA and APEX could be secured. The afterglow showed very complex features, which did not allow a straightforward interpretation. But the campaign proved the approach of getting simultaneous data despite observatories distributed around the globe.

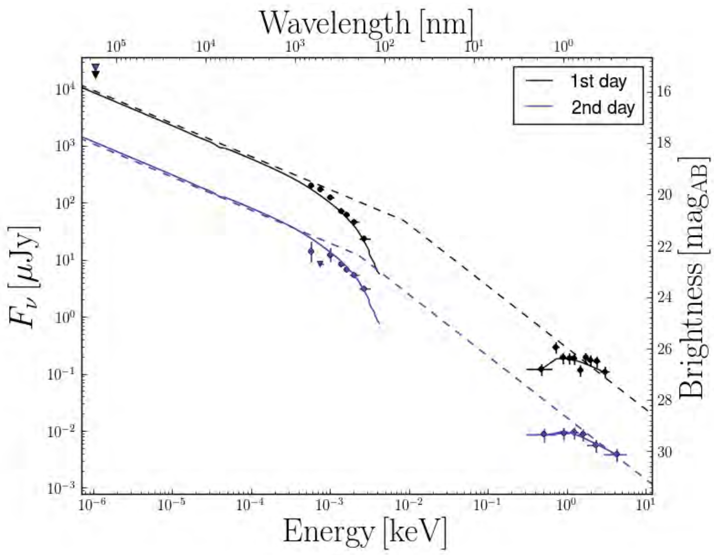

Our most recent campaign was for GRB 121024A (Fig. 3). Unfortunately, the APEX/LABOCA limits are just above the extrapolation of the GROND SED, and thus do not provide constraints on the fireball model. With APEX only the top 1-2% of GRBs are detectable in the sub-mm. Only with ALMA will a larger sample become available for systematic studies.

References:
- Greiner J. et al. 2013, A&A (subm.)
- Varela K., PhD work

K. Varela, J. Greiner, T. Krühler, M. Nardini and the GROND Team

Intervening MgII illuminated by GRB afterglows: Evidence of bias in spectroscopic surveys?

We investigate the unusual overabundance of intervening MgII absorption line systems in GRB sight-lines. We test for signatures of a dust extinction bias, and probe for an excess of field galaxies clustered around GRB afterglow positions. We find that a bias against heavy dust extinguished quasars is only likely to account for the observed MgII overabundance by ~10%, and that there are no signs of anomalous clustering of galaxies around GRB sight-lines. Therefore, there are likely still unknown biases in current spectroscopic surveys.

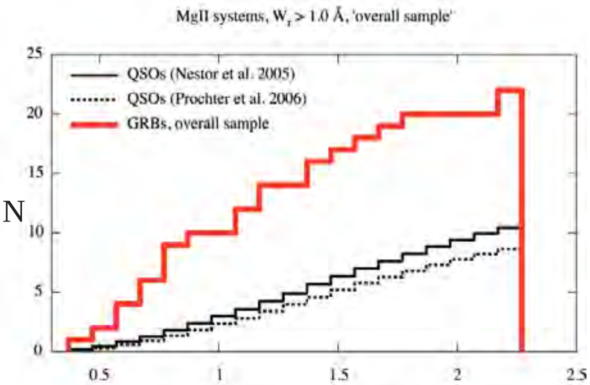

Fig. 1: Observed number density of inter-vening MgII absorbers among different samples. The number of observed absorbers seemingly depends on the background source.

MgII absorption line systems are strongly associated with DLAs and galaxies. These absorbers can be detected in spectra of bright, cosmological sources at all relative velocities. For this latter reason, it is surprising that the observed number density of these systems seemingly depends on the class of background source -- suggesting a significant observational bias in current spectroscopic surveying techniques.

This excess is represented in Figure 1, where the cumulative number of absorbers is found for GRB and QSO samples (Vergani+ 2009).

(Top) SDSS i-band distribution of quasars before and after correcting for dust extinction introduced by simulated MgII absorbers. The distributions are statistically consistent with an input MgII number density of 0.273, which corresponds to a 10% increase relative to the observed value. This implies that the contribution of a bias due to excluding dust extinguished quasars to the MgII problem is also on order ~10%. **(Bottom)** GRB-field galaxy two point correlation function computed from 80 GRB fields observed with GROND. The data are consistent with the best fit galaxy-galaxy correlation derived also from GROND data, represented with the solid black line. This result implies that the galaxies hosting the MgII absorbers are either not preferentially found in GRB fields, or that they represent a sample that is beyond the survey's limiting magnitude.

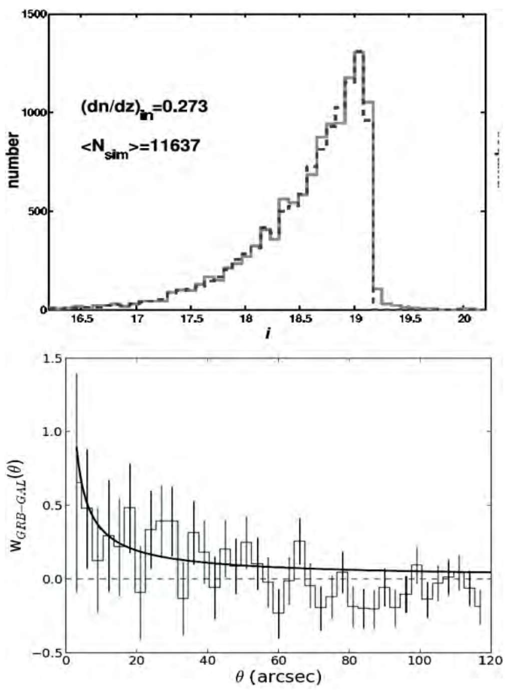

References:
- Vergani, S. D., Petitjean, P., Ledoux, C., et al. 2009, A&A, 503, 771
- Sudilovsky, V., Savaglio, S., et al. 2007, ApJ, 669, 741
- Sudilovsky, V., Smith, D., & Savaglio, S. 2009, ApJ, 699, 56
- Sudilovsky, V., Greiner, J., Rau, A. et al. 2012, A&A (in press)

S. Sudilovsky, S. Savaglio, J. Greiner and the GROND team

The Cosmic Chemical Enrichment as seen with GRB Afterglow Spectroscopy

Long duration gamma-ray bursts (GRBs) have been used for more than a decade now to explore the metal content in the interstellar medium (ISM) of high-redshift galaxies. This effort has revealed an unexpected picture, with metallicities that are on average above those measured in QSO damped Lyman-α systems (DLAs), a large spread and a mild evolution with time.

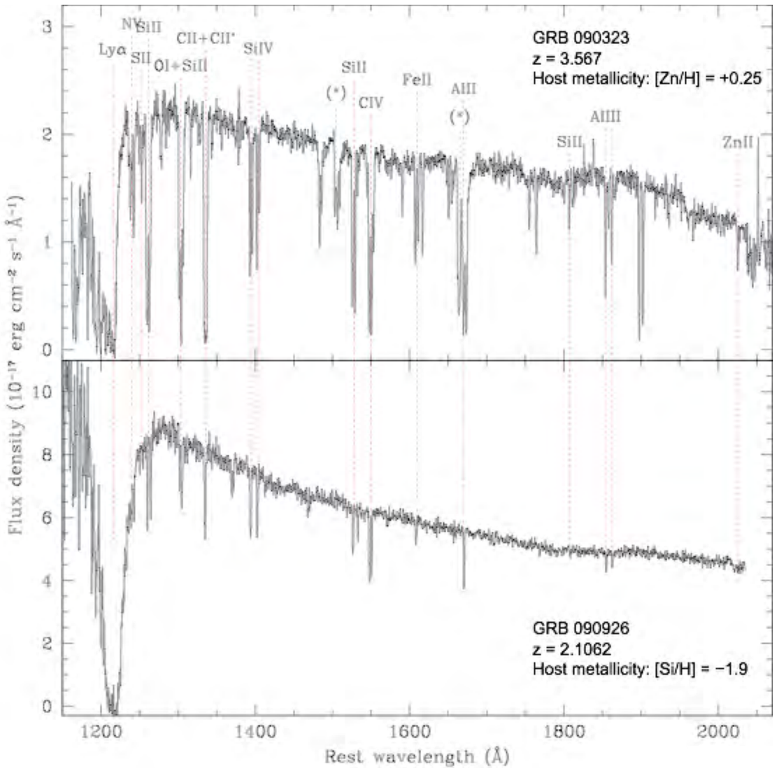

Two extreme cases are shown in the left Figure. Metal lines, detected in afterglow VLT spectra, probe the cold ISM of the host galaxies. In the upper panel, GRB 090323 at z = 3.567 has two DLAs with super-solar metallicity and separated by 660 km s^{-1} [1]. In the lower panel, GRB 090926 at z = 2.106 is characterized by a strong DLA with weak metal lines, resulting in a metallicity $Z/Z_\odot$ = 1/80 [2]. This large spread in chemical enrichment suggests that GRB hosts do not necessarily select metal poor galaxies, as depicted by most popular theoretical scenarios, and generally found at low redshift. Star formation is likely a more dominant parameter. It is well known that in the local universe, star formation happens predominantly in small galaxies.

At high redshift, big systems are still young and active. Here metallicity is generally high, as shown by the mass-metallicity relation [3]. Thus, a large spread in metallicity seen in GRB-DLAs for z > 2 is expected (red squares in the right Figure). Blue triangles are low-z GRB host metallicities measured using emission lines [4]. QSO-DLA metallicities are black crosses (the dashed line is the linear correlation). Solid curves are estimated metallicities for star-forming galaxies with different stellar masses [3], and suggest that high-z GRBs do not have to choose small galaxies. To confirm this, we need more mass measurements for GRB hosts at z > 2.

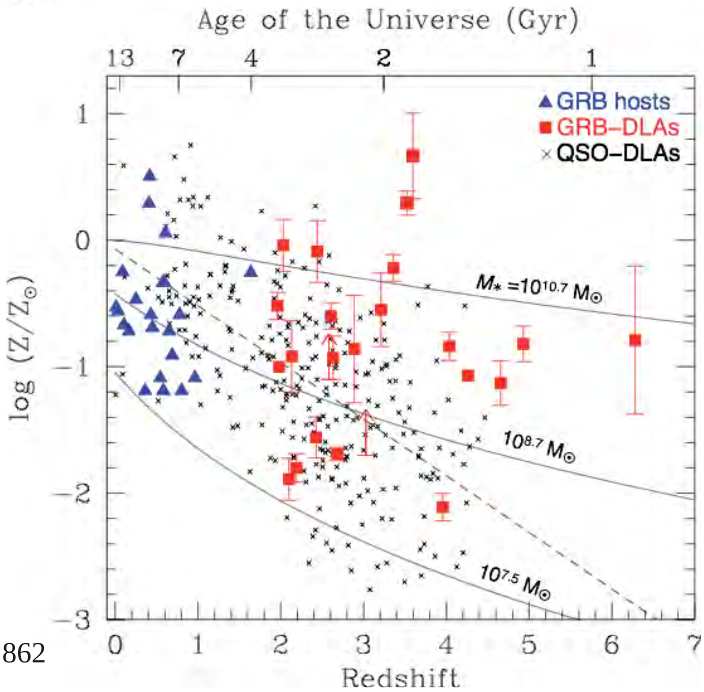

References:
- [1] Savaglio, S., et a1. 2012, MNRAS, 420, 627
- [2] Rau, A., Savaglio, S., Greiner, J., et al. 2010, ApJ, 862
- [3] Savaglio, S., et al. 2005, ApJ, 635, 260
- [4] Savaglio, S., et al. 2009, ApJ, 691, 182

S. Savaglio, A. Rau, T. Krühler, J. Greiner, S. McBreen and the GROND team

The Extremely Red Galaxy Hosting GRB 080207

We present results from our Herschel proposal to observe the more massive and chemically enriched subset of gamma-ray burst (GRB) host galaxies. These are exemplified by the host of GRB080207[1], which is an extremely red object (ERO), and dust-obscured galaxy (DOG) at z=2.1, towards the end of the peak of the star-formation rate (SFR). This galaxy may represent an increasing sample of high-z, massive and dusty systems that hold the link between GRB hosts, submillimeter galaxies, and other star-forming galaxy populations.

The link between long GRBs and the death of massive stars has now been indisputably established, as has their high redshift origin. Their extremely luminous and unobscured high-energy emission pinpoints regions of star formation irrespective of host galaxy luminosity, and as such makes GRBs compelling tracers of the cosmic SFR[2]. Through a series of Herschel programmes to follow-up GRB hosts (PIs: Schady & Hunt), our group and collaborators have exploited the use of GRBs to probe dust-rich, high-z galaxies otherwise challenging to study, and which are largely missing from optically-selected GRB afterglow and host samples[3].

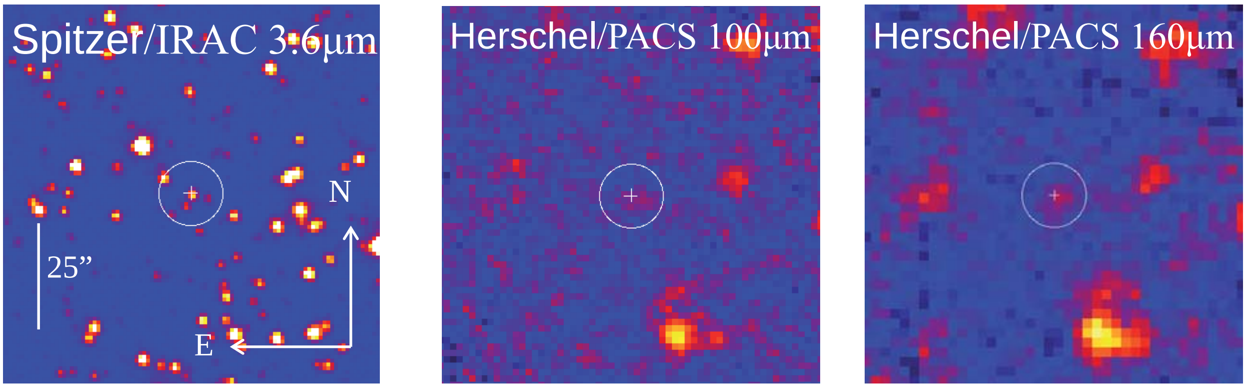

The host galaxy of GRB080207 is the first high-redshift host detected by Herschel. The galaxy SED is well fit by a nearby starburst template (M 82-like), yielding a high SFR_{IR}= 110 $M_\odot$ yr^{-1}, metal-rich stellar population, and significant dust extinction within the galaxy (A_V = 1−2; M_{dust}= 1.4×10^8 $M_\odot$). Our current results indicate that ~30% of our Herschel sample are luminous at FIR wavelengths, implying that an important fraction of GRB host galaxies are more massive and chemically evolved than previously believed[4]. This result has significant implications for the use of GRBs as tracers of the cosmic SFR density.

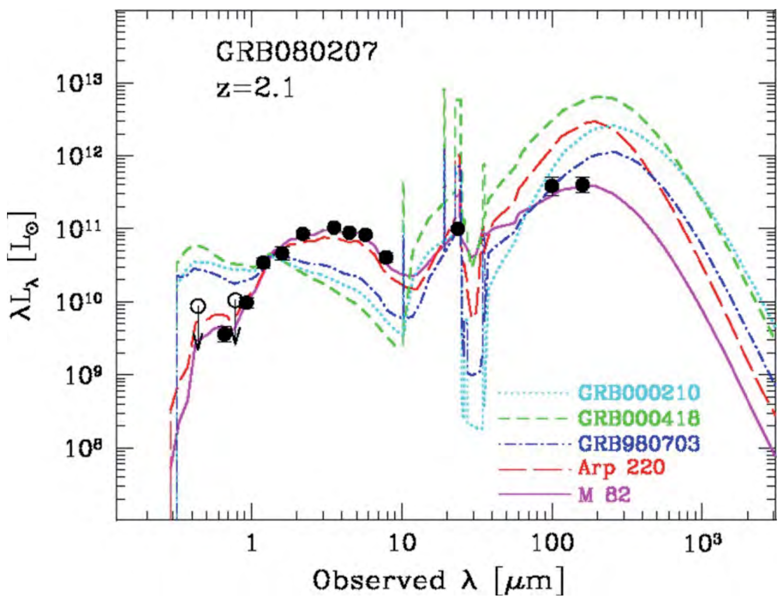

References:
- [1] Hunt et al. 2011, ApJ, 736, 36
- [2] Elliott et al. 2012, A&A, 539, 113
- [3] Krühler et al. 2011, A&A, 534, 108
- [4] Savaglio et al. 2012, MNRAS, 420, 627

P. Schady, S. Savaglio, J. Greiner et al.

The Connection between Gamma-Ray Bursts & Supernovae

We studied three of the latest SN associations with GRBs using GROND optical/near-infrared (NIR) data and *Swift X-ray and UV data. Through the early spectral energy distribution (SED),* the host-galaxy dust extinction is obtained for each event. By means of the extinction corrected light curves (LCs), the SN luminosity is computed. We derived luminosities 15% and 46% brighter than SN 1998bw for SN 2009nz and SN 2010ma, respectively, and a luminosity 68% fainter for SN 2008hw. The physical explosion parameters such as nickel, ejecta mass, and kinetic energy are delivered by the bolometric LC modelling. The full GRB- SN sample was completed with the addition of the SN bump of GRB 111209A and SN 2012bz/GRB 120422A. We discovered two populations when comparing the nickel and ejecta masses, which reveals a duality in the mass-loss histories of GRB-SN progenitors. The comparison between GRB and SN energetics suggests that the bimodal GRB-SN explosion could have a fixed energy budget.

1. SED modelling: (broken) power-law attenuated by host ISM

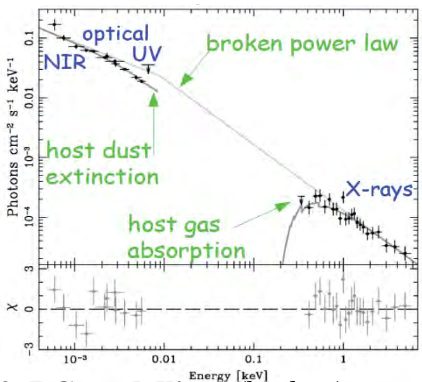

2. LC modelling: (broken) power-law, SN 1998bw templates, and host constant flux

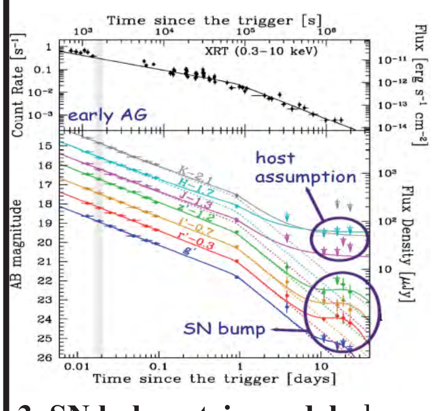

3. SN bolometric model: by Arnett (1982) delivers the nickel-56 mass (MNi), the ejecta (Mej), and the kinetic energy (Ek).

4. The full GRB-SN sample

15 events with MNi, Mej, and Ek; 5 measured with GROND data; (yellow circles); 10 from the literature (green filled circles). **A double correlation in the MNi-Mej plane hints at two different mass-loss records for the progenitors:**

Group 1**: high mass loss at the** end of their lives only allowing the core growth at earlier stages, which translates into a larger Ni production

Group 2: higher mass loss at early stages inhibited the core growth, hence less Ni is synthesised

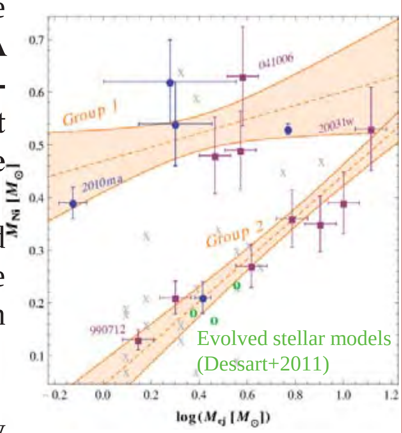

Sne Ibc in grey crosses (Drout+2011)

The gamma-ray energy Epeak was obtained from the GRB prompt emission for a subset of 10 events. With the exception of the peculiar GRB events connected to SNe 2010bh and 2006aj, **an anti-correlation shows more energetic GRBs associated with SNe producing less nickel. The core-collapse** energy might be partitioned between central accretion (GRB) and envelope expansion (SN).

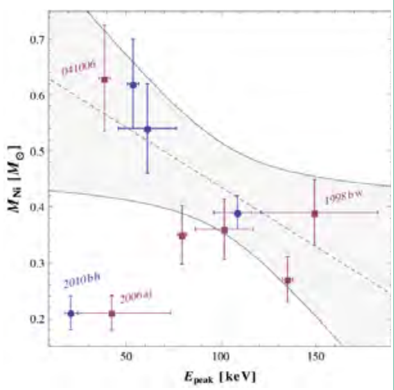

References:
- Arnett, W. D. 1982, ApJ, 253, 785
- Drout, M. R., et al. 2011, ApJ, 741, 97
- Dessart, L., et al. 2011, MNRAS, 414, 2985

F. Olivares E., J. Greiner, P. Schady, T. Krühler, A. Rau, et al.

The XMM-Newton Survey of the SMC

With the XMM-Newton survey of the Small Magellanic Cloud (SMC, PI: F. Haberl, 900 ks), a complete coverage of this galaxy is reached with imaging X-ray optics in the (0.2-12.0) keV band for the first time. The moderate distance of ~60 kpc and the low Galactic foreground absorption enables us to study complete X-ray source populations, like supernova remnants (SNRs), high-mass X-ray binaries (HMXBs), and super-soft X-ray sources (SSSs) down to $L_X = 5 \quad 10^{34}$ erg s^{-1}, which is difficult for the Galaxy or more distant galaxies. Besides of detailed studies of individual sources (e.g. newly discovered pulsars), the SNR distribution was found to extend to larger and older remnants than known before, the Be/X-ray binary luminosity function could be measured precisely and deviates from the expectations of the universal HMXB luminosity function and we showed that the diffuse X-ray emission correlates with star formation. A large sample of AGN behind the SMC will be useful for subsequent studies.

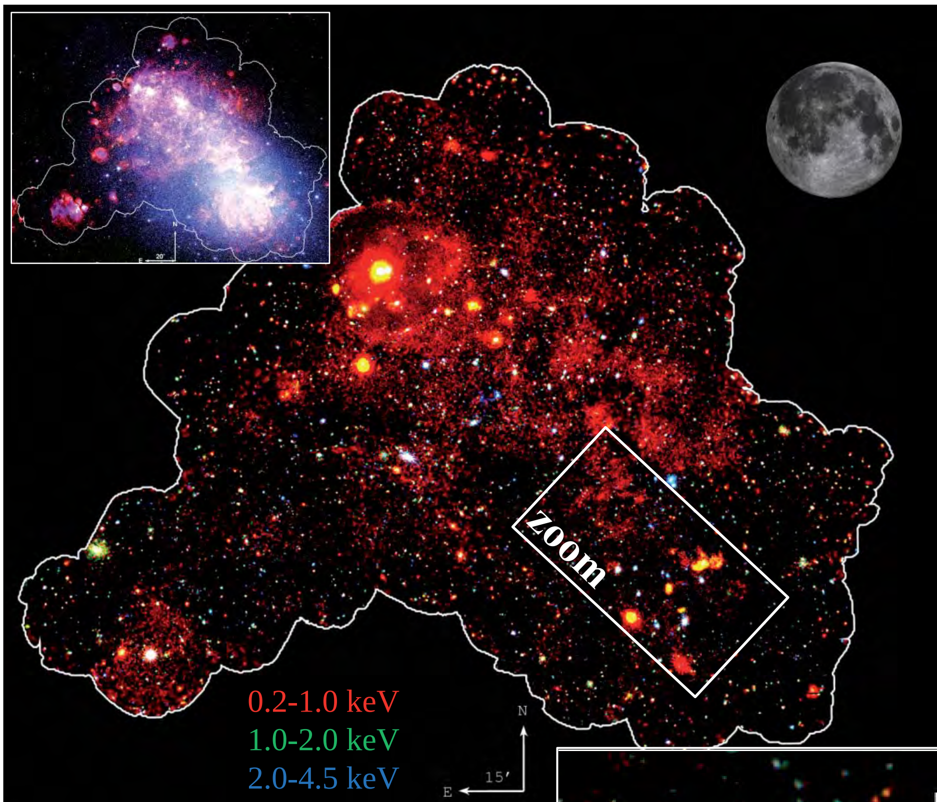

Figure: The mosaic EPIC colour image of the SMC reveals more than 3000 X-ray sources and diffuse X-ray emission in a field of 5.7 deg^2 (the moon demonstrates the size). In the *top left*, the field is compared with an optical image from MCELS. In the zoom-in *below*, sources within the SMC are labeled, (HMXB with their pulse period, if known, SNRs with their name, SMC3 is an SSS). Most of the other point sources are AGN behind the SMC.

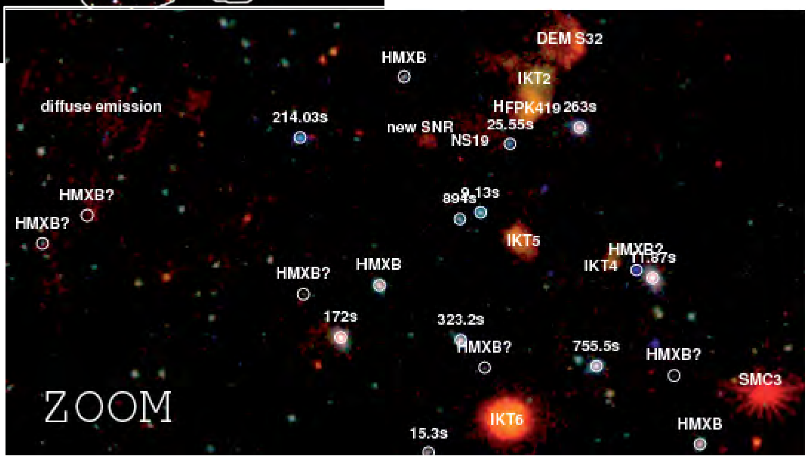

References:
- Haberl et al. 2012, A&A 545, 128
- Sturm 2012, PhD thesis, TU Munich
- Sturm et al. 2012, A&A 537, 76
- Coe et al. 2012, MNRAS 424, 282
- Sturm et al. 2011, A&A 527, 131
- Sturm et al. 2011, A&A 529, 152
- Novara et al. 2011, A&A 532, 153
- Townsend et al. 2011, MNRAS 410, 1813
- Coe et al. 2011, MNRAS 414, 3281
- Mereghetti et al. 2010, A&A 519, A42
- Sturm et al. 2013, A&A 551, 96

R. Sturm, F. Haberl, W. Pietsch

The Monitoring of the Remnant of SN 1987A with *XMM-Newton*
Evolution of the X-ray Light Curve and Properties of Fe K lines

Recent observations of the supernova remnant SNR 1987A in the Large Magellanic Cloud with *XMM-Newton* offer a unique opportunity to follow the early evolution of a core-collapse SNR. In particular, we can probe the complex circumstellar ring-like structures shaped by the supernova progenitor star by monitoring the evolution of the X-ray emission. We homogeneously (re-)analyse all observations from 2007 to 2011, three of which have not been published so far, using mainly data from the EPIC-pn camera. Fitting the integrated spectra with a three-component plane-parallel shock model, we measure soft and hard X-ray fluxes with high accuracy, and examine the presence and properties of Fe K lines. Our findings are interpreted in the framework of a hydrodynamics-based model.

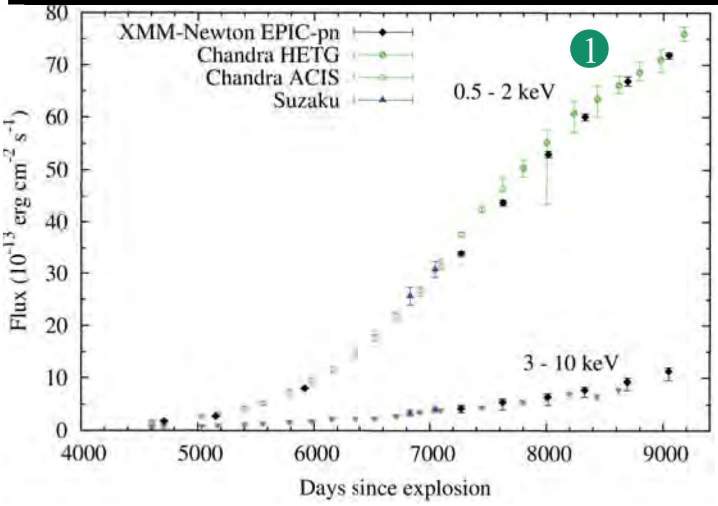

X-ray light curve: The soft (0.5-2 keV) and hard (3-10 keV) X-ray fluxes are shown on Fig. 1, along with *Chandra* and *Suzaku* measurements. Although a mild flattening of the soft X-ray light curve is seen in recent data, *the source has not reached a turn-over yet,* a picture confirmed by recent *Chandra* observations. We conclude that material in the equatorial ring and out-of-plane HII regions are still being swept up.

From the hydrodynamics-based model of Dewey et al. (2012), we estimate the thickness of the equatorial ring to be at least 4.5×10^{16} cm (0.0146 pc). This lower limit will increase as long as the soft X-ray flux has not reached a turn-over.

Fe K lines : Taking advantage of the superior high-energy effective area of *XMM-Newton*, we studied the properties of the Fe K lines, which are significantly detected in all spectra since 2008. *The data suggest the presence of various iron ionisation stages*, from Fe XVII to Fe XXIV. The low statistics preclude conclusions on the flux and centroid energy evolution in recent years.

The thermal emission model, which fits the integrated spectra, *under-predicts* the low-energy part of the line complex (Fig. 2). This points to the presence of shocked material with *shorter ionisation ages*, and/or contribution from *fluorescence* by low ionisation iron, including Fe in unshocked ejecta.

We find that the main contribution to the Fe K emission comes from the out-of-plane H II region.

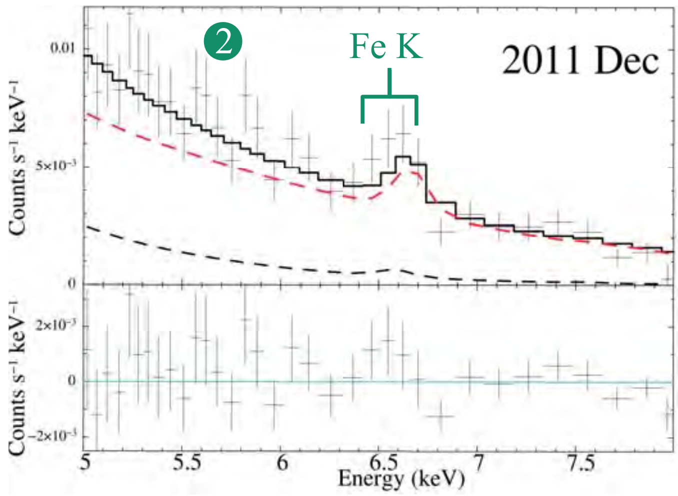

Conclusions: Recent *XMM-Newton* observations of SNR 1987A showed that the equatorial ring is more extended than previously thought, providing clues to pre-explosion scenarios. Following the evolution of the Fe K lines is crucial in order to constraining their origin.

References:
Maggi P., Haberl F., Sturm R., & Dewey D. 2012, A&A, 548, L3
Dewey D., Dwarkadas V.V., Haberl F., Sturm R., & Canizares C.R. 2012, ApJ, 752, 103

P. Maggi, F. Haberl, R. Sturm, et al.

RASS Supernova Remnant Candidates and their Prospects for eROSITA

Identified radio supernova remnants (SNRs) in the Galaxy comprise an incomplete sample of the SNR population due to various selection effects. ROSAT performed the first All-Sky Survey (RASS) with an imaging X-ray telescope and thus provided another window for finding SNRs and compact objects that may reside within them. Meanwhile, 14 new SNRs were identified in multi-wavelength identification campaigns based on this RASS data (cf. Prinz & Becker 2013 for a summary) . The current list of RASS SNR candidates still includes 73 sources, which will be very promising to study with eROSITA.

All 73 sources have a diameter of $> 5'$, are at a low Galactic latitude (|**b**| < 15 deg) and have a signal-to-noise ratio greater than 4σ. eROSITA, planed to be launched at the end of 2014, will provide a survey sensitivity of more then 10 times of what was available in the RASS. It supports to continue the previous SNR identification campaign and to search for new SNRs with a much higher sensitivity than was possible before.

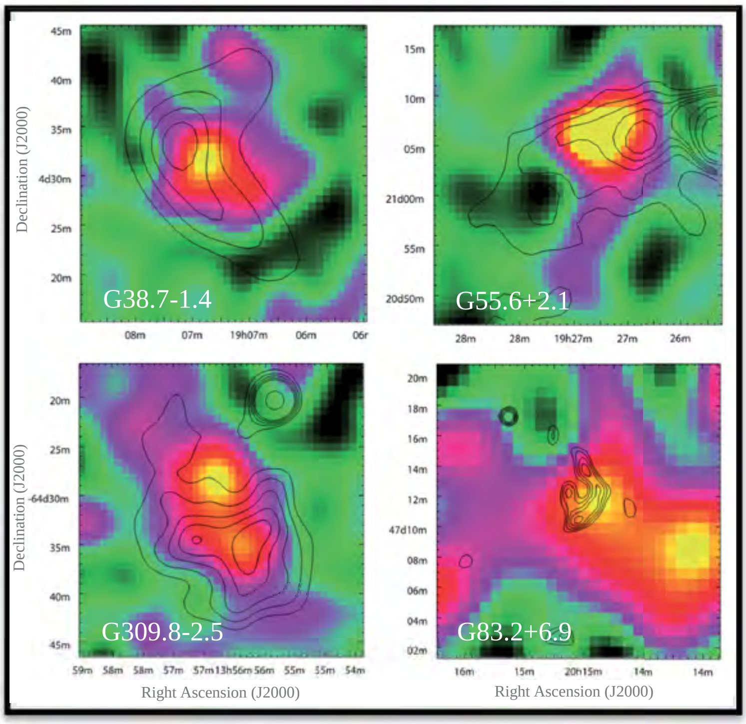

Figure 1: RASS images of SNR candidates with a good positional match between X-ray and radio emission:

G38.7–1.4 shows X-ray emission with an extent of 13'x10'. Radio data show a strong radio shell. With an Effelsberg follow-up observation at 6 cm a radio spectral index of -0.65 is determined. The radio emission is polarized, all in strong favour towards a SNR interpretation

G55.6+2.1 depicts X-ray emission with an extent of 13'x12'. Radio emission from the Parkes-MIT-NRAO (PMN) survey and infrared emission matches perfectly the shape of the X-ray source.

G309.8-2.5 reveals X-ray emission in the RASS with an extent of 18'x12'. The Molonglo sky survey (SUMSS) shows a bright radio shell.

G83.2+6.9 shows X-ray emission with an extent of 6'x6'. In the NRAO VLA Sky Survey (NVSS) an incomplete radio shell can be seen. With Effelsberg data taken in a follow-up observation, a spectral index of -0.9 is deduced. The radio data are not polarized.

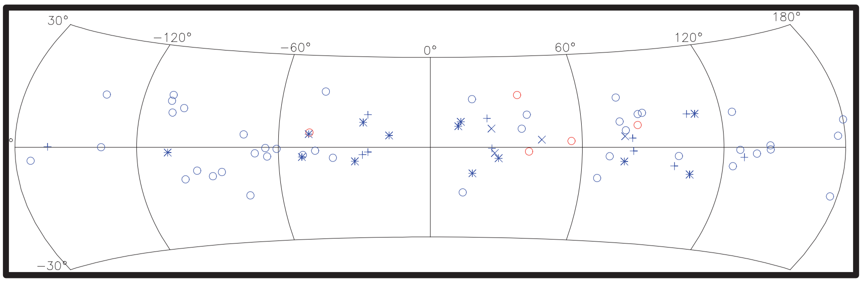

Figure 2: The location of the 73 RASS supernova remnant candidates in an Aitoff-Hammer projection. Sources with an extent of less than 30 arc minutes are indicated by (○). (+) indicates SNR candidates with an extent of 30 – 60 arc minutes, (X) with an extent of 60 – 120 arc minutes and sources with an extent greater than 120 arc minutes are indicated by (*).

References:

- Prinz, T., Becker, W., Supernova Remnant Candidates in the ROSAT All-Sky Survey, 2013, in preparation
- Prinz, T., Becker, W., Exploring the supernova remnant G308.4-1.4, 2012, A&A, 544, 7
- Prinz, T., Becker, W., Supernova Remnant G296.7-0.9 in X-rays, 2013, A&A, 550, 33

T. Prinz and W. Becker

Investigating Star- and Supernova-Interiors

The photospheric surfaces of stars and supernovae only indirectly convey what happens in their interiors. Other messengers could be neutrinos or gravitational waves. Here we explore radioactive isotopes whose creation reflects the physical conditions in deep interiors of stars and of supernovae. Such isotopes decay in the source surroundings after being ejected through winds and explosions, and can be measured in characteristic gamma-ray lines.

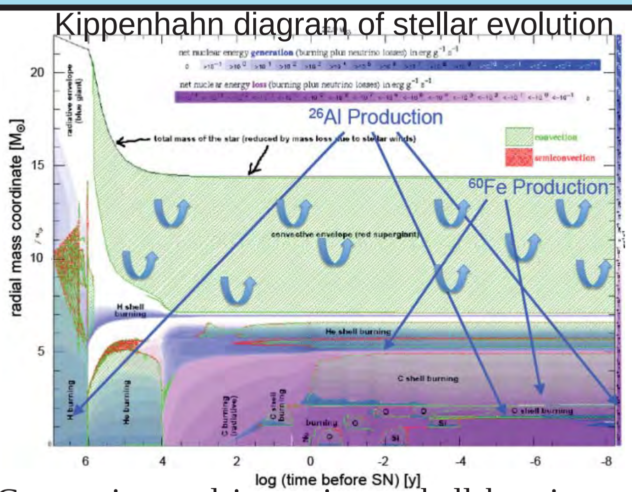

Convection and intermittent shell burning are complex processes, whose modeling is approximate and unphysical in current massive-star models. Nuclear fusion products are among the most-sensitive probes to test the validity of models. ^{26}Al is synthezised in core H burning, late C and O shell burning, and explosive nucleosynthesis, while ^{60}Fe is synthezised only in C and H shell burning regions. Measuring the isotopic ratio ^{60}Fe/^{26}Al therefore characterizes the massive-star source population as a whole, and provides a global test. Both isotopes have been measured through their decay γ-ray lines with INTEGRAL. Our observed ratio in γ-ray brightness is in conflict with predictions, but is consistent with meteoritic studies of the early solar system. Discussed model revisions are direct black-hole formation in larger stellar-mass regimes, convection models, and also nuclear rate uncertainties [1,2].

The γ-ray lines from decay of ^{44}Ti probe deep interiors of core-collapse supernovae, as this isotope originates from α-rich freezeout near the mass cut. INTEGRAL γ-ray line width measurements constrain current ejecta velocities [3]. Cas A and SN1987A ^{44}Ti yields have been derived from INTEGRAL γ-ray observations, and exceed by factors model predictions for typical core-collapse events. The γ-ray survey finds fewer sources in the Galaxy than expected [1,2].

INTEGRAL's spectrometer is unique in being capable of measuring the gamma-ray lines from decay of radioactive ^{56}Ni, which powers supernova light. The γ-ray emission conveys key information on the explosion mechanism and on how the explosion unfolds. It essentially complements photospheric SNIa obser–vations, as their modeling from the original ^{56}Ni power input is complex and indirect, and understanding of SNIa physics is key to cosmological applications. Suffiently-nearby SNIa are rare (expected rates ~0.5/y). SN2011fe came close, though not quite enough (see Figure below) [1,4,5].

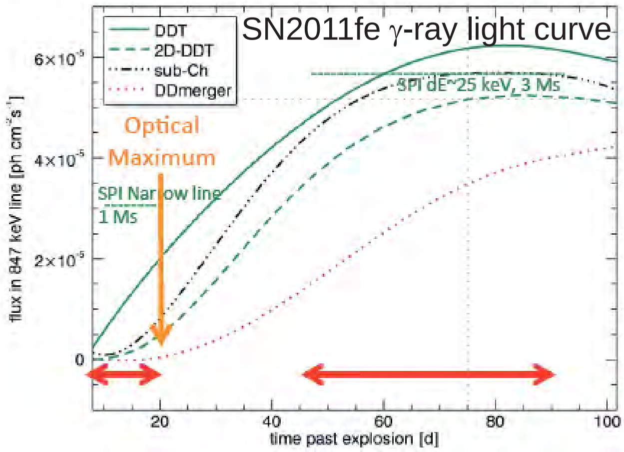

References:

[1] Diehl R.: *Nuclear-Astrophysics Lessons from INTEGRAL*. Rep. Prog. Phys., 76, 2, 026301 (2013).

[2] Thielemann F.-K., et al.: *Massive Stars and Supernovae.* Springer Lect.Notes in Physics, Vol. 812, Ch. 4 (2011)

[3] Martin P., et al.: *Kinematics of the ^{44}Ti ejecta of Cas A from INTEGRAL/SPI.* A. & A., 502, 131 (2009)

[4] Isern J. et al.: *Observation of SN2011fe.* A.&A. *(in press)* (2013); ATels (2011,2012)

[5] Maeda K., et al.: *Hard X- and Gamma-Rays from Type Ia Supernovae.* ApJ 76, 54 (2012)

R. Diehl, F. Knust, K. Kretschmer, M. Lang, P. Martin, W. Wang, X. Zhang

Positron Annihilation in the Galaxy

The SPI imaging spectrometer on ESA's INTEGRAL spacecraft is uniquely suited to observing the 511 keV gamma-ray line due to annihilation of positrons in the Galaxy. SPI provides simultaneously high spectral resolution, allowing the line shape to be studied, and imaging of the distribution of the annihilation events over the sky. By the end of 2012 more than 10 years of data have been accumulated and are being analysed.

Detection of the 511 keV gamma-ray line from the Galaxy implies the annihilation of ~10^{43} electron-positron pairs per second. The origin of the positrons remains unclear. Many possible explanations have been proposed [1], including decay of dark matter, pair plasmas in pulsars and near black holes. The observation of the 1809 keV line from ^{26}Al implies that at least some positrons must be produced by radioactive decay following nucleosynthesis in supernova explosions.

Early results from INTEGRAL/SPI showed that the 511 keV emission was surprisingly concentrated towards a comparatively compact, region around the Galactic centre ('the bulge'). Emission from the disk, where positrons from nucleosynthesis are most likely to be produced, was found to be significant, but relatively weak, with an indication of an asymmetry (Fig. 1).

Fig 1

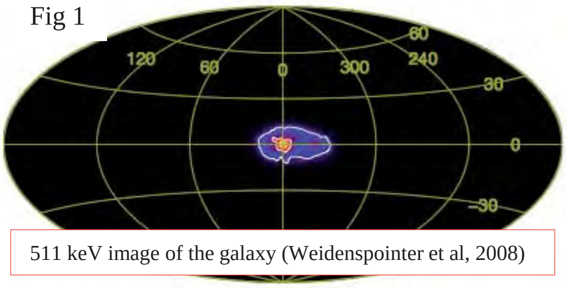

511 keV image of the galaxy (Weidenspointer et al, 2008)

Analysis of data from the 10 years of observations improves the statistical significance of the results and reduces systematic effects. The general conclusion remains that the bulge-to-disk ratio is high and difficult to reconcile with many of the possible origins for the positrons.

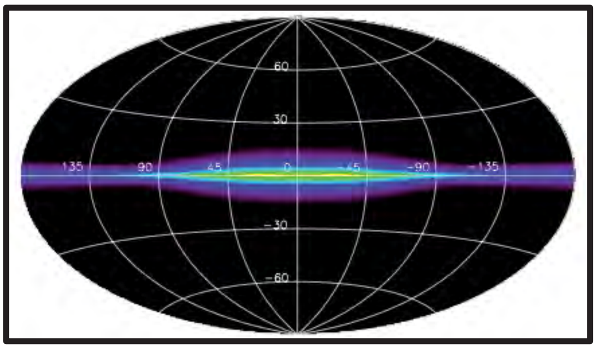

Fig. 2. A simulation of the expected 511 keV line distribution from nucleosynthesis positrons, allowing for propagation in a turbulent magnetic field (Ref 3).

It has become increasingly apparent that in order to understand the observations the propagation in Galaxy of the positrons and their slowing down must be taken into account. Simulations [2,3] (*e.g.* Fig. 2) show that, in contrast to some predictions, positrons from radioactive decay following nucleosynthesis in supernova explosions do not travel large distances before annihilation, leading to emission largely confined to the disc of the Galaxy. This implies a different origin for most of the positrons and a low escape fraction for positrons produced in this way.

References:

•1) N. Prantzos, C. Boehm, A. Bykov, R. Diehl, et al. "*The 511 keV emission from positron annihilation in the Galaxy*" Rev.Mod. Phys. 83, 1001, 2011

•2) P. Martin, J. Vink, S. Jiraskova, P. Jean, R. Diehl, "*Annihilation emission from young supernova remnants*" A&A 519, A100 (2010)

•3) P. Martin, A. W. Strong, P. Jean, A. Alexis, R. Diehl, "*Galactic annihilation emission from nucleosynthesis positrons*" A&A 543, A3 (2012)

G. Skinner, R. Diehl, P. Martin, A. Strong, G.Weidenspointner, X. Zhang

Triggering star formation in Scorpius-Centaurus

With the objective of studying the complex structure and evolution of the interstellar medium in the region of the Scorpius-Centaurus OB association - the nearest region of recent massive star formation - we will analyse INTEGRAL data in order to reveal the structure of the emitted ^{26}Al which was spread into the interstellar medium through supernova explosions and the winds of Wolf-Rayet stars. The characteristic γ-rays enable us to probe the history of activity of the massive stars on a time scale of My. Together with results from different wavelengths and the predictions of numerical simulations the project provides the basis for understanding how the feedback of massive stars shapes the interstellar medium.

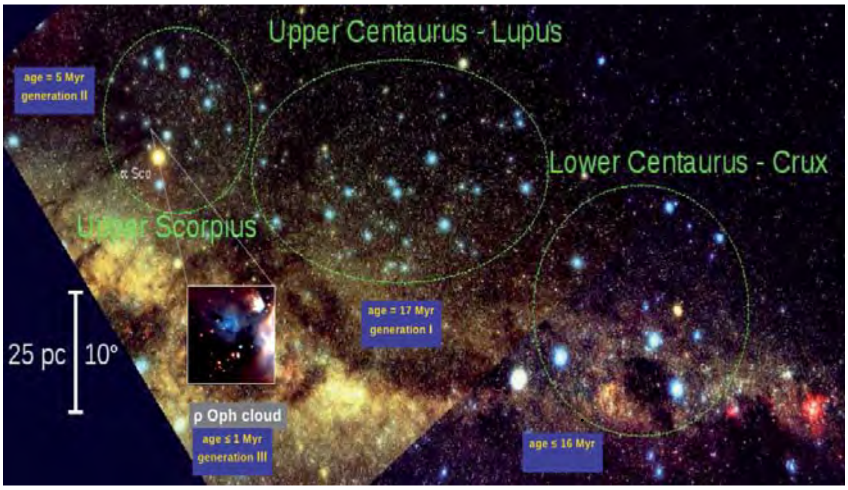

Fig.1: Optical image of the Sco-Cen region. The three subgroups are marked. As an outcome of triggered star formation there are three generations of stellar groups.

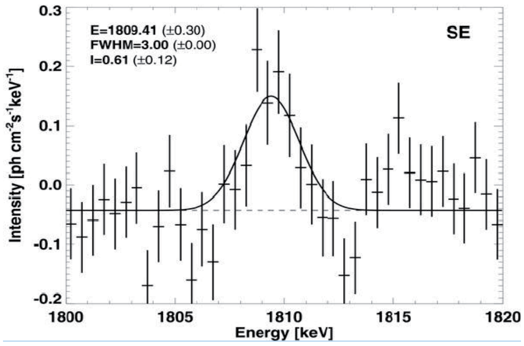

Fig.2: The signal from Sco-Cen enables us to make an independent age estimate for the subgroups and to gain information on the bulk motion from measuring the line centroid and the width..The figure shows the INTEGRAL/SPI spectrum from 2010. The line is significantly blue-shifted which indicates that the radioactive ejecta are moving towards us.

The Scorpius-Centaurus OB Association (Sco OB2) is, at a distance of 145 pc, the nearest region of recent massive star formation. It consists of three subgroups, Upper Scorpius, Upper Centaurus-Lupus, and Lower Centaurus-Crux which have ages of about 5, 17, and 16 Myr. The γ-ray-spectrometer SPI on INTEGRAL enables us to probe the nearby massive stars by means of radioactive ejecta from massive-star nucleosynthesis. The ^{26}Al is expelled via winds during the Wolf-Rayet phase and core-collapse supernovae over 10-20 My after formation of a stellar group. ^{26}Al emits γ-rays with an energy of 1809 keV and a radioactive decay lifetime of ~1 Myr. Compared to the evolutionary time scales of a stellar group this is a short time, while significantly beyond the characteristic time of other observables.

Using all available observables, such as radioactive ejecta, bubble shells, ionized-gas emissions, and remaining-star counts, population synthesis exploitation gives us the unique opportunity to test our understanding of massive star groups for consistency. Moreover, nucleosynthesis ejecta from the Sco-Cen subgroups, through their location and Doppler line shifts, can provide constraints on models of triggering successive generations of star formation, and on bulk motion, thus revealing the star formation history in the Scorpius-Centaurus OB association.

References:

Diehl et. al. “Radioactive ^{26}Al from the Scorpius-Centaurus Association” A&A, 522, A51 (2010)
Preibisch & Mamajek 2008, Handbook of Star Forming Regions, Vol. II, ed. B. Reipurth, p. 235

F. Alexander, R. Diehl

Exospheric X-ray Emission of Venus

The solar wind interaction with planetary atmospheres plays an important role for their evolution. By utilizing the fact that the solar wind contains heavy ions which emit X-rays when they are discharged in a planetary exosphere, we have pioneered a novel method for remote, global imaging of this interaction by X-ray observations. After having successfully applied this method to Mars, we demonstrate that it works also at Venus.

Despite its prominence in the optical sky and its general importance as the „twin“ of the Earth, virtually nothing was observationally known about the X-ray properties of Venus before 2001, when we succeeded with Chandra in detecting our neighbouring planet for the first time ever as an X-ray source. In this pioneering observation, which took place during solar maximum, we found the X-ray radiation to be dominated by fluorescent scattering of solar X-rays. An additional component, caused by charge exchange between solar wind ions and atoms in the Venusian exosphere, was suspected, but could not be unambiguously identified. In order to reveal the presence of any exospheric charge exchange X-ray emission in subsequent observations, we utilized the fact that around solar minimum the fluorescence component should become considerably fainter, and succeeded, as illustrated below.

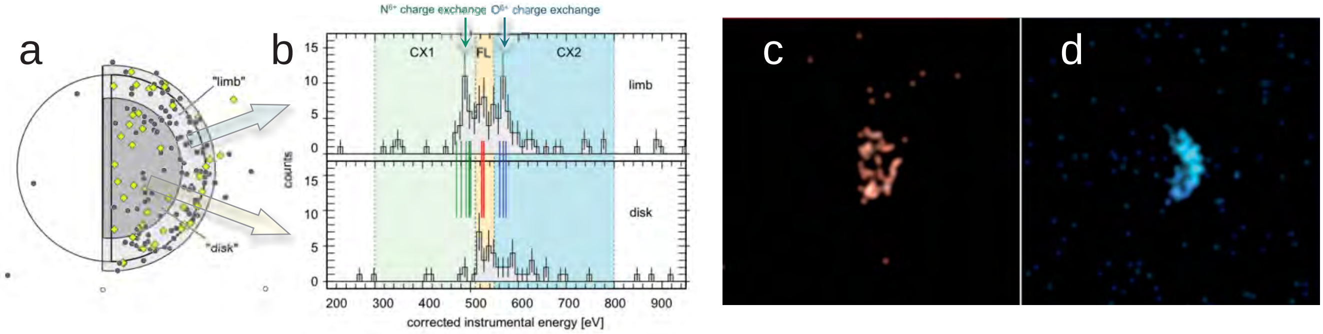

a) Spatial distribution of X-ray photons over the disk of Venus (large circle) as observed with Chandra. Yellow diamonds mark photons with energies consistent with O-K fluorescence of solar photons, while dark circles identify photons with energies consistent with solar wind charge exchange. **b)** Spectral distributions for the „disk“ and „limb“ regions, exhibiting clear differences: while the disk spectrum is dominated by emission from O-K fluorescence, the limb spectrum shows evidence for emission from N^{6+} and O^{6+} ions. **c, d)** Smoothed images composed of „fluorescence photons“ (c) and of „charge exchange photons“ (d). The fact that the charge exchange emission is more confined to the Venusian limb is in agreement with simulations.

With this detection, Venus becomes the second planet, after Mars, which we have shown to exhibit charge exchange induced exospheric X-ray emission. These findings reveal the unique, unparalleled capabilities of X-ray observations for remote, global imaging of the solar wind interaction with planetary atmospheres, a process which may have considerable impact on the atmospheric evolution and even on astrobiology.

References:

- Dennerl, K. et al., “Solar system X-rays from charge exchange processes”, AN 333, No. 4, 324-334, 2012
- Dennerl, K., “Charge Transfer Reactions”, Space Sci. Rev. 157, 57-91, 2010
- Dennerl, K., “X-rays from nonmagnetic planets”, Adv. in Geosciences., 53-74, 2009
- Gunell, H. et al., “Simulations of solar wind charge exchange X-ray emissions at Venus”, GRL 34, 3107, 2007
- Dennerl, K. et al., “Discovery of X-rays from Venus with Chandra”, A&A 386, 319-330, 2002

K. Dennerl

The non-thermal interstellar medium

The non-thermal components of the interstellar medium related to relativistic particles are studied via models which predict the photon emission from radio to gamma rays, supplemented by particle measurements near the earth. This project contributes to the science of Fermi and other missions. A global multi-wavelength spectral energy distribution of the non-thermal Galaxy illustrates one major application of the model.

Relativistic particles - hadronic and leptonic - in the Galaxy produce a wide range of emissions from radio to gamma rays, and observations thus allow very detailed studies of the non-thermal processes in the interstellar medium. Space missions including Fermi, CGRO, INTEGRAL, WMAP, Planck are relevant, as well as direct measurements of cosmic rays – the Milky Way is the only galaxy for which such *in-situ* data are available in addition to electromagnetic. Our information is hence far more complete than for extragalactic objects. The GALPROP project, an international collaboration originated and coordinated at MPE, models the non-thermal Galaxy in 3D, using a theory-based numerical approach to particle propagation, and extensive astronomical input on Galactic structure.

Fig 1 shows the high-energy spectrum of the inner Galaxy from 100 keV to 100 GeV, showing how each of the components contributes. This forms the basis for a detailed understanding of the astrophysics of the processes involved.

Fig 2 shows the spectral energy distribution of the Galaxy as would be as seen by an external observer, from radio to gamma rays, as well as the escaping relativistic particle injection into the intergalactic medium. This had not been possible previously at this level of detail, now based on the current model. It demonstrates that the Galaxy is a "lepton calorimeter", and that the energy outputs in radio and gamma rays are about equal.

The model has also been used to analyse the synchrotron emission and magnetic fields in the Galaxy using WMAP polarization data, and use in the Planck mission data analysis is ongoing.

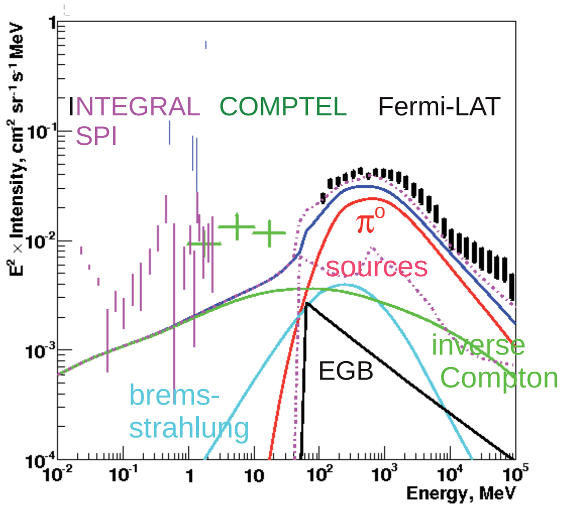

Fig 1: Inner Galaxy spectrum. GALPROP model and data

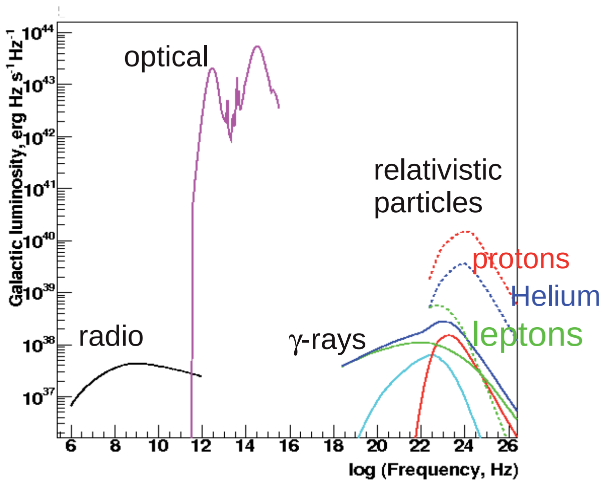

Fig 2: SED of the Galaxy for an external observer.

References

- Strong et al., 2007, Ann Rev Nuc Part Sci. 57, 285
- Strong et al., 2010, A&A 722, L58
- Strong, Orlando & Jaffe, 2011, A&A 534, A54

A. Strong, et al.

A catalogue sharing and data products access tool

A catalogue sharing and data access tool was developed for the study of the X-ray sources in the region of the Small Magellanic Cloud based on an XMM-Newton survey covering about 5.7 square degrees. The X-ray catalogues comprise ~5000 detections of ~3000 individual X-ray sources. The aim of the tool is to provide an easy and flexible access to selected source samples with all available information including X-ray source properties and created products, as well as results from correlations with various other catalogues (X-ray and other wavelengths). The tool is adopted for the use with eROSITA.

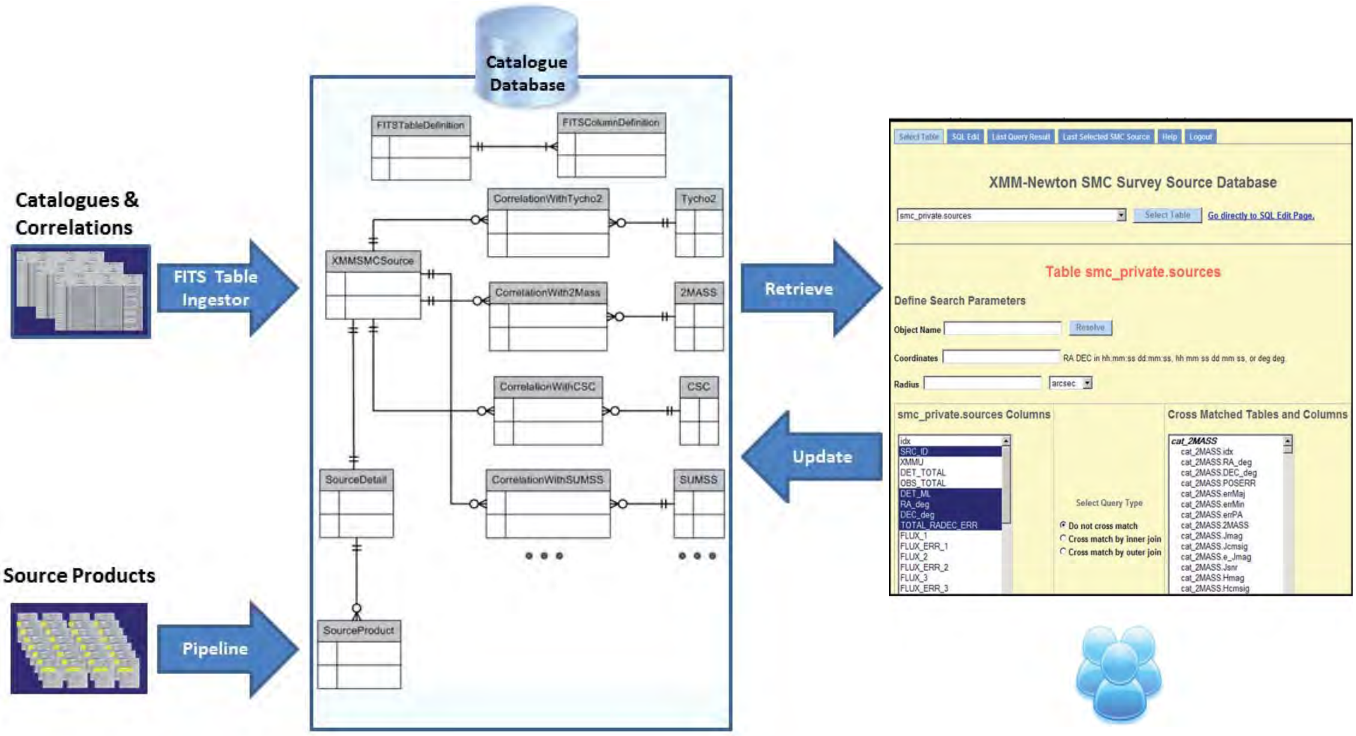

The tool consists of two main parts, a command line script (FITS table ingestor) which enters all available information into a database and an access interface which retrieves and visualises the information requested by the user from the database (see figure).

A. FITS table ingestor and database design - Generic FITS binary table upload to MySQL database in Java. - Multiple database schemas, and tables. - Upload any number of catalogues, and correlation results. - Extract metadata from the uploaded table which are used in the database browser in the web interface (e.g. units, parameter descriptions). - Additional metadata of source products can easily be entered into the database with MySQL scripts by the pipeline process.

B. Access interface - Authorisation support for access to different parts of database (core users, collaborators, public). - Simple cone search and links to external services e.g., Simbad, Vizier. - Full SQL query editing. - Complex SQL query generation, joining multiple catalogues and cross-match results. - Download query results in various file formats. - Enter additional information (comments, references) on sources manually.

F. Haberl, J.W. Kim, R. Sturm, H. Brunner, G. Lemson

eROSITA – Instrument Overview

eROSITA is the main instrument on board of the Russian „Spektr-Rentgen-Gamma“ (SRG) mission, scheduled for launch late 2014. The primary mission goal is to perform an X-ray all-sky survey lasting for 4 years. eROSITA consists of 7 identical telescopes, each equipped with nested Wolter-I mirror modules + pnCCD-cameras. The design of the instrument is driven by the goal to detect 100.000 clusters of galaxies in order to constrain cosmological parameters including Dark Energy. MPE is responsible for the design, development and integration of the instrument. Furthermore, also the software development for the data analysis is led by MPE.

Status: The complete instrument („protoflight model“) successfully survived the qualification tests (acoustic noise, vibration, pyro-shock, thermal-vacuum). The first four mirror modules are already delivered to MPE, and their expected X-ray performances have been verified.

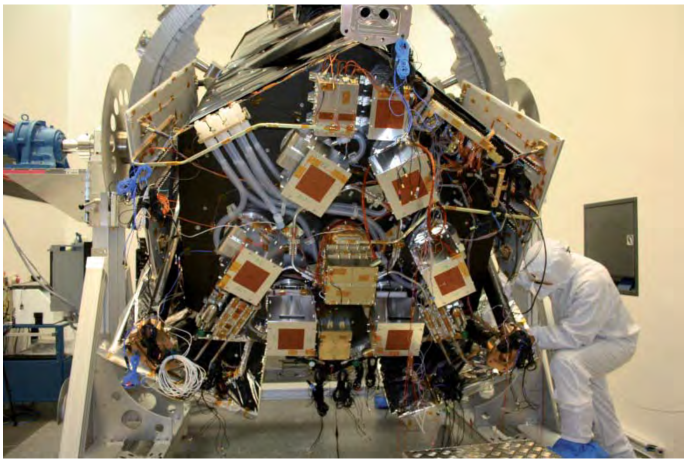

eROSITA, 3.5m tall, 800kg heavy, hanging on a crane during the qualification tests (left); inspection of the front entrance after vibration tests (top right); the camera platform before mounting the MLI (bottom right). The 9 electronics boxes, and the complicated cooling and purging system are seen. This protoflight model was equipped with one real mirror and camera plus six mass dummies each.

P. Predehl on behalf of the eROSITA Team

Simulating the eRosita extragalactic sky

Starting 2015, eRosita onboard SRG will map the entire sky in X-rays up to 10 keV, with an angular resolution and a sensitivity unprecedented over this area. The extragalactic part of the survey will unveil ~10^5 galaxy clusters and ~3 millions of Active Galactic Nuclei (AGN) forming the basis of cosmological and evolutionnary studies. Accurate simulations of the eRosita sky are required for the mission preparation and for the scientific analysis phase.

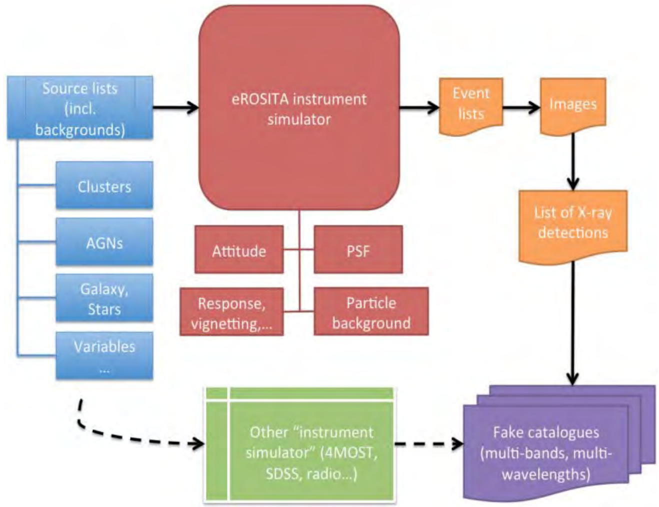

Fig. 1 – *the eRosita simulation process. Current works make use of the SIXTE software (C. Schmid, Bamberg Obs.) to generate "raw" simulated event lists describing the arrival of photons onto the detectors.*

As part of the **pre-launch** effort, realistic simulations are essential in order to formulate forecasts, coordinate follow-up strategies and prepare analysis tools adapted to the scientific goals (Merloni+ 2012).

After launch, simulations will be key in interpreting the large samples of extragalactic objects (AGN and clusters) collected during the survey. For example, the derivation of precise cosmological constraints using galaxy cluster mass functions requires precise knowledge of selection biases and measurement uncertainties, only achievable through realistic simulations (e.g. Böhringer+ 2001, Vikhlinin+ 2009, Clerc+ 2012).

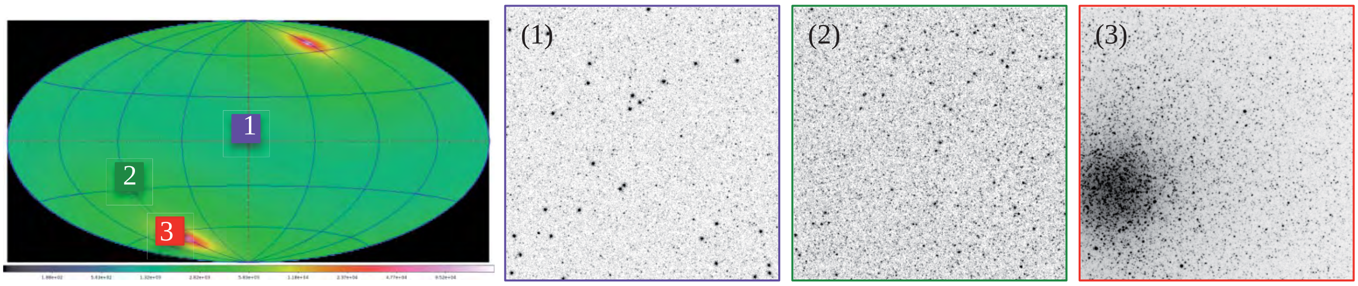

Fig. 2 – *Left: simulated eRosita exposure in equatorial coordinates (J. Robrade, Hamburg Obs.) Right: simulated 3.6×3.6 deg^2 fields at different locations: (1)* ***equatorial*** *(T_{exp}~1.6 ks) ; (2)* ***intermediate*** *(~4 ks) ; (3)* ***polar*** *(20-200 ks). Simulated fields are actually more than single images and embed the spectral signal of X-ray sources: AGN at different obscuration levels, galaxy clusters at various temperatures and distances, etc.*

References:
• Böhringer, H. et al. 2001, A&A, 369, 826
• Clerc, N. et al. 2012, MNRAS, 423, 3561
• Merloni, A. et al. 2012, eRosita science book, arXiv 1209:3114
• Schmid, C. et al. 2010, AIP Proceedings, 1248, 591-592
• Vikhlinin, A. et al. 2009, ApJ, 692, 1033

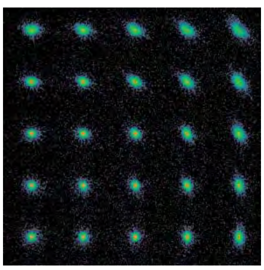

Fig. 3 – *Knowledge of the eRosita point spread function is critical in discriminating clusters from AGN. Measurements on real mirrors from* PANTER *(shown here at different focal plane positions, on-axis being at the bottom-left, grid step of 5 arcmin) are used as input of our simulations.*

N. Clerc on behalf of the eRosita collaboration

eROSITA point source follow-up: strategies and resources

The eROSITA survey is expected to detect about 4.000.000 point-sources, most being AGN. Thus, there is strong need for an interface capable of dealing with large amount of data and that allows the exploitation of the data in real time. Here we present the basic concept and the structure that we are planning for the database and the interface.

The eROSITA data will provide an all-sky X-ray map 30 time deeper than ROSAT. This, together with the plethora of wide or all-sky maps at other wave-lengths (see GALEX, WISE, PanSTARRs, Skymapper, VHS, DES, etc), will allow us an unprecedented synergy across the entire spectrum. In order to do that, two things needs to be taken into account:

A: The resolution of eROSITA is not good enough for a simple match in coordinates between the X-ray and any other catalog. For these purpose, following Budavari&Szalay, (2008) we developed a code that, using Baeysian statistics, takes into account spatial and physical properties (e.g. magnitude) information simultaneously in at least 2 wavelength, in order to obtain the most likely correct association. At the moment the code is tested on XMM-COSMOS data, cut at the depth of eROSITA and using simultaneously Optical and MIR photometric catalogs for the associations. Comparing the results with the Maximum Likelihood technique on the same field (Brusa+ 2010) we find perfect agreement, suggesting that we can proceed in extending the number of catalogs and properties simultaneously used for the match (Salvato+, 2013 in prep).

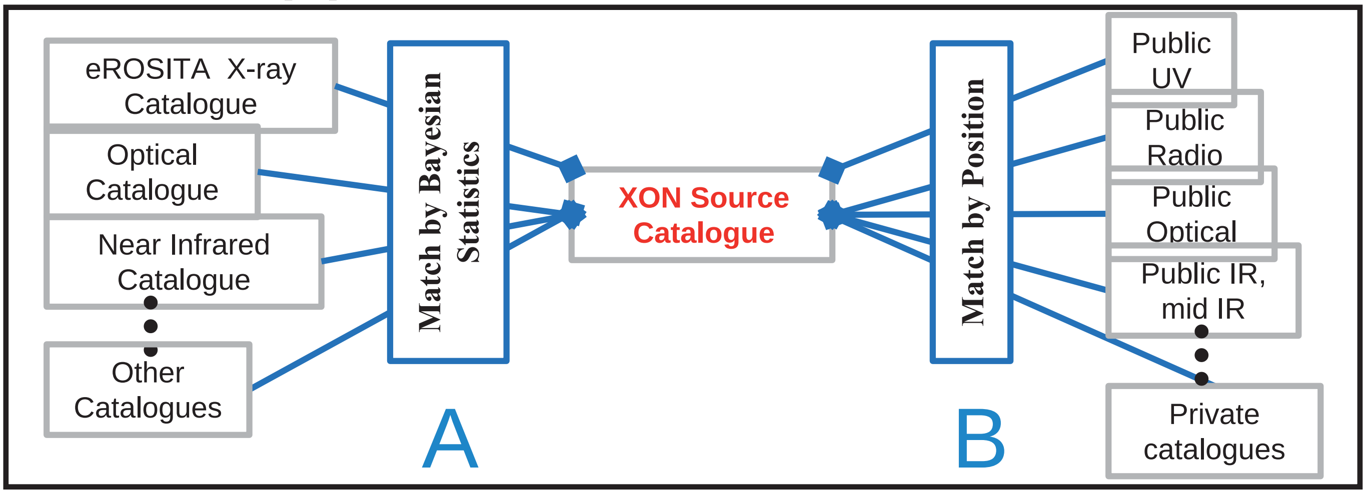

B: For each of the likely counterparts to a X-ray source, a reliable Spectral Energy Distribution (SED) needs to be construct using multi-band photometry measured in the same aperture. Once an association from the X-ray to a counterpart at longer wavelength is available, we can proceed in gathering all the information from other public or private catalogs. In case of photometric catalogs, we need to assure that only catalogs with total aperture are uploaded. When this is not the case, the catalog needs to be previously converted, accordingly.

We are currently trying to quantify the necessary resources, both in terms of hardware, software and man power for the implementation of such a system.

References: *Budavari&Szalav, 2008, ApJ, 679, 301, Brusa+, 2010, ApJ, 716, 348*

M. Salvato, J. Kim, G. Lemson, F. Haberl, H. Brunner, A. Merloni, T. Budavari
for the eROSITA consortium

The eROSITA Ground Segment

From Photons to Source Catalogs

In parallel with the eROSITA hardware development, work on a software system to support the operation of the eROSITA telescope is under way. As its core component, an eROSITA data processing pipeline creates a standard set of calibrated data products and X-ray source catalogs. In addition, tools for an interactive, in-depth analysis of the data are provided. Other functions include instrument health monitoring, archiving and managing data access. The software system is developed by an MPE-led team of up to 15 staff members, postdocs, and PhD students at six eROSITA consortium and associated institutes. It is currently transitioning from code developement to testing and integration.

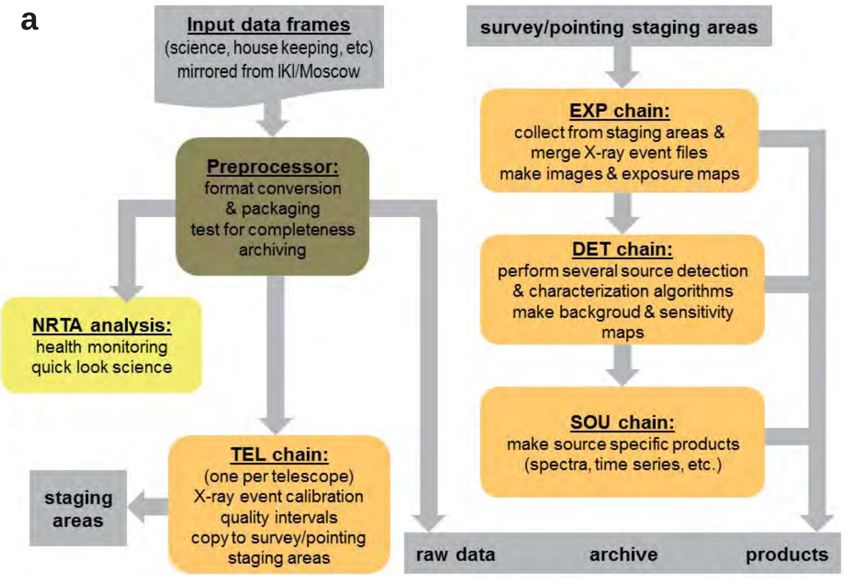

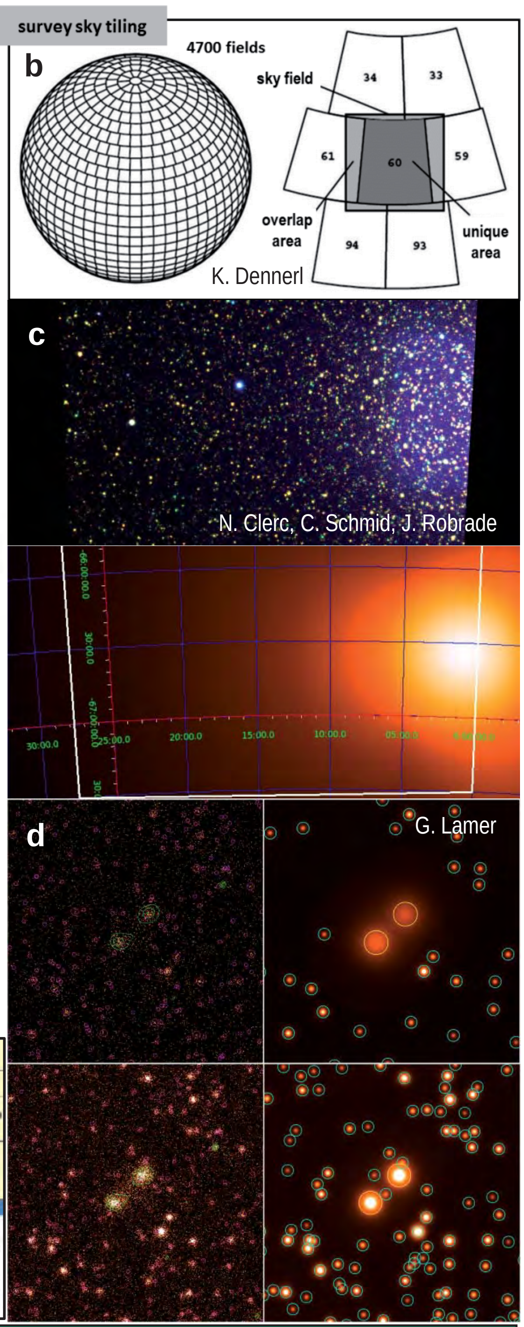

Clockwise from top left: **a.** Layout of eROSITA data processing pipeline: four task chains create calibrated event lists (TEL), images and exposure maps (EXP), source catalogs (DET), and calibrated source level products (SOU) **b.** Sky tiling: all-sky survey data are processed in 4700 approx. equal-area fields **c.** Simulated eROSITA image of all-sky survey ecliptic pole region and corresponding exposure map **d.** Results of source detection runs: shallow and deep fields; left: photon images, right: best fit models **e.** Sample screen shot of preliminary version of eROSITA source catalogs access and cross-matching tool

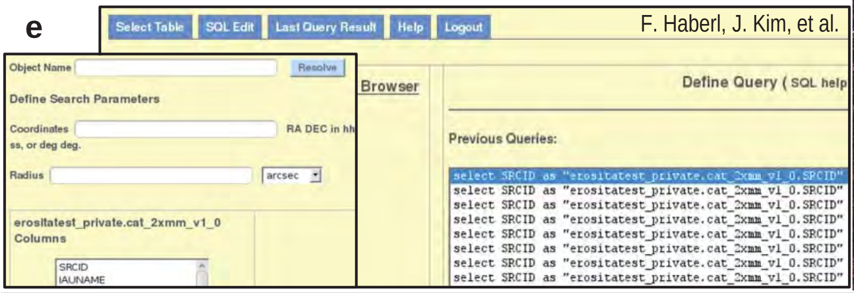

H. Brunner on behalf of the eROSITA software team

The eROSITA in-orbit calibration and performance verfication

Changes of the on-ground calibration performed at PUMA and PANTER has to be verified and adjusted after launch due to (e.g.) finite PANTER source distance and radiation damage increasing the CTI. This is done via celestial sources and an internal Fe-55 calibration source.

Several important celestial targets are only visible for a short period, and thus a flexible programme will be set up to observe as many as possible of these targets. The order of the calibration subjects will have to be adjusted according to the actual launch date. Images below show A2199 (left) and Cygnus Loop (right). A detailed list of target candidates is available at http://www.mpe.mpg.de/~mjf/CalPV/

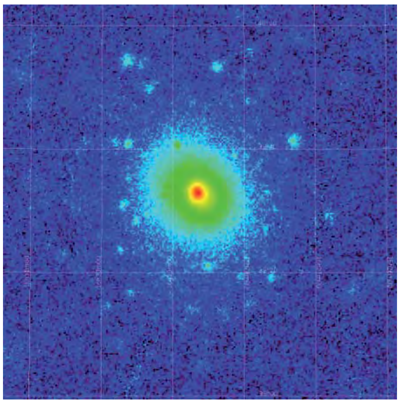

Calibration subject:
Commissioning
Plate scale and boresight of the 7 modules
Gain and CTI
Filter integrity (launch and micrometeorites)
Soft X-ray response and contamination monitoring
XUV response and contamination monitoring
Power-law type spectrum
Effective area and vignetting
Flatfield and vignetting
PSF
X-ray baffle (mosaic or mini-survey)
Masked mode
Timing
Miscellaneous
Performance verification

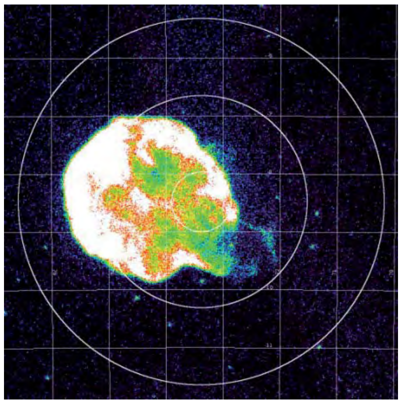

Commissioning: During the transfer phase to L2 switch-on of the cameras will take place one after another. After initial health checks the cameras will be operated with ``Closed" and ``CalClosed" filter wheel positions. Several instrument parameters will be fine-tuned such as lower event (trigger and split) thresholds or parameters related to the on-board rejection of minimum ionizing particles (MIPs). After turning the filter wheel into science position the filter integrity can be checked by the response to optical light, e.g., of globular clusters.

Calibration: Celestial targets dedicated for a specific calibration subject have to be chosen, which should be X-ray bright (statistics) but not too bright in X-rays (pile-up) and optically. Simultaneous observations of the 7 eROSITA cameras are an important tool for cross-calibrating the instruments. A mini-survey (several great-circle scans across the ecliptic poles) would be useful to determine spacecraft parameters (e.g., time delays of star tracker relative to CCD cameras) or single-reflection straylight effects, e.g., by passing close to Sco X-1.

Monitoring: To verify presumably variable calibration parameters such as CTI or contamination, non-variable sources on times scales of the eROSITA lifetime are preferred for monitoring, such as the internal Fe-55 calibration source or supernova remnants or isolated neutron stars.
These targets should be scheduled regularly like every 6 months after each all-sky survey, and restart of the survey phase without gap afterwards.

References:

. M. Freyberg & K. Dennerl, SPIE 8448, 2012

M. Freyberg, H.Brunner, K. Dennerl, P. Friedrich

Spectral response of the ROSITA detectors

The eROSITA instrument will perform observations in the low and medium X-ray energy regime. For the characterization of the seven PNCCDs for this instrument, we conducted spectral measurements and quantum efficiency measurements at the synchrotron BESSY II. In addition, we performed simulations in order to reproduce the measured spectra and to understand their formation.

The quantum efficiency (QE) of a detector describes the ratio of detected photons to incident photons. The QE is mainly influenced by the material and thickness of the detector photon entrance window. The QE curve exhibits absorption edges characteristic for the elements contained in the entrance window (Fig. 1).

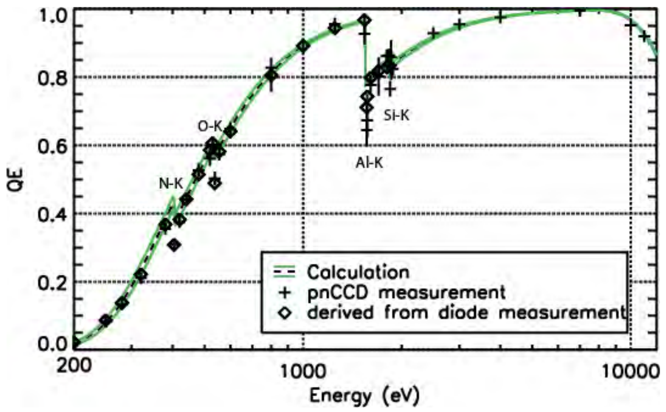

Fig. 1: Quantum efficiency measured at the synchrotron BESSY II and compared to calculations.

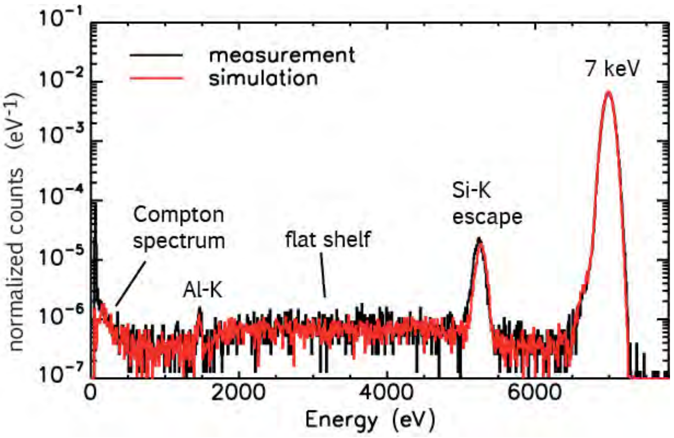

Fg. 2: Spectrum of monochromatic photons with E=7 keV, measured at the synchrotron BESSY II and simulated with Cosima/Geant4.

The spectral redistribution function describes the distribution of photon counts in a spectrum. A detector typically shows an intrinsic instrumental background that has to be separated from the astronomical data. In order to be able to interpret the measurement results correctly it requires the characterization and understanding of even small features of the PNCCD spectral resdistribution function. As shown in Fig. 2, the spectral redistribution function shows a Gaussian peak at the incident photon energy (7 keV), but also features with reduced event energies caused by different physical mechanisms inside the detector. For example, the escape of Si-K fluorescence photons out of the sensitive detector volume causes the Si-K escape peak. The transport of electrons across the interface between sensitive and insensitive volume in the photon entrance window is responsible for the flat shelf in the spectrum. By comparing Monte-Carlo simulations with the measured spectrum, all relevant mechanisms in the formation of a spectrum could be identified for the entire energy range of interest from 0.3 keV to 10 keV.

References:

- S. Granato, “The response of silicon PNCCD sensors with aluminum on-chip filter to visible light, UV- and X-ray radiation,” Ph.D. dissertation, Universität Siegen, Oct. 2012.
- S. Ebermayer et al. , “Quantum efficiency measurements of eROSITA pnCCDs,” in Proc. SPIE, vol.7742.. 2010, pp. 77 420U–10.

S. Granato on behalf of the eROSITA team

Bayesian inference for signal separation -
A feasibility study for eROSITA on SRG

The Background-Source Separation (BSS) technique provides for a rigorous approach to source detection and characterization in image analysis. Bayesian probability theory is used to gain insight into the co-existence of background and source signals through a probabilistic two-component mixture model, providing consistent uncertainties of background and sources. Applications to real data, collected in the X-ray part of the electromagnetic spectrum, have shown that the BSS technique improves the detection of sources and their structural parameters, especially the ones with low-surface brightness, with respect to standard techniques.

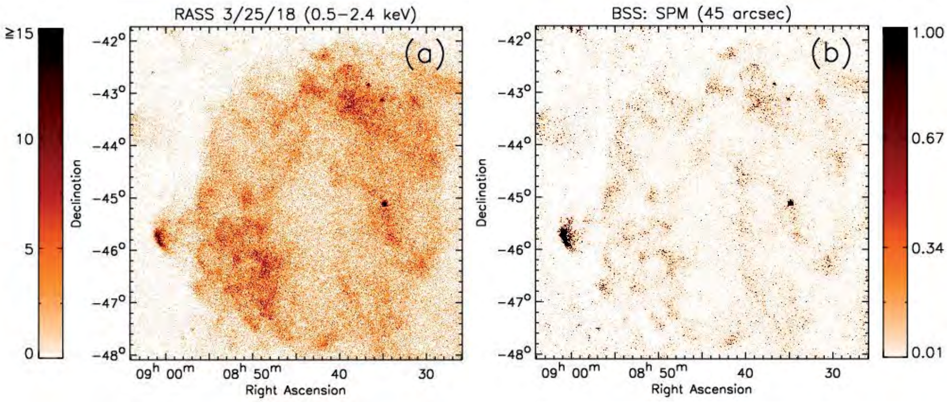

Application of the BSS algorithm [1] to *ROSAT* All Sky Survey (RASS) [2] data sets. *ROSAT* performed the first imaging all sky survey in the energy range (0.1-2.4) keV. e*ROSITA* [3] will perform an all sky survey 20 times more sensitive than RASS in the common energy range and it will extend the imaging survey up to energies of 10 keV.

Panel (a) Photon count image of the RASS field RS932518n00 in the hard energy band. The original image shows values in the range 0-136 photon count/pixel. **Panel (b)** The BSS algorithm provides source probability maps (SPM) in a multiresolution analysis (above an SPM at 45 arcsec resolution is shown). SPMs display the probability that source counts are present in pixels and in pixel cells, i.e. collecting information of neighbouring pixels. The color bar indicates source probability/pixel.

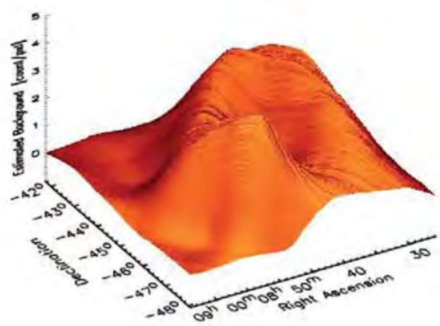

On the left: Background amplitude map derived analysing the image in panel (a) with the BSS algorithm. The background amplitude map is well-defined and capable to cope with steep gradients in the data. Note: the foreground peak is a diffuse emission caused by the Vela Junior supernova remnant (SNR), the central emission is the shock front caused by the Vela SNR and in the background is the emission caused by Puppis A SNR.

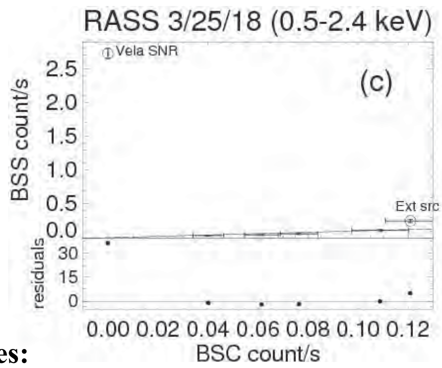

Panel (c) Comparison of estimated source fluxes as obtained by the BSS algorithm and the Bright Source Catalogue (BSC) [2]. The BSS technique provides larger values on fluxes for the Vela pulsar. The flux of the Vela pulsar and recovered by the BSS algorithm is confirmed by *XMM-Newton* observations.

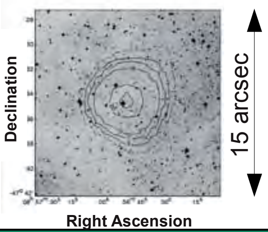

On the left: POSS-II R plate, centered on a newly discovered X-ray object. RASS contours in the (0.5-2.4) keV energy range are superposed.

References:

·[1] F. Guglielmetti, R. Fischer, V. Dose, 2009, MNRAS, 396, 165

·[2] W. Voges et al., 1999, A&A, 349, 389

·[3] P. Predehl et al., 2011, SPIE, 8145E, 247

F. Guglielmetti and the eROSITA team

Data Analysis for eROSITA CCD Detectors

X-ray measurements of eROSITA CCD detectors are analyzed in a standard way to gain comparable results. The analysis contains filtering of X-ray events, several correction steps, and generation of maps, overviews, and summaries. The results are used to monitor changes in performance when testing different operation parameters (timing, voltages, currents) and will help to compare setups (laboratory versus flight electronics). They are of special importance as basis for selecting the flight detectors and test models.

The eROSITA CCDs are single-photon X-ray detectors with energy and spatial resolution. The analysis extracts and corrects the events from the data. The main steps are

- Offset subtraction and applying event thresholds: Both calculations are necessary for data from laboratory setups; the flight electronics will carry them out by itself for data reduction reasons.
- Recombination: Charges from an interaction may be collected in more than one pixel. The analysis has to recombine them.
- Calculation and application of gains and charge transfer efficiencies which are inherent to the electronics and CCD.
- Calculation and application of non-linearity factors: correct small non-linearities of the electronics.

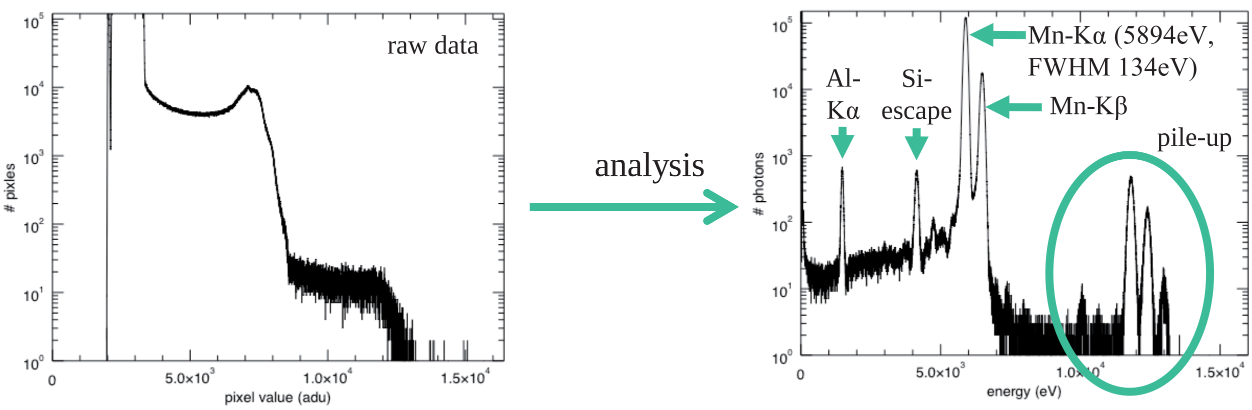

The analysis extracts a couple of characteristic numbers from measurements such as energy resolution, channel-by-channel gain and charge transfer efficiency, charge splitting (distribution of charges generated in X-ray interactions over the pixels), pixel-by-pixel offsets and noise, bad pixels.

These numbers are usually used for comparing measurements in order to determine the impact of varied timings, voltages, or currents on performance, i.e. to optimize parameters. Keeping parameters constant but changing the CCD allows to compare these CCDs. This way the best CCDs are selected for flight. Using a well tested CCD in a new setup such as the flight version of the readout electronics will help to debug and optimize this setup. Finally the gained numbers document the performance for later reference.

The analysis software is

- in a mature state: the standard algorithms are widely tested and well understood
- kept “simple” and stable: there is one file containing all the parameters and no interactive GUI to avoid unnecessary and error-prone complexity of the code; this makes the analysis easy to use
- modular: parts of the software (i.e. classes) can be reused e.g. for special analysis tasks such as health monitoring with test pulses or inject pulses
- able to read full CCD frames as well as reduced data
- optimized for speed by using fast internal structures

References:

• R. Andritschke, et al., “Data analysis for characterizing PNCCDs”, Proc. IEEE NSS, 2008, pp. 2166-2172

R. Andritschke, G. Hartner

The eROSITA thermal control system

eROSITA is the core instrument on the Spektrum-Röntgen-Gamma (SRG) mission. The thermal control system mainly consists of the following components: temperature control of the telescope structure, heating of the mirror modules, cooling of the camera electronics and cooling of the CCD detectors. Special attention is paid to the last point, since it is the most critical one. The complex assembly with the sevenfold symmetry of the eROSITA telescope requires an innovative design. Large distances in combination with a very low operating temperature between -90°C and -100°C place high demands on the cooling chain. In total, three different types of low-temperature ethane heat pipes are used to transport the heat from the cameras to two radiators outside the telescope structure. Extreme environmental temperature gradients with the Sun on the one side and the cold space on the other present a real challenge not only to the cooling systems, but to the overall thermal control.

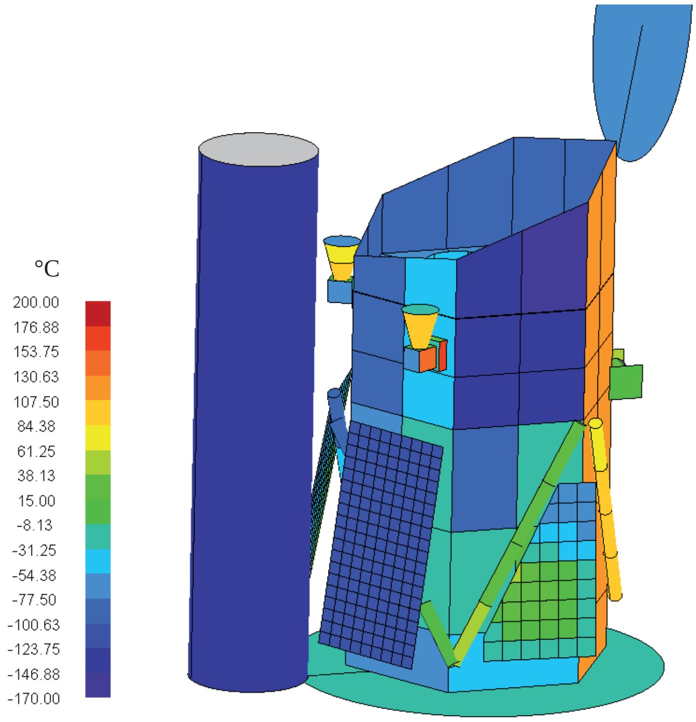

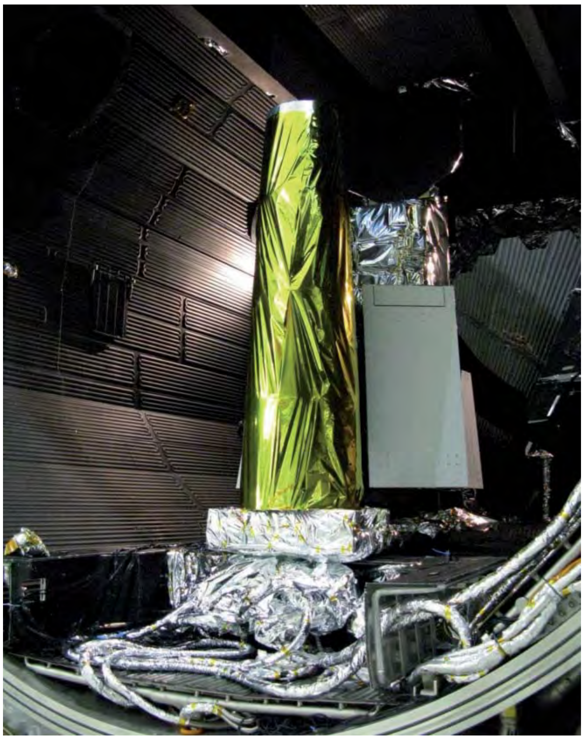

A thermal model of the complete telescope was used to predict the thermal behaviour of the telescope and its subsystems (left). Through various tests, this model could be improved step by step. The most complex one was the solar simulation test with a dummy of the Russian ART-XC telescope and the complete eROSITA telescope, including a flight-like thermal control system. The test was done in January 2013 at the IABG facilities in Ottobrunn, Germany (right).

About 200 temperature sensors, distributed over the whole structure and all subsystems, monitored the relevant temperatures during the test. They were within the predicted intervals and therefore not only verified the complete concept but also enabled a further refining of the thermal model. This, in turn, allows for a reliable prediction of the thermal behaviour during the mission.

M. Fürmetz for the eROSITA team

Development and Optical Performance of the eROSITA Mirror Modules

After an extended mirror development program, the integration of eROSITA flight mirror modules started in early 2011 and shall be finished in November 2013. Parallel to the mirrors we have developed an X-ray baffle to suppress stray light. X-ray tests after delivery, X-ray baffle mounting and environmental tests follow. Final steps will be calibration and integration into the telescope structure.

eROSITA’s X-ray telescope consists of 7 co-aligned mirror modules (MM), each with 54 nested Wolter-1 electro-formed mirror shells with a focal length of 1600 mm and maximum diameter of 357 mm. The optical performance of each MM is being tested in MPE’s X-ray test facility PANTER. After the acceptance test the X-ray baffle is being mounted and aligned by optical means. It consists of precisely shaped and welded concentric Invar foils designed to reduce about 90% of the single reflections from off-axis sources while the on-axis collecting area is preserved; the impact on the off-axis area is acceptably low.

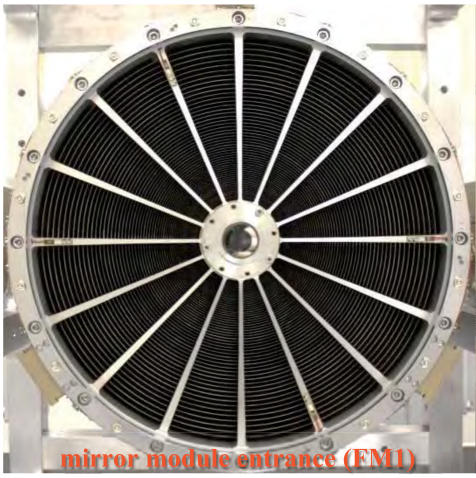
mirror module entrance (FM1)

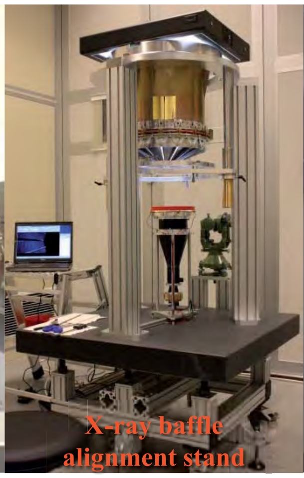
X-ray baffle alignment stand

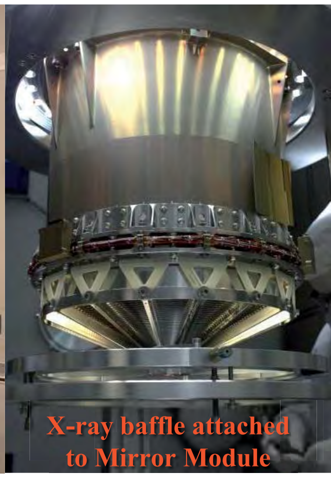
X-ray baffle attached to Mirror Module


mirror module on the shaker

The first completed eROSITA mirror module – FM1 – was delivered in December 2012 and is subject to an extended sequence of X-ray tests in the PANTER facility. Seven of eight requirements are fulfilled, while one is marginally out of specification.

	Requirement		Measurement		
	Orbit	derived for PANTER	Acceptance test	test with X-ray baffle	test after vibration
HEW @ 1.49 keV	< 15’’	< 15’’	16.1’’±0.2’’	16.5’’ ± 0.3’’	16.8’’ ± 0.2’’
HEW @ 8.04 keV	< 20’’	< 20’’	15.2’’±0.1’’	14.6’’ ± 0.3’’	15.0’’ ± 0.3’’
W90 C-K @ 0.28 keV	< 90’’	< 90’’	~89.8’’	~91.6’’	~91.0’’
Eff. Area @ Al-K	> 350 cm^2	> 363.6 cm^2	387.5 cm^2 ± 7.2 cm^2	406 cm^2 ± 30.6 cm^2	387.5 cm^2 ± 8.3 cm^2
Eff. Area @ Cu-K	> 20 cm^2	> 21.0 cm^2	24.8 cm^2 ± 0.8 cm^2	23.3 cm^2 ± 0.5 cm^2	23.8 cm^2 ± 0.5 cm^2
Micro-roughness	< 0.5 nm	Scattering Cu-K < 15.7%	Scattering Cu-K 10.8%	Scattering Cu-K 9.5%	Scattering Cu-K 13.4%
Focal length	1600±10 mm	1600±10 mm	1600.58±0.5 mm	1600.90± 0.5 mm	1600.82± 0.5 mm
Optical axis alignment	< 30’’	< 30’’	0’’±21’’	0’’ ± 21’’	36’’ ± 14’’

References:

- Bräuninger et al, “Calibration of hard X-ray optics at the MPE test facility PANTER”, SPIE 5168, 283 (2004)
- Friedrich, P. et al., “Development and testing of the eROSITA mirror modules”, SPIE 84431S (2012)
- Predehl, P, “eROSITA”, SPIE 84431R (2012)

P. Friedrich on behalf of the eROSITA team and the PANTER team

Determination of the eROSITA mirror HEW with subpixel resolution

The Point Spread Function (PSF) of the eROSITA mirror modules is specified to have an on-axis Half Energy Width (HEW) of 15 arcsec. This is only slightly larger than the eROSITA pixel size of 75 microns, which corresponds to 9.6 arcsec at the PANTER test facility, where we measure the PSF with a prototype of the eROSITA CCD. We have developed a fast algorithm which provides a substantially higher spatial resolution by utilizing the information contained in the charge ratios of split events. By applying this algorithm to measurements where the CCD is systematically shifted in subpixel increments (typically in a 12 x 12 pattern), we are able to achieve an effective resolution of ~2 arcsec for specific pixel patterns.

Simulated CCD resolution for various combinations of patterns at different energies, for 12 x 12 subpixel raster scans

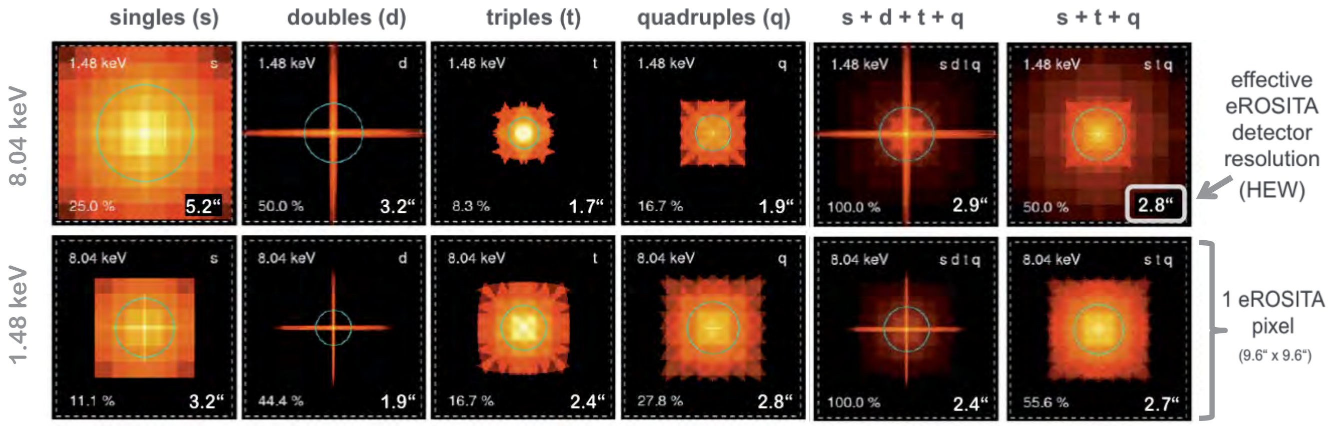

This algorithm can also be used to compute the two dimensional probability distribution for detecting a photon from an incident point-like beam, for each combination of photon energy, low energy (split) threshold, selected pixel patterns, and subpixel scan properties. These maps allow us to deconvolve the measured PSF and thus to minimize the influence of the spatial detector resolution on the determination of the eROSITA mirror HEW. After launch, we will apply the algorithm for improving the spatial resolution by reconstructing the subpixel positions to the science data.

Application of the subpixel reconstruction algorithm to ‚static' images obtained with eROSITA mirror shells
(left/right: without/with subpixel resolution)

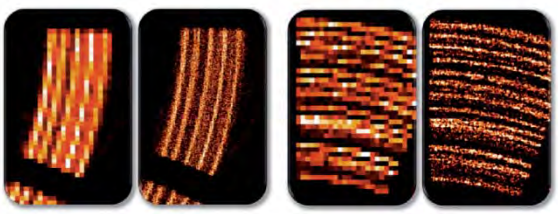

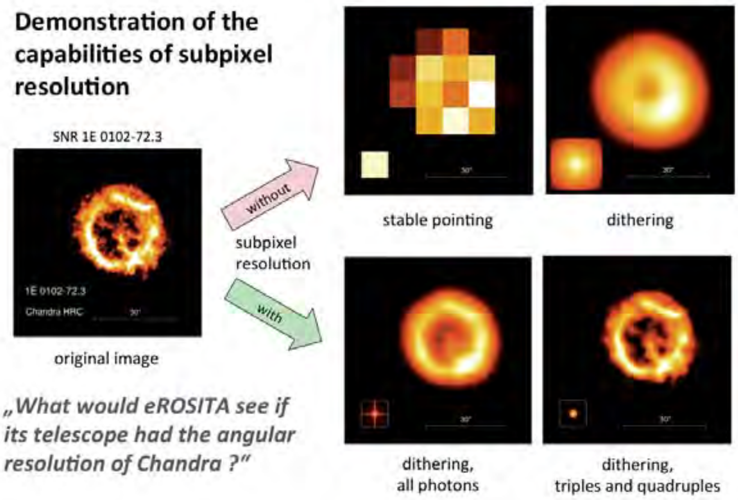

References:

- Dennerl, K. et al., "Determination of the eROSITA mirror half energy width (HEW) with subpixel resolution", Proc. SPIE 8443, 2012

K. Dennerl on behalf of the eROSITA team

eROSITA CCD Camera

The focal plane of the eROSITA space telescope will be equipped with seven CCD cameras developed by MPE. Their PNCCD sensor has been produced in the MPI semiconductor laboratory and measures precisely the energy in the range from 0.3 keV to 10 keV, position and time of incidence of single X-ray photons with high quantum efficiency. In various tests we determined the detector performance for eROSITA which means a significant improvement compared to the precursor camera on board of XMM-Newton.

We determined the camera properties by simulations and experimental tests. The spectral response and quantum efficiency of an eROSITA detector was measured at the synchrotron BESSY II. Verification of radiation hardness against protons in space was done in a series of irradiations tests at a TANDEM accelerator. The thermal model was studied at MPE and external test facilities to assure that the desired operating temperature of -95°C will be achieved. Tests on a shaker demonstrated the robustness of the camera against the vibrational load during satellite launch.

PNCCD	back-illuminated	450 µm thickness fully sensitive
Frame transfer CCD	image: 384 x 384 pixel	pixel size: 75 µm x 75 µm
Time resolution	9 ms / frame	50 ms / frame @ 0.7 W
Read noise	2.5 electrons rms	≈ no pixel defects
Energy resolution	52 eV @ 200 eV	131 eV @ 5.9 keV
Quantum efficiency	89% @ 1 keV	98% @ 10 keV
Radiation hardness	ΔFWHM/FWHM < 10%	7 years in space @ L2, T ≈ -100°C

Table I

eROSITA camera: X-rays hit the CCD image area via the aperture.

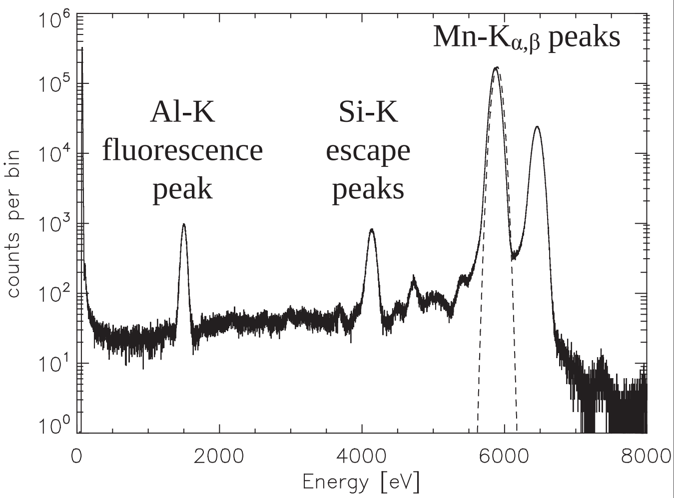

^{55}Fe spectrum measured with eROSITA EM detector under operating conditions as used for space.

References:
- N. Meidinger, R. Andritschke, F. Aschauer et al., Proc. SPIE, 8453, 2012
- N. Meidinger, R. Andritschke, W. Assmann et al., IEEE Nucl. Sci. Symp., 2010

N. Meidinger on behalf of the eROSITA team

Tests of operating parameters for eROSITA flight detectors

MAX-PLANCK-GESELLSCHAFT

MPE

The eROSITA mission will be equipped with seven identical PNCCD detector modules for time-, spatially- and energy-resolved detection of x-rays in the range of 0.3 keV to 10 keV. In our x-ray test facilities the optimal operating parameters for the eROSITA flight detectors including electronics and data acquisition system are precisely evaluated. This concerns in particular the voltage supply and the timing of analog and digital signals.

The supply voltages for the CAMEX readout ASIC and the PNCCD detector as well as the signals for the control and synchronization of signal readout and digitalization have been optimized with regard to detector performance and energy consumption. The results helped to establish benchmarks for the flight detector performance.
At our test facilities equipment is available to access all relevant signals and to check the signal quality of digital pulses. The signal timing can be monitored on a nanosecond scale, i.e. through the LVDS break-out flex (Fig. 1). For the test of the seven flight modules a standard test procedure has been developed. It includes the cross-checking of all electronic signals and the programming of the various components of the DAQ-System before every step of integration. Thus it provides maximum safety for the flight equipment while having good control of the actual detector performance.

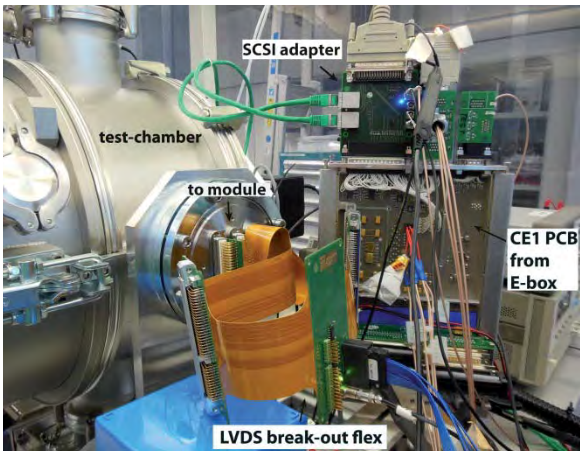

Fig 1: Test chamber for eROSITA flight detectors with front-end PCB, break-out flex for LVDS signals and various custom made adapters.

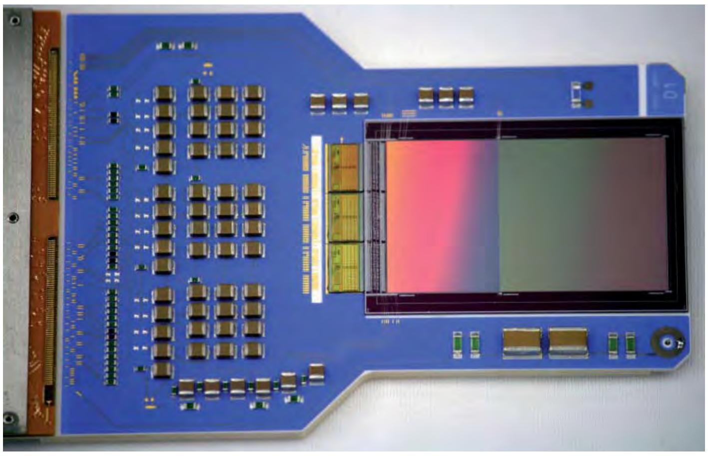

Fig 2: PNCCD detector module on printed ceramic board with three CAMEX chips and electronic circuits.

For the extensive testing of the detector a high degree of flexibility is required. In some pre-launch tests cooling or evacuation of the detector will not be possible. Thus the test procedure includes the possibility of checking the basic functionality of the detector and readout electronics under ambient conditions, as well as the precise determination of energy resolution, electronic noise and charge transfer inefficiency in UHV at 180 K. Envisaged values for the flight detectors are:
FWHM = 138eV @ 5.9 keV (Mn-Kα)
equivalent noise charge = 2.5 RMS
Measurements of already existing modules have shown that they fulfill these requirements.

References:

• N. Meidinger, R. Andritschke, F. Aschauer et al., Proc. SPIE, 8453, 2012
• J. Elbs, R. Andritschke, O. Hälker et al., Proc. SPIE, 7742, 2010

V. Emberger, S. Walther

4MOST - Facility Simulator

MAX-PLANCK-GESELLSCHAFT

MPE

The 4-metre Multi-Object Spectroscopic Telescope (4MOST) is a new instrument concept proposed for ESO's VISTA telescope. 4MOST team members at MPE have designed and implemented key parts of a complex simulator, which is used to optimise & evaluate 4MOST's instrumental design, and to maximise the scientific return from a planned 5-year sky survey.

The 4MOST focal plane will contain 2400 independently manoeuvrable Echidna-style fibre spines arranged over a ~4 deg^2 field, leading to several fibre-fed high-throughput spectrographs, capable of simultaneously collecting up to 1600 low resolution (R~5000) and 800 high resolution (R~25000) spectra. Crucially, 4MOST is both an instrument *and* a science project; at the heart of the 4MOST proposal is a 5-year duration sky survey, the main aim of which is to follow up targets detected by the soon-to-be-launched eROSITA and Gaia space telescopes, and to obtain redshifts for >10 million galaxies. The success of this complex project requires a detailed understanding of the strengths and limitations of 4MOST as it surveys the sky. This can only be achieved by modelling the whole system in software, hence we built the 4MOST Facility Simulator (4FS).

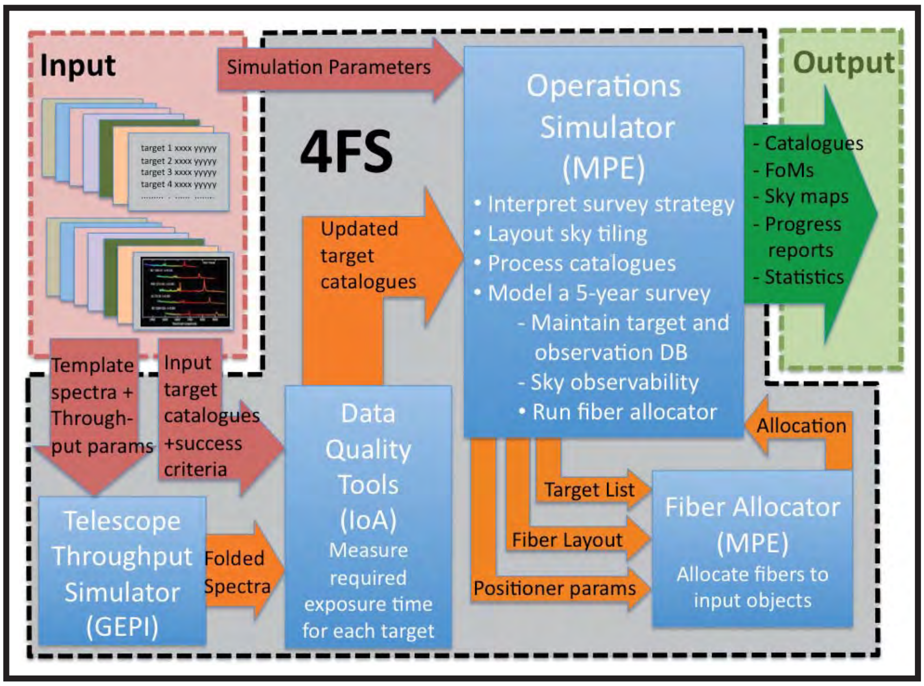

Figure 1. The components of the 4FS and their interfaces. The Throughput Simulator and Data Quality Tools are used to estimate required exposure times for a set of well-specified input targets. The 4FS Operations Simulator (OpSim) models realistically the planning, execution and evaluation of a 4MOST sky survey. The 4FS implements a prioritised targeting algorithm and incorporates the effects of adverse weather, lunation pattern and seasonal night length, as well as handling instrument failures and scheduled maintenance.

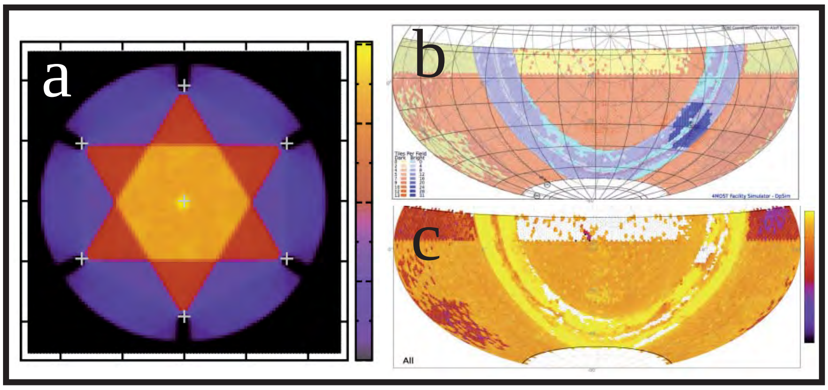

Figure 2. a) the density of fibre positioner deflections, **b)** executed sky tiling density map, and **c)** the success rate of observed targets. These are all standard OpSim data products which have already been used to inform the optimisation of the 4MOST instrument design, operation plan, and survey strategy.

References:
• De Jong et al,Proc.SPIE,2012,8446E..0TD
• Boller&Dwelly,Proc.SPIE,2012,8446E..0XB

T. Dwelly, Th. Boller, H. Böhringer and the 4MOST Facility Simulator team

Testing Optics for Future X-ray Missions

As part of a program to test new lightweight optics for future ATHENA+ type ESA X-ray missions, the MPE PANTER X-ray test facility beamline has been extended to allow the testing of silicon pore (SPO) and slumped glass (SGO) X-ray optic modules with focal lengths of up to 20m. In July 2012 the PANTER beamline extension, partly supported by ESA, was comissioned and a first set of SPO and SGO test optics were measured. The analysis of the measured PSFs yields half energy widths (HEWs) of ~22“ for the SPO module and ~55“ for the best SGO mirror. These values are in line with what is expected from the ray tracing predictions.

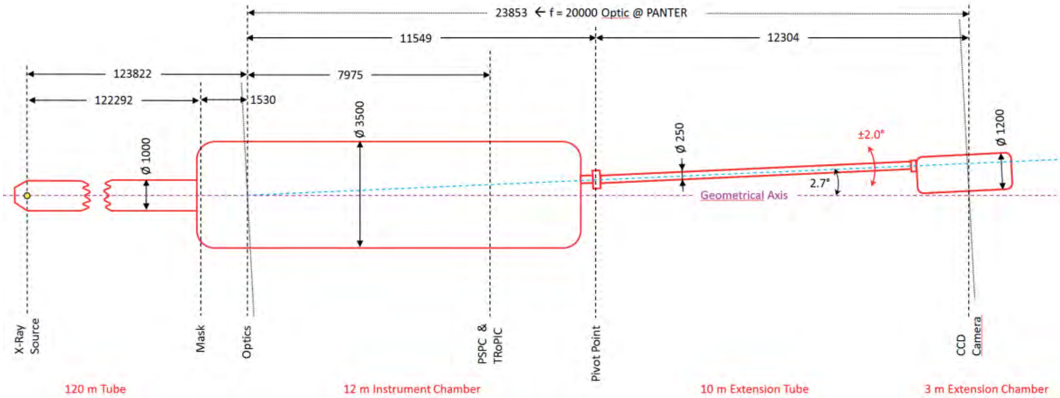

Figure 1: Schematic view of the fundamental dimensions of the X-ray test facility including the IXO extension as seen from above. All lengths are given in millimeters.

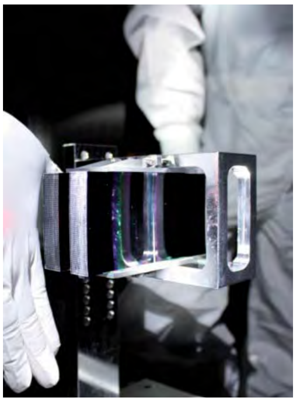

Figure 3: Two 21 layered SPO modules placed on PANTERs geometrical axis.

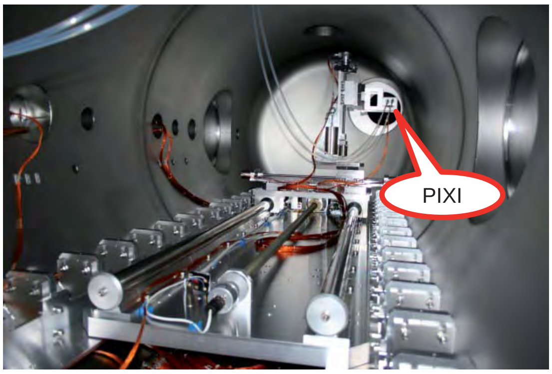

Figure 2: View into the new movable detector vacuum chamber with the translation stage holding the PIXI CCD camera.

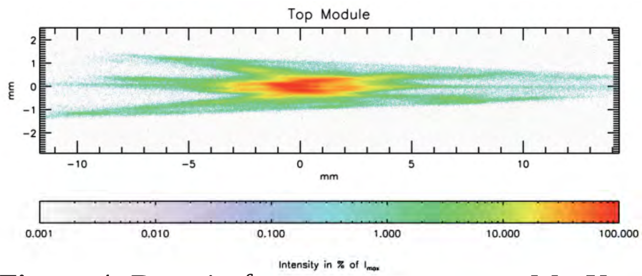

Figure 4: Deep in-focus measurement at Mg-K 1.25 keV of the PSF obtained for the top silicon pore optic (SPO) module (see Fig. 3 module on the right).

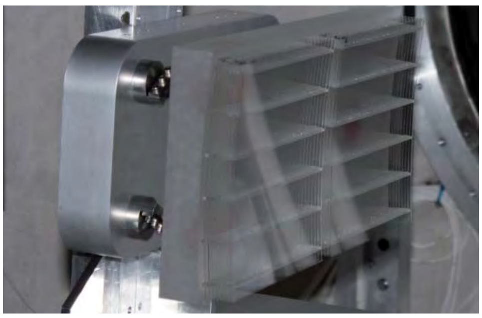

Figure 5: A8 layer (SGO) slumped glass optic mounted in the vacuum chamber at PANTER.

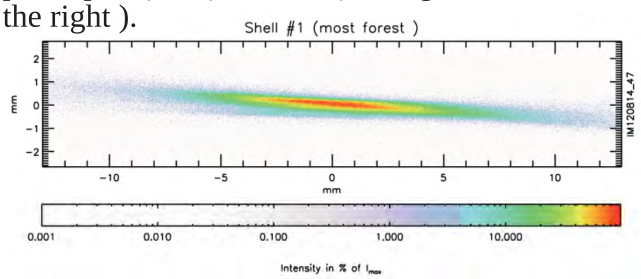

Figure 6: Deep in-focus measurement at Mg-K 1.25 keV showing the extent of PSF measured for the outermost shell of the slumped glass optics (see Fig 5 top-most shell).

V. Burwitz, W. Burkert, M. Freyberg, G. Hartner, B. Menz

Light-weight Segmented X-Ray Mirrors Made of Slumped Glass

Future X-ray observatories require a large collecting area combined with very good angular resolution. Light-weight mirror materials, such as thin glass sheets, are needed to achieve these aims within the mass limits. We are developing a technology based on indirect hot slumping of thin glass segments, which enables the production of parabola and hyperbola in one piece. Here we present the slumping process, our metrology methods and the results of a recent X-ray tests of several integrated glass sheets.

THERMAL SLUMPING ON CERAMIC We perform slumping processes using glass sheets of the type D263 with a thickness of 0.4mm on a mould made of a ceramic based on aluminium oxide. This material has a thermal expansion coefficient (CTE) close to the CTE of the glass type, and it is porous, so a vacuum pump can be used to improve the contact between glass and mould surface. The typical temperature profile uses a maximum temperature of typically 620°C; the entire slumping process takes 3 days.

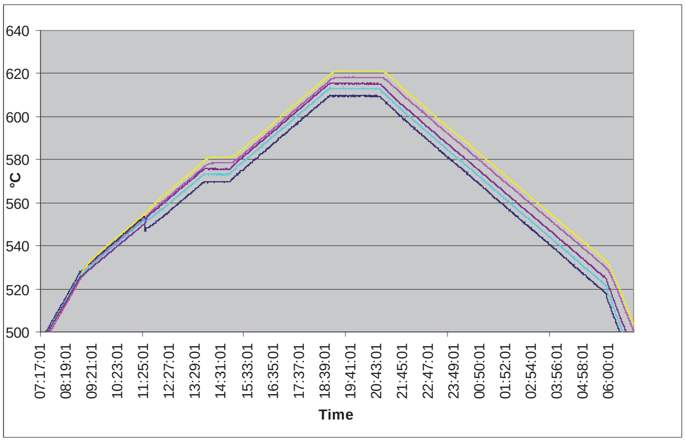

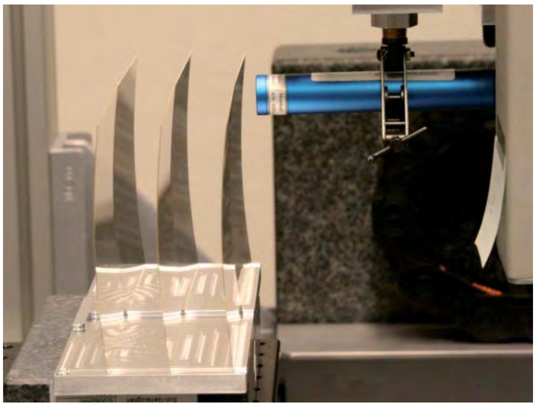

OPTICAL MEASUREMENT The slumped glass sheets are then integrated and measured on our high-precision 3D measuring table. Measurements are being carried out using a 1mm-grid along the optical axis of the mirror. The measured shape is compared with simulations, which shows the quality of the slumping process itself and where improvements can be made. Furthermore we made predictions for the X-ray test performed subsequently at the MPE testing facility PANTER. The image shows three glass sheets integrated for the PANTER test; the intersection between parabola and hyperbola is visible.

X-RAY TEST Three selected glasses have been measured at PANTER for their X-ray imaging qualities. The results for the half-energy width (HEW) lie between 64“ and 77“ for the three glasses. The two main error sources are the slumping mould (~50“) and the thickness variations of the glass (~15“), suggesting a very good reproduction of the mould surface by the glass. We now focus on improving the mould surface and remove the thickness variations of the glass sheets to enhance the quality of the mirror segments.

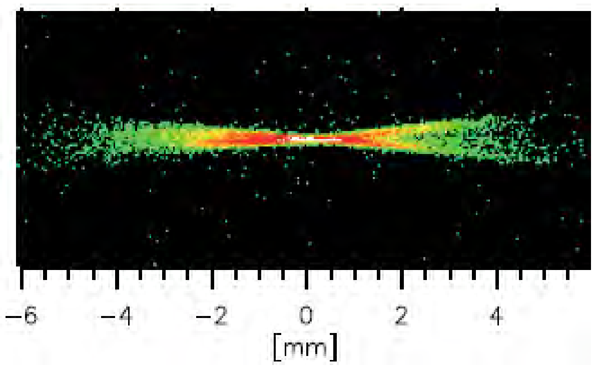

Within the last year we have started research on the integration of segmented glass mirrors, for measurements as well as the final telescope mounting. See poster by E. Breunig for details.

References:

• A. Winter et al.: “Light-weight glass optics for segmented X-ray mirrors”, 2012, Proc. SPIE, 8450, p. 84502E

A. Winter, P. Friedrich and E. Breunig

Alignment and Integration of modular X-Ray Mirrors

Future X-Ray observatory concepts are designed around a mirror systems with considerably larger collecting area than current missions but still require arc-second resolution to enable new scientific discoveries. To realize such mirror systems, modular optics, based on thin segmented glass mirrors have been investigated at MPE in the recent years. This Phd project focuses on advancing technology and procedures needed to align and integrate such optics, maintaining or even improving the shape accuracy of it‘s individual mirror segments. The research effort can be summarized in three main areas briefly described below.

Handling and initial Alignment

The first and very crucial step in the integration process is the transfer of the raw mirror from ist production mould or coating jig into the alignment and integration system. It is important to control the influence of temporary handling mounts and the inevitable gravitational distortion of the mirror. We are investigating several variants of a gravity compliant transfer mount and handling sequence which also uses an semi-isostatic interface to the mirror to achive optimal performance.

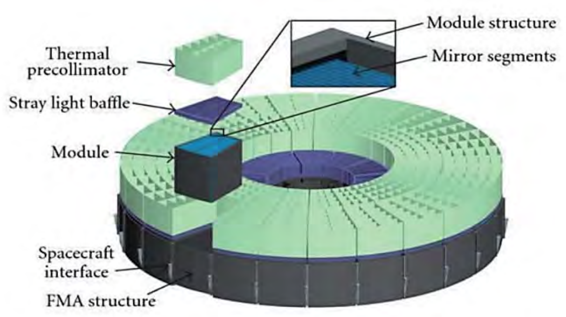

Fig. 1: Overview of a X-Ray mirror based on modular segmented optics. *Biskach et al. 2011*

Performance and Optimization of a bonded Mirror Interface

The permanent interface between mirror segments and mirror module structure (compare Fig. 1) can be formed by an adhesive. Even though this has been done many times on classical x-ray mirrors the influence on mirror performance it is not well understood. We study a number of different geometries (compare Fig. 2) and types of adhesive (epoxies & silicones) with numerical and experimental methods to evaluate their applicability for modular x-ray mirrors.

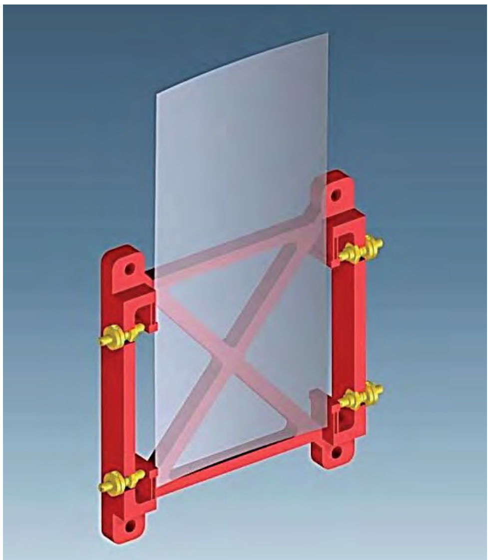

Fig. 3: Adjustable mount prototype. Adjustable elements in yellow.

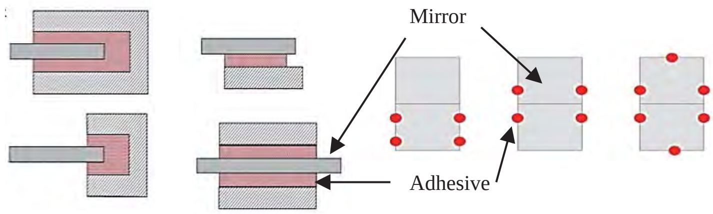

Fig. 2: Bonding geometries and locations under evaluation

Design and Test of an adjustable Mounting System

Several concepts exist to improve the shape accuracy of a mirror segment during integration or even after launch for example by using a bimorph piezo coated mirror. We are investigating an adjustable mounting system which enables control of the precision alignment and longwave shape of the mirror. Such a system can also be used to optimize the required thickness of the adhesive layer (compare Fig. 2) and therefore reduce it‘s performance impact.

A first demonstrator is currently build (compare Fig. 3).

E. Breunig, P. Friedrich, A. Winter

Studies to generate a collimated beam for PANTER: the Zone Plate approach

We have started a study of how to collimate X-rays using a zone plate. A collimated X-ray beam with a diameter of several centimeters to meters is needed to characterize X-ray optics by measuring the focal length and shape of the point response of a source at infinite distance. Here we present the results of our study with a zone plate of 122 m focal length at Al-K 1.49 keV and a diameter of 5 cm.

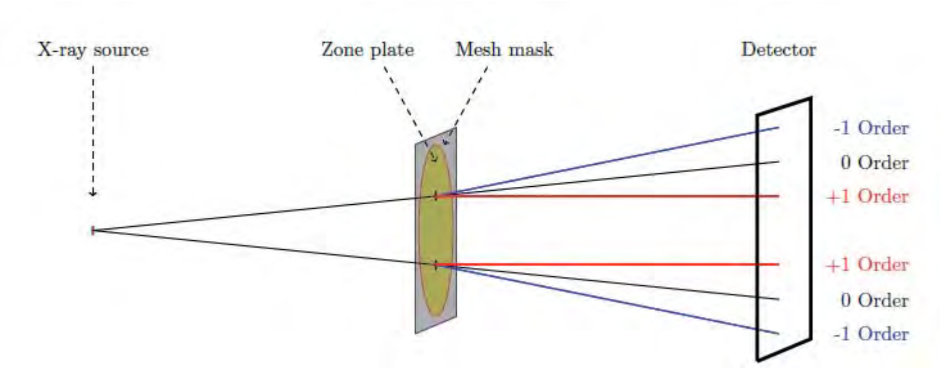

Fig. 1: The setup to study the zone plate: A mesh mask is used to separate the effects of the different orders on the detector. The parallel +1 order is highlighted in red.

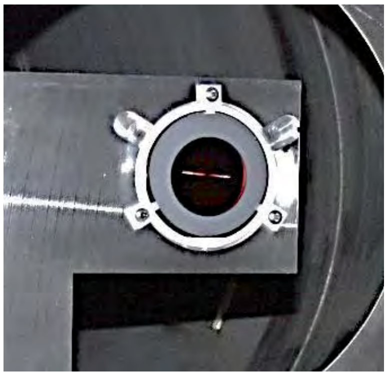

Fig. 2: The zone plate mounted in the PANTER vacuum chamber.

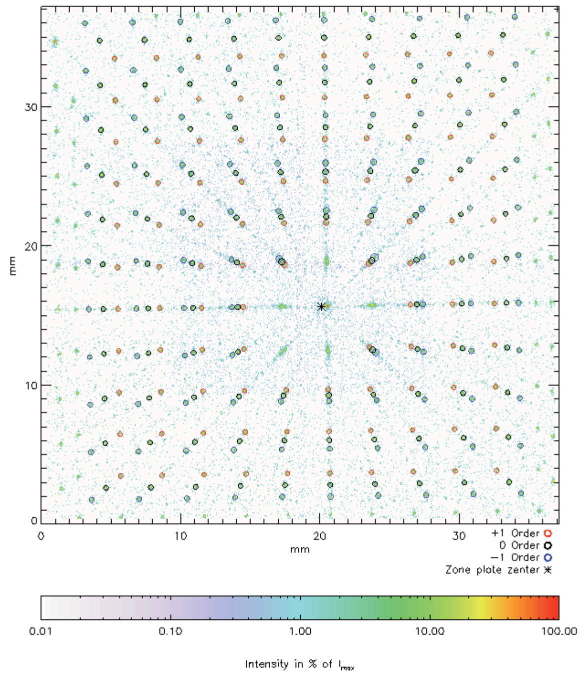

Fig. 3: Detector image of the zone plate shadowed by a mesh mask: A source detection algorithm is used to find the point sources.

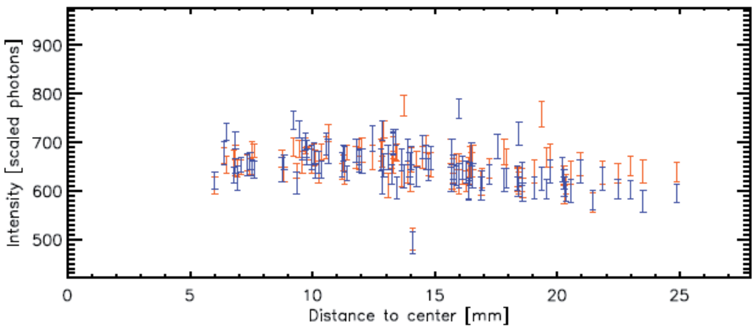

Fig. 4: The intensity distribution of point sources (indicated as circles in Fig. 3). The homogeneous intensity distribution over the whole zone plate shows that it can be used as a collimator for X-ray optics.

Moreover the parallelity of the X-ray beam (+1 order) is tested by measuring the distances of the point source positions. Within the current detector resolution and counting statistics no deviations from a parallel beam can be detected.

B. Menz, V. Burwitz, G. Hartner, et. al.

Technology Development for CCD- and DEPFET-Sensors

The Technology group at the MPI Halbleiterlabor (HLL) produces detectors for various research activities of the Max-Planck institutes - in particular for X-ray astronomy, and high-energy physics. CCD and DEPFET sensors have been fabricated for the X-ray astronomy mission eROSITA, the Mercury imager MIXS, Free Electron Laser experiments CAMP, LAMP and DSSC and for the envisioned X-ray satellite ATHENA.

The silicon sensors are fabricated in a 300 m^2 class I cleanroom. Since the installation of an ion implanter in 2009, all processing steps - starting from the bare silicon wafers and finishing with cut and mounted dies - can be done reliably within this cleanroom. The main distinction of HLL to commercial sensor manufacturers is the use of double-side polished high-purity silicon and the capability to fabricate reliably specialized sensors in small numbers with large sensitive areas. Double polysilicon and double metal layers are standard, a third metal layer (Cu) and flip-chip interconnection technique have been developed during the last years.
All detectors have some common features: Full depletion of the bulk material enabling backside illumination with 100% fill factor and thin entrance windows for maximum quantum efficiency. High frame rates with very low noise values are achieved through integrated readout amplifiers and parallel readout nodes. All manufacturing steps, starting from the device idea through simulation, layout and photomask design, sensor fabrication and test of the final dies are done inhouse.

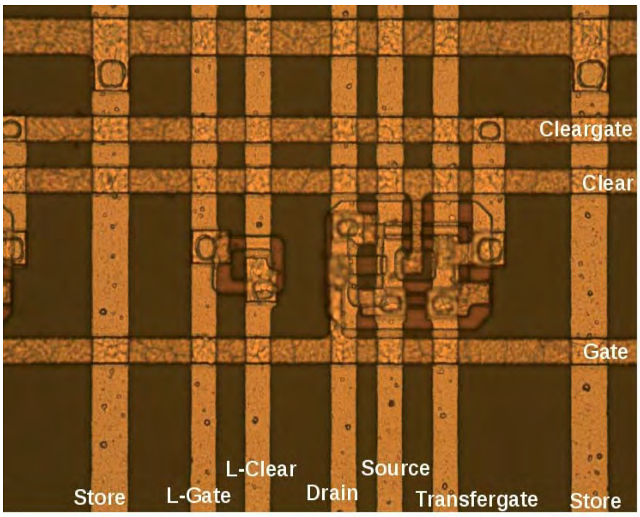

Prototype DEPFET-Sensor for the proposed ATHENA X-ray mission. The pixel structure contains an integrated storage area where charge can be integrated while the information of the previous frame is read out. If these sensors work as good as device simulation showed, problems with dead time and signal charge corruption can be avoided even for very high countrates.

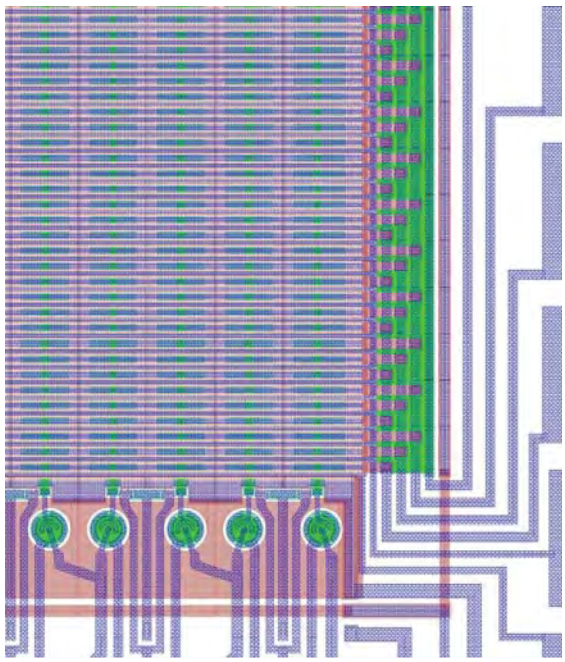

Layout of the CCD-Sensors produced for the eROSITA satellite mission. Each pixel is defined by three consecutive shift-registers which are connected by the bus structure on the right. The on-chip amplifiers for each readout channel are visible at the bottom.

F. Schopper, G. Schaller

The Wide Field Imager for the Next-Generation X-ray Observatory

The Wide Field Imager (WFI) is an imaging X-ray spectrometer with high-time resolution capability over a wide field of view. It has a solid technological heritage from previous X-ray mission concepts (XEUS, IXO, ATHENA) and is currently in continued development for ATHENA+ in preparation for ESA's the next L-Class mission call (anticipated for early 2014). The WFI for ATHENA+ would operate in the energy band from 0.1-15keV with a field of view of approx. 40'x40', an energy resolution of ~125eV at 6keV, and a count rate capability of 1 Crab. It is developed by a collaboration of MPE with a consortium of German universities (ECAP, IAAT, TUD), the company PNSensor, and partners in UK and France.

Science: The WFI can provide essential wide-field capabilities for observatory workhorse science. Among many things, WFI observations will determine the energy flows given rise to cosmic feedback and quantify the growth of supermassive black holes and the evolution of nuclear obscuration over cosmic time. It will also allow to trace the evolution of intracluster medium through temperature, metallicity and turbulent velocity changes with redshift. Performance simulations[1] are shown on the right.

Technology: The WFI uses active pixel sensors based on the DePFET technology [2,3] developed in the MPE Semiconductor Lab. This technology offers the important advantage over standard CCDs of allowing very high read-out rates and flexible read-out modes. The figure below shows a 24'x24' field of view WFI prototype on a 6-inch wafer including periphery electronics.

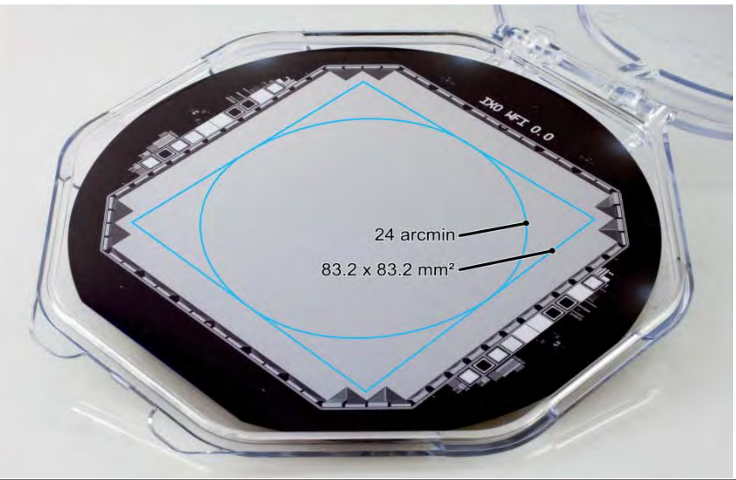

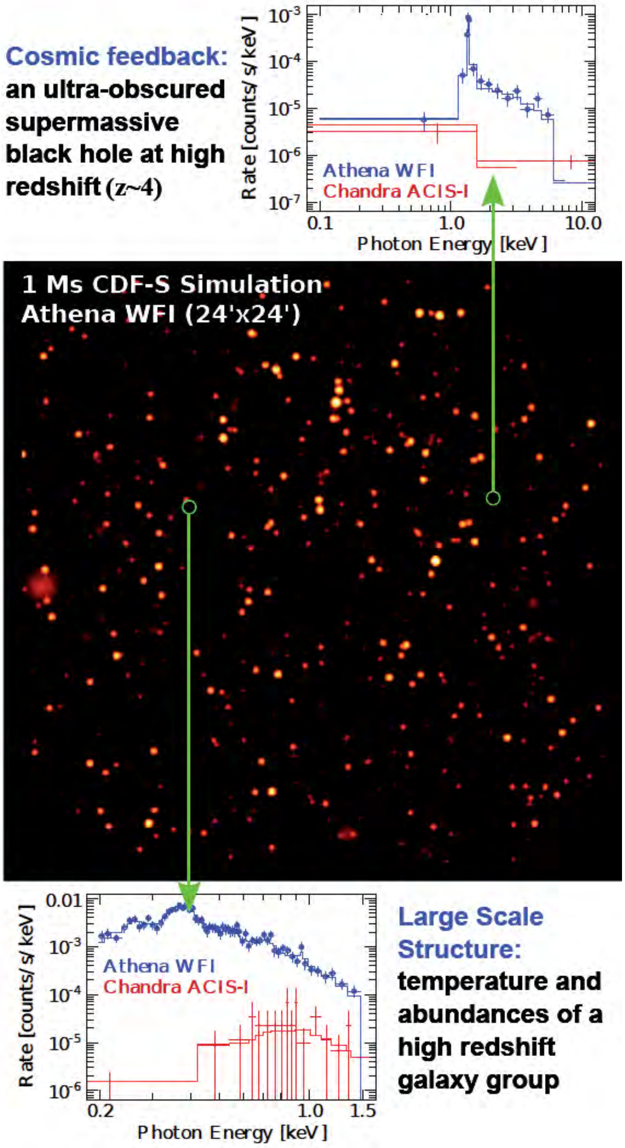

References:

- [1] ATHENA Yellow Book
- [2] see poster by B. Günther
- [3] see poster by A. Bähr

A. Rau, N. Meidinger, M. Porro, K. Nandra

Development of Gated DEPFET detectors for ATHENA

For the observation of bright x-ray sources, as planned for the ATHENA project, a high time resolving detector is mandatory. A detector well suited for this task is the so called gateable DePFET. Based on the DePFET concept this device provides a built-in shutter capability, allowing the observation of high photon fluxes without a degradation of the spectral performance. First measurements showing the outstanding performance will be presented.

In x-ray astronomy the concept of out of time events is a well known issue. Due to the readout used for DePFET sensors, charges arriving at an arbitrary moment of the readout phase will be evaluated with a false energy value.
Based on the DePFET principle the so called gateable type was developed. These devices provide a built-in shutter which can be used to suppress false event energies during signal processing.
The expected benefit in terms of reachable peak to background values for the ATHENA project is illustrated in Figure 1.

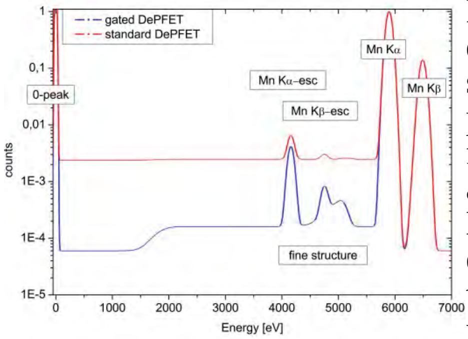

Figure 1: difference of spectral performance for a standard and a gated DEPFET expected for the ATHENA project.

Principle description:
The depletion p-channel field effect transistor (DePFET) can be used as base cell of an active pixel sensor. A n+ implantation below the transistor gate forms a local potential minimum for electrons, the so called internal gate. Each electron collected in this minimum will modulate the transistor current and can thus be detected.
The shutter capability can be achieved by adding an anode. In normal operation it is biased such that the internal gate is the most positive potential and electrons will be collected as usual. To close the shutter a positive voltage is applied to the anode. Electrons generated in the bulk will be attracted by the thus formed positive potential and be removed. While the shutter is active charge collection is suppressed by a factor of .

Measurement results:
The measured values for the charge suppression vary depending on operation parameters and design between and .
Figure 2 presents timing measurements on a macropixel prototype device. The central readout node is a gateable DePFET which is surrounded by several driftrings giving an overall collection area of 10mm².

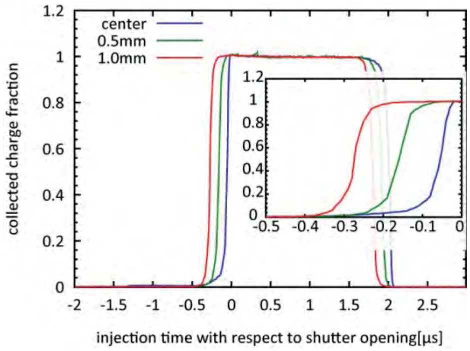

Figure 2: The change from insensitive to sensitive state happens in less than 200 ns.

Charge injection was done using a laser with a pulse duration of 50ps. The charge was injected at three different positions of the macropixel. As shown the charge collection only happens when the built-in shutter is in the open state. The change from the sensitive to the insensitive state takes less than 200ns, which is one order of magnitude faster than the typical readout and integration times.
Measurements to evaluate the spectroscopic performance of the gateable DePFET devices are currently performed.

References:
•Bähr et al. "New simulation and measurement results on gateable DEPFET devices", *Proc. SPIE* 8453, High Energy, Optical, and Infrared Detectors for Astronomy V, 84530N

A. Bähr

Analysis of DEPFET detector designs for ATHENA on die-level

For ATHENA wafer-scale DEpleted P-channel Field Effect Transistor (DEPFET) detectors will be needed as well as excellent detector performance. Therefore smaller prototypes with different pixel layout were produced to allow studies of suitable designs. The prototype chips are spread over the whole wafer area to gain information about homogeneity with respect to the wafer position.

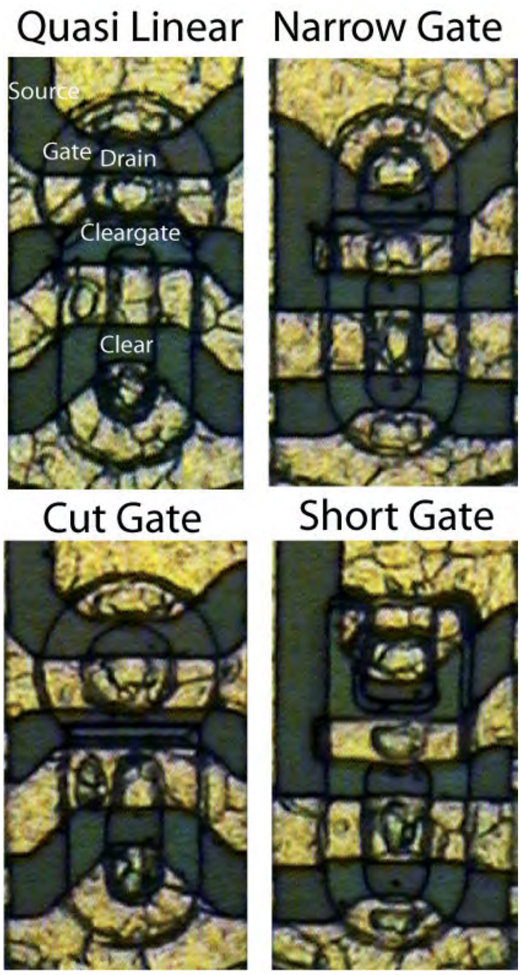

For analysing different DEPFET designs (see picture on the left) on die-level a probe station located inside a dark box was used. The dark box is located in a clean room controlled environment. The chip is mounted on a chuck and contacted electrically by a needle card and an automated probe head (see picture below).

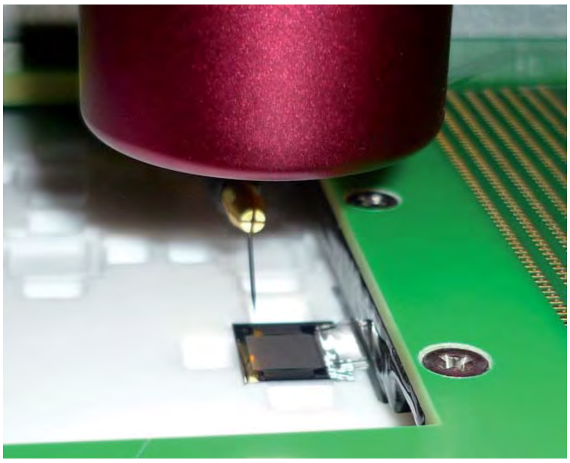

In the DEPFET equivalent circuit diagram below can be seen that the device consists of two transistors. They can be characterized by four different measurements performed with the probing setup.

From the characterization measurements we learned that the gate voltage variation is less than 0.4 V for all devices and even less within every design. That demonstrates a great homogeneity over the whole wafer area and indicates a homogenous production process. Devices of the same design group show similar values for all extracted performance parameters. This allows to clearly see differences in the operational parameters needed for different designs.

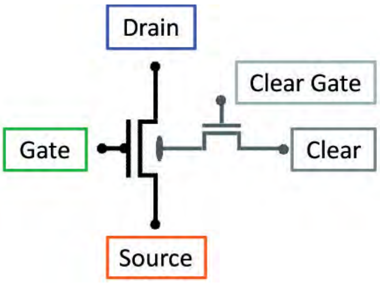

References: P. Majewski et al., DEPFET Macropixel Detectors for MIXS: Integration and Qualification of the Flight Detectors, IEEE Trans Nucl Sci, vol. 59, no. 5, p2479 (2012)

B. Günther

Development of large-area CCD detectors for X-ray free electron laser experiments

CCD detector modules developed and manufactured by MPE have been used in various XFEL (X-ray free electron laser) experiments at LCLS (Linac Coherent Light Source, USA) and SACLA (Spring-8 Angstrom Compact Free Electron Laser, Japan) resulting in numerous publications covering fields from atomic physics to biological investigations.

The semiconductor sensor of the detector is a backside illuminated fully depleted PNCCD. X-rays are being detected with a resolution of 1024^2 pixels, where each pixel has a size of 75µm. Additionally to the outstanding imaging capabilities the detector can also measure photon energies from 50eV to 25keV and single photons can be detected. The typical frame rate is 120Hz. The PNCCD detectors in the CAMP (**C**FEL-**A**SG-**M**ulti-**P**urpose) chamber stimulated experiments carried out from December 2009 to July 2012, including measurement of fluorescence of highly ionized noble gas atoms, nanocluster dynamics, nanocrystallography, and recording diffraction patterns for 3D reconstruction of small particles and biological samples like proteins and viruses (see Fig. 1).

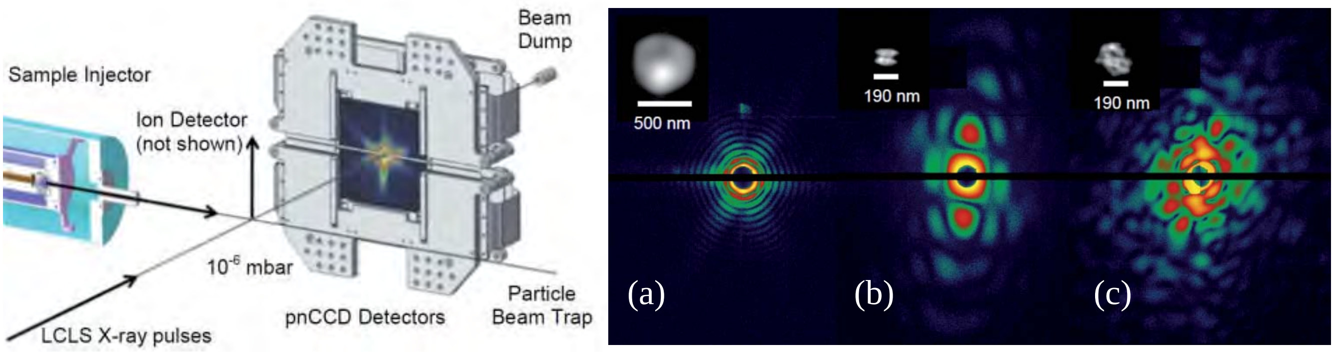

Figure 1. Diffraction experiments with two PNCCD detectors done at LCLS in 2011 (see Ref.): X-ray pulses hit samples injected from the left by an aerodynamic lens stack. Multiple X-ray diffraction patterns are recorded by the PNCCDs, allowing 3D reconstructions of samples such as mimivirus (a) and clusters of nanorice (b-c).

The next generation of PNCCD detector modules is currently under development at the MPE for LAMP (**L**CLS-**A**SG-**M**ichigan **P**roject, successor of CAMP). Enhancements include optimizations on the reset structures of the PNCCD, better thermal and stray light management, a modified center hole for FEL pass-through, and FPGA-assisted digital signal management on the detector module. Operation at LCLS is expected to start in Autumn 2013.

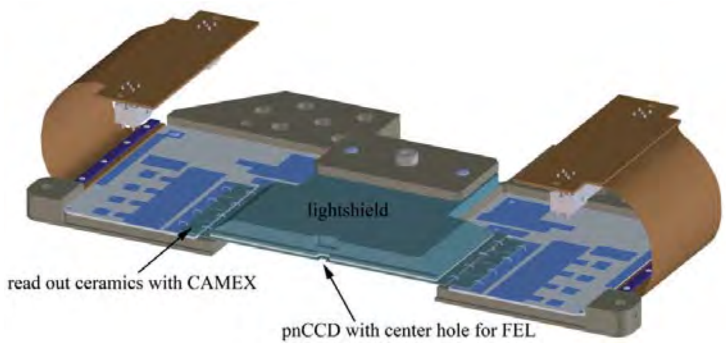

Figure 2. Next generation PNCCD detector module without rear electronic board. The CCD is attached to a light shield reducing stray light signals and ensuring homogenous temperature distribution on the CCD.

References:

- A. V. Martin, et al, “Single particle imaging with soft x-rays at the Linac Coherent Light Source”, Proc. SPIE 8078, 807809 (2011)

L. Englert, G. Hauser

The DSSC Detector for the European XFEL

The DSSC (DEPFET Sensor with Signal Compression) will be a new 1Mpixel X-ray camera for the European XFEL in Hamburg. The XFEL facility will e.g. investigate ultra-fast dynamic processes of atomic and molecular clusters, biomolecules and nanocrystals. The DSSC must be able to operate at a frame rate of 4.5 MHz and to achieve high dynamic range (~ 10000 ph./pixel) and single photon detection at the same time. The DSSC will be the only instrument able to achieve single photon resolution even in the low energy range down to 0.5 keV.

The most challenging property of the DSSC is the capability to acquire a full image every 220 ns. The DSSC is based on a new non-linear DEPFET pixel sensor with full parallel readout. Even if the DEPFET is a well established technology, the production of the DSSC sensors requires the development of new complex process steps. In particular, in order to achieve high-dynamic range, the new DEPFET must provide a non-linear current/charge characteristic. The challenges of the project go beyond the development of the DEPFET array. It is necessary, e.g., to design ASICs with more than 4000 ADCs per chip. The very high frame rate and the low noise specifications imply considerable power consumption and new sophisticated thermal designs had to be conceived.

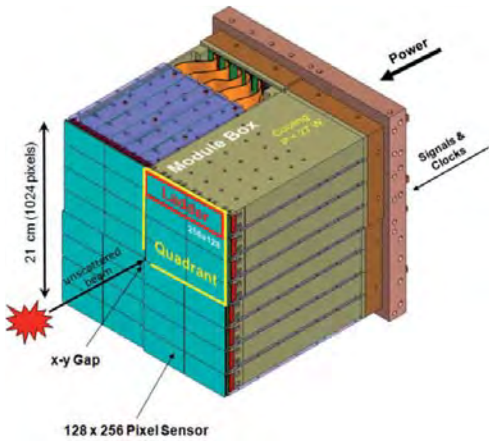

3-D view of the DSSC focal-plane comprising 4 quadrants. Each quadrant is composed of 4 ladders and 8 monolithic sensors of the size of 128x256 pixels each.

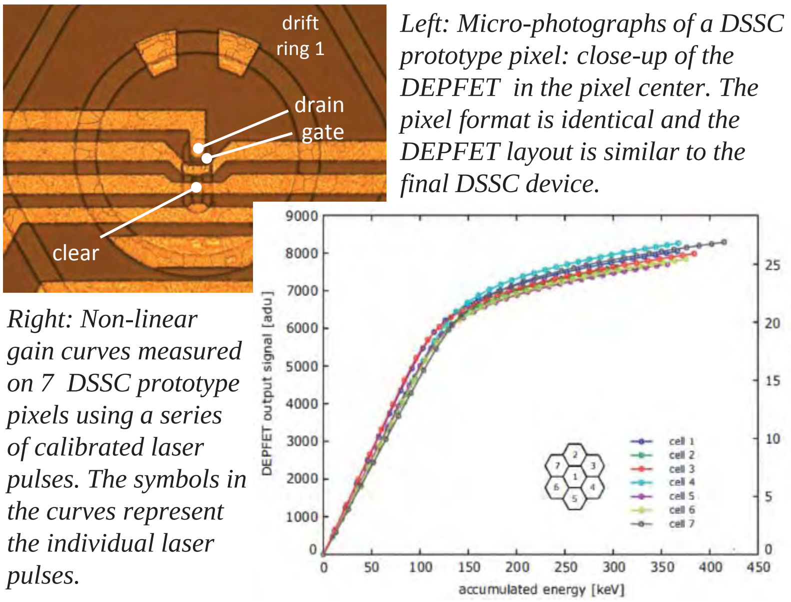

Left: Micro-photographs of a DSSC prototype pixel: close-up of the DEPFET in the pixel center. The pixel format is identical and the DEPFET layout is similar to the final DSSC device.

Right: Non-linear gain curves measured on 7 DSSC prototype pixels using a series of calibrated laser pulses. The symbols in the curves represent the individual laser pulses.

During the first 4 years of development, prototypes of all the main building blocks have been designed, produced and tested. The non-liner DEPFET working principle has been experimentally verified.

Estimates based on the first measurements with prototype ASICs show that it will be possible to achieve simultaneously single photon detection and high dynamic range even at low energies.

References:
• M. Porro et al., Nuclear Instruments and Methods in Physics Research A 624 (2010) 509–519
• M. Porro et al., IEEE Transaction on Nuclear Science, vol. 59, no. 6, 3339-3351, 2012

M. Porro on behalf of the DSSC Consortium

DSSC detector testing for XFEL.EU

The DSSC (DEPFET Sensor with Signal Compression) is a new instrument designed for the European X-ray Free Electron Laser (XFEL.EU) currently being built in Hamburg, Germany. The DSSC will be a 2d photon counting detector featuring single photon sensitivity, non-linear compression of the input signal and parallel signal processing for all pixels. A DSSC prototype setup has been used for testing and determining basic calibration functionalities and parameters of the read-out electronics. Subsequently a first calibration of the non-linear system response of a DSSC prototype pixel has been achieved.

The DSSC prototype setup consists of a prototype DEPFET sensor connected to a prototype read-out ASIC. Initial tests of the DSSC prototype included ASIC functionalities (e.g. offset and gain settings) and the determination of the bin boundaries of the system's 8-bit ADC. Then a first calibration of the Non-Linear System Response (NLSR) of a DSSC prototype pixel for counting 1 keV X-ray photons was accomplished. The NLSR is the non-linear relation between the charge collected inside the sensor and the corresponding digital output. The NLSR calibration can be achieved by using ^{55}Fe X-ray lines and pulsed electrical charge injection.

An additional test bench with an 14-bit ADC was used to obtain the spectral response of the prototype DEPFET for ^{55}Fe photons.

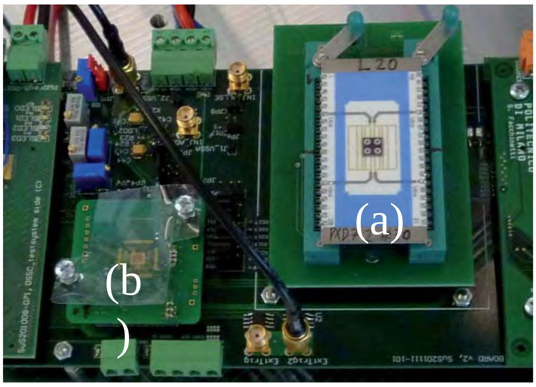

Above: The DSSC prototype setup showing the prototype DEPFET sensor (a) and the read-out ASIC prototype (b)

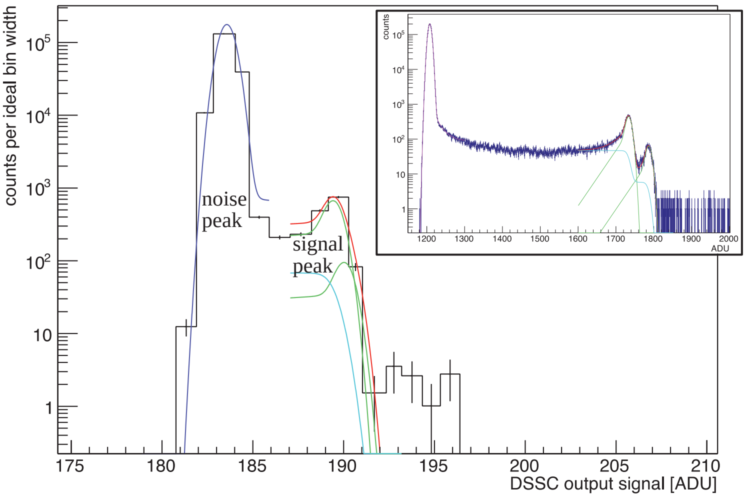

Above: ^{55}Fe spectrum obtained with the prototype setup for a calibration to count 1 keV X-ray photons. In this calibration one photon is assigned to one ADC bin, therefore the signal peak at about 6 keV has to be set at a distance of about 6 ADU from the noise peak. This leads to a spectrum consisting of only a few bins.

The insert shows the ^{55}Fe spectral shape of the prototype DEPFET acquired with the test bench at 14-bit resolution. This model has been used to fit the DSSC 8-bit spectrum. Both plots show the ^{55}Fe K-alpha and K-beta X-ray lines painted in green and the noise peak coloured in blue/violet.

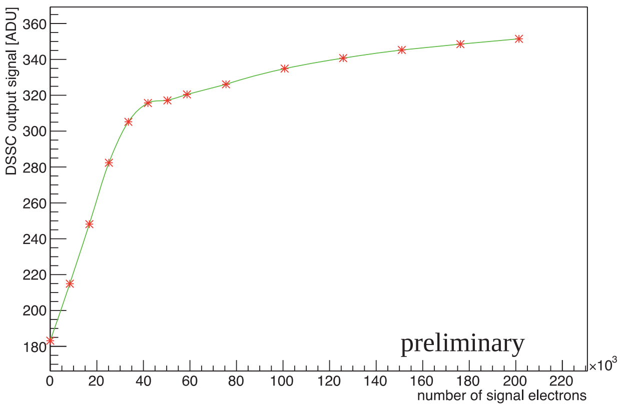

Left: First preliminary experimental calibration of the non-linear relation between charges collected in a DSSC pixel and the corresponding digital output.

References:
• Weidenspointner et al., IEEE NSS, 468, 2011 • Weidenspointner et al., IEEE NSS, 2012
• Porro et al., IEEE TNS, vol. 59, no. 6, 3339-3351, 2012

D. Moch and the DSSC consortium

Calibration and System Simulation of the DSSC Detector for XFEL.EU

The DSSC (DEPFET Sensor with Signal Compression) is a new instrument with non-linear compression of the input signal in the sensor and with parallel signal processing (filtering, linear amplification, and digitization) for all pixels. The DSSC will serve as imaging photon counting detector at the European X-ray Free Electron Laser (XFEL.EU) under construction in Hamburg, Germany. Calibration and system simulation of the DSSC are intimately connected and of paramount importance for achieving the scientific goals of XFEL.EU.

The DSSC design goal is to achieve at the same time single photon detection and high dynamic range of about 10^4 photons, both for photon energies down to 0.5 keV and read-out speeds up to 4.5 MHz. Realization of this goal requires an accurate calibration of the characteristics of each of the 1024×1024 DSSC pixels in the laboratory. System simulation is an indispensable tool not only for testing calibration software and for preparing and optimizing calibration measurements and procedures, but also for planning scientific experiments.
The DSSC is a 2d photon counter with 8 bit resolution; to achieve single photon detection the DSSC calibration settings are a function of the energy of the incident XFEL photons.

The three main DSSC characteristics that must be calibrated are:

• Non-linear system response (NLSR), i.e. the non-linear relation between the charge collected in a DEPFET pixel and the corresponding digital output of the system. The NLSR allows at the same time single photon counting and large dynamic range.

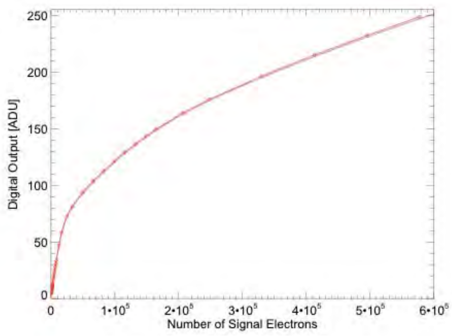

Demonstration of NLSR calibration, based on simulated data, of a DSSC pixel adjusted to count 1 keV photons: assumed NLSR (black), and calibration result (red). The calibration can recover the assumed NLSR very well.

• Collected-charge distribution function (CCDF), i.e. the distribution of the charge collected in a DEPFET pixel as function of the energy of an incident photon.

• Point spread function (PSF), i.e. the splitting of charge generated by incident photons amongst neighboring pixels.

System simulation of the measurement of a T4 virus diffraction image:

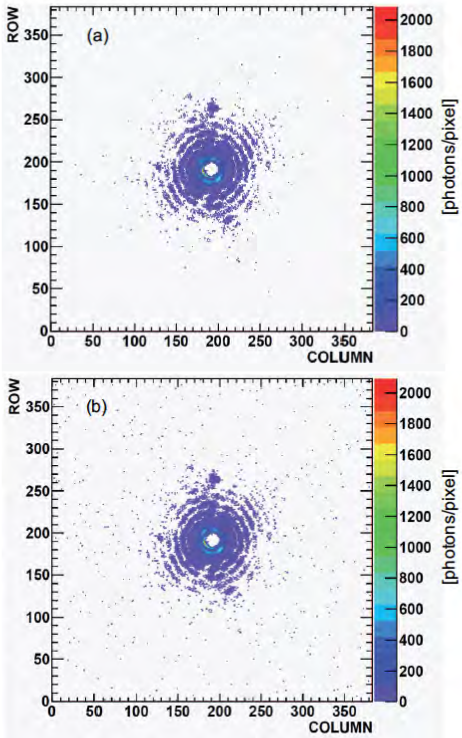

Panel (a): simulated input distribution of incident photons, randomly drawn from a diffraction image measured at the Linear Coherent Light Source at SLAC. Panel (b): reconstructed diffraction image. The reconstructed image and the incident photon distribution agree within the Poisson uncertainty of the input.

References: • Weidenspointner et al., IEEE NSS, 468, 2011 • Weidenspointner et al., IEEE NSS, 2012
• Porro et al., IEEE TNS vol. 59, no. 6, 3339-3351, 2012

G. Weidenspointner and the DSSC consortium

IV) MPE Research Groups

IV.1) Group: Dr. Sadegh Khochfar

Proto-galaxies reionizing the Universe

One of the major challenges in modern cosmology is identifying the nature of the sources responsible for reionizing the Universe. The contribution of stars in galaxies to cosmic reionization depends on the star formation history in the Universe, the abundance of galaxies during reionization, the escape fraction of ionizing photons and the clumping factor of the intergalactic medium. We compute the star formation rate and clumping factor during reionization in a cosmological volume using the *First Billion Years* (FiBY) simulation. We post-process the output with detailed radiative transfer simulations to compute the escape fraction of ionizing photons. Together, this gives us the opportunity to assess the contribution of galaxies to reionization self-consistently.

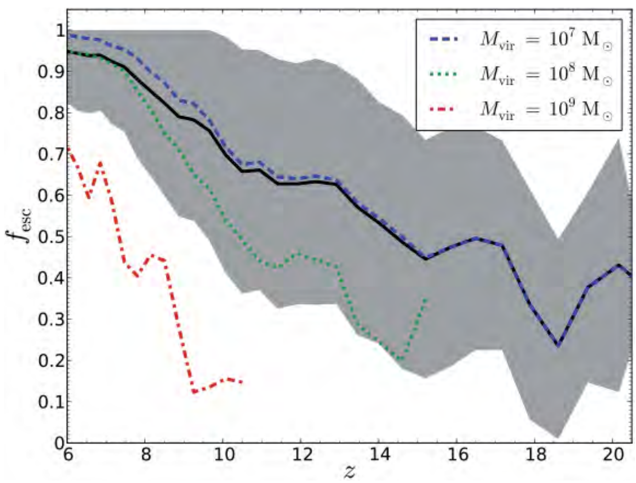

Left: We find a strong mass and redshift dependence of the escape fraction that indicates that reionization occurred between z = 15 and 10 and was mainly driven by proto-galaxies forming in dark matter haloes with masses between 10^7 and 10^8 $M_\odot$. More massive galaxies (that are rare at these redshifts) have significantly lower escape fractions and thus contribute less photons to the reionization process than the more-abundant low-mass galaxies.

Right: The cumulative number of ionizing photons per baryon as function of redshift shows that galaxies with mass between 10^5 and 10^6 $M_\odot$ dominated the ionizing photon budget for reionization (denoted by the dashed line). Star formation in these galaxies is suppressed by radiative feedback from reionization, therefore these proto-galaxies only contribute when the part of the Universe they live in is still neutral. After z~10, massive galaxies become more abundant and provide most of the ionizing photons.

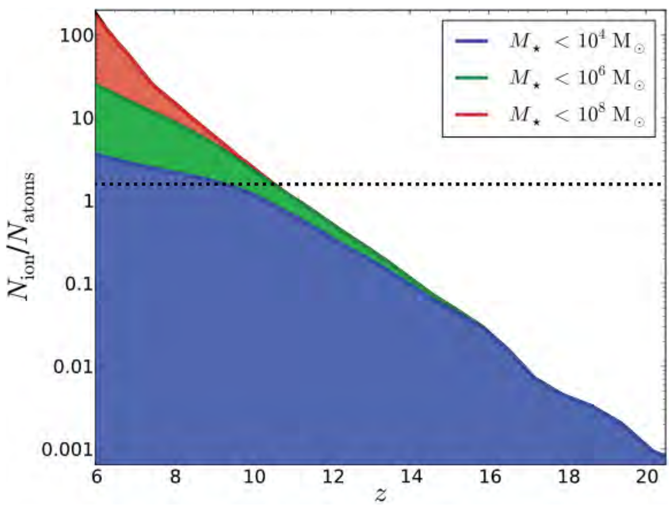

References:

• Paardekooper, J.-P., Khochfar, S., Dalla Vecchia, C., 2013, MNRAS, 429

J.-P. Paardekooper, S. Khochfar, C. Dalla Vecchia

Cores and Cusps in the First Galaxies

Much progress has been made using dark matter only simulations to understand the properties of high redshift dark matter halos. However, the structural properties of the dark matter halo are also affected by the presence of baryons. We use the First Billion Years (FiBY) simulation [2] to study the connection between the earliest galaxies and their host dark matter halos [1]. We study the role of stellar feedback in modulating the density profile of the dark matter in over 5,000 halos. The central profile can alternate between a core and a cusp in cycles following the star formation rate in the galaxies. We find that the energy injected by the early supernovae is enough to completely unbind the gas in the central regions of the halo, resulting in the expansion of dark matter as the gas is pushed out.

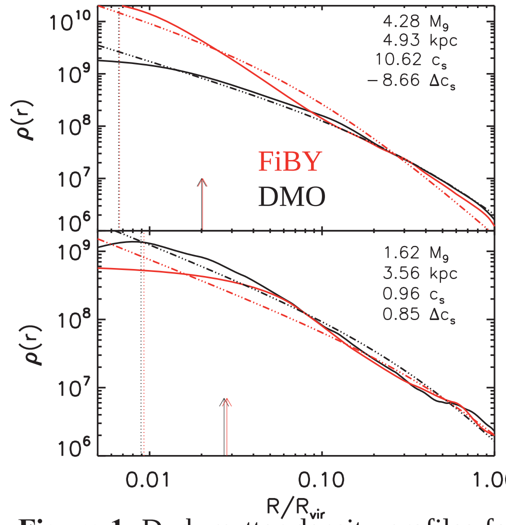

Figure 1: Dark matter density profiles for two halos in the FiBY simulation (red) and the same halos in a dark matter only (DMO) simulation (black), as well as best fit NFW profiles (dashed). We find halos can show an enhancement (top) or a decrement (bottom) of dark matter in the galaxy core. We quantify this enhancement, η, as the ratio of dark matter mass inside 100 pc: $\eta = M_{FiBY}/M_{DMO}$ (<100pc). The annotations give the halo mass, virial radius, best fit FiBY NFW concentration parameter, and the difference in concentration (DMO-FiBY) between the two simulations.

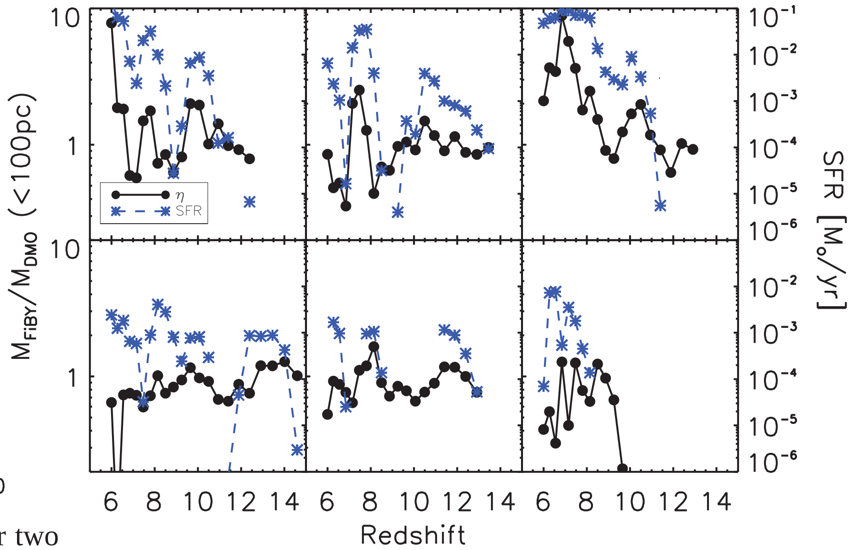

Figure 2 (Top): Evolution of the dark matter enhancement, η, (black) and star formation rates (blue) for six halos. We find the two quantities are correlated, and that the dark matter halo in the FiBY run can rapidly respond to the changing potential when gas is evacuated from the center of the galaxy.

Figure 3 (Right): Phase diagrams of the gas in a halo as it cycles from η < 1 to η > 1 and back. As the dense gas collapses to the center, the dark matter adiabatically contracts. When the central dense gas is blown out, the dark matter responds non-adiabatically to the new potential well, creating a cored dark matter profile.

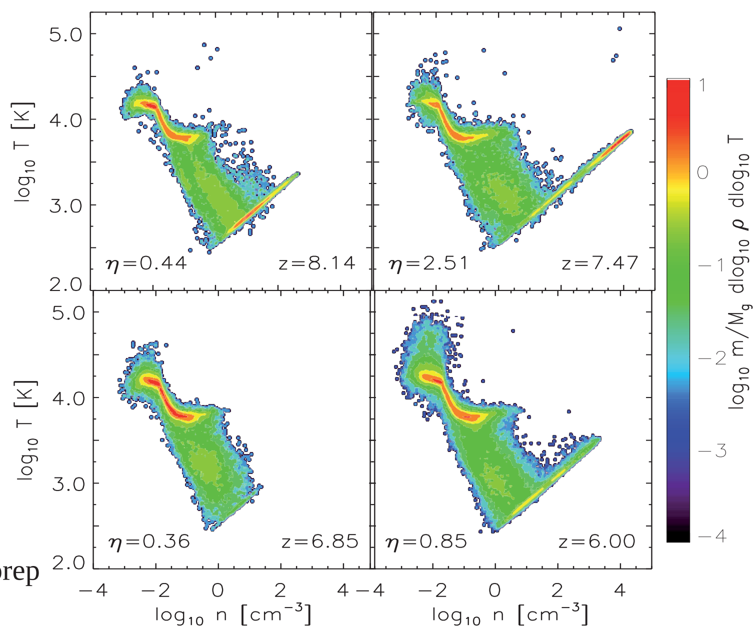

References:
[1] Davis, Khochfar & Dalla Vecchia, 2013, in prep
[2] Khochfar et al. 2013, in prep

A. Davis, S. Khochfar, C. Dalla Vecchia, TMoX Group

Unravelling a new class of galaxies at z > 6

The presence of supermassive black holes (SMBH) at z > 6 is well established via observations of quasars[1]. However, the formation of the seeds of SMBHs is still highly uncertain. We explore the direct collapse scenario[2] where a high level of Lyman-Werner (LW) radiation (11.2 − 13.6 eV) can dissociate all the molecular hydrogen in a metal-free atomic-cooling halo causing the gas to collapse isothermally to form a dense core. The core can then undergo direct collapse (DC) into a black hole with mass $M = 10^{4-5}\ M_\odot$. We probe the formation and evolution of these DCBHs using our self consistent semi-analytical-model[3a] and comment on their detectability and plausibility of this scenario.

After identifying the DCBHs, we allow the DCBHs to grow by gas accretion with f_{lim} times the Eddington rate. In our model[3b] the stellar host of a DCBHs grows either by merging with other galaxies or by in-situ star formation. The evolution of galaxies hosting DCBHs in the M_{BH}-M_{star} plane is clearly off-set form the local relation (Fig 1). Note that since in these galaxies, the DCBH forms first, the BH is always more luminous than the stellar component and we coin the name ‘Obese Black Hole Galaxies (OBGs)’ for these objects.

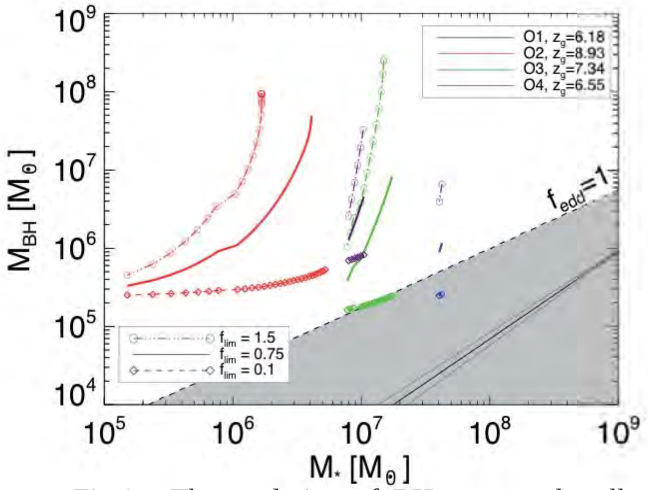

Fig.1 : The evolution of BH mass and stellar mass in the OBGs.

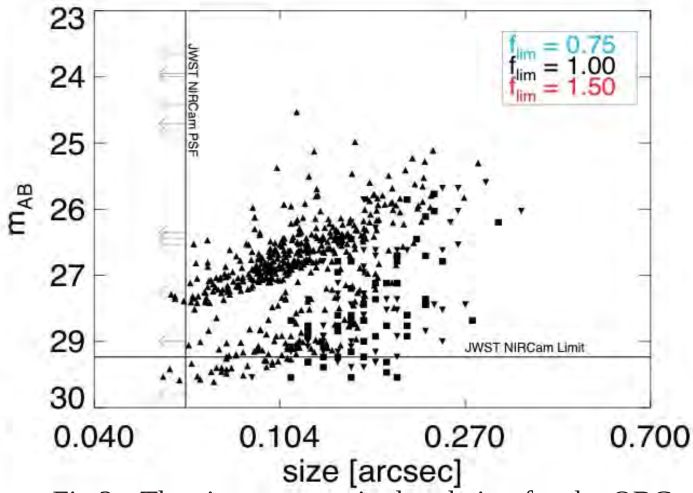

Fig.2 : The size vs. magnitude relation for the OBGs at z~6 indicated by the arrows. The solid symbols represent the galaxies seen by HUDF at z>6.

These OBGs have peculiar observational characteristics like the absence of a Balmer break (amongst other features) which if detected by the JWST would conclusively prove that DCBHs existed in the early universe. OBGs are as bright as or brighter than the galaxy population already seen at z>6 with the HUDF,[5] but should appear as unresolved point sources (Fig. 2). Their number densities of 0.04 Mpc^{-3} suggest that present surveys are not large enough to detect them, but that future JWST surveys will be able to do so. Furthermore, they are abundant enough to be the possible seeds of SMBHs at z=6.

[1] Mortlock et al. 2011, Nature vol. 474 pp. 616[2] Eisenstein and Loeb 1995, ApJ 1995 vol. 443 pp. 11[3a] Agarwal et al. 2012, MNRAS, 2012 vol. 425 pp. 2854
[3b] Agarwal et al. 2013 submitted[4] Häring and Rix 2004, ApJ, vol. 604 pp. L89
[5] Personal communication with Dr. Rychard Bouwens

B. Agarwal, S. Khochfar, A. Davis, J. Johnson,
Pr. Natarajan, C. Dalla-Vecchia, E. Neistein

AnarchySPH: state of the art smoothed particle hydrodynamics and entropy mixing

We present a novel numerical implementation of smoothed particle hydrodynamics (SPH) including state of the art algorithms for force calculation and time dependent artificial viscosity, as well as a new algorithm for entropy/energy diffusion that we developed. Hydrodynamical instabilities and phase mixing are successfully reproduced in all numerical tests.

The cosmological code AnarchySPH includes a generalised formulation of SPH [1], time dependent artificial viscosity [2] and high order SPH kernel functions [3]. We implemented numerical diffusion of internal energy which allows for better mixing of gas phases in turbulent regions [4]. Diffusion is triggered by large values of the second spatial derivative of the internal energy, and normalised in order to keep contact discontinuities sharp over a couple of resolution lengths. The evolution of simulated Kelvin-Helmholtz instabilities is shown in Fig. 1.

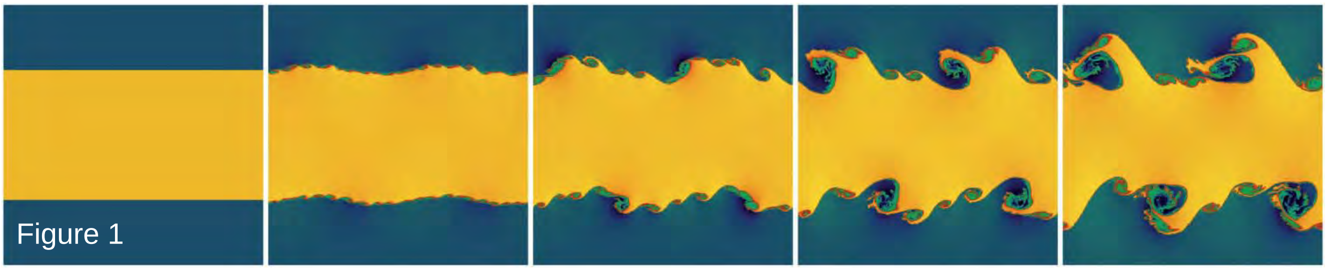

Figure 1

We ran a cosmological simulation test using the initial conditions of the Santa Barbara cluster comparison project [5]. Entropy mixing allows the formation of an entropy core similar to that obtained with mesh codes (Fig. 2). Without energy diffusion, we recover the entropy profile produced with the standard SPH of Gadget-2. The accurate treatment of hydrodynamical instabilities translates into efficient gas stripping from satellite haloes and, together with entropy mixing, into a smoother gas distribution of the inter-galactic medium when using our code (Fig. 3). AnarchySPH is a major step in overcoming failures of traditional SPH formulations and converges towards results from grid-based techniques, allowing to take full advantage of the SPH approach in modelling structure formation.

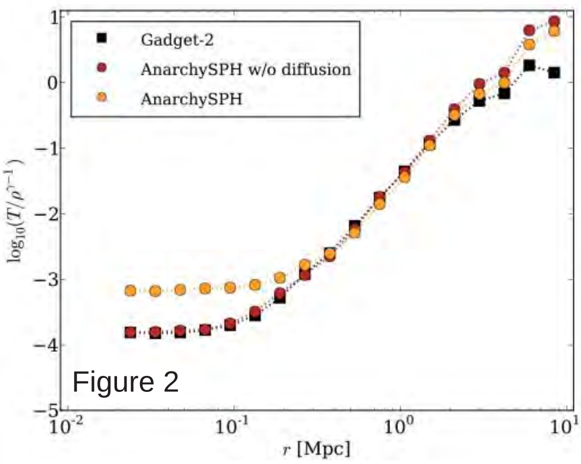

Figure 2

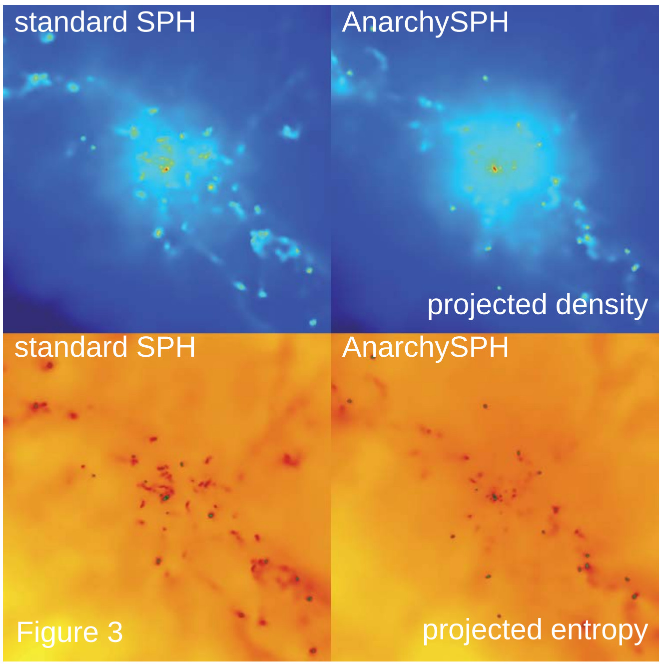

Figure 3

References:
[1] Hopkins, 2013, MNRAS, 428
[2] Cullen & Dehnen, 2010, MNRAS, 408
[3] Dehnen & Aly, 2012, MNRAS, 425
[4] Dalla Vecchia & Khochfar, in preparation
[5] Frenk et al, 1999, ApJ, 525

C. Dalla Vecchia, S. Khochfar

Clustered star formation in major mergers

Mergers with significant off-nuclear, induced star formation, often in the form of massive star clusters (e.g. [1]), have shown that there is deviation from the nuclear starburst picture. Simulations capture the formation of such star clusters, but focus on extreme starbursts, e.g. the Antennae [2]. We study a sample of 5 randomly chosen mergers to establish if they also exhibit induced cluster formation and to study the mechanism for this and its impact. Merger-induced star cluster formation was suggested as an explanation for the bimodality in the Kennicutt-Schmidt relation seen in recent observations [3,4]. While we see clustered star formation in all the mergers, we do not find evidence for a clear bimodality.

During the mergers the gas density probability density function (PDF) evolves significantly, resulting in an enhanced fraction of very dense gas (Fig. 1a). The change in its shape could explain enhanced HCN/CO ratios in ULIRGs since their emission traces $n>10^4 cm^{-3}$ and $n>100 cm^{-3}$, respectively. The PDFs also predict that there should be a lower α_{CO} in mergers compared to quiescent discs, since increasing CO emission is expected due to the enhanced probability of collisional excitation in a denser environment.

More dense gas leads to a peak in the star formation rate (SFR), which also coincides with a peak in the gas velocity dispersion (Fig 1b). We demonstrate this is not due to turbulence driven by supernova (SN) feedback by re-running one merger for the duration of its starburst with SN feedback switched off. The velocity dispersion peak still occurs (Fig 2a). We attribute the increase in turbulence to the interaction itself, in-keeping with recent observations of the Antennae [5]. We propose a turbulent fragmentation process is driving clump formation in the gas (Fig 2a).

Mergers are offset above the quiescent Kennicutt-Schmidt (K-S) relation during their starbursts, but there is no distinct bimodality (Fig 2b). This is in agreement with recent results using a volume-limited, rather than an M_*-SFR selected, sample of mergers [6].

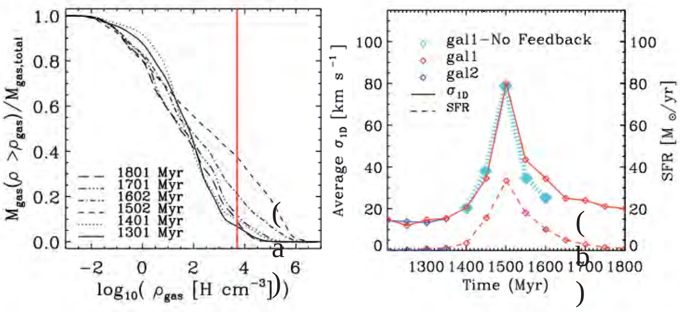

Fig. 1 (a) Density PDF of the gas in galaxy 1 for one merger. The vertical red line shows the density threshold for star formation. **(b)** Average velocity dispersion (solid line) and SFR (dashed line) for both galaxies. The cyan line shows the average velocity dispersion when SN feedback is switched off.

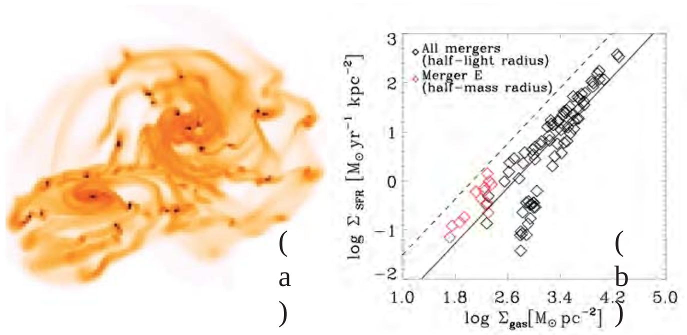

Fig. 2 (a) Gas density map showing the clumpy structure as the two galaxies interact. **(b)** The K-S relation. Data from [3] for the starburst (dashed line) and quiescent (solid line) sequences are over-plotted.

References:

1. Whitmore B. C., Schweizer F., 1995, AJ, 109, 960
2. Teyssier R. etal., 2010, ApJ, 720, L149
3. Daddi E. et al., 2010, ApJ, 714, L118
4. Genzel R. et al., 2010, MNRAS, 407, 2091
5. Herrera C. N., et al., 2011, A&A, 534, A138
6. Saintonge A. et al., 2012, ApJ, 758, 73

L. C. Powell, F. Bournaud, D. Chapon, R. Teyssier

Hydrodynamics and semi-analytic models of galaxy formation

We develop a new method to turn a state-of-the-art hydrodynamical cosmological simulation of galaxy formation (HYD) into a simple semi-analytic model (SAM). Surprisingly, by turning the HYD into a SAM, we conserve the mass of individual galaxies, with deviations at the level of 0.1 dex, on an object-by-object basis, with no significant systematics. This is true for all redshifts, and for the mass of stars and gas components. We show that the same level of accuracy is obtained even in case the SAM uses only one phase of gas within each galaxy. Moreover, we demonstrate that the formation history of one massive galaxy provides sufficient information for the SAM to reproduce the population of galaxies within the entire cosmological box. The method developed here can be applied in general to any HYD, and can thus serve as a common language for both HYDs and SAMs.

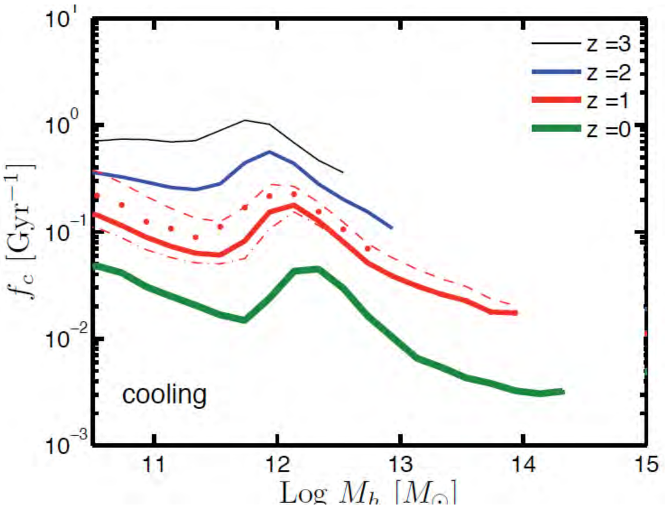

Figure 1: The cooling efficiencies extracted from the HYD, and averaged as a function of halo mass and time. M_h is the host subhalo mass; f_c is defined as the ratio of the cooling rate over the mass of hot gas. Each *solid line* represents a different redshift bin, all the other lines are shown only for z=1: The *dashed line* shows the average plus one standard deviation in f_c; The *dotted-dashed line* shows the average minus one standard deviation, after averaging out f_c for all the progenitors within each tree; The *dots* represent the average plus one standard deviation of f_a after averaging over different progenitors within a tree, but not within different snapshots.

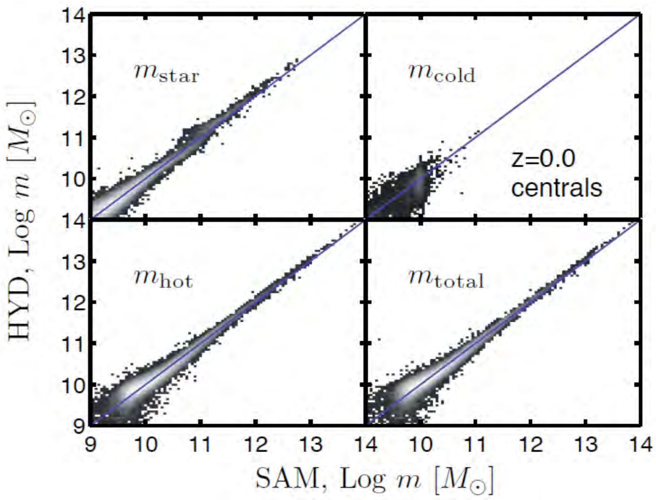

Figure 2: Comparing the masses of individual galaxies, SAM against the HYD. Each panel represents a different mass component as labeled, using only central subhaloes at z=0. The panels show the two dimensional histogram of the pairs (m_{SAM}, m_{HYD}), describing the mass of the same objects in both models. The pixels are color-coded according to the log of the number of objects.

Figure 3 (Right): Comparison of star-formation rate (SFR) for individual galaxies within the models, SAM against the HYD. Central and satellite subhaloes are plotted in dots and circles respectively. The solid red line shows the values where SFRs from both models agree. Results are shown for z = 2 only.

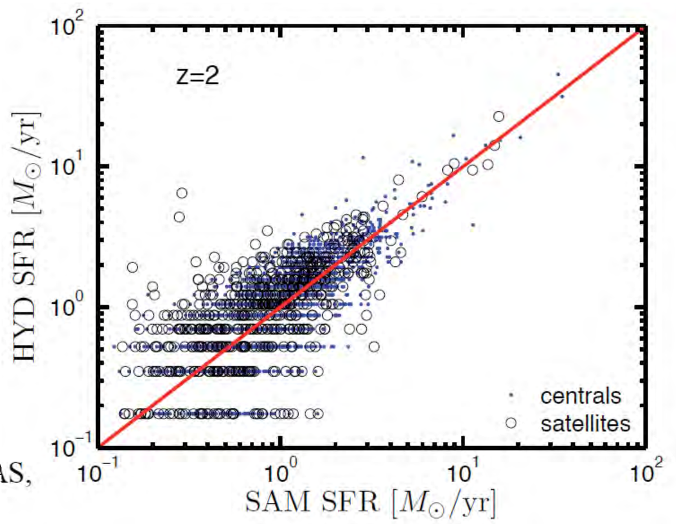

Published in:
Neistein, Khochfar, Dalla Vecchia, Schaye, 2012, MNRAS, 421, 3579

E. Neistein, S. Khochfar, C. Dalla Vecchia, J. Schaye (TMoX Group)

IV.2) Group: Prof. Andreas Burkert

Massive-star feedback on their surroundings

Massive stars influence their environment via radiation, winds and supernova explosions. They often occur in clusters. We investigated[1] with 3D-mesh-refining hydrodynamics simulations how the effect on the environment depends on the distance between the massive stars. We find that the energy transferred to the environment may change by a factor of a few when changing this distance, but for distances up to 10-30 pc it remains essentially constant. Supernova energy is quickly dissipated. We further find that the Vishniac instability leads to shell clumping, which makes a strongly radiative shell appear thick, as observed in many observations.

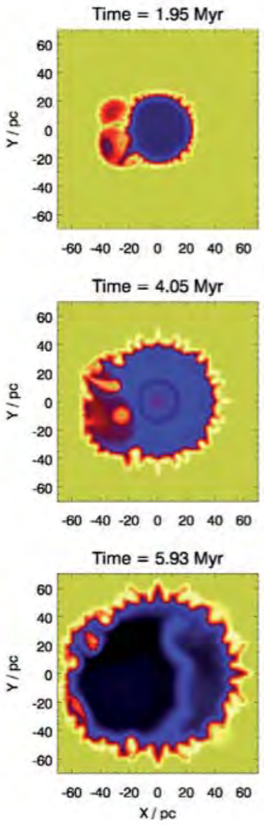

Left: 3D-mesh-refining simulations of emerging superbubbles. We simulate the entire evolution of a 25, 32 and a 60 solar mass star varying the respective distances. Shown here is a time sequence of midplane log-density slices (top: 1.95 Myr, middle: 4.05 Myr, bottom: 5.93 Myr). The bubble interfaces are swept away because of the strong pressure differences in the individual wind bubbles. A substantial superbubble develops even before the first supernova (4.6Myr). The filament in the bottom plot is a sign of the Rayleigh-Taylor instability occurring after each supernova due to the acceleration of the shell. A movie is supplied with the online article[1].

Right: Logarithmic column density at 12.56 Myr. The shell shows a filamentary network with dense knots due to the Vishniac instability. The knots have up to about 100 solar masses and are expected to become also gravitationally unstable and form further stars. The Vishniac instability makes the shell appear thick although it is radiative, in agreement with bubble observations[2].

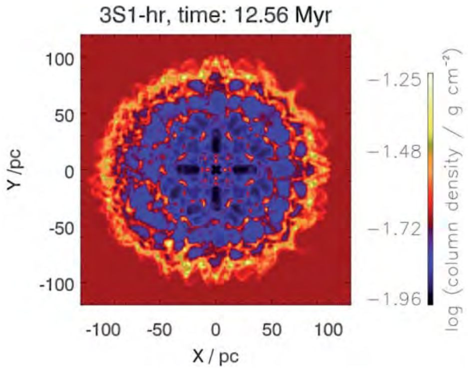

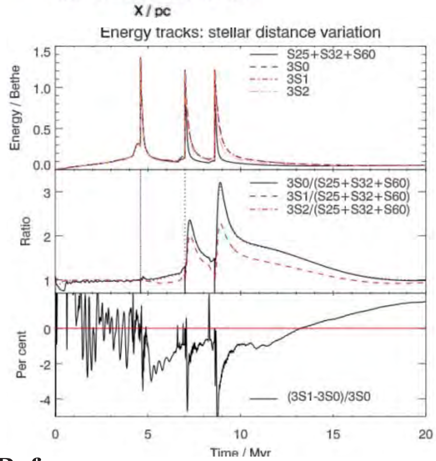

Left: Energy evolution of the interstellar medium in response to massive star action. *Top*: energy content of the interstellar medium over time for varying distances between the stars (3S0: 0 pc, 3S1: ≈ 30 pc, 3S2: ≈ 60pc, S25+S32+S60: separate simulations). The spikes correspond to the supernovae. Energy is built up in the wind phases. The energy from supernovae is radiated within about 10^6 yrs, even though the supernovae explode in a pre-shaped superbubble. Middle: Ratio of energy tracks from the top plot relative to the case where the stars are in separate simulations, i.e. effectively at very large distances. There is essentially no difference in the energy of the interstellar medium until the second supernova. Different separations affect the energy stored in the interstellar medium by a factor of a few, but configurations where the stars are closer than a few 10s of pc all show the maximum energy response, which is highlighted in the bottom plot.

References:

- Krause et al. A&A 550, A49 (2013)
- Churchwell et al. ApJ, 649, 759 (2013)

M. Krause, K. Fierlinger, R. Diehl, A. Burkert, R. Voss and U. Ziegler

A compact source scenario for the Galactic Centre cloud G2

With hydrodynamical simulations we modeled the compact source scenario suggested origin of the Galactic Centre cloud G2 (Gillessen et al., 2012; 2013). We studied different spherically symmetric winds of an invisible source in the centre of G2, finding that any interaction with the ambient medium and the extreme gravitational field of the supermassive black hole strongly affect the evolution. Comparing our results to the observed G2 properties, the best model has a wind mass loss rate equal to 8.8 x 10^{-8} $M_\odot$/yr and wind velocity equal to 50 km/s.

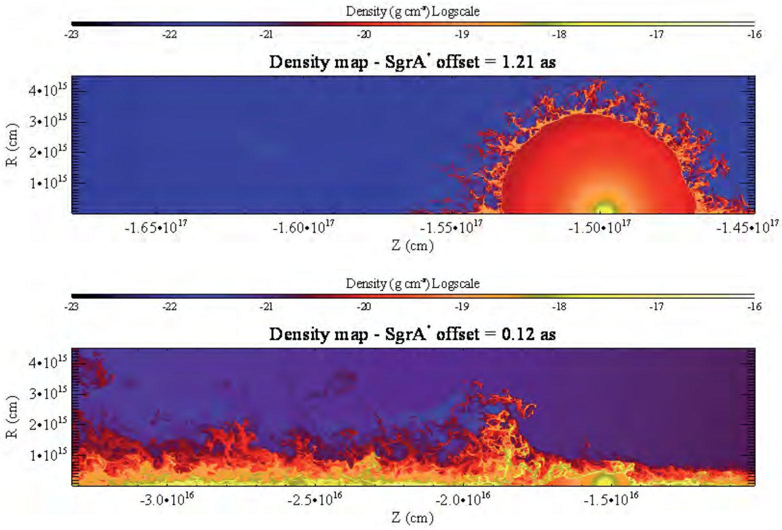

The interaction with the dense and hot atmosphere around SgrA* strongly affects the structure of the winds: a free-wind region with uniform velocity and density $\propto 1/r^2$ is surrounded by a thin, dense and Rayleigh-Taylor unstable shell of shocked wind material. The density maps show that, approaching SgrA*, the ambient ram pressure forms a long tail of stripped material which mixes with the atmosphere. The tidal force is also strongly stretching the wind material in the direction of the motion.

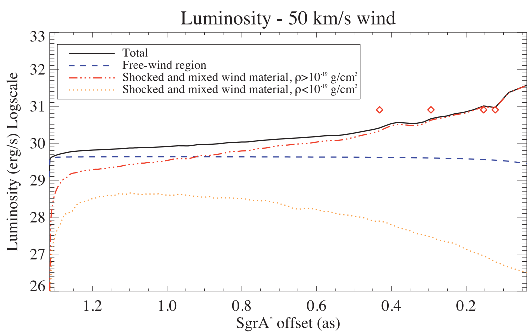

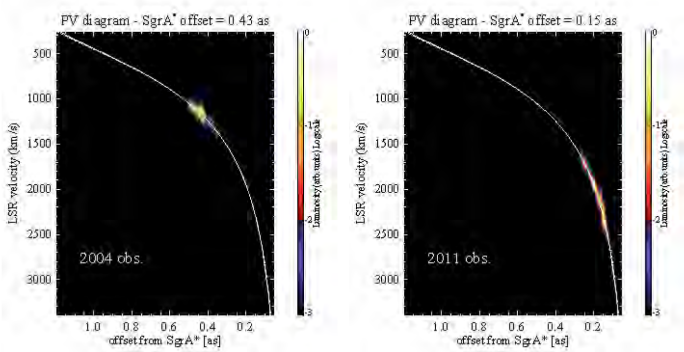

A combination of total luminosity and size can constrain the wind parameters. Here we show a comparison for our best model. The red diamonds in the plot on the left mark the observed Brγ luminosity. Significantly, most of the luminosity of the object comes from the densest shocked wind material, as shown by the red curve on the left. In the position-velocity diagrams on the right, the white line tracks the G2 orbit and the green crosses fix the observed G2 size in this space.

References:
• Gillessen, Genzel, Fritz, Quataert, Alig, Burkert, Cuadra, Eisenhauer, Pfuhl, Dodds-Eden, Gammie, Ott, 2012 Nature, 481, 51
• Gillessen, Genzel, Fritz, Eisenhauer, Pfuhl, Ott, Cuadra, Schartmann, Burkert, 2013, ApJ, 763, 78
• Burkert, Schartmann, Alig, Gillessen, Genzel, Fritz, Eisenhauer, 2012, ApJ, 750, 58
• Murray-Clay & Loeb, 2012, Nature Communications, 3, 1049

A. Ballone, M. Schartmann, A. Burkert, S. Gillessen

Hydrodynamical Simulations of the Compact Cloud G2

We perform Hydrodynamical Simulations of the evolution of the recently discovered gas and dust cloud G2, which will reach its peri-centre approach of the SMBH in the Galactic Centre in September 2013. We investigate the possibility of a single compact cloud (CC), which enables us to model the head component found in observations and of a spherical shell (SS) being able to account for both, the head and tail component in the so-called position-velocity diagrams. Depending on the model as well as the characteristics of the hot atmosphere, an increase in central activity can be expected in the coming years.

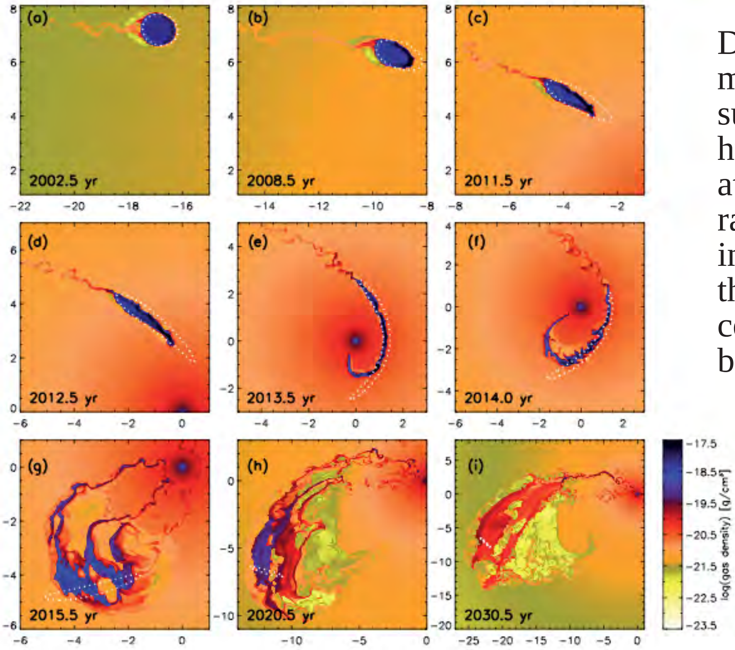

Density distribution of the compact cloud model. The initially spherical cloud suffers from tidal stretching as well as the hydrodynamical interaction with the hot atmosphere close to Sgr A*, mainly by ram pressure and Kelvin-Helmholtz-instability, which leads to disruption of the cloud and feeding of gas towards the centre in a nozzle-like feature. A similar behaviour is found for the spherical ring.

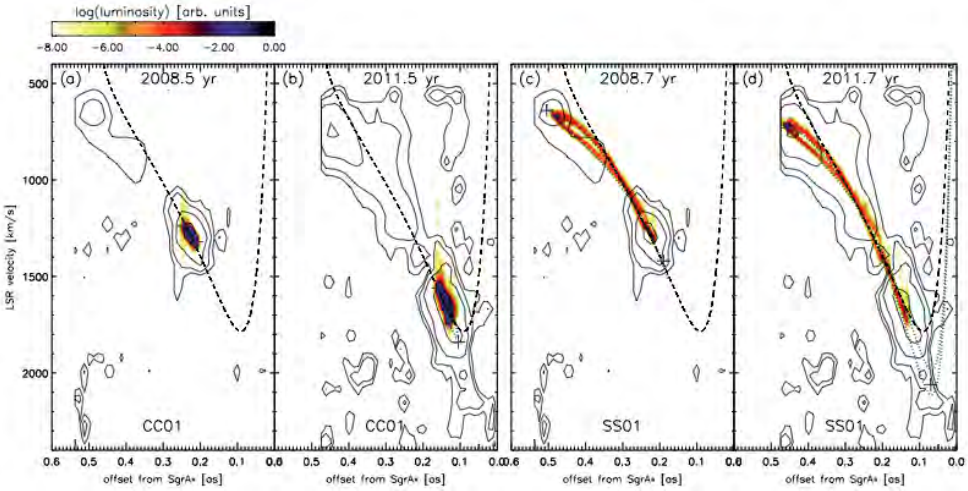

Comparison of hydro models with observations: the CC model (left two panels) is able to explain the evolution of the G2 component itself, whereas the spherical shell is able to describe both, G2 and the extended tail structure.

References:

- Gillessen, Genzel, Fritz, Quataert, Alig, Burkert, Cuadra, Eisenhauer, Pfuhl, Dodds-Eden, Gammie, Ott, 2012 Nature, 481, 51
- Gillessen, Genzel, Fritz, Eisenhauer, Pfuhl, Ott, Cuadra, Schartmann, Burkert, 2013, ApJ, 763, 78
- Burkert, Schartmann, Alig, Gillessen, Genzel, Fritz, Eisenhauer, 2012, ApJ, 750, 58
- Schartmann, Burkert, Alig, Gillessen, Genzel, Eisenhauer, Fritz, 2012, ApJ, 755, 155

M. Schartmann, A. Burkert, Ch. Alig, S. Gillessen,
R. Genzel, T. Fritz, F. Eisenhauer, A. Ballone

Origin of the Galactic Centre stellar discs

We suggest a new formation mechanism for the inclined, sub-parsec scale and counter-rotating stellar discs observed around the central black hole in the Milky Way Galactic Centre. The simulation of a molecular cloud crashing into a circum-nuclear ring of gas leads to the inflow of multiple streams of gas towards the central parsec region. The time delayed arrival of those streams creates multiple accretion discs, with their orbital parameters and their angular momentum depending on the ratio of cloud and circum-nuclear ring material. These accretion discs could be the progenitors which fragmented into the observed stellar discs

Evolution of the surface density in the central 2 pc showing the interaction of a gas cloud with the circum-nuclear ring. The first plot gives a large scale view (10 pc boxsize) of the initial setup. In plot 5 and 9 we present the two high mass accretion discs at peak mass. The last plot shows again a large scale view at the final simulation timestep. During the simulation gas flows from the inner boundary of the circum-nuclear ring towards the central black hole. This gas winds up around the black hole and forms multiple accretion discs.

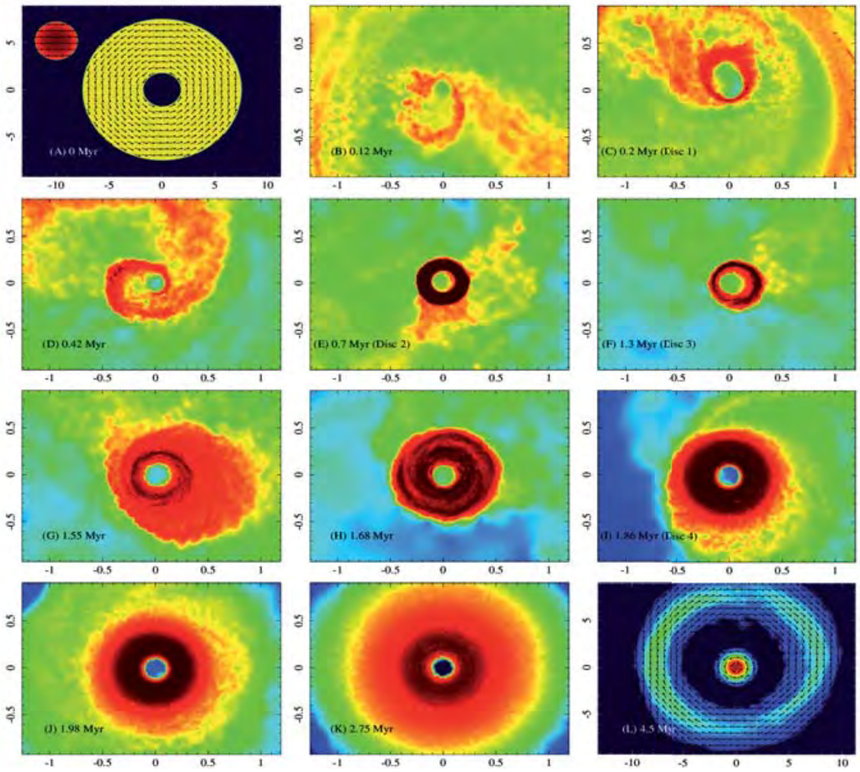

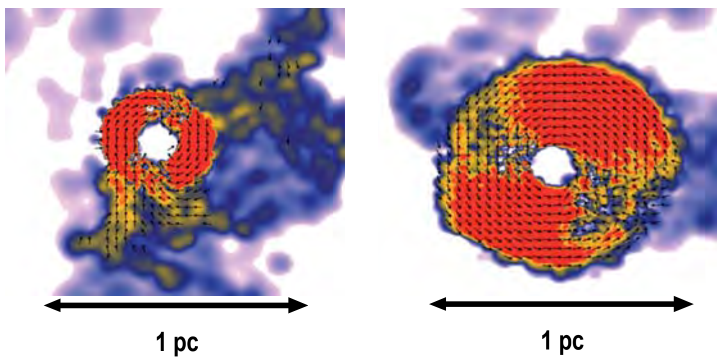

Surface density and velocity field of the two high mass accretion discs forming at 0.7 Myrs and 1.86 Myrs into the simulation. The discs are clearly counter-rotating. Also the discs radii are very similar to the observed stellar discs radii of 0.5 pc.

References:
- Alig, Schartmann, Burkert, Dolag, 2013, Submitted to ApJ
- Alig, Burkert, Johansson, Schartmann, 2011, MNRAS, 412, 469-486
- Montero-Castaño, Herrnstein, Robeson, Ho, ApJ, 695, 1477-1494

C. Alig, M. Schartmann, A. Burkert, K. Dolag

Dynamics of gas and dust clouds in AGN

We analyse the motion of single optically thick clouds in the potential of a central mass under the influence of an anisotropic radiation field $\propto |\cos\theta|$, a model applicable to the inner region of active galactic nuclei. Resulting orbits are analytically soluble for constant cloud column densities. All stable orbits are closed, although they have non-trivial shapes. Furthermore, there exists a stability criterion in the form of a critical inclination, which depends on the luminosity of the central source and the column density of the cloud.

The family of stable orbits features a range of different orbit shapes, depicted on the right. For this set of parameters, the near elliptical orbit (a) is the most circular orbit possible. Both orbits (b) and (d) still show an axis of symmetry related with the position of the typical two maxima of the cloud's distance to the central mass. In contrast to that orbit (c) is completely asymmetric, which is the most prevalent shape.

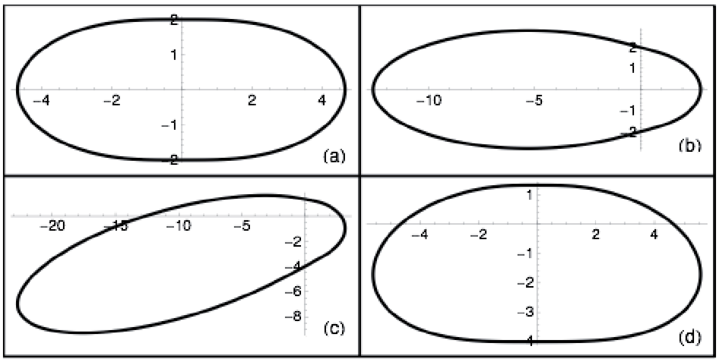

There is a critical orbit inclination above which all orbits are unstable for any particular choice of column density and luminosity.
For example, in a typical Seyfert galaxy with Eddington ratio of 0.1, a cloud with column density $10^{23}\ \mathrm{cm}^{-2}$ is restricted to angles smaller than 10°. If the column density is only greater by a factor of about 6, polar orbits become allowed.

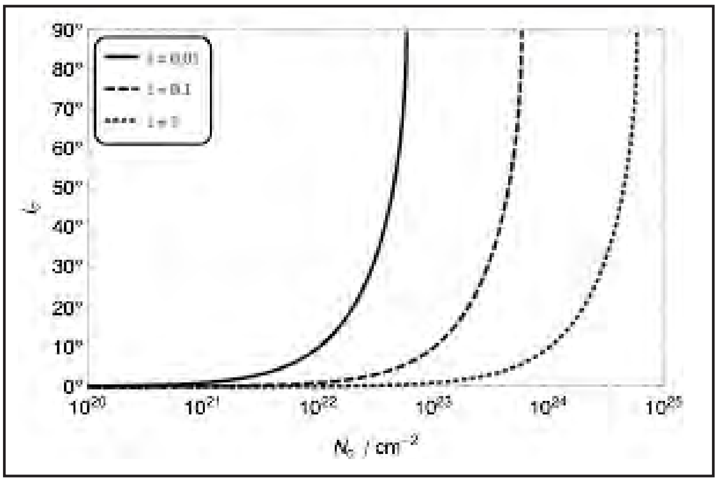

To apply this model to AGN tori (or the BLR), several simplifications are necessary, such as neglecting the intercloud medium (e.g. ram-pressure interaction or an underlying disk) and the related issue of cloud confinement, as well as cloud-cloud interactions (e.g. shadowing of the central light source, secondary radiation pressure from heated dust or collisions and mergers).

However, radiation pressure is still likely to influence the dynamics of clumpy AGN tori significantly. Compared to the derived limit on the inclination of stable cloud orbits, the geometrical thickness of a real torus might be amplified due to an outflow consisting of ejected clouds. When supply for the outflow has ceased, there could still be left a rather thin but long-lived torus.

References:
• Plewa, Schartmann & Burkert, 2013, MNRAS, 431, L127-L130 (and references therein)

P.M. Plewa, M. Schartmann, A. Burkert

The Dark Halo – Spheroid Conspiracy

Dynamical modeling and strong lensing data indicate that the total density profiles of early-type galaxies are close to isothermal, i.e., $\rho_{tot} \sim r^{\gamma}$ with $\gamma \approx -2$. To understand the origin of this universal slope we study a set of simulated spheroids formed in isolated binary mergers as well as the formation within the cosmological framework. The total stellar plus dark matter density profiles can always be described by a power law with an index of $\gamma \approx -2.1$ with a tendency toward steeper slopes for more compact, lower-mass ellipticals. In the binary mergers the amount of gas involved in the merger determines the precise steepness of the slope. This agrees with results from the cosmological simulations where ellipticals with steeper slopes have a higher fraction of stars formed in situ. Each gas-poor merger event evolves the slope toward $\gamma \sim -2$, once this slope is reached further merger events do not change it anymore. All our ellipticals have flat intrinsic combined stellar and dark matter velocity dispersion profiles. We conclude that flat velocity dispersion profiles and total density distributions with a slope of $\gamma \sim -2$ for the combined system of stars and dark matter act as a natural attractor. The variety of complex formation histories as present in cosmological simulations, including major as well as minor merger events, is essential to generate the full range of observed density slopes seen for present-day elliptical galaxies.

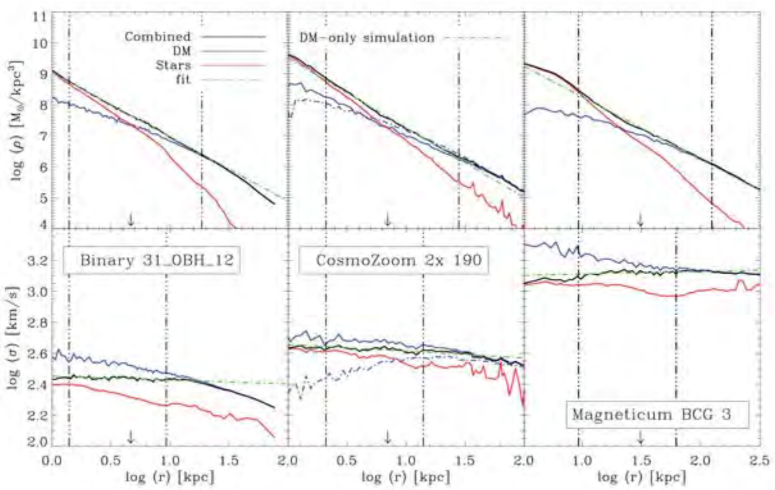

Density (upper panel) and velocity dispersion (lower panel) profiles for a 3:1 Binary merger elliptical (left), a cosmological zoom-in elliptical (center) and a BCG (right). Red lines: stellar component; blue solid lines: dark matter component; black lines: combined profiles. Green line: power law fit to the combined profile. Dashed black lines: 1Reff, 2Reff and 4Reff. Blue dashed line: dark matter only simulation.

Slopes of the stellar velocity dispersion β against the slopes of the total density profiles γ: Binary merger ellipticals (blue cirlces), cosmological zoom-in ellipticals (blue cirlces), Magneticum BCGs (yellow circles) as well as observations (Coma ellipticals, Thomas et al 2007, open stars; Lensing elliptical, Sonnenfeld et al 2012, filled star)

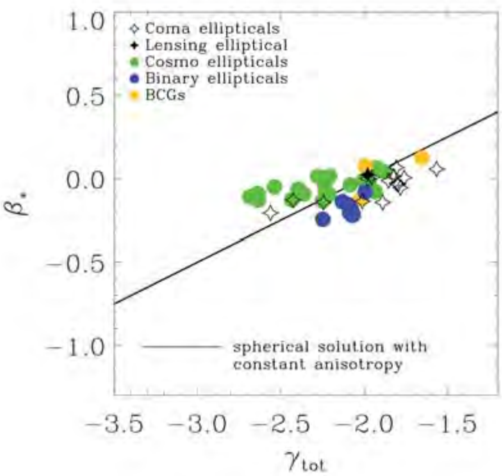

References:

- Remus, Burkert, Dolag, Johansson, Naab, Oser, Thomas, 2013, ApJ, 766, 71
- Johansson, Burkert, Naab, 2009, ApJ, 707, L184
- Oser, Ostriker, Naab, Johansson, Burkert, 2010, ApJ, 725, 3212
- Sonnenfeld, Treu, Gavazzi, Marshall, Auger, Suyu, Koopmans, Bolton, 2012, ApJ 752 163
- Thomas,Saglia, Bender, Thomas,Gebhardt, Magorrian, Corsini,Wegner, 2007, MNRAS, 382, 657

R.-S. Remus, A. Burkert, K. Dolag, P. H. Johansson, T. Naab, L. Oser, J. Thomas

Origin and Properties of Clumps in z=2 Disk Galaxies

We perform high resolution hydrodynamical simulations of gas-rich disks to get a better understanding of the origin and peculiar properties of the dominating structures in z=2 massive disk galaxies. Their structure is irregular, they have highly turbulent motions and high gas fractions of 30-80%. Stars form with enormous rates of a factor of 10-100 higher than in the Milky Way. The star formation is concentrated in a few gigantic clumps of molecular gas, about 1000 times larger than present day molecular clouds. In our simulations, we follow the fragmentation process induced by gravitational instabilities from the beginning and the evolution up to a few orbital times. We show that gravitationally bound, highly substructured clumps can grow from mergers of smaller structures, which can explain the substructure, indicated in some observations. A revised 'Toomre' criterion for thick disks is developed that can describe the early fragmentation process precisely and enables us to predict random motions and clump sizes in good agreement with our simulations as well as observational data.

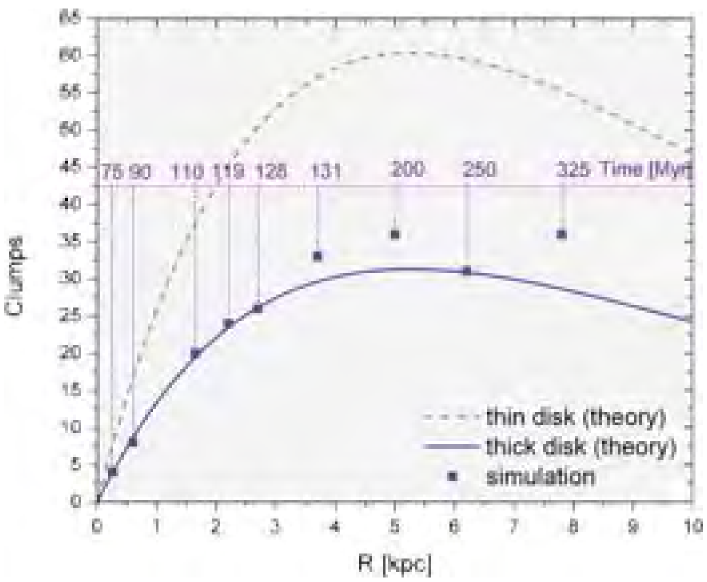

The perturbations grow in the centre first where the dynamical time is the shortest and spread outwards with time. Ring-like density perturbations break into several clumps, which can be predicted very precisely by our theory. We find that neglecting the thickness of the disk, one would overestimate the number of clumps by a factor of two.

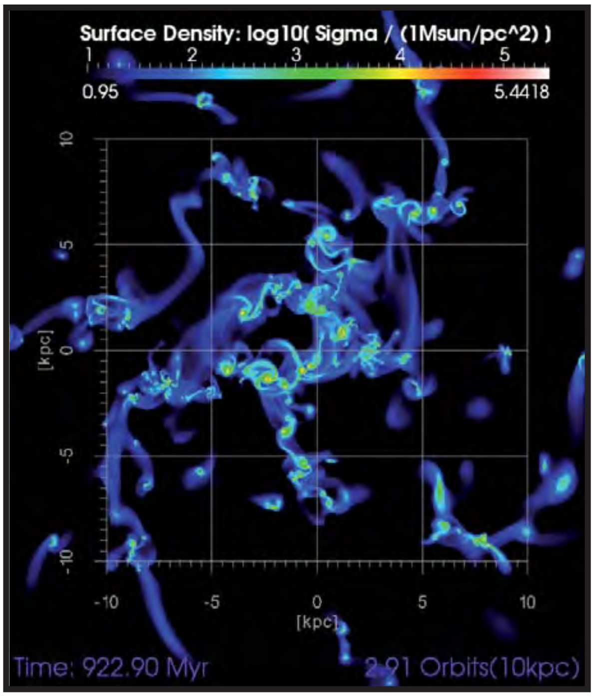

The disk runs through different phases from smaller objects merging into larger ones with masses and sizes comparable to the observations. This requires that small clumps live longer than typical clump merger timescales, indicating inefficient star formation in low-mass clumps.

References:
- Ceverino et al., 2012, MNRAS, 420,3490–3520
- Genzel R. et al., 2011, ApJ, 733, 101
- Toomre, A. 1964, ApJ, 139, 1217

M. Behrendt, A. Burkert, M. Schartmann

Front Cover:

Time series of position-velocity-diagrams of the Brackett-gamma line emission from the recently discovered gas cloud G2 falling toward the Sgr A*, the massive black hole in the Galactic Center. The diagram is a composite using seven epochs of adaptive optics based, near-infrared integral field spectroscopy obtained at the VLT with SINFONI. G2 approaches the pericenter of its orbit during these years. The time of closest approach is predicted for late 2013. While the radial velocity steadily increases, the cloud is tidally torn apart, developing a shear visible as continuously increasing velocity width.

For datails see the poster at page 24.